# SAP2017


13th Symposium on Accelerator Physics — Jishou, Hunan Province, China

第十三届加速器物理学术交流会

湖南·吉首 2017.8.28-30

ISBN: 978-3-95450-199-1

# Contents

ISBN: 978-3-95450-199-1

ISBN: 978-3-95450-199-1

# SAP2017 Committees

## Chairmen

Qin, Qing (IHEP,CAS)
Huang, Wenhui (TUB)
Yan, Xueqing (PKU)

## Scientific Programme Committee

Tang, ChuanXiang (TUB), Chair
Li, Weimin (USTC)
Wang, Dong (SINAP, CAS)
Zhang, Tianjue (CIAE)
An, Shizhong (CIAE)
Luo, Gwo-huei (NSRRC)
Long, Jidong (CAEP)
Liu, Kexin (PKU)
Su, Ping (IHEP, CAS)
Shen, Baifei (SIOM, CAS)
Li, Yutong (IPHY CAS)
Lu, Wei (TUB)
Xu, Gang (IHEP,CAS)
Fan, Kuanjin (HUST)
Sheng, Zhengming (SJTU)

## Local Organization Committee

Ma, Yanyun (NUDT), Chair
Zhou, Huawen (NUDT)
Fan, Xue (TUB)
Zhou, Jie (IHEP, CAS)
Zhao, Ning (IHEP, CAS)
Ji, Daheng (IHEP, CAS)
Zhuo, Hongbin (NUDT)
Yang, Xiaohu (NUDT)

## Editorial Team

Ning Zhao (IHEP)
Daheng Ji (IHEP)
Lu Li (IMP)
Volker RW Schaa (GSI)

ISBN: 978-3-95450-199-1 doi:10.18429/JACoW-SAP2017-MOBH1

# EXPERIMENTAL STUDY ON THE ELECTRON SUPERCONDUCTING LINAC AND ITS APPLICATION*

Kexin Liu†, Shengwen Quan, Jiankui Hao, Senlin Huang, Lin Lin,
Liwen Feng, Fang Wang, Feng Zhu, Huamu Xie, Limin Yang, Jia-er Chen
Institute of Heavy Ion Physics & State Key Laboratory of Nuclear Physics and Technology
Physics and Technology, Peking University, Beijing, China

*Abstract*

Experimental study on superconducting electron linac has been developed at Peking University. Stable operation of a DC-SRF photoinjector and a 2×9-cell SRF linac has been realized with an average beam current of mA scale in macro pulses of several ms with a repetition rate of 10 Hz. A compact high repetition rate THz radiation source has been developed based on DC-SRF photo-injector through velocity bunching. Superradiant THz radiation with a repetition rate of 16.25 MHz and a frequency that can be tuned from 0.24 to 0.42 THz was generated by varying the electron beam energy from 2.4 to 3.1 MeV. MeV UED at MHz repetition rate has been demonstrated experimentally using electron pulses from the DC-SRF photoinjector. THz undulator radiation of ~1 THz central frequency with an average power of 1 W has been achieved with 13 MeV electron beam from SRF linac and applications are underway.

## INTRODUCTION

To obtain electron beams with high average current and low emittance, superconducting radiofrequency (SRF) photocathode guns, which combine the high brightness of normal conducting RF photocathode guns with the advantage of CW operation of superconducting RF cavities, have been developed in many laboratories worldwide [1, 2].

DC-SRF photoinjector, which combines a DC Pierce gun and a superconducting cavity, was first proposed by Peking University in 2001 [3] and demonstrated with a 1.5-cell TESLA type superconducting cavity in 2004 [4]. An upgraded DC-SRF injector with a 3.5-cell large grain niobium cavity was then designed and constructed [5]. Electron beam with a current of mA level has been obtained at long-term stable operation. At the same time, a 1.3 GHz superconducting linac containing two 9-cell cavities was designed, setup and commissioned. Electron beam of 8-25 MeV was obtained by combination of the DC-SRF photoinjector and SRF linac.

Some applications with superconducting electron linac have been carried out at Peking University. Based on the DC-SRF photoinjector, a compact THz radiation source through velocity bunching was constructed to generate THz pulses with a high repletion rate. MeV ultrafast electron diffraction (UED) at MHz repetition rate has been demonstrated experimentally using electron pulses from the DC-SRF photoinjector. With 13 MeV electron beam from SRF linac, THz undulator radiation are generated and an average power of 1 W in macro pulse has been achieved.

In this paper, the experimental studies on DC-SRF photoinjector and superconducting linac, the applications with electron beam from superconducting injector and linac are reported.

## STUDY ON DC-SRF PHOTOINJECTOR

### *DC-SRF Photoinjector*

Figure 1 shows the schematic view of the upgraded DC-SRF photoinjector, which consists of the DC pierce gun, 3.5-cell SRF cavity, helium vessel, liquid nitrogen shield, input power coupler, tuner and auxiliary systems.

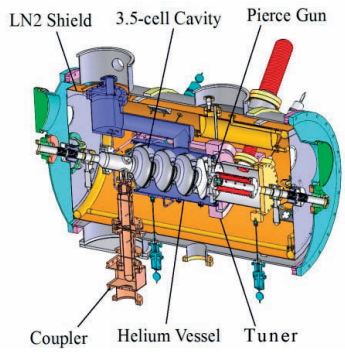


Figure 1: Schematic view of the DC-SRF photoinjector.

The designed DC voltage of Pierce gun is 90 kV. The surface electric field on the cathode is almost 5 MV/m and the peak electric field is lower than 13 MV/m. The 3.5-cell large grain niobium superconducting cavity comprises three TESLA type cells and a special designed half-cell. The accelerating gradient of the cavity reaches 23.5 MV/m and the intrinsic quality factor $Q_0$ is higher than $1.2\times10^{10}$ in vertical test [5]. The input power coupler adopts compact capacitive coupling structure [6].

$Cs_2Te$ photocathode is used for DC-SRF injector. The upgraded drive laser system composes of a Time-Bandwidth GE-100 XHP seed laser, amplifier, second harmonic generator, fourth harmonic generator and optical beam line to transport the UV pulses to the photocathode. The repetition rate of laser pulses is 81.25 MHz. The drive laser system can provide 1 W power in a train of 6 ps UV (266 nm) pulses with 5% power instability. The deposition of photocathode is accomplished in the vacuum of about $1.2\times10^{-8}$ mbar. The $Cs_2Te$ cathode is activated again with cesium just before

*Work supported by National Key Programme for S&T Research and Development (Grant NO.:2016YFA0401904)
† kxliu@pku.edu.cn

ISBN: 978-3-95450-199-1 doi:10.18429/JACoW-SAP2017-MOBH1



transferring it into the cryomodule. Quantum efficiency (QE) and life time of the cathode have been improved obviously after reactivation. The QE was more than 10% at the beginning and then stabilized at about 4% for more than 10 days. After one more week, the photocathode was illuminated again by drive laser and the QE was still 2% and lasted for a long time.

In order to stabilize the accelerating field of the 3.5-cell SRF cavity, a digital LLRF control system was designed. By comparing the pick-up signal with the set point, the PI controller in FPGA can adjust output signal to compensate the deviation, thus maintain stable field in the cavity [7]. To allow pulse operation, gate signal has been added to the feedback loop and the control algorithm has been modified to handle Lorentz force detuning.

A diagnostic beam line is designed and constructed, as shown in Fig. 2. Two solenoid lenses, a quadrupole magnet and a dipole magnet are adopted for beam focusing and deflecting. The first solenoid lens is installed as close as possible to the cryomodule for emittance compensation. The dipole magnet is used to deflect the electron beam to a Faraday cup with water cooling as dump. Beam diagnostic devices including YAG screen, Faraday cups and a beam emittance meter are installed in beam line.

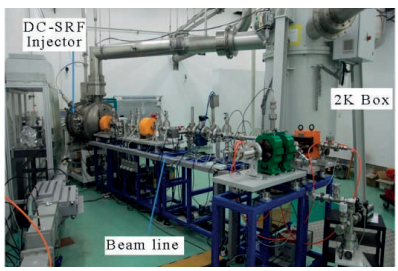


Figure 2: Beam line of the 3.5-cell DC-SRF injector.

## *RF and Beam Experiments*

The $E_{acc}$ of 3.5-cell cavity reached 14.5 MV/m in CW mode and 17.5 MV/m in pulsed mode with a duty factor of 10% and a repetition rate of 10 Hz. The amplitude (up) and phase (below) signals of 3.5-cell DC-SRF injector without beam load is shown in Fig. 3. The instability is less than 0.1% for amplitude and 0.1 degree for RF phase.

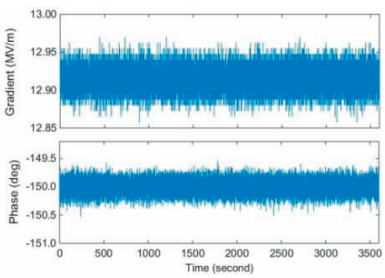


Figure 3: Long-term running of LLRF control system.

The beam experiments were carried out at $E_{acc}$ of 8.5 MV/m for stable operation and at a low average current in order to avoid electron beam bombarding the beam tube. We reduced the duty factor of drive laser instead of the laser pulse energy to keep the same bunch charge for different average current. The average beam current was about 2.5 μA when the duty factor of the drive laser was 1% at a repetition rate of 10 Hz. The duty factor was then increased to 100% gradually and the average current increased to 250 μA at CW mode operation. The beam current was increased further by increasing laser power, but the degassing of the dump Faraday cup became serious. Pulsed mode was applied for long term beam test to protect the superconducting cavity. The duty factor of RF power was 7% with a repetition rate of 10 Hz. The average beam current in a macro pulse reached 1 mA and was kept at 0.55 mA for long term operation.

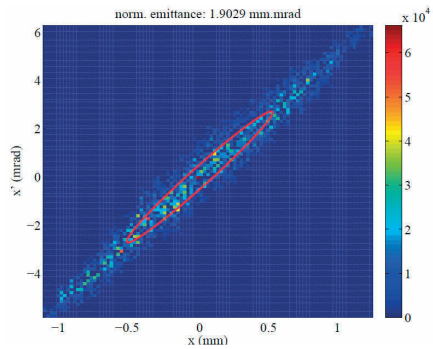


Figure 4: measured emittance of electron beam.

The kinetic energy of electron beam of 3.4 MeV was measured with the bending magnet. This was consistent with the value derived from the accelerating gradient. The measured normalized emittance was about 1.9 mm·mrad, see Fig. 4. More simulation work is underway to reduce the emittance of the DC-SRF photoinjector.

# APPLICATIONS OF DC-SRF PHOTOINJECTOR

## *Superradiant THz Undulator Radiation*

Based on the DC-SRF photoinjector, we constructed a compact THz radiation source through velocity bunching to generate THz pulses with a high repetition rate, see Fig. 5. A solenoid, following the DC-SRF photo-injector, is used to focus the electron beam and compensate emittance growth. A 10-period planar undulator is installed 6.0 m downstream of the photocathode. Velocity bunching [8, 9] by the rf field of the superconducting cavity is applied to compress electron bunches. Between the solenoid and the undulator are only several pairs of steering coils. A dipole magnet is placed after the undulator to bend the electron beam to a dump.

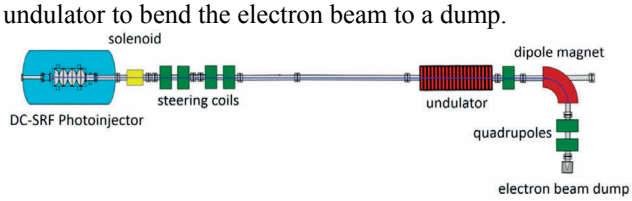


Figure 5: Layout of the compact THz system at PKU.

The simulated longitudinal distribution of electrons was obtained using the tracking code ASTRA. In the simulation, the space charge effect was taken into account

ISBN: 978-3-95450-199-1 doi:10.18429/JACoW-SAP2017-MOBH1

and the wake field effect was not implemented due to the low beam peak current. The electron beam parameters used for the simulation, as well as the undulator parameters, are listed in Table 1. To determine the maximum THz radiation power, we investigated electron distribution at the undulator entrance in the longitudinal phase space under different rf phases of 0° to −40°. Here, 0° is defined as the on-crest acceleration phase. For each phase, the solenoid magnetic field was adjusted to focus the electron beam to form a waist at the undulator center. The longitudinal position of the electrons was derived from the ASTRA output, and the coherent enhancement factor $F_{ce}$ was obtained. A maximum coherent enhancement factor of $4.3\times10^6$ was obtained at an acceleration phase of −24°. The corresponding electron distribution in the longitudinal phase space and the current profile of the electron bunches are shown in Fig. 6. This asymmetric current profile with a sharp peak in the tail confers high $F_{ce}$ because some electrons are squeezed into a very narrow region.

Table 1: Operation Parameters of DC-SRF Photo Injector

| Parameter | Value |
|---|---|
| **Electron beam at photocathode** | |
| Beam size (rms) | 1.0 mm |
| Bunch length (FWHM) | 5 ps |
| Repetition rate | 16.25 MHz |
| Bunch charge | 25 pC |
| **Undulator** | |
| Number of Periods | 10 |
| Period length $\lambda_u$ | 27 mm |
| **rms strength parameter $a_u$** | **1** |

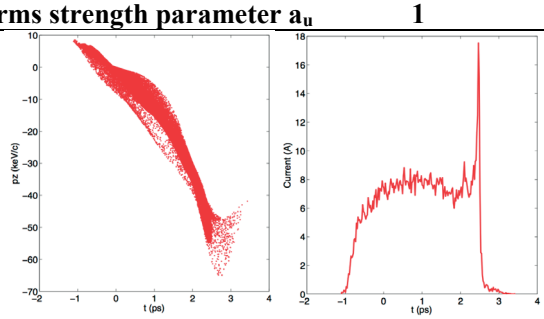


Figure 6: Electron distribution in the longitudinal phase space (left) and the current profile of electron bunches (right) at the undulator entrance when the rf phase is −24°.

The calculated maximum power of the superradiant THz radiation from the undulator is ~1 W. The maximum THz power obtained at the exit of the dipole magnet chamber is 5.7 mW if the propagation loss is considered.

Figure 7 shows the experimental setup for THz radiation power and spectrum measurement, which is composed of two off-axis parabolic reflecting mirrors, two identical z-cut quartz windows with a transparency of 70% each, a Fourier transform far-infrared spectrometer (FTS) for spectrum measurement, and a Golay cell detector for radiation power measurement. An attenuator is installed before the Golay cell to avoid saturation. THz radiation is transported in vacuum (100 Pa) to reduce THz absorption by water vapor and CO2.

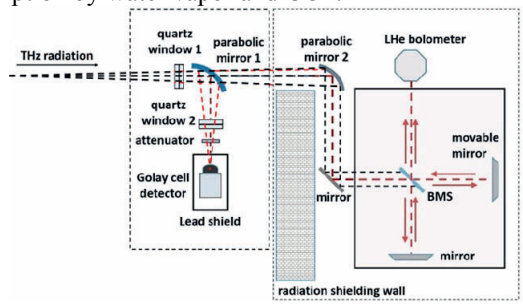


Figure 7: Schematic of the THz measurement system.

The production and measurement of THz is straight forward. The photoinjector was operated in macro pulse mode for safe operation. The macro pulse repetition rate is 7 Hz, and the duty factor is 2.8%. Accelerating gradients were varied to generate THz radiation with different central wavelengths. For each accelerating gradient, the solenoid and steering coils were optimized to ensure effective electron beam transport in the vacuum chamber of the undulator. The accelerating phase was also adjusted to obtain the maximum THz radiation power.

The measured THz radiation spectra are shown in Fig. 8. The central frequency ranges from 0.24 THz to 0.42 THz when electron beam energy varies from 2.4 to 3.1 MeV, and the FWHM bandwidth is approximately 0.05 THz. Electron beam transport is more difficult at electron beam energy lower than 2.4 MeV.

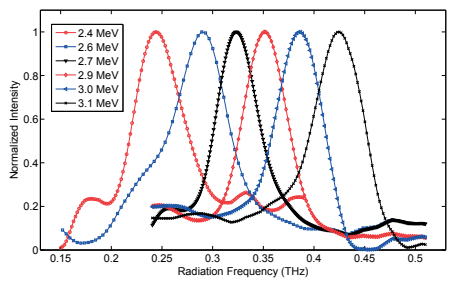


Figure 8: Measured THz spectra with different electron beam energies.

THz radiation power was measured at different rf phases of the SRF cavity with an interval of 5°. Fig. 9 shows the measured THz radiation power and the calculated results, wherein propagation losses were considered. The power at mW level in macro pulses was obtained at about −25°. The figure shows good agreement between calculation and experimental measurements.

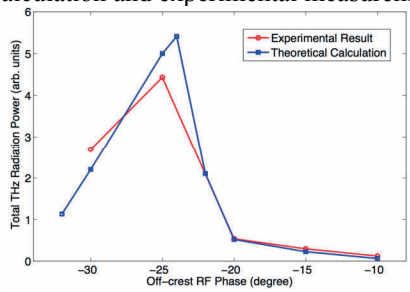


Figure 9: Measured and calculated THz power at different rf phases.

ISBN: 978-3-95450-199-1 doi:10.18429/JACoW-SAP2017-MOBH1



The total superradiant radiation power is evaluated to be about 5.65 mW, which comprises 4.76 mW (84%) fundamental radiation and 0.89 mW (16%) higher-order harmonic radiation. The fundamental radiation contributes more than 80% to the measured mW level THz radiation power.

### *MHz MeV UED*

The first MeV UED that operates at the MHz repetition rate regime was carried with electron beams from DC-SRF photoinjector. The layout of the MHz MeV UED proof-of-principle experiment is shown in Fig. 10.

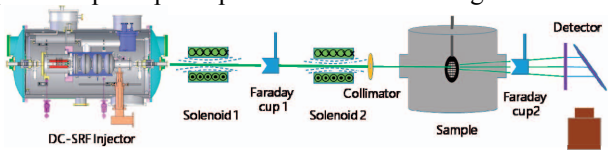


Figure 10: Schematic layout of the MeV MHz UED beam line.

The MHz MeV pulsed electron beam is produced with DC-SRF photoinjector. The repetition rate of the electron beam can be varied from 162.5 kHz up to 81.25 MHz and the average beam current can be varied from about 1 nA up to 1 mA by changing the laser power and laser repetition rate. The electron pulse length is expected to be about 5 ps (FWHM), which is limited by the pulse length of the photocathode drive laser. By running the electron beam at off-crest phase in the superconducting rf cavities, the electron pulse can be significantly shorter than the laser pulse due to velocity bunching.

After exiting the injector, the beam is focused by a solenoid to maintain a reasonable beam size during the transportation to the UED beam line. Then a second solenoid is used to minimize the beam size at the phosphor screen to maximize the contrast of the diffraction pattern. A collimator with 2 mm diameter is put upstream of the sample chamber to remove beam halo that would otherwise contribute to a large background to the diffraction pattern. Both single crystalline Au and polycrystalline Al samples were used in the experiments, which were mounted on a motorized stage in the sample chamber. The detector was composed of a phosphor screen, located at 2.6 m downstream of the sample, a 45° mirror, and a high-efficiency CCD camera. The average beam current at the exit of the photoinjector and at the exit of the sample can be measured with Faraday cups.

Figure 11 shows the measured diffraction patterns for a 20 nm thick single-crystal Au foil and a polycrystalline Al foil. The diffraction pattern was obtained by integrating the signal over 200 ms when the beam repetition rate is 812.5 kHz. The total beam charge (after the sample) for Fig. 11 is measured to be about 33 pC, corresponding to about 0.2 fC per pulse. To protect the phosphor screen and the sample, we intentionally lowered the drive laser energy and repetition rate to reduce the number of electrons passing through the sample.

The projection of the diffraction spots taken along the line indicated in Fig. 11a is shown in Fig. 11c. All spots including the direct beam have approximately the same width which is found to be about 0.1 $A^{-1}$ (FWHM), implying good spatial coherence of the beam. To quantify the spatial coherence of the beam, we compared the sharpness of the diffraction spots with that calculated from multi-slit interference [10, 11] where the half angle spread is related to the beam transverse coherence as $\Delta\theta=\lambda/Nd$, where $N$ is the number of slits in the coherently illuminated area and $d$ is the distance of the slits. With the spot width being about 0.7 mm (FWHM), the spatial coherence of the beam is estimated to be about 1.5 nm. With the diffraction angle being $\theta=\lambda(k^2+l^2+m^2)^{1/2}/a_0$, where $\lambda$ is the De Broglie wavelength, $k$, $l$, $m$ are the Miller indices and $a_0$ is the lattice constant, the electron De Broglie wavelength is determined to be about 0.42 pm and the corresponding beam energy is quantified to be about 3.0 MeV, in good agreement with that measured with an energy spectrometer.

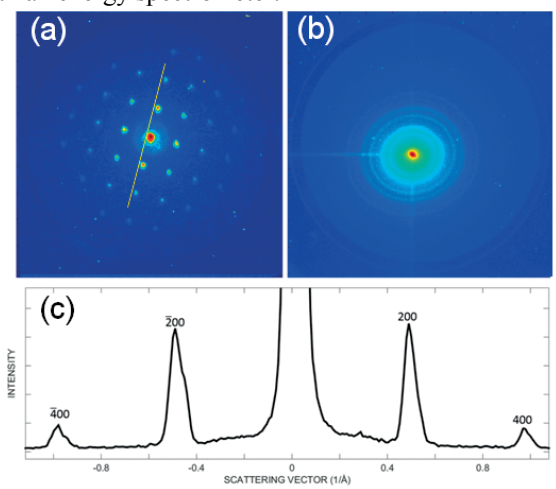


Figure 11: Measured electron diffraction patterns from a single-crystalline Au foil (a) and a polycrystalline Al foil (b) taken at 812.5 kHz repetition rate with an integration time of 200 ms; (c) Intensity projections along the (200) and (400) spots in (a).

## STUDY AND APPLICATION OF 2×9-CELL SRF LINAC

### *Commissioning of 2×9-cell SRF Linac*

To improve the energy of electron beam, a main SRF linac is designed and constructed, which contains two 9-cell TESLA cavities, input power couplers, frequency tuners, helium vessel, liquid nitrogen shield, magnetic shield and its associated auxiliary systems. Fig. 12 gives the sectional view of the 2×9-cell linac.

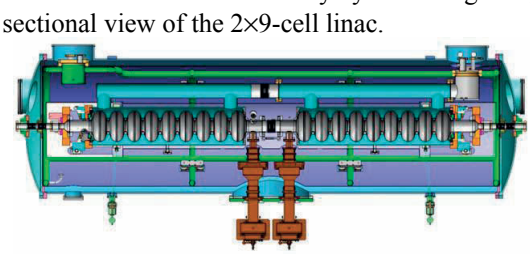

Figure 12: The sectional view of 2×9-cell SRF linac.

ISBN: 978-3-95450-199-1 doi:10.18429/JACoW-SAP2017-MOBH1

Both 9-cell cavities (PKU2 and PKU4) are made from Ningxia large grain niobium material and fabricated by PKU. The accelerating gradients in vertical test are 22.4 MV/m for PKU2 and 32.6 MV/m for PKU4. Quality factor of both cavities are higher than $1\times10^{10}$ at the quench gradients.

An improved LLRF system was designed and setup for SRF linac. A compact LO/Digital clock generation board using commercial PLL ICs was developed. A Digital Phase Lock Loop (DPLL) based reference racking algorithm was developed to cancel the LO/Digital clock noise. Stability of the upgraded LLRF system is 0.01% for amplitude and 0.02° for phase.

Commissioning of SRF linac was finished in Oct. 2015. Due to the capacity limit of the cryogenic system, the SRF linac can only run at long macro pulse mode. The accelerating gradient of both cavities in horizontal test are ~20 MV/m. Electron beam loading test was carried out by combination of DC-SRF photoinjector and SRF linac. An average current of ~1 mA was obtained with macro pulse duration of 5 ms and duty factor of 5%.

### *THz Undulator Radiation with SRF Linac*

Based on the stable operation of DC-SRF photo-injector and SRF linac, THz undulator radiation experiments are carried out with high repetition rate ~15 MeV electron beam. The layout of the THz system is shown in Fig. 13. A Chicane structure is installed after the SRF linac for further electron bunch compression. An upgraded 10-period undulator with tuneable gap is installed downstream of the Chicane. FTS and Golay cell detector are used for spectrum and radiation power measurements.

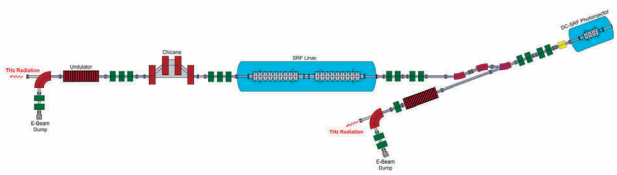

Figure 13: Layout of the compact THz system at PKU.

The coherent enhancement factor $F_{ce}$ was obtained with the longitudinal position of the electrons derived from the ASTRA output. Coherent enhancement factor is $2\times10^{7}$ at 350 μm central wavelength with electron beam of 14 MeV energy, 450 μA average current and 27 MHz repetition rate, when the undulator gap is 10 mm.

The measured THz radiation spectra with different electron beam energies and undulator gaps are shown in Fig. 14. The central frequency ranges from 0.83 THz to 1.02 THz with fixed gap of 10 cm when the electron beam energy varies from 11.4 MeV to 12.6 MeV. With fixed electron beam energy of 11.4 MeV, the central frequency changes from 0.92 THz to 1.28 THz when the gap varies from 10 mm to 12 mm. The FWHM bandwidth is approximately 0.1 THz.

THz radiation power was measured at macro pulse length of 2 ms, duty cycle of 1% and macro pulse length of 7 ms, duty cycle of 3.5%, see Fig. 15. The average power in macro pulse is 1.2 W and 1.1 W. Applications with watt scale, high repetition rate THz radiation are carried out.

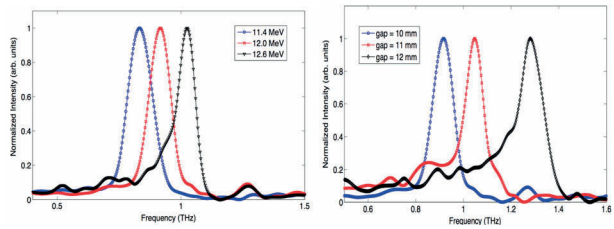


(a) (b)

Figure 14: Measured THz spectra with different electron beam energies (a) and undulator gaps (b).

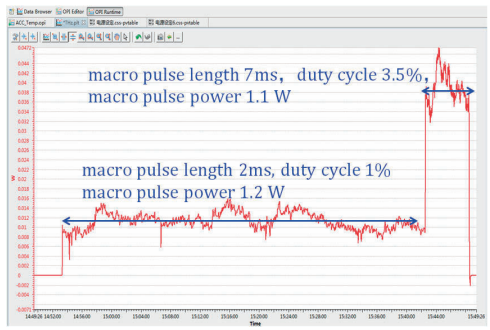


Figure 15: Measured THz power at different macro pulse.

## CONCLUSIONS

Stable operation of the DC-SRF photoinjector and 2×9-cell SRF linac has been realized based on a series of improvements of drive laser, photocathode preparation, LLRF control system and diagnostic devices. Electron beam with energy of 8-25 MeV can be obtained with superconducting linac. The average beam current in macro pulses reached ~1 mA and was kept for long term operation at ~0.5 mA with the RF duty cycle up to 7% and repetition rate of 10 Hz. A series of applications have been carried with high repletion rate electron beam. A compact MHz repetition rate THz source was developed based on the DC-SRF photo-injector through velocity bunching. An average THz radiation power of mW level within macro pulses was experimentally detected, which is consistent with the calculation results considering the current low propagation efficiency of about $5.7\times10^{-3}$. MeV electron diffraction at MHz repetition rate has been demonstrated experimentally using electron pulses from a superconducting rf photoinjector, which shows the potential of high repetition rate pulses from the DC-SRF photoinjector for applications in UED. After improving the electron beam bunch energy to ~13 MeV with SRF linac and compressed with a Chicane structure, THz undulator radiation with an average power of 1 W has been achieved with gap-tuneable undulator. More applications with high repetition rate THz radiation are underway.

ISBN: 978-3-95450-199-1 doi:10.18429/JACoW-SAP2017-MOBH1



## REFERENCES

[1] A. Arnold and J. Teichert, *Phys. Rev. ST Accel. Beams*, vol. 14 (2011), p. 024801.

[2] S. Belomestnykh, in *proc. FEL13*, New York, NY USA, 2013, p. 176.

[3] K. Zhao *et al*., *Nucl. Instr. and Meth. A*, vol. 475 (2001), p. 564.

[4] J. Hao *et al*., *Nucl. Instr. and Meth. A*, vol. 557 (2006) 138.

[5] Shengwen Quan, Feng Zhu, Jiankui Hao *et al*., *Phys. Rev. ST Accel. Beams*, vol. 13 (2010), p. 042001.

[6] He Fei-Si, Hao Jian-Kui, Zhang Bao-Cheng, Zhao Kui, *Chinese Physics C*, vol. 32 (2008), p. 584.

[7] H. Zhang, J.-K. Hao, Lin Lin, K.X. Liu, F. Wang, B.C.Zhang, in *Proc. IPAC2011*, San Sebastián, Spain, 2011, p. 304.

[8] S.G. Anderson, P. Musumeci *et al*., *Phys. Rev. ST Accel. Beams*, vol. 8 (2005), p. 014401.

[9] L. Serafini, M. Ferrario, in: S. Chattopadhyay *et al*. (Eds.), in *Proc. the AIP Conference* 581, *19th Advanced ICFA Beam Dynamics Workshop*, AIP, vol. 87, 2001.

[10] F. Kirchner, S. Lahme, F. Krausz and P Baum, *New J. Phys.*, vol. 15, p. 063021 (2013).

[11] M. Born and E. Wolf, "Principles of Optics: Electromagnetic Theory of Propagation, Interference and Diffraction of Light" (Oxford: Pergamon).

ISBN: 978-3-95450-199-1 doi:10.18429/JACoW-SAP2017-MOBH2

# STATUS OF HEPS LATTICE DESIGN AND PHYSICS STUDIES*

Y. Jiao†, X.H. Cui, Z. Duan, Y.Y. Guo, D.H. Ji, J.Y. Li, X.Y. Li, Y.M. Peng, Q. Qin,
S.K. Tian, J.Q. Wang, N. Wang, Y.Y. Wei, G. Xu, H.S. Xu, F. Yan, C.H. Yu, Y.L. Zhao
Key Laboratory of Particle Acceleration Physics and Technology, IHEP, CAS, Beijing, China

*Abstract*

The High Energy Photon Source (HEPS) is a 6-GeV, kilometer-scale, ultralow-emittance storage ring light source to be built in Beijing, China. The HEPS is now under extensive design and study. In this report we will introduce the status of the HEPS lattice design and physics studies, including storage ring design, booster design, injection design, collective effects, error study, insertion device effects, longitudinal dynamics, etc.

## INTRODUCTION

The High Energy Photon Source (HEPS) is a 6-GeV, kilometer-scale, ultralow-emittance storage ring light source to be built in the Huairou District, northeast suburb of Beijing, and now is under extensive design.

As the R&D project for HEPS, the HEPS test facility (HEPS-TF) has started in 2016, and is to be completed by the end of Oct., 2018. The goal of the HEPS-TF project is to develop key hardware techniques that are essentially required for constructing a diffraction-limited storage ring light source, meanwhile, to complete the design for HEPS. One of the goals of the HEPS-TF project is to obtain an 'optimal' lattice design for the HEPS, study the related accelerator physics issues and ensure there is no show-stopper from beam dynamics point of view, and give as detailed parameter list and tolerance budget table as possible for various hardware systems.

This year, we start to prepare the conceptual design report and the feasibility study report of the HEPS project. After iterative discussions, the goal emittance of the HEPS storage ring lattice design is to obtain a natural emittance of below 100 pm.rad, and the ring circumference is fixed to 1360.4 m.

For the sake of the R&D of key hardware techniques and related physics issues, a hybrid-7BA lattice with a natural emittance of ~60 pm.rad and large ring acceptance that promises different candidate injection schemes was proposed (see below for details).

Based on this lattice, we carry out related physics studies for the HEPS, including collective effect study, error effect and lattice calibration simulation, injection system design, injector design, etc. In addition, we also continuously do optimizations to look for lattice with even better performance.

In the following we will briefly introduce the status of the lattice design, and recent progress of studies on the related physics issues.

## LATTICE DESIGN & PHYSICS STUIDES

### *Storage Ring Lattice Design*

After various attempts of ultralow-emittance lattice designs and nonlinear optimizations [1-8], now the hybrid-7BA is chosen to be the basic layout of the HEPS storage ring. The optical function of one 7BA of the present lattice is shown in Fig. 1, and the main parameters of the ring are listed in Table 1.

After systematic optimization of both linear and nonlinear dynamics, as shown in Figs. 2 and 3, the 'effective' on-momentum dynamic aperture (DA) and momentum acceptance (MA) are 8 mm and 3.3 mm in $x$ and $y$ planes, and ~3.5%, respectively (see [9] for definition and discussion of the 'effective' DA and MA). The large ring acceptance makes it feasible to use on-axis swap-out, on-axis longitudinal accumulation, or even off-axis multipole injection method in the HEPS storage ring.

It is worth mentioning that there is a trade-off between the emittance (which is positively correlated to the available maximum brightness) and the ring acceptance. On the other hand, the choice of injection method is related to the available of the ring acceptance. Generally speaking, conventional local-bump injection method requires a DA of larger than 10 mm, off-axis injection with multipole requires a DA of at least 5 mm, on-axis longitudinal injection requires that both on-momentum and off-momentum DAs are 1 to 2 mm, on-axis swap injection only requires an on-momentum DA of 1 to 2 mm.

Actually, this lattice is selected among those obtained from the global optimization of the hybrid-7BA lattice, where the linear and nonlinear dynamics are simultaneously optimized and all the available tenable element parameters are scanned. The results are presented in Fig. 4. It shows that with the hybrid-7BA lattice, if satisfying only the DA requirement of on-axis swap-out injection, the HEPS ring emittance can be down to ~45 pm.rad; if pursuing large ring acceptance that allows for accumulation injections, the DA can be optimized to be close to (if not larger than) 10 mm in the injection plane, while keeping the emittance to be around 60 pm.rad.

Except the layout presented in Fig. 1, we are exploring and comparing different types of lattice structures and globally scanning all tuneable parameters of the ring with stochastic optimization methods, with the aim to achieve lattice with even better performance. This will be reported in a forthcoming paper.

* Work supported by by NSFC (11475202, 11405187, 11205171)
† email address: jiaoyi@ihep.ac.cn

ISBN: 978-3-95450-199-1 doi:10.18429/JACoW-SAP2017-MOBH2



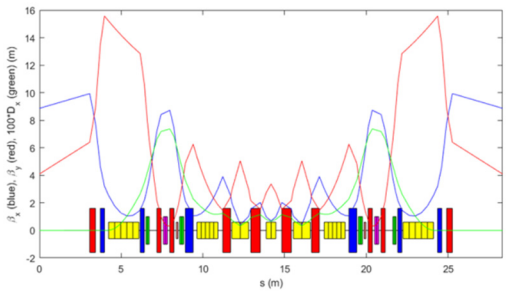


Figure 1: Optical functions and lattice layout of one 7BA of the present HEPS lattice.

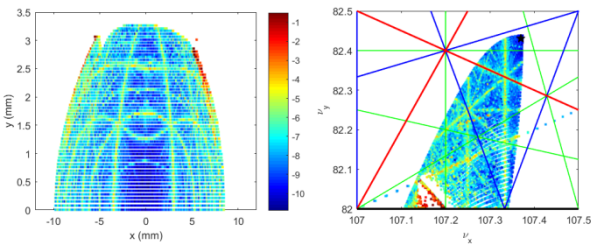


Figure 2: Effective (on-momentum) dynamic aperture and the corresponding frequency map of the present HEPS lattice.

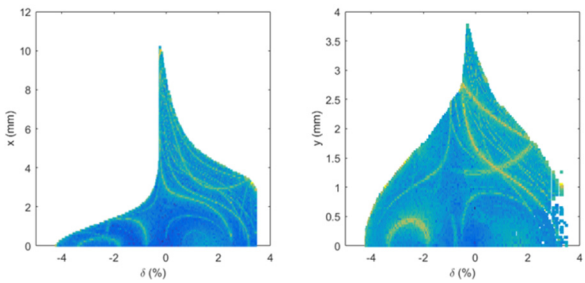


Figure 3: Effective momentum acceptance of the present HEPS lattice.

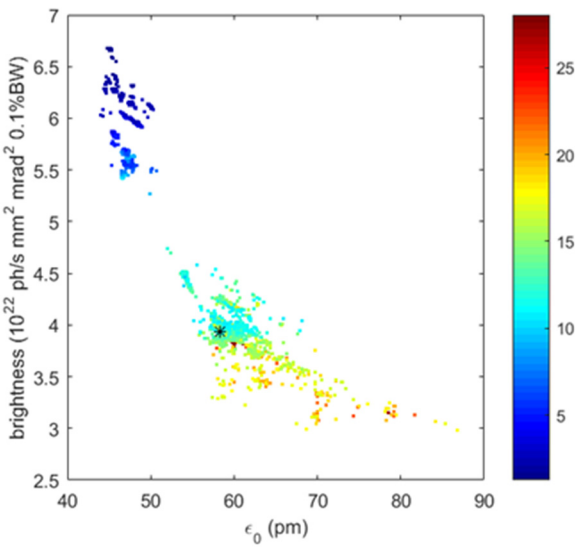


Figure 4: Solutions of global optimization of the hybrid-7BA lattice, the present lattice is represented with a black asterisk.

Table 1: Ring Parameters of Present HEPS Lattice

| Parameters | Values |
|---|---|
| Energy $E_0$ | 6 GeV |
| Beam current $I_0$ | 200 mA |
| Circumference | 1360.4 m |
| Natural emittance $\varepsilon_{x0}$ | 58.4 pm.rad |
| Working point $\upsilon_x/\upsilon_y$ | 107.37/82.43 |
| Natural chromaticities (H/V) | -214/-133 |
| No. of superperiods | 48 |
| ID section length $L_{ID}$ | 6.15 m |
| Beta functions at ID sect. (H/V) | 8.9/4.1 m |
| Energy loss per turn | 1.959 MeV |
| Rms energy spread | $8.20\times10^{-4}$ |
| Momentum compaction | $3.43\times10^{-5}$ |

## *Injection to the Ring*

The nominal injection scheme presently under consideration is the on-axis swap-out injection. The design also leaves space for other injection schemes, especially the on-axis longitudinal injection [e.g., 10]. Two operational modes with different filling patterns are considered, i.e., low-charge mode (200 mA with 680 bunches) and high-charge mode (200 mA with 63 bunches).

To inject a high-charge bunch to the ring, while avoiding the strong collective effects at the low energy of the booster ramping loop, a transport line from the storage ring to the booster (STB) has been designed [11] to allow for accumulation of the extracted bunches from the storage ring in the booster at 6 GeV. Especially for the high-charge mode, when the charge of the stored bunch of the ring reduces, this bunch will be extracted and injected to the booster after passing through the STB. The bunch will merge with existing bunch in the booster, and then be extracted from the booster and re-injected to the ring.

## *Error Study and Lattice Calibration*

Associated with the compact layout and strong focusing of the ultralow-emittance design, the ring performance is sensitive to various errors, such as the alignment error, magnetic field error, BPM error, etc.

One critical concern is that whether we can smoothly and quickly store the beam in such an ultralow-emittance ring. To this end, we simulate the beam injection of the first several turns, and develop an automatic correction procedure to gradually reduce the amplitude of the particle oscillation and finally realize storage of the beam [12].

We evaluate the error effects by modelling these errors in the lattice and simulate the lattice calibration process, including orbit correction, optics correction and coupling control [13]. From this study we will also get detailed tolerance table for related hardware systems.

ISBN: 978-3-95450-199-1 doi:10.18429/JACoW-SAP2017-MOBH2

### *Collective Effects*

The fundamental frequency of the HEPS RF system is chosen to 166.6 MHz. To release the strong intrabeam scattering (IBS) and Touscheck effects related to the increasing beam density with the decreasing emittance, we adopt third-order harmonic RF cavities with frequency of 499.6 MHz. With the harmonic cavities, the bunch length can be lengthened by about 3 times so as to greatly release the IBS and Touschek effects. The Touschek lifetime is about 20 hours for the low-charge mode and 3 hours for the high-charge mode.

The impedance budget of the HEPS storage ring is estimated [14]. It is found that the main contributions to the longitudinal impedance are resistive wall impedance and elements with large quantity, and the transverse broadband impedance is dominated by the resistive wall impedance due to the small-aperture vacuum chamber.

Based on the impedance model, the collective effects are evaluated with both analytical analysis and numerical simulations, especially for the high-charge mode.

Among the single bunch instabilities, the transverse mode coupling instability is the strongest one. It leads to a threshold current of ~ 0.1 mA at zero chromaticity. This problem, however, can be resolved with a positive chromaticity, e.g., +2. Actually, in HEPS design, we set the corrected chromaticities to (+5, +5).

For the coupled bunch instabilities, the main contributors are the high-order modes of RF cavities and the resistive wall impedance (the full aperture of the vacuum chamber is on the level of 25 mm). To cure the instabilities and ensure stable operation, feedback system with damping time of shorter than 0.5 ms is required.

### *Injector Design*

The booster will accelerate the beam from 300 MeV to 6 GeV, and is assumed to be located in a separate tunnel, so as to reduce the effect of the ramping cycle of the booster to the particle motions of the ring.

To fulfil the requirements for the expected light source performance, it is required that the booster should have the ability to provide high enough charge bunch, i.e., 15 nC. Study shows that the single bunch instability causes stringent limitation to available stored bunch charge at the low energy.

Efforts are made to release this limitation as much as possible. The lattice is changed from a 15BA layout to a FODO structure. The latter one allows larger momentum compaction factor, which is helpful to increase the bunch charge threshold. In addition, the average beta function of the lattice is reduced. And, it is required that the electron bunch from the linac should have a long bunch length, i.e., not less than 25 ps or namely 7.5 mm. Even with these measures, the bunch charge threshold cannot be increased to be above 15 nC. As mentioned above, it is determined to build an additional transport line between ring and booster to overcome this problem.

## ACKNOWLEDGEMENT

The authors would thank A. Chao, B. Hettel, K. Bane, X. Huang of SLAC, L. Yu, Y. Li, G. Wang of BNL, B. Jiang, S. Tian of SINAP, P. Raimondi, B. Nash, S. Liuzzo of ESRF, M. Borland of ANL, etc. for helpful discussions on the HEPS design and physics studies.

## REFERENCES

[1] X. Jiang *et al*., "BAPS Preliminary Design Report", internal report, 2012.

[2] G. Xu, and Y. Jiao, "Towards the ultimate storage ring: the lattice design for Beijing Advanced Photon Source", *Chin. Phys. C*, 37(5), 057003 (2013).

[3] Y. Jiao, G. Xu and D.H. Ji, "Latest design and optimization of the PEPX-type lattice for HEPS", *SAP2014*, Lanzhou, 2014.

[4] Y. Jiao, G. Xu, S.Y. Chen, Q. Qin, and J.Q. Wang, "Advances in physical design of diffraction-limited storage ring", *High Power Laser and Particle Beams*, 27(04): 045108, 2015.

[5] Y. Jiao and G. Xu, "PEPX-type lattice design and optimization for the High Energy Photon Source", *Chin. Phys. C*, 39(6), 067004, 2015.

[6] G. Xu, Y. Jiao and Y. Peng, "ESRF-type lattice design and optimization for the High Energy Photon Source", *Chin. Phys. C*, vol. 40, p. 027001, 2016.

[7] Y. Jiao, "Improving nonlinear performance of the HEPS baseline design with a genetic algorithm", *Chin. Phys. C*, vol. 40, p. 077002, 2016.

[8] Y. Jiao, and G. Xu, "Optimizing the lattice design of a diffraction-limited storage ring with a rational combination of particle swarm and genetic algorithms", *Chin. Phys. C*, 41(2): 027001, 2017.

[9] Y. Jiao, Z. Duan and G. Xu, "Characterizing the nonlinear performance of a DLSR with the effective acceptance of the bare lattice", *IPAC2017*, WEPAB055, Copenhagen, Denmark.

[10] G. Xu *et al*., "On-axis beam accumulation enabled by phase adjustment of a double-frequency RF system for diffraction-limited storage rings", *IPAC2016*, WEOAA02, Busan, Korea.

[11] Y.Y. Guo *et al*., "High energy transport line design for the HEPS project", *IPAC17*, Copenhagen, Denmark, TUPAB063, this conference.

[12] Y. L. Zhao et al., "First turns around strategy for HEPS", IPAC2017, MOPIK082, Copenhagen, Denmark.

[13] D.H. Ji *et al*., "Study of HEPS performance with error model and simulated correction", *IPAC17*, MOPIK081, Copenhagen, Denmark.

[14] N. Wang *et al*., "Development of the impedance model in HEPS", *IPAC2017*, WEPIK078, Copenhagen, Denmark.

ISBN: 978-3-95450-199-1 doi:10.18429/JACoW-SAP2017-MOBH3

# CEPC PARAMETER CHOICE*

D. Wang†, C. Yu, Y. Zhang, Y. Wang, J. Zhai, B. Sha, H. Geng, N. Wang, X. Cui, T. Bian, J. Gao,
IHEP, Beijing, China

*Abstract*

The 100km Double Ring configuration with shared super conducting RF systems has been defined as baseline by CEPC steering committee. CEPC is compatible with W and Z experiment. Requirement for energy acceptance of Higgs has been reduced from 2% to 1.1% by enlarging the ring to 100 km. For CDR, W and Z will use the same lattice as Higgs, and the luminosity for Z is at the level of $10^{34}cm^{-2}s^{-1}$.

## INTRODUCTION

According to the physics goal of CEPC at Higgs and Z-pole energy, it is required that the CEPC provides e+e- collisions at the center-of-mass energy of 240 GeV and delivers a peak luminosity of $2\times10^{34}cm^{-2}s^{-1}$ at each interaction point. At Z-pole the luminosity is required to be at least larger than $1\times10^{34}cm^{-2}s^{-1}$ per IP.

In the beginning of 2015, Pre-CDR of CEPC-SppC [1] has been completed with 54km circumference and single ring scheme. After that the size and the collision scheme of CEPC-SPPC was reconsidered. The 100km Double Ring configuration with shared SCRF has been defined as baseline by CEPC steering committee on Jan. 14th of 2016. The CDR report with 2mm βy* and 31 MW beam power will be finished by the end of 2017.

CEPC was proposed as a compatible machine which will allow stringent tests of the Standard Model (SM) with precision measurements at the Z pole and WW thresholds. At Higgs energy, all bunches distribute in the half ring due to the shared RF system. While for W and Z, bunches can distribute in the whole ring thanks to the independent RF system so that more bunches are possible. The scheme of CEPC bunch distribution is shown in Fig. 1.

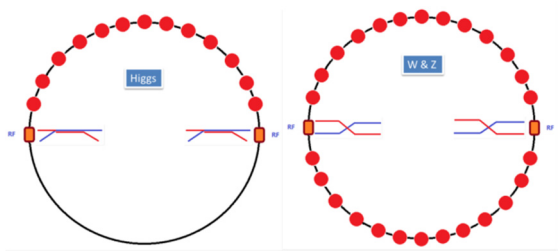


Figure 1: CEPC bunch distribution scheme (left: Higgs, right: W&Z).

## BEAM LIFETIME LIMIT AND ENERGY SPREAD LIMIT DUE TO BEAMSTRAHLUNG

When two head-on colliding electron and positron beams penetrate each other, every particle in each beam will feel the electromagnetic field of the other beam and will be defected. This deflection process has some undesirable effects. Firstly, the deflected particle will lose part of its energy due to the synchrotron radiation, called as beamstrahlung, which will increase the energy spread of the colliding beams, and hence increase the uncertainty of the physical experiments. If the beamstrahung is so strong that particles' energy after collision is beyond the ring's energy acceptance, they may leave the beam and strike the vacuum chamber's walls, and hence beam lifetime is decreased. Secondly, the deflected particles will emit photons, hadrons, etc., which will increase the noise background level in the detector. Additionally, after the collision particles will change their flying direction with respect to the axis by a certain angle. If this angle is large enough the particles after the collision will interfere with the detection of small-angle events.

In order to control the extra energy spread by beamstrahlung to a certain degree, we introduce a constraint in this paper as

$$\delta_{BS} \le \frac{1}{5}\delta_0 \tag{1}$$

where $\delta_0$ is the nature energy spread and $\delta_{BS}$ is the extra energy spread due to beamstrahlung.

V. I. Telnov [2] pointed out that at energy-frontier e+e− storage ring colliders, beamstrahlung determines the beam lifetime through the emission of single photons in the tail of the beamstrahlung spectra. Unlike the linear collider case, the long tails of the beamstrahlung energy loss spectrum are not a problem because beams are used only once. If we want to achieve a reasonable beamstrahlung-driven beam lifetime of at least 30 minutes, we need to confine the relation of the bunch population and the beam size as follows [3]

$$\frac{N_e}{\sigma_x\sigma_z} \le 0.1\eta\frac{\alpha}{3\gamma r_e^2} \tag{2}$$

where $\eta$ is the energy acceptance of the ring and $\alpha$ is the fine structure constant (1/137).

## COLLISION SCHEME WITH LARGE PIWINSKI ANGLE AND CRAB WAIST

The crab waist scheme of beam-beam collisions can substantially increase the luminosity of a collider since it combines several potentially advantageous ideas. The first one is the large Piwinski's angle.

It is well known that decreasing $\beta_y$ at the IP is very profitable for the luminosity, but the main limitation is set by the lower limit on the achievable bunch length. With

* Work supported by the National Key Programme for S&T Research and Development (Grant NO. 2016YFA0400400) and the National Natural Science Foundation of China (11505198, 11575218, 11605210 and 11605211).
† wangd93@ihep.ac.cn

ISBN: 978-3-95450-199-1 doi:10.18429/JACoW-SAP2017-MOBH3

large Piwinski's angle the overlapping area becomes much smaller than $\sigma_z$, allowing significant $\beta_y$ decrease:

$$\beta_y \approx \frac{\sigma_x}{\theta} \ll \sigma_z \quad (3)$$

And this can give us very significant gain in the luminosity! The additional advantages of such collision scheme are:

1. It's not necessary to decrease the bunch length which is the key factor of luminosity. This will certainly ease the problems of HOM heating, coherent synchrotron radiation of short bunches, excessive power consumption, etc.
2. The problem of parasitic collisions (PC) is automatically solved since with higher crossing angle and smaller horizontal beam size the beams separation at the PC is very large in terms of σx.

However, such a scheme of collision induces strong X-Y betatron resonances, which may cause troubles in making choice of the working point, and lower the achievable luminosity. Fortunately, the Crabbed Waist (CW) can solve this problem, which is the other attractive idea accomplishing the concept of crab waist collision. As it is seen in Fig. 2, the beta function waist of one beam is oriented along the central trajectory of the other one. In practice the CW vertical beta function rotation is provided by sextupole magnets placed on both sides of the IP in phase with the IP in the horizontal plane and at π/2 in the vertical one.

The crab sextupole strength should satisfy the following condition depending on the crossing angle and the beta functions at the IP and the sextupole locations [4]:

$$K_2 = \frac{1}{2\theta}\frac{1}{\beta_y^* \beta_y}\sqrt{\frac{\beta_x^*}{\beta_x}} \quad (4)$$

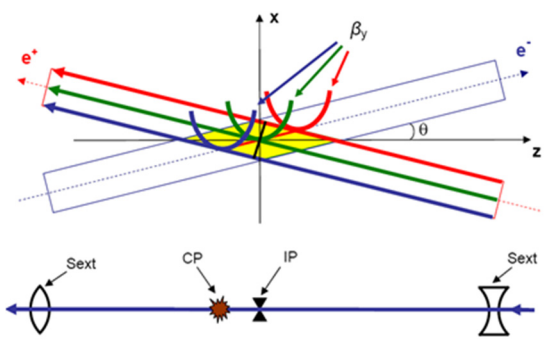


Figure 2: Collision in "Crabbed Waist" scheme.

## BEAM-BEAM PARAMETER LIMIT COMING FROM BEAM EMITTANCE BLOW-UP

In e+ e- storage ring colliders, due to strong quantum excitation and synchrotron damping effects, the particles are confined inside a bunch. The position for each particle is random and the state of the particles can be regarded as a gas, where the positions of the particles follow statistic laws. Apparently, the synchrotron radiation is the main source of heating. Besides, when two bunches undergo collision at an interaction point (IP), every particle in each bunch will feel the deflected electromagnetic field of the opposite bunch and the particles will suffer from additional heating. With the increase of the bunch particle population $N_e$, this kind of heating effect will get stronger and the beam emittance will increase. There is a limit condition beyond which the beam emittance will blow up. This emittance blow-up mechanism introduce a limit for the first part of beam-beam tune shift [5]

$$\xi_y = \frac{2845}{2\pi}\sqrt{\frac{U_0}{2\gamma E_0 N_{IP}}} \times F_l \quad (5)$$

where $F_l$ is the luminosity enhancement factor by crab waist scheme and so far we assume it is 1.5 for Higgs, 1.9 for W and 2.6 for Z.

## CEPC PARAMETER CHOICE FOR 100KM DOUBLE RING

To make an optimization for a collider, started from the goals, such as energy, luminosity/IP, number of IPs, etc, one has to consider very key beam physics limitations, such as beam-beam effects and beamstrahlung effect, and also take into account of economical and technical limitations, such as synchrotron radiation power and high order mode power in each superconducting RF cavity. By taking into account all these limitations in an analytical way, an analytical electron positron circular collider optimized design method has been developed both for head-on collision [6] and carb-waist collision [7].

### *Constraints for Parameter Choice*

1. Limit of Beam-beam tune shift
2. Beam lifetime due to beamstrahlung
3. Extra energy spread due to beamstrahlung
4. HOM power per cavity

$$P_{HOM} = k(\sigma_z) e N_e \cdot 2I_b \le 2kw \quad [8] \quad (6)$$

where the HOM loss factor is $k(\sigma_z) = \frac{1.8}{\sqrt{\sigma_z / 0.00265}}$ $V/pC$.

### *CEPC Intermediate Parameters toward CDR*

Since the FFS design and DA study is the bottleneck for CEPC physics design, as the first step, we decided to choose 2mm βy* and lower SR power (31MW) for CDR report which will be published by the end of 2017. Using the method in reference 7, we got the parameter table for 2mm βy* as Table 1.

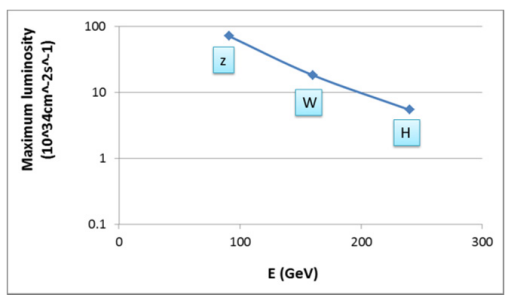


Figure 3: Luminosity potential of 100km CEPC with 1mm βy* and 50MW SR power/beam.

ISBN: 978-3-95450-199-1 doi:10.18429/JACoW-SAP2017-MOBH3



We have found the vertical emittance growth for Z mode is most dangerous among the three energies due to the detector solenoid (3T) coupling effect. So we chose larger coupling factor (2.2%) at Z pole, while it is 0.3% for Higgs and W.

### *CEPC Upgrade*

We have considered the upgrade of CEPC with higher luminosity using higher SR power and smaller βy*. Luminosity potential of 100km CEPC with 50MW SR power and 1mm βy* is shown in Fig. 3. Here we assume Z mode can use different lattice rather than Higgs and W, because Z needs larger emittance to increase luminosity which can be realized by closing half quadrupoles in Higgs lattice. Also Z mode may need dedicated 1 cell cavities to control the HOM power.

Table 1: CDR Parameters for 100km CEPC Double Ring with 2mm βy*

| | **Pre-CDR** | **Higgs** | **W** | **Z** | |
|---|---|---|---|---|---|
| Number of IPs | 2 | 2 | 2 | 2 | |
| Energy (GeV) | 120 | 120 | 80 | 45.5 | |
| Circumference (km) | 54 | 100 | 100 | 100 | |
| SR loss/turn (GeV) | 3.1 | 1.61 | 0.32 | 0.033 | |
| Half crossing angle (mrad) | 0 | 16.5 | 16.5 | 16.5 | |
| Piwinski angle $\Phi$ | 0 | 2.28 | 3.6 | 6.33 | |
| *N*e/bunch ($10^{11}$) | 3.79 | 9.68 | 3.6 | 2.3 | |
| Bunch number | 50 | 420 | 5700 | 3510 | 27000 |
| Beam current (mA) | 16.6 | 19.5 | 98.6 | 38.8 | 298.5 |
| SR power /beam (MW) | 51.7 | 31.4 | 31.3 | 1.3 | 9.9 |
| Bending radius (km) | 6.1 | 11.4 | 11.4 | 11.4 | |
| Momentum compaction ($10^{-5}$) | 3.4 | 1.15 | 1.15 | 1.15 | |
| $\beta_{IP}$ x/y (m) | 0.8/0.0012 | 0.36/0.002 | 0.36/0.002 | 0.36/0.002 | |
| Emittance x/y (nm) | 6.12/0.018 | 1.18/0.0036 | 0.52/0.0017 | 0.17/0.0038 | |
| Transverse $\sigma_{IP}$ (um) | 69.97/0.15 | 20.6/0.085 | 13.7/0.059 | 7.81/0.087 | |
| ξx/ξy/IP | 0.118/0.083 | 0.025/0.085 | 0.014/0.068 | 0.017/0.053 | |
| RF Phase (degree) | 153.0 | 128 | 134.7 | 151 | |
| $V_{RF}$ (GV) | 6.87 | 2.03 | 0.45 | 0.069 | |
| $f_{RF}$ (MHz) | 650 | 650 | 650 | 650 (217800) | |
| Nature $\sigma_z$ (mm) | 2.14 | 2.75 | 2.98 | 2.92 | |
| Total $\sigma_z$ (mm) | 2.65 | 2.85 | 3.0 | 3.0 | |
| HOM power/cavity (kw) | 3.6 (5cell) | 0.42 (2cell) | 0.38 (2cell) | 0.096 (2cell) | 0.74 (2cell) |
| Energy spread (%) | 0.13 | 0.096 | 0.064 | 0.036 | |
| Energy acceptance (%) | 2 | 1.1 | | | |
| Energy acceptance by RF (%) | 6 | 1.98 | 1.46 | 1.2 | |
| $n_\gamma$ | 0.23 | 0.19 | 0.11 | 0.12 | |
| Life time due to beamstrahlung_cal (minute) | 47 | 63 | | | |
| *F* (hour glass) | 0.68 | 0.93 | 0.963 | 0.987 | |
| $L_{max}$/IP ($10^{34}$cm$^{-2}$s$^{-1}$) | 2.04 | 2.0 | 5.6 | 1.0 | 7.7 |

## CONCLUSION

We have developed a consistent method for CEPC parameter choice with carb waist scheme by using analytical expression of maximum beam-beam tune shift and beamstrahlung beam lifetime started from given IP vertical beta, beam power and other technical limitations. The luminosity can be crosschecked by beam-beam simulations. Based on double ring scheme with 100 km circumference, the requirement of energy acceptance for Higgs was reduced to 1.1%, and also the beam loading effect and sawtooth effect can be solved.

We chose 2mm βy* and 31MW SR power for CDR. The luminosity goal for Higgs is $2\times10^{34}$cm$^{-2}$s$^{-1}$ and the luminosity for Z is at the level of $10^{34}$cm$^{-2}$s$^{-1}$.

## ACKNOWLEDGEMENT

The authors thank Professors Katsunobu Oide, Yunhai Cai, Frank Zimmermann, Michael Koratzinos, and Valery Telnov for their helpful discussions.

ISBN: 978-3-95450-199-1 doi:10.18429/JACoW-SAP2017-MOBH3

## REFERENCES

[1] The CEPC-SPPC Study Group, "CEPC-SPPC preliminary Conceptual Design Report, Volume II- Acceleraor", IHEP-CEPC-DR-2015-01, IHEP-AC-2015-01, March 2015.

[2] V. Telnov, arXiv:1203.6563v, 29 March 2012.

[3] V. Telnov, HF2012, November 15, 2012.

[4] P. Raimondi *et al.*, e-Print:physics/0702033, 2007.

[5] J. Gao, *Nucl. Instr. Meth.*, vol. 533, pp. 270-274, 2004.

[6] D. Wang *et al.*, "Optimization parameter design of a circular e+e- Higgs factory", *Chinese Physics C*, vol. 37, no. 9, p. 097003, 2013.

[7] D. Wang *et al.*, "CEPC partial double ring scheme and crab-waist parameters", *International Journal of Modern Physics A*, vol. 3, p. 1644016, 2016.

[8] J. Zhai, private communication, 2015.

ISBN: 978-3-95450-199-1 doi:10.18429/JACoW-SAP2017-MOCH1

# PHASE SPACE GYMNASTICS

Alexander Chao, SLAC National Accelerator Laboratory

*Abstract*

Phase space gymnastics is a highly evolved accelerator physics technique based on the finest properties of the phase space. As modern accelerators become increasingly demanding, these techniques are finding a sharp increase in their applications. Here we intend only to introduce this topic to bring attention to the direction it points to.

## INTRODUCTION

As accelerator technology advances, the requirements on accelerator beam quality become increasingly demanding. Facing these new demands, the topic of phase space gymnastics is becoming a new focus of accelerator physics research. In a phase space gymnastics, the beam's phase space distribution is manipulated and precision-tailored to meet the required beam qualities. On the other hand, all realization of such gymnastics will have to obey accelerator physics principles as well as technological limitations. Recent examples of phase space gymnastics include

1. Adapters
2. Emittance exchanges
3. Phase space exchanges
4. Emittance partitioning
5. Seeded free electron lasers
6. Steady-state microbunched storage rings

Each one of these applications involves half a dozen to a dozen inventions to special cases. It can only be expected that many more applications are yet to be found. This research filed is very rich and active. In this report, however, we aim only to illustrate the subject and we will only breifly address the case of adapters (item 1 above) and give some of their example applications.

Just like the physical gymnastics, e.g. in the Olympic games, the skills needed in phase space gymnastics are highly technical and precise, while the resulting performance exquisite and beautiful. A comparison of these two gymnastics skills is shown in Fig. 1. Earlier phase space gymnastics have been mostly applied to the 2D longitudinal phase space, and took the form of RF manipulations in beam injection, extraction, and phase space displacement acceleration [1]. The recent advances, led by the seminal papers by Derbenev [2], begin to incorporate the transverse dimensions and become much more sophisticated, yielding a new wealth of additional applications mentioned above.

It should be mentioned here that phase space gymnastics permit precision manipulations because phase space is conserved to its finest details. Liouville theorem (more accurately, the condition of symplecticity) is the root cause of this possibility of phase space technology. The very concept of phase space (a bold extension and abstraction of the 3D real space), and its intricate physical and mathematical properties (that pave the foundation of these phase space techniques), however, are not the subject of this report.

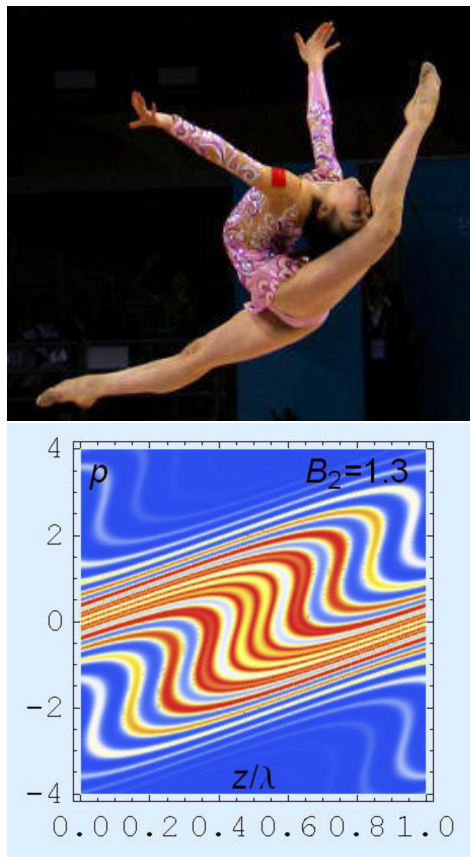


Figure 1: A comparison of phase space gymnastics and physical gymnastics.

## ADAPTERS

The idea of adapters was first introduced by Derbenev [2] and later rapidly extended by him and many others [3]-[14]. A few adapters of a different variety are shown in Fig. 2. Derbenev first envisioned applying it to a storage ring collider to form round beams at the collision point to mitigate the effect of the encountered beam-beam nonlinear resonances. This adapter idea has also been adapted for electron cooling [3,7]. Furthermore, the production of a very flat beam from a round photocathode immersed in a solenoid followed by a round-to-flat adapter has been experimentally demonstrated [10–12].

ISBN: 978-3-95450-199-1 doi:10.18429/JACoW-SAP2017-MOCH1

Figure 2: A few adapters of a different variety.

During this time, as mentiond earlier, several other kinds of adapters have been invented, including emittance exchange adapters and phase space exchange adapters and nonsymplectic applications for emittance partitioning have also been developed, but we do not cover those applications below.

Consider the 4D canonical phase space $X_{\text{can}} = (x, p_x, y, p_y)$. We have two representations to describe particle motion in this phase space:

1. For an uncoupled case, use the Courant-Snyder basis of planar modes ($x$ and $y$ modes) in a matrix form:

$$X_{\text{can}} = Va \tag{1}$$

where

$$V = \begin{bmatrix} \sqrt{\beta_x}\cos\phi_x & \sqrt{\beta_x}\sin\phi_x & 0 & 0 \\ \frac{-\alpha_x\cos\phi_x - \sin\phi_x}{\sqrt{\beta_x}} & \frac{-\alpha_x\sin\phi_x + \cos\phi_x}{\sqrt{\beta_x}} & 0 & 0 \\ 0 & 0 & \sqrt{\beta_y}\cos\phi_y & \sqrt{\beta_y}\sin\phi_y \\ 0 & 0 & \frac{-\alpha_y\cos\phi_y - \sin\phi_y}{\sqrt{\beta_y}} & \frac{-\alpha_y\sin\phi_y + \cos\phi_y}{\sqrt{\beta_y}} \end{bmatrix} \tag{2}$$

and

$$a = \begin{bmatrix} \sqrt{2\epsilon_x}\sin\chi_x \\ \sqrt{2\epsilon_x}\cos\chi_x \\ \sqrt{2\epsilon_y}\sin\chi_y \\ \sqrt{2\epsilon_y}\cos\chi_y \end{bmatrix} \tag{3}$$

These equations describe the motion of a particle in a planar beamline whose $x$ and $y$ emittances are $\epsilon_x, \epsilon_y$ and initial betatron phases of $\chi_x$ and $\chi_y$. Lattice functions $\alpha_{x,y}, \beta_{x,y}, \phi_{x,y}$ are the familiar betatron parameters in this representation. Indeed by direct multiplication, we have

$$x_{\text{can}} = Va = \begin{bmatrix} \sqrt{2\beta_x\epsilon_x}\sin(\phi_x + \chi_x) \\ \sqrt{\frac{2\epsilon_x}{\beta_x}}[\cos(\phi_x + \chi_x) - \alpha_x\sin(\phi_x + \chi_x)] \\ \sqrt{2\beta_y\epsilon_y}\sin(\phi_y + \chi_y) \\ \sqrt{\frac{2\epsilon_y}{\beta_y}}[\cos(\phi_y + \chi_y) - \alpha_y\sin(\phi_y + \chi_y)] \end{bmatrix} \tag{4}$$

Equation (4) is a very familar result. What may be less familiar, and it might come as a surprise, is the fact that this familiar result is actually factorizable according to Eq. (1).

2. For a fully coupled beam with rotational symmetry (e.g. in a solenoidal field), one can describe particle motion using the basis of circular modes (left-handed and right handed modes) [8]:

$$X_{\text{can}} = Ub \tag{5}$$

where

$$U = \frac{1}{\sqrt{2}}\begin{bmatrix} \frac{\sqrt{\beta}\cos\phi_+}{\frac{-\sin\phi_+ - \alpha\cos\phi_+}{\sqrt{\beta}}} & \frac{\sqrt{\beta}\sin\phi_+}{\frac{\cos\phi_+ - \alpha\sin\phi_+}{\sqrt{\beta}}} & \frac{-\sqrt{\beta}\cos\phi_-}{\frac{\sin\phi_- + \alpha\cos\phi_-}{\sqrt{\beta}}} & \frac{-\sqrt{\beta}\sin\phi_-}{\frac{-\cos\phi_- + \alpha\sin\phi_-}{\sqrt{\beta}}} \\ \frac{-\sqrt{\beta}\sin\phi_+}{\frac{-\cos\phi_+ + \alpha\sin\phi_+}{\sqrt{\beta}}} & \frac{\sqrt{\beta}\cos\phi_+}{\frac{-\sin\phi_+ - \alpha\cos\phi_+}{\sqrt{\beta}}} & \frac{-\sqrt{\beta}\sin\phi_-}{\frac{-\cos\phi_- + \alpha\sin\phi_-}{\sqrt{\beta}}} & \frac{\sqrt{\beta}\cos\phi_-}{\frac{-\sin\phi_- - \alpha\cos\phi_-}{\sqrt{\beta}}} \end{bmatrix} \tag{6}$$

and

$$b = \begin{bmatrix} \sqrt{2\epsilon_+}\sin\chi_+ \\ \sqrt{2\epsilon_+}\cos\chi_+ \\ \sqrt{2\epsilon_-}\sin\chi_- \\ \sqrt{2\epsilon_-}\cos\chi_- \end{bmatrix} \tag{7}$$

for a particle with left-handed and right-handed emittances $\epsilon_+$ and $\epsilon_-$ and initial betatron phases $\chi_+$ and $\chi_-$. Lattice parameters are $\alpha, \beta, \phi_+, \phi_-$, i.e., there is only one $\beta$-function, one $\alpha$-function, but two (left-handed and right-handed) phases. Direct multiplication gives

$$X_{\text{can}} = Ub = \begin{bmatrix} \sqrt{\beta}(\sqrt{\epsilon_+}\sin\Delta_+ - \sqrt{\epsilon_-}\sin\Delta_-) \\ \frac{1}{\sqrt{\beta}}(\sqrt{\epsilon_+}\cos\Delta_+ - \sqrt{\epsilon_-}\cos\Delta_- - \alpha\sqrt{\epsilon_+}\sin\Delta_+ + \alpha\sqrt{\epsilon_-}\sin\Delta_-) \\ \sqrt{\beta}(\sqrt{\epsilon_+}\cos\Delta_+ + \sqrt{\epsilon_-}\cos\Delta_-) \\ -\frac{1}{\sqrt{\beta}}(\sqrt{\epsilon_+}\sin\Delta_+ + \sqrt{\epsilon_-}\sin\Delta_- + \alpha\sqrt{\epsilon_+}\cos\Delta_+ + \alpha\sqrt{\epsilon_-}\cos\Delta_-) \end{bmatrix}$$

where $\Delta_+ = \phi_+ + \chi_+, \Delta_- = \phi_- + \chi_-$.

ISBN: 978-3-95450-199-1 doi:10.18429/JACoW-SAP2017-MOCH1



Once we have the planar basis $V$ and the circular basis $U$ — both are symplectic — we are now in a position to consider "adapters". So far we considered transverse phase space only. Adapters can also be applied to transverse-longitudinal coupled systems.

### *Flat-to-flat Adapters*

Flat-to-flat adapter from $s_1$ to $s_2$ is well known. The job is to design a lattice that provides the map from the basis $V(s_1)$ to the basis $V(s_2)$, i.e. the optics matching from one set of lattice parameters to another. A moment's reflection shows that the needed matching map is given by $V(s_2)V(s_1)^{-1}$, and a simple calculation gives

$$V(s_2)V(s_1)^{-1} = \begin{bmatrix} \sqrt{\frac{\beta_{x2}}{\beta_{x1}}}(\cos\mu_x + \alpha_{x1}\sin\mu_x) & \sqrt{\beta_{x1}\beta_{x2}}\sin\mu_x & 0 & 0 \\ \frac{(\alpha_{x1}-\alpha_{x2})\cos\mu_x-(1+\alpha_{x1}\alpha_{x2})\sin\mu_x}{\sqrt{\beta_{x1}\beta_{x2}}} & \sqrt{\frac{\beta_{x1}}{\beta_{x2}}}(\cos\mu_x - \alpha_{x2}\sin\mu_x) & 0 & 0 \\ 0 & 0 & \sqrt{\frac{\beta_{y2}}{\beta_{y1}}}(\cos\mu_y + \alpha_{y1}\sin\mu_y) & \sqrt{\beta_{y1}\beta_{y2}}\sin\mu_y \\ 0 & 0 & \frac{(\alpha_{y1}-\alpha_{y2})\cos\mu_y-(1+\alpha_{y1}\alpha_{y2})\sin\mu_y}{\sqrt{\beta_{y1}\beta_{y2}}} & \sqrt{\frac{\beta_{y1}}{\beta_{y2}}}(\cos\mu_y - \alpha_{y2}\sin\mu_y) \end{bmatrix} \tag{8}$$

Equation (8) of course is a well known result; $\mu_x = \phi_{x2} - \phi_{x1}, \mu_y = \phi_{y2} - \phi_{y1}$ are the betatron phase advances from $s_1$ to $s_2$. A particle with initial condition (3) is now brought from position $s_1$ to position $s_2$.

Let us make a few side comments here concerning Eqs. (1) and (8):

- Equation (1) is not to be confused with a similar-looking expression $X_{\text{out}} = MX_{\text{in}}$, which relates the final coordinates $X_{\text{out}}$ to the initial coordinates $X_{\text{in}}$ through a beamline element with map $M$ and is the job of Eq. (8). This should become apparent when one observes that the final product of the multiplication of $Va$ yields Eq. (4).

- Equation (1) factorizes the particle's motion into a product of a factor $V$ that depends only on the accelerator optics, and a factor $a$ that depends only on the particle's initial conditions. It is important to note that $V$ has nothing to do with the particle while $a$ has nothing to do with the accelerator.

- Now Eq. (8) goes further in factorization. It says that the map that brings the accelerator optics from $s_1$ to $s_2$ can be factorized into a factor $V(s_1)^{-1}$ that depends only on the optical properties at $s_1$ and a factor $V(s_2)$ that depends only on the optical properties at $s_2$.

The elegance of this formalism should be very apparent.

### *Round-to-round Adapters*

Round-to-round adapter from $s_1$ to $s_2$, i.e., from one set of circular lattice parameters to another, is given by the map $U(s_2)U(s_1)^{-1}$. Although the algebra is somewhat involved, it can be shown that the result can be written as

$$U(s_2)U(s_1)^{-1} = R^{-1}(\theta)T \tag{9}$$

where $R(\theta)$ is a rotation matrix with rotation angle $\theta$,

$$R(\theta) = \begin{bmatrix} \cos\theta & 0 & \sin\theta & 0 \\ 0 & \cos\theta & 0 & \sin\theta \\ -\sin\theta & 0 & \cos\theta & 0 \\ 0 & -\sin\theta & 0 & \cos\theta \end{bmatrix} \tag{10}$$

and

$$T = \begin{bmatrix} \sqrt{\frac{\beta_2}{\beta_1}}(\cos\mu + \alpha_1\sin\mu) & \sqrt{\beta_1\beta_2}\sin\mu & 0 & 0 \\ \frac{(\alpha_1-\alpha_2)\cos\mu-(1+\alpha_1\alpha_2)\sin\mu}{\sqrt{\beta_1\beta_2}} & \sqrt{\frac{\beta_1}{\beta_2}}(\cos\mu - \alpha_2\sin\mu) & 0 & 0 \\ 0 & 0 & \sqrt{\frac{\beta_2}{\beta_1}}(\cos\mu + \alpha_1\sin\mu) & \sqrt{\beta_1\beta_2}\sin\mu \\ 0 & 0 & \frac{(\alpha_1-\alpha_2)\cos\mu-(1+\alpha_1\alpha_2)\sin\mu}{\sqrt{\beta_1\beta_2}} & \sqrt{\frac{\beta_1}{\beta_2}}(\cos\mu - \alpha_2\sin\mu) \end{bmatrix} \tag{11}$$

The left-handed and right-handed betatron phases at $s_2$ are then given by $\phi_{+2} = \phi_{+1} + \mu - \theta$ and $\phi_{-2} = \phi_{-1} + \mu + \theta$.

There are two ways to realize this desired map (9):

- a quadrupole channel that provides the map (11), followed by rotating the entire subsequent beamline (not including the quadrupole channel) by $\theta$.

- A uniform solenoid with strength $k_s$ and length $L$ (including its two ends) will produce this map with $\theta = -k_sL/2, \mu = k_sL/2, \beta_1 = \beta_2 = 2/k_s, \alpha_1 = \alpha_2 = 0$,

ISBN: 978-3-95450-199-1 doi:10.18429/JACoW-SAP2017-MOCH1

where the solenoid strength is specified by $k_s = \frac{B_s}{(B\rho)_0}$ with $B_s$ the solenoid magnetic field and $(B\rho)_0$ the magnetic rigidity of the electron beam.

### *Round-to-flat Adapters*

A round-to-flat adapter is given by the map $V(s_2)U(s_1)^{-1}$, which can be shown to have a general form of a round-to-round adapter, followed by a specific round-to-flat insertion with map $(VU^{-1})_0$, followed by a flat-to-flat adapter.

These three adapters have the following parameters:

- The first round-to-round transformation is from $(\alpha, \beta, \phi_+, \phi_-)$ to $(\alpha = 0, \beta, \phi_+ = \phi_y + \mu + \pi/4, \phi_- = \phi_y + \mu - \pi/4)$.
- The second round-to-flat transformation $(VU^{-1})_0$ is from $(\alpha = 0, \beta, \phi_+ = \phi_y + \mu + \pi/4, \phi_- = \phi_y + \mu - \pi/4)$ to $(\alpha_x = \alpha_y = 0, \beta_x = \beta_y, \phi_x = \phi_y)$.
- The last flat-to-flat transformation from $(\alpha_x = \alpha_y = 0, \beta_x = \beta_y, \phi_x = \phi_y)$ to $(\alpha_x, \beta_x, \phi_x, \alpha_y, \beta_y, \phi_y)$.

Combining all steps, we then have finally an adapter from $(\alpha, \beta, \phi_+, \phi_-)$ to $(\alpha_x, \beta_x, \phi_x, \alpha_y, \beta_y, \phi_y)$. Each step, although stated in language of mathematics, is directly translatable to conventional lattice designs.

The special round-to-flat map $(VU^{-1})_0$ has a simple form [3, 9, 10]

$$(VU^{-1})_0 = R\left(-\frac{\pi}{4}\right)\begin{bmatrix} -\sqrt{\frac{\beta_y}{\beta}}\sin\mu & -\sqrt{\beta\beta_y}\cos\mu & 0 & 0 \\ \frac{\cos\mu}{\sqrt{\beta\beta_y}} & -\sqrt{\frac{\beta}{\beta_y}}\sin\mu & 0 & 0 \\ 0 & 0 & \sqrt{\frac{\beta_y}{\beta}}\cos\mu & -\sqrt{\beta\beta_y}\sin\mu \\ 0 & 0 & \frac{\sin\mu}{\sqrt{\beta\beta_y}} & \sqrt{\frac{\beta}{\beta_y}}\cos\mu \end{bmatrix} R\left(\frac{\pi}{4}\right) \quad (12)$$

It is easy to see that $(VU^{-1})_0$ represents a regular quadrupole channel (miminum of three quadrupoles in general) rotated 45°. The 45° rotation renders the quadrupoles skew quadrupoles. Design of the adapter therefore reduces to a regular lattice matching problem.

Inserting a round-to-flat adapter brings a beam from a round optics to a flat optics. A round beam with left-handed and right-handed emittances of $(\epsilon_+, \epsilon_-)$ is transformed to a planar beam with $x$- and $y$-emittances given by $(\epsilon_x = \epsilon_+, \epsilon_y = \epsilon_-)$.

### *Flat-to-round Adapter*

Reversing the round-to-flat adapter, a flat beam with $x$- and $y$-emittances of $(\epsilon_x, \epsilon_y)$ is transformed to a round beam with left-handed and right-handed-emittances $(\epsilon_+ = \epsilon_x, \epsilon_- = \epsilon_y)$. This adapter can also be achieved by an insertion with three skew quadrupoles.

### *Applications of Flat-to-round and Round-to-flat Adapters*

As mentioned, the idea of adapters was first suggested by Derbenev 1993 to control the beam-beam effect in storage ring colliders. But it has subsequently been much extended for other applications.

*Storage Ring Colliders* In this collider application [2], a planar flat beam in regular arc cells is transformed by a flat-to-round adapter to become a round beam at the collision region. The collision region is immersed in a solenoidal field. After the collision region, the beam is brought back to the regular arc by a round-to-flat adapter. With a round beam at the collision point, this possibly reduces the beam-beam effect due to much reduced number of nonlinear resonances.

*Linear Colliders* In this application [5], a round beam is produced at the cathode immersed in a solenoidal field. After exiting the solenoid, a round-to-flat adapter transforms the beam into a flat planar configuration, which is what is needed for linear collider applications. The use of adapter here avoids the need of a damping ring to provide flat beams.

*Electron Cooling* Applying a flat-to-round adapter to a very flat beam ($\epsilon_x \gg \epsilon_y$), a round beam can be produced with $\epsilon_+ \gg \epsilon_-$. Immersing the beam in a matched solenoid with appropriate magnetic field, particles in the beam will move in the solenoid with very small angular divergence, i.e., the beam becomes extremely laminar with all particles moving almost straight ahead along the solenoidal field with zero Larmor radius and as a result almost zero transverse temperature. This is an ideal beam for performing electron cooling [3, 7].

*Diffraction Limited Synchrotron Radiation* While the application to electron cooling is most likely performed in a linac environment, the same configuration can also be installed in a synchrotron radiation storage ring. By an insertion with the configuration (flat-to-round adapter + solenoid + round-to-flat adapter), a conventional 3rd generation synchrotron radiation storage ring can in principle reach diffraction limit for X-rays [6, 13].

Perhaps one can illustrate the point as follows. To reach diffraction limit for X-rays, much efforts have been dedicated to the design of "ultimate storage rings" aiming for exceedingly small $\epsilon_x$. The beam also has an even much smaller $\epsilon_y$. To reach diffraction limit, we operate the beam fully coupled, so that the coupled beam has both its horizontal and vertical emittances given by the arithmatic mean of $\epsilon_x$ and $\epsilon_y$, i.e. they are both equal to $(\epsilon_x + \epsilon_y)/2$. In contrast, the round beam adapter scheme yields a beam with its horizontal and vertical emittances equal to the geometric mean of $\epsilon_x$ and $\epsilon_y$, i.e. they are both given by $\sqrt{\epsilon_x\epsilon_y}$. Since $\epsilon_y \ll \epsilon_x$, it is clear that the adapter round beam scheme has a great advantage in reaching small emittances. If, for example, $\epsilon_y = 10^{-3}\,\epsilon_x$, then one potentially gains a factor of 15 reduction in the beam emittances.

ISBN: 978-3-95450-199-1 doi:10.18429/JACoW-SAP2017-MOCH1



In principle, therefore, the adapter round beam scheme could be applied to conventional 3rd generation storage ring facilities to provide coherent soft X-rays. If so, one can save the effort of developing ultimate rings. In practice, however, the catch is that there is missing a way to match the electron optics to that of the laser optics [15]. As it stands, the requires solenoid field turns out too strong and the required solenoid length is too long.

## REFERENCES

[1] See, for example, R. Garoby, *RF Gymnastics in a Synchrotron*, in *Handbook of Accelerator Physics and Engineering*, 2nd Edition, p. 376, World Scientific, Singapore (2013).

[2] Y. Derbenev, Michigan Univ. Report No. 91-2 (1991); UM HE 93-20 (1993); Workshop on Round Beams and Related Concepts in Beam Dynamics, Fermilab (1996).

[3] Y. Derbenev, Michigan Univ. Report UM HE 98-04 (1998).

[4] A. Burov and V. Danilov, FNAL Report No. TM-2040 (1998); FNAL Report TM-2043 (1998).

[5] R. Brinkmann, Y. Derbenev, and K. Flöttmann, *Phys. Rev. Special Topics – Accel. & Beams*, 4, 053501 (2001).

[6] R. Brinkmann, *Proc. European Part. Accel. Conf.*, TUPRI044 (2002).

[7] A. Burov, S. Nagaitsev, A. Shemyakin, and Ya. Derbenev, *Phys. Rev. Special Topics – Accel. & Beams*, 3, 094002 (2000).

[8] A. Burov, S. Nagaitsev, and Ysroslov Derbenev, *Phys. Rev. E* 66, 016503 (2002).

[9] Kwang-Je Kim, *Phys. Rev. Special Topics – Accel. & Beams*, 6, 104002 (2003).

[10] D. Edwards *et al.*, *Proc. 2001 Part. Accel. Conf.*, Chicago, IL (IEEE, Piscataway, NJ, 2001), p.73.

[11] J. Ruan, A. S. Johnson, A. H. Lumpkin, R. Thurman-Keup, H. Edwards, R. P. Fliller, T. Koeth, Y.-E Sun, *Phys. Rev. Lett*, 106, 244801 (2011).

[12] P. Piot, Y.-E. Sun, K.-J. Kim, *Phys. Rev. Special Topics – Accel. & Beams*, 9, 031001 (2006).

[13] Alexander Wu Chao and Panteleo Raimondi, SLAC-PUB-14808, unpublished (2011).

[14] D.F. Ratner and A.W. Chao, *Phys. Rev. Lett.* 105, 154801 (2010).

[15] See, for example, J. Chavanne, Mini-Workshop on Round Beams, SOLEIL, France, 2017.

ISBN: 978-3-95450-199-1 doi:10.18429/JACoW-SAP2017-MOCH2

# FABRICATION, ASSEMBLY AND TEST OF THE 2×4-CELL SUPERCONDUCTING LINAC MODULE FOR THE CAEP FEL-THz FACILITY *

X. Luo, C. L. Lao, L. J. Shan, K. Zhou†, T. H. He, X. M. Shen, L. D. Yang,
H. B. Wang, D. Wu, D. X. Xiao, J. X. Wang, S. F. Lin, X. F. Yang, M. Li
Institution of Applied Electronics, CAEP, Mianyang, China
X. Y. Lu, S. W. Quan, F. Wang, Peking University, Beijing, China

*Abstract*

A 2×4-cell superconducting linac module for the THz-FEL facility has been developed at the China Academy of Engineering Physics, which is expected to provide 6~8 MeV quasi-CW electron beams with an average current of 1~5 mA. The module consists of two 4-cell cavities, two power couplers, two tuners and the cyromodule. The main components are tested before the module assembly. The cavity test includes microwave measurement at room temperature and vertical test at 2 K. The conditioning and test of the couplers are also finished. The performances of the main components and the whole module are presented in this paper. The horizontal test indicated that the effective field gradients of both cavities have reached 10 MV/m, which have satisfied our designed goal.

## INTRODUCTION

The FEL-THz facility in the China Academy of Engineering Physics (CAEP) is under construction at Chengdu, China. It is expected to provide 1 ~ 3 THz FEL with average power greater than 10 W [1]. Because of the advantages on working at CW mode or long pulse mode with high accelerating gradient, RF superconducting technology is employed in this project. As shown in Fig. 1, the superconducting module is used to accelerate the CW 1~5 mA beam from 320 keV to 6~8 MeV. The design of the module is based on the requirement of CW mode operation, such as beam loading and HOMs issues [2]. Two 4-cell TESLA-type cavities are adopted instead of one original 9-cell cavity, because of the limit of coupler power tolerance.

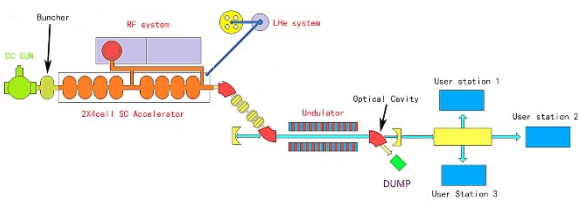


Figure 1: Layout of the CAEP THz-FEL facility.

Fig.2 shows the sectional view of the module. It consists of two 4-cell cavities, two power couplers, two tuners [3] and the cyromodule [4]. After the components are tested alone, the module are assembled and tested in Chengdu, China. The test technology and results are presented in this paper, as well as the components test.

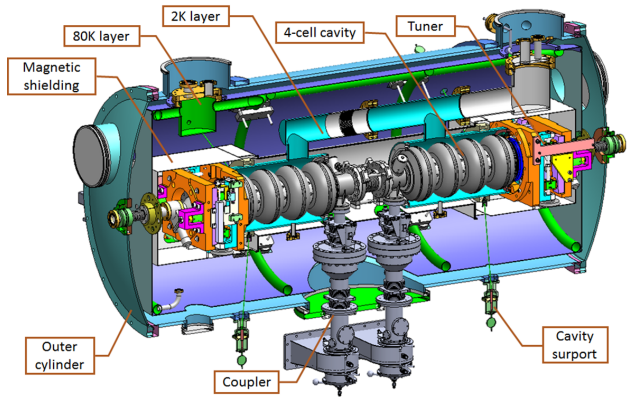


Figure 2: Schematic of the 2×4-cell module.

## CAVITY PERFORMANCE

The 4-cell cavities are fabricated by Peking University. The RF character are measured by low power microwave test at room temperature. The frequency and electric field distribution of the fundamental mode and higher order modes are measured. After carefully adjust every cell length, the field flatness of each cavity reaches 95% (see Fig.3), and the fundamental mode frequency is adjusted to 1297.3 MHz, in order to make the frequency 1300 MHz after cooling down.

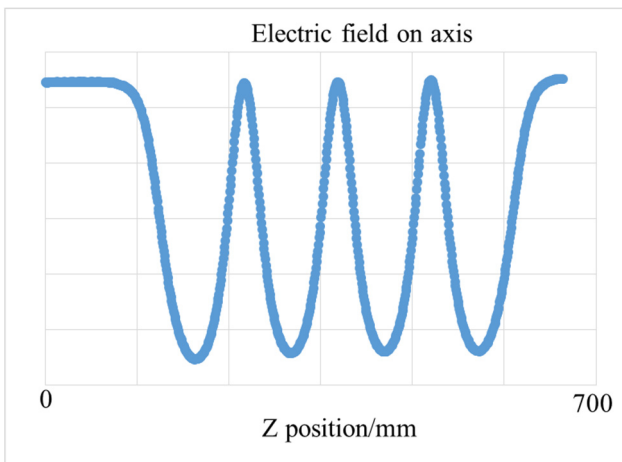


Figure 3: The electric field distribution of the fundamental mode in the 4-cell cavity.

The frequency and the field distribution of the HOMs are also measured. The modes type are identified by comparing with the simulation results before. The perfor-

* Work supported by China National Key Scientific Instrument and Equipment Development Project (2011YQ130018), National Natural Science Foundation of China with grant (11605190,11475159, 11505173 and 11576254).
† Email address: zhoudakui@163.com

ISBN: 978-3-95450-199-1 doi:10.18429/JACoW-SAP2017-MOCH2



mance of the HOM coupler are measured by S-parameters. To avoid fundamental mode leak out from HOM couplers, the $S_{21}$ of the fundamental mode is adjusted to lower than -100dB, as shown in Fig. 4. The $Q_e$ of the HOMs are $10^3$~$10^6$, which means the HOM couplers are able to damp HOM power effectively.

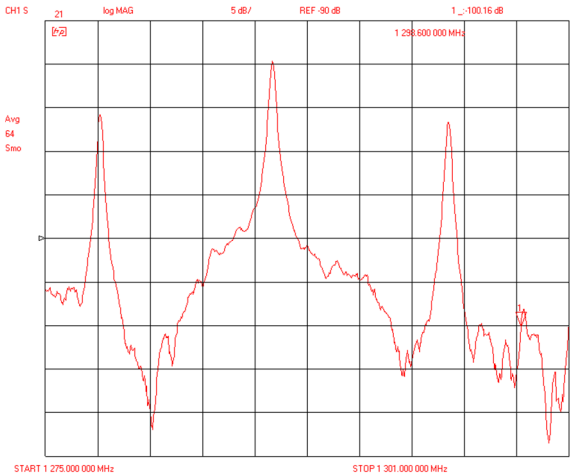


Figure 4: The $S_{21}$ parameter of the HOM coupler.

In order to make sure the accelerating gradient can reach our target (10MV/m), one 4-cell cavity was transported to JLAB (USA) for 2K vertical test. A series of surface treatment were processed at JLAB, such as BCP, ultrasonic cleaning and drying, outgassing baking, HPR, etc. The $Q_0$ versus $E_{acc}$ curve measured by VTA is shown in Fig. 5. $Q_0$ is larger than $2\times10^{10}$ for gradients of 8~18 MV/m. The test is stopped at 30MV/m, due to the field emission effect.

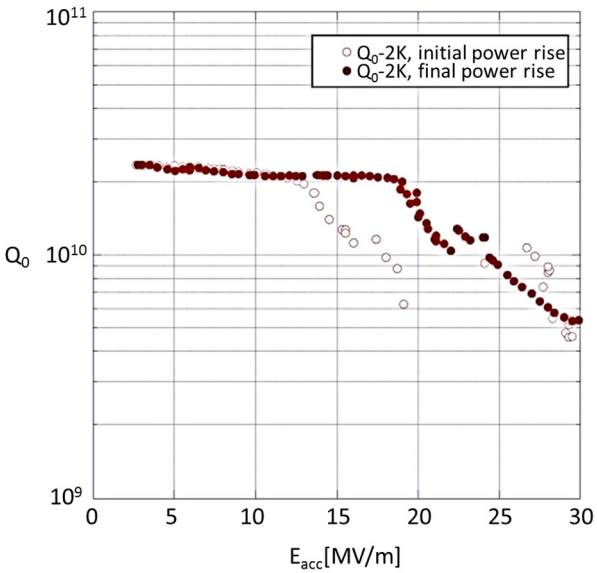


Figure 5: $Q_0$ versus $E_{acc}$ for a 4-cell cavity at 2 K temperature.

## COUPLER PERFORMANCE

The power couplers (CPI Company produced) are coaxial type with the presence of both warm and cold windows. They are fabricated by CPI company (USA) based on the design of the CORNELL ERL couplers [5]. The couplers are conditioned at Chengdu to get the maximum transfer power. Figure 6 shows the conditioning structure. Liquid nitrogen is used for cooling the dissipation power at cold window part. Temperature sensors and arc sensors are connected into interlock protect loop, in case that the power is too high. By about two months conditioning, the maximum power reaches 30 kW in CW mode (as shown in Fig.7), which was limited not by the coupler performance but by the power source.

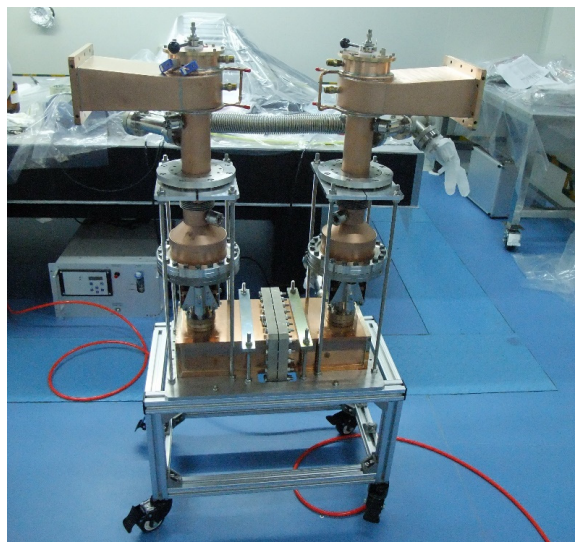

Figure 6: The conditioning structure equipped with couplers.

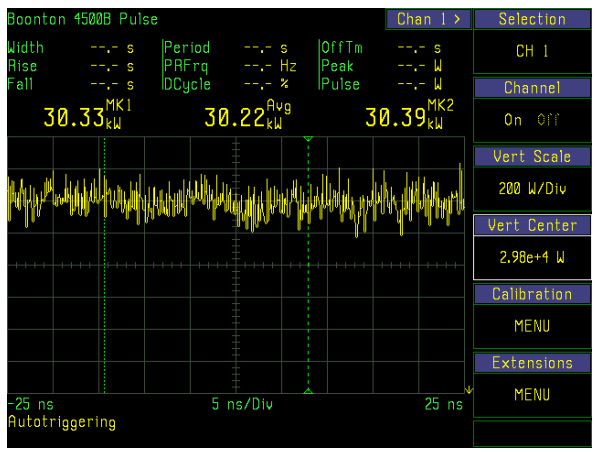


Figure 7: The max power reaches 30 kW in CW mode.

After power conditioning, the couplers were disassembled, and the cold parts were transported to Peking University to install on cavities.

## ASSEMBLY

The assembly procedure is composed of two stage. Since there is no 100-class ultra-clean room in our lab in Chengdu, the cavity string assembly was done in Peking University. As shown in Fig. 8. The coupler cold parts, tuner planks and valves were installed on the jacketed cavities. And the string was carried back to Chengdu as a whole. Then the rest parts were assembled at the facility hall, such as 80K layer, magnetic shielding, coupler warm

ISBN: 978-3-95450-199-1 doi:10.18429/JACoW-SAP2017-MOCH2

parts, sensors, and so on. Figure 9 shows the accomplished superconducting module which has been connected with the cryogenic system and the microwave system.

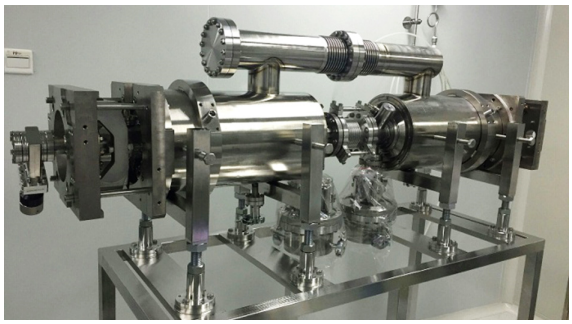

Figure 8: The cavity string assembled in 100-class ultra-clean room.

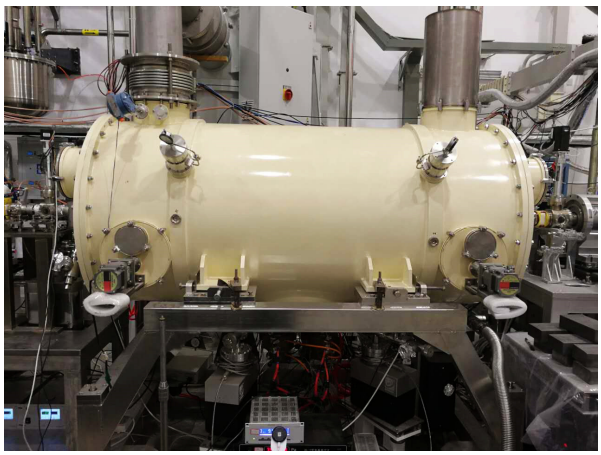

Figure 9: The superconducting module accomplished ssembly.

## HORIZONTAL TEST

The cool down procedure from room temperature costs about ten days. All the components work well at 2K state. The vacuum of every layer can satisfy our requirement. The static heat loss is 17.4 W, including the heat loss along the helium transmission line (about 5 W).

The field in the cavity is build up and controlled by the LLRF system and protective interlock system. The forward and reflect signal is monitored by the power meter and the oscilloscope. The linear relation between the accelerating gradient $E_{acc}$ and the amplitude of the pickup signal $V_{pickup}$ are calibrated at 4 K state, by Eq. (1) and Eq. (2). The measured $E_{acc}$ versus $V_{pickup}$ at 4 K state is shown in Fig. 10.

$$E_{acc} = K \cdot V_{pickup} \tag{1}$$

$$E_{acc} = \frac{\sqrt{P_0 \cdot Q_0 \cdot \frac{R}{Q_0}}}{L_{cav}} \tag{2}$$

[6] K. Zhou *et al.,* "Progress of the 2×4-cell superconducting accelerator for the CAEP THz-FEL facility", in *Proceedings of the 18th International* Conference *on RF Superconductivity*, Lanzhou China, July 17-21, 2017, paper MOPB037.

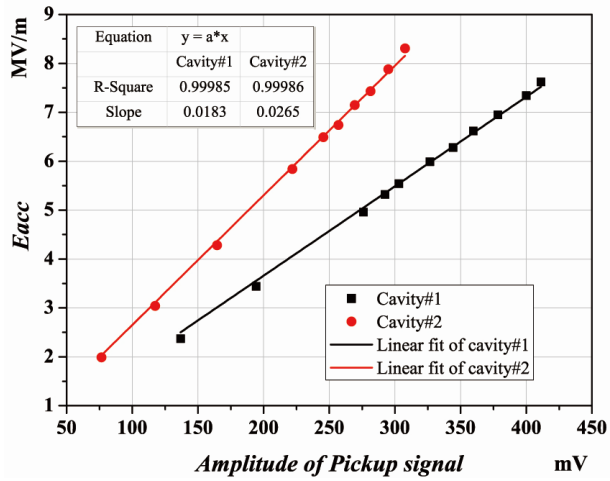


Figure 10: Eacc versus Amplitude of pickup signal at 4 K.

Then the module was cooled down to 2K, and the max $E_{acc}$ are measured. The effective field gradients of both cavities have reached 10 MV/m, which have satisfied our designed goal. More detailed results of horizontal test can be seen in Ref. [6].

## SUMMARY

The 2×4-cell superconducting accelerator for THz-FEL facility has finished its construction and horizontal test. The accelerating gradient of the 4-cell cavity reaches 18MV/m while $Q_0$ is $2\times10^{10}$ in vertical test. And the max power of couplers reaches 30 kW after conditioning. The 2K horizontal test shows that the whole superconducting cyomodule works well and stably. The effective field gradients of both cavities have achieved our target, 10 MV/m.

## ACKNOWLEDGEMENT

The authors would like to thank Peking university and Institute of High Energy Physics (IHEP) for their help with the coupler conditioning and cryomodule assembly.

## REFERENCES

[1] X. Zhou *et al.,* "Design of high average power terahertz-FEL facility", in *Journal of Terahertz Science and Electronic Information Technology*, 2013, 11(1): pp.1-6

[2] X. Luo *et al.,* "Design and fabrication of the 2×4-cell superconducting linac module for the free-electron laser", *Nuclear Instruments and Methods in Physics Research Section A*, 2017, 871: pp.30-14.

[3] M. Zhenghui *et al.,* "Design and test of frequency tuner for CAEP high power THz free-electron laser", *Chinese Physics C*, 2015, 39: pp.95-100.

[4] X. Luo *et al.,* "Design of the 2x4-cell superconducting cryomodule for the free-electron laser", in *Proceedings of the 18th International Conference on RF Superconductivity*, Lanzhou, China, July 17-21, 2017, paper MOPB010.

[5] V. Veshcherevich *et al.,* "Design of high power input coupler for Cornell ERL injector cavities", in *Proceedings of the 12th International Workshop on RF Superconductivity*, edited By H. Padamsee and S. Belomestnykh, New York, USA, 2005, p.54.

ISBN: 978-3-95450-199-1 doi:10.18429/JACoW-SAP2017-MODH3

# ANALYSIS OF BEAM OPTICS FOR A HIGH POWER ION SOURCE*

Y. H. Xie, C. D. Hu# , NBI Team, ASIPP, Hefei, China

*Abstract*

The high power ion source is the key parts of neutral beam injector. Generally speaking, the beam power should matching the extraction voltage for a given accelerator. In order to get higher beam power with lower beam extraction voltage, the beam optics of accelerator was analyzed based on the structure of EAST-NBI tetrode accelerator. The beam optics of a tetrode accelerator and a new designed three-electrode accelerator was analyzed with beam energy of 50 keV. The results shown that, the two types of accelerator can get high beam perveance (4.6μp) with lower beam divergence angle compare to the EAST-NBI accelerator (2.8 μp ). And the tetrode accelerator can gets lower beam divergence angle compare to the three-electrode accelerator, but the electric field between two electrode is much higher than three-electrode accelerator. The results can help for the ion source design of high power ion source.

## INTRODUCTION

The Experimental Advanced Superconducting Tokamak (EAST) is the first fully superconducting tokamak in the world. It aims at the long-pulse operation (1000s) to study the physics and engineering questions of steady-state operation for controlled nuclear fusion sciences[1]. High auxiliary heating power was needed to support the physical research of EAST. So, a Neutral Beam Injection (NBI) system was designed and developed in the Institute of Plasma Physics, Chinese Academy of Sciences (ASIPP) for the EAST plasma heating and current driving[2-5].

The EAST-NBI system consist two ion sources, which has the same structure and designed parameters. According to the physical requirements of the EAST, a hot cathode multi-cusp ion source with four stage accelerator girds was employed for the EAST-NBI since the year of 2010. In September of 2013, one beam line with two ion sources are installed on the EAST and high power neutral beam of 2MW were injected into EAST in July of 2014. In the same year, other beam line with two modified accelerator with diamond plasma grids were installed on the EAST and it was contributed in the next campaign experiment of the EAST in 2015. The parameters of NBI can be achieved was mainly decided by the performance of ion source. In order to achieve high beam power with lower beam energy, the beam optics of a new designed accelerator based on the EAST-NBI accelerator was analyzed.

*Work supported by the National Natural Science Foundation of China (NNSFC) (Contract No. 11405207, 11507215 & 11675215)
#cdhu@ipp.ac.cn

## THE HIGH POWER ION SOURCE OF EAST-NBI

The hot cathode bucket ion source with tetrode accelerator was employed on the EAST-NBI system[6-7]. The ion source contains a plasma generator and a tetrode accelerator. The plasma generator has a rectangle cross section arc chamber with the dimension of 650 mm × 260 mm × 300 mm (W×L×H). In the top side, 32 pure tungsten filaments with diameter of 1.6 mm are installed near the back electron plate, which was used to provide sufficient primary electrons. The accelerator is a multiple slit type. It has a high transparence of 60%. Each layer of accelerator grid has 64 rails, which made of molybdenum and has cavity structure. The cooling water runs through the inner of rails, so, it has good performance of heating remove. The schematic map of ion source is shown in Figure 1. The cross-sectional picture of accelerator is shown in Figure 2. The designed beam energy of ion source is 50-80 keV, beam power is 2-4 MW. The beam cross section is 120mm×480mm and can be changed. The designed divergence angle in X direction is 0.6 degree and Y direction is 1.2 degree.

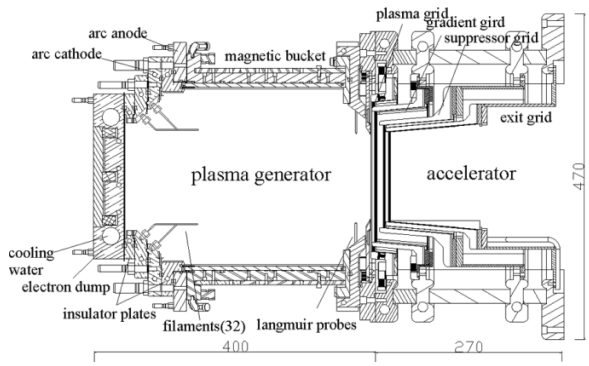


Figure 1: Schematic of high current ion source.

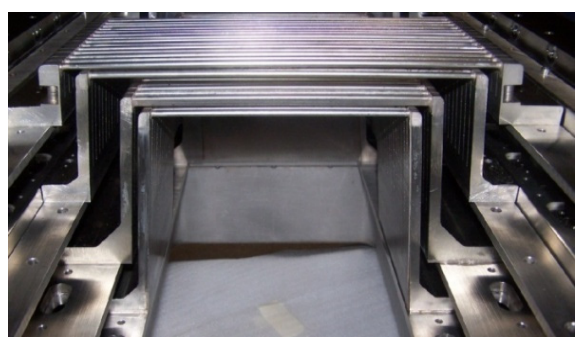

Figure 2: Cross sectional picture of accelerator with four stages of grids.

ISBN: 978-3-95450-199-1 doi:10.18429/JACoW-SAP2017-MODH3

## ACCELERATOR MODIFICATION BACKGROUND

When the neutral beam injected into the EAST plasma, the beam energy should matching the EAST plasma density to heating the core plamsa. For the ion source, the extracted beam current also should matching the extraction voltage (beam energy), thus, the beam power can not change with given beam energy. In order to achieve high beam power with lower beam energy, the ion source should be modificated.

The accelerator of EAST-NBI has a four stage electrode grids, which are plasma grid (PG), gradient grid (GG), suppressor grid (SG) and exit grid (EG). The schematic map of accelerator is shown in Figure 3. The extracted ion current $I_E$ can be calculated by equation (1)[8].

$$I_E = \frac{4\varepsilon_0}{9}\sqrt{2\eta}\frac{V^{3/2}}{d^2} \quad (1)$$

When $\varepsilon_0$ is the permittivity of vacuum, $\eta = q/m_i$, $d$ is the distance between two extraction grids, $V$ is the extraction voltage.

In order to increase the extracted ions, the distance between grids should be decreased, which is shown in Figure 3.

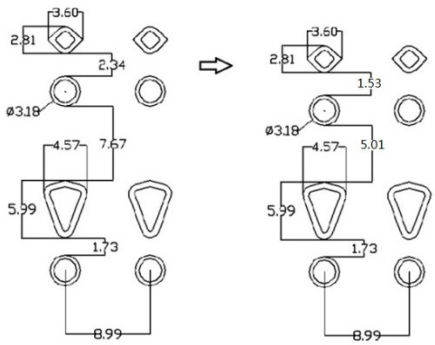


Figure 3: Schematic map of original and modified accelerator for the high current ion source.

## THE SIMULATION MODE OF ACCELERATOR FOR EAST-NBI

The prototype draw of accelerator is shown in Figure 4. The thickness of PG, GG, SG and EG are t1, t2, t3 and t4, respectively. The distance between PG and GG, GG and SG, SG and EG are d1, d2 and d3, respectively. The half-gap of rails of each layer are a1, a2, a3 and a4. The a1 = 2.7mm, a2 = 2.9 mm, a3 = 2.26 mm, a4 = 2.9 mm, d3 = 1.73 are not changed during the simulation.

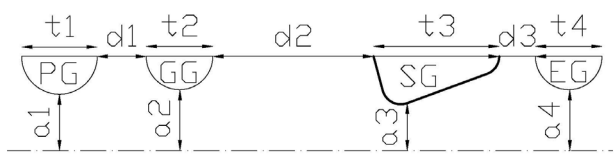


Figure 4: The simulation prototype of accelerator.

## SIMULATION RESULTS WITH MODIFIED TETRODE ACCELERATOR

The optics of the accelerator was simulated with the EAST-NBI accelerator[9,10] and the modified accelerator. The voltage applied on the GG is 80% of the voltage on PG. The voltage applied on SG is -2.5 kV. The beam perveance (perv = $A/V^{3/2} \times 10^6$, A: beam current [A], V: applied beam voltage [V]) and the beam divergence angle are two important parameters to estimate the beam optics. The simulation parameters and the results were shown in table 1. The divegence angle was analyzed with different beam perveance and extracted ion density, which shown in Figure 5 and Figure 6.

It can be seen that, the modified accelerator can got high optimum beam perveance of 4.6 μp compare with the original structure of accelerator (2.8 μp). The beam power can be increased about 62%. The beam divegence angle is 0.8 degree and almost keep no change. The extraced ion density is increased from 0.11 A/cm$^2$ to 0.18 A/cm$^2$ and also acceptable by the plasma generator. But the maximum electric field is 123 kV/cm compare to the original accelerator of 88 kV/cm. It may has the high risk of beam break down and may not good for the stable beam extraction.

Table 1: Simulation Results of Tetrode Accelerator with 50 keV Beam Energy

| Item | Used in ASIPP | Modified |
|---|---|---|
| d1 | 2.34 mm | 1.53 mm |
| d2 | 7.67 mm | 5.01 mm |
| d3 | 1.73 mm | 1.73 mm |
| Optimum beam perveance | 2.8 μp | 4.6 μp |
| Ion density at optimum beam perveance | 0.11 A/cm$^2$ | 0.18 A/cm$^2$ |
| Divergence angle | 0.8 degree | 0.8 degree |
| Maximum electric field | 88 kV/cm | 123 kV/cm |

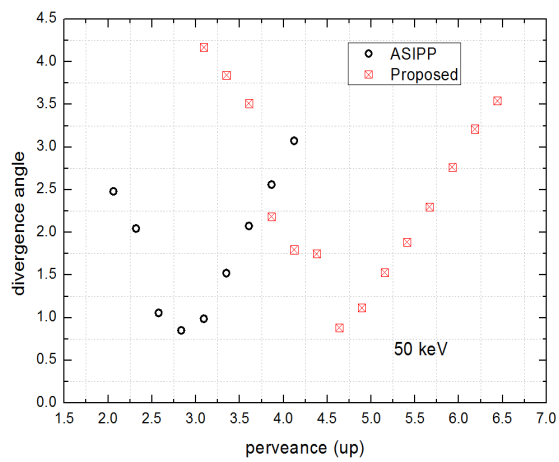


Figure 5: Divergence angle as a function of beam perveance with 50keV beam energy.

ISBN: 978-3-95450-199-1 doi:10.18429/JACoW-SAP2017-MODH3



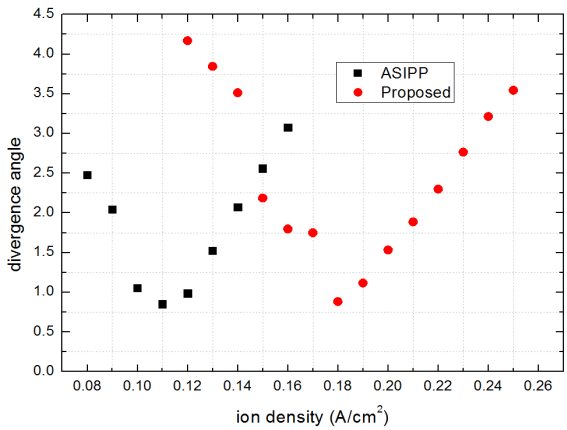


Figure 6: Divergence angle as a function of ion density with two type of accelerator.

## SIMULATON RESULTS WITH THREE-ELECTROD ACCELERATOR

Consider the beam energy is 50 keV, a three-electrod accelerator was designed, which is PG, SG and EG. In order to extract high beam current, the distance between PG and SG was estimated according to the original and modified tetrode accelrator, which is during 52.5 × 1.53/10 = 8.02 mm to 52.5×2.43/10 = 12.76 mm. The beam optics was simulated with different parameters which listed in Table 2. The divergence angle, extracted ion density and the optimum beam pervance was analized and shown in Table 2 too.

It can be seen that, the divergence angle is much larger (about two times) compare to the tetrode accelerator, more beam will losed during the beam transmission channel. The beam perveance is about 3.6 μp with the lowest divergence angle (1.55 degree) and is lower than the modified tetrode accelerator. The ion extraction density is from 1.3 A/cm2 to 1.9 A/cm2 when the beam divergence angle close to 1.6 degree, which also acceptable. The maximum electric field is 68.82 kV/cm with the optimum beam perveance. It was much lower compare to the tetrode accelerator (88-123 kV/cm).

Table 2: Simulation Results of Three-electrod Accelerator with 50 KeV Beam Energy

| D1 mm | D2 mm | Ion density A/cm² | Optimum beam perveance μp | Divergence angle | Maximum field kV/cm |
|---|---|---|---|---|---|
| 7.75 | 1.73 | 0.28 | 7.2 | 2.45 | 106.86 |
| 8.75 | 1.73 | 0.25 | 6.44 | 2.29 | 98.16 |
| 9.75 | 1.73 | 0.25 | 6.44 | 2.11 | 90.42 |
| 10.75 | 1.73 | 0.21 | 5.41 | 1.63 | 84.04 |
| 11.75 | 1.73 | 0.19 | 4.89 | 1.6 | 77.59 |
| 12.75 | 1.73 | 0.17 | 4.38 | 1.58 | 73.21 |
| 13.75 | 1.73 | 0.14 | 3.61 | 1.55 | 68.82 |
| 14.75 | 1.73 | 0.13 | 3.35 | 1.58 | 64.96 |

## DISCUSSIONS AND CONCLUSIONS

The ion optics of modified tetrode accelerator and designed three-electrod accelerator were simulated with beam energy of 50 keV for the high current extraction. The minimum divergence angle of 0.8 degree is almost the same compare with the original accelerator. The optimum perveance increased from 2.8 μp to 4.6 μp. The ion density is increased from 0.11 A/cm² to 0.18 A/cm². But the maximum electric field is 123 kV/cm and the accelerator has the risk of break down. The minimum divergence angle is about 1.6 degree for the three-electrod accelerator. The optimum beam perveance is about 3.6 μp, and the ion density is also acceptable for the original plamsa generator. The maximum electric field is 68.82 kV/cm and much lower than the original accelerator.

The results shown that, the modified accelerator can achieve high beam power. But the divergence angle of three-electrod accelerator is large and the maximum electric field of modified tetrode accelerator is very high. A new ion source with modified tetrode accelerator was assembled and will be tested soon. The simulation results can help for the design and optimization of high curent ion source.

## REFERENCES

[1] Y. X. Wan, J. G. Li and P. D. Weng, *Plasma. Sci. Technol*. 8, 253 (2006).
[2] C. D. Hu and NBI Team, *Plasma Sci. Technol*. 14, 567 (2012).
[3] Hu C D, Xie Y H, Xie Y L, *et al.,* Plasma Sci. Technol., 17, 817-825(2015).
[4] B. Wu, J. F. Wang, J. B. Li, J. Wang and C. D. Hu, *Fusion Eng. Des*. 86, 947 (2011).
[5] J. F. Wang, B. Wu and C. D. Hu, *Plasma Sci. Technol*. 12, 289(2010).
[6] C. D. Hu, Y. H. Xie and N. Team, *Plasma Sci. Technol*. 14, 75 (2012).
[7] Wei J L, Li J, Hu C D, *et al., Rev. Sci. Instrum.,* 85, 073504(2014).
[8] S.A Self., Physics of Fluids, 6, 1762-1768 (1963).
[9] R. Becker, W.B. Herrmannsfeldt, *Rev. Sci. Instrum*., 63, 2756–2758(1992).
[10]Y. H. Xie, C. D. Hu and H.W. Zhao, *Nucl. Instrum. Methods Phys. Res.*, Sect. A, 791, 22-26(2015).

ISBN: 978-3-95450-199-1 doi:10.18429/JACoW-SAP2017-MOPH01

# THE ACCELERATION AND EXTRACTION SIMULATION FOR PULSED BEAM WITH DIFFERENT PHASE WIDTH FOR CYCIAE-100

Shizhong An†, Luyu Ji, Sumin Wei, Ming Li, Fengping Guan, Tianjue Zhang, Chuan Wang, Dongsheng Zhang, LiPeng Wen, Yang Wang, Xiaotong Lu, Lei Cao
China Institute of Atomic Energy, Beijing, P.R. China

*Abstract*

A 100 MeV H- compact cyclotron (CYCIAE-100) has started operation from 2016 at China Institute of Atomic Energy (CIAE). The continuous proton beams of 75 MeV - 100 MeV has been extracted in dual opposite directions by charge exchange stripping devices. In order to analyze the extracted proton beam characteristics and control the beam loss for extracting 200 μA proton beam, the acceleration and stripping extraction process for the pulsed beam for CYCIAE-100 are simulated with the code of COMA in detail in this paper. The simulations are mainly done for the different RF acceptance or acceleration phase width. Due to the simulation results, the extraction turns are more for the large phase width and it will be reduced effectively with small phase width. The transverse beam distribution and the extracted beam profile are not affected by the initial phase width due to the simulation, that's the characters of the cyclotron with the stripping extraction mode.

## INTRODUCTION

The project of Beijing Radioactivity Ion-beam Facility (BRIF) has been constructed at China Institute of Atomic Energy (CIAE) for fundamental and applied research [1] [2]. As a major part of the BRIF project, the 100MeV compact cyclotron (CYCIAE-100) will provide proton beam with an intensity of 200μA ～ 500μA [3]. The extracted proton energy range is 75MeV～100MeV with dual direction foil stripping system [4]. The first beam of CYCIAE-100 was extracted on July 4, 2014 [5], the operation stability have been improved and beam current have been increased gradually. The main parameters for CYCIAE-100 are presented in Ref. [2]. For CYCIAE-100, the diameter of main magnet is 6160mm, corresponding to 4000mm for the magnet pole with the sector angle of 47o. The magnet is 2820mm high with a total weight of 435 tons. Two identical 100 kW RF amplifiers have been adopted to drive two cavities with the Dee angle of 38 o independently.

The CYCIAE-100 extraction system use two sets of stripping probes, can extract the beam from the symmetry direction to the various terminals. Two stripping probes with carbon foil are inserted radially in the opposite directions from the hill gap region and the two proton beams after stripping are transported into the crossing point in a combination magnet center separately under the fixed main magnetic field. The combination magnet is fixed between the adjacent yokes of main magnet in the direction of valley region at (R=2.75 m, θ=100°).

The basic optic trajectories of extracted proton beams with various energies have been studied with the code CYCTR [6] and the transport matrix from the stripping foil to the crossing point is got from the code GOBLIN [7] including the dispersion effects. With the multi particle tracking code COMA [8], the beam dynamics are studied and the acceleration and stripping extraction process for the pulsed beam are simulated. The accelerate phase for the pulsed beam are selected after the simulation and the exatracted proton beam turns are studied in detail for the pulsed beam with different initial phase width. The simulation results will give the references for the designing the beam pulsing system for CYCIAE-100. In order to analyze the extracted proton beam parameters for the pulsed beam, the simulation is mainly done for the different RF acceptance or acceleration phase width with the fixed initial transverse emittances.

## THE BASIC CONSIDERATION FOR THE SIMULATION

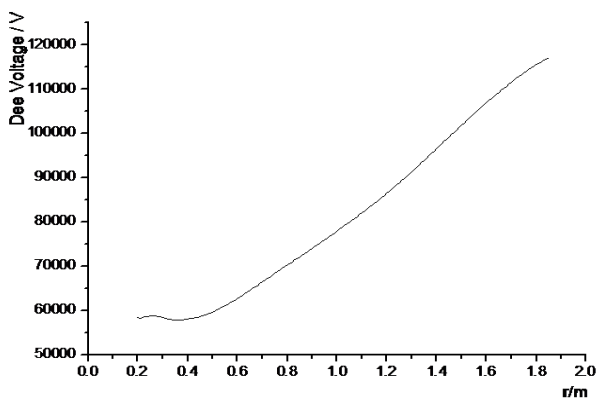


Figure 1: The voltage distribution versus along the radius of accelerating gap.

For CYCIAE-100, the outer radius of magnet yoke is 3.08 m and the combination magnet is located inside the yoke (R=2.75 m, θ=100º). The stripping foil is at the radial position of (1.609 m, 57.8 º) for extraction energy of 70MeV and (1.875m, 59.6 º) for extraction energy of 100MeV. The Dee Voltage is changed continuously from 60kV to 120kV along the radius of accelerating gap. Figure 1 shows the voltage distribution versus along the radius of accelerating gap.

† email address Szan@ciae.ac.cn

ISBN: 978-3-95450-199-1 doi:10.18429/JACoW-SAP2017-MOPH01



The initial matched beam condition with the fixed energy and fixed emittance can be obtained from the beam dynamic calculation at any position in the cyclotron. The chosen initial H- beam for the simulation is at the symmetry center of valley with azimuth θ=0 o, and the beam will be tracked along the inserting direction of stripping probe with azimuth θ =57.8 o. The initial beam parameters: E0=1.49MeV, R=23.1Cm, phase extension in RF with Δφ=±20o, normalized transverse emittance is 0.01Cm2 or 4pi-mm-mrad. The input phase distributions are random in both transverse and longitudinal directions with the initial zero energy spread and 20000 macro particles are used. Figure 2 shows the initial normalized distribution with the normalized emittance of 4.0π-mm-mrad.

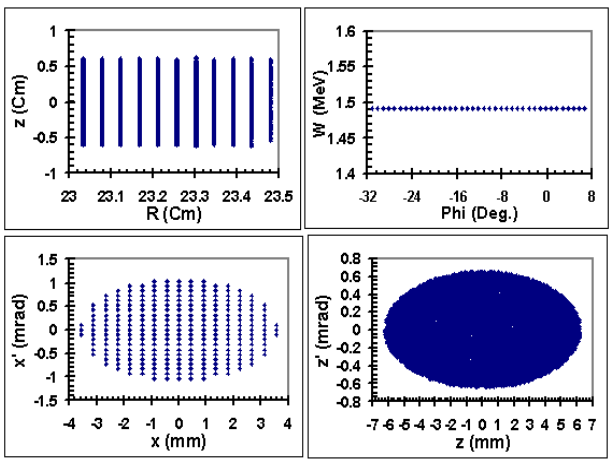


Figure 2: Initial normalized distribution with the normalized emittance of 4.0π-mm-mrad.

The extraction orbits and the extracted beam parameters are compared in detail between the measured fields and the theoretic fields [9]. Both the results are almost the same between the measured fields and the theoretic fields. So, all of the calculation results for CYCIAE-100 extraction orbits based on the theoretic fields can be used under the measured fields.

## THE ACCELERATING PROCESS FOR THE BUNCH

The RF acceptance is 40º for CYCIAE-100. In order to get the accelerating phase for the pulsed beam, four initial phases with the bunch length of 40º are simulated. Figure 3 shows the simulated results for the extracted 100 MeV beam with the different initial phase. Due to the simulation results, the central accelerating phase of the bunch with the bunch length of 40º should be -5º with the initial phase of -25º for the bunch. From the simulation, the particles will be extracted in the 302th turn and they will be extracted completely after 320th turn. The total extracted turns is about 18 for the whole bunch.

The accelerating process is simulated with COMA for the bunch with the initial phase of -25º. Figure 4 shows changes of the energy and RMS phase with the turns during the acceleration. The average extraction radius is 1.6m for the energy of 70MeV and 1.85m for the energy of 100MeV. This keeps the agreement with the calculation results which got from the code CYCTR. The RMS phase is constant during the acceleration, which means the bunch length is almost un changed during the acceleration.

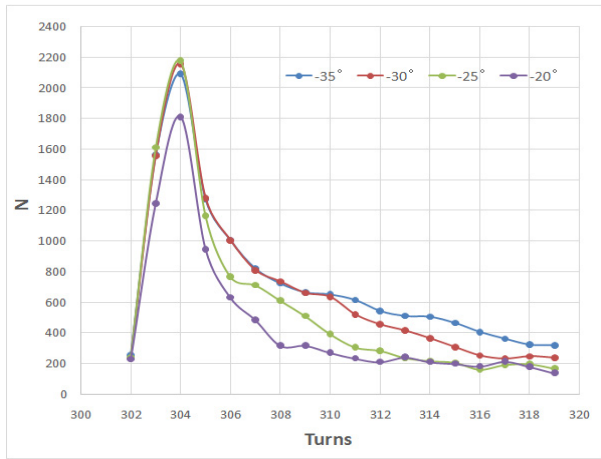


Figure 3: The simulated results for the extracted 100 MeV particles with the different initial phase of the 40º bunch.

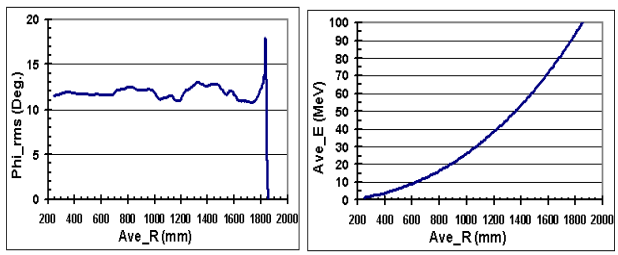


Figure 4: The changes of the energy and RMS phase with the turns during the acceleration.

## STRIPPING EXTRACTION SIMULATION WITH DIFFERENT PHASE WIDTH

In order to study the extracted pulsed beam characters and time structure, the stripping extraction simulations for 100MeV beam with different phase width are done with the multi-particle tracking code COMA too. The maximum of the initial phase width is chosen as Δφ=±20° and the minimum of the initial phase width is chosen as Δφ=±5°. Other initial input simulation conditions are the same as the case for the different bunch simulation. From the simulation results, the transverse distributions are almost the same for all kinds of case. Just the extracted longitudinal distributions and the extracted turns are different. Figure 5 shows the distributions with the initial phase width of ±20°, ±10°, ±5°. It is clear, the extracted phase width is larger with the long bunch and it is smaller with the smaller bunch. The average extracted energy and

ISBN: 978-3-95450-199-1 doi:10.18429/JACoW-SAP2017-MOPH01

the phase for the extracted bunch are almost the same for all of the case. The energy spread is about +-0.6% and the phase extension is about 55° for the extracted beam distribution with the initial phase width of ±20°. The energy spreads are almost the same for the different initial phase width.

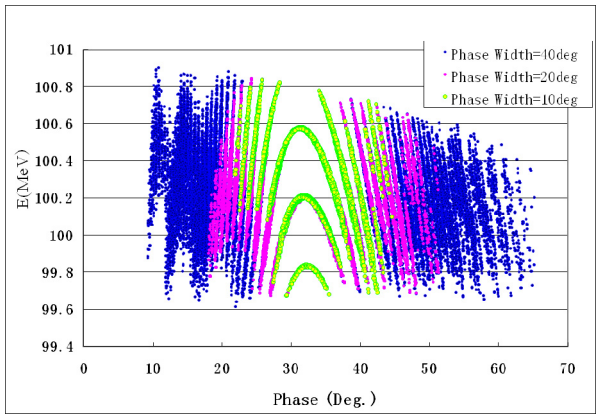


Figure 5: The extracted particle distributions on the stripping foil with different initial phase width.

Figure 6 shows the extracted beam particles with the turns for the different initial phase width. From the simulation results, it is less than 5 turns to extracted the whole bunch with the initial phase width of 10° and 5°. More than 95% particles will be extracted after 8 turns for the long bunch with 40° phase width. So it is possible to get the pulsed beam for CYCIAY-100. Of course, the phase slit is needed in order to get the very good time structure for the cyclotron with the stripping extraction system.

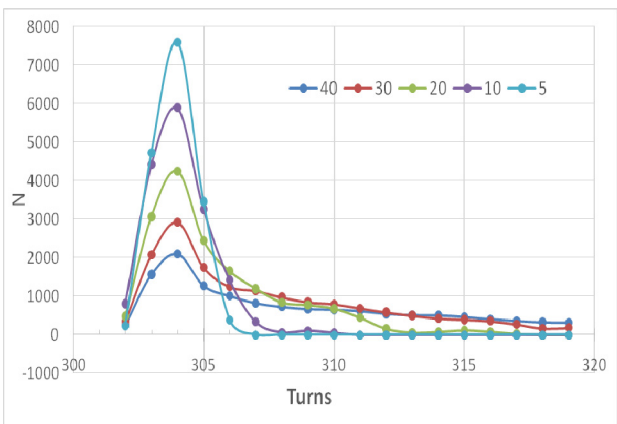


Figure 6: The extracted particle numbers at 100MeV with different initial phase widths.

## SUMMARY

For CYCIAE-100, the first beam had been got in 2014 and about 300 hours proton beam were provided last year. In order to get the pulsed beam with CYCIAE-100, the accelerating process for different initial bunch are simulated in detail. From the simulation results, RF acceptance for different bunch length is almost no effect to the transverse beam distribution. Large initial phase width will lead to more extracted turns and short initial phase width will lead to less extracted turns. It is very hard to get the single turn extraction for the compact cyclotron with the stripping extraction system even with very short bunch width if the sine waveform voltage is used for the acceleration. The transverse space distributions and the energy spread of the extracted beam are almost the same for the case of long initial phase width and short phase width. Large phase width means high beam intensity. The transverse beam distribution and the extracted beam profile are not affected by the initial phase width due to the simulation, that's the characters of the cyclotron with the stripping extraction mode. It is possible to get the pulsed beam for CYCIAY-100 because more than 95% particles can be extracted after 8 turns even with large RF acceptance. The phase slit is needed in order to get the very good time structure for the cyclotron with the stripping extraction system.

## ACKNOWLEDGEMENTS

The authors are very much grateful to Dr. Yi-Nong Rao from TRIUM, who give us considerable help and providing materials concerning the cyclotron and the use of the code COMA and CYCLOP. Also the authors would like to give the grateful acknowledge to Dr. Gerardo Dutto, George Mackenzie, R. Baartman from TRIUM, Dr. Wernor. Joho from PSI, Jingyu Tang from IHEP-Beijing, for the extraction discussion and lots of useful suggestions.

## REFERENCES

[1] Tianjue Zhang *et al.*, "A new project of cyclotron based radioactive ion- beam facility", in *Proc. APAC'04*, Gyeongju, Korea, pp.267-269.

[2] Tianjue Zhang *et al.*, "Progress on construction of CYCIAE-100", in *Proc. of 19th International Conference on Cyclotrons and Their Applications*, Sept. 6 - 10, 2010, Lanzhou, China, pp.308-313.

[3] Tianjue Zhang *et al.*, "Physics problem study for a 100 MeV, 500 microAmp H- beam compact cyclotron", in *Proc. ICAP'09*, 2009, San Francisco, pp. 224-228.

[4] "Stripping extraction system for CYCIAE-100", CYCIAE Design note in Chinese, 2006.

[5] Tianjue Zhang *et al.*, "The beam commissioning of brif and future cyclotron development at CIAE", *NIM in Physics Research Section B: Beam Interactions with Materials and Atoms*. 10.1016/j.nimb.2016.01.022. pp. 434-439.

[6] Shizhong An, Fengping Guan *et al.*, "Stripping extraction calculation and simulation for CYCIAE-100", *China Physics C (HEP & NP)*, 2009, 33 (Suppl. Ⅱ), pp. 42-46.

[7] *GOBLIN User Guide and Reference* V3.3, TRI—CD-90-01, TRIUMF.

[8] C.J. Kost, G. H. Mackezie, "COMA – a linear motion code for cyclotron", *IEEE Transactions on Nuclear Science*, Vol.NS-22, No.3, June 1975, pp. 1922 - 1925.

[9] Shizhong An, Junqing Zhong, Sumin Wei, Lei Cao, "The calculation for the CYCIAE-100 extraction orbit based on the measured magnet fields", *Annual report of CIAE*, 2013.

ISBN: 978-3-95450-199-1 doi:10.18429/JACoW-SAP2017-MOPH02

# BEAM EXTRACTION SIMULATION FOR A 230 MeV SUPERCONDUCTING CYCLOTRON

Ming Li†, Tianjue Zhang, Tao Cui, Tao Ge, Chuan Wang, Dongsheng Zhang, Jiuchang Qin, Sumin Wei, Shizhong An
China Institute of Atomic Energy, Beijing

*Abstract*

Introducing superconducting technologies, China Institute of Atomic Energy has designed a cyclotron to extract 230 MeV proton beam for cancer therapy. Extracted beam loss is one of the very crucial parameter in this machine. A low beam loss has benefit in reducing the dose level inside the cyclotron and preventing device damage, and consequently keeps the machine operate stable in long time. Two electrostatic deflectors are installed in the adjacent magnet hills to deflect the beam for extraction. The $\nu_r$ =1 resonance and precession motion are introduced in extraction region to enlarge the turn separation. After the deflectors, passive magnetic channels provide radial focusing force to restrain the beam dispersion in the edge field. In this paper, the design process and simulation results will be presented in detail.

## INTRODUCTION

Proton therapy is an effective way for cancer treatment with minimal side effect and widely investigated recent years. Due to the progress of superconducting techniques, very compact cyclotron can be manufactured with lower cost and less power consumption, which could be very suitable to be installed in hospital. In order to promote the development of proton therapy in china, CIAE (China Institute of Atomic Energy) has designed a superconducting cyclotron to extract 230 MeV, 300 nA proton beam [1]. The overall structure of the cyclotron is listed in Fig.1. The diameter and height of the magnet is 320 cm and 140 cm respectively, and the weight of the magnet is about 70 ton. The main parameters of the cyclotron are listed in Table 1 in detail. The excitation and field mapping of the coil has completed, the results of which shows the system operates stable and could generate the desired field. Meanwhile, the rough machining of the magnet is finished and the precision machining is ongoing.

As a proton therapy machine installed in hospital, beam extraction efficiency is very critical to reduce the dose level, which could prevent the devices from damage and hence increase the reliability of the machine in long time operation. There are four sectors in this machine. Spiral structure of the pole is adopted to increase the vertical focusing. Unlike the normal temperature magnet, the edge field of pole is very soft, i.e. the field drops slowly at the edge, leading to a long drift before extracted to the outside of the cyclotron. In order to drag the beam from acceleration, two deflectors placed at the adjacent hills are adopted to accelerate the beam deflection. Moreover, many magnetic channels are used to prevent the beam from blowing up resulted from the long drift in edge field.

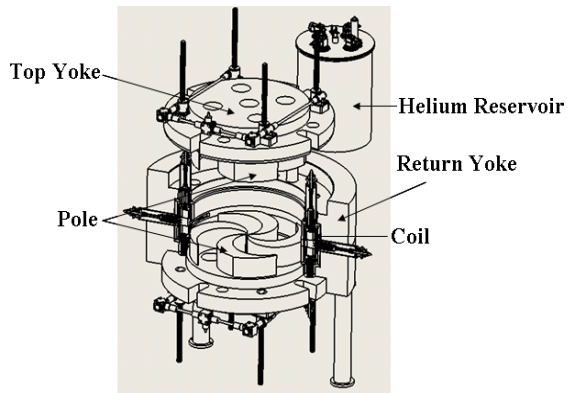


Figure 1: The overall structure of the cyclotron.

Table 1: The Main Parameters of the Cyclotron CYCIAE-230

| | |
|---|---|
| **Beam** | |
| Extracted beam energy | 240 MeV |
| Extracted beam current | 300 nA |
| **Magnet** | |
| Pole structure | Spiral |
| Pole radius | 85.0 cm |
| Outer radius of yoke | 160.0 cm |
| Hill gap | 5.0 cm |
| Central field | 2.3 T |
| **Coils** | |
| Coil type | NbTi low temperature superconducting |
| Ampere-Turn Number | ~600000 A.T×2 |
| **RF Cavity** | |
| Number of cavity | 4 |
| RF frequency | 72.0 MHz |
| Harmonic Mode | 2 |
| Cavity Voltage | 80～110kV |

## BEAM PRECESSION

Beam precession with off center injection is always used to enlarge the turn separation in separated sector cyclotrons. A particle travel in the cyclotron with radial oscillation, the position of which at nth turn can be expressed as:

$$r = r_{seo} + x \sin(n(\nu_r - 1)\theta + \varphi) \quad (1)$$

Where $r_{seo}$ is the according position of the static equilibrium, x and φ is the oscillation amplitude and phase, $\nu_r$ is the tune value in radial direction and θ is the azimuth of the particle. Then the turn separation can be deduced,

†email address 393054642@qq.com

ISBN: 978-3-95450-199-1 doi:10.18429/JACoW-SAP2017-MOPH02

$$\Delta r = \Delta r_{seo} + \Delta x \sin(n(\nu_r-1)\theta+\varphi) + n(\nu_r-1)x\cos(n(\nu_r-1)\theta+\varphi) \quad (2)$$

Where $\Delta r_{seo}$ is the separation from energy gain, the second term is from blow up of the amplitude taken from the resonance crossing, and the last term is from precession. From the formula we can know a large enough coherent oscillation amplitude is the precondition for the precession to generate a turn separation. Moreover in superconducting cyclotron, the compact structure results in beam overlap of neighbouring turns and precession in long time of acceleration could increase the effective emittance, thereby off center injection is not allowed in this cyclotron. Actually, beam centering is a very critical work in the commissioning of this cyclotron to improve the extraction efficiency. A clever solution is to introduce the precession in the last many turns instead of the whole acceleration process, where mixing of the phase space is far from sufficient to overlap together.

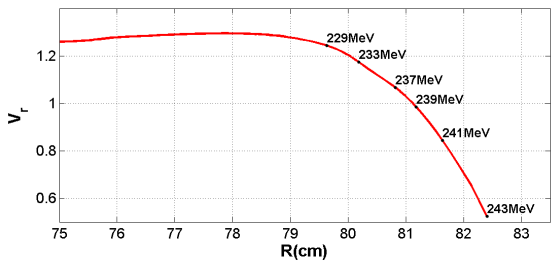


Figure 2: vr vs R at the extraction region.

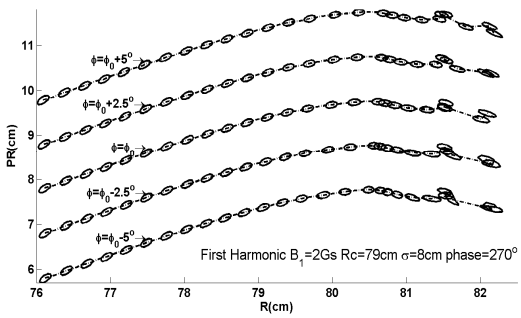


Figure 3: Phase space during the acceleration with different initial RF phase ($Ø_0$ is the central RF phase) , where a first harmonic distribution with maximum B1=2 Gs, center position Rc=79 cm, width σ=8 cm, phase =270°.

In CYCIAE-230, beam is accelerated near the pole edge where field is not isochronous and $\nu_r$ drops quickly as shown in Fig.2. A first harmonic near $\nu_r$=1 is added through Trim Rods [2] to excite a coherent oscillation, i.e. the x in formula (2), when the beam passes the resonance. Then procession near the $\nu_r$=0.75 could generate enough turn separation for the electrostatic deflector to extract the beam. We start the simulation from 200 MeV, selecting points on the radial phase space ellipse with normalized emittance of 0.5 πmm·mrad, which are accelerated to high energy, and then we can observe the precession near extraction. Figure 3. records the phase space during acceleration with different initial RF phase. From Fig.3 we can see the position and turn separation of beam with different initial phase is more or less overlapped, meaning beam loss at the entrance of the deflector is inevitable with large phase width beam. Figure 4 clearly shows the particles numbers along radius by simulation, which stars from 2 MeV with particle in an ellipse of 0.5 πmm·mrad, so the first electrostatic deflectors can be placed at r = 81.8 cm, where less particles is at the entry of septum and the beam envelop in the deflector is relatively small.

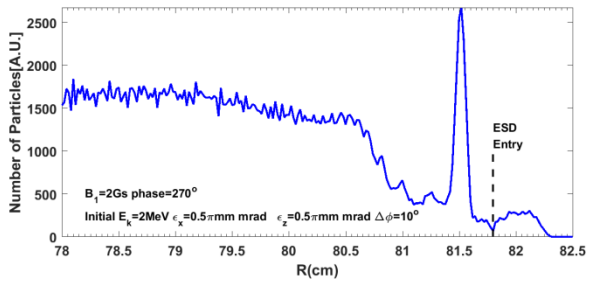


Figure 4: Particles numbers along radius. The entry of the first electrostatic deflector could be placed at r = 81.9 cm.

## EXTRACTION DESIGN

### *Extraction Trajectory*

Particle circulates in the cyclotron due to the effect of centripetal force coming from the magnetic field. In order to deflect the particle out of cyclotron, it is essential to drag the particle out as fast as possible, preventing a sharply blow up of the beam in a long drift. As the valley is occupied by the four cavities, two electrostatic deflectors (ESD) are placed in the adjacent hills, pushing the beam deviate from the pole. Then the sharply dropped edge field decreases the centripetal force to the particles, which are extracted after traveling about half turn. Besides, the magnetic channels, which are used to focus the beam, have a negative dipole field component [3], helping to accelerate the beam deflection. Figure 5 gives the trajectories of the particles. In this simulation, many particles are selected in the phase ellipse with emittance of 0.5 πmm·mrad at 200 MeV and the RF phase width is 10°. The electric fields of the ESD are 85 kV/cm and 75 kV/cm respectively.

In the extraction process, the beam has to pass the gap of ESD, MC and also the gap between the joint board of DEE and liner after the second the ESD. The joint board links the top and bottom DEE in large radius. Moreover, the beam can not touch the board in the DEE after the first ESD. The extraction position and electric field in the two ESDs can be changed here to adjust the beam path through the gaps. The increase of the electric field is restricted due to the high voltage discharge in such a compact space. A shimming bar at the outer edge of the pole is added, providing a method to adjust the local field and further change the extraction position.

ISBN: 978-3-95450-199-1 doi:10.18429/JACoW-SAP2017-MOPH02



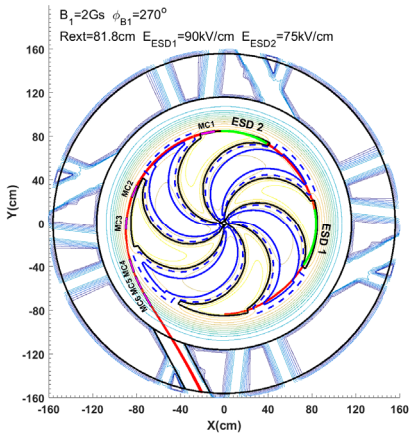


Figure 5: Particle Trajectories in the extraction process passing the electrostatic deflectors (ESD) and magnetic channel (MC) to the outside of the cyclotron.

### *Extraction Envelop*

In the long drift, only the magnetic channel can be used to focus the beam in radial direction. As the space is very limited, passive magnetic channel (MC) are adopted generate a radial field gradient and also with a small dipole field component [3]. The MC is comprised with three iron bars and designed for the beam to pass fitly, so the effect on the main field is relatively weak. Figure 6 gives the cross section of one MC, which has a aperture of 6 mm and can generate a field gradient of 2.6 kGs/cm.

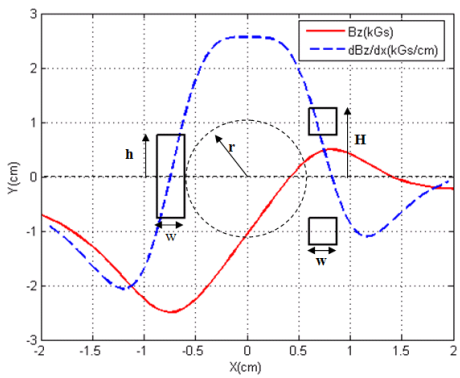


Figure 6: Field distribution in the cross section of the magnetic channel comprised with three iron bars. The size of the bars is given with r=6 mm, w=3 mm, h=8 mm, H=1.25 mm.

Through multi-particles simulation and optimizing the parameters of the six MCs, the beam envelop in the extraction process is illustrated in Fig.7. The radial and vertical envelops at the exit of the cyclotron are 8 mm and 1 mm. Here the start energy of the simulation is 200 MeV and initial emittance is 1π mm·mrad in both directions.

### *Beam Loss*

Following the above the results, the distribution of beam loss is given in Fig.8. Most of the beam lost at the first ESD, especially at the entrance of the septum, which is easy to observe from Fig.4. Due to the thermal effects by the hitting of many particles, the Ti with high melting point is selected as septum material and a cool system is equipped with the first ESD to decrease the temperature of the septum.

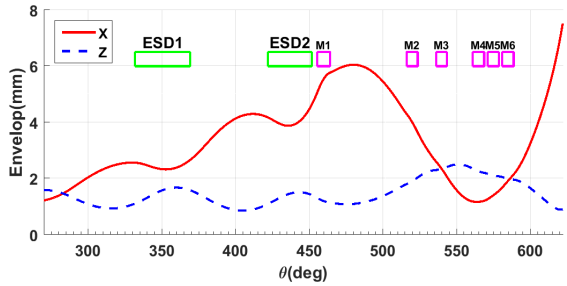


Figure 7: Beam envelop in the extraction process.

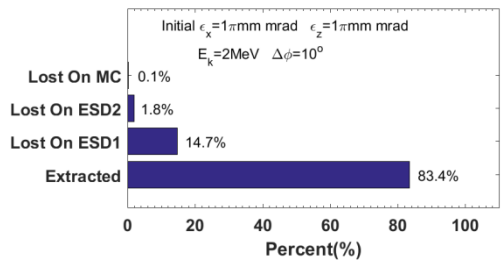


Figure 8: Beam loss distribution in extraction process.

## CONCLUSION

The extraction simulation, including the trajectory, envelop and beam loss, is implemented in the CYCIAE-230. Through two ESDs and six MCs, the beam can be extracted to the outside of the cyclotron with reasonable transverse beam envelop. Results show the beam extraction efficiency could achieve 80%, providing a possibility to upgrade the current of cyclotron to about 1 μA in the future. High voltage discharge in the ESD is a critical issue in this machine. A test stand and 1:1 scale model of ESD 1 are designed and under machining to verify the feasibility of the design. Furthermore results on the experiments and the layout of the elements in the extraction process will be illustrated soon.

## REFERENCES

[1] T. Zhang, C Wang *et al.*, "Developments for 230 MeV superconducting cyclotrons for proton therapy and proton irradiation", *Nuclear Instruments and Methods in Physics Research Section B*, Volume 406, Part A, 1 September, 2017, Pages 244-249.

[2] D. Zhang, M. Li *et al.*, "Physical Design of the Extraction TRIM-RODS in a 230 MeV Superconducting Cyclotron", in *Proc. Cyclotron 2016*, Zurich, Switzerland, 2016, Pages 61-63.

[3] G. Bellomo, "Design of Passive Magnetic Channels", in Proc. *the 13th International Conference on Cyclotrons and their Applications*, Vancouver, BC, Canada, Pages 592-595.

ISBN: 978-3-95450-199-1 doi:10.18429/JACoW-SAP2017-MOPH03

# ENVELOPE CONTROL OF THE EXTRACTED BEAM FROM COMPACT CYCLOTRON

Sumin Wei†, Ming Li, Tianjue Zhang, Shizhong An, Guofang Song, Pengzhan Li
China Institute of Atomic Energy, Beijing, China

*Abstract*

Along with the fast development of cyclotrons, more and more compact cyclotrons are used in the medical treatment and the scientific research. Because of the compact structure, the magnetic field in the extraction area is complex and there is no room for the focusing elements, the new methods to control beam envelope in extraction area are needed. In this paper, the influence of envelope caused by the angle between the foil and the beam has been studied, the experiment on a 10 MeV compact cyclotron that construct in CIAE (China Institute of Atomic Energy) has been done, the result is well agrees with the theoretic design. For the small medical cyclotrons, this method can be used to adjust the beam spot on the liquid target which installs just on the exit of the cyclotron.

## INTRODUCTION

A majority of the medical cyclotrons for the radiopharmaceuticals production are compact cyclotrons, 10 MeV-30 MeV proton beams are extracted to produce radioactive nuclide for diagnosis such as F-18[1]. Usually, these kinds of cyclotron accelerate H- and extract proton beam by stripping foil because of the compact structure. Stripping is one of the most important methods in beam extraction of compact cyclotron because of the simple mechanical structure, the high extraction efficiency, the low cost, and the adjustable extraction energy.

For compact cyclotron, the dispersion caused by fringe field on the extract region will be obviously because of the small gap of the magnet, on the other hand, the energy dispersion of beams extracted by stripping foils usually large, which caused large increase in beam envelope and emittance, beam loss will be increased too. The extracted beam from these compact medical cyclotrons usually hit liquid target directly without long beam transfer line to produce short lifetime radioactive nuclide, there is no room for the focusing elements such as quadrupole, so we can't control beam envelope at this area and beam spot on target by focusing elements. The influence of envelope caused by the angle between the foil and the beam has been studied to control beam characteristic, both theoretical study and experiment study have been done. The results shows that one can control beam envelope effectively at extraction area only by adjusting the foil angle, it is of great significance for beam spot control on target, increasing the yield of radioactive nuclide and increasing of target lifetime.

For other cyclotrons with small extraction region that hard to install focusing elements, this method can be used to control the extracted beam envelope, which is very important for the later beam transport, especially for high current cyclotron.

## ANGLE EFFECT OF THE FOIL

Normally, the foil is perpendicular to beam direction and bring no influence for beam envelope. When there is an angle α between foil and the normal direction of beam, as shown in Fig. 1, it will bring a increment on x' after foil, could be expressed as formula 1.

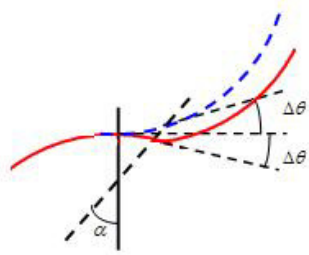


Figure 1: The angle between the foil and the beam.

$$\begin{aligned}\Delta x' &= 2\int \frac{B_z}{B\rho} ds \\ &= \frac{2}{(1+\delta)}\int \frac{B_0 + \frac{\partial B}{\partial x}x}{(B\rho)_0} ds \\ &= \frac{2}{(1+\delta)} \frac{1+\frac{\partial B}{\partial x}\frac{x}{B}}{\rho} x\tan\alpha \\ &= \frac{2}{\rho}(1-\frac{n}{\rho}x)(1-\delta)x\tan\alpha \\ &= \frac{2\tan\alpha}{\rho}x - \frac{2n\tan\alpha}{\rho^2}x^2 - \frac{2\tan\alpha}{\rho}x\delta\end{aligned} \quad (1)$$

In which α is the angle between foil and the normal direction of beam, ρ is the bending radius of the particles, δ is the momentum dispersion, n is the field-gradient index. Ignore higher order terms, the formula 1 can be wrote as:

$$\Delta x' = \frac{2\tan\alpha}{\rho}x \quad (2)$$

Which means when there is an angle between foil and the normal direction of beam, it is a focusing effect in x direction, such as the pole-face rotation angle of the bending magnet.

Similarly, for z direction, the increment on z' after foil can be shown in formula 3.

† weisumin@tsinghua.org.cn

ISBN: 978-3-95450-199-1 doi:10.18429/JACoW-SAP2017-MOPH03

$$\begin{aligned}\Delta z' &= 2\int \frac{Bx}{B\rho} ds \\ &= \frac{2}{(1+\delta)} \int \frac{\frac{\partial Bx}{\partial z} z}{(B\rho)_0} ds \\ &= \frac{2}{(1+\delta)} \int \frac{\frac{\partial By}{\partial x}}{(B\rho)_0} dsz \\ &= -\frac{2}{(1+\delta)} \frac{n}{\rho^2} xz \tan\alpha \\ &= \frac{2\tan\alpha}{\rho^2} n(1 \quad \delta) xy \\ &= \frac{2n\tan\alpha}{\rho^2} xz \quad \frac{2n\tan\alpha}{\rho^2} xz\delta\end{aligned} \tag{3}$$

Ignore higher order terms, $\Delta z' = 0$, which means there is no angle change in z direction, so the angle between foil and the normal direction of beam brings no change of transfer matrix in z direction, the vertical envelope has no change.

In summary, ignore higher order terms, the angle between foil and the normal direction of beam can be used as focusing/defocusing lens in x direction with no effect in z direction. So the beam envelope can be controlled only by rotate a small angel of the stripping foil, especially for the cyclotrons whose target is at the exit, the beam spot on the target can be adjusted.

## SIMULATION RESULTS OF CYCIAE-14

To produce short lifetime medical radioactive nuclide, promote development of medical cyclotron in China, a compact medical cyclotron CYCIAE-14 is designed and constructed in CIAE [2], this cyclotron using a dual stripping extraction system to get proton beam with highest current 400 μA, for each extract direction, the beam with energy 14 MeV and 14.4 MeV are extracted , as shown in Figure 2, in which the beam with energy 14 MeV will hit liquid target directly for F-18 production, beam with energy 14.4 MeV is for solid target to produce radioactive nuclide such as C-11.

As shown in chapter III, the beam envelope in x direction can be controlled by using the angle between foil and the normal direction of beam, which can be used as focusing/defocusing lens. Also the circular beam spot can be got by this angle, which is good for radioactive nuclide production.

The particles distribution on foil is simulated with the multi-particle tracking code COMA [3]. A particle tracking code developed with MATLAB has been done for beam tracking after stripping foil.

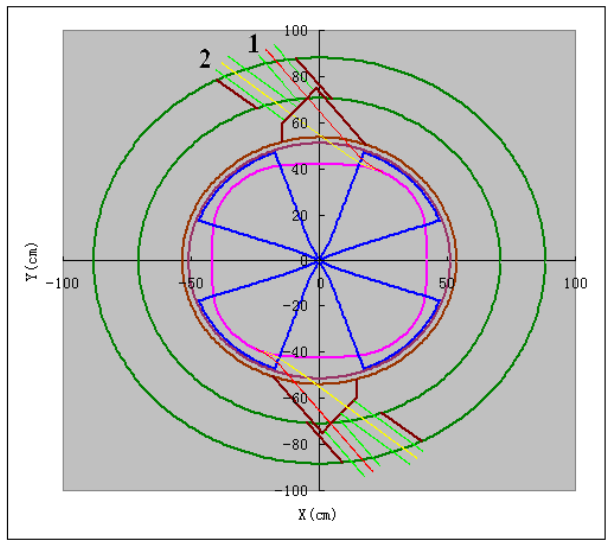


Figure 2: Dual extracted beam of CYCIAE-14.

Figure 3 shows the envelope after foil, in which the upper one is the results of beam 1 (as shown in figure 2), the nether one is beam 2. In the upper figure, the blue lines shows the vertical envelope and red lines shows the horizontal envelope, 2 cases are simulated: foil is perpendicular to beam direction and foil rotated by 20°, simulation shows that the vertical envelopes are same in these 2 cases, but for horizontal, the envelope can be reduced by almost 20%. As the liquid target is installed inside the return yoke of cyclotron, just at the exit, the beam spot can be adjusted as a circular with diameter 8 mm on the target, as shown in this figure. The other beam can be extracted outside cyclotron and transfer into a beam line for solid or gas target. If different beam spots are required, we can rotate the foil by different angles, the beam on target can be adjusted easily.

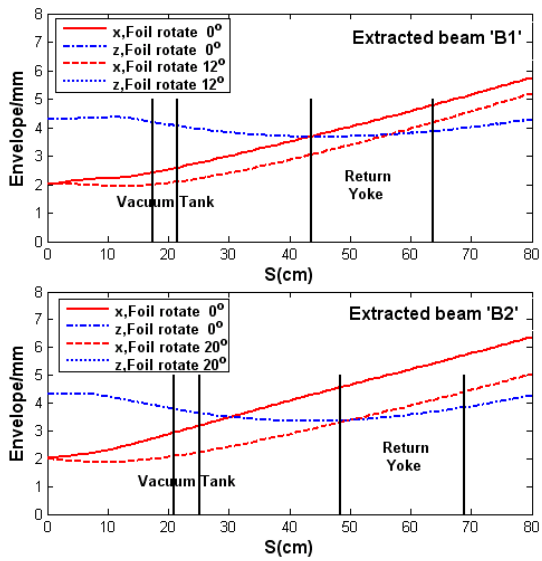


Figure 3: Extracted envelope with foil rotated.

ISBN: 978-3-95450-199-1 doi:10.18429/JACoW-SAP2017-MOPH03

## SIMULATION AND MEASUREMENT ON CYCIAE-CRM

The measurement has been done to prove this method on CYCIAE-CRM, a compact cyclotron build in CIAE. This cyclotron is the first compact medical cyclotron that design and construct all by ourselves in China, with highest beam energy 10 MeV [4].

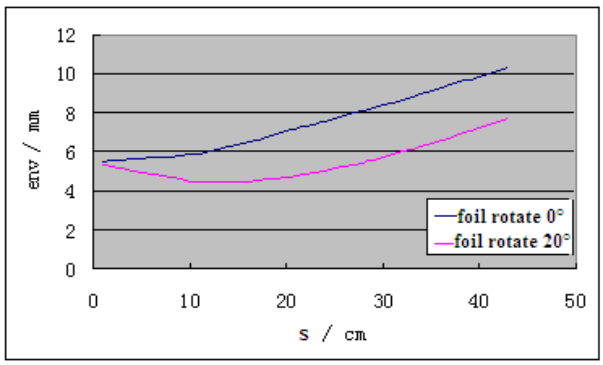


Figure 4: The influence of envelope caused by the foil angle in CYCIAE-CRM.

Figure 4 shows the simulation on influence of envelope caused by the foil angle in CYCIAE-CRM, in the figure, s is the beam trajectory, the blue line shows the envelope which the foil is perpendicular to beam direction, if the foil rotate by 20º, we can get the red line as beam envelope, at target place (where s is 40 cm), the envelope will reduce by almost 3mm because of the foil rotation.

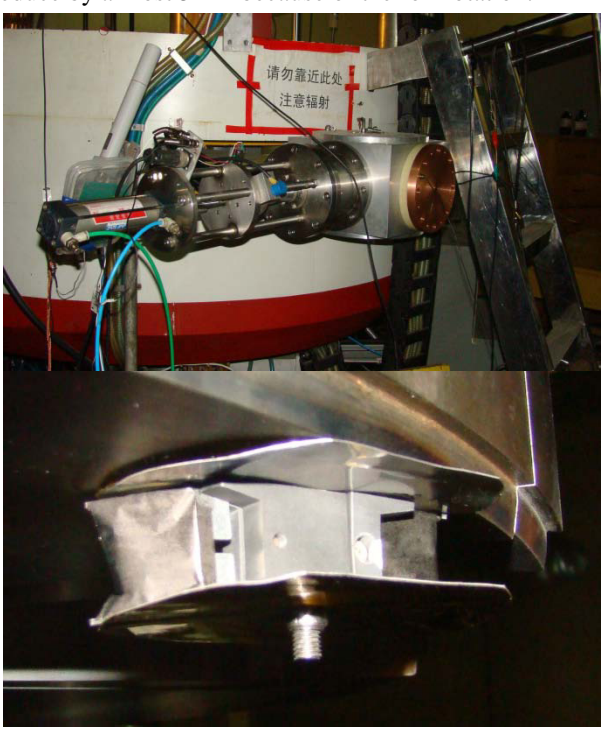


Figure 5: Experimental equipment of influence for foil.

The experiment has been done on CYCIAE-CRM to validate the simulation, the experimental equipment are shown in Figure 5,the cyclotron CYCIAE-CRM can install two stripping foils one time, in this experiment, one of the foil is perpendicular to beam direction, and the other one is rotate by 20º, a wire scanner is installed at the target place to measure the cross section of the beam extracted by two different foils. The result is shown in Figure 6, in which the dotted lines are measured results and the solid lines are the fitting results. The results shows that when the angle between foil and the normal direction of beam is 20º, the beam envelope will reduce by about 3~5mm, which is well agrees with the theoretic simulation.

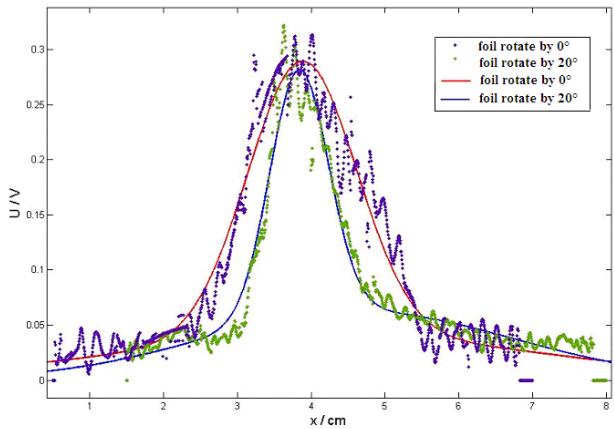


Figure 6: Measurement results of influence caused by different foil angles on CYCIAE-CRM.

## SUMMARY

The influence of envelope caused by the angle between the foil and the beam has been studied both by theoretical study and experiment study, the experimental result agreeing well with the theoretic design. This result can not only be used to control beam envelope on the extraction region and beam spot on the target of small medical cyclotron to increasing the yield of radioactive nuclide and increasing of target lifetime, but it can also be used in the improve the envelope in extraction region of high current compact cyclotron without focusing element.

## REFERENCES

[1] TianJue Zhang *et al.,* "The present situation and the prospect of medical cyclotrons in China", *SCIENCE CHINA Physics, Mechanics & Astronomy,* Vol.54 Suppl. 2: 1–6, 2011.

[2] TianJue Zhang *et al.,* " Overall design of CYCIAE-14, a 14MeV PET cyclotron", ECAART2010, Athens, Greece, 2010.

[3] C. J. Kost, G. H. Mackezie, COMA – A Linear Motion Code for Cyclotron, *IEEE Transactions on Nuclear Science,* Vol.NS-22, No.3, June 1975.

[4] Tianjue Zhang *et al.,* "Comprehensive test stand for high-intensity cyclotron development", *Chinese Science Bulletin,* Vol.56 No.3: 238-244, 2011.

ISBN: 978-3-95450-199-1 doi:10.18429/JACoW-SAP2017-MOPH04



# SOME INITIAL RESULTS OF CENTRAL REGION ORBIT TRACKING FOR SUPERCONDUCTING CYCLOTRON CYCIAE-230*

Dongsheng Zhang†, Xianlu Jia, Ming Li, Fengping Guan,
Shizhong An, Tianjue Zhang, Chuan Wang, Sumin Wei,
China Institute of Atomic Energy, Beijing

*Abstract*

CYCIAE-230 superconducting cyclotron, a medical accelerator for proton therapy, is designing and constructing at CIAE now [1]. An internal PIG source was adopted to attain a compact and simple design. Central region electric and magnetic field design will directly affect the beam quality and reliability of the cyclotron in terms of phase selection, beam loss and beam stability. Moreover, a favourable central region will ensure single-turn extraction efficiency. The central region study was based on detailed orbit tracking results, including the beam behaviour in the push-pull RF mode and phase selection and axial focusing in the latest magnetic field and electrical field distribution from calculation. The physical design results of central region beam dynamics are presented here.

## INTRODUCTION

CYCIAE-230 is a compact isochronous cyclotron with four spiral pole sectors and four spiral Dees in the valleys given the central field of 2.33 T and Dee voltage of 72 kV. This machine is designed to accelerate proton beam from the ion source to extraction energy of 230 MeV. Aims for clear single-turn extraction by electrostatic deflectors, second harmonic acceleration as well as push-pull RF mode was employed to get enough turn separation, which also benefits the central region design for larger energy-gain in the first turns. Internal ion source was adopted to simplify the machine, lead to a compact central region. Protons at the opening slit of the ion source was considered nearly zero energy, extracted by the puller at proper RF phase and accelerated in the first gap subsequently. Under the circumstances of internal ion source, the beam behaviour is strongly sensitive to the initial parameters of particles and the electric field distribution at the first gap. Meanwhile, without the injection beam line it is hard to satisfy all the demands of beam input properties (including energy, RF phase, radial phase space matching and vertical focusing) only by adjusting the position and opening direction of ion source. The general solution is to abandon the radial phase space matching in central region and rectify the radial oscillation by trim-rods or trim-coils located in the accelerator region. In our machine, four sets of trim-rods will be installed to provide radial beam alignment, but difficulties still remain in the ion source and central region design.

* This work was supported by the National Natural Science Foundation of China under Grand Nos.11375273 and 1146114103
† 18810681102@163.com

## ORBIT CALCULATION

The calculation was conducted by single-particle tracking code CYCLONE [2] with the magnetic field in the symmetric plane and 3-dimensional electrical potential map in central region. The magnetic field calculations were carried out by 3-dimension finite element method code and the electric field was calculated by 2- or 3-dimension Laplace and Poisson equations solver RELAX3D [3]. The shape of central region electrodes was drawn in AutoCAD and imported to RELAX3D as boundary condition of electric potential.

Two electric field maps were used in CYCLONE. The small field, only covered the first gap, was fine meshed to make a more accurate orbit-tracking result, the field area is 1.6×1.6 cm and the grid size is 0.01×0.01×0.01 cm, The large field in CYCLONE has an area of 20×20 cm and grid size of 0.05×0.05×0.05 cm, contains about first 5 orbit turns. Simulation results implied such small grid in the small field region is necessary and the number of nodes in the large field is suitable for rapid iteration.

The initial coordinates of reference particle was chosen at the zero-potential surface in the opening of ion source, as recommended by Forringer's thesis [4] to provide accurate radial phase-space prediction. And the initial energy and RF phase of reference particle were scanned and determined in orbit-tracking.

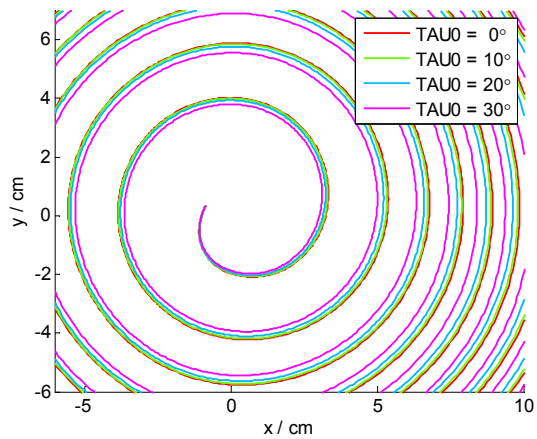


Figure 1: Orbits of particles with different initial RF phase.

The orbit tracking result shown in Fig. 1 contains the acceleration orbit of several particles within 30° phase width. In the current single-particle simulation period, the results shown that the phase acceptance of more than 30° is approachable, however a fixed phase slit will be

ISBN: 978-3-95450-199-1 doi:10.18429/JACoW-SAP2017-MOPH04

mounted in the central region to select particles in about 20° phase width to prevent beam loss at larger energy. The phase history of particles is shown in Fig. 2, in which displays the phase of particles when they across 0 degree azimuth, implies that the phase width of proton beam was compressed from 30° to less than 20° in first one or two gap, moreover, about 8° phase slip in first 5 turns test to be proper to provide electric focusing. Figure 3 gives particle energy with azimuth (turn number), shows four times of accelerations per turn, and the energy-gain per turn of 0.40 MeV is complying with the design parameters. In Fig.4 the acceleration phases of particles at each gap are marked, indicating fast acceleration and vertical electric focusing in the central region.

In the next step, the 3-dimensional computing electric field results of RF system will be import to CYCLONE to make the design more realistic.

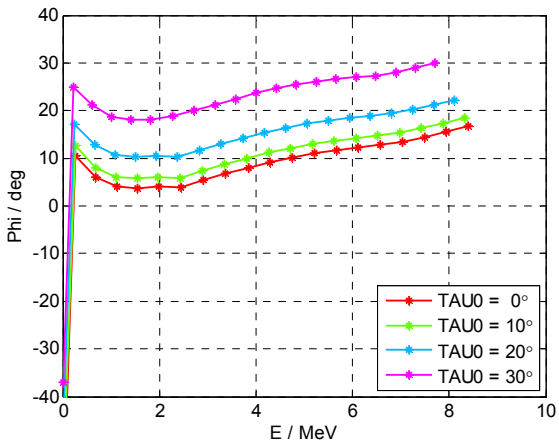


Figure 2: Phase slip of particles in central region.

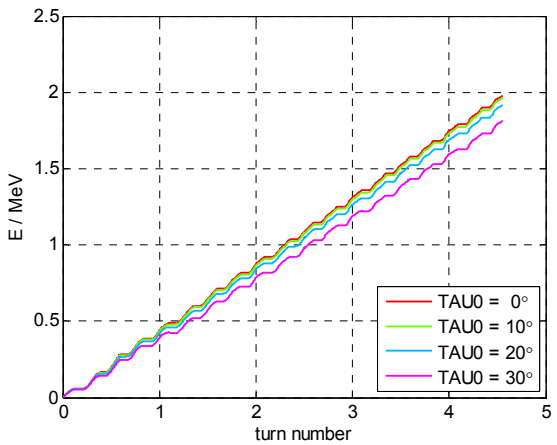


Figure 3: Energy gain diagram.

## RADIAL MOTION

Since the internal ion source is adopted in CYCIAE-230, it is hard to reach radial alignment by adjusting the position and opening direction of ion source, the trim-rods in the outer area should provide enough first harmonic to revise the radial oscillation. Moreover, the extraction system stipulates a radial emittance of 2 π mm-mrad within 5° phase width to achieve clear extraction. These claims should be followed in central region design.

Figure 5 shows the radial motion of particles with different initial RF phase but with the same initial coordinates, in which we can easily calculate the radial oscillation amplitude from peaks to illustrate radial alignment. The Y-label 'x' is a direct output of CYCLONE, means the radial offset compare to static equilibrium orbit at corresponding energy ($x = r - r_{eo}$). In the iteration steps of central region design, the maximum radial oscillation amplitude was about 0.8 cm. Therefore we provide that the trim-rods should reduce radial oscillation of 1 cm amplitude and arbitrary phase angle. The physical design of trim-rods is completed.

A preliminary multi-particle tracking contain particles in 5° phase width and different initial coordinates in symmetric plane shows that the radial oscillation amplitude range is about 0.22 cm, equivalent to 1.3 π mm-mrad radial emittance, and the radial oscillation amplitude and phase angle is more sensitive to the initial coordinates of particles rather than RF phase. The detailed calculation using a composed magnetic field of main magnet and well-positioned trim-rod is going on.

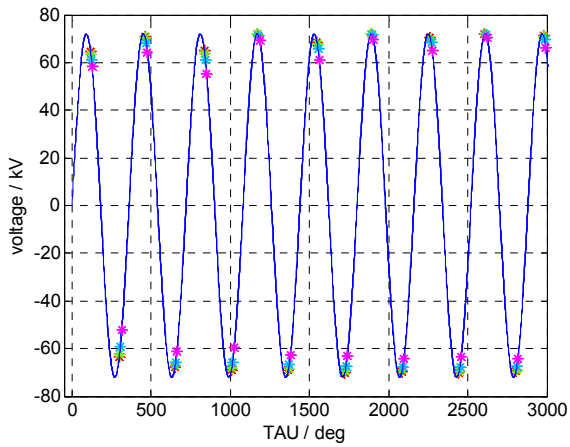


Figure 4: Acceleration phase of particles with different initial RF phase.

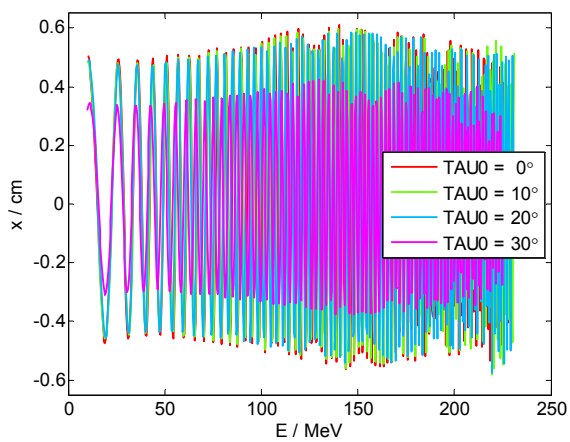


Figure 5: radial oscillation of particles with different initial RF phase.

ISBN: 978-3-95450-199-1 doi:10.18429/JACoW-SAP2017-MOPH04



## VERTICAL MOTION

In the first period of central region design, the position and opening angle of ion source were determined to obtain minimum vertical oscillation amplitude. Then the shape of electrodes is designed to get enough vertical focusing by iterative process.

The vertical motion of particles in central region of CYCIAE-230 combines vertical focusing effect of electric field and magnetic field. In the first 3 turns, the average magnetic field is ascendant and defocusing the beam, while the electric focus effect with proper acceleration phase is strongest in first turns, the vertical oscillation amplitude would not grow much. In the 5rd to 10th turn, beam energy is larger than 2 MeV and the electric focusing effect is rather weak, thus we intentionally build a slowly drop average field to ensure magnetic focusing. In the later turns the magnetic field flutter becomes the main force of vertical focusing and maintains the vertical oscillation amplitude.

The vertical oscillation of particles is shown In Fig. 6 and Fig. 7. In Fig. 6, the particles starting at z-coordinate of 0.1 cm within 30° phase width will not crash on the RF Dees in z-direction. In Fig.7, the particles have the same initial RF phase as reference particle, and the initial axial position ranges from 0.05 cm to 0.20 cm, the amplitude is nearly proportional to the initial z-coordinates.

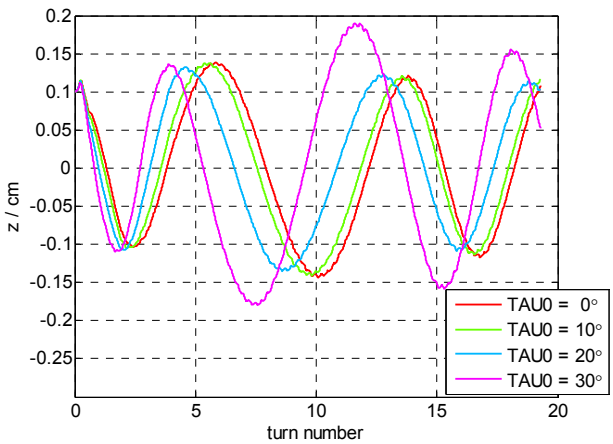


Figure 6: Vertical oscillation of particles with different initial RF phase.

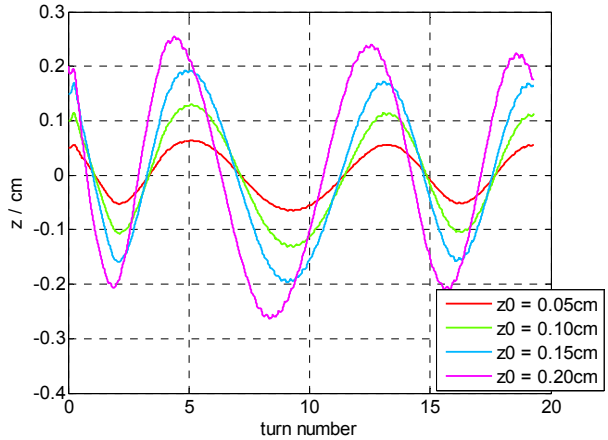


Figure 7: Vertical oscillation of particles with different initial z-coordinates.

## CONCLUSION

The physical design results of CYCIAE-230 central region based on single-particle orbit tracking is introduced in this paper. The position of internal ion source and the shape of electrodes are optimized by iterative design process to meet the requirements of extraction system. A detailed simulation using particles of different initial position, momentum and RF phase will proceed in the next step.

## ACKNOWLEDGEMENT

We are grateful to thank Jianjun Yang for valuable discussions and experiments in the central region preliminary design stage, and thank Y.N. Rao for helpful suggestions regarding the optimizing goals of CYCIAE-230 central region.

## REFERENCES

[1] T. J. Zhang *et al*., "Developments for 230 MeV Superconducting Cyclotrons for Proton Therapy and Proton Irradiation", presented at Proc. ECAART'12, Finland, July 2016, unpublished.

[2] B. F. Milton, "Cyclone 8.4 User Manual", TRI-DN-99-4, 1999.

[3] C. J. Kost, F. W. Jones, "RELAX3D User's Guide and reference Manual", TRI-CD-88-01, Vancouver, 1988.

[4] E R. Forringer, "Phase space characterization of an internal ion source for cyclotrons", 2004.

ISBN: 978-3-95450-199-1 doi:10.18429/JACoW-SAP2017-MOPH05

# DESIGN STUDY OF HEPS BOOSTER DESIGN*

Yuemei Peng†, Zhe Duan, YuanYuan Guo, Daheng Ji, Yi Jiao, Cai Meng, Jingyi Li, Saike Tian, Haisheng Xu, Gang Xu, Key Laboratory of Particle Acceleration Physics and Technology, Institute of High Energy Physics, CAS, China

*Abstract*

The High Energy Photon Source (HEPS) is a 6GeV ultra-low emittance light source proposed to be built in Beijing. It will utilise a full energy booster synchrotron operating at a frequency of 1Hz as its injector. For meeting the requirement of high charge when using swap-out mode, the booster need to have the ability of beam accumulation. In this paper, a FODO lattice with 4 dispersion-free straight sections is presented.

## INTRODUCTION

The light source HEPS with emittance less than 0.1nm.rad is proposed to be built in the suburb of Beijing. It will be composed of four main parts, a 0.3 GeV linac as the pre-injector, a full energy booster to accelerate the electrons from 300 MeV to 6 GeV, a storage ring at 6 GeV and the radiation synchrotron experimental hall.

The booster is located in a separate tunnel with a circumference about 453.5 m, 1/3 of that of the storage ring. It raises the energy of a 300 MeV electron beam up to 6 GeV in approximately 400 ms and operates at repetition rate of 1Hz.

Two filling patterns are mainly considered in HEPS storage ring, high-brightness mode (or low-bunch-charge mode, 90% buckets uniformly filled by about 680 bunches with beam current of 200 mA) and timing mode (or high-bunch-charge mode, 63 bunches uniformly filled in the ring). For the latter filling pattern, we need inject about 14nC charge to each bucket, this is a big challenge for injector, and so, the booster also used for beam accumulation is proposed.

For meet the storage ring operation requirements, the booster need support the beam with 2nC single bunch charge. The high bunch charge is a big challenge when beam energy is 300MeV.Under the detailed instability analysis, we change the booster lattice from TME cell with combined dipole [1] to FODO cell with separated dipole for larger momentum compact factor.

This paper is entirely about the lattice design and beam dynamics of the booster.

## LATTICE DESIGN

The booster employs a classical FODO lattice structure as standard cell. It is a four-fold symmetry lattice with 14 identical cells together with two modified cells containing dispersion suppressors. The booster lattice is presented in Figure 1.The circumference is about 453.5 m, 1/3 of that of the storage ring.

There are four 8-m long straight sections with dispersion-free suitable for the installation of RF cavity, injection, and extraction systems. The main parameters are listed in Table 1.

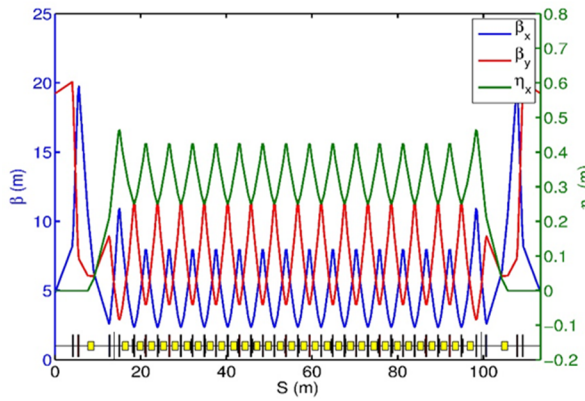


Figure 1: Optical functions and lattice structure of quarter.

Table 1：Main Parameters of HEPS Booster Lattice

| Parameter | Unit | Value |
|---|---|---|
| Injection energy | GeV | 0.3 |
| Extraction energy | GeV | 6 |
| Number of super-periods | | 4 |
| Length of the straight sections | m | 8 |
| Circumference | m | 453.5 |
| Repetition rate | Hz | 1 |
| Emittance @ 6 GeV | nm.rad | 43 |
| Emittance @ 0.3 GeV | nm.rad | 70 |
| Tune(H/V) | | 16.30/10.73 |
| Energy spread @ 6 GeV | | $9.6\times10^{-4}$ |
| Energy spread @ 0.3 GeV | | 0.5% |
| Natural chromaticity(H) | | -17.70 |
| Natural chromaticity(V) | | -14.70 |
| Momentum compaction factor | | $4.2\times10^{-3}$ |
| Energy loss per turn @ 6 GeV | MeV | 4 |
| Long. damping time @ 6 GeV | ms | 4.56 |
| Hor. damping time @ 6 GeV | ms | 4.51 |
| Ver. damping time @ 6 GeV | ms | 2.24 |
| Maximum $\beta_x$ | m | 19.8 |
| Maximum $\beta_y$ | m | 20.1 |
| Maximum dispersion | m | 0.5 |

We use six families of chromatic sextupoles to correct the chromaticity and nonlinear optimization. The nonlinear dynamics is simulated with AT program. The dynamic aperture of bare lattice and physical aperture in the middle of long straight is presented in Figure 2. The horizontal and vertical aperture can meet the requirements of beam

* Work supported by NSFC (11475202, 11405187, 11205171)
† pengym@ihep.ac.cn

ISBN: 978-3-95450-199-1 doi:10.18429/JACoW-SAP2017-MOPH05



stay clear and tousheck lifetime. The chromaticity curve is shown in Figure 3, and the transverse momentum acceptance is about 2.8%.

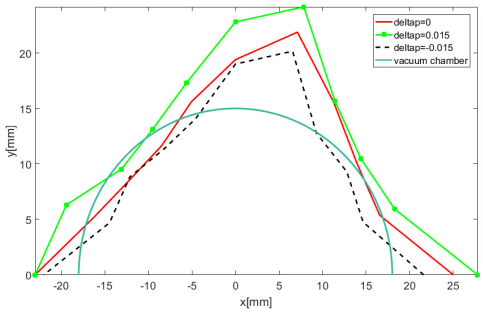


Figure 2: The DA in middle of long straight without error.

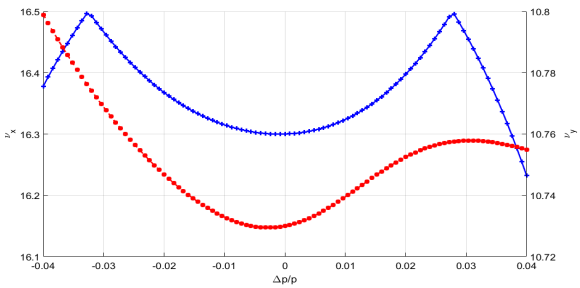


Figure 3: The chromaticity curves of HEPS booster lattice.

## ANALYSIS OF RAMPING PROCESS

### *Ramp Cycle*

HEPS booster operates with repetition rate of 1Hz, a ramp cycle is shown in Figure 4. The ramping curve has a flat bottom of 200 ms for 10 bunches injecting to booster from the linac, and also a flat top of 200 ms to allow the bunch inject to booster from storage ring merge to the bunch already in the booster at 6GeV and extraction to storage ring, 400ms for energy ramping up and 200ms for energy ramping down.

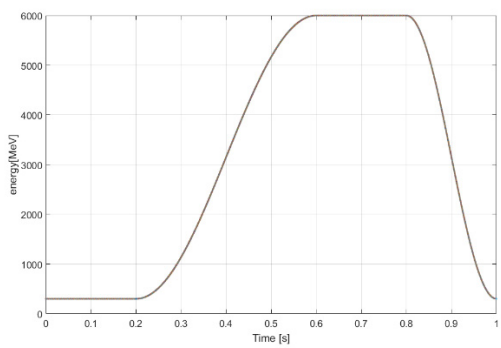


Figure 4: An energy ramp cycle in the booster.

### *Eddy Current Effect*

Magnetic field ramping in booster induces eddy current in the dipole vacuum chambers. This produces an effective sextupole field superimposed on the nominal dipole fields, leading to changes in the chromaticity. The sextupole strength inside the vacuum chamber due to the eddy currents is calculated by the formula given in ref.[2] .We consider using a stainless steel vacuum chamber of height $g$ =30 mm and elliptical aspect ratio $g/w$ = 0.75, the thickness of vacuum chamber is 0.7mm, with these element parameters, we can get the sextupole strength induced by eddy current in ramping up process like shown in Figure5, the maximum value of the sextupole field is about 0.08m$^{-3}$.

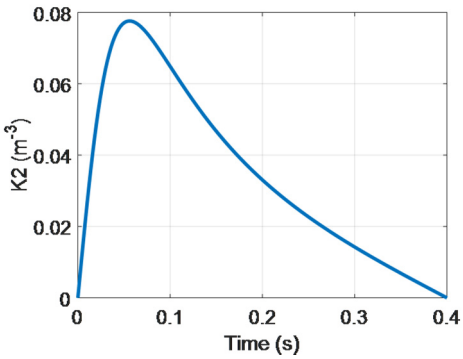


Figure 5: The sextupole strength induced by eddy current in ramping up process.

Corresponding calculated values of chromaticity are +3.3 horizontally and –4.7 vertically, which can be compensated by local modification of the sextupole ramp. The chromaticity evolution curve and the strength of compensate sextupole is shown in Figure 6.

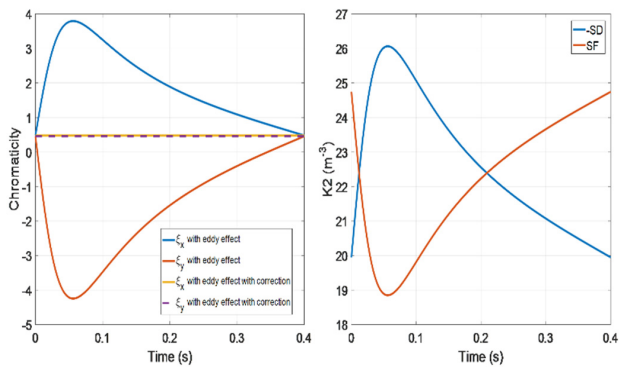


Figure 6: The curves of chromaticity evolution and strength of compensate sextupole.

### *Emittance and Energy Spread Evolution*

Beam energy spread and emittance evolution with energy ramping can calculate by the formula [3]

$$\frac{dA_i}{dt} = -A_i\left(\frac{\dot{E}}{E} + J_i\frac{P_\gamma}{E}\right) + C_q\frac{P_\gamma\gamma^2}{E}G_i \quad , \quad (2)$$

where $A_i$ with $i$ = 1 and 2 represents the energy spread $(\sigma_E/E)^2$ and horizontal emittance $\varepsilon_x$, respectively. The first two damping terms in right hand side come from the adiabatic damping process which results from the evolution of the beam energy and the effect of radiation damping, and the last excitation term comes from the quantum fluctuation. $J_i$ is the damping partition number, $J_1$ is the longitudinal damping partition, $J_2$ is the horizontal damping partition number. $P_\gamma$is the synchrotron radiation pow-

ISBN: 978-3-95450-199-1 doi:10.18429/JACoW-SAP2017-MOPH05

er, $C_q=3.83*10^{-13}m$. $G_1=I_3/I_2$, $G_2=I_5/I_2$, $I_2$, $I_3$ and $I_5$ are the synchrotron radiation integration. The emittance and energy spread evolution are given in Figure 7.

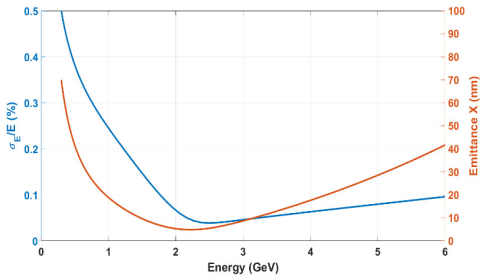


Figure 7: Emittance and energy spread evolution in ramping.

### *RF Cavity*

There are six 5-cell 499.8MHz RF cavities placed in the booster which offer 6MV voltage and support 0.6% bucket height in extraction energy.

At injection energy, we set the RF voltage 1.2MV. The RF voltage ramping up curve is set like Figure 8, the RF voltage linear ramp from 1.2MV to 6MV in 300ms, and then hold in 6MV until the beam is extracted.

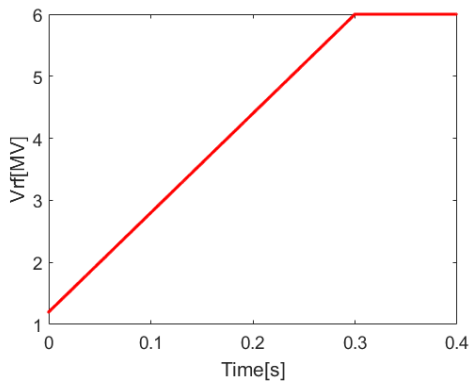


Figure 8: RF voltage during the energy ramp.

The bucket height and beam energy spread evolution in the ramping process with this RF voltage setting is presented in Figure 9. The bucket height is much larger than the beam energy spread, so that the energy spread of the accepted beam is limited by the physical aperture and/or the transverse off energy dynamic aperture of the lattice, not by the RF system.

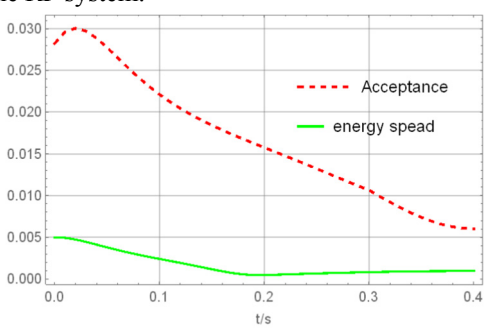


Figure 9: Bucket height and beam energy spread evolution during the energy ramp.

## BOOSTER AS AN ACCUMULATION RING

When the storage ring operating in swap-out mode, the booster need provide about 14nC bunch charge. So, HEPS booster also need to have the ability of beam accumulation.

The accumulation process is realized with four steps, which is presented in Figure 10.

First, injecting the required charge to booster from linac, second, ramping up the booster energy to 6GeV, then the beam swapped out from storage ring is injected to the booster bucket with charge, after a few damping time, the accumulated beam with enough charge is extracted from booster and injected to storage ring.

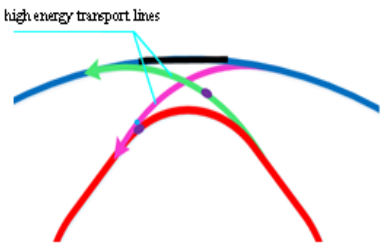


Figure10: The diagram of on-axis swap-out injection.

## INJECTION AND EXTRACTION SYSTEM

The HEPS booster injection is a simple single turn on-orbit injection with the injection system consists of a lambertson and a kicker.

We choose vertical off-axis injection system as the extraction and reinjection scheme.

In the reinjection system, there are 2 kickers with phase advance π to generate a local orbit bump in the vertical plane and the beam will be deflected by a lambertson horizontally.

The extraction system consists of 4 slow bumper dipole, a kicker and a lambertson. The 4 slow bumper dipole are used to form an 8 mm bump for reducing the required strength of the kicker. The phase advance between the kicker and lambertson is π/2, making zero vertical angle at extraction point.

## CONCLUSION

In this paper, we presented the lattice design, preliminary studies of ramping progress and so on. For meet the injection requirement, the booster is also used for beam accumulation. Reinjection system uses 2 kickers instead of 4 kickers to increase impedance.

## REFERENCE

[1] Y. Peng *et al.*, "The progress of heps booster design", in *Proc. IPAC'17*, Copenhagen, Denmark, May 2017, paper TUPAB065, pp.1472-1474.

[2] J.C. Bergstrom, L.O. Dallin, "Effects of Eddy Current Induced Sextupole Moments in the Booster during Ramping", CLS DESIGN NOTE - 3.2.69.2 Rev. 0, pp.1-8

[3] Edwards D.A., Syfers M. J. "An introduction to the Physics of High Energy Accelerators". New York: John Wiley and Sons, Inc. 1993, p110-115.

ISBN: 978-3-95450-199-1 doi:10.18429/JACoW-SAP2017-MOPH07



# STUDY OF THE STABILITY OF LONGITUDINAL BEAM DYNAMIC OF CEPC FOR UNEVEN FILLING

Yuansheng SUN†, Yuan Zhang, Na Wang, Jiyuan Zhai, Dianjun Gong
Institute of High Energy Physics, CAS, Beijing ,China

*Abstract*

PDR is a choice of CEPC design scheme, at any given time will contain a train of 50-70 bunches populate adjacent buckets and the remaining buckets unfilled. A consequence of an uneven filling scheme in the storage ring is that within train the synchronous phase will vary from bunch to bunch. This paper is to describe the tracking of the stability of longitudinal beam dynamic for CEPC, with the aim of including the main effects affecting the beam dynamics (i.e. the bunch-by-bunch feedback, the effect of the HOMs, the synchrotron radiation)..

## INTRODUCTION

Table 1: The Machine Parameters of CEPC Partial Double Ring Scheme

| Parameters | |
|---|---|
| Beam energy[GeV] | 120 |
| Beam revolution frequency [MHz] | 5475.46 |
| Energy spread total[%] | 0.16 |
| Number of IP | 2 |
| Circumference[km] | 54 |
| SR loss/turn[GeV] | 3.1 |
| Bunch number | 50 |
| Bunch current[mA] | 16.67 |
| Bunch length[mm] | 6 |
| Momentum compaction[$10^{-5}$] | 3.4 |
| RF Voltage[GV] | 6.87 |
| RF frequency[MHz] | 650 |
| Harmonic number | 117081 |
| Quality factor | 4E10 |
| Coupling factor | 1.82E4 |
| RF frequency[MHz] | 650 |
| Harmonic number | 117081 |
| Shunt impedance[MΩ] | 5.72E2 |

CEPC is a circular electron-positron collider operate at 240GeV center-of-mass energy with a circumference of 54 km, serve as a Higgs factory. The parameters of CEPC is shown in Table 1.The main constraint in the design is the beam lifetime due to beamstrahlung(a process of energy loss by the incoming electron due to its interaction with the electron (positron) bunch moving in the opposite direction) and the synchrotron radiation power, which should be limited to 50MW per beam, in order to control the AC power of the whole machine. A new scheme called partial double ring was development recently and crab waist was adopted on CEPC. The layout of the CEPC partial double ring scheme is shown in Figure 1. The main advantage of crab waist is that the beam-beam limit can be significantly increased. At any given time, the ring contains a train of 50-70 bunches. Within the train bunches populate adjacent buckets and there is an extreme long gap that extends over 11731-11001 buckets. The time structure of bunch train is shown in Figure 2. A consequence of such uneven filling scheme is that within train the synchronous phase will vary significantly from bunch to bunch. For superconducting cavities with heavy beam loading, the transient effects result from fierce beam-cavity interaction should be carefully explored to provide information to the low level feedback system to ensure the accelerator can operate stabilized. In this paper we will study the beam loading of fundamental mode ignore the effect of other high order modes.

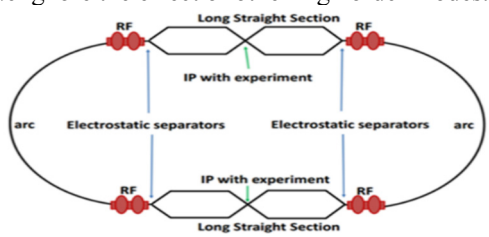


Figure 1: The layout of CEPC partial double ring.

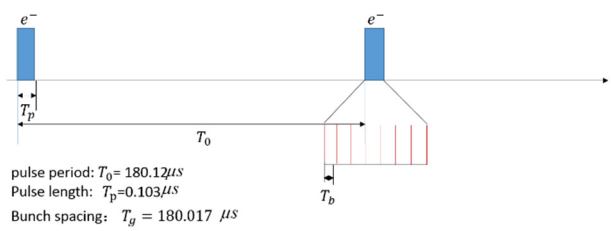


Figure 2: Time structure of bunch train.

## COMPUTER SIMULATION OF THE BEAM LOADING

### *Tracking Model*

† sunys@ihep.ac.cn

ISBN: 978-3-95450-199-1 doi:10.18429/JACoW-SAP2017-MOPH07

To find the steady-state fundamental voltage and phase along the bunch train, we model each bunch as a macroparticle. The main purpose of this paper is to explore the effects of main cavity on the bunch train and the status of the asymmetric fill pattern. The difference equation for the synchrotron oscillations of each bunch can be expressed as [1],

$$\varepsilon_{j+1} = (1 - 2\lambda_{rad})\varepsilon_j + \frac{1}{E}\left[eV_g(\phi_{j+1}) + eV_b - U_0\right] \quad (1)$$

and

$$\phi_{j+1} = \phi_j + 2\pi\alpha h\varepsilon_j \quad (2)$$

where ε is the relative beam energy deviation, and ϕ is the bunch phase with respect to the nominal synchronous phase. $\lambda_{rad}$ is the radiation damping rate expressed in units of the rotation frequency and 1U0 is the radiation loss per turn. $V_g$ and $V_b$ are the generator and beam-induced voltages in the main cavities.$V_g$ is given by

$$V_g(\phi_i) = \sin(\phi_i + \phi_0 + \psi) \quad (3)$$

where $\phi_0$ is the stable phase for the rf voltage,ψ is the tuning angle of the rf cavity.

The relation of tuning angle to the detuning of the cavity is

$$\tan\psi = 2Q_L\frac{f_{res} - f_{rf}}{f_{res}} \quad (4)$$

where $Q_L$is load quality factor.

### *Beam-induced Voltage*

We assume that the beam-cavity energy exchange at a single point in the ring. In the tracking code each bunch is modeled as a macroparticle of charge q. Under this condition it is possible to simulate only the "rigid" oscillation that, however, are the most dangerous for the beam stability. When a charge q crosses the cavity, it perturbs the total voltage. The induced voltage of each mode depends on the shunt impedance $R_m$, the quality factor $Q_m$ and the angular frequency $\omega_m of\ the\ mode$,

$$v_m = -2\frac{\omega_m R_m}{2Q_m}q = -2k_m q \quad (5)$$

where $k_m$is the loss factor and m labels the cavity number. In this paper we mainly focus on the beam loading of the fundamental mode (m=0). The induced beam voltage resonance with the frequency of fundamental mode and decay in magnitude by a factor $e^{-\tau}$, where $\tau = \frac{2Q}{\omega_0}$ is the cavity filling time and $\omega_0$ is the fundamental resonance angular frequency. In storage ring, the particle bunches go through the cavity periodically, so we should consider the cumulative build up of the beam voltage. The voltage induce by the bunches is found from the difference equation

$$V_{b,i+1} = V_{b,i}e^{[j\omega_0 - \frac{1}{\tau}]\Delta t} - 2kq \quad (6)$$

Δt is arrive time between the current (ith) bunch and previous (i-1th) bunch given by

$$\Delta t = \frac{\phi_{t,i} - \phi_{t,i-1}}{\omega_0} + T_b \quad (7)$$

$T_b$ is the spacing of bunches which is equivalent to the number of buckets between the bunches multiplied by main rf period.

For the purpose of taking the bunch length into consideration, assuming a Gaussian distribution, the shunt impedance is corrected by a factor [2-7],

$$\exp[-(\omega_m\sigma_t)^2] \quad (8)$$

where $\omega_m$is the resonance angular frequency of the mode and the $\sigma_t$is the RMS bunch length. The build up of beam induced voltage is shown in Figure 3.

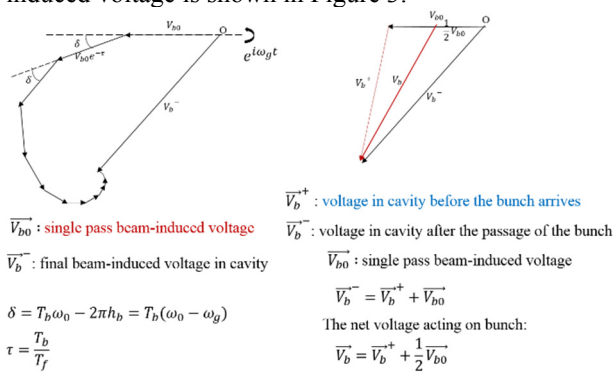


Figure 3: The build up of beam induced voltage in cavity.

From the fundamental theorem of beam loading, when a point charge crosses a cavity, it leaves behind a voltage $V_{b0}$, the point charge itself decelerated by $V_{b0}/2$. Therefore the final effective beam-induced voltage given by

$$V_{t,i} = V_{t,i} - (-k_0 q_i \exp[-(\omega_m\sigma_t)^2]) \quad (9)$$

## SIMULATION RESULT

Use the difference equation of the synchrotron motion we can track the bunch motion of arbitrary number turn by turn. In this section we present the result of beam loading of CEPC partial double ring scheme with a train of 50 bunches adjacent in the fill pattern.

Assuming that the cavity is operated at optimum tuning frequency and the revolution period $\boldsymbol{T_r}$ is much shorter than the filling time of the cavity $\boldsymbol{T_f}$,namely $\boldsymbol{T_r/T_f} \ll \mathbf{1}$,the phase shift of the bunch train caused by the long gap can be estimated analytically by [8]

$$\Delta\theta_{1N} \approx \frac{-2kq}{V_{c0}\sin\phi_0}\left[\frac{(N-1)N_g}{N+N_g}\right] \quad (10)$$

ISBN: 978-3-95450-199-1 doi:10.18429/JACoW-SAP2017-MOPH07

where k is loss factor , q the charge per bunch,N the bunch number per train ,$N_g$the number of missing bunch in the gap. The analytical bunch phase shift is 4.6969 degree.

The author is still working on debug the code, the simulation result cannot be shown for the moment.

## ACKNOWLEDGEMENT

The author thank the Y.Zhang, N.Wang, J.Y.Zhai, D.J.Gong for helpful discussion.

## REFERENCES

[1] J.M. Byrd, S. De Santis , J. Jacob *et al.*, *Physical Review Special Topics - Accelerators*, 2002 , 5 (9) :409-425.

[2] H.FAN, C.F.WU, "Tracking simulation for the HLS-II with a passive harmonic cavity in the symmetric and asymmetric fill patterns." *Chinese Physics C*, 36, (2012-11-01), 2012, 36 (11): 1111-1115

[3] P.B. Wilson, SLAC-PUB-6062, 1993.

[4] P.B.Wilson, "Transient beam loading in electron-potron storage rings", ISR-TH-78-23-rev

[5] M. Bassetti, A. Ghigo, *et al.*, " A time domain simulation code of the longitudinal multibunch instabilities", *INFN-LNF*, July 18, 1995 Note.

[6] R.Garoby, "Beam loading in RF cavities", *Lecture Notes in Physics*, 1992 , 400 :509-541

[7] H.P.Wang, "Transient beam loading effects in RF systems in JLEIC", in *Proc. IPAC'16,* Busan, Korea, MOPMY003, pp.518-521.

[8] Tetsuya Kobayashi, "Advanced simulation study on bunch gap transient effects", *Physical Review Accelerators and Beams*, Volume 19, Issue 6, id.062001

ISBN: 978-3-95450-199-1 doi:10.18429/JACoW-SAP2017-MOPH08

# MULTI-OBJECTIVE OPTIMIZATION OF DYNAMIC APERTURE AT OFF-AXIS INJECTION LATTICE OF HEPS

J. Wu†, Y. Zhang, Y. M. Peng, IHEP, Beijing, China

*Abstract*

The off-axis injection scheme is also considered at HEPS. A large beta insertion section is need in the case, which breaks the symmetry of the machine. We introduce two designs of the injection section. There exist clear difference for the dynamic aperture between the two designs. The low-order nonlinear resonance driving terms is calculated and compared. The results show a correlation between momentum acceptance and the off-momentum driving terms. We enlarge the dynamic aperture by tuning the on-momentum and off-momentum non-linear driving terms with a multi-objective optimization code.

## INTRODUCTION

Both on-axis injection scheme and off-axis injection scheme are considered in High Energy Photon Source (HEPS). Technology of off-axis injection is matured and it is well demonstrated in existing light sources. For ultra-low emittance storage ring, dedicated effort is required to reach the required dynamic aperture, but maybe at the expense of larger emittance.

Different lattices are adopted in different injection schemes. Compared with the standard 48-cell lattice, which is used for on-axis injection scheme, large-beta section is inserted in off-axis injection scheme that breaks the symmetry. As a result, dynamic aperture (DA) and momentum acceptance (MA) decrease a lot, especially MA, which falls from 3% to 2%. This result will be mentioned later.

Minimizing of the resonance driving terms (RDTs) is widely used for optimizing the dynamic aperture. This correction method is described in [1]. In consideration of the large reduction in momentum acceptance, we adopt both on-momentum and off-momentum resonance driving terms to carry out the optimization.

In this paper, we first introduce the lattice that includes the large-beta section and compare the DA and MA of two schemes. Then we give a short description for the resonance driving terms theory and analysis the 3rd and 4th order (Hamiltonian) terms with this method. According to the analytical results, we try to choose the objection functions to do the optimization.

## LATTICE

To meet the demands of off-axis injection, standard 48-cell structure should be inserted large-beta ($\beta_x$=90.86m) linear section. As a result, the lattice includes: standard cell with 44 H7BA structure, injection cells with a high-beta section for injection, and the opposite two cells. See Figure 1 and Table 1.

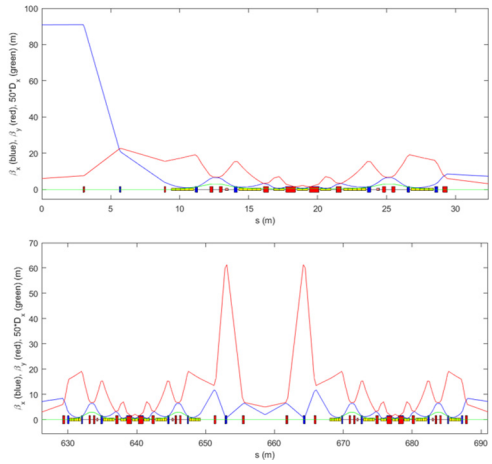


Figure 1: Half injection cell (above) and opposite cell for RF (below) [2].

Table 1: Main Parameters of the Lattice

| Parameter | Value |
|---|---|
| Circumference(m) | 1317.2783 |
| Emittance(pm·rad) | 60.2248 |
| $Q_x, Q_y$ | 111.2839/41.1428 |
| $\xi_x, \xi_y$ | -2.4469/-2.3962 |
| $\beta_x, \beta_y$(m) | 90.8581/5.9937 |
| Damping time(ms) | 16.68/24.97/16.61 |
| $U_0$(Mev) | 2.11 |

After inserting the high-beta section, we used this design lattice to do the particle tracking (1000 turns) and compared the DA result with the same work in the standard 48-cell lattice. Results are given below (See Figure 2).

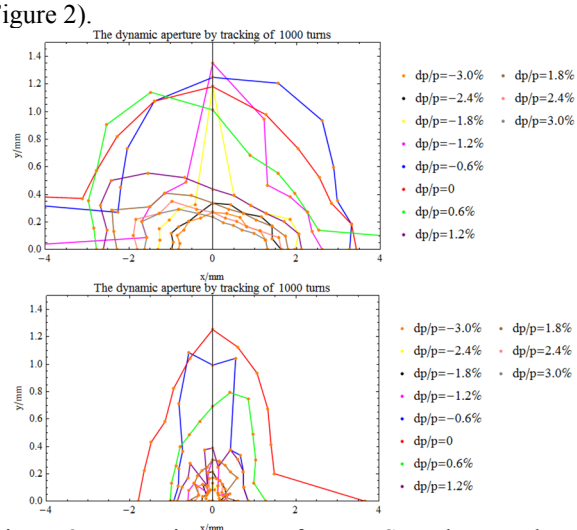


Figure 2: Dynamic aperture for HEPS on the x-y plane at the injection point for different off-energy values.

† wujin@ihep.ac.cn

ISBN: 978-3-95450-199-1 doi:10.18429/JACoW-SAP2017-MOPH08



Intuitively, DA and MA decrease a lot, especially the small DA at momentum deviation dp/p>1%.

## RDT THEORY

The RDT correction method is described in [1]. The theory can be introduced within different equivalent theoretical frameworks, in which Lie algebra is common used.

In [3], the 3rd RDTs arising from the sextupoles (1st order to strength) can be calculated using this kind of formulas [4]:

$$h^3_{jklmp} \propto \sum_{n=1}^{N_{sext}} (b_3 l)_n \beta_{xn}^{\frac{j+k}{2}} \beta_{yn}^{\frac{l+m}{2}} \eta_{xn}^{p} e^{i\{(j-k)\mu_{xn}+(l-m)\mu_{yn}\}} \quad (1)$$

where j, k, l, m and p are integers which satisfy j+k+l+m+p=3, $b_3 l$ is the integrated sextuple strength, $\beta_{x,y}$ and $\eta_x$ are the usual Twiss parameters and dispersion function and $\mu_{x,y}$ are the horizontal and vertical phase advance.

The 4th order RDTs can be written as follow:

$$h^4 = \sum_i^{N_{oct}} f_i^4 + \frac{1}{2}\sum_{j>i=1}^{N_{sext}} [f_i^3, f_j^3] \quad (2)$$

the contributions to which arising from the octupoles (1st order to strength) are similar to $h^3_{jklmp}$:

$$h^4_{jklmp} \propto \sum_{n=1}^{N_{oct}} (b_4 l)_n \beta_{xn}^{\frac{j+k}{2}} \beta_{yn}^{\frac{l+m}{2}} \eta_{xn}^{p} e^{i\{(j-k)\mu_{xn}+(l-m)\mu_{yn}\}} \quad (3)$$

where j, k, l, m and p are integers which satisfy j+k+l+m+p=4, $b_4 l$ is the integrated octupole strength. The contributions to RDTs arising from the sextupoles (2st order to strength) can be derived in Mathematica [5]. Explicit formulas can also be consulted in [6].

In this paper, we only consider geometric terms and tune shift with amplitude. Chromaticity related terms can be controlled with other method. The impact of these 3rd order and 4th order driving terms on the beam dynamics are summarized in Table 2 (16 terms total).

Table 2: RDT Effects on Beam Dynamics

| RDT | Effect |
|---|---|
| $h_{30000}$ | $3\nu_x$ resonance |
| $h_{21000}, h_{10110}$ | $\nu_x$ resonance |
| $h_{10200}$ | $\nu_x + 2\nu_y$ resonance |
| $h_{10020}$ | $\nu_x - 2\nu_y$ resonance |
| $h_{40000}$ | $4\nu_x$ resonance |
| $h_{31000}, h_{20110}$ | $2\nu_x$ resonance |
| $h_{00400}$ | $4\nu_x$ resonance |
| $h_{00310}, h_{11200}$ | $2\nu_x$ resonance |
| $h_{20200}$ | $2\nu_x + 2\nu_y$ resonance |
| $h_{20020}$ | $2\nu_x - 2\nu_y$ resonance |
| $h_{22000}, h_{11110}, h_{00220}$ | $\frac{\partial \nu_x}{\partial J_x}, \frac{\partial \nu_x}{\partial J_y}, \frac{\partial \nu_y}{\partial J_y}$ |

## ANALYSIS

Multi-objective approaches to DA optimization with RDTs had been successfully applied to the NSLS-II [7]. The results demonstrated a correlation between DA and low-order nonlinear driving terms. To give a reasonable explanation for why MA decreased, we try to find some relevance between off-momentum RDTs and off-energy DA.

Code is written in SAD [8], which is easy to use for calculating the RDTs with different momentum devitation. It is well to be reminded that the latest code to calculate the 3rd and 4th RDTs of the whole ring is efficient that time used is less than 10 seconds, and the results are proved to be consistent with those of PTC [9]. Subsequent work of optimization is also based on SAD.

We compared the on and off-momentum ($\delta = \pm 0.02$) RDTs (16 terms for each $\delta$) in the two versions of lattice, standard 48-cell structure (marked by CEL) and large-beta section involved structure (marked by INJ). Results shows that all on-momentum ($\delta = 0$) RDTs appeared minute difference, just translation of image according to the length. We take an example with 3 terms of tune shift in Figure 3. Not surprisingly, off-momentum ($\delta = \pm 0.02$) RDTs appeared huge differences, especially the terms $h_{31000}$ and $h_{00310}$. We also give the pictures in Figure 4.

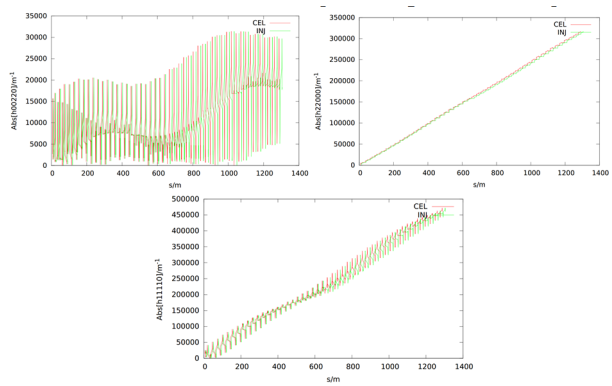


Figure 3: $h_{22000}, h_{00220}, h_{11110}$ with $\delta = 0$ in two versions of lattice.

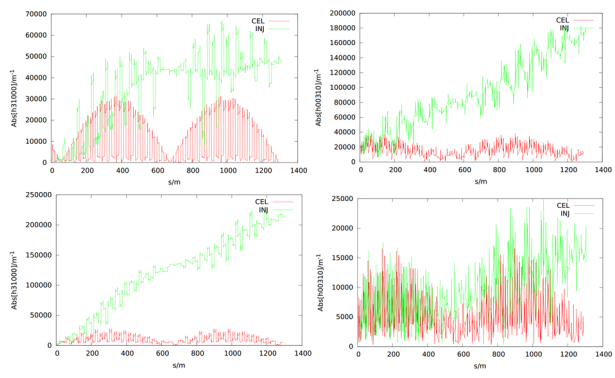


Figure 4: $h_{31000}$ (left) and $h_{00310}$ (right) with $\delta = 0.02$ (up) and $\delta = -0.02$ (down) in the two versions.

These results inspired us to set suitable objective functions in the subsequent optimization work.

ISBN: 978-3-95450-199-1 doi:10.18429/JACoW-SAP2017-MOPH08

## OPTIMIZATION FOR THE HIGH-BETA SECTION INCLUDED LATTICE

We use Multi-Objective optimization by Differential Evolution (MODE) [10]. In our optimization strategy, we use the geometric sum of RDTs in different energy deviation $f_1$, with $f_2$ related to the chromaticities and $f_3$ characterizing the DA area of on-momentum and off-momentum particles:

$$\begin{cases} f_1 = \sum_{\delta=0,\pm0.02}[a\sqrt{\sum(h^3_{jklmp})^2} + b\sqrt{\sum(h^4_{jklmp})^2}] \\ f_2 = \xi_x, \xi_y \\ f_3 = \sum_{\delta=0,\pm0.02} S_{DA}(\delta) \end{cases} \quad (4)$$

where am is the weight coefficients of 3rd and 4th RDTs according to the values, $\xi_x, \xi_y$ contains linear and nonlinear chromaticities.

In our optimization strategy, we only changed the strength of multipoles, while the linear lattice remained with $\nu_x$ =111.28, $\nu_y$ = 41.14 . All six families of sextupoles are used as parameters added with four families of octupoles.

Actually, suppression of 3rd RDTs can also control the 4th terms to some extent and save considerable time. After several iterations, we choose a relatively better solution. Here we give the comparison about RDTs (also $h_{31000}$ and $h_{00310}$ ), chromaticities and DA after optimization (See Figure5- Figure 7). It is important to mention that other terms are decreased more or less, but not presented here due to limited length.

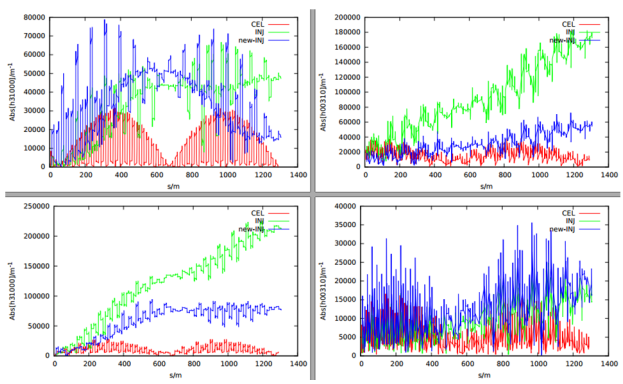

Figure 5: the change of $h_{31000}$ (left) and $h_{00310}$ (right) with $\delta = 0.02$ (up) and $\delta = -0.02$ (down) after the optimization (blue is new).

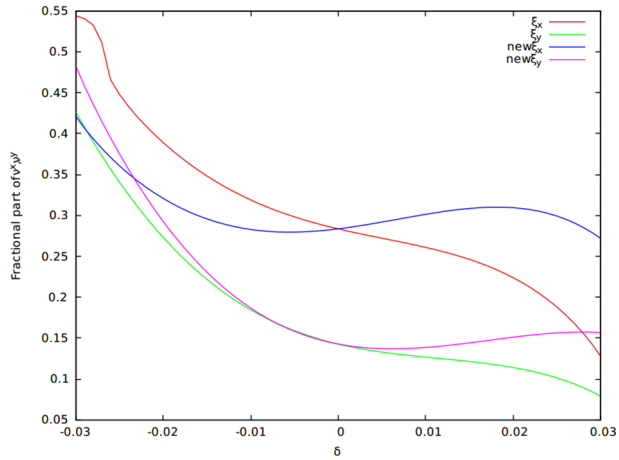


Figure 6: chromaticities turn to be smooth after optimized (blue and pink), while tunes ( $\delta = \pm0.03$ ) are still deviating much.

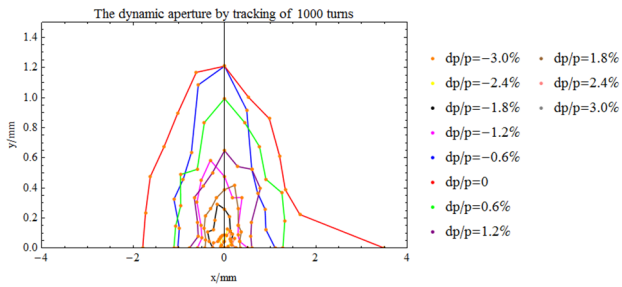


Figure7: compared with Figure 2, area of DA ($|\delta| \geq 1.2\%$) increased, but not so much.

## CONCLUSION

From analysis we could see that the decreasing of DA and MA has some correlation to the off-momentum RDTs. Contrasted with the on-momentum RDTs, off-momentum terms deviated a lot.

The optimization had a little bit better result but it is not so obvious. In consideration of the symmetry of the whole ring, six families of sextupoles were not split more. Next work may use more variables and objective functions may contains more RDTs that would spend more time.

Frequency map analysis (FMA) is also useful to check the tunes and resonances. If needed, linear part of lattice could be changed. As a consequence, more work is necessary.

## ACKNOWLEDGEMENT

The author would like to thank Chenghui Yu for providing the early version of lattice, and Yi Jiao for providing the latest version and discussing some key questions.

ISBN: 978-3-95450-199-1 doi:10.18429/JACoW-SAP2017-MOPH08



## REFERENCES

[1] J. Bengtsson, I.P.S. Martin, J.H. Rowland and R. Bartolini, "On-line control of the nonlinear dynamics for synchrotrons", *Phys. Rev. ST Accel. Beams*, vol. 18, p.074002, 2015.

[2] Y. M. Peng, talk on LERLD 2016 workshop.

[3] J.Bengtsson, "The sextupole scheme for the Swiss Light Source (SLS): an analytic approach", SLS Note 9/97, 1997.

[4] I.P.S. Martin, M. Apollonio, R. Bartolini, "Online suppression of the sextupole resonance driving terms in the diamond storage ring", in *Proc. IPAC'16*, Busan, Korea, May 2016, paper THPMR001, pp. 3381-3384.

[5] Mathematica, http://www.wolfram.com/mathematica/

[6] Chun-xi, Wang, "Explicit formulas for 2nd-order driving terms due to sextupoles and chromatic effects of quadrupoles", Argonne National Laboratory (ANL), USA, ANL/APS/LS-330, April 2012.

[7] L. Y. Yang, Y. J. Li, W. M. Guo, Samuel Krinsky, "Multiobjective optimization of dynamic aperture", *Phys. Rev. ST Accel. Beams*, vol. 14, p.054001, 2011.

[8] SAD, http://acc-physics.kek.jp/SAD/

[9] PTC, http://madx.web.cern.ch/madx/

[10] Y. Zhang, D. Zhou, "Application of differential evolution algorithm in future collider optimization", in *Proc. IPAC'16*, Busan, Korea, May 2016, paper TUOBA03, pp. 1025-1027.

ISBN: 978-3-95450-199-1 doi:10.18429/JACoW-SAP2017-MOPH10

# THE BEAM DYNAMICS SIMULATION OF AN L-BAND ELECTRON GUN USING GENETIC ALGORITHM

Peiliang Fan†, Xiaozhong He, Jian Pang, Liu Yang
Institute of Fluid Physics, China Academy of Engineering Physics, Mianyang, China

*Abstract*

The China Academy of Engineering Physics (CAEP) plans to build XFEL light source. In the beam dynamics simulation there are many parameters to be considered, so we need a high efficient method to find the optimal parameters. Genetic algorithm (GA) [1] is wildly used as one kind of evolutionary algorithm and it can help us to find the optimal parameters in a shorter time. In this paper, we will use genetic algorithm to do the beam dynamics simulation of an L-band electron gun used for the XFEL. We put emphasis on the optimization of the transverse normalized projected emittance and the relevant result will be given and discussed.

## INTRODUCTION

The China Academy of Engineering Physics (CAEP) plans to build XFEL light source. A normal conducting L-band photocathode electron gun will be used to produce high quality electron beam and its working frequency is 1.3 GHz. One of the most important parameters that influence the FEL process is the normalized transverse projected emittance, hereafter called emittance. There are many parameters to be considered in the beam dynamics simulation of the electron gun in order to get an optimized result. We need one efficient way to find these optimal parameters. Genetic algorithm is wildly used as one kind of evolutionary algorithm and it can help us to find the optimal parameters in a shorter time. In this paper, we will use genetic algorithm to do the beam dynamics simulation.

## THE BEAM LINE AND GA

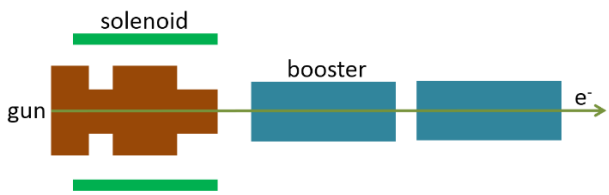


Figure 1: The simplified schematic of the beam line.

The electron source used for the XFEL is one normal conducting 1.6-cell L-band RF gun and its working frequency is 1.3 GHz (the field is shown in Fig. 2). The photocathode will use $Cs_2Te$ or Cu, and they will be illuminated by UV laser pulses to produce high quality electron beams. The produced beams will be focused with solenoid installed around the gun. The beam will be further accelerated by the superconducting TESLA booster (9-cell). The simplified schematic of the beam line is shown in Fig. 1.

† fanpeiliang@163.com

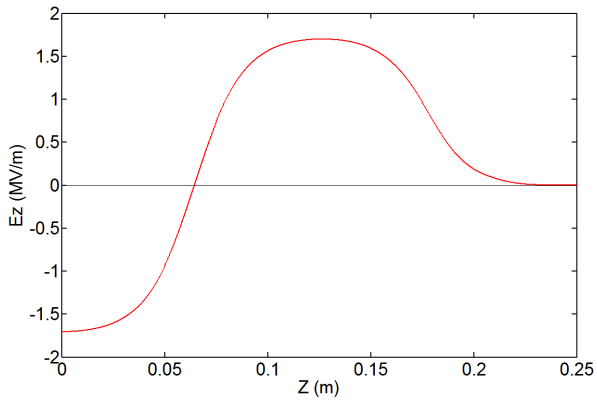


Figure 2: The electric field of the L-band gun.

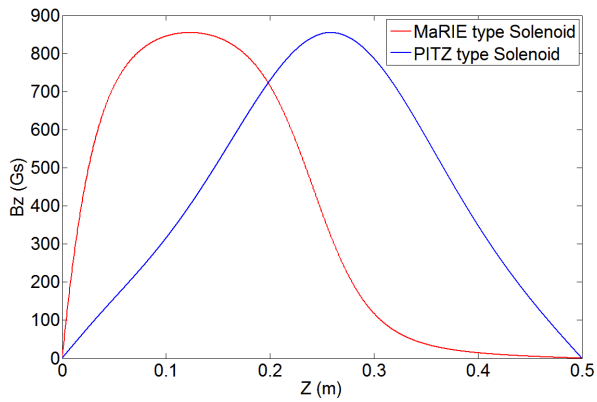


Figure 3: The magnetic field of solenoids.

In the simulation we compared the MaRIE [2] type solenoid, hereafter called M type, and the PITZ [3] type solenoid (P type). The magnetic field of the solenoids is shown in Fig. 3. We use ASTRA code [4] to do the beam dynamics simulation.

The initial condition is FWHM pulse length $Lt$ = 20ps and the rise time $rt$ = 2ps. The laser pulse longitudinal shape is plateau distribution, and the transverse distribution is 2D uniform distribution. The $E_{acc}$ of the booster is 20 MV/m and the gain energy is about 20 MeV for each 9-cell superconducting cavity.

Genetic algorithm solver is in the optimization tool of MATLAB. The GUI interface of the GA solver in MATLAB is shown in Fig. 4. We need to write the fitness function and set constrains. The population type is double vector and the population size is 50 ~ 100 for 4 variables. In the stop criteria option, *Generations* specifies the maximum number of iterations the genetic algorithm performs. In the plot function option, *Best fitness* plots the best function value in each generation versus iteration number.

ISBN: 978-3-95450-199-1 doi:10.18429/JACoW-SAP2017-MOPH10



Table 1: Results from the GA Simulation for the L-band Electron Gun

| Solenoid type | Photo-cathode | Bunch charge (pC) | $E_{cath}$ (MV/m) | Sig_x (mm) | Phase (degree) | MaxB (Gs) | [b]Pos(2) (m) | Emittance (mm-mrad) |
|---|---|---|---|---|---|---|---|---|
| M | [a]$Cs_2Te$ | 200 | 55 | 0.163 | 7.0 | 1892 | 2.05 | 0.241 |
| M | $Cs_2Te$ | 200 | 60 | 0.147 | 7.2 | 2030 | 2.15 | 0.226 |
| M | $Cs_2Te$ | 200 | 65 | 0.142 | 7.5 | 2167 | 2.29 | 0.214 |
| M | $Cs_2Te$ | 100 | 55 | 0.106 | 7.9 | 1875 | 2.56 | 0.161 |
| M | $Cs_2Te$ | 100 | 60 | 0.097 | 7.8 | 2018 | 2.49 | 0.148 |
| M | [a]Cu | 100 | 60 | 0.112 | 8.1 | 2031 | 2.09 | 0.074 |
| M | Cu | 200 | 60 | 0.156 | 7.3 | 2035 | 1.95 | 0.114 |
| P | $Cs_2Te$ | 100 | 60 | 0.113 | 3.3 | 2102 | 2.86 | 0.190 |
| P | $Cs_2Te$ | 200 | 60 | 0.157 | 2.3 | 2093 | 3.14 | 0.259 |

[a] LE of the $Cs_2Te$ is 1.2 eV and 0.132 eV for Cu. [b] Pos(2) is the distance from the cathode to the first booster cavity.

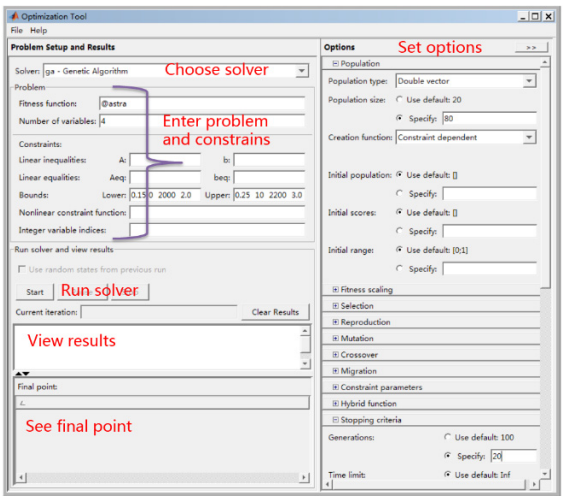


Figure 4: Genetic algorithm solver in MATLAB.

## THE SIMULATION RESULT

Figure 5 shows one optimization result from the GA solver, we can see that the minimum emittance decreases gradually with the increase of generation. The average emittance of each generation has the same trend as the minimum emittance. Eventually, the average emittance coincides with the minimum emittance, it means that the result is converged.

Table 1 gives the results from the GA simulation for the L-band electron gun. From the result we can see that using M type solenoid gets lower emittance. With higher $E_{cath}$ we can get better result. When the bunch charge changed, e.g from 100 pC to 200 pC, the phase of the cavity and the magnetic field of the solenoid have the similar value.

$$\frac{\rho_1}{\rho_2} = \frac{Q_1 / S_2}{Q_2 / S_1} = \frac{r_2^2 Q_1}{r_1^2 Q_2} . \quad (1)$$

Actually, the charge density is basically constant for different bunch charge, the charge density relationship of between different bunch charge is shown in Eq. (1). $Q$ is the bunch charge and $r$ is the radius of the bunch.

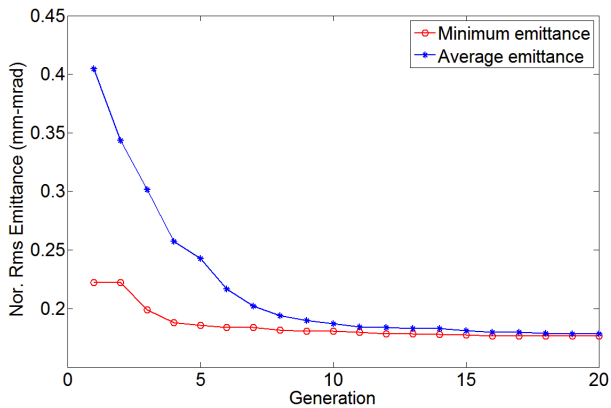


Figure 5: One optimization result from the GA solver.

For the P type solenoid and $Cs_2Te$ photocathode case, $0.157^2/0.113^2/2 = 0.97$, for the M type solenoid and $Cs_2Te$ case, $0.147^2/0.097^2/2 = 1.15$, and for the M type solenoid and Cu photocathode case, $0.156^2/0.112^2/2 = 0.97$.

## SUMMARY

When there are many parameters to optimize we need one efficient way to find the optimal results. Here we choose genetic algorithm to realize this goal, and it proves that GA is very available. It help us save a lot of time. In the current optimization procedure we just have one objective function, in the future work we will use multi-objective genetic optimizer for the further optimization.

## REFERENCES

[1] J. Holland, Adaptation in Natural and Artificial Systems, University of Michigan Press, Ann Arbor, MI, 1975; MIT Press, Cambridge, MA, 1992.

[2] J. W. Lewellen *et al.*, "Status of the MaRIE X-FEL accelerator design", in *proc. IPAC'15*, Richmond, VA, USA, 2015, paper TUPMA026, pp. 1894-1896.

[3] M. Otevrel *et al.*, "Report on gun conditioning activities at PITZ in 2013", in *proc. IPAC'14*, Dresden, Germany, 2014, paper THPRO044, pp. 2962-2964.

[4] K. Floettmann, *A Space Charge Tracking Algorithm*, user manual (Version 3.0), 2011.

ISBN: 978-3-95450-199-1 doi:10.18429/JACoW-SAP2017-MOPH12

# BEAM DYNAMICS OF A 325 MHz IH-DTL WITH KONUS

R.Tang, S. X. Zheng , Q. Z. Xing , X. L. Guan, X. W. Wang, C.X. Tang†, Key Laboratory of Particle & Radiation Imaging (Tsinghua University), Ministry of Education, Beijing, China
also at Laboratory for Advanced Radiation Sources and Application, Tsinghua University, Beijing,
also at Department of Engineering Physics, Tsinghua University, Beijing, China

*Abstract*

A 325 MHz interdigital H-mode drift tube linac (IH-DTL), which is aimed at proton medical facilities, has been proposed and developing at Tsinghua University. The proton beam can be accelerated from 3 MeV to 7 MeV and the peak current of the beam at the exit of the cavity is about 15 mA. A KONUS dynamics without focusing element is applied in this cavity. The co-iteration of dynamics simulation and RF simulation is done. The process and result of the design is presented in this paper.

## INTRODUCTION

Since Munich University built the first IH-DTL accelerator at 1977, IH-DTL is widely used for heavy ion accelerators because of its high shunt impedance at low β range (beta<0.1) [1, 2]. As facilities used for proton and carbon therapy increase and the 3D RF simulation becomes reliable. IH DTL has been used widely in the injector of medical synchrotrons. A 216 MHz IH-DTL has been developed for HICAT (Heidelberg Heavy Ion CAncer Therapy) project. There are 4 KONUS (Kombinierte Null Grad Struktur) sections and three triplets in the tank. The proton beam can be accelerated from 0.4 MeV to 7 MeV in 3.76 m. The high effective gradient is 5.5 MV/m [3]. Another kind of proton IH DTL is developed via APF (Alternating Phase Focusing) beam dynamics. The length of this cavity is ~1.7 m. It can accelerate 10mA proton beam to 7.4 MeV at 200 MHz [4].

Considering the beam test on XiPAF (Xi`an Proton Application Facility) project, a 325 MHz IH-DTL is proposed and developing at Tsinghua University. The design parameters of this IH-linac is shown in Table1.

The optimization of single cell geometry and the dynamics model is introduced in reference [5]. To get high accelerating gradient and high shunt impedance, there is no focusing elements in this 1 m cavity. The power loss of the cavity is 145 kW and the average accelerating gradient is 5.45 MV/m. While the peak surface electric field is 2.25Kp, which seems a little higher [6].

For both APF and KONUS beam dynamics design, it needs the approximation of E field distribution (or voltage versus gaps) at first. And the synchronous phase calculated by beam dynamics at each cell determines the cell length which changes the E field distribution meanwhile. Thus, an IH-DTL design needs the co-iteration of beam dynamics and RF field simulation [4]. The design process and results is presented in this paper.

Table 1: Parameters of 325 MHz IH-DTL

| **Parameters** | |
|---|---|
| Particle species | proton |
| Frequency | 325 MHz |
| Particle input energy | 3 MeV |
| Particle output energy | 7 MeV |
| Peak current | 15 mA |
| Pulse width | 40 μs |
| Energy spread | <±0.3%(>8mA) |

## BEAM DYNAMICS DESIGN

To design an IH-DTL, the gap voltage and the transit time factor (TTF) for different cell is necessary. The TTF of cell is determined by interpolation with some typical cells like Parmila code. The gap voltage is given by designers at first which is shown in Fig. 1. The code and model of the dynamics design is introduced in reference [5].

This 325MHz IH-DTL is divided into 3 sections: bunching, acceleration, de-bunching. There are 4 gaps used for bunching which`s synchronous phase is -80 deg. The phase spread of the beam becomes bigger than ±20 deg because of a long MEBT after RFQ. This bunching section can bunch this beam without big distortion in longitudinal phase space. The acceleration section is designed in a KONUS way [7]. The structure is designed with 0 deg synchronous phase and the designed injecting energy is a little lower than the real bunch central energy. The injecting phase is 8 deg. As the real bunch central energy is bigger than the synchronous energy, the RF phase of bunch center decreases as shown in Fig. 2. The synchronous phase at de-bunching section is 10 deg and there are 5 gaps. This section are used to suppress the beam envelop growth as there is no focusing elements in the cavity. Meanwhile, this positive synchronous phase design can defocusing beam at longitudinal phase space. The energy spread is too big for injection and a de-buncher is needed after the DTL. This de-bunching section makes the beam spread at the exit of IH-DTL widely, which decreases the drift length between the DTL and the de-buncher. There are 21 gaps for this design and the total length is 1m. The phase space evolution is shown in Fig. 3. The blue lines are the bucket plot. The red

† tang.xuh@tsinghua.edu.cn

ISBN: 978-3-95450-199-1 doi:10.18429/JACoW-SAP2017-MOPH12



ellipses are calculated by linear matrices and the star lines are calculated by single particle tracking.

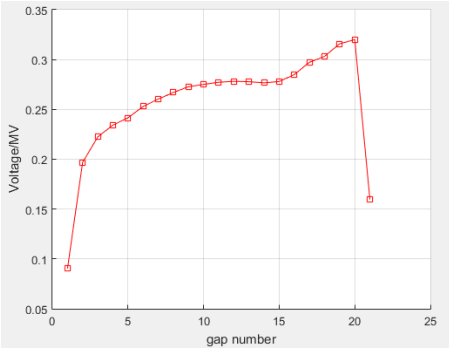


Figure 1: Voltage versus gaps.

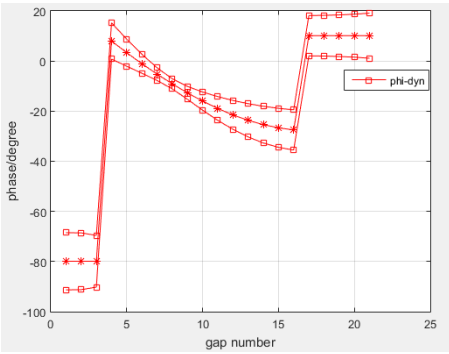


Figure 2: RF phase and phase spread for bunch centre versus gaps.

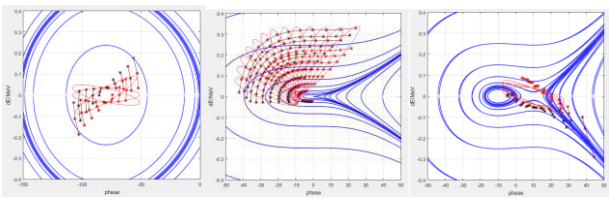

Figure 3: Phase evolution in bucket plot (left: bunching, middle: acceleration, right: de-bunching).

Those above are calculated with MATLAB code based on the simple model [5]. After getting the structure of this IH-DTL, it is checked with Tracewin code. The input parameter for multi-particle simulation is in Table 2.

Table 2: Beam Parameters at IH-DTL Entrance

| Beam at IH-DTL entrance | |
|---|---|
| Peak current | 15mA |
| $\alpha_{x/y}$ | 9.26 |
| $\beta_{x/y}$ | 2.55mm/mrad |
| Normalized RMS transverse emittance | 0.2π mm• mrad |
| $\alpha_z$ | -1 |
| $\beta_z$ | 0.75mm/mrad |
| Normalized RMS longitudinal emittance | 0.19deg*MeV |

The simulation results are shown in Fig. 4. The biggest beam spot is Ø16 mm. The transmission of the IH-DTL is >99%. The phase ellipse in longitudinal direction seems strong nonlinear effect. The energy spread is bigger than 0.32 MeV and the phase spread is bigger than 35 deg. But if there is a de-buncher at the 500 mm distance from the DTL exit. The phase ellipse is shown in Fig. 5. The energy spread of almost all particles is <±50keV, which satisfies the design requirement.

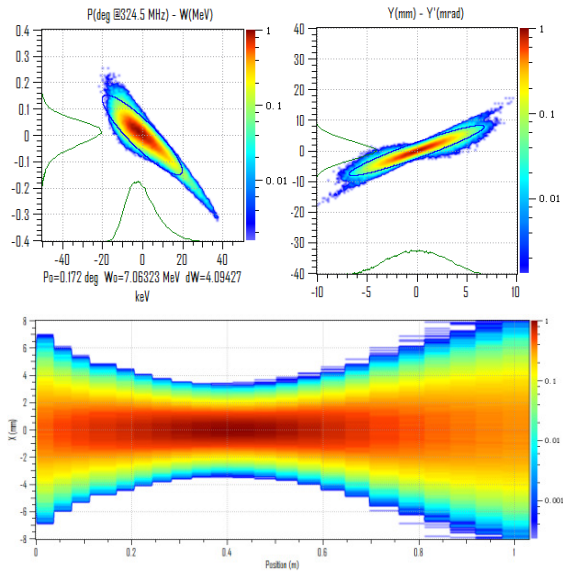


Figure 4: Multi-particle simulation results (left: longitudinal phase space, right: Y-Y' plot, bottom: beam envelop in X, X and Y are the same).

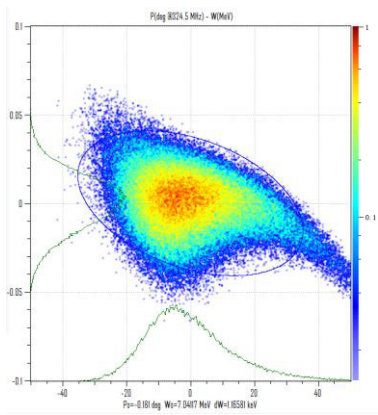

Figure 5: Longitudinal phase space after de-buncher.

## RF SIMULATION

After the dynamics design, the structure (cell length and numbers) of IH-DTL is determined. Based on the single cell geometry, a cavity is constructed with CST code. 8 tuners and 1 coupler has been mounted in the cavity. The 3D plot of vacuum area is shown in Fig. 6. The field map and RF parameters are calculated with CST`s Eigen mode solver. The RF results are shown in Table 3. The magnitude of Ez on Z axis is shown in Fig. 7. There is a little difference between the voltage used for dynamics design and voltage calculated by RF simulation,

ISBN: 978-3-95450-199-1 doi:10.18429/JACoW-SAP2017-MOPH12

shown in Fig. 7. If the difference is big, the re-design of the structure is needed to make the difference small enough. That`s the co-iteration process.

Table 3: RF Results of this 325 MHz IH-DTL

| Parameters | |
|---|---|
| Frequency | 324.87MHz |
| Power loss | 145kW |
| Q0 | 11760 |
| Cavity length | 0.983m |
| Shunt impedance | 201MΩ/m |
| Effective shunt impedance | 112MΩ/m |
| Epeak | 2.25Kp |

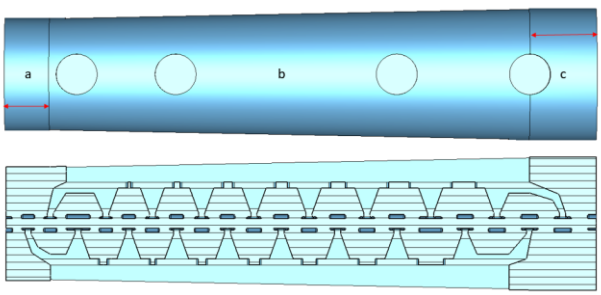


Figure 6: Vacuum area of the cavity(a/c: cylinder, b:cone).

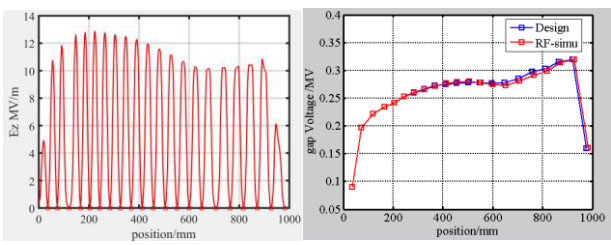


Figure 7: Ez distribution and voltage difference between the design and simulation.

As there is some difference between the dynamics design and RF simulation, 3D field map is used to do multi-particle tracking. The results seem similar to the dynamics design, which proves that this little difference is not important and the simple dynamics model is good enough to produce the structure of the IH-DTL. The tracking results is shown in Fig. 8.

## CONCLUSION

The design process of a 325 MHz IH-DTL at Tsinghua University is presented. The co-iteration of dynamics design and RF simulation is the key of this design process. The dynamics design divides the cavity into 3 sections: bunching, acceleration, de-bunching. This design don`t need a re-buncher after RFQ and decreases the distance between the DTL and the de-buncher. The RF simulation results agree well with the dynamics ones. The power loss of this cavity is 145 kW and the average accelerating gradient is 5.45 MV/m. This makes it a high efficient DTL for such a short cavity.

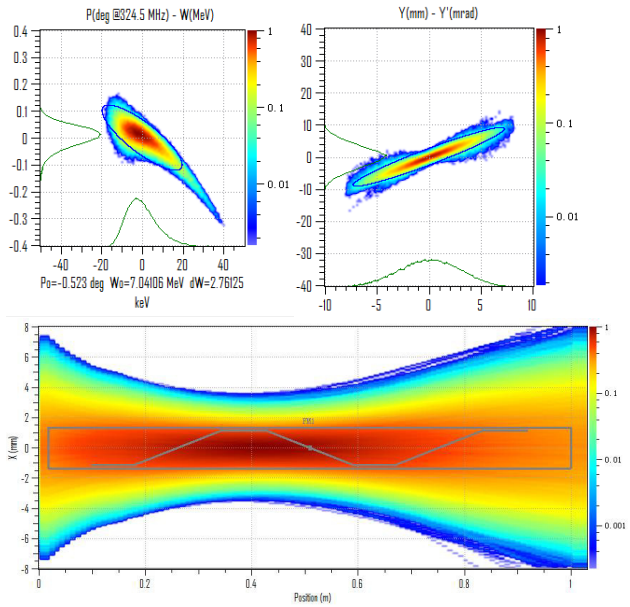


Figure 8: Multi-particle simulation results with 3D field map (left: longitudinal phase space, right: Y-Y' plot, bottom: beam envelop in X, X and Y are the same).

## ACKNOWLEDGEMENT

The authors wish to thank to Prof ZhiHui Li for his help with IH-DTL RF design and KONUS lattice design. And Prof. YuanRong Lu give a lot of advice on RF structure and process also.

## REFERENCES

[1] E. Nolte, G. Geschonke, K. Berdermann *et al.,* The Munich Heavy Ion Post Accelerator[J]. IEEE Transactions on Nuclear Science, 1977, 24(3): 1153-1155.

[2] S.S. Kurennoy, J.F. O'Hara, E.R. Olivas *et al.*, "H-mode Accelerating Structures with PMQ Focusing for Low-beta Ion Beams[J]", in *Proc. IPAC'10*, Kyoto, Japan, 2010, p. 828.

[3] Y. Lu, "Development of an IH-DTL Injector for the Heidelberg Cancer Therapy Project", (Ph.D. thesis), Physics Department, Frankfurt University, Frankfurt, Germany, 2005.

[4] K. Yamamoto, H. Tanaka, H. Harada *et al.,* "Experimental verification of an APF Linac for a Proton Therapy Facility[J]", *Nuclear Instruments and Methods in Physics Research Section B: Beam Interactions with Materials and Atoms,* vol. 269(24), pp. 2875-2878, 2011.

[5] R. Tang *et al.,* "RF AND PRIMARY BEAM DYNAMICS DESIGN OF A 325 MHz IH-DTL", in *Proc. IPAC'17*, Copenhagen, Denmark, May 2017, paper TUPVA104, pp. 2332-2335.

[6] M. Otani *et al.*, "APF IH-DTL Design for the Muon Lianc in the J-PARC Muon G-2/EDM Experiment", in *Proc. IPAC'16*, Busan, Korea, May 2016, paper TUPMY002, pp. 1539-1542.

[7] R. Tiede *et al.,* "KONUS beam dynamics designs using H mode cavity" in *Proc. HB2008*, Nashville, USA, 2008, paper WGB11,pp.223-230.

ISBN: 978-3-95450-199-1 doi:10.18429/JACoW-SAP2017-MOPH13



# MULTI-BEND ACHROMAT LATTICE WITH INTERLEAVED DISPERSION BUMPS FOR A DIFFRACTION-LIMITED STORAGE RING

Zhenghe Bai†, Derong Xu, Penghui Yang, Lin Wang*
National Synchrotron Radiation Laboratory, USTC, Hefei, China

*Abstract*

In this paper, we propose a new lattice concept of multi-bend achromat (MBA) for designing a diffraction-limited storage ring, which is inspired by the hybrid MBA concept proposed by ESRF EBS and the locally symmetric MBA concept recently proposed by ourselves. In this new MBA concept, two pairs of dispersion bumps are created in each cell, which accommodate sextupoles to correct chromaticities. For each pair of dispersion bumps, from the point of view of two different representations of a cell, many nonlinear effects caused by itself are cancelled out within one cell. For the two pairs of dispersion bumps, from the nonlinear cancellation point of view, they are interleaved. Compared to the hybrid MBA where only one pair of dispersion bumps is created in each cell, this new MBA can provide more knobs so as to better control tune shift terms, which is especially beneficial for enlarging dynamic momentum aperture.

## INTRODUCTION

In the recent two years the MAX IV light source has opened the door to the next-generation synchrotron radiation sources, the so-called diffraction-limited storage rings (DLSRs). Today many advanced light sources are being constructed or designed around the world towards lower emittances than MAX IV, even on the order of tens of pm·rad. Following MAX IV, these DLSRs adopt multi-bend achromat (MBA) lattices to reduce the emittance. Lower emittance generally means stronger nonlinear dynamics. For DLSRs with emittances of about one hundred or tens of pm·rad, the nonlinear dynamics is extremely strong, which is a big challenge for lattice designers.

To combat the very serious nonlinear dynamics in DLSRs with even lower emittances, some MBA lattice concepts with different nonlinear cancellation schemes have been proposed. PEP-X proposed a fourth-order geometric achromat MBA concept, in which the nonlinear cancellation was done over some cells. There are many knobs (i.e. families of nonlinear multipoles) in this concept so that tune shift terms and higher-order resonance driving terms can be well controlled. ESRF EBS proposed a hybrid MBA concept [1], in which the nonlinear cancellation was done within one cell that can be more effective than the cancellation over some cells due to interleaved sextupoles. However, it is hard to control tune shift terms in the hybrid MBA concept due to limited knobs. For the APS-U and HEPS lattices that adopt the hybrid MBA concept but have lower emittances than ESRF EBS, the tune shift with momentum is large and half-integer resonance line will be crossed for particles with relative momentum deviation of about 2~3%.

† baizhe@ustc.edu.cn
* wanglin@ustc.edu.cn

Recently we proposed a locally symmetric MBA (LS-MBA) concept by making the beta functions locally symmetric about two mirror planes in each cell [2], in which the nonlinear cancellation was done within one cell and also many knobs could be used. The LS-MBA concept was applied to the design of Hefei Advanced Light Source (HALS), and the designed lattices with emittances of tens of pm·rad had excellent on- and off-momentum nonlinear dynamics, especially the dynamic momentum aperture being larger than 7% or even 10%.

In this paper, we develop a new MBA concept following the same philosophy as for the LS-MBA, i.e. doing nonlinear cancellation within one cell and having many knobs to be used. In this new MBA concept, the dispersion in the arc section will have several bumps as in the hybrid MBA so as to reduce the strengths of sextupoles. We will first give a description for this new MBA concept and then apply it to the design of HALS.

## MBA LATTICE WITH INTERLEAVED DISPERSION BUMPS

In the hybrid MBA one pair of dispersion bumps is created at both ends of the arc section with a separation of $-I$ transformation, which is very effective for nonlinear cancellation and also can reduce the strengths of sextupoles. However, for each cell there can be placed only three families of sextupoles at most in the dispersion bumps. Due to that two knobs have to be used for correcting horizontal and vertical chromaticities, it is very hard to well control tune shifts with amplitude and momentum simultaneously using the other knobs (including one family of octupole). Our idea is to create an additional pair of dispersion bumps in each cell to increase the number of knobs. However, the problem for this idea is how to make a nonlinear cancellation for the additional pair of bumps. Inspired by the LS-MBA of the second kind that we proposed, the nonlinear cancellation for the additional pair of bumps can also be realized within one cell from the point of view of an unusual representation of a cell.

In the usual representation, we can write a cell as *ABBA*, where *A* represents one half of the long straight section and *B* one half of the arc section. In an unusual representation, we can also write it as *BAAB*. Using these two representations, we have classified the LS-MBA lattices into two kinds. For the hybrid MBA lattice, the nonlinear cancellation between the pair of two dispersion bumps is referred to using the representation of *ABBA*. For a MBA lattice, like the hybrid MBA lattice, with one pair of dispersion bumps satisfying the condition of nonlinear cancellation, if we create a second pair of dispersion bumps, generally the phase advance between the two bumps of the second pair

ISBN: 978-3-95450-199-1 doi:10.18429/JACoW-SAP2017-MOPH13

will not satisfy the condition of nonlinear cancellation using the representation of *ABBA*. But if using the representation of *BAAB*, the problem of phase advance for the second pair could be solved. Considering the real lattice design, a MBA lattice with interleaved dispersion bumps, as shown in the lower plot of Fig. 1, could realize the nonlinear cancellation within one cell for two pairs of dispersion bumps. In the upper plot of Fig. 1, a MBA lattice with only two dispersion bumps is also shown. From the nonlinear cancellation point of view, the pairs of bumps in the lower plot are interleaved, while the pairs of bumps in the upper plot are non-interleaved. The phase advances for the nonlinear cancellation between one pair of two bumps are

$$\mu_x=(2m+1)\pi,\ \mu_y=n\pi \quad (1)$$

for normal sextupoles, where $m$ and $n$ are integers. If $n$ is an odd number, the transformation between one pair of two bumps will be $-I$ transformation. We have found that the MBA lattice with interleaved dispersion bumps can be easily realized based on the hybrid 7BA lattice as will be designed in the next section for HALS.

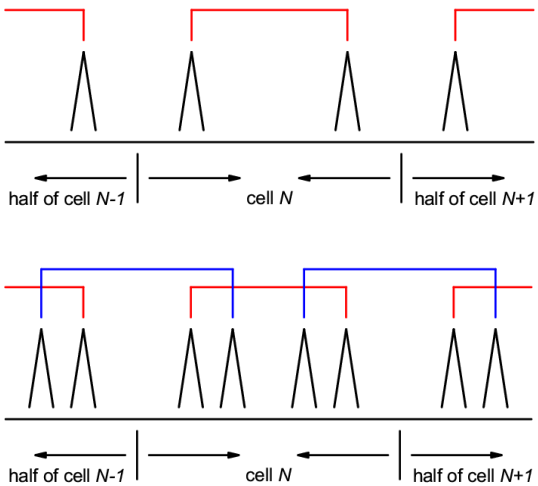


Figure 1: Schematics of MBA lattices with two dispersion bumps (upper) and interleaved dispersion bumps (lower). The nonlinear cancellation is made between each pair of dispersion bumps.

## HALS LATTICE DESIGN AND OPTIMIZATION

Now we apply the new MBA concept described above to the design of HALS. HALS is a soft X-ray DLSR proposed by NSRL two years ago, which is being designed aiming at an emittance of tens of pm·rad. An 8BA and a 6BA lattices had been designed for HALS using the LS-MBA concept. Following part of the feature of the hybrid 7BA lattice but using the new MBA concept, a 7BA lattice was recently designed for HALS. The linear magnet layout and linear optical functions are shown in Fig. 2, and some main parameters of the 7BA storage ring are listed in Table 1. In this lattice all bending magnets are combined function ones. From Fig. 2 we can see that four dispersion bumps are created in one cell, which is different from the case in the hybrid 7BA lattice. The 1st and the 4th dispersion bumps in the same cell form the first pair of bumps, and the 2nd bump of the present cell and the 3rd bump of the previous cell form the second pair of bumps. The phase advances between two bumps of the first or the second pair are $3\pi$ and $\pi$ in the horizontal and vertical directions, respectively (i.e. $-I$ transformation). The multi-objective particle swarm optimization (MOPSO) algorithm was applied in the linear lattice optimization, where the magnet layout and strengths are simultaneously optimized to search for the lowest emittance.

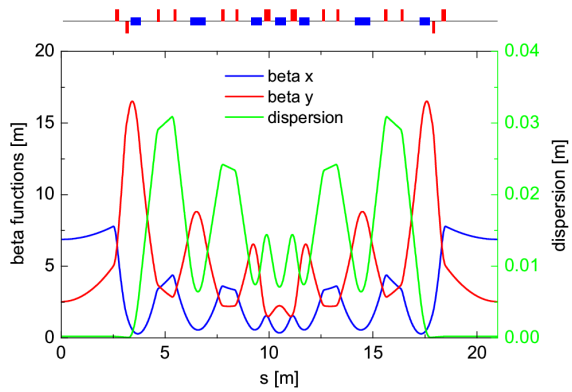


Figure 2: Linear magnet layout and linear optical functions of the HALS 7BA lattice.

Table 1: Main Parameters of the HALS 7BA Lattice Ring

| Parameter | Value |
|---|---|
| Beam energy | 2.4 GeV |
| Circumference | 672 m |
| Number of cells | 32 |
| Natural emittance | 30.9 pm·rad |
| Transverse tunes | 77.211, 28.281 |
| Natural chromaticities | -105, -103 |
| Momentum compaction factor | $6.08\times10^{-5}$ |
| Length of long straights | 5 m |
| Beta functions at long straights | 6.873, 2.526 m |

Six families of sextupoles (three families for each pair of bumps) were employed for chromaticity correction and nonlinear dynamics optimization, and no octupole was employed. MOPSO was also applied in the nonlinear optimization. Fig. 3 shows the part of the optimized dynamic aperture (DA) with tunes not crossing the integer resonance line. The tunes and horizontal DAs at different relative momentum deviations are shown in the upper and lower plots of Fig. 4, respectively. From Fig. 3 and Fig. 4 we can see that rather good on- and off-momentum dynamics are achieved, which is beneficial for long beam lifetime and implementation of longitudinal injection scheme in HALS. The maximum strength of sextupoles is in the range of (4000, 4500) T/m$^2$.

ISBN: 978-3-95450-199-1 doi:10.18429/JACoW-SAP2017-MOPH13



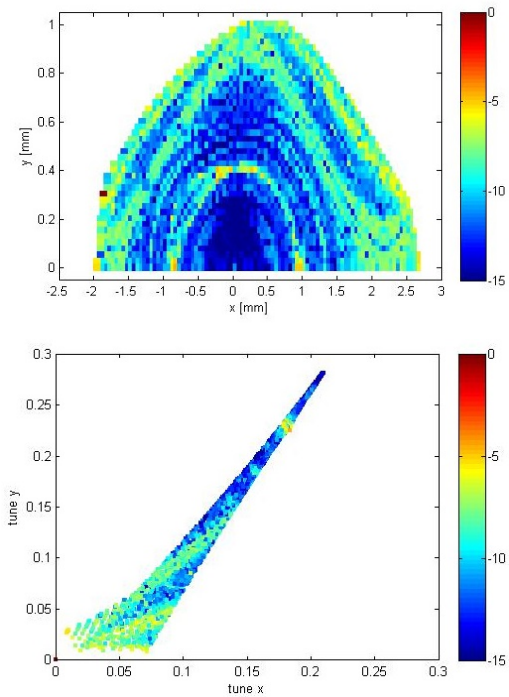


Figure 3: Frequency map analysis for the optimized DA.

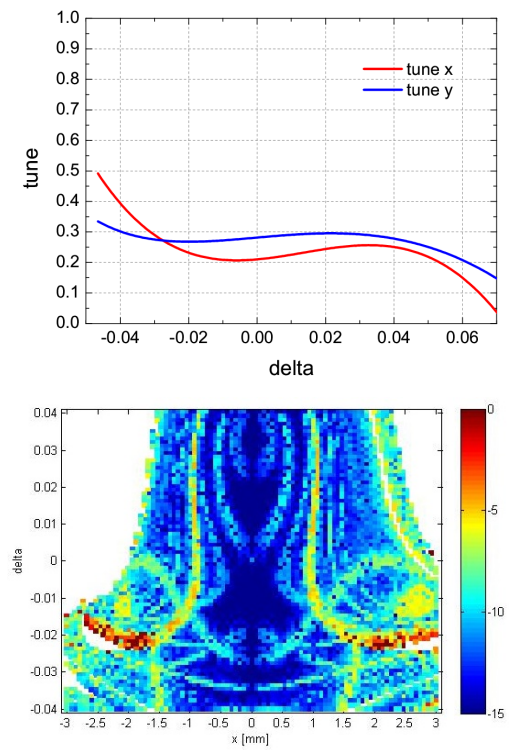


Figure 4: Tunes (upper) and horizontal DAs (lower) versus relative momentum deviations.

## CONCLUSION AND OUTLOOK

Inspired by the hybrid MBA and the LS-MBA of the second kind, we developed a new MBA concept, which had two pairs of dispersion bumps in each cell. For each pair of bumps the nonlinear cancellation was done within one cell, and the two pairs of bumps were interleaved from the nonlinear cancellation point of view. Compared to the hybrid MBA, this new MBA can provide more knobs to better control tune shifts with amplitude and momentum. The application of the new MBA concept to the design of HALS showed rather good nonlinear dynamics was achieved, especially the off-momentum nonlinear dynamics.

Besides, following some parameters of HEPS, we also applied the new MBA to the design of a 6.0 GeV DLSR with a circumference of about 1.4 km. A lattice with an emittance of about 50 pm·rad was achieved, and the preliminary nonlinear optimization result showed that the dynamic momentum aperture was larger than 4% without tune crossing half-integer resonance lines. This work will not be reported in this paper. In the coming work, we will consider using octupoles for further nonlinear optimization, and using longitudinal gradient and reverse bending magnets to lower emittance.

## ACKNOWLEDGEMENTS

This work was supported by the National Natural Science Foundation of China (11605203, 11475167), the National Key Research and Development Program of China (2016YFA0402000), and the Chinese Universities Scientific Fund (WK2310000058).

## REFERENCES

[1] L. Farvacque *et al.*, "A Low-Emittance Lattice for the ESRF", in *Proc. IPAC2013*, Shanghai, China (2013).

[2] Zhenghe Bai *et al.*, "Design Study for the First Version of the HALS Lattice", in *Proc. IPAC2017*, Copenhagen, Denmark (2017).

ISBN: 978-3-95450-199-1 doi:10.18429/JACoW-SAP2017-MOPH14

# OPTIMIZATION OF CLOSED ORBIT CORRECTION USING ANT COLONY ALGORITHM IN HALS

Derong Xu, Zhenghe Bai, Gangwen Liu, Hongliang Xu*, Lin Wang†
National Synchrotron Radiation Laboratory, USTC, Hefei 230029, China

*Abstract*

In this paper, we present a method using correctors as few as possible while controlling the residual closed orbit within an acceptable level based on ant colony optimization algorithm instead of the ideal optical properties. We prove that this method works well with HALS.

## INTRODUCTION

The Hefei Advanced Light Source (HALS) project [1], as a soft X-ray diffraction limited storage ring (DLSR), was proposed by National Synchrotron Radiation Laboratory with a beam energy around 2.4 GeV and the detailed lattice design is in progress.

To reduce the emittance of a DLSR, multi-bend achromat (MBA) lattices have been adopted. The main method to reduce emittance is to employ many strong quadrupoles which depress dispersion function and introduce chromatic aberrations that must be corrected with strong sextupoles [2]. In our first version lattice, the ring consists of 32 identical 6BAs with a nature emittance of 26.5 pm · rad [3]. The strong quadrupoles and sextupoles make the lattice sensitive to closed orbit distortion. Therefore, the closed orbit correction plays an important role in HALS's design.

Ant colony optimization (ACO) is a heuristic technique for optimization that was introduced in the early 1990's [4]. ACO, which is inspired by the ants' foraging behavior, is very suitable for combinatorial optimization problem. A scientific description for ACO algorithm can be found in [5].

In this paper, we develop a method to correct the closed orbit using Rank-based Ant System (RAS) – a variant of ACO [6]. The goal is to apply correctors as few as possible while controlling the residual closed orbit within an acceptable level.

## ERROR ESTIMATION AND BPMs LAYOUT OF HALS

The magnet elements of a storage ring can never be placed at their ideal positions. To simulate a real machine, we have to assume a statistical variation of their positions. The orbit distortion is caused by dipole errors which can be produced by bending magnets tilt, bending magnets strength or length error and transverse misalignment of quadrupoles etc. In addition, the orbit at quadrupoles or sextupoles concern with a closed orbit a lot in DLSR. If the closed orbit without correction exceed the vacuum chamber aperture limits, the orbit correction is impossible. Tracking the closed orbit with elegant [7] for 10,000 seeds, we find that the misalignment should be less than $8\,\mu m$ which is impossible technically. Tab. 1 shows the dipole error in the following simulations.

Table 1: Error Sheet for Magnets. All values are rms, and the truncation is $2\sigma$.

| | | |
|---|---|---|
| dipole | misalignment | $5\,\mu$m |
| | rotation error | 0.2mrad |
| | strength error | $5 \times 10^{-4}$ |
| quadrupole | misalignment | $5\,\mu$m |
| | strength error | $10^{-3}$ |
| | multipole error | [8] |
| sextupole | misalignment | $5\,\mu$m |
| | strength error | $10^{-2}$ |
| | multipole error | [8] |

Once a closed orbit is established, the position of this closed orbit is measured by a large number of Beam Position Monitors (BPM) and small corrector magnets are used to correct the closed orbit towards the ideal orbit. There are several guildlines to place BPMs along the ring.

- BPMs should be spaced by 90° in phase advance.
- The orbit at light source points should be stable enough. So both sides of radiation elements must be measured by BPMs.
- Maximum position measured by BPMs (MAX-BPM) have to approximately equal to the maximum closed orbit distortion(MAX-COD).
- BPMs are close to the sextupoles. In theory, the dynamic aperture can be restored if the beam pass through the center of the sextupoles.

In accordance with the above principles, we place 17 BPMs per cell in HALS as shown in Fig. 1. We also compare MAX-BPM with the MAX-COD for 10,000 seeds in Fig. 2. From the figure, we know that there is 93% possibility at least when the tolerance is 10%. That is

$$P\left(\left|\frac{u_c - u_b}{u_c}\right| < 10\%\right) > 93\%, \quad (1)$$

where $u_c$ is MAX-COD and $u_b$ is MAX-BPM. So our BPMs system is reasonable that the BPM measured value can reflect the real closed orbit.

## ALGORITHM DESCRIPTION

Tab. 2 summarizes all elements contained in the HALS lattice cell. Every drift line is a possible position to place a corrector. Because the last drift is connected to the first line

* hlxu@ustc.edu.cn
† wanglin@ustc.edu.cn

ISBN: 978-3-95450-199-1 doi:10.18429/JACoW-SAP2017-MOPH14



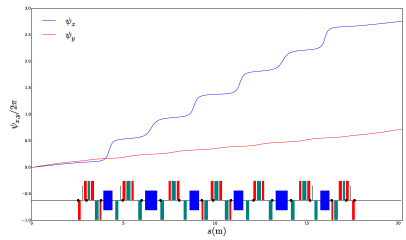

Figure 1: 17 BPMs' location in one cell. The blue and red lines are phase advance in horizontal and vertical plane respectively. The dark points on the baseline are where BPMs placed, The blue, red and cyan blocks are dipoles, quadrupoles and sextupoles respectively.

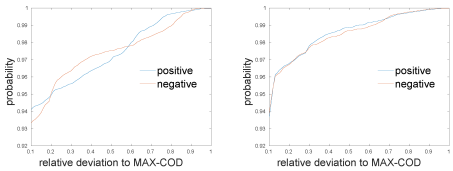


(a) Horizontal (b) Vertical

Figure 2: Probability of different tolerance. The blue and red lines are corresponding to positive and negative maximum closed orbit.

Table 2: All Elements Per Cell in HALS

| | |
|---|---|
| defocussing combined dipoles | 6 |
| quadrupoles | 20 |
| sextupoles | 19 |
| octupoles | 4 |
| drifts | 50 |

in the next cell, there are 49 optional locations for correctors. Except that the first location is chosen at the starting point in the first line, the rest locations are chosen at the midpoints of the drift lines. There are $2^{49} \approx 5.6 \times 10^{14}$ combinations in all. RAS is a powerful tool to deal with this situation. For convenient description, we number the locations from $C_1$ to $C_{49}$. We also mark $C_0$ as the origin where an artificial ant begins its trip and $C_{50}$ as its destination. Every tour from $C_0$ to $C_{50}$ indicates a correction scheme. The ant chooses its trajectory according to the pheromone left by the ant clony.

### *Initialize*

Let $e_{ij}$ be a edge from node $C_i$ to $C_j$, and $\tau_{ij}$ be the pheromone on edge $e_{ij}$. The complete graph is composed by edges $e_{ij}(0 \le i < j \le 50)$. At the very beginning, all edges have the same pheromone

$$\tau_{ij} = \tau_0, \qquad (0 \le i < j \le 50). \tag{2}$$

### *Finish a Tour*

When the ant is at the node $i$, the probability that node $j(j > i)$ is selected to be visited immediately can be written in the following formula:

$$p_{ij} = \frac{\tau_{ij}^{\alpha}}{\sum_{k=i+1}^{50} \tau_{ik}^{\alpha}}, i < j \le 50 \tag{3}$$

where $\alpha$ is a parameter to regulate the influence of $\tau_{ij}$. This selection process is repeated until the ant arrives at the destination $C_{50}$. Then a new lattice file is generated based on the tour and we run elegant to perform the correction. The same seed is used in each correction. The optimization objective function is

$$u = \sqrt{u_{bx}^2 + u_{by}^2}, \tag{4}$$

where $u_{bx}(u_{by})$ is MAX-BPM of horizontal(vertical) plane.

### *Update Pheromone*

After all $M$ ants have generated a tour $\Omega_m(1 \le m \le M)$ and the corresponding correction have been done, the ants are sorted by optimization objective function in Eq. 4. Then $(\omega-1)$ elitist ants are considered to update pheromone. Additionally, the best solution until the current iteration is also taken into account. Expressed by formula as

$$u_* \le u_1 \le u_2 \le \ldots \le u_{\omega-1}. \tag{5}$$

The corresponding tours are $\Omega_*, \Omega_1, \ldots, \Omega_{\omega-1}$. Each tour appears in the elite group only once to avoid the danger of over-emphasized pheromone caused by many ants using the same paths.

The updating formula is

$$\tau_{ij}(n+1) = \rho\tau_{ij}(n) + \sum_{k=1}^{\omega-1}(\omega-k)\Delta\tau_{ij}^{k} + \omega\Delta\tau_{ij}^{*}, \tag{6}$$

$$\Delta\tau_{ij}^{k} = \begin{cases} \frac{Q}{u_k} & \text{if } e_{ij} \in \Omega_k \\ 0 & \text{otherwise} \end{cases} \quad \Delta\tau_{ij}^{*} = \begin{cases} \frac{Q}{u_*} & \text{if } e_{ij} \in \Omega_*, \\ 0 & \text{otherwise} \end{cases} \tag{7}$$

where $n, \rho$ and $Q$ are parameters of the current iteration, the pheromone reduction and the quantity of pheromone laid by an ant per tour respectively.

## SIMULATION RESULT

All parameters mentioned in the previous section are listed in Tab. 3. The MAX-BPM described in Eq. (4) decreases with the increase of correctors as we excepted. The

Table 3: Parameters Used in the Simulation

| | | |
|---|---|---|
| $\tau_0$ | initial pheromone | 10 |
| $\alpha$ | influence of $\tau_{ij}$ | 2.0 |
| $\rho$ | reduction of pheromone | 0.8 |
| $Q$ | pheromone quantity laid by a ant | 20 |
| $M$ | number of ants in the colony | 20 |
| $\omega$ | number of elite ants | 6 |
| $\nu$ | random search limit | 49 |

ISBN: 978-3-95450-199-1 doi:10.18429/JACoW-SAP2017-MOPH14

result is shown in Fig.(3). If the MAX-BPM is required to be less than the misalignments(5 $\mu m$ in this case), 12 correctors at least are needed. When correctors are more than BPMs, a complete correction is possible for a reasonable scheme.

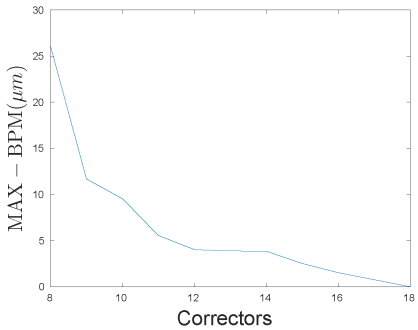


Figure 3: Best correction result for different number of correctors.

Figure 4 shows how the 12 correctors are placed. Figure 5 shows closed orbits before and after the correction using 130 sets of random errors. The corresponding statistical results of the maximum COD measured in the BPMs are shown in Fig. 6. It is clear that the maximum COD along the ring in x- and y-directions before the correction are bigger than 1mm which is the dynamic aperture of the bare lattice at $s = 0$. After the correction, the MAX-CODs along the ring are all smaller than 60 $\mu$m in x-direction, and 25$\mu$m in y-direction. Meanwhile, most MAX-BPMs are smaller than 5 $\mu$m which satisfies our requirment. So we can roughly say that the 12 corrector scheme works well in our case, but an exact estimation will have to be made upon dynamic tracking in the future. The maximum corrector strengths used in our correction does not exceed the corrector capacity which is about 1mrad.

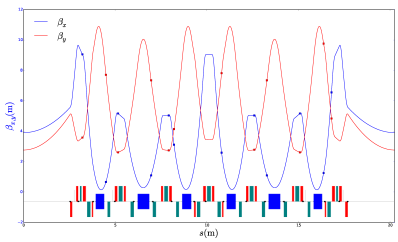

Figure 4: The 12 correctors scheme and $\beta$ functions. All the 12 correctors are used to correct both horizontal and vertical directions. The abscisse of squares on $\beta_x$ and $\beta_y$ are where to place the correctors. Elements on baseline are the same with Fig. 1.

## CONCLUSION

We explore the threshold of different kinds of dipole errors causing COD at first. To measure COD as accurate as possible, we propose a 17-BPMs layout scheme per cell in HALS and the simulation result also prove that it works well. Then we develop a method to correct the COD with different numbers of correctors. This method can find out a well worked correctors lawout of a fixed number ( maybe not the best one). Our simulation result indicates that a 12 correctors correction scheme is suitable for the current HALS lattice. A dynamical tracking will be done in the future and the generic algorithm will be considered to replace the random search step for improving efficiency. Besides, the parameters used in Tab. 3 will be further optimized.

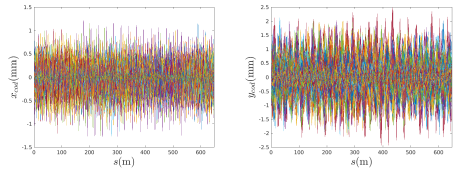

(a) Before correction,$x_{cod}$ (b) Before correction,$y_{cod}$

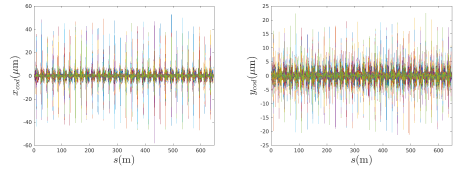

(c) After correction,$x_{cod}$ (d) After correction,$y_{cod}$

Figure 5: COD along the storage ring before and after the 12 correctors scheme is applied. 130 sets of random error are used.

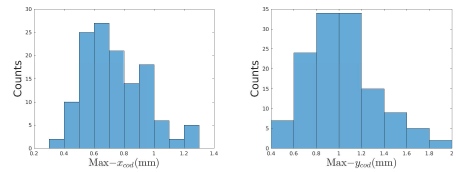

(a) Before, Max-$x_{BPM}$ (b) Before, Max-$y_{BPM}$

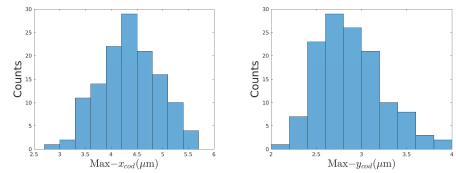

(c) After, Max-$x_{BPM}$ (d) After, Max-$y_{BPM}$

Figure 6: Counts of MAX-BPM before and after the 12 correctors scheme is applied. The same 130 sets of error are used.

## ACKNOWLEDGEMENTS

This work was supported by the National Key Research and Development Program of China (2016YFA0402000), the National Natural Science Foundation of China (11605203, 11475167), and the Chinese Universities Scientific Fund (WK2310000058).

ISBN: 978-3-95450-199-1 doi:10.18429/JACoW-SAP2017-MOPH14



## REFERENCES

[1] Z. Bai *et al.*, "Initial Lattice Design for Hefei Advanced Light Source: A VUV and Soft X-ray Diffraction-limited Storage Ring", in *Proc. IPAC'16*, Busan, Korea, May 2016, paper WEPOW027, pp. 2889–2891.

[2] R. Hettel and M.Borland, "Perspectives and Challenges for Diffraction-Limited Storage Ring Light Sources", in *Proc. NA-PAC'13*, Pasadena, CA, USA, 2013.

[3] Z. Bai, P. Yang, W. Li and L. Wang, "Design study for the first version of the HALS lattice", in *Proc. IPAC'17*, Copenhagen, Denmark, May 2017, paper WEPAB060, pp. 2713–2715.

[4] M. Dorigo, "Optimization, learning and natural algorithms", Ph.D. thesis, Politecnico di Milano, Italy, 1992.

[5] Christian Blum, "Ant colony optimization: Introduction and recent trends", *Physics of Life reviews*, vol. 2, no. 4, p.353–373, Oct. 2005.

[6] Bernd Bullnheimer *et al.*, "A new rank based version of the Ant System. A computational study.", 1997

[7] M. Borland, "elegant: A Flexible SDDS-Compliant Code for Accelerator Simulation ", Technical report, Argonne National Lab., IL (US), 2000.

[8] L. Rivkin *et al.*, "Precise magnetic measurements of the sls storage ring multipoles", in *Conference Program and Abstract of the Second Asian Particle Accelerator Conference*, 2001,pp. 209-211.

ISBN: 978-3-95450-199-1 doi:10.18429/JACoW-SAP2017-MOPH16

# RF EXCITATION PARAMETERS IN RESONANT EXTRACTION*

J. Li†, Y. J. Yuan, Institute or Modern Physics, CAS, Lanzhou, China

*Abstract*

Ion beam resonant slow extraction from synchrotron is extensively used in experimental nuclear and particle physics, material radiation science, and deep-seated malignant tumours radiotherapy. In this paper, the ion motion of resonant extraction under RF excitation are discussed. The expression for sweeping frequency waveforms used in tracking code for resonant extraction are presented.

## INTRODUCTION

The transverse excitation or RF-Knockout resonant extraction has been developed in the last twenty years as a popular method in slow beam extraction from synchrotron [1]. It also promotes the application of heavy ion radiotherapy due to the advantages of quick response on beam start and cut-off, and simple operation in controlling beam at therapy terminals [1]. The domestic heavy-ion synchrotron in operation e.g., CSRm and HIMM take this method to realize the slow extraction for experimental research and radiotherapy [2].

The process of RF transverse excitation is described as below. During the storage beam being accelerated to the energy for extraction, the betatron tune of synchrotron is adjusted to be closer to the third order resonance and synchronously introduced sextuple fields help to produce three separatrixes in phase space and confine the stored beam inside the stable region that is larger than transversal beam emittance. The RF excitation heats the circulating stored beam at horizontal plane, so that the transverse emittance blows up rapid until some ions escape away the stable region along the separatrixes and jump into the gap of electrostatic septum for extraction. To suppress the beam loss along the synchrotron, the electrostatic spectrum is required that further limits the dynamics aperture and deflects lost beam away from close orbit for those that jump into the septum gap. The extraction beam intensity is controlled by the RF excitation parameters. This method features fixed stable area in phase space or unchanged sextuple fields and synchrotron lattice parameters during the RF excitation process at extraction plateau. In additional, a orbit bump system upstream the electron spectrum and longitudinal RF capture are helpful to improve the extraction efficiency.

## ION MOTION UNDER RF EXCITATION

The ion motion equation under sextuple field and RF transverse excitation is written as:

$$X''(\mu) + X(\mu) + \tfrac{1}{2}\beta_x^{5/2} k_2 X^2(\mu) = \beta_x^{3/2}\frac{\beta c}{B\rho}\sum_{n\geq 0} E_x \delta(\mu - 2\pi Q_x m - \mu_k) \quad (1)$$

in which $\mu_k$ and $\mu$ are the Betatron phases of RF exciter and ions respectively, $Q_x$ is the horizontal working point, $k_2$ is the field strength of sextuple, $\beta_x$ is Twiss parameter, m is any integer greater than 0, $E_x = E_{x0}\sin(2\pi f_k t)$ represents the transverse excitation strength of RF electric field, $\delta$ at the right denotes Dirac function. If we replace the variable $\mu$ with revolution turn number $n$, i.e. $d\mu/dn \approx \Delta\mu/1 = 2\pi Q_x$ then equation (1) is rewritten as

$$X''(n) + (2\pi Q_x)^2(X(n) + +\tfrac{1}{2}\beta_x^{5/2} k_2 X^2(n)) = (2\pi Q_x E_x)\frac{\beta_x^{3/2}\beta c}{B\rho}\sum_{n,m}\cos(2\pi\frac{f_k}{f_{rev}}n)\delta(n-m) \quad (2)$$

with $f_k$ is the RF excitation frequency, $f_{rev}$ is the revolution frequency of ion beam in synchrotron. The homogeneous solution of equation (2) can be expressed as

$$X(n) = a\cos(2\pi q_x n + b) \quad (3)$$

where $q_x$ is fraction part of the horizontal working point $Q_x$, a and b represent any constants. The summation part at the right side of equation (2) is further written as

$$\sum_n \cos(2\pi\frac{f_k}{f_{rev}}n)$$

In comparison with the right side of equation (3), we find that the horizontal excitation works only when the RF frequency satisfies the following relationship

$$\frac{f_k}{f_{rev}} = Integer \pm q_x \quad (4)$$

This is required by applying RF excitation to the circulating ion beam.

The betatron amplitude of 10 ions under influence of sextuple and RF excitation is shown in Fig. 1, in which, sextuple field is applied after 500 revolution turns, and RF excitation starts up at the $1000^{th}$ turn.

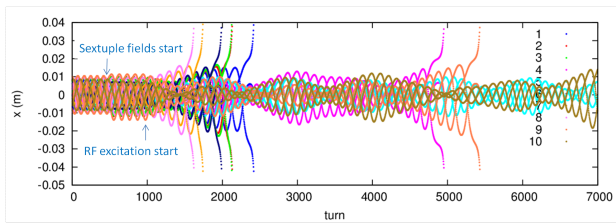


Figure 1: The betatron amplitude under influence of sextuple fields and RF excitation.

Because the betatron tune of ion also depends on momentum spread, betatron amplitude, and the magnetic field deviation and ripple etc., thus the circulated beam has a

* Work supported by NSFC (Grant No. 11475235, 11375245, 11575264)
† lijie@impcas.ac.cn

ISBN: 978-3-95450-199-1 doi:10.18429/JACoW-SAP2017-MOPH16



certain tune spread $\delta q_x$. According to equation (4), therefore, the extraction of more ions require RF exciter cover a frequency width

$$\Delta f_{ks} \geq f_{rev}\delta q_x \tag{5}$$

Generally, this is realized by white noise band or sweeping frequency back and forth around the resonance point.

## RF EXCITATION PARAMETERS

When the RF excitation is applied on the third-order resonance slow extraction, it have to sweep over a certain frequency width for a continuous extraction according to equation (5). In addition, the ion density decreases with extraction due to fixed area of stable region in phase space. For this reason, the uniform extraction needs adjustable amplitude of RF excitation throughout the extraction.

Therefore, uniform and continuous resonance extraction by RF excitation need the following adjustable parameters to the RF system:

- central frequency $f_k = (Integer \pm q_x)f_{rev}$
- sweeping frequency width $\Delta f_{ks}$
- sweeping frequency period $T_{ks}$
- excitation amplitude upon ion beam $U_{k0}$

Figure 2 shows the kick angle variation by RF excitation in three sweeping cycles when the central frequency is modulated by a sine waveform. The horizontal axis shows the normalized time of three cycles.

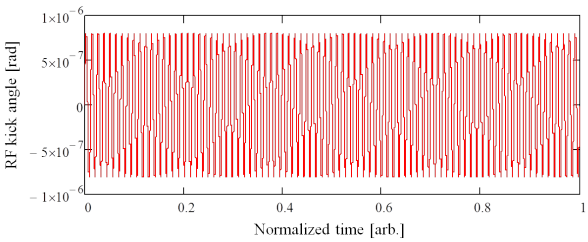


Figure 2: The kick amplitude variation over time under the modulation of sine waveform sweeping frequency.

## SWEEP FREQUENCY WAVEFORM

The waveform of rising sawtooth and triangular are typically used for sweeping frequency of RF excitation. To investigate the effect of different sweeping waveform, we list the expressions of kick angle dependence upon revolution turns in cases of sine, triangular, and sawtooth waveforms and implant them into the tracking code. We assume a sweeping bandwidth $\Delta f_{ks} = \pm 0.0005\Delta f_k$ at the following calculation in this section.

### *Sweeping in Sine Wave*

The sweep kick expression in sine waveform implanted in tracking is expressed as

$$\begin{cases} U_{k1}(N) = U_{k0}(N)\sin(2\pi N\frac{f_k}{f_{rev}} + P_{ks1}(N)) \\ P_{ks1}(N) = \frac{1}{2}\Delta f_{ks}T_{ks}\sin(\frac{2\pi N}{f_{rev}T_{ks}}) \end{cases} \tag{6}$$

in which $U_{k1}$ and $U_{k0}$ denote the kick angle by RF excitation, N is revolution turns, $p_k s1$ is a phase modulation term contributed by sweeping sine waveform.

### *Sweeping in Triangle Waveform*

The implanted sweep kick expression in triangle waveform is written as

$$U_{k2}(N) = U_{k0}(N)\sin(2\pi N\frac{f_k}{f_{rev}} + P_{ks2}(N)) \tag{7}$$

in which $U_{k2}$ denote the modulated kick angle by RF excitation, $p_{ks2}(N)$ is the modulated phase term contributed by sweeping triangle waveform.

Figure 3 shows the triangular waveform sweeping process of RF excitation central frequency over 3 sweeping cycle or $3 \cdot T_{ks}$ when the relative central frequency is showed as vertical axis and normalized time of three cycles as the horizontal coordinate.

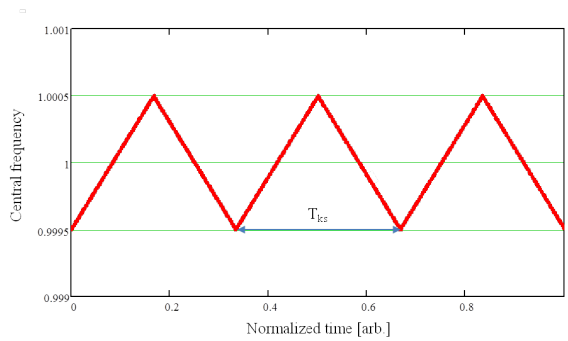


Figure 3: The relative central frequency variation over three sweeping cycles in case of triangle waveform.

The phase modulation parameter by triangle waveform sweeping frequency is expressed as

$$P_{ks2}(N) = \begin{cases} \frac{25}{4}\frac{\Delta f_{ks}}{f_{rev}^2 T_{ks}}(mod(N, T_{ks}f_{rev}) - \frac{T_{ks}f_{rev}}{4})^2, \\ \quad if \quad mod(N, T_{ks}f_{rev}) - \frac{f_{rev}-T_{ks}}{2} < 0 \\ \frac{25}{4}\frac{\Delta f_{ks}}{f_{rev}^2 T_{ks}}(mod(N, T_{ks}f_{rev}) - \frac{3T_{ks}f_{rev}}{4})^2, \\ \quad else \end{cases} \tag{8}$$

The phase variation by sweeping triangle waveform over three cycles is shown in Fig. 4.

ISBN: 978-3-95450-199-1 doi:10.18429/JACoW-SAP2017-MOPH16

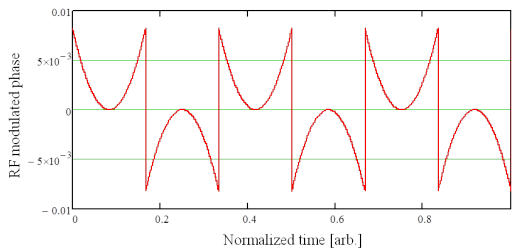


Figure 4: The phase variation over three sweeping cycles in case of triangle waveform.

### *Sweeping in Rising Sawtooth Wave*

The implanted kick expression in sweeping rising sawtooth waveform has the form

$$\begin{cases} U_{k3}(N) = U_{k0}(N)\sin(2\pi N\frac{f_k}{f_{rev}} + P_{ks3}(N)) \\ P_{ks3}(N) = \frac{25}{8}\frac{\Delta f_{ks}}{f_{rev}^2 T_{ks}}(mod(N, T_{ks}f_{rev}) - \frac{T_{ks}f_{rev}}{2})^2) \end{cases} \quad (9)$$

with $U_{k3}$ denotes the kick angle by RF excitation, $p_{ks3}(N)$ the modulated phase term by sweeping rising sawtooth waveform. Figure 5 shows variation of central frequency and modulated phase in case of rising sawtooth waveform while sweeping over three cycles.

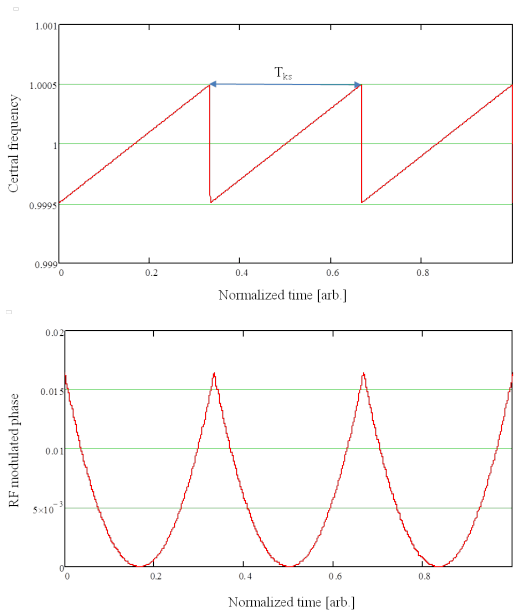


Figure 5: The dependence of central frequency and modulated phase variation on normalized time of three sweeping cycles in case of rising sawtooth waveform.

## BEAM UNIFORMITY WITH DUAL FM

In order to improve the time uniformity of extracted spill, the dual modulated RF frequency method is proposed by HIMAC [3]. The dual FM waveforms of triangular and rising sawtooth are implanted into simulation code. Fig. 6 shows the dependence of central frequency and modulated phase on normalized time in three sweeping cycles in which red and blues represent the two RF modulations with half cycle of phase shift.

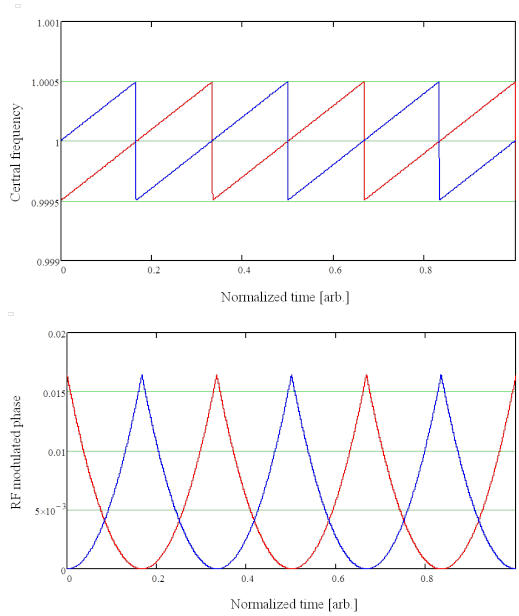


Figure 6: The variation of modulated central frequency and phase over three sweeping cycles in case of dual FM rising sawtooth waveform.

As an example of simulation, Figure 7 shows extracted intensity at the first y axis by histogram in red and the ratio of extracted ions to the total number one at the secondary vertical axis by green line in about 6 sweeping cycles. The left figure in Fig. 7 shows extraction at single RF modulation mode, while the right is the result of dual FM one but with smaller excitation amplitude. The RF sweeps in rising sawtooth waveform and starts at the $500^{th}$ revolution turn. Simulation shows that the uniformity of extracted ions gets improved with the dual FM methods.

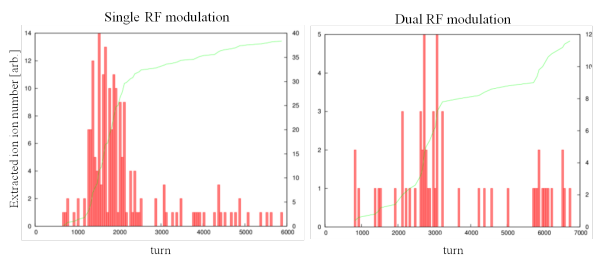


Figure 7: Comparison of extracted ion numbers and extraction ratio between single (left) and dual modulation (right).

## CONCLUSION

We discussed the ion motion of resonant extraction under RF excitation. Particularly, the expression of sweeping frequency waveforms are given which can be added into other tracking code for resonant extraction. As an example of simulation, the beam uniformity with dual FM is present.

ISBN: 978-3-95450-199-1 doi:10.18429/JACoW-SAP2017-MOPH16



## REFERENCES

[1] K. Noda *et al.*, "Slow beam extraction by a transverse RF field with AM and FM", *Nucl. Instr. and Meth. A*, vol. 374,pp. 269-277, 1996.

[2] Q. Li *et al.*, "Progress in heavy ion cancer therapy at IMP", *AIP Conference Proceedings*, vol. 1533, pp. 174-178, 2002.

[3] K. Noda *et al.*, "Advanced RF-KO slow-extraction method for the reduction of spill ripple", *Nucl. Instr. and Meth. A*, vol. 492, pp. 253-263, 2002.

ISBN: 978-3-95450-199-1 doi:10.18429/JACoW-SAP2017-MOPH17

# SIMULATION OF BEAM INTENSITY LIMITATIONS UNDER SPACE CHARGE EFFECTS AT BRing OF HIAF *

J. Li†, J. C. Yang, HIAF design group, Institute or Modern Physics, CAS, Lanzhou, China

*Abstract*

The booster ring (BRing) of the new approved High Intensity heavy-ion Accelerator Facility (HIAF) in China is designed to stack $^{238}U^{35+}$ ions at the injection energy of 17MeV/u and deliver $1.0{\cdot}10^{11}$ of uranium ions at 800MeV/u. Two injection modes, with or without the electron cooling, are introduced. The transverse emittance evolution and beam lifetime are investigated by simulation of RF capture process for the fast cycle mode.

## INTRODUCTION

### *HIAF Layout*

The High Intensity heavy-ion Accelerator Facility (HIAF) is a new heavy ion accelerator complex under detailed design by Institute of Modern Physics [1]. Two typical particles of uranium and proton is considered in the design. The beam is generated by a Superconducting Electron Cyclotron Resonance (SECR) ion source or an intense proton source, and accelerated mainly by an ion linear accelerator (iLinac) and an booster ring (BRing). The iLinac is designed to deliver $H_2^+$ at 48 MeV and $^{238}U^{35+}$ at 17 MeV/u. Before entrancing into the BRing, $H_2^+$ is stripped to proton, then accumulated by two-plane painting and accelerated to 9.3 GeV. The $^{238}U^{35+}$ is injected by multi-turn two-plane painting scheme, after accumulation or cooling by an electron cooler at the BRing, then accelerated to 0.2-0.8 GeV/u for extraction. After being stripped at the HIAF FRagment Separator (HFRS), the secondary beam like $^{238}U^{92+}$ is injected to the Spectrometer Ring (SRing) for the high precision physics experiments. Besides, five external target stations of T1 - T5 is planned for nuclear and atomic experimental researches covering the energy range from 5.8-800 MeV/u for uranium beam. The global layout of the HIAF complex is illustrated in Fig. 1.

### *Overview of the BRing*

The BRing is designed to accumulate beam intensity up to the space charge limit at injection energy and deliver over $1.0{\cdot}10^{11}$ $^{238}U^{35+}$ ions or $1.0{\cdot}10^{12}$ protons in extraction. Two operation modes of fast and slow are considered. The fast mode feathers multi-turn two-plane painting injection within around 120 revolution turns whereas the slow one by over 10 s injection time for electron cooling helped accumulation. Main parameters of the BRing are listed in Table 1. The BRing has a three-folding symmetry lattice around its circumference of 549.45 m. Each super-period consists of an eight-FODO-like arc and an over 70 m long dispersion-free straight section featured with length of 15.7 m drift reserved for electron cooler, two-plane painting injection, or RF cavities. Lattice layout of the BRing for one super-period is shown in Fig. 2.

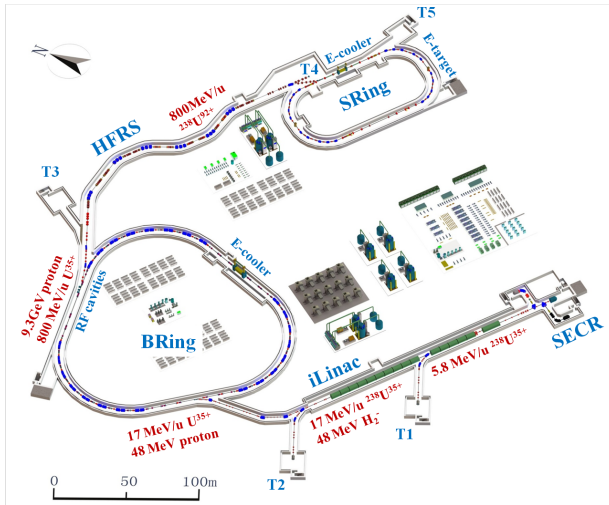


Figure 1: General layout of the HIAF complex.

Table 1: Main Parameters of the BRing

| Parameter | Proton | $^{238}U^{35+}$ |
|---|---|---|
| Injection energy | 48 MeV | 17 MeV/u |
| Injection mode | EX [a]+PT [b] | PT, PT+EC[c] |
| Betatron tune | - | (8.45,8.43) |
| Circumference | 549.45 m | |
| Max. magnetic rigidity | 34 Tm | |
| Super-periodicity | 3 | |
| Bunching factor | 0.2~0.4 | |
| Acceptance ( $H/V, \delta p/p$ ) | $200/100\pi mmmrad, \pm 5.0\%$ | |

[a] Charge exchange.
[b] Two-plane painting.
[c] Electron cooling.

### *Factors Concerning to Space Charge Effect*

Space charge effect induced resonances dominate the limit on beam intensity and density especially at low energy heavy-ion synchrotron. Factors concerning to this effect at the BRing are list below.

**Painting Injection** Two-plane painting multi-turn injection scheme is adopted to accumulate high intensity beam. The injected storage beam has a momentum spread $\pm 2.0\%$, and horizontal emittance 200 $\pi$mmmrad and vertical one of 100 $\pi$mmmrad with a quasi-uniform or Gaussian distribution in transverse phase space according to the simulation [2, 3].

* Work supported by NSFC (Grant No. 11475235, 11375245, 11575264)
† lijie@impcas.ac.cn

ISBN: 978-3-95450-199-1 doi:10.18429/JACoW-SAP2017-MOPH17



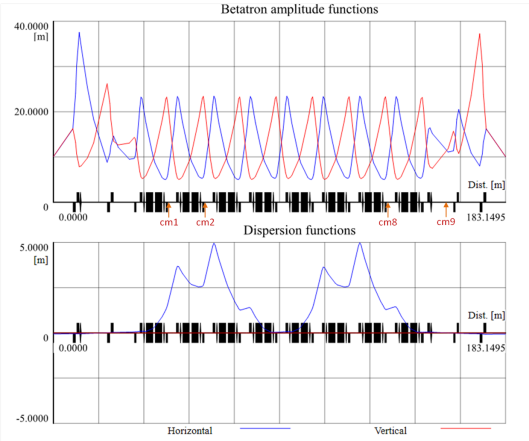


Figure 2: BRing lattice for one super-period.

**RF System** An intermediate plateau is planed within acceleration from injection to extraction energy. The capture and first stage of acceleration works at a harmonic number of three for $^{238}U^{35+}$, and harmonic number of two for proton at a ramping speed of 12 T/s. To depress the space charge effect, a dual harmonic RF system is considered to increase the bunching factor up to 0.4 whereas it's about 0.2 in the case of a single harmonic.

**Electron Cooling** To obtain intense beam at injection energy and short bunch at middle acceleration plateau, the magnetized electron cooling is adopted for accumulation at 17 MeV/u and cools bunched beam at 200 MeV/u. It is expected that the injected uranium beam will be cooled to a emittance less than 50 $\pi mmmrad$ and a momentum spread less than $3.0 \cdot 10^{-4}$ at the injection energy [4].

**Collimation System** To keep the vacuum condition ~ $1.0 \cdot 10^{-11}$ mbar, each super-period is placed eight collimators ($cm1 \ldots cm8$) just behind each defocusing quadruple at arc section and one more ($cm9$) at the position between the first focusing and defocusing quadruple at straight section. The total number of collimator is 27 around the ring.

**Stop-bands Compensation** Stop-bands correction system is proposed to depress the main resonance for a larger space for tune spread by high intensity beam. Compensation of linear coupling and the $3^{rd}$-order stop-bands are considered at the nominate working point (8.45,8.43) for uranium beam. The valid tune space after compensation is expected to reach ~ 0.4.

## RESONANCES AND TUNE SPREAD

### *Resonances*

The charged particle beam produces repulsive force and resulting in depressed distribution in tune space. During the injection and accumulation process of $^{238}U^{35+}$ beam at BRing, the nominal working point is set as (8.45, 8.43) with safety distance from dangerous low-order structure resonances shown in Fig.3 as the blue solid lines, i.e. $3^{rd}$-order $2Q_y - Q_x = 9$ and $2Q_x - Q_y = 9$. Whereas it sits next to the linear coupling difference resonance $Q_x - Q_y = 0$ and about 0.1 above the $3^{rd}$-order betatron resonances $3Q_y = 25$, $Q_x + 2Q_y = 25$, $3Q_x = 25$, $2Q_x + Q_y = 25$ shown as dotted lines. Thus the valid vertical space is 0.1 without any stop-bands compensation and a little larger than 0.4 after compensating the linear coupling resonance and $3^{rd}$-order ones above the integer resonance of $Q_y = 8$. They are indicated in Fig. 3 by short heavy diagonal line and long double line respectively. The $4^{th}$-order resonances indicated as pink lines in figure are ignored due to weak effect considering operation experiences.

For operation at the design intensity of $1.0 \cdot 10^{11}$, the linear coupling will be compensated by skew quadruple field which is produced by additional windings on steering magnets at the straight lattice section. The $3^{rd}$-order stop-bands is planned to be compensated by sextuple fields produced by windings on existed normal and new skew sextuple magnets.

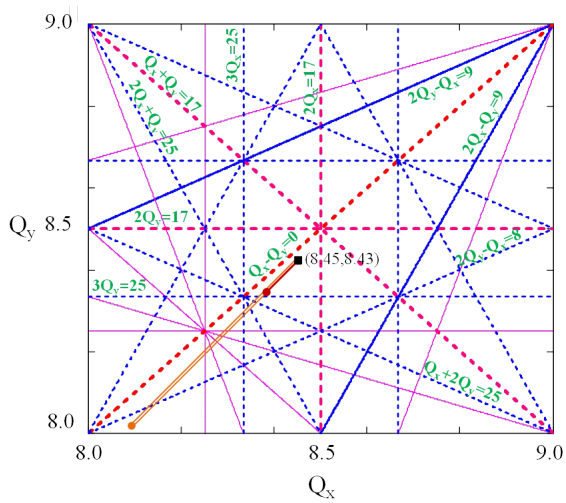


Figure 3: Resonances in tune diagram at the BRing: half-integer and linear difference coupling (red dotted line), $3^{rd}$-order structure (blue solid line), $3^{rd}$order betatron (blue solid line), and $4^{th}$-order structure (pink solid line). The nominal working point (■) for $^{238}U^{35+}$ injection is set as (8.45, 8.43).

### *Tune Spread*

The maximum allowed intensity of storage beam at BRing is limited by transverse space charge effect through valid space for tune spread that can been evaluated by:

$$\Delta Q_{y\_inc} = -\frac{N_i r_i}{\beta\gamma^2}\frac{G_t}{B_f \epsilon_{y\_n}}\left(1 + \sqrt{\frac{\epsilon_{y\_n} Q_h}{\epsilon_{x\_n} Q_v}}\right) \quad (1)$$

in which $\Delta Q_{y\_inc}$ is incoherent tune spread, $N_i$ is particle number, $\beta$ and $\gamma$ are relativistic factors, $r_i = 7.93 \cdot 10^{-18} m$ is the classical radius of $^{238}U^{35+}$, $\epsilon_{x\_n}$ and $\epsilon_{y\_n}$ are the normalized transverse beam emittance. $G_t$ is transversal distribution factor and equals to 2 for Gaussian distribution

ISBN: 978-3-95450-199-1 doi:10.18429/JACoW-SAP2017-MOPH17

in real space, $B_f$ longitudinal bunching factor and equals to 1.0 for coasting beam and reaches 0.4 here in the case of dual harmonic RF system, $Q_h$ and $Q_v$ are the nominal horizontal and vertical working points. Table 2 lists the calculation result of beam intensity limitation by transverse space charge at injection energy and vertical incoherent tune spread at design intensity when the emittance comes up to the designed acceptance.

Table 2: Intensity Limitation and Tune Spread at the BRing

| **Parameters** | **Proton** | $^{238}U^{35+}$ |
|---|---|---|
| $\Delta Q_{y\_inj}$ [a] | 0.09 | 0.14 |
| $\Delta Q_{y\_mid}$ [b] | - | 0.01 |
| Intensity limitation [c] | $4.38{\cdot}10^{12}$ | $2.87{\cdot}10^{11}$ |
| Bunching factor | 549.45 m | |
| Max. magnetic rigidity | 34 Tm | |
| Valid tune space | 0.4 | |
| RF bunching factor | 0.4 | |
| Normalized emittance ( $H/V$) | $38.4/19.2\pi mmmrad$ | |

[a] Tune spread at injection energy with design intensity.
[b] Tune spread at middle platform with design intensity.
[c] RF bunched beam at injection plateau.

Figure 4 shows the simulation for $^{238}U^{35+}$ when the beam emittance equals to the transverse acceptance and momentum spread of ±2.0%, at its design intensity of $1.0{\cdot}10^{11}$ and is bunched after RF capture with a bunching factor of 0.4. The simulation result indicates a vertical tune spread width about 0.16 that is bigger than 0.14 by calculation. The difference of tune spread can been explained by ions with larger betatron amplitude. Moreover, the spread crosses four $3^{rd}$-order betatron resonances and the linear coupling difference resonance. Compensation or correction of these resonances is considered for normal operation.

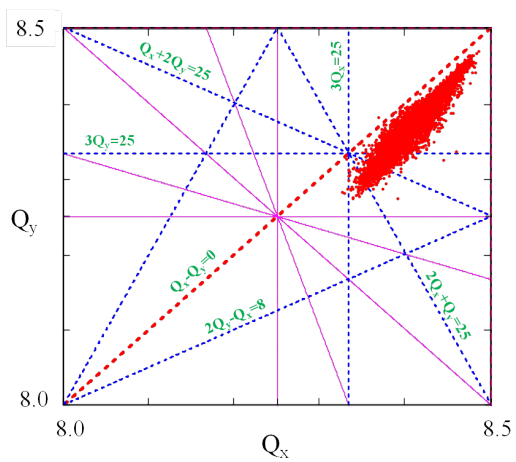


Figure 4: Tune spread of $^{220}U^{35+}$ beam at the design intensity $1.0{\cdot}10^{11}$ at the BRing, and resonances of linear coupling (red dotted diagonal), $3^{rd}$-order betatron (blue dotted lines), $4^{th}$-order structure (pink solid lines).

## EMITTANCE EVOLUTION UNDER SPACE CHARGE EFFECT

To observe the transverse beam emittance change and beam survival of $^{238}U^{35+}$ at its designed intensity of $1.0{\cdot}10^{11}$, ten thousands of macro particles is tracked about 5000 turns during the RF capture process from initial coasting beam after injection. We applied adiabatic RF voltage variation from zero to 23.4 kV [5], zero phase and three number of harmonic frequency upon one of six cavities at the injection energy. The simulation is performed by modified pyORBIT code under 2.5D space charge model [6]. We symmetrically set three elliptical aperture limits at the positions of straight section collimator ($cm9$). The aperture limit is set as 50 mm larger than the beam envelope size (129 mm, 64 mm) at the case of designed beam acceptance. The lost ions will been collected when their betatron amplitude exceeds the aperture limit at the three places and get their related message recorded in simulation. Figure 5 shows the dependences of relative or normalized emittance and beam intensity on revolution turns in logarithmic coordinate.

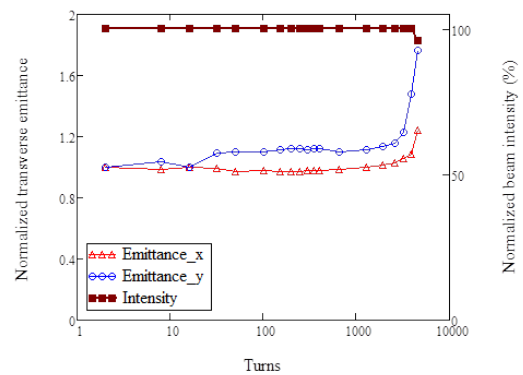


Figure 5: Evolution of normalized horizontal (△) and vertical (○) emittance and survived beam intensity (■) during the RF capture process from initial coasting beam.

The simulation indicates emittance exchange between the horizontal and vertical planes in the first 1000 turns and a gradually accelerating growth of emittance variation. The exchange is explained by tune spread overlapping with the stop-band of linear difference coupling, while a slow emittance variation by beam rotation in longitudinal phase space during the early RF bunching process. The emittance growth is caused by spread staying on the $3^{rd}$-order resonances with longer time when the preliminary bunch is formed.

## CONCLUSION

We list factors concerning to space charge effect for high intensity at beginning. Then the resonances and tune spread at BRing are discussed. The emittance evolution under space charge effect suggests to compensate the linear coupling resonance stop-bands and the one of $3^{rd}$-order at the BRing.

ISBN: 978-3-95450-199-1 doi:10.18429/JACoW-SAP2017-MOPH17

## REFERENCES

[1] J.C. Yang *et al.*, "High Intensity heavy ion Accelerator Facility (HIAF) in China", *Nucl. Instr. and Meth. B*, vol. 317, p. 263-265, 2013.

[2] W.P. Chai, private communication, Jun. 2016.

[3] T. Katayama, private communication, Jun. 2017.

[4] L.J. Mao, private communication, Mar. 2016.

[5] D.Y. Yin, private communication, Jun. 2016.

[6] A. Shishlo *et al.*, "The Particle Accelerator Simulation Code PyORBIT", *Procedia Computer Science*, vol. 51, p. 1272-1281, 2015.

ISBN: 978-3-95450-199-1 doi:10.18429/JACoW-SAP2017-MOPH18

# INVESTIGATION ON THE SUPPRESSION OFINTRABEAM SCATTERING IN THE HIGHINTENSITY HEAVY ION BEAM WITH THE HELP OF LONGITUDINAL DOUBLE-BUNCH OF ELECTRON*

X. D. Yang†, L. J. Mao, J. Li, X. M. Ma, T. L. Yan, M. T. Tang, H. Zhao, G. H. Li
Institute of Modern Physics, CAS, Lanzhou, China

*Abstract*

Intrabeam scattering is the main reason of degradation of the beam brightness and shortening of brightness lifetime in the collider, light source and storage ring. The intrabeam scattering presents dissimilar influence in the different facilities. Electron cooling was chosen to suppress the effect of intrabeam scattering and another unexpected effect happened during the cooling. The distribution of ion beam quickly deviates from the initial Gaussian type, then form a denser core and long tail. The ions standing in the tail of beam will loss soon owing to large amplitude. This solution will focus on the investigation on the suppression of intrabeam scattering in the high intensity heavy ion beam in the storage ring with the help of longitudinally modulated electron beam. The stronger cooling was expected in the tail of ion beam and the weaker cooling was performed in the tail of ion beam. The particle outside will experience stronger cooling and will be driven back into the centre of ion beam during which the ion loss will decrease and the lifetime will increase. The intensity of ion beam in the storage ring will be kept and maintain for a long time.

## INTRODUCTION

This solution will focus on the investigation on the suppression of intrabeam scattering in the high intensity heavy ion beam in the storage ring with the help of longitudinally modulated electron beam. The traditional DC electron beam in the electron cooler was modulated into electron bunch with different longitudinal distribution. The stronger cooling was expected in the tail of ion beam and the weaker cooling was performed in the tail of ion beam. The particle outside will experience stronger cooling and will be driven back into the centre of ion beam. The ion loss will lessen and the lifetime will be increased. The intensity of ion beam in the storage ring will be kept and maintain for a long time. Two functions will be combined into one electron cooler. The more short pulse, the more high intensity and more low emittance heavy ion beam was expected in the cooler storage ring. In the future, these results of this project will be constructive to the upgrade and improvement for existing machine and also be helpful to the design and operation for future storage and high energy electron cooler.

## SOME CONSIDERATIONS

The final equilibrium transverse emittance and longitudinal momentum spread were determined by the cooling effect and intra-beam scattering heating effect together in the case of fixed ion energy and particle number. If we want to get more particle number, in other words, more intensive ion beam, a new parameters configuration will be necessary in the new equilibrium state. In the absence of electron cooling, the transverse ion beam will be blown-up due to not suppression intra-beam scattering effect. The transverse dimension and longitudinal length of ion beam will increase with time, as a result, some ion will loss and the lifetime of ion beam will become short.

## LIFETIME AND INTENSITY OF ION BEAM

The ion beam of $^{238}U^{92+}$with population $1*10^{11}$ particle was required in the high energy high intensity accelerator facility [1]. In this situation, the final emittance and momentum spread were the key parameters which the physics experiments concerned, more important parameters of ion beam were lifetime and the ion number in the detectors.

## MOTIVATION

Two essential questions should be certainly answered and clearly described in advance.

The first question concerned by physics experiment is that whether enough particle [2] be provided to the experiments terminals.

The second one concerned the lifetime [3] of the ion beam with so high intensity whether enough to satisfy the requirements of physics experiments, because it determines the efficiency of experiments.

## NEW SOLUTION PROPOSED

There are three points in this solution. The first point, the intensity of electron bunch presents certain distribution according to the ion bunch distribution in the longitudinal direction. The second point, the electron bunch distribution will change actively according to the ion beam distribution in the cooling process. As a result, the electron beam will provide different strength cooling in the different periods. The third point, the transverse intensity distribution can change also, the electron beam can present different transverse distribution according to the transverse distribution of ion beam in the cooling process. The purpose of this solution will aim to suppress the effect of IBS, increase the lifetime of ion beam and reduce the ion loss during cooling [4].

* Work supported by The National Natural Science Foundation of China, NSFC (Grant No. 11375245, 11475235, 11575264 )
† yangxd@impcas.ac.cn

ISBN: 978-3-95450-199-1 doi:10.18429/JACoW-SAP2017-MOPH18



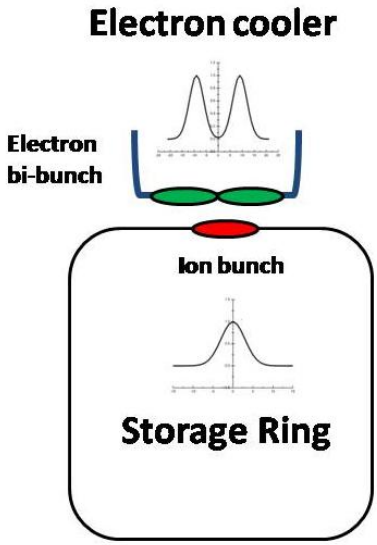


Figure 1: The longitudinal relation between the ion bunch in the storage ring and electron double-bunch in the electron cooler.

In the interest of cooling the un-Gaussian distribution ion beam and suppressing the IBS in the ion beam, we plan to modulate the electron beam in longitudinal direction [5]. In the first step, two proximate electron bunches were delivered by the electron gun, and triggered isochronously. An ion bunch will be cooled by this two electron bunches, it was shown in the Fig. 1. We hope this solution can provide stronger cooling in the tail of ion pulse, and relatively weaker cooling in the core of ion bunch. Further, The hollow electron beam will be united with the longitudinal electron bunches. We hope decrease the ion loss caused by recombination. The hollow electron beam in which the radial distribution of electron can be changed will be combined with the longitudinal modulated electron bunch chain in which the longitudinal distribution presents proper distribution as demonstrated in the Fig.2.

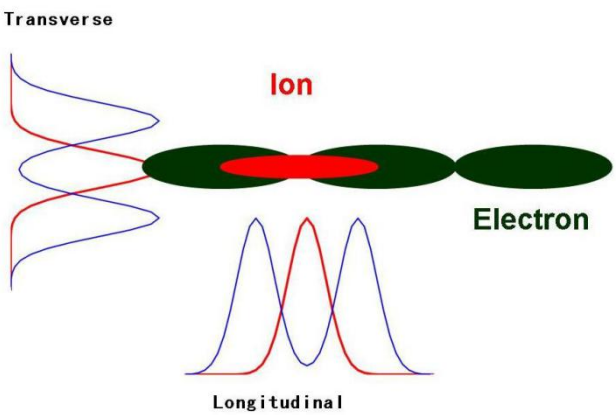


Figure 2: Diagram of ion bunch and electron double-bunch distributions in the transverse and longitudinal directions respectively.

If we use the pulsed electron beam, as one possible result, we can use higher average electron density than the DC electron beam, the ion in the beam can experience higher cooling than DC electron beam, and these ion were expected to be cooled down quickly, and to avoid escaping from the RF bucket.

### *Betacool Simulation*

Betacool program [6] has the ability to simulate the cooling and intrabeam scattering processes together in the various conditions, such as electron bunches and it can give the information about the lifetime of ion beam and final equilibrium emittance and bunch length, etc. Another function was developed for calculating the cooling and scattering intrabeam in the case of bunched electron beam.

According to the information from the IBS measurement results, the electron beam will be provided different distribution in the different periods, such as in the beginning of cooling and intrabeam scattering, before achieve the equilibrium and final equilibrium situation. In the beginning, the ion beam needs to cool down fast with the lowest ion loss, while before the equilibriumit needs modest cooling, and in the period of equilibrium, it just needs maintaining the proper cooling to counteract IBS effect.

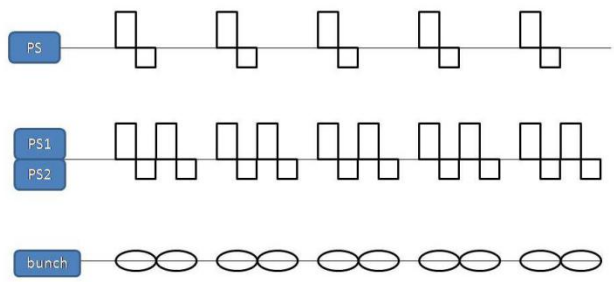


Figure 3: Sketch of two electron bunches generated by two independent HV power supplies with the help of delay trigger.

### *Scheme and Scenario*

In order to get the double-bunch with the certain frequency corresponding the ion beam revolution frequency, two independent HV power supplies were arranged in parallel connection. Delay trigger was used in this solution, as illustrated in the Fig. 3. Every electron bunch was driven by the independent HV power supply, and the strength, width and space will be adjusted independently. In additional, the time relation between the double electron bunch can be triggered slightly advance precede and trail before and after the ion pulse in the electron cooler, and ion pulse will be timely, earlier or later.

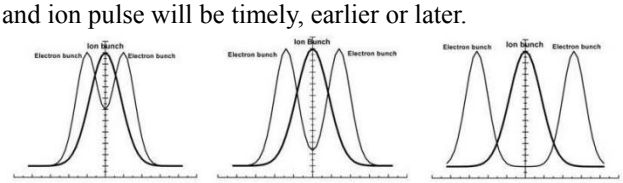

Figure 4: The longitudinal distributions of ion bunch and electron double-bunch with different interval.

ISBN: 978-3-95450-199-1 doi:10.18429/JACoW-SAP2017-MOPH18

### *Implement*

In order to optimize and improve the effect of this double-bunch chain, we plan to vary the strength, interval of individual bunch and delay time with respect to the ion bunch to investigate the efficiency of cooling and suppression of IBS as presented in Fig. 4.

A double-bunch chains were expected to deliver form the electron gun of cooler in order to implement the different cooling in the different position of ion beam, the ion in the centre of ion beam will be cooled mildly and the ion located in the tail of ion beam will be cooler intensively and fleetly. As a result, the ions outside of the beam was drug into the central part of ion beam, the ion loss caused by larger oscillation amplitude will be reduced, and the ion beam intensity was retained.

### *Experimental Investigation*

Intrabeam scattering not only depends on the lattice optical parameters of storage ring, but also depends on the parameters of ion beam, such as population, energy and charge state of ion. Furthermore, IBS depends on the condition and mode of cooling system.

The intrabeam scattering in the cases of different ion beam energy and population will be studies as well as the electron cooling process. The transverse emittance and longitudinal bunch length will be measured after the electron beam was switched off, the transverse growth rate and longitudinal growth rate, ion loss, and ion beam lifetime will be derived from these experiments.

The transverse emittance and longitudinal bunch length will be measured with the help of beam profile monitor and Schottky probe, and their developing with time will be recorded in the case of different energy and population in the ion beam with different initial ion beam parameters.

The normal uniform DC electron beam was chosen as the reference, the cooling time, equilibrium emittance and momentum spread will be measured in this condition, and the information of beam lifetime and beam loss during the cooling was derived from the data of beam current transformer.

The second step, the perform of a double-bunch chain with a certain space but uniform distribution in transverse direction was studied.

The third step, the behavior of transverse hollow electron beam with uniform longitudinal distribution will be investigated in CSRm.

The forth step, the perform of a double-bunch chain with a certain space, and hollow distribution in transverse direction was studied.

The fifth step, the parameters of electron bunch amplitude, interval, width and delay time were varied to optimize and improve the cooling process.

## ACKNOWLEDGMENTS

We would like to thank Xiaolong Zhang for many useful discussions on this subject. We also acknowledge collaboration on thissubject with the power supplies group. Special thanks go to D. Q. Gao, Z. Z. Zhou, and J. B. Shangguan for many fruitful suggestions and very constructive comments on many aspects of this work.

## SUMMARY

The high energy and high intensity accelerator facility was required to provide high density and high charge state ion beam with long lifetime in the storage ring to satisfy the requirements of physics experiments. To maintain the ion beam density for longer time and reduce the ion loss, lifetime is the critical subject. Due to intrabeam scattering, the quality and the lifetime of ion beam will degrade during accelerating and storing. The electron cooling was chosen as a way to suppress the IBS and improve the quality of ion beam. There is a shortage point in the case of conventional DC electron cooling. The solution proposed in this paper was expected to overcome the deficiency of DC electron beam. The longitudinal modulated electron beam was adapted to suppress the IBS effects. The electron beam was constructed into certain strength distribution longitudinally. The stronger cooling was expected in the tail of ion beam, and the weaker cooling was applied in the core of ion beam. As a consequence, the ion loss was reduced and the lifetime of ion beam was lengthened. Meanwhile, the ion beam density was maintained for longer time in the storage ring, and ensued the certain luminosity in the physics experiment terminals. The detailed investigation will carry out in the future.

This exploration was expected to provide some helpful information for the design of electron cooler and operation parameters and mode in the case of high density high charge state ion beam.

## REFERENCES

[1] J.C. Yang, J.W. Xia, G.Q. Xiao *et al.,* "High Intensity heavy ion Accelerator Facility (HIAF) in China", in *Nucl. Instr. and Meth. in Phys. Res. B* 317, pp. 263-265, 2013.

[2] V.V. Parkhomchuk, V.B. Reva, X. D. Yang, "Using electron cooling for obtaining ion beam with high intensity and brightness", in *Proceedings of HB2010*, Morschach, Switzerland, paper MOPD25, pp. 110-114.

[3] A. Krämer, O. Boine-Frankenheim, E. Mustafin *et al.,* "Measurement and calculation of $U^{28+}$ beam lifetime in SIS", in *Proceedings of EPAC 2002*, Paris, France, paper WEPLE116 , pp. 2547-2549.

[4] L.J. Mao, J.C.Yang, J.W.Xia *et al.,* "Electron cooling system in the booster synchrotron of the HIAF project", in *Nuc. Instr. and Meth. in Phys. Res. A* 786, pp. 91-96, 2015.

[5] Xiaodong Yang, Lijun Mao, Xiaoming Ma *et al.,* "Formation of bunched electron beam at the electron cooler of CSRm", in *Proceedings of COOL2015*, Newport News, VA, USA, paper TUYAUD03, pp. 85-88.

[6] A. Sidorin, A. Smirnov, A. Fedotov *et al.,* "Electron cooling simulation for arbitrary distribution of electrons", in *Proceedings of COOL 2007*, Bad Kreuznach, Germany, paper THAP01, pp. 159-162.

ISBN: 978-3-95450-199-1 doi:10.18429/JACoW-SAP2017-MOPH20



# SIMULATION OF ELECTRON COOLING ON BUNCHED ION BEAM

H. Zhao1, L. J. Mao†, X. D. Yang, J. C. Yang, J. Li, M. T. Tang,
Institute of Modern Physics, Chinese Academy of Sciences, Lanzhou, China
[1]also at University of Chinese Academy of Sciences, Beijing, China

*Abstract*

A combination of electron cooling and RF system is an effective method to compress the beam bunch length in storage rings. A simulation code based on multi-particle tracking was developed to calculate the bunched ion beam cooling process, in which the electron cooling, Intra-Beam Scattering (IBS), ion beam space charge field, transverse and synchrotron motion are considered. In the paper, the cooling process was simulated for C beam in HIRFL-CSRm, and the result was compared with experiments, according to which the dependence of the minimum bunch length on beam and machine parameters was studied in the paper.

## INTRODUCTION

Electron cooling is a powerful method for shrinking the size, the divergence and the momentum spread of stored charged-particle beams in storage rings for precision experiments [1]. It also supports beam manipulations involving RF system to provide beams with short bunch length. Short-bunched ion beam has a wide range of application in rare isotope production, high energy density physics experiment, collider and cancer therapy [2]. In order to study the cooling process of bunched ion beam, a simulation code was developed, in which the electron cooling, IBS and space charge effect are considered, and simulation of electron cooling with a sinusoidal wave RF field were carried out in CSRm under various intensities of cooled 6.9 MeV/u $C^{6+}$ ion beams. The simulation results have also compared with the experiment in CSRm. The simulation results show a good agreement with the experiment. Meanwhile, the investigation about the limitation of the bunch length is give in the paper.

## SIMULATION CODE

The simulation code is developed based on multi-particle tracking, in which the ion beam is represented by a number of model particles and the beam dynamics is calculated by statistical method. In the code, a certain number of charged particles are generated according to the initial beam emittance, momentum spread and bunch length. Particularly, it assumes that the initial ion beam distribution is Gaussian in transverse and longitudinal. Each particle is presented as a six-coordinate vector: ($x$, $x'$, $z$, $z'$, $\varphi$, $\Delta v$), where $x$ and $z$ are the horizontal and vertical coordinates, $x'$ and $z'$ are the corresponding angles in horizontal and vertical, $\varphi$ is the phase angle with respect to the ring, and $\Delta v$ is the relative velocity of particle in Laboratory Reference Frame (LRF). For each turn, the coordinate of model particle will be tracked and the beam dynamics is based on the synchrotron and transverse motion [3].

The calculation of electron cooling is based upon the energy exchange between ions and electrons, which can be described in terms of a velocity-dependent friction force. In the simulation, the Parkhomchuk force formula was used to calculate the friction force on each particle at Particle Reference Frame (PRF) [4]. Additionally, the longitudinal velocities of electrons at a certain radius due to space charge effect should be corrected by

$$\frac{\Delta V_e}{V_e} = \frac{I_e}{4\pi\varepsilon_0\beta^3\gamma^3 c}\frac{e}{m_e c^2}\frac{r^2}{r_b^2} \tag{1}$$

where $\varepsilon_0$ is the vacuum permittivity, $I_e$ is the electron beam current, $\beta,\gamma$ and $c$ are Lorentz factors and $r_b$ the radius of electron beam.

On the other hand, the heating effects which can induce beam blows up should be analysed seriously. However, the IBS effect is the most important effect, which is a multiple Coulomb interaction of the charged particles within the beam. In the code, the Martini IBS model was applied in the calculation, in which the growth rates are calculated from a complicated integration that connected the 6-dimentional phase space density of the beam with the optics of the storage ring [5].

The ion beam density will increase as it was cooling down, during which the space charge effect becomes much stronger to prevent the cooling effect on bunch length and beam profile accordingly. In the code, the space charge effect is considered only in longitudinal and this effect is represented by a potential applying to particles which is similar to the RF voltage, the space charge potential is given by [6].

$$V_{SC} = \frac{gh^2}{2R\varepsilon_0\gamma^2}\frac{d\rho(\phi)}{d\phi} \tag{2}$$

in which $\rho$ is the linear charge density of ion beam, $h$ is the harmonic number, $R$ the radius of the ring. The geometric factor $g=1+2ln(b/a)$ depends on the radio of beam radius a to pipe radius b. The change of particle velocity caused by the space charge potential together with the RF voltage for each turn is applied based on the synchrotron motion.

† maolijun@impcas.ac.cn

ISBN: 978-3-95450-199-1 doi:10.18429/JACoW-SAP2017-MOPH20

## SIMULATION ON CSRM

An application on CSRm is dedicated to the bunched beam cooling of the typical ion beam C at the injection energy of 6.9 MeV/u. The main parameters used in the simulation are listed in Table 1. The variations of beam emittance, momentum spread and bunch length with time under the combined actions of the IBS, space charge and electron cooling are shown in Fig. 1. The distribution of momentum spread and bunch length in the cooling process are showed by the contour map in Fig. 1 to reveal the evolution of particle distribution.

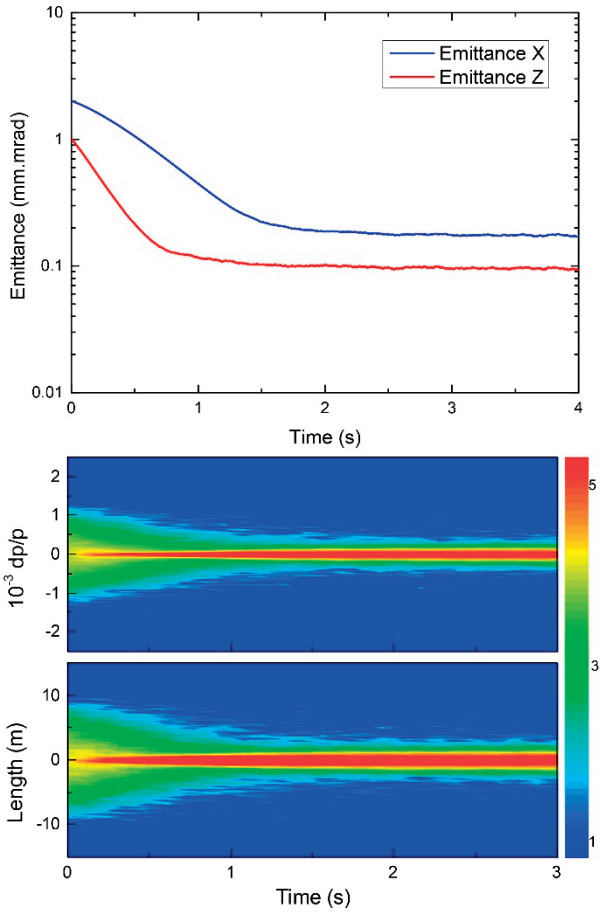


Figure 1: Evolution of beam emittance (RMS), distribution of momentum spread and bunch length in the procedure of cooling combined with RF field ($V_{RF}$=1.0 kV for 6.9 MeV/u C beam.

The particle distribution in longitudinal phase space and the corresponding separatrix orbits, and beam space charge potential during cooling process are given in Fig. 2. The space charge potential shows the behaviour increasing with the decrease of bunch length as it was cooling down, during which the beam bunch length is prevented from being cooled to much shorter together with the IBS effect. However, the space charge potential at 1 second is larger than that at equilibrium state and there are many particles cooled to the centre as shown in Fig. 2. It is mainly because of that the cooling force in longitudinal is larger than in transverse. Many particles will be quickly cooled to the centre in longitudinal at the beginning of cooling and then diffuse slowly due to Intra-Beam Scattering effect and space charge effect until the equilibrium state achieved. For a cooled ion beam with stationary distribution, the particle charge density in longitudinal can be described by the Fokker-Plank equation [7], which is used to fit the beam distribution during cooling and the fitting results have a good agreement with the simulation results before and after cooling as shown in Fig. 2.

Table 1: Initial Parameters used in Simulation

| Name | Initial Value |
|---|---|
| Ion energy | 6.9 MeV/u |
| Particle number per bunch | 1E8 |
| Emittance (RMS) | 2.0/1.0 pi mm mrad |
| Momentum spread (RMS) | 5E-4 |
| Betatron function @cooler | 10/10 m |
| RF voltage | 1.0 kV (h=2) |
| Transition gamma | 5.42 |
| Electron beam density | 3.8E6 $cm^{-3}$ |
| E-beam Temp. | 0.5/1E-5 eV |
| Magnetic field @cooler | 365 Gs |

## BENCHMARK FOR SIMULATION CODE

The experiments were performed with C beam at the energy of 6.9 MeV/u at CSRm, in which the beam shape is measured by a position pick-up. The beam parameters are close to the value in Table 1. Because the cooling time is too small to measure the cooling process and there is no facility to measure the beam emittance, we only studied the final bunch length at the equilibrium status and it dependence on particle number. The experimental and simulation results are shown in Fig. 3.

In order to investigate the limitation of bunch length for high intensity ion beam, more calculations on 6.9 MeV/u C beam with RF voltage 1.0 kV were done. The particle number is from 1E7 to 1E10 per bunch. However, the IBS and space charge effect are considered independently in the calculation, and the results comparing with the measurement are shown in Fig. 3. According to the results considered the IBS effect only, the experiments of C in CSRm are clearly belong to the IBS dominant regime. The bunch length is proportional to $N^{1/4}$. The space charge dominated beam will attained when the particle number per bunch exceeds 6E8. When only space charge effect is considered, it is observed that the dependency of the particle number is divided into two regions which is mainly due to the amplitude of oscillation in RF bucket.

According to the simulation and experiments, we can know the simulation results is rather well and can give an estimation on the limitation of cooled ion beam bunch length. The limitation result calculated by simulation code can almost apply to any kind of heavy ion beams with different energies and the IBS dominated beam or Space-Charge dominated beam can be distinguished.

ISBN: 978-3-95450-199-1 doi:10.18429/JACoW-SAP2017-MOPH20



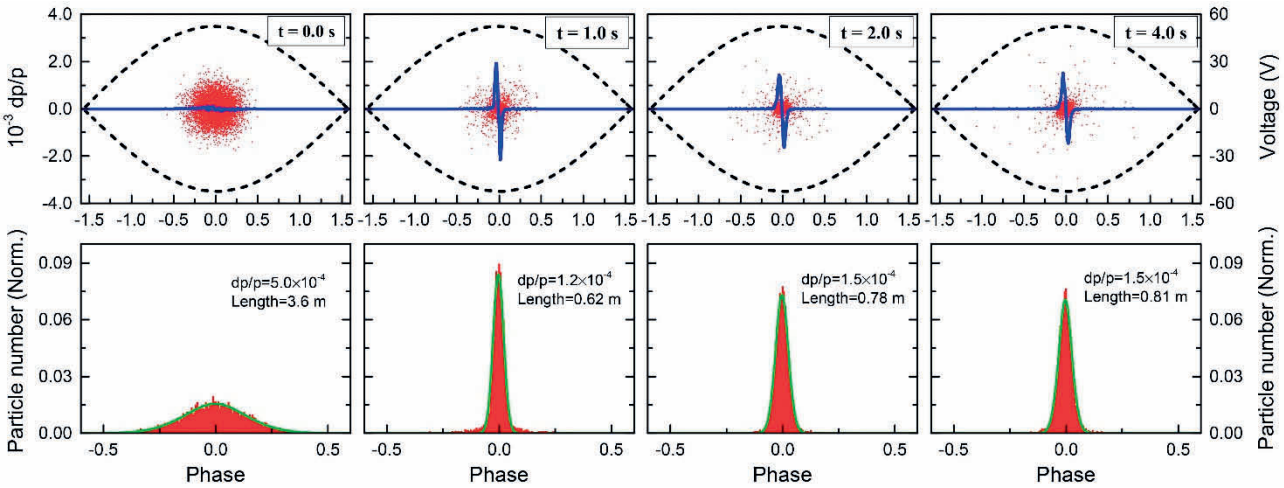


Figure 2: Evolution of model particles distribution in longitudinal phase space (red dot) and space charge potential (blue line) and the particles distribution in longitudinal for one bunch of C beam in CSRm. The black dash line is the RF bucket with $V_{RF}$=1.0 kV, the green line is the fitted line by Fokker-Plank equation.

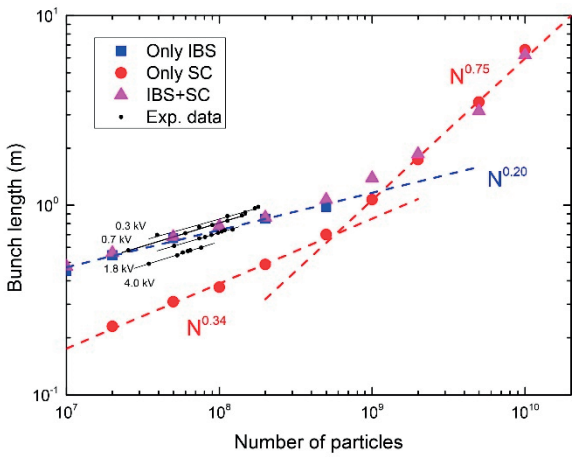


Figure 3: The bunch length versus particle number in the simulation (colored) and experiment (black) for 6.9 MeV/u C ion beam. In the simulation, the IBS and space charge effect are considered independently. The dash lines are fitted to the simulation results.

## CONCLUSION

In this paper, we reported bunch beam cooling simulation code and its application in CSRm. According to the benchmark with experimental results, the experimental results in CSRm shown a good agreement with the simulation results in the IBS dominated regime. We also studied the dependence of bunch length on particle number and finally give the estimation of the limitation of bunch length for that condition.

## ACKNOWLEDGEMENT

The authors would like to express their thanks to members of the HIRFL-CSR operation group. We also thanks to Dr.Takayama and Dr. Smirnov for the help on the simulation code. This work is supported by the National Natural Science Foundation of China (Project No.11575264, No.11375245 and No.11475235) and the Hundred Talents Project of the Chinese Academy of Sciences.

## REFERENCES

[1] H. Poth, "Electron cooling: theory, experiment, application", *Phys. Rep*., vol. 196, Nos. 3 & 4, p. 135, 1990.

[2] K. Noda *et al.,* "Electron cooling of bunched ion beam at NIRS-HIMAC", *Nucl. Instrum. Methods Pys. Res.Sect. A*, vol. 532, p. 129, 2004.

[3] S.Y. Lee, "Accelerator Physics", USA: World Scientific, 2006, p. 255.

[4] V.V. Parkhomchuk, "New insights in the theory of electron cooling", *Nucl. Instrum. Methods Pys. Res, Sect. A*, vol. 441, p. 9, 2000.

[5] M. Martini, CERN, Geneva, Switzerland, Rep. CERN-PS/84-9 (AA), 1984.

[6] C.R. Prior and E.Fellow, TRACK1D Guide for Users.

[7] S. Nagaitsev *et al.*, "The investigation of space charge dominated cooled bunched beams in a synchrotron", in *Proc. Workshop on Beam Cooling and Related Topics*, Montreux, Swichzerland, 1993, Vol. 94(3), pp. 405.

ISBN: 978-3-95450-199-1 doi:10.18429/JACoW-SAP2017-MOPH21

# RADIATION EFFECTS STUDY FOR BEAM LOSSES ON THE ELECTRO-STATIC DEFLECTOR IN HUST SCC250

S. W. Hu, K. J. Fan†
Institute of Applied Electromagnetic Engineering, Huazhong University of Science and Technology, Wuhan, China

*Abstract*

China has payed comprehensive attention to the study of proton therapy in recent years. Radiation effects induced by beam losses in compact, high energy superconducting cyclotrons are being taken into crucial considerations. The proton beam is extracted out of HUST SCC250 superconducting cyclotron by electrostatic deflectors. The fierce impinging between proton beam and the deflector septum is the main cause of beam losses, which will bring about radiation effects leading to activations in devices and coil quenching. This paper presents the simulation result of radiation effects between beam and septum by utilizing Geant4 code based on Monte Carlo method. The energy deposition of beam losses is figured. Meanwhile, the yields and energy distributions of secondary particles are investigated. The result focused on radiation effects will provide us with valuable implications for the design of this superconducting cyclotron.

## INTRODUCTION

HUST SCC250, being developed for/at Huazhong University of Science and Technology, is a superconducting cyclotron applied for proton therapy. The extracted proton beam is expected to be 250MeV and the beam current is about 800nA. The electrostatic deflector in this cyclotron is the research subject of this paper, whose structure has been introduced in [1]. In real operation conditions, the deflector undergoes intense interactions with beam that will directly influence the beam quality and extraction efficiency. These interactions subsequently trigger severe cooling problem and radiation effects affecting the operating performance of the cyclotron. The cooling problem has been discussed in [1], then the radiation effects will be studied in this paper.

Radiation effects mainly exerts considerable influences on the operation of superconducting cyclotron from the following two aspects: the nuclear heating of the cryogenic magnet and radiation damage or activation of certain materials [2]. To gain a deeper insight into radiation effects, Geant4 toolkit has been used to simulate the radiation with the septum after impacted by proton beam. The energy deposition and secondary particles have been analysed which gives a reference to the future study and configuration of the cyclotron.

This paper is structured as follows: Section 2 introduces details on the simulation model and parameters employed in Geant4 toolkit, Section 3 presents results and discussion and then the conclusion is proposed in Section 4.

† kjfan@hust.edu.cn

## MATERIAL AND METHODS

### *Geant4 Toolkit*

Geant4 is a software toolkit for the simulation of the passage of particles through matter [3]. It is applied in a variety of domains including high energy physics, space applications, medical physics and radiation shielding. Geant4 code, which is written in C++ programming language, earns much favour from a large number of researchers whereby its abundant particle data libraries and open-source capability. Since plenty of examples adapted to various occasions contains in Geant4 data package, the users can modify the example codes as they need to satisfy their applications. Moreover, self-defining simulation models and physics lists give users much more setting options.

It is noted that Geant4 10.1.2 edition is employed in this study and the application platform is Win10 x64 system.

### *Incident Beam Properties*

As the proton beam is propagated down the +Z axis into the deflector, its transverse motion can be represented by two ellipses in the phase spaces [4]（X, $X_P$）and （Y, $Y_P$）, where $X_P = P_x/P_z$, $Y_P = P_y/P_z$, represent respectively the beam angular divergences θ and φ , and $P_x$ , $P_y$ , $P_z$ stand for the three components of the beam momentum. The phase ellipse is defined with Twiss parameters and beam emittance. The beam emittance is 1mm · mrad. Twiss parameters taken from beam dynamics calculation are tabulated in Table 1

Table 1: Margin Specifications

| X planar | Y planar |
|---|---|
| $\alpha_x = -0.533862$ | $\alpha_y = 0.219913$ |
| $\beta_x = 1.303566$ | $\beta_y = 0.668318$ |
| $\gamma_x = 0.985764$ | $\gamma_y = -1.568657$ |

Subsequently, the respective phase ellipse in X, Y directions and the beam profile in X-Y cross-section are plotted in Figure 1.

It is noteworthy to mention that Geant4 code package doesn't contain beam phase ellipse defining class so that users can only achieve this by employing mathematic manipulation. To define the phase space, the users should specify the four variables X, Y, $X_P$, $Y_P$ into random Gaussian distribution respectively. Geant4 code provides the function--SetParticleMomentumDirection( ) for users to set the momentum direction of particles. The proton beam energy in our study is set to be monoenergetic 250 MeV.

ISBN: 978-3-95450-199-1 doi:10.18429/JACoW-SAP2017-MOPH21



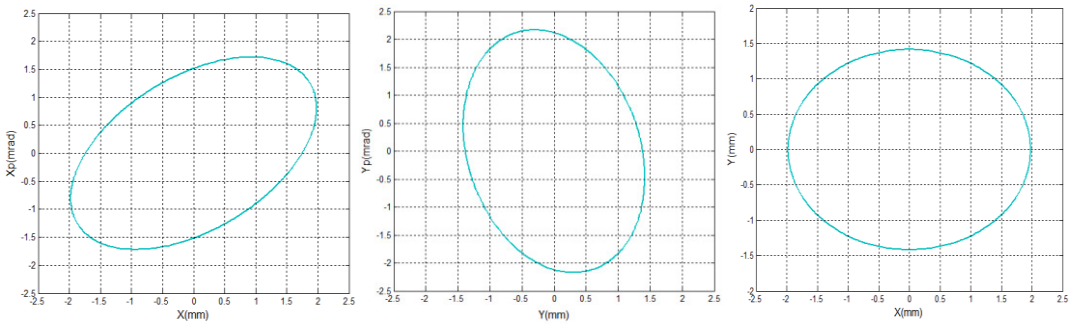


Figure 1: left: ( X, $X_P$) phase ellipse; middle:( Y, $Y_P$) phase ellipse; right:( X, Y) beam profile.

### *Simulation Set-ups*

To simplify the calculation, we establish 1/4 length of the overall deflector to be our simulation model whose 3D dimension is 50mm × 40mm × 120mm. The septum is made of Tungsten and only 0.3mm thick. While the liners and housing are copper styled. The model is placed in $2\times10^{-5}$Pa, 20℃ vacuum environment. Figure 2 displays the simulation model.

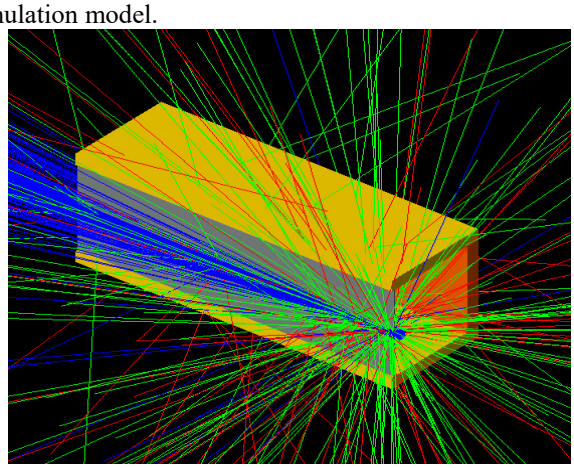

Figure 2: Simulation model in Geant4.

To make the best compromise between calculation accuracy and CPU time, we choose the FTRP_BERT from several physics lists [5]. The range cut is set to 0.1 μm, therefore the cutoff energy for transport is fixed to 0.01MeV. The monoenergetic 250MeV beam of $2\times10^6$ protons irradiates the center of the septum lateral surface along +Z axis, inducing p-W nuclear interactions.

As shown in Figure 2, the incident proton beam (blue in the figure) impinges the septum producing numerous secondary particles, most of which are gammas (red in the figure) and neutrons (green in the figure). Gamma and neutron are also the types of secondary particles that contribute most to the radiation effects.

## RESULTS AND DISCUSSION

### *Energy Deposition on the Septum*

The energy deposition curve is plotted in Figure 3, when the 250MeV proton beam irradiates tungsten bulk and its energy is postulated to be completely deposited in the bulk. The maximum energy deposition locates in the depth of 37.7mm, which agrees well with the value calculated by SRIM software.

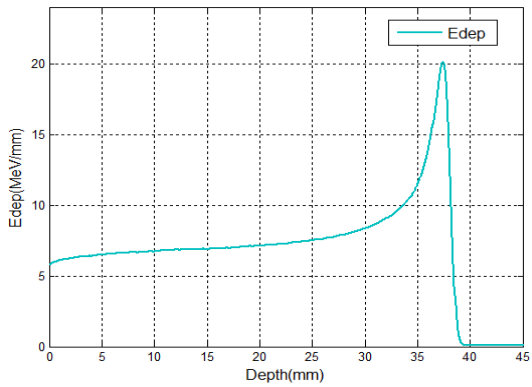


Figure 3: Energy deposition curve of 250MeV proton beam in tungsten.

Obviously the above curve cannot illustrate our simulation case, for the tungsten septum is so thin, only 0.3mm, that the energy of the proton beam won't be totally deposited in it. Figure 2 shows that thin septum splits the proton beam into diverse directions. Since the positon where the maximum energy deposition locates indicates the fiercest heating effect and nuclear interactions happening, it is essential to investigate the distribution of energy deposition on the septum shown in Figure 4.

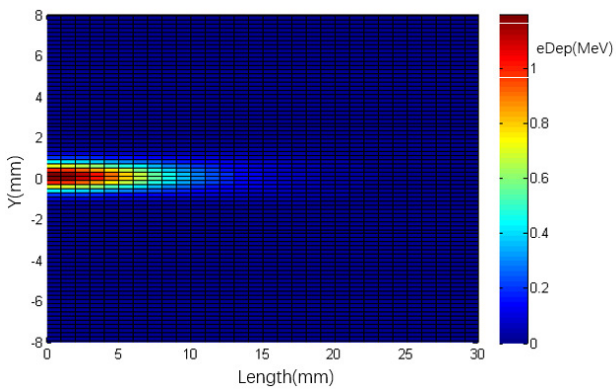


Figure 4: Distribution of energy deposition on the tungsten septum.

As displayed in Figure 4, the leading edge of the septum receives the maximum energy deposition. The dimension of the main energy deposition area reaches nearly

ISBN: 978-3-95450-199-1 doi:10.18429/JACoW-SAP2017-MOPH21

20mm×3mm where the fiercest nuclear interactions happens. Maybe we can settle lower Z material in the front of the septum to weaken the nuclear interactions.

### *Energy Deposition of Secondary Particles on the Housing*

Large amount of gammas and neutrons are generated due to the collision between proton beam and tungsten septum. Those secondary particles may penetrate the housing to hit on the superconducting coils possibly inducing quenching. Figure 5 presents the energy deposition of secondary particles on the housing.

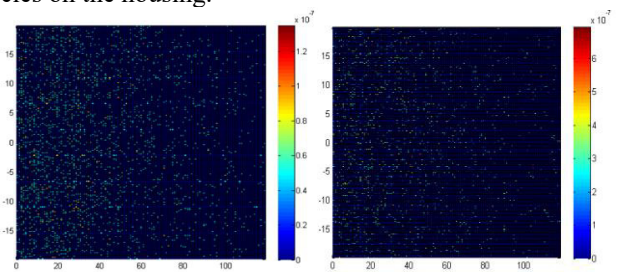

Figure 5: left: energy deposition of gamma; right: energy deposition of neutron.

We can see from Figure 5 that the energy depositions of gammas and neutrons on the housing are extremely tiny. The number of stopped secondary particles just accounts for less than 0.1% based on calculation which means that most of the secondary gammas and neutrons penetrate the housing and emanate to outer space. It is suggested that the material of housing should show an excellent performance to shield gammas and neutrons.

### *Yields and Energy Distributions of Secondary Particles*

The ratio between secondary particles productions and beam source proton number present the yields of secondary particles existing from the target. The tabulated results of yields appear in Table 2.

Table 2: Yields of Gammas and Neutrons

| Type | Yield |
|---|---|
| Gamma | 0.11734 |
| Neutron | 0.26634 |

The energy distributions of outgoing gammas and neutrons are shown in Figure 6 and Figure 7. As shown in Figure 6, the energy of secondary gammas is relatively low mainly ranging from 0-8MeV and the number of 0-2MeV secondary gammas accounts for over half of the total. While the Figure 7 shows that the energy of secondary neutrons mostly settles in 0-50MeV and neutrons lower than 10MeV occupy nearly 90% of total. Those results may bring some implications for the radiation shielding designers.

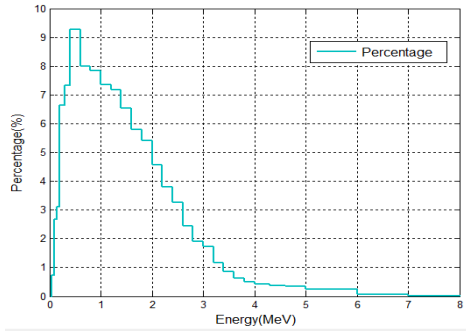


Figure 6: Energy distribution of secondary gammas.

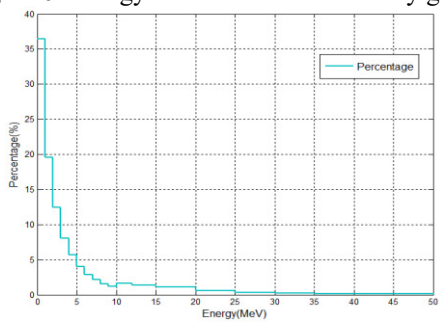


Figure 7: Energy distribution of secondary neutrons.

## CONCLUSION

This paper exhibits a comparably detailed study into radiation effects caused by beam losses on the septum. The energy depositions on the septum and housing in the simulation demonstrate that radiation effects on the deflector deserves serious considerations. The yields and energy distributions of secondary particles provide useful implications for researchers when designing the radiation shielding structure. This study will be carried out more deeply in the near future.

## REFERENCES

[1] S. Hu *et al.,* "Design and fluid-solid-heat coupling analysis of an electrostatic deflector for HUST SCC250 proton therapy facility", in *Proc. 8th Int. Particle Accelerator Conf. (IPAC'17)*, Copenhagen, Denmark, May 2017, paper THPVA 109, pp. 4713-4715.

[2] Z. S. Hartwig *et al.*, "Nuclear heating and radiation damage studies for a compact superconducting proton cyclotron", submitted for publication.

[3] J. Allison *et al.,* "Recent developments in Geant4", *Nucl. Instr. Meth,* vol. 835, pp. 186-225, 2016.

[4] S. Incerti *et al.,* "Simulation of cellular irradiation with the CENBG microbeam line using Geant4", submitted for publication.

[5] J. Apostolakis *et al.,* "GEANT4 physics lists for HEP", submitted for publication.

ISBN: 978-3-95450-199-1 doi:10.18429/JACoW-SAP2017-MOPH22

# PRIMARY DESIGN OF 4 A S-BAND LINAC USING SLOTTED IRIS STRUCTURE FOR HOM DAMPING*

J. Pang†, S. Chen, X. He, IFP, CAEP, Mianyang, China
S. Pei, H. Shi, J. Zhang, IHEP, Beijing, China

*Abstract*

A S-band LINAC with the operating frequency of 2856MHz and beam current of 4 A was designed for flash X-ray radiography for hydrodynamic test. The optimization of the parameters of the LINAC was processed to achieve the minimum beam radius and the proper energy efficiency. For the purpose of reducing the beam orbits offset at the exit of LINAC, a slotted iris accelerating structure would be employed to suppress the transverse Higher Order Modes (HOMs) by cutting four radial slots in the iris to couple the HOMs to SiC loads. In this paper, we present the design of the LINAC and the results of beam dynamic analysis.

## INTRODUCTION

Linear induction accelerators were used in large-size or full-size radiographic hydrodynamic test with dose of hundreds of Rad by accelerating several-kA electron beam to tens of MeV. In addition, small machine, such as pulsed X-ray machine with several hundreds kV and anode-pinch diode, was used in small-size hydrodynamic subdivision experiments for dynamic material characteristic study, micro jetting diagnosis, et al.

In the past twenty years, intense-beam normal conducting RF accelerator has been developed with great achievement due to the development of large collider technology. The CLIC Test Facility, CTF3, has accelerated the beam with current of up to 5A to150MeV with full beam loading [1-2]. The HOM was damped by using slotted iris constant aperture (SICA) accelerating structures. The 100MeV/100kW linac, constructed by IHEP and used as a driver of a neutron source in KIPT, Ukraine, has accelerated a beam of 2A to 100MeV by using detuning accelerating tubes [3-5].

The great progress in intense-beam linac motivates the compact radiographic facility driven by a 4A 30MeV linac, which might be utilized for multi-pulse radiographic with the material planar density of several to tens g/cm$^2$. The most considered parameter, FWHM of transverse distribution of electron beam, should be limited less than 1 mm. A radiographic system has been discussed before [6]. The Monte Carlo codes, Geant4, has been used to simulate bremsstrahlung characteristic, such as exposure dose, energy deposit in target and increment of X-ray spot size by electron scatter, with 30 MeV electron beams bombarding tantalum target with various thickness in a certain radiography layout. Simulation results showed that the exposure dose 1 m away from the target right ahead was about 9.1 R and the X-ray spot sizes were not increased with the increment of the thickness of target material. The results also shown that pulse number was limited by temperature rise in target, which was increased intensely with a very tiny beam transverse size.

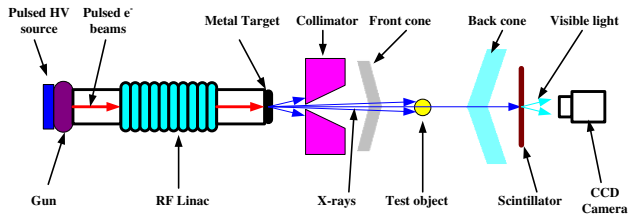


Figure 1: Layout of a typical flash X-ray radiography system using RF accelerator.

In this paper, the design of accelerator was described. A beam dynamic analysis was carried out with the primary design of the accelerating structure. BBU effect calculation was also carried out.

## GENERAL DESCRIPTION OF THE ACCELERATOR

Layout of the accelerator, which consists of a DC gun, 3 accelerating tube, a chicane and matching beam line, was shown in Fig. 2. The total length is about 14m and could be reduced by farther optimization. Table 1 lists main parameters.

Table 1: Main Linac Parameters

| Parameter | Value |
|---|---|
| RF frequency | 2856MHz |
| Energy | >30MeV |
| Beam current (max) | 4A |
| Energy spread (FWHM) | <1% |
| Emittance (RMS) | <50mm mrad |
| Beam pulse length | 100ns |
| Number of pulses in a train | 4-8 |
| RF pulse duration | 10μs |
| Pulse repetition rate | 10Hz |
| Klystron power | 65MW |
| Number of klystron | 3 |
| Number of ACC. structure | 3 |
| Gun voltage | ~120 kV |
| Gun beam current | 10A |

## ACCELERATING STRUCTURE

The goal of the design of accelerating structure is to achieve a high RF-beam power efficiency with short length as much as possible. Two type of structure was considered: the conventional disk-load structure and

* Work supported by Key Laboratory of Pulsed Power, CAEP (Contract NO. PPLF2014PZ05) and Key Laboratory of Particle Acceleration Physics &Technology，IHEP, CAS (Contract Y5294109TD)
† email address jpang@caep.cn

ISBN: 978-3-95450-199-1 doi:10.18429/JACoW-SAP2017-MOPH22

constant-aperture structure. Both of them should be slotted on the iris to suppress the HOM modes, which would be introduced by the beam. The input power, limited by klystron power and transmission efficiency, was determined as 45MW. There were 3 rules to determine cell arrangements for constant gradient along the axis when there is no beamloading:

1. The structure is solvable. The group velocity of all accelerating cells should not be negative and smaller than the maximum one when the length of nose cone is 0;
2. The unloaded gradient should be chosen carefully making the surface electric field as small as possible;
3. The acceleration structure should be as short as possible to make microwave - beam conversion efficiency as high as possible. We determine the conversion efficiency to be 0.95 times the maximum conversion efficiency by abandoning part of the acceleration cells to improve the average loading gradient.

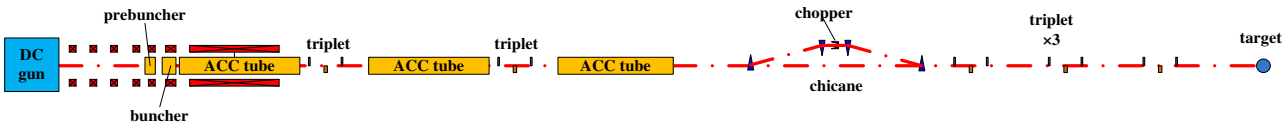


Figure 2: Layout of the accelerator.

The arrangement of disk-load structure has only a unique solution in the case of certain input power and average unload gradient. Some results with unloaded gradient of 12MV/m with the different input power calculation are shown in Figure 3. With a certain beam load and unloaded gradient, the number of cells required to achieve specific microwave-beam efficiency (90% for example) increased linearly with input power, and the loaded gradient satisfying the above requirements did not change.

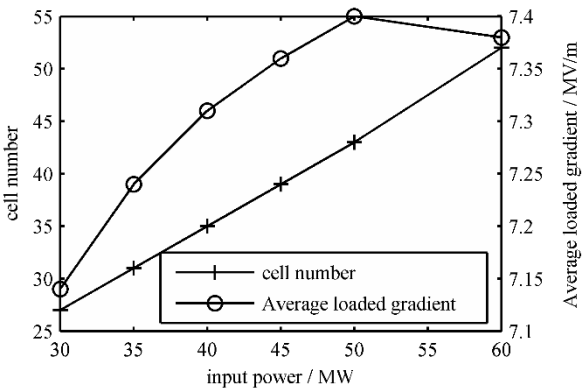


Figure 3: Calculation results of disk-load structure with a certain unloaded gradient of 12MV/m with various input power.

With the employee of nose cone to achieve constant-aperture, the arrangement is also determined by the iris diameter. With a certain input power, there will be an appropriate value of iris diameter resulting minimum surface electric field as shown in Fig. 4.

The design of two types of structure for 45MW input power is list in Table 2. The average loaded gradient is larger to CTF3 2998MHz structure (6.5 MV/m for beam current of 3.5A [1]), but more critical to the RF breakdown threshold with about 6 times larger RF pulse length. The uniform un-loaded gradient design will bring a lower surface electric field of whole accelerating structure. The results are shown in Fig. 5.

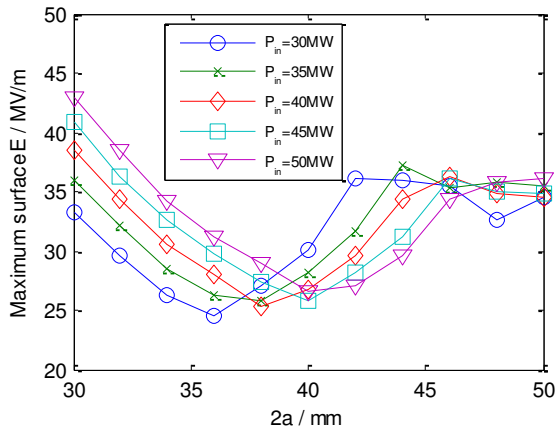


Figure 4: Maximum surface electric field of different structure design.

Table 2: Design of Two Type Accelerating Structures

| Parameter | Unit | Disk-load | Constant-aperture |
|---|---|---|---|
| Input power | MW | 45 | 45 |
| $E_{acc}$ (no beamloading) | MV/m | 12.0 | 12.1 |
| $E_{acc}$ (max beamloading) | MV/m | 7.36 | 7.38 |
| $E_{max}$ on surface | MV/m | 27.66 | 29.70 |
| Phase advance per cell | | $2\pi/3$ - mode | |
| RF-beam effeciency | | 0.893 | 0.895 |
| Number of cells | | 39 | 39 |
| Iris diameter ($2a$) | mm | 36.010-35.051 | 36 |
| Length of nose cones | mm | - | 0.031-0.706 |
| Ratio of $v_g$ to $c$ | | 0.05576-0.05151 | 0.0550-0.0504 |
| Energy gain | MeV | 9.95 | 9.98 |

ISBN: 978-3-95450-199-1 doi:10.18429/JACoW-SAP2017-MOPH22



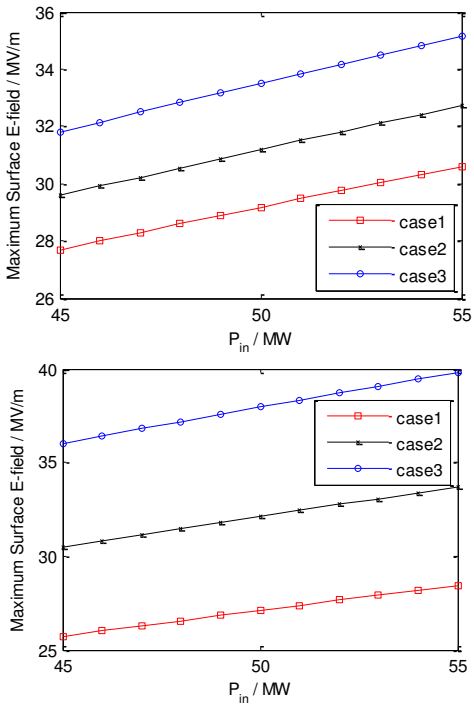


Figure 5: The maximum surface electric field with different unloaded gradient arrangements. Upper: disk-load structure; lower: constant-aperture structure. Case 1: uniform unloaded gradient; case 2: unloaded gradient linearly changed within ±10%; case 3: unloaded gradient linearly changed within ±20%.

## BEAM DYNAMIC

Beam dynamic analysis was carried out using PARMELA code without consideration of BBU. The FWHM of beam horizontal distribution at the end of the accelerator can be controlled less than 1 mm in the case of the 4A beam load. Fig. 6 shows the beam envelop along *z* axis. Fig. 7 and Fig. 8 shows beam transverse distribution, energy spectrum and longitudinal distribution, respectively. If the BBU effect is taken into account, the beam lateral size jitter will be in the order of mm, and after preliminary calculation, it can be known that when the Q of dipole modes were reduced less than 20, the beam position jitter can be controlled less than 0.1mm, shown in Fig. 9.

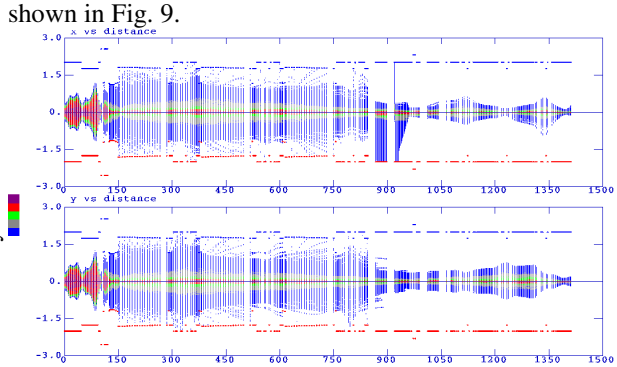


Figure 6: Beam envelope calculation result.

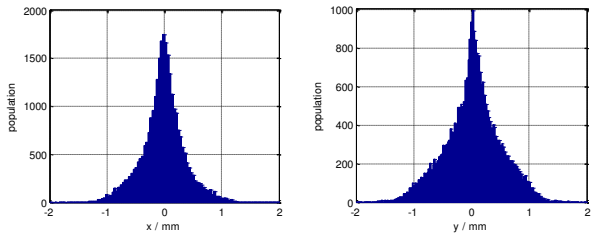


Figure 7: Beam transverse distribution at the exit

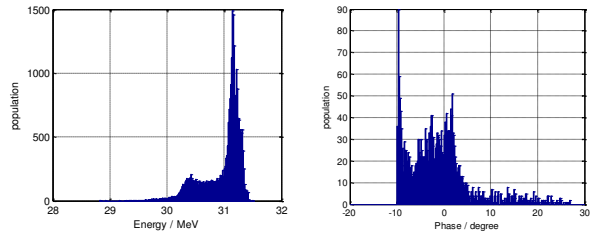


Figure 8: Beam energy spectrum and longitudinal distribution at the exit.

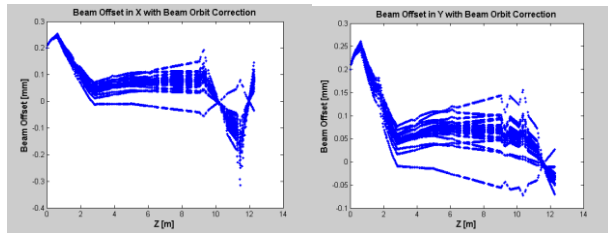


Figure 9: Beam offset calculation with a 100ns RF duration considering long-range wakefield.

We will use the uniform-gradient disk-load structure. The accelerating structure will be designed carefully to suppress Q of most dipole modes less than 20.

## REFERENCES

[1] P. Urschütz, H. H. Braun, R. Corsini *et al.,* "Efficient long-pulse fully loaded CTF3 LINAC operation", in *Proc. LINAC'2006,* Knoxville, Tennessee, USA, 2006, paper MOP002, pp. 31-33.

[2] M. Aicheler *et al.,* "A Multi-TeV linear collider based on CLIC technology: CLIC Conceptual Design Report", CERN, Geneva, Switzerland, Rep. CERN-2012-007, Oct. 2012.

[3] Y. Chi, S. Pei, S. Wang *et al.*, "Design studies on 100MeV/100kW electron linac for NSC KIPT neutron source on the base of subcritical assembly driven by linac", in *Proc. IPAC'11*, San Sebastián, Spain, 2011, paper TUPC034, pp. 1075-1077.

[4] M. Aizatskiy, O. Bezditko, I. Karnaukhov *et al.,* "100MeV/100kW electron linear accelerator driver of the NSC KIPT neutron source", in *Proc. IPAC2013*, Shanghai, China, 2013, peper THOAB203, pp. 3121-3123.

[5] S. Pei, private communication, May. 2017.

[6] J. Pang *et al.*, "Analysis of bremsstrahlung characteristic by 30 MeV multi-pulse beams bombarding rotated tantalum-based target", *High power laser and particle beams*, vol. 29, no. 6, p. 065101, Jun. 2017.

ISBN: 978-3-95450-199-1 doi:10.18429/JACoW-SAP2017-MOPH23

# STUDIES ON THE S-BAND BUNCHING SYSTEM WITH THE HYBRID ACCELERATING STRUCTURE*

S. Pei†, B. Gao, Key Laboratory of Particle Acceleration Physics & Technology, Institute of High Energy Physics, Chinese Academy of Sciences, Beijing, China

*Abstract*

A standard bunching system is usually composed of a SW PB, a TW B and a standard accelerating structure. In the industrial area, the bunching system is usually simplified by eliminating the PB and integrating the B and the standard accelerating structure together to form a β-varied accelerating structure. The bunching efficiency for this kind of simplified system is lower than that for the standard one. The HB has been proved to be an innovative attempt to reduce the cost but preserve the beam quality as much as possible. Here, the HAS is proposed by integrating the PB, the B and the standard accelerating structure together to exclusively simplify the standard bunching system. Compared to the standard bunching system, the one with the HAS is more compact, and the cost is lowered to the largest extent without fairly degrading the beam performance. The proposed HAS can be widely applied in the industrial area.

## INTRODUCTION

Generally, a standard bunching system is composed of a standing wave (SW) pre-buncher (PB), a travelling wave (TW) buncher (B) and a standard accelerating structure; all of them operate at the same radio frequency (RF) and are powered by one single klystron. However, for various reasons and different applications, the bunching system can be complicated or simplified. The complicated bunching system is always happened in the scientific area, and it is usually accompanied with better beam performance and higher construction cost. One typical example is the BEPCII subharmonic bunching system. Two sub-harmonic bunchers (SHB) were used to replace the PB [1]. In the industrial area, the usual way to simplify the bunching system and lower the cost is to eliminate the PB and integrate the B and the standard accelerating structure together to form a β-varied accelerating structure. However, the bunching efficiency will be lowered.

The hybrid buncher (HB) has been proved to be an innovative attempt to reduce the bunching system construction cost [2-4], and it is a combined structure of the PB and the B. Using the HB to replace the PB and B can simplify the bunching system to certain extent but not exclusively, it has been proved that the beam performance can be preserved as much as possible [4]. In this scenario, further simplification of the standard bunching system by integrating the PB, the B and the standard structure to form a hybrid accelerating structure (HAS) is proposed. It is worth to note that this paper focuses on the simplification studies of the standard bunching system operating at one single S-band frequency (2856 MHz). The bunching system with the $\beta$-varied structure was studied first, and then that with the HAS was investigated.

* Work supported by the National Natural Science Foundation of China (11475201) and the Youth Innovation Promotion Association of Chinese Academy of Sciences, China.
† email address: peisl@ihep.ac.cn.

## BUNCHING SYSTEM LAYOUTS

Figure 1 shows the layouts of the standard bunching system applied in the linac of the NSC KIPT (National Science Center, Kharkov Institute of Physics and Technology, Ukraine) [5], the bunching system with the $\beta$-varied structure and that with the HAS. For both the simplified bunching systems, although the total linac length for S-band can only be shortened by several to twenty centimeters, but all the RF devices connected with the PB and B can be completely removed, this is more exclusive than the one with the HB [4]. Simplifying the bunching system with the HAS can lower the construction cost, facilitate the mechanical design and the tunnel installation, and less parameters need to be adjusted in the beam tuning process, while relatively accurate HAS design is needed, which depends on the gun emitted beam energy.

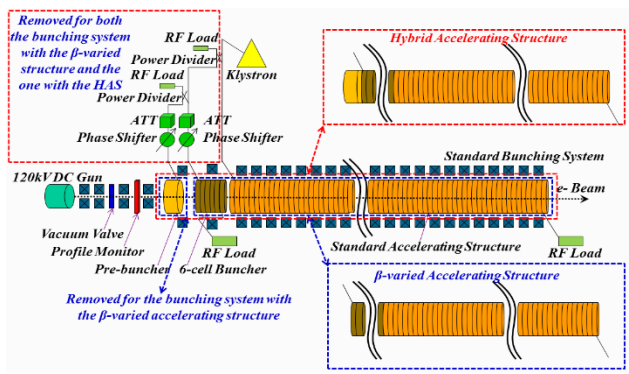


Figure 1: The bunching system layouts.

To easily compare the beam performance, the bunching system with the HAS was introduced into the KIPT linac [5] to replace the standard one. EGUN [6] and PARMELA [7] were used for the beam dynamics study. The RF power fed into the bunching system was all fixed to be 14.4 MW. The solenoid field distribution along the bunching system and the parameter setup for the chicane system were also adjusted to get the best beam quality at both the bunching system and the linac exits. At the bunching system exit, the higher the efficiency the better, and the energy spectrum should also be appropriate for the collimation process realized by a chicane system with a collimator deployed [8]. For the collimated beam, the RF phase for each accelerating structure downstream the chicane was optimized to minimize the energy spread at the linac end. At the linac exit, the more the particles within ±4% peak-to-peak (p-to-p) energy spread the better. This is demanded by the energy

ISBN: 978-3-95450-199-1 doi:10.18429/JACoW-SAP2017-MOPH23



spread acceptance of the 90° beam transport line from the linac end to the neutron target [8].

## BEAM DYNAMICS WITH THE BETA VARIED STRUCTURE

5 variants of the $\beta$-varied structure were studied. For each variant, the phase velocities of the first 8 cells are listed in Table 1. Besides, each $\beta$-varied structure still has 36 regular cells with $\beta$=1. The beam dynamics results are listed in Table 2. The efficiency at the linac exit is relative to the gun emitted beam current.

Table 1: The $\beta$ Values for the First Few Cells of the $\beta$-varied Accelerating Structure

| Cell # | Variant | | | | |
|---|---|---|---|---|---|
| | 1 | 2 | 3 | 4 | 5 |
| 1 | 0.88 | 0.75 | 0.75 | 0.75 | 0.75 |
| 2 | 0.92 | 0.88 | 0.75 | 0.75 | 0.75 |
| 3 | 0.95 | 0.92 | 0.88 | 0.75 | 0.75 |
| 4 | 1 | 0.95 | 0.92 | 0.88 | 0.75 |
| 5 | 1 | 1 | 0.95 | 0.92 | 0.88 |
| 6 | 1 | 1 | 1 | 0.95 | 0.92 |
| 7 | 1 | 1 | 1 | 1 | 0.95 |
| 8 | 1 | 1 | 1 | 1 | 1 |

Table 2: The Beam Dynamics Results for the Bunching System with the $\beta$-varied Accelerating Structure

| Variant | The linac exit | | |
|---|---|---|---|
| | Efficiency / % | $E_{ave}$ / MeV | δE / MeV |
| 1 | 26.3 | 98.8 | ±4.0 |
| 2 | 40.6 | 100.7 | ±3.9 |
| 3 | 48.1 | 101.5 | ±4.0 |
| 4 | 70.4 | 95.0 | ±10.1 |
| 5 | 73.1 | 83.4 | ±20.8 |

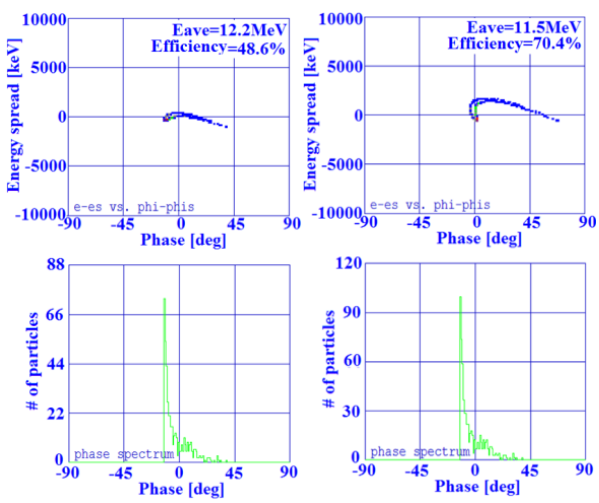


Figure 2: The spectrums at the chicane system exit (left for the variant 3; right for the variant 4).

After carefully analysing the results, one can get the following conclusions: a) By putting the p-to-p energy spread limit at the linac end to be ±4%, the variant 3 is the best, however the efficiency at the lianc exit is ~20% lower than the demanded ~70% [5]; b) Concerning the transportation efficiency, the variant 4 and 5 can meet the ~70% design goal, while the p-to-p energy spread is fairly bigger than ±4%, this will result in a severe beam loss along the 90° beam transport line located at the linac end.

Figure 2 shows the beam spectrums at the chicane system exit for the variants 3 and 4. The more the cells with $\beta$<1 introduced into the $\beta$-varied accelerating structure, the longer the bunch length and the bigger the energy spread of the collimated electron beam, which is the main reason of the bigger p-to-p energy spread at the linac exit.

For the bunching system with the variant 3, if the bunching efficiency at the bunching system exit can be increased by ~20% but not increasing the bunch length of the collimated electron beam, the design requirements for both the transportation efficiency and the p-to-p energy spread at the linac exit can be met, this is also true for the bunching system with the variant 4 if the bunch length of the collimated beam can be shortened to a certain level similar to that of the variant 3. All these problems can be solved by integrating the PB with the $\beta$-varied structure together to form the HAS. The $\beta$-varied structure is a pure TW structure, in which only TW RF field exists. While for the HAS, both the SW and TW RF fields exit, it combines all the functions of the PB, the B and the standard accelerating structure. The $\beta$-varied structures with the variant 3 and 4 are the most promising candidates for the TW section design of the HAS.

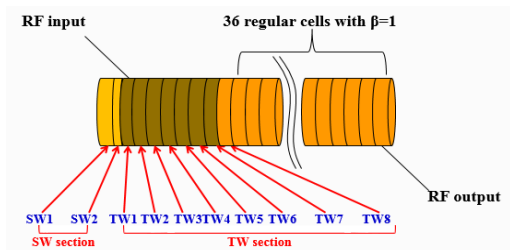


Figure 3: The schematic layout of the HAS.

## BEAM DYNAMICS FOR THE HAS

Figure 3 shows the schematic layout of the HAS. The SW1 and SW2 are two cells operating at the SW π/2 mode, while the cells from TW1 to TW8 are eight cells operating at the TW 2π/3 mode. By a large amount of beam dynamics simulations, it was found that the variant 4 listed in Table 2 is the best candidate for the TW section design of the HAS, the corresponding β values for the SW1, SW2 are 0.94 and 0.56 respectively. The SW section of the HAS is generally the same as that of the HB [3, 4], while the iris aperture between SW2 and TW1 was re-tuned to obtain an optimized field amplitude ratio of ~0.4 between the SW and the TW sections.

Figures 4 to 6 show the beam phase and energy spectrums at the exits of the bunching system, the chicane system and the linac. The spectrums for both the standard

ISBN: 978-3-95450-199-1 doi:10.18429/JACoW-SAP2017-MOPH23

bunching system and the one with the HAS are listed. The bunching system with the HAS fulfils the transportation efficiency requirement of the electron linac. However, the bunching system with the HAS has relatively bigger absolute energy spread than the standard one.

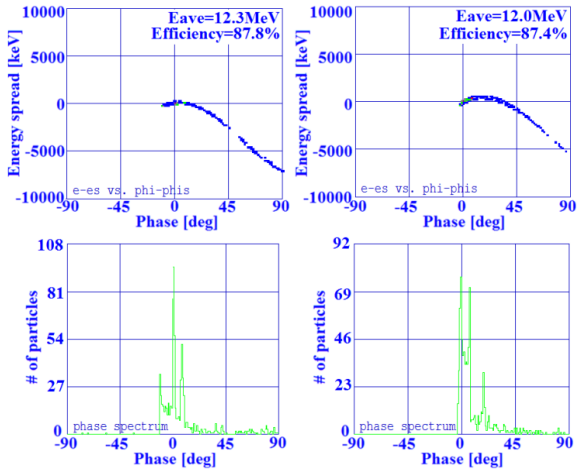


Figure 4: The spectrums at the bunching system exit (left for the standard one; right for the one with the HAS).

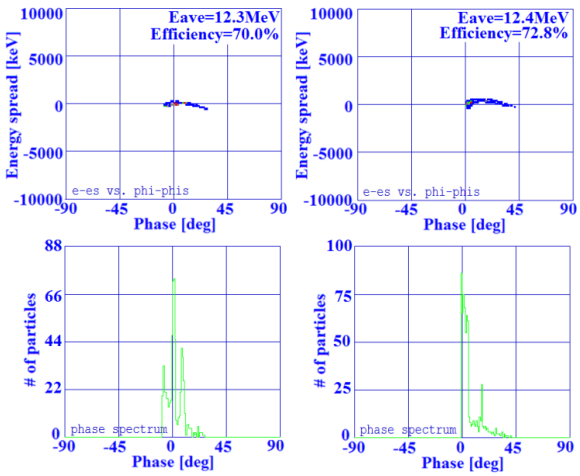


Figure 5: The spectrums at the chicane system exit (left for the standard one; right for the one with the HAS).

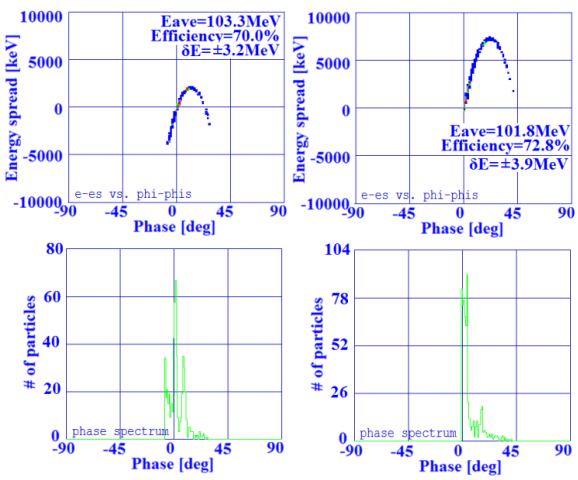


Figure 6: The spectrums at the linac exit (left for the standard one; right for the one with the HAS).

Figure 7 shows the transverse emittance evolution along the linac. For the bunching system with the HAS, the emittance at the linac exit is ~60% bigger, which is because of the relatively hasty bunching process. To obtain the best beam performance, the energy modulation in the SW section of the HAS is bigger than that in the PB of the standard bunching system. The drift space between the SW and TW sections for the HAS is also shorter than that between the PB and the B of the standard bunching system. For the bunching system with the HAS, it is unlikely to obtain the same emittance as the standard one; the drift length between the SW and TW sections cannot be too long for the RF power coupling reason, which means that a relatively bigger energy modulation by the SW section is always needed. At the linac exit, although the bunching system with the HAS has relatively bigger energy spread and emittance, it is still a better choice if the primary concern for the linac is the bunching or transportation efficiency, this is especially true for the industrial linacs.

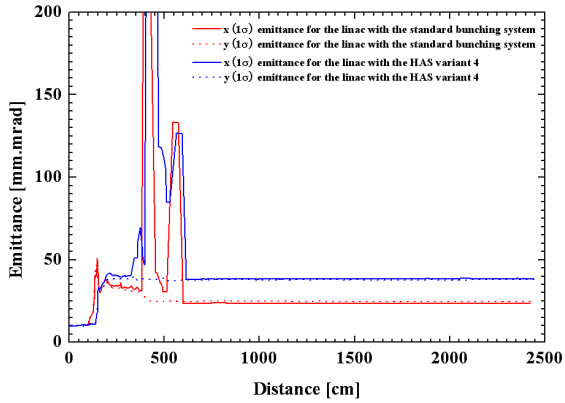


Figure 7: The emittance evolution along the linac.

## SUMMARY

Compared to the standard bunching system, the one with the HAS is more compact, and the cost is lowered to the largest extent without fairly degrading the linac beam performance. In terms of the bunching efficiency and the construction cost, the proposed bunching system with the HAS can be widely applied in the industrial linacs, and can greatly increase the linac efficiency. Additionally, the compactness of the bunching system with the HAS also allows it to be easily scaled to a higher frequency, which is a better choice for the future table-top linac.

## REFERENCES

[1] S. Pei, "Studies on Two-bunch Acceleration in Electron Linear Accelerator", PhD thesis, Beijing: IHEP, 2006.

[2] Y. C. Nie, C. Liebig *et al.*, "Tuning of 2.998 GHz S-band Hybrid Buncher for Injector Upgrade of LINAC II at DESY", *Nucl. Instrum. Methods Phys. Res., Sect. A* 761, 2014, 69-78.

[3] S. Zhao, S. Pei *et al.*, "Field Distribution Measurement and Tuning of the Hybrid Buncher", *High Power Laser Part. Beams* 29, 2017, 065104.

[4] S. Pei, O. Xiao, "Studies on an S-band Bunching System with Hybrid Buncher", *Chin. Phys. C* 37, 2013, 117001.

ISBN: 978-3-95450-199-1 doi:10.18429/JACoW-SAP2017-MOPH23

[5] S. Pei, Y. Chi *et al.,* "Beam Dynamics Studies on the 100 MeV / 100 kW Electron Linear Accelerator for NSC KIPT Neutron Source", *Chin. Phys. C* 36, 2012, 653-660.

[6] W. B. Herrmannsfeld, Developments in the Electron Gun Simulation Program, SLAC-PUB-6726, 1994.

[7] L. M. Young, PARMELA, LA-UR-96-1835, 2005.

[8] Y. Chi, S. Pei *et al.,* "Progress on the Construction of the 100 MeV / 100 kW Electron Linac for the NSC KIPT Neutron Source", *Chin. Phys. C* 38, 2014, 047005.

ISBN: 978-3-95450-199-1 doi:10.18429/JACoW-SAP2017-MOPH24

# ELECTROMAGNETIC AND MECHANICAL DESIGN OF HIGH GRADENT S-BAND ACCELERATING STRUCTURE IN TTX

Cao Dezhi[1†], Shi Jiaru[1], Zha Hao[1], Du Yingchao[1],
Tang Chuanxiang[1], Huang Wenhui[1], Chen Huaibi[1], Wei Gai[2]
Department of Engineering Physics, Tsinghua University, Beijing, China
[1]also at Key Laboratory of Particle and Radiation Imaging of Ministry of Education, Tsinghua University, Beijing, China
[2]also at High Energy Physics Division, Argonne National Laboratory, USA

*Abstract*

Thomson scattering x-ray source is an essential scientific platform and research tool in x-ray imaging technology for various fields. Upgrading plan that replacing the 3-meter S-band old linac with shorter high-gradient structure in Tsinghua Thomson scattering X-ray source (TTX) is undergoing so far, aiming to enhance accelerating gradient from 15 MV/m to 30 MV/m. Detailed parameters of couplers and electromagnetic simulation results of whole acceleration structure are presented in this paper. Finally, mechanical structure and further upgrading research on energy with X-band structures are also discussed.

## INTRODUCTION

The Advanced X-ray sources, including X-ray free-electron-lasers facilities and Thomson scattering facilities, are widely used in molecular biology and material sciences research area. In Tsinghua University, we have built the compact Thomson x-ray scattering source, which is specialized in hard x-ray generating in china firstly [1]. The current beam line layout of TTX is presented in Fig. 1 (a).

In the latest proposal, we are planning to add two X-band accelerating structures and replace the S-band travelling wave (TW) tube with a shorter one in 1.5-meter, maintaining high-energy x-ray photos generation meanwhile. The layout of beam line after the upgrading is showed in Fig. 1(b).

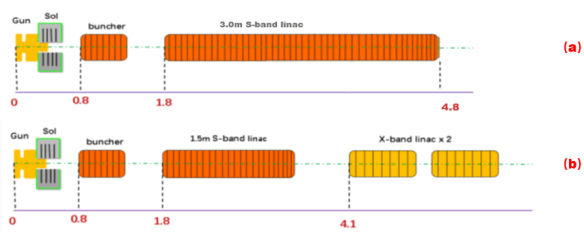


Figure 1: Present linac layout and upgrade proposal.

In the new acceleration structure, we have adopted the constant gradient design in chambers to achieve a higher acceleration gradient as well as a shorter distance. The S-band TW tube are supposed to working in 3π/4 mode through electromagnetic simulation. The method and the concrete parameters of the design of the cavity structure has been demonstrated previously [2-3]. The following section we will present input/output couplers design parameters and the whole integrated structure with acceleration chambers. The completely electromagnetic structure and mechanical structure of the S-band TW tube are also showed here.

## ELECTROMAGNETIC DESIGN

Completely single-cell design procedure of S-band TW tube has finished [2]. Continuous feedback brings adjustments dynamically between the electromagnetic design and realistic mechanical manufacturing procedure.

The simulated parameters of S-band TW tube without couplers are updated in Table 1.

Table 1: Completely Parameters of S-band TW Tube

| Parameters | Value |
|---|---|
| Frequency | 2856.00 MHz |
| Phase advance per cell | 3π/4 |
| Length | 1.456 m |
| Cell numbers | 37 |
| Period | 39.36 mm |
| Iris half aperture | 10.22 mm~8.13 mm |
| Cell radius | 42.53 mm~42.17 mm |
| Elliptical iris long axis | 9.54 mm |
| Elliptical iris thickness | 5.3 mm |
| Filling time | 999 ns |
| Group velocity ($v_g$/c) | 0.00724~0.00302 |
| Shunt impedance | 66.2 MΩ/m~72.0 MΩ/m |
| Input power | 30 MW |
| Gradient | 31.5 MV/m~29 9 MV/m |

Separate design process of dual-feed coupler was simulated in working frequency of 2856MHz to match the chambers as microwave input/output port.

### *Coupler Design*

The input and output couplers have been designed in order to implement the power feeding into structure. Dual-feed coupler structure and its separated model with four cells are showed in Fig. 2 [4]. One fourth of side coupler are showed in Fig.3 [4].

† cdz16@mails.tsinghua.edu.cn

ISBN: 978-3-95450-199-1 doi:10.18429/JACoW-SAP2017-MOPH24



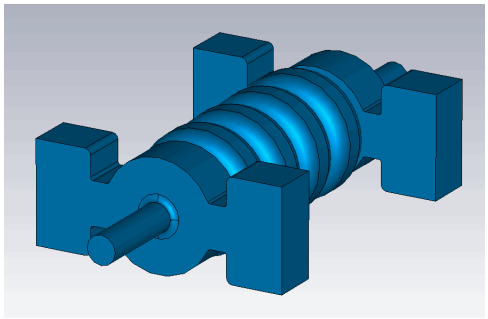

Figure 2: Model of coupler with four cells.

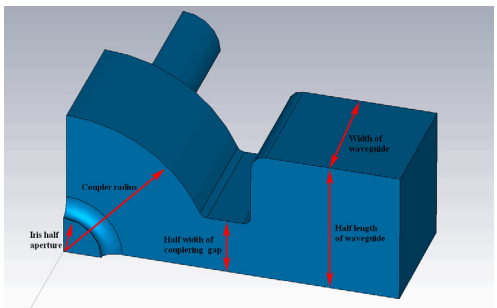


Figure 3: Symmetric split of coupler model in simulation.

We have optimized radius of coupler and width of coupling gap for lower reflection. Parameters of couplers working in 2856 MHz are listed in Table 2.

Table 2: Input / Output Couplers Parameters

| Parameters | Input coupler | Output coupler |
|---|---|---|
| Iris half aperture | 10.22mm | 8.13mm |
| Coupler radius | 39.46mm | 39.52mm |
| Half-width of coupling gap | 15.23mm | 13.94mm |
| Half-length of waveguide | 36.07mm | 36.07mm |
| Width of waveguide | 34.04mm | 34.04mm |

The input and output coupler convert TE mode to TM mode and transmit power through waveguide. The simulated reflection coefficient of individual input/output coupler with four cells are showed in Fig. 4.

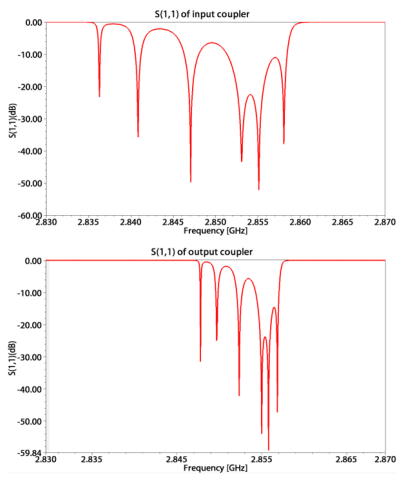


Figure 4: S (1, 1) parameter of input/output coupler.

### *Completely Electromagnetic Accelerating Structure*

In the whole design process, feedback between the electromagnetic design and realistic mechanical design procedure has been necessary.

Combined cell-chains consists of each cell and power feeding couplers are integrated with beam pipe. The whole S-band accelerating structure are showed as Fig. 5 [4].

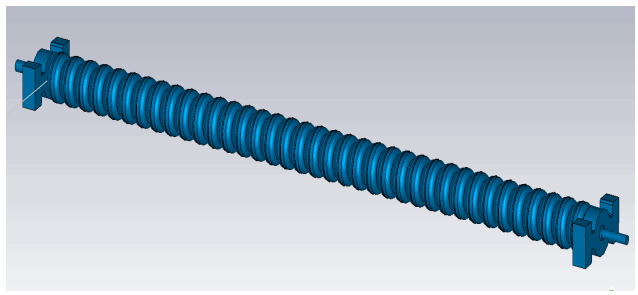

Figure 5: Completely electromagnetic model of S-band TW tube.

Initial tuning and simulation results shows that microwave reflection of whole structure is -14 dB.

Optimizing the radius for every cell and the size of coupling port is continuing in process to match the microwave working frequency in 2856 MHz.

### *Mechanical Design*

The electromagnetic model of the vacuum area wrapped in the metal boundaries. Division of whole acceleration structure are cavities, input coupler and output coupler.

The cell design was split up in the middle position of cavity for the industrial manufacturing procedure consideration. The section chart of cavity has demonstrated as Fig. 6 [5].

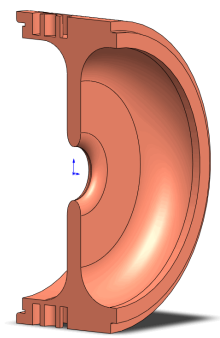

Figure 6: Mechanical model of individual cavity design.

Couplers was split into two parts for conventional milling process. Half of coupler component combined with one cell part to form the first cavity and the last cavity.

The accelerating structure is consisting of 37 vacuum chambers by adding input couples, output couples and 36 similar parts above combing. The completely mechanical design with flanges are showed as Fig. 7 [5].

ISBN: 978-3-95450-199-1 doi:10.18429/JACoW-SAP2017-MOPH24

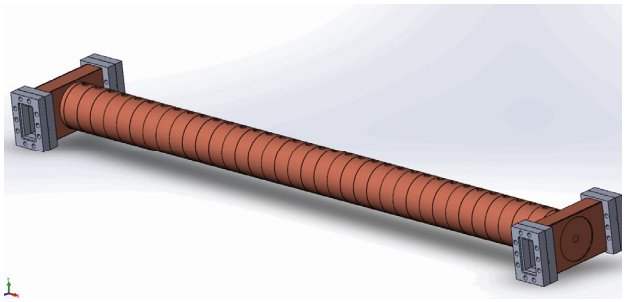

Figure 7: Completely mechanical model of acceleration structure.

Mechanical drawing is real-time adjustment with results of electromagnetic simulation process. Subsequent fabricating procedure will be carry out when the optimistic process finished.

## CONCLUSION

The initial design of S-band TW tube with nearly 1.5m length is finished and overall parameters have mentioned previously. Mechanical drawing design are in progress depended on optimistic simulation results. Next several months, manufacturing procedure will carry out. After that, frequency measurement of cold test and high power test of the structure will proceed in platform. Final experiment results will characterize the performance of tube.

Structure optimization in upgrading proposals is aiming to improve electron energy into 150 MeV. Meanwhile, synchronically structure design of another two X-band accelerating tube is in progress. Furthermore, mechanical design of X-band acceleration structure keeps pace with the fabrication of X-band TW tube.

## REFERENCES

[1] Zhen Zhang, Yingchao Du *et al,* "High time resolution beam-based measurement of the rf-to-laser jitter in a photocathode rf gun", *Physical Review Special Topics – Accelerators and Beam*. 17,032803 (2014).

[2] Cao Dezhi *et al,* "S-band Accelerating Structure for High-Gradient Upgrade of TTX", in *International Particle Accelerator Conference (IPAC'17)*, Copenhagen, Denmark, paper TUPAB070.

[3] PEI. Yuanji,*Design of Electron Linear Accelerator*. Beijing, China: Science Press. 2013.

[4] CST, *http://www.cst.com*

[5] SolidWorks, *http://www.solidworks.com/*

ISBN: 978-3-95450-199-1 doi:10.18429/JACoW-SAP2017-MOPH25

# DEVEOPMENT OF LLRF SYSTEM FOR TSINGHUA X-BAND HIGH POWER TEST FACILITY

M. Peng†, J. Shi*, P. Wang, Department of Engineering Physics,
Tsinghua University, Beijing, China
also at Key Laboratory of Particle & Radiation Imaging, Tsinghua University,
Ministry of Education, Beijing, China
Z. Sun, D. Zhang, HZCY Technologies Co., Ltd., Beijing, China

*Abstract*

Tsinghua X-band high power test stand is under construction. A new LLRF system based on the original S-band LLRF system has been designed and tested. A 1 U chasses called X-Adapter was constructed, which has the ability of up-converting and down-converting the signals between 2.856 GHz and 11.424 GHz. The goal of the LLRF system development is to modulate and measure the phase and amplitude of the RF signals. The test results are presented and analysed.

## INTRODUCTION

Tsinghua has been preparing for a high power test stand based on the 50 MW klystron. The 50 MW CPI klystron and ScandiNova modulator will be installed in this September, and then are the waveguides, cooling system, and RF load. Some tests of RF components and high power experiments are under planning. To do these experiments, one or more amplitude and phase tunable RF signals are required.

There are basically two ways to approach this goal. One is to quadruple the frequency of the 2856 MHz signal directly to 11.424 GHz. The other one is to triple the 2856 MHz signal and then multiply it with the original one. The first method has been tested on CERN's Xbox 2 [1]. Since the limited input power range of quadrupler, the output power of 11.424 GHz can only vary in a very small range, which is not suitable for some RF tests. So we chose the second way.

All the components used in the X-Adapter are small in size. So this adapter can be packaged in an individual 1 U chassis or assembled with the S-band LLRF chasses by adding 1 U in height. For preliminary research on the feasibility of the X-Adapter, we packaged the RF circuits on a plate. The test results show that the X-Adapter can generate RF signal with modulated phase or amplitude, which is enough for the experiments of the high power test stand in the early stage. More functions of the X-Adapter will be added in the future.

## SCHEMATIC DESIGN

The signal flow of the X-Adapter is shown in Fig. 1. The whole adapter has at most seven connectors, three S-band input signals for three phase and amplitude modulated X-band outputs, one X-band input signal for S-band output to be measured in S-band LLRF.

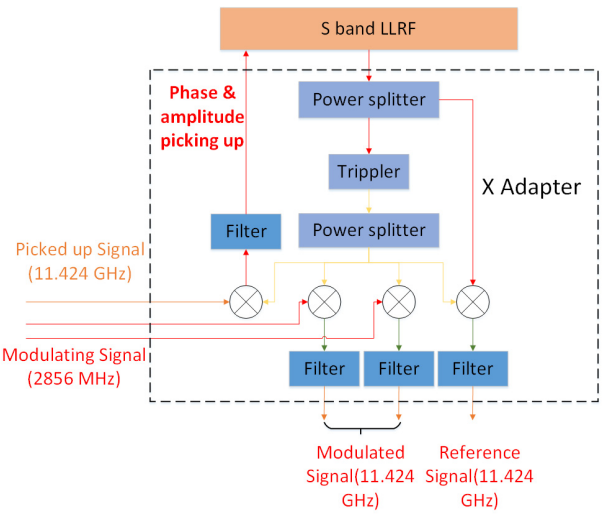


Figure 1: Schematic diagram of the X-Adapter.

### *Generation of RF Signal*

The generation of X-band signal is achieved by the up conversion of S-band RF signal. A prerequisite signal $\cos(\omega_0 t + \varphi_0)$ from S-band LLRF, named input reference signal, first split into two same one by the power splitter. One of them then becomes $\cos(3\omega_0 t + 3\varphi_0)$ after the Tripler, as the LO of the four frequency mixers, the other one becomes the IF of one frequency mixer. It is obvious that the RF of this frequency mixer is $\cos(\omega_0 t + \varphi_0) \times \cos(3\omega_0 t + 3\varphi_0) = \frac{1}{2}[\cos 4(\omega_0 t + \varphi_0) + \cos 2(\omega_0 t + \varphi_0)]$. At the output of the filter, we have the reference X-band RF signal $\cos 4(\omega_0 t + \varphi_0)$, named output reference signal. The phase and amplitude of the reference signal is only depending on the input reference signal of S-band LLRF.

Two alternative modulated X-band signals are provided by inputting modulating S-band signals. For modulating signal $A\cos(\omega_0 t + \varphi_1)$, the modulated X-band signal is $\frac{1}{2}A\cos(4\omega_0 t + \varphi_0 + \varphi_1)$ after frequency the mixer and filter. The input S band signals and output X band signals are called modulating signal and modulated signal. The relative phase and amplitude of the modulated signals are alterable by changing A and $\varphi_0$.

† pmm15@mails.tsinghua.edu.cn
*shij@tsinghua.edu.cn

ISBN: 978-3-95450-199-1 doi:10.18429/JACoW-SAP2017-MOPH25

### *Phase and Amplitude Picking Up*

As the LO has provided when generating 11.424 GHz signal, the input signal for phase and amplitude picking up can be easily down converted to 2856 MHz. We suppose the input signal is $\cos(4\omega_0 t + \varphi_2)$, and the output to S-band LLRF is $\cos(\omega_0 t + \varphi_2 - 3\varphi_0)$. We should notice that the phase of S band LLRF get is not $\varphi_0$ but $\varphi_2 - 3\varphi_0$.

## EXPERIMENTS

The photograph of the X-Adapter is shown in Fig. 2. For the convenience to test, all the components are fixed on a slab by tape. Only phase and amplitude modulating are tested up to now, the RF picking is still untested. For there are only two outputs of the original S-band LLRF chasses, we tested one reference signal and one modulated signal.

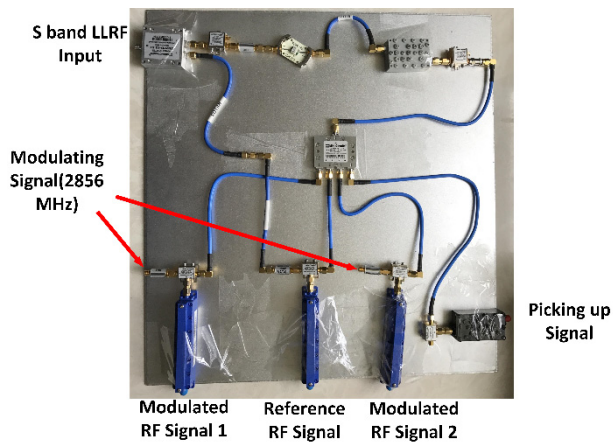


Figure 2: The X-Adapter.

The 11.424 GHz reference and modulated signal were measured by a Lecroy oscilloscope in Fig. 3, which has sampling rate of 80GHz and passband of 25GHz. Then we get the phase and amplitude by I/Q demodulating the data saved in the oscilloscope. The output signal's power was measured by a ROHDE&SCHWARZ power meter in Fig.4. The GUI of the power meter gives the profile of the pulse, and peak value and period. A wide band frequency from 50MHz to 18 GHz with power from -60 dBm to +20dBm can be measured safely.

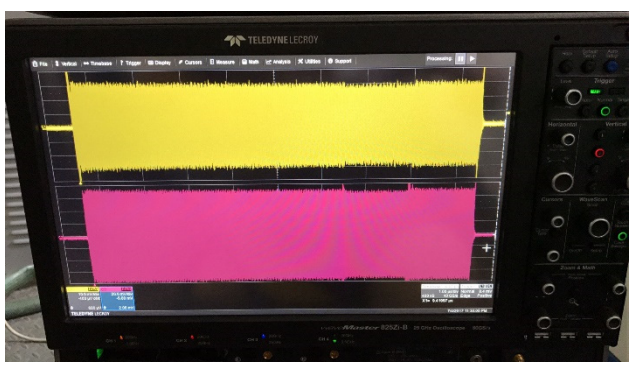

Figure 3: The reference and modulated signal measured by Lecroy oscilloscope.

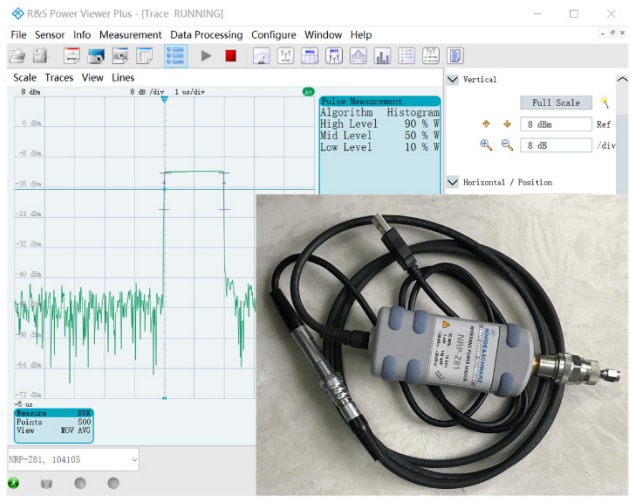


Figure 4: ROHDE&SCHWARZ power meter and its GUI on computer.

### *Amplitude Modulating*

We modulated the amplitude of the RF signal and the results are shown in the Fig. 5. With the reference input signal fixed, the amplitude at last 1.5μs of input S-band modulating signal becomes half of the front. The amplitude of output X band RF changes from 80 mV to 40 mV. This result indicates that the LLRF system can generate RF signal with different amplitude. Moreover, we can modulate the amplitude the amplitude of the RF signal in the RF pulse.

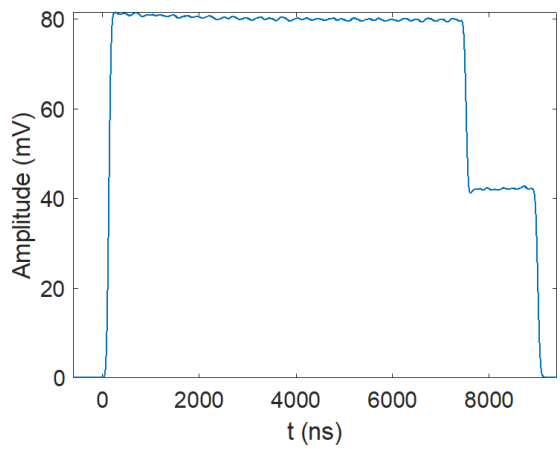


Figure 5: Amplitude modulating of the modulated signal.

### *Phase Modulating*

Keeping the input reference signal and the amplitude of modulating signal constant, we reverse the phase of modulating signal at 6μs and reverse it back at 7.5μs. In Fig. 6, Fig. 7, Fig. 8, Fig. 9 are the amplitude and phase of output reference and modulated signals.

In Fig. 4, the amplitude of output reference signal keeps 52.5 mV and low noise from time 0 to 9μs, which means no interference from the modulated signal. At beginning and end of Fig. 7, there are some phase oscillations, but it doesn't matter because of the zero amplitude.

ISBN: 978-3-95450-199-1 doi:10.18429/JACoW-SAP2017-MOPH25



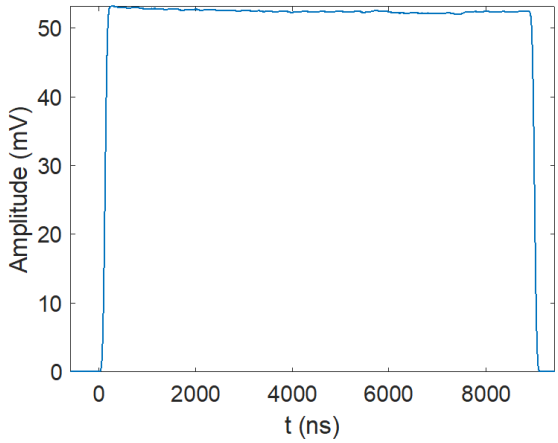


Figure 6: Amplitude of the output reference signal.

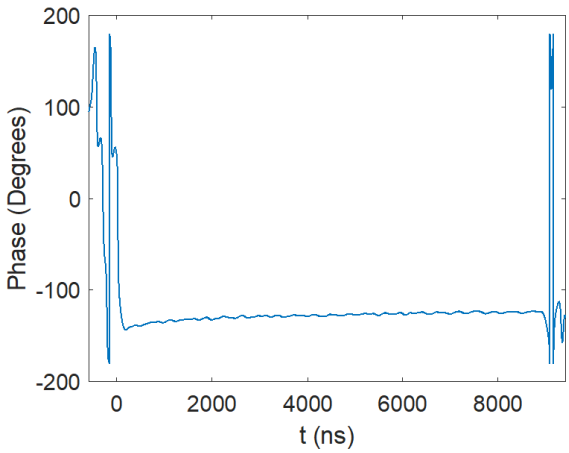


Figure 7: Phase of the output reference signal.

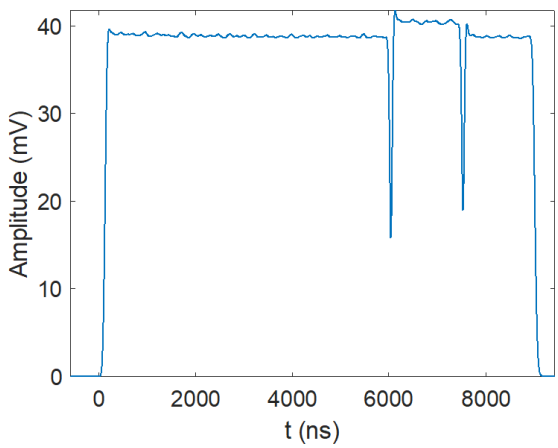


Figure 8: Amplitude of the modulated signal.

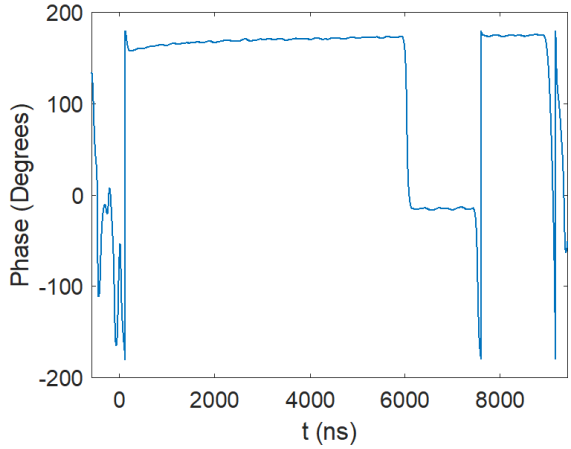


Figure 9: Phase of the modulated signal.

The modulated signals are shown in Fig. 8 and Fig. 9. The amplitude changes about 2.5% when its phase reversed and then coming back. This result is caused by the reflection of the wires and other components. The phase of modulating signal in S-band LLRF is changed by increasing or decreasing its frequency [2]. For a signal $\cos(\omega_0 t + \varphi_0)$, to advance its phase, we first add a frequency $\Delta\omega$ and becomes $\cos((\omega_0 + \Delta\omega)t + \varphi_0)$. At $t = t + \Delta t$, the signal turns into $\cos(\omega_0 t + \varphi_0 + \Delta t \cdot \Delta\omega)$. As 11.424 GHz output is on the edge of passband of the filter, there is a downward peak when the phase is changing. In Fig. 9, the phase reversed from 180° to 0° as expected. However, the rising time of reversing phase is 100 ns, which is beyond the acceptance of pulse compressor tests. Replace the output filter should help.

## CONCLUSION

The X-Adapter provides a highly flexible and low cost solution for X-band high power RF test stand and make full use of the S-band LLRF system. Further experiments needed to be conducted after adding external isolator and replacing the filter with one have a suitable passband.

## REFERENCES

[1] Woolley B, Dexter A, Syratchev I *et al.*, High power X-band RF test stand development and high power testing of the CLIC crab cavity[D]. Lancaster University, 2015: 44-48.

[2] Jin, Yang, Research on Synchronization System based on Tsinghua Thomson scattering X-ray source [D].Beijing: Tsinghua University, 2016: 51-83.

ISBN: 978-3-95450-199-1 doi:10.18429/JACoW-SAP2017-MOPH26

# CEPC LINAC DESIGN AND ERROR STUDY*

C. Meng†, Y. Chi, X. Li, G. Pei, S. Pei, D. Wang, J. Zhang
Institute of High Energy Physics, Beijing, China

*Abstract*

Circular Electron-Positron Collider (CEPC) is a 100 km ring $e^+ e^-$ collider for a Higgs factory, including the double ring for collider and the injector. The injector is composed of the linac and booster. The linac of CEPC is a normal conducting S-band linac with frequency in 2856.75 MHz and provide electron and positron beam at an energy up to 10 GeV with bunch charge in 1.0 nC and repetition frequency in 100 Hz. The linac scheme will be detailed discussed. The beam dynamic results with short-range Wakefields and detailed error study including misalignment errors and field errors also be presented.

## INTRODUCTION

With the discovery of the Higgs particle at the Large Hadron Collider at CERN in July 2012, further re-search and measurement in Higgs is very important for particle physics. In September 2012, Chinese scientists proposed a Circular Electron Positron Collider (CEPC) in China at 240 GeV centre of mass for Higgs studies [1]. It could later be used to host a Super proton proton Collider (SppC) in the future as a machine for new physics and discovery. After that a great effort have been made in parameter choice and physics design [2][3]. With the deep study and more consideration in CEPC the scheme has several versions compared with the pre-CDR [4]. The latest scheme has some updates, the baseline design of main ring is double ring with circumference 100 km and the linac energy is 10 GeV and also some more detailed optimizations.

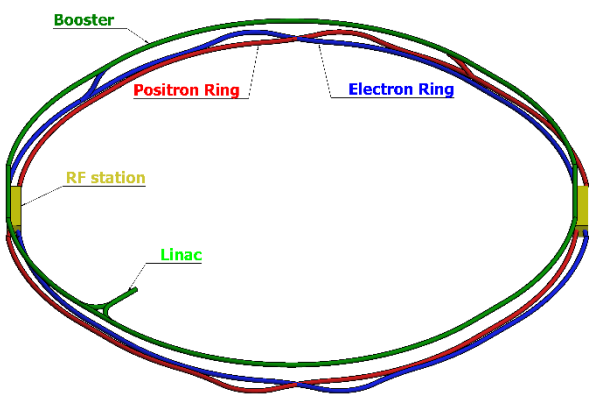


Figure 1: Layout of CEPC.

CEPC is composed of double ring for collider and the injector including linac and booster. The Booster provides 120 GeV electron and positron beams to the CEPC collider and is installed above the collider in the same tunnel, which is shown in Fig.1. Considering the very low magnetic field at the injection of booster, one pre-booster with energy in 45 GeV given consideration to Z study have been proposed.

The first part of the injector is a normal conducting S-band linac with frequency in 2856.75 MHz and provide electron and positron beam at an energy up to 10 GeV. The main parameters are shown in Table 1. With the study of CEPC booster and injection scheme, one-bunch-per-pulse mode is considered and the bunch charge is decreased to 1.0 nC from 3.2 nC at pre-CDR, however we also keep the ability to provide a 3.2 nC bunch beam by now. In the baseline design a 4 GeV primary electron beam with bunch charge in 10 nC hit a tungsten target to obtain a 3.2 nC positron beam.

Table 1: Main Parameters of CEPC Linac

| Parameter | Unit | Value |
|---|---|---|
| $e^-/e^+$ beam energy | GeV | 10 |
| Repetition rate | Hz | 100 |
| $e^-/e^+$ bunch population | nC | 1.0 |
| Energy spread ($e^-/e^+$) | | $<2\times10^{-3}$ |
| Emittance ($e^-/e^+$) | mm-mrad | <0.3 |
| $e^-$ beam energy on Target | GeV | 4 |
| $e^-$ bunch charge on Target | nC | 10 |

Based on a lot of discussions of linac scheme, we choose the linear scheme as the baseline design, which is shown in Fig.2 and composed of electron source and bunching system (ESBS), the first accelerating section (FAS) where electron beam is accelerated to 4 GeV, positron source and pre-accelerating section (PSPAS) where positron beam is accelerated to 200 MeV, and the second accelerating section (SAS) where electron and positron beam are accelerated to 10 GeV. The electron bypass method, electron transport line bypass or target bypass, have not yet been determined. The beam dynamics will be presented. The errors study has been considered carefully, including the misalignment errors of magnets and accelerating tubes, correction scheme, filed errors and accelerating gradient errors of accelerating tube.

* Work supported by National Key Programme for S&T Research and Development (Grant NO.: 2016YFA0400400)and National Natural Science Foundation of China (NO. 11505198)
† mengc@ihep.ac.cn

ISBN: 978-3-95450-199-1 doi:10.18429/JACoW-SAP2017-MOPH26



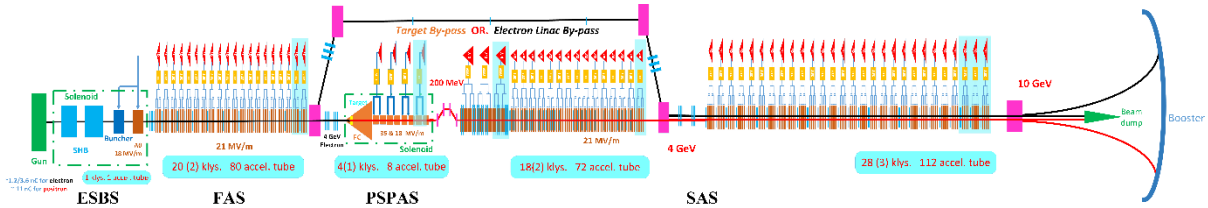


Figure 2: CEPC linac layout.

## BEAM DYNAMICS OF LINAC

The linac is composed of ESBS, FAS, PSPAS and SAS , which provide electron and positron beam with the energy in 10 GeV. The detailed design and beam dynamics results can been proposed [5].

There are different transverse focusing structures in different sections. The solenoid focusing structure is adopted in ESBS and PSPAS section to obtain large beam transmission. For the FAS section there are 2 period structures shown in Fig.3: one triplet group 4 accelerating tubes and one triplet group 8 accelerating tubes. Because the emittance of positron beam is much larger. There are four period structures changing with energy increasing in SAS section shown in Fig.4: FODO structure where the quadrupoles are nesting on accelerating tube, one triplet group one accelerating tube, one triplet group two accelerating tubes and one triplet group four accelerating tubes.

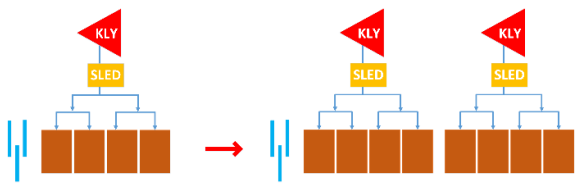


Figure 3: Period structure of FAS.

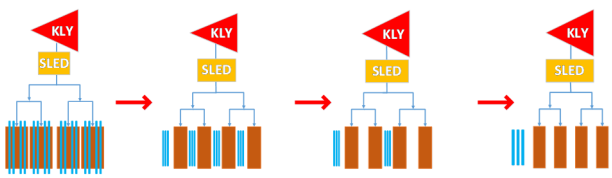


Figure 4: The focusing structures of SAS.

To shorten linac length and improve power efficiency, the SLAC energy doubler (SLED) and one klystron drive 4 accelerating tubes mode have been adopted. Beam is accelerated by S-band accelerating tube with frequency in 2856.75 MHz and accelerating gradient in 21 MV/m. To get higher positron yield constant impedance S-band accelerating tubes with radius in 15 mm and accelerating gradient in 35 MV/m are used in PAPAS. Considering one-bunch-per-pulse mode and high bunch charge for positron generation, the short-range longitudinal Wakefield and transverse Wakefield are included in beam dynamics simulation, using Yokoya's Wakefield model for periodic linac structure [6].

Because the positron beam has larger emittance, we focused on the beam dynamics of positron beam. Considering the short-range Wakefield, one can get beam simulation results with bunch charge 3.2 nC including energy spread, emittance, longitudinal phase space distribution, energy and beam sizes, which are shown in Fig.5 and can meet the requirements.

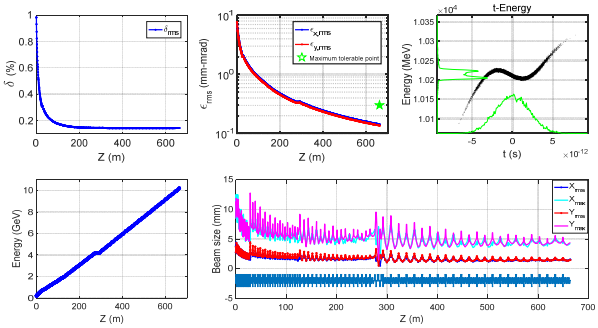


Figure 5: The simulation results along the linac: energy spread (top left), emittance (top middle), longitudinal phase space distribution (top right), energy (down left) and beam sizes (down right).

## ERROR STUDY

All the devices having electromagnetic field influence over the beam have installation errors including translational errors and rotational errors, and also field errors. We can classify the possible error sources into three groups:

1. Misalignment errors: affecting all the elements with translational errors and rotational errors, e.g. solenoids, quadrupoles, accelerating cavities, etc.
2. Field errors: affecting the fields as well as the phases of accelerating tubes and the fields of magnets.
3. BPM uncertainty errors: affecting the orbit correction effect.

All the errors mentioned above can be also classified in two different types according to their variation properties with time: static errors and dynamic errors.

### *Vibration of Magnet*

Because the beam orbit jitter caused by quadrupole vibration caused by ground vibration cannot be corrected, we should control the beam orbit jitter carefully to meet the requirement of booster injection. Figure 6 shows the rms beam orbit jitter with different quadrupole vibration amplitude. If the rms orbit jitter should smaller than 0.2 mm which means the maximum orbit jitter is about 0.6 mm,

ISBN: 978-3-95450-199-1 doi:10.18429/JACoW-SAP2017-MOPH26

quadrupole vibration amplitude need be controlled within 5 μm.

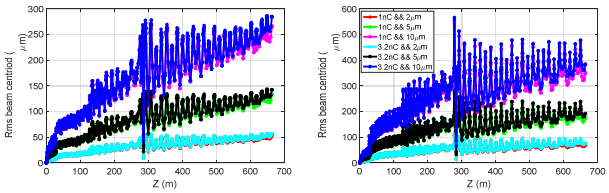


Figure 6: The rms beam orbit jitter with different quadrupole vibration amplitude along the linac.

### *Misalignment Errors and Correction*

Following the engineering experience, the errors used for error study are shown in Table 2, which in the values of errors are RMS value with 3σ truncated Gaussian distribution. The RMS beam orbit with errors are shown in Fig.7. From the simulation results one can get the beam orbits with errors are too large and correction is necessary. One-to-one correction method is used and each period have one pair of correctors and one BPM in the correction scheme. The simulation results with correction are shown in Fig.7 and the rms beam orbit is smaller than 0.3 mm. If the requirement of beam orbit is loose, we can reduce the number of BPM and corrector. According to the simulation results, it is predictable that the number of BPM and corrector can be reduced by half.

Table 2: Errors Settings for Error Study

| Error description | Unit | Value |
|---|---|---|
| Translational error | mm | 0.1 |
| Rotation error | mrad | 2 |
| Magnetic element field error | % | 0.1 |
| BPM uncertainty | mm | 0.1 |

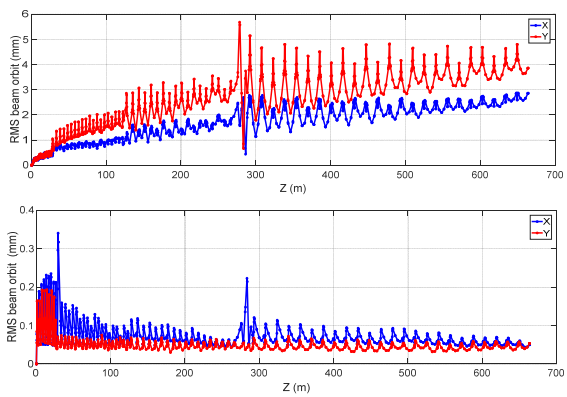


Figure 7: The RMS beam orbit with errors without correction (up) and with correction (down).

### *Phase Errors and Accelerating Gradient Errors*

The phase errors and accelerating gradient errors of accelerating tubes can cause energy jitter. Considering the requirement of booster in energy spread is 0.2% and the energy spread without errors is about 0.15%, the energy jitter should smaller than 0.1%. Figure 8 shows the energy jitter with different phase errors and accelerating gradient errors. According to the simulation results, one can get the phase errors should be controlled in 0.5 degree and accelerating gradient errors should be controlled in 0.5%.

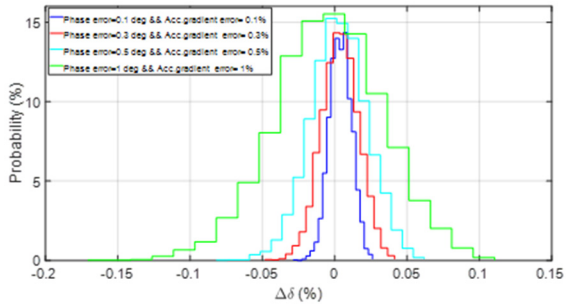


Figure 8: Energy jitter with different phase errors and accelerating gradient errors.

## CONCLUSION

The linac of CEPC is a normal conducting S-band linac with frequency in 2856.75 MHz and provide electron and positron beam at an energy up to 10 GeV. The detailed simulation results and error study are presented and the linac design can meet the requirements of CEPC. There is no issue that defies solution for CEPC linac and more optimizations should be continued.

## ACKNOWLEDGEMENT

The authors would like to thank Professors T. Kamitani, M. Akemoto and CEPC group members' valuable suggestions and comments.

## REFERENCES

[1] Y.F. Wang, "A proposal on ring-based Higgs factory in China", 2nd Symposium on Accelerator-based HEP Strategy and Development in China, Sept. 2012.

[2] Q. Qin *et al.*, "Overview of the CEPC Accelerator", in *Proceedings of HF2014*, Beijing, China, 2014, paper THP3H2.

[3] J. Gao, "CEPC-SppC Accelerator Status", in *Proceedings of RuPAC2016*, St. Petersburg, Russia, 2016, paper MOZMH01.

[4] The CEPC-SppC Study Group, "CEPC-SppC preliminary Conceptual Design Report", Volume II- Accelerator, IHEP-CEPC-DR-2015-01, IHEP-AC-2015-01, March 2015.

[5] C. Meng *et al.*, "CEPC Linac Design and Beam Dynamics", in *Proceedings of IPAC'17*, Copenhagen, Denmark, 2017, paper THPAB008, p.1315.

[6] K. Yokoya, "The Longitudinal High–frequency Impedance of a Periodic Accelerating Structure", in *Proceedings of the 1999 Particle Accelerator Conference*, New York, 1999, pp.1725-1727.

ISBN: 978-3-95450-199-1 doi:10.18429/JACoW-SAP2017-MOPH27

# DESIGN STUDIES ON AN S-BAND HYBRID ACCELERATING STRUCTURE*

B. Gao†, S. Pei, Y. Chi, Key Laboratory of Particle Acceleration Physics and Technology, Institute of High Energy Physics, Chinese Academy of Science, Beijing, China

*Abstract*

In an electron linac, the composition of the bunching system is determined by the synthetical consideration of the beam performance and the construction cost. In the industrial area, the bunching system is usually simplified to reduce the construction cost by eliminating the PB and integrating the B and the standard accelerating structure to form the $\beta$-varied structure. The bunching performance for this kind of system is relatively worse than that for the standard one. To keep the beam performance of the standard bunching system and reduce the construction cost as much as possible, the HAS is proposed by integrating the PB, the B and the standard TW accelerating structure together. The HAS can be widely applied in the industrial area to enhance the beam performance of the industrial linac but not increase the cost. In this paper, the design studies on an S-band (2856 MHz) HAS is presented. The HAS studied here is composed of 2 SW cells, 40 TW cells and 2 coupler cells. The on-axis electric field amplitude distribution simulated by HFSS can fully meet the beam dynamics requirement.

## INTRODUCTION

The standard bunching system consists of a standing wave (SW) prebuncher (PB), a traveling wave (TW) buncher (B) and a TW accelerating structure in an electron liner accelerator. Inspired by the ingenious idea of the hybrid photo-injector developed by the INFN-LNF/UCLA/ SAPIENZA collaboration [1], we successfully built the hybrid buncher (HB) [2]. It has been proved that the HB is an innovative attempt to reduce the construction cost of the standard bunching system but preserve the beam quality as much as possible [3]. In this scenario, to exclusively simplify the standard bunching system, the hybrid accelerating structure (HAS) shown in Fig. 1 is proposed by integrating the PB, the B and the standard accelerating structure together [4]. Compared to the standard bunching system, the one with the HAS is more compact, and the cost is lowered to the largest extent without fairly degrading the beam performance.

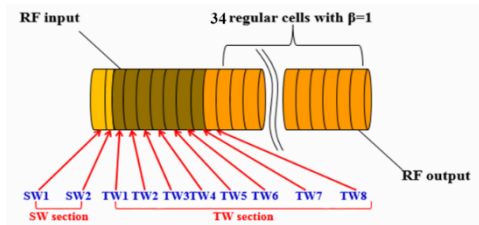


Figure 1: The schematic layout of the HAS.

Supported by the National Natural Science Foundation of China and the Youth Innovation Promotion Association of Chinese Academy of Sciences, China, we are building an S-band (2856 MHz) HAS prototype. The HAS prototype is composed of 2 SW cells, 40 TW cells and 2 coupler cells. The 2 SW cells operate at $\pi/2$ mode, while the 40 TW cells operate at $2\pi/3$ mode. The SW section of the HAS is generally the same as that of the HB [2, 3], while the iris apertures between the SW cells and the input RF coupler cell need to be adjusted carefully to obtain the appropriate field distribution. Beam dynamics study on the bunching system with the HAS has been done, it is shown that the HAS bunching system can keep the beam performance of the standard one as much as possible [4].

In this paper, the RF design of the HAS prototype is presented. Initially, 2D code SUPERFISH [5] was used to determine the dimensions of all the cells. Secondly, 3D code HFSS [6] was used to optimize the input and output RF coupler cells. Finally, the on-axis RF field distribution of the whole HAS prototype was calculated, which can fully meet the beam dynamics requirement determined by PARMELA [7].

## INITIAL 2D DESIGN

The initial 2D design for the SW and the TW sections of the HAS were performed separately in SUPERFISH by setting appropriate boundary conditions and material properties. Table 1 lists the basic design requirement of the HAS [4],

In the TW section, the 1st and 42nd cells correspond to the RF input and output coupler cells respectively. The 2nd to 6th are $\beta$-varied cells and the rests are regular cells.

*Work supported by the National Natural Science Foundation of China (11475201) and the Youth Innovation Promotion Association of Chinese Academy of Sciences, China.
† email address: gaobin@ihep.ac.cn.

ISBN: 978-3-95450-199-1 doi:10.18429/JACoW-SAP2017-MOPH27

Table 1: The Basic Design Requirement of the HAS

| Section | Cell # | β | Cell length [mm] |
|---|---|---|---|
| SW section | 1 | 0.94 | 32.80 |
| | 2 | 0.56 | 19.68 |
| TW section | 1 | 0.75 | 26.24 |
| | 2 | 0.75 | 26.24 |
| | 3 | 0.75 | 26.24 |
| | 4 | 0.88 | 30.79 |
| | 5 | 0.92 | 32.19 |
| | 6 | 0.95 | 33.24 |
| | 7~42 | 1 | 34.98 |

### *TW Section Design*

The TW section is the traditional disk-loaded type waveguide structure, which operates at 2π/3 mode. By using the SUPERFISH model shown in Fig. 2, the RF characteristics (frequency $f$, quality factor $Q$, shunt impedance $r_0$, group velocity $v_g/c$, etc) of each cell are calculated. Finally, by colligating all the calculated results for the TW cells together, the main specifications for the TW section listed in Table 2 can be obtained.

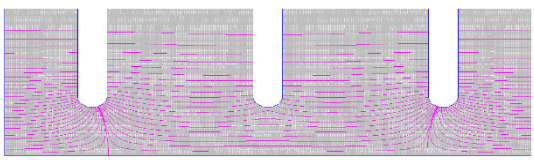

Figure 2: The 2D SUPERFISH model for the TW cells.

Table 2: The Main Specifications of the TW Section

| Parameters | Value |
|---|---|
| Frequency $f$ [MHz] | 2856 |
| Operating temperature [°C] | 35±0.1 |
| Number of cells | 40 |
| Phase advance per cell [°] | 120 |
| Cell length [mm] | 26.24~34.98 |
| Disc thickness [mm] | 5.843 |
| Iris diameter $2a$ [mm] | 28.52~23.73 |
| Cell diameter $2b$ [mm] | 85.47~82.77 |
| Shunt impedance $r_0$ [MΩ/m] | 28.36~57.05 |
| Quality factor $Q$ | 10980~13753 |
| Group velocity $v_g/c$ | 0.0246~0.0141 |
| Filling time [ns] | 239 |
| Attenuation coefficient [Np] | 0.16 |

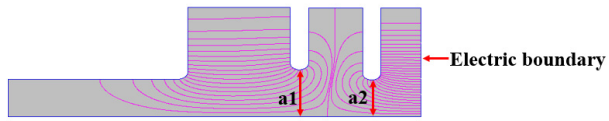


Figure 3: The 2D SUPERFISH model for the SW section.

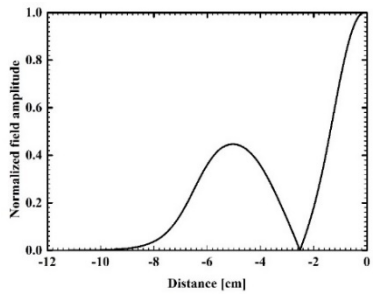


Figure 4: The field amplitude distribution along the axis of the SW section.

### *SW Section Design*

It is well known that half of the coupler cell in the TW accelerating structure operates at the SW mode, thus by using the SUPERFISH model shown in Fig. 3 the SW section of the HAS can be designed and optimized. The left two cells are the 2 SW cells of the HAS, while the right half-cell corresponds to the input RF coupler cell. By tuning the dimensions of a1 and a2, the field amplitude ratio between the SW and the TW sections can be changed.

Figure 4 shows the optimized electric field amplitude distribution along the axis of the SW section. The ratio of the value for the 1st peak to that for the 2nd peak is ~0.45, which is ~4% smaller than the optimized value of ~0.47 [4]. Due to the existence of simulation and fabrication errors, this small deviation is within the tolerance and can be acceptance.

## 3D DESIGN OF THE HAS

The 2D RF design of the HAS is the starting point of the 3D design. Similarly, the SW and the TW sections of the HAS are designed separately.

There may be some frequency difference between the 2D and the 3D simulations. To recover the resonate frequency of each cell back to the nominal value of 2856 MHz, the cell diameter of each cell needs to be adjusted in the 3D simulation. However, all the other dimensions of each cell determined by 2D simulation should be fixed.

### *Coupler Design*

Both the input and output RF couplers can be designed based on the matching procedure for the 2π/3 structure proposed by Dr. R. L. Kyhl and confirmed with the field transmission method. However, for the input coupler, attachment of the SW section with the TW section will change the coupler matching status. Fortunately, it has been proved that the power dissipation in the SW section is much smaller than the power transmitted to the TW section [3]. Therefore, when the field transmission method is used to confirm the input RF coupler matching status,

ISBN: 978-3-95450-199-1 doi:10.18429/JACoW-SAP2017-MOPH27



only minor modification of the dimensions for the coupler cell is needed. Table 3 shows the matching results of the input RF coupler based on the Kyhl method. Fig. 5 shows the 3D HFSS model of the RF input coupler based on the transmission method. By slightly tuning the cavity size and the coupling iris width of the coupler cavity, the S11 curve shown in Fig. 6 can be obtained. The S11 value at the operating frequency 2856 MHz is ~-40dB, which means the matching of the input RF coupler is very well.

Table 3: The Matching Results of the Input RF Coupler

| Frequency [MHz] | Phase I [°] | Phase II [°] | Phase rotation [°] | $\beta$ & $\Delta f$ [MHz] |
|---|---|---|---|---|
| 2829.7 | 57.4 | -62.4 | 119.8 | 1.01 & -0.04 |
| 2842.8 | 51.0 | -130 | 181.0 | |
| 2856.0 | 44.7 | 164 | 240.7 | |

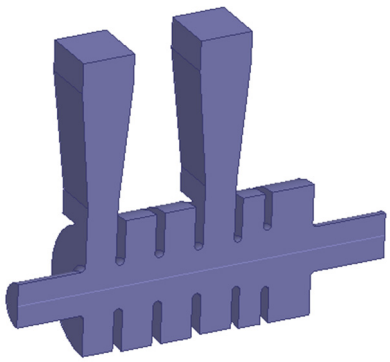

Figure 5: The 3D HFSS model of the input RF coupler based on the transmission method.

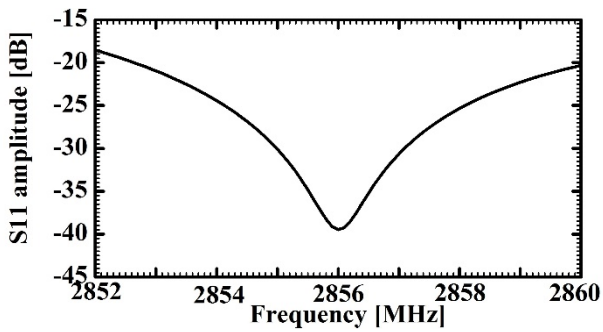


Figure 6: The S11 curve for the input RF coupler.

## *Design of the Whole Structure*

By assembling the SW section, the TW section and the two RF couplers together, the 3D structure of the HAS can be determined and constructed.

In recent years, with the development of the computer technology, simulation of the full 3D structure of the HAS becomes possible. In this situation, calculation of the HAS was carried out in HFSS. To minimize the CPU time and the memory use, only 1/2 model of the HAS shown in Fig. 7 was created and simulated by setting appropriate boundary conditions.

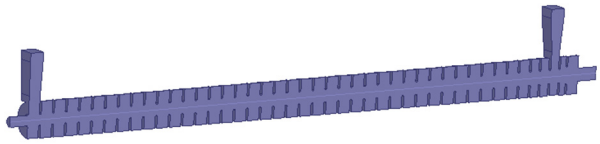

Figure 7: The 1/2 model of the HAS created in HFSS.

Figure 8 shows the electric field amplitude distribution along the axis of the HAS. For comparison, the field distribution used in PARMELA is also shown. One can see that there are 43 peaks, 1st of which corresponds to the 1st cell in the SW section. The 2nd and 43rd peaks correspond to the input and output couplers, respectively. The other 40 peaks correspond to the 40 TW cells. The HFSS simulation result is consistent with the beam dynamics requirement. the axis of the HAS. Figure 9 shows the electric field phase distribution along the axis of the HAS. The phase jump between the SW and the TW sections is 180°, which indicates the operating mode in the SW section is π/2 mode. In the TW section, the phase advance from one cell to another is 120°, which is the case of 2π/3 mode.

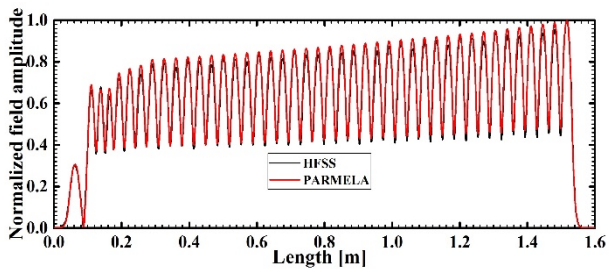


Figure 8: The electric field amplitude distribution along the axis of the HAS.

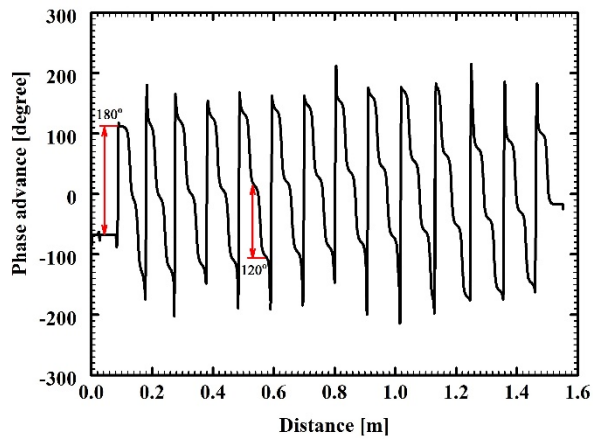


Figure 9: The electric field phase distribution along the axis of the HAS.

## CONCLUSION

The RF design studies on the HAS has been conducted by SUPERFISH and HFSS. The obtained distribution can fully meet the beam dynamics requirement. The HAS combines the functions of the PB, the B and the standard TW accelerating structure, it can be widely applied in the industrial area.

ISBN: 978-3-95450-199-1 doi:10.18429/JACoW-SAP2017-MOPH27

## REFERENCES

[1] D. Alesini *et al.*, The Design of a Hybrid Photon Injector for High Brightness Beam Applications, in *Proc. EPAC2006*, Edinburgh, Scotland, 2006, WEPLS048, p.2487.

[2] S. Zhao *et al.*, Field Distribution Measurement and Tuning of the Hybrid Buncher, *High Power Laser and Particle Beams*, 2017, 29(6): 065104.

[3] S. Pei *et al.*, Studies on an S-band Bunching System with Hybrid Buncher, *Chinese Physics C*, 2013, 37(11): 117001.

[4] S. Pei *et al*, Studies on the S-band Bunching System with the Hybrid Accelerating Structure , presented at *SAP2017*, this proceedings, paper MOPH23.

[5] J. Billen *et al.*, POSSION SUPERFISH, LA-UR-96-1834, LANL, 2006.

[6] HFSS, *www.ansys.com*

[7] L. Young *et al.*, PARMELA. LA-UR-96-1835, LANL, 2005.

ISBN: 978-3-95450-199-1 doi:10.18429/JACoW-SAP2017-MOPH30

# COMMISSIONING OF THE 2×4-CELL SUPERCONDUCTING ACCELERATOR FOR THE CAEP THz-FEL FACILITY *

K. Zhou, X. Luo†, C. L. Lao, D. Wu, J. X. Wang, D. X. Xiao, L. J. Shan
T. H. He, X. M. Shen, S. F. Lin, H. B. Wang, X. F. Yang, M. Li
Institution of Applied Electronics, CAEP, Mianyang, China
X. Y. Lu Peking University, Beijing, China

*Abstract*

The CAEP THz-FEL facility is the first high average power THz radiation user facility in China. The superconducting accelerator including double 4-cell superconducting radio frequency (SRF) cavities is one of the most important components for this facility. The construction and horizontal test of the superconducting accelerator have been finished. At 2K state, the effective gradients of both cavities have reached our designed goal, 10 MV/m. This paper mainly presents the commissioning results of the superconducting accelerator. In the commissioning experiments, the kinetic energy of 5mA electron beams can be accelerated to 8 MeV successfully, with the energy spread less than 0.2%, much better than our design goal. Further beam loading experiments are in progress.

## INTRODUCTION

At present, China Academy of Engineering Physics (CAEP) is developing a THz radiation facility (THz-FEL), which is the first high average power THz user facility in China based on SRF drived oscillator type free electron laser [1]. The THz-FEL facility consists of a high-brilliance electron gun, a superconducting accelerator, a high-performance undulator and so on, as shown in Fig. 1. The designed frequency of the THz radiation is 1-3 THz with the average output power beyond 10 W. Correspondingly, the superconducting accelerator is expected to provide 6-8 MeV quasi-CW electron beams with the average current of 1-5 mA.

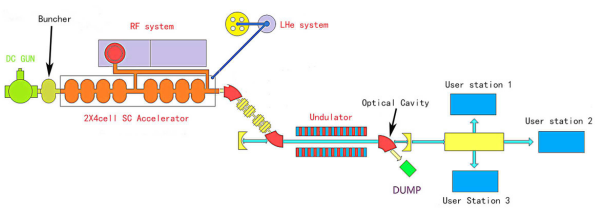


Figure 1: General layout of the CAEP FEL-THz facility.

The superconducting accelerator is one of the most important components for this facility, which contains a cryostat, double 4-cell TESLA SRF cavities, double tuners, double main couplers and some auxiliary systems, including the microwave system, the cryogenic system and the low level RF control system, as shown in Fig. 2. The design and fabrication of these subsystems have been finished [3]. All these components have reached their designed goals and the linac module has also finished its assembling and horizontal test at Chengdu. At 2 K state, the whole superconducting accelerator works well and stably. The effective field gradients of both cavities have achieved 10 MV/m [4]. This paper mainly presents the commissioning results of the 2x4-cell superconducting accelerator, including some beam loading experiments and the measurement of energy and energy spread of the electron beams.

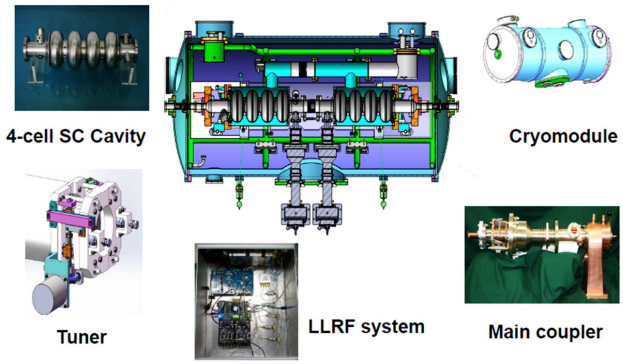


Figure 2: The cross-section and components of the superconducting accelerator [2].

Table 1: Designed Parameters of the 2×4-cell Superconducting Accelerator.

| *Parameters* | *Designed value* |
|---|---|
| Frequency | 1.300 GHz |
| $Q_0$ | $\geq 5\times10^9$ |
| $Q_e$ | $8\times10^5$-$5\times10^6$ |
| $E_{acc}$ | 8-10 MV/m |
| $I_b$ | 1-5 mA |
| Repetition rate | 54.17 MHz |
| Energy gained | 6-8 MeV |
| Energy spread | 0.75% |
| 2 K heat loss | $\leq$ 20 W |
| Magnetic field @ central axis | $\leq$20 mGs |

## BEAM LOADING EXPERIMENTS

The superconducting linac module has been connected with the beam line after the horizontal test. Figure 3 shows

* Work supported by China National Key Scientific Instrument and Equipment Development Project (2011YQ130018), National Natural Science Foundation of China with grant (11475159, 11505173, 11576254 and 11605190).
† Email address: luox8688@163.com

ISBN: 978-3-95450-199-1 doi:10.18429/JACoW-SAP2017-MOPH30

the sketch map of the straight beam line and Figure 4 is a picture of the CAEP THz-FEL facility after installation. The first and most important component is the photocathode DC injector. The high voltage acting on the surface of the photocathode is up to 320 kV. Before the superconducting accelerator, there is a buncher cavity to provide longitudinal manipulation of electron beams. The bunch length of electron beams at the entrance of the superconducting cavity should be compressed to 6-8 ps.

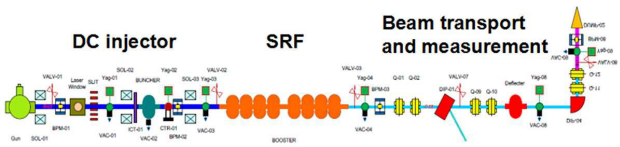


Figure 3: Sketch map of the straight beam line.

Figure 4: Picture of the CAEP THz-FEL facility.

Some beam loading experiments have been done with the straight beam line. The beam loading effect has been observed successfully in pulse mode, as shown in Fig. 5. The repetation rate and macro pulse length of the microwave are 10 Hz and 10 ms. The macro pulse length of the electron beams is 200 us and the measured beam current is 5 mA. The electron beams taking away microwave power when travelling through the cavity, which leads to the decrease of the storage energy as well as the field gradient of the cavity. To maintain the stablity of the field gradient, the low level RF (LLRF) system will increase the forward power. Meanwhile, when beam loading exists, the loaded quality factor $Q_L$ decreses, which causes the decrease of transmission resistance and reflected power.

## ENERGY AND ENERGY SPREAD MEASUREMENT

The basic principle of measuring energy and energy spread is based on the deflection of electron beams in the perpendicular dipole magnetic field due to Lorentz force, as shown in Fig. 6. The radius curvature of our analysis magnet is 300 mm. The beam spot can be adjusted to the center of the YaG screen by changing the current of the analysis magnet. So the kinetic energy of the electron beams can be calculated from the following formula:

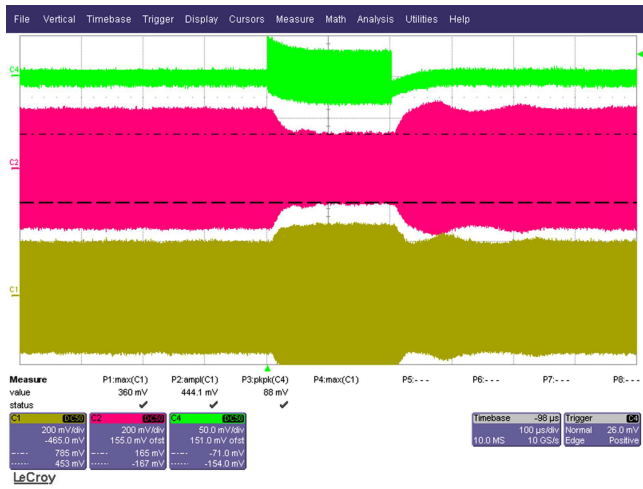


Figure 5: Beam current signal (green), reflected signal (red) and forward signal (yellow) in pulse mode.

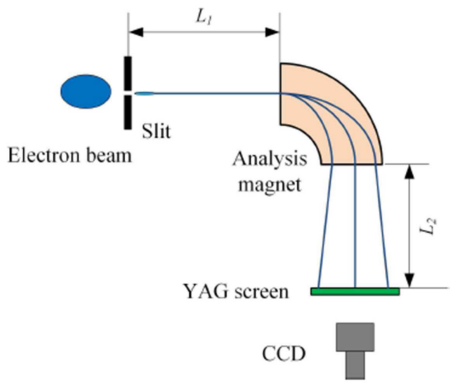


Figure 6: The energy and energy spread measuring principle.

$$E_k[\mathrm{MeV}]=2.1224\ I[\mathrm{A}]-0.2977$$

Where $E_k$ is the kinetic energy of electron beams and I is the current of the analysis magnet. Table 2 lists some measurement results with different electron energies. $E_{acc,cav\#1}$ and $E_{acc,cav\#2}$ are field gradients of the upstream cavity and the downstream cavity correspondingly. To maintain the longitudinal compression of electron beams, the initial accelerating phases of both cavities are set to be about $-10°$ comparing to the optimal accelerating phase. So the measured energy gained is a bit smaller than the maximum energy gained in theory. The kinetic energy of electron beams can be accelerated to 8 MeV successfully.

Figure 7(a) shows the colored beam spot after analysis magnet, when the beam current is 5 mA and the macro pulse length is 400 ns. The measured current of the analysis magnet is 4.02 A. So, the measured central kinetic energy of the electron beams is 8.22 MeV. Figure 7(b) gives the energy

ISBN: 978-3-95450-199-1 doi:10.18429/JACoW-SAP2017-MOPH30

Table 2: Measurement Results with Different Electron E ergies

| $E_{acc,cav\#1}$ (MV/m) | $E_{acc,cav\#2}$ (MV/m) | I (A) | $E_k$ (MeV) | Measured energy gained (MeV) | Maximum energy gained (MeV) |
|---|---|---|---|---|---|
| 6.2 | 0 | 1.64 | 3.17 | 2.85 | 3.01 |
| 8.4 | 0 | 2.13 | 4.22 | 3.90 | 4.06 |
| 4.2 | 6.6 | 2.79 | 5.30 | 4.98 | 5.22 |
| 7.5 | 6.7 | 3.40 | 6.92 | 6.60 | 6.88 |
| 8.25 | 8.7 | 3.96 | 8.11 | 7.79 | 8.2 |

distribution curve of the electron beams, and the measured rms energy spread is 0.19%, which is much better than our designed goal.

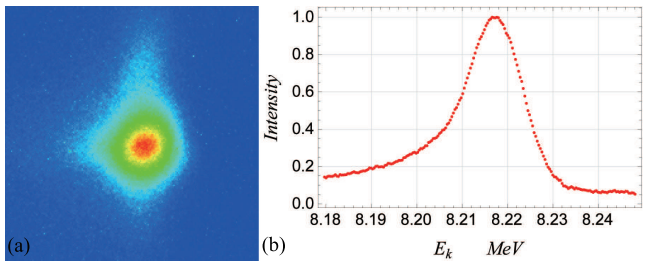


Figure 7: (a) Colored beam spot on YaG screen after analysis magnet, (b) the energy distribution curve of the electron beams.

## CONCLUSION

The 2×4-cell superconducting accelerator for the THz-FEL facility has finished its construction, performance test and commissioning. In the commissioning experiments, the beam loading effect has been observed successfully and the measured kinetic energy of 5 mA electron beams is beyond 8 MeV, with its rms energy spread less than 0.2%, much better than our designed goal. So far, the debugging of this facility has made significant progress with the support of the superconducting accelerator.

## ACKNOWLEDGEMENT

The authors would like to thank Peking university for their help with the debugging of the low level RF system.

## REFERENCES

[1] X. Zhou *et al.*, "Design of a high average power terahertz-FEL faiclity", in *Journal of Terahertz Science and Electronic Information Technology*, 2013, 11(1): p.1-6.

[2] X. Luo *et al.*, "Design of the 2x4-cell superconducting cryomodule for the free-electron laser", Presented at the 18th International Conference on RF Superconductivity, Lanzhou, China, July 17-21, 2017, paper MOPB010, unpublished.

[3] X. Luo *et al.*, "Design and fabrication of the 2×4-cell superconducting linac module for the free-electron laser", *Nuclear Instruments and Methods in Physics Research Section A*, 2017, 871: pp.30-34.

[4] K. Zhou *et al.*, "Progress of the 2x4-cell superconducting accelerator for the CAEP THz-FEL facility", Presented at the 18th International Conference on RF Superconductivity, Lanzhou, China, July 17-21, 2017, paper MOPB037, unpublished.

ISBN: 978-3-95450-199-1 doi:10.18429/JACoW-SAP2017-MOPH31

# FRINGE FIELD OVERLAP MODEL FOR QUADRUPOLES

Huan Jia, Institute of Modern Physics, CAS, Lanzhou, China
Michael Plum, Oak Ridge National Laboratory, Oak Ridge, USA

*Abstract*

In the large aperture-to-length ratio quadrupoles, there will be long fringe field. When putting three of this type quadrupoles next to each other, the field will overlap and change the beam dynamics of "hard-edge" model. By numeric integration, we find that the transfer matrix difference is quite significant at the first part of MEBT of CADS Injector II. By re-exploring the "hard-edge" model, the traditional definition of quadrupole's effective length and effective gradient are found to be just rough approximations and not right in this condition. The finding explains the good prediction of beam dynamics model of MEBT by emittance measurements with different current settings of the triplet quadrupoles, and may be also helpful in explaining some discrepancies in beam lines around the world

## INTRODUCTION

At the MEBT of CADS Injector II, quadrupoles have very large bore aperture to bore length ratio, i.e. 54 mm/52 mm for QL80 and 54 mm/ 74 mm for QL100 [1]. At the same time, due to the strong focusing properties at MEBT, the distance between quadrupoles is quite near. The distance between the first three adjacent quadrupoles is 180 mm, which is smaller than the sum of quadrupole bore length and 3 times of apertures.

Thus, the fringe field is quite significant for the quadrupoles at MEBT, and the overlap effect between adjacent quadrupoles is also significant. This effect is analysed by comparison of beam properties after tracking through both the hard-edge model and fieldmap overlap model.

In the past, people try to treat the field overlap problem by multiplying some factors for the three quadrupoles [2]. But our finding is that such a method is not right, because it is not the effective length or effective gradient making effect. It is the total transfer matrix integration making change, and the change is different in horizontal and vertical plane.

The emittance measurement at MEBT of CADS Injector II shows good agreement to multi particle tracking simulation, with 1-D fringe field overlap model [3]. The new finding in the paper explains the agreement between simulation and measurement.

## HARD EDGE MODEL

The hard edge model has been prompted for the quadrupoles for many years. The "hard edge" means that quadrupole's gradient is a square-like waveform, with two step-function "edges" in both sides, as shown in Fig. 1.

The transfer matrix of "hard edge" model is that:

$$R_{xx} = \begin{bmatrix} \cos(k\Delta s) & \frac{\sin(k\Delta s)}{k} \\ -ksin(k\Delta s) & \cos(k\Delta s) \end{bmatrix}. \quad (1)$$

$$R_{yy} = \begin{bmatrix} \cosh(k\Delta s) & \frac{\sinh(k\Delta s)}{k} \\ ksinh(k\Delta s) & \cosh(k\Delta s) \end{bmatrix}. \quad (2)$$

Where $k = \sqrt{\frac{G}{B\rho}}$ is the focusing strength, $G = \frac{\partial B_y}{\partial x}$ is the quadrupole gradient. $B\rho$ is the magnetic rigidity.

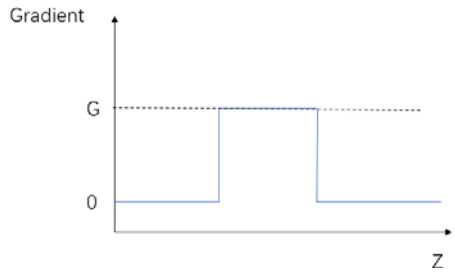


Figure 1: "hard edge" gradient along the quadrupole.

In reality, there is no quadrupole that is "hard edge". The model is right for "thick" quadrupoles, which means that quadrupole has small aperture-to-length ratio. But for "thin" quadrupoles, which means that quadrupole has large aperture-to-length ratio, the model is not right and need to be re-investigated.

For example, because of the large aperture-to-length ratio, the QL80s in MEBT of CADS Injector II can be regard as "thin" quadrupoles, as shown by field gradient simulation and measurements in Fig. 2.

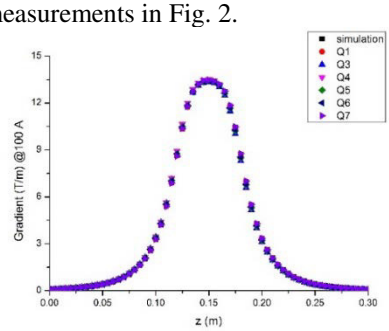


Figure 2: Simulated (black) and measured gradient along axis for six QL80 at MEBT of CADS Injector II [1].

If we treat the quadrupole with "hard edge" approximation, the effective length and effective gradient will be

$$L_{eff} = \int_0^{300} \frac{G*dL}{G_{z=150\,mm}} = 80\,mm \quad (3)$$

$$G_{eff} = G_{z=150\,mm} = 13.5\,T/m \quad (4)$$

## FRINGE FIELD MODEL

For the same quadrupole field distribution, we integrate the transfer matrix by sliced pieces $M_i$, where each $M_i$ is treated as "hard edge" quadrupole, then,

$$M = \prod_{i=1}^{n} M_i \quad (5)$$

Here we define the new effective length as $l$ and effective gradient as $k$, thus, the new transfer matrix is [4],

ISBN: 978-3-95450-199-1 doi:10.18429/JACoW-SAP2017-MOPH31

$$M=\begin{pmatrix} C & S \\ C' & S' \end{pmatrix}=\begin{pmatrix} 1 & \lambda \\ 0 & 1 \end{pmatrix}\begin{pmatrix} \cos\varphi & \frac{1}{k}\sin\varphi \\ -k\sin\varphi & \cos\varphi \end{pmatrix}\begin{pmatrix} 1 & \lambda \\ 0 & 1 \end{pmatrix} \quad (6)$$

where $\varphi = kl$, $\lambda = m - l/2$, $f = \frac{1}{Kl}$ and $K = k^2$.

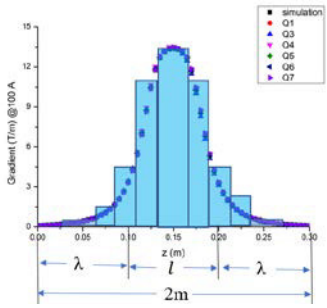


Figure 3: New definition of the effective length of quadrupole based on the numerical gradient integration.

By numeric integration of the field distribution, as shown in Fig. 3, the M can be achieved. After solving Equation (6), the new $l$ and $k$ will be got.

For the focusing of the quadrupole, the Equation is [5]

$$\begin{aligned} C_f - \tfrac{1}{2}LC'_f &= \cos\varphi_f + \tfrac{1}{2}\varphi_f \sin\varphi_f \\ C'_f \ell_f &= -\varphi_f \sin\varphi_f . \end{aligned} \quad (7)$$

where $k_f = \varphi_f / l_f$.

For the defocusing of the quadrupole, the Equation is

$$\begin{aligned} C_d - \tfrac{1}{2}LC'_d &= \cosh\varphi_d - \tfrac{1}{2}\varphi_d \sinh\varphi_d \\ C'_d \ell_d &= -\varphi_d \sinh\varphi_d . \end{aligned} \quad (8)$$

where $k_d = \varphi_d / l_d$.

From Equation (1) and Equation (2), for the same quadrupole, the effective length and effective gradient are different in focusing and defocusing plane. We investigate this effect by comparing the quadrupole parameters with different magnet current, as shown in Fig. 4.

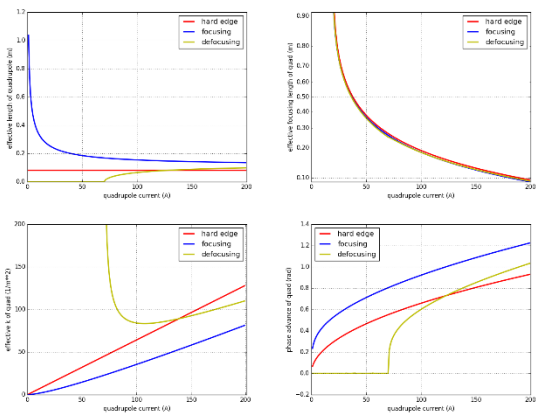


Figure 4: Effective length (left up), effective focusing length (right up), effective focusing strength (left down) and effective phase advance (right down) in focusing plane (blue), defocusing plane (green) and hard edge model (red) of the quadrupole with different quadrupole magnet currents.

Although the focusing length is same in focusing plane, defocusing plane and hard edge model, the effective length, effective gradient and effective phase advance are different.

Comparing the transfer matrix of fieldmap model to hard edge model, the difference will be

$$\Delta x_{ij} = \frac{(\tilde{x}_{ij} - x_{ij})}{x_{ij}} \quad \Delta y_{ij} = \frac{(\tilde{y}_{ij} - y_{ij})}{y_{ij}} \quad (9)$$

From Fig. 5, we can see that when the magnet current is around 130 A, the difference is quite big. The reason is that in this region the transfer matrix elements are around zero, as shown in Fig. 6 and Fig. 7.

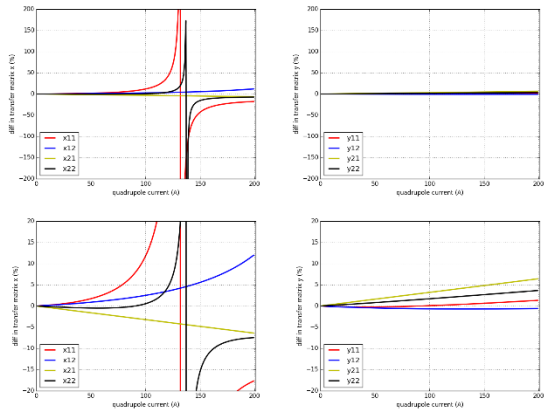


Figure 5: Transfer matrix elements difference with focusing in x plane (left up) and y plane (right up), with defocusing in x plane (left down) and y plane (right down).

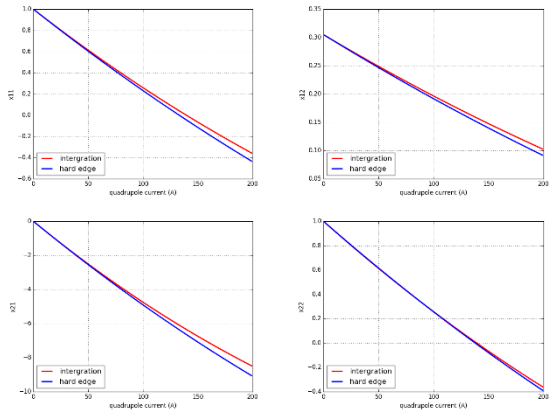


Figure 6: Transfer matrix elements of Q1 fringe field model (red) and hard edge model (blue) in x plane.

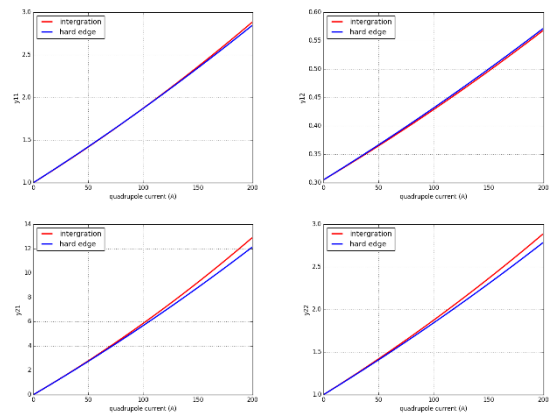


Figure 7: Transfer matrix elements of Q1 fringe field model (red) and hard edge model (blue) in y plane.

ISBN: 978-3-95450-199-1 doi:10.18429/JACoW-SAP2017-MOPH31

## FRIGE FIELD OVERLAP MODEL

For the first three adjacent quadrupoles of the MEBT, we add them together with current ratio of 1:-1:1, and normalize current to 1 A. The field is overlapped, as shown in the new 1D fieldmap distribution in Fig. 8. The parameters of quadrupoles are listed in Table 1.

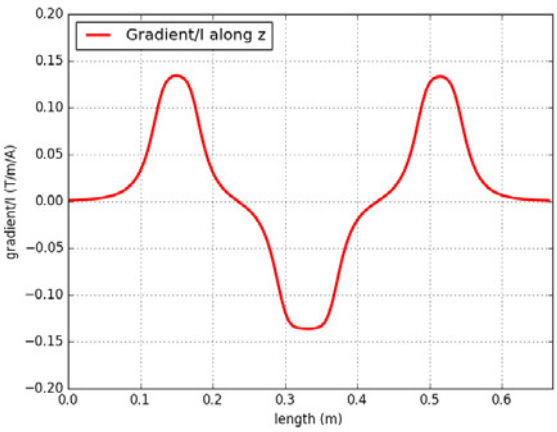


Figure 8: Field overlap distribution of Q1, Q2 and Q3.

Table 1: The Three Adjacent Quadrupole Parameters

| Quadrupole | Aperture (mm) | Iron length (mm) | Hard edge effective length (mm) |
|---|---|---|---|
| Q1 | 54 | 52 | 80 |
| Q2 | 54 | 74 | 100 |
| Q3 | 54 | 52 | 80 |

The difference of the transfer matrix elements between hard edge model and fringe field overlap model is shown in Fig. 9. In y plane, the transfer matrix is significant different to the hard edge model, as shown in Fig. 10 and Fig. 11, while in x plane the difference is not very big. The difference grows as the magnet current increase. Thus, it is impossible to find "multiplying factors" for the three quadrupoles to get good approximation in both x and y plane.

The larger difference in y plane than in x plane is explained that beam envelope is bigger in y plane when the Q1 is focusing in x plane [1]. Beam will experience more fringe field effect with larger envelope.

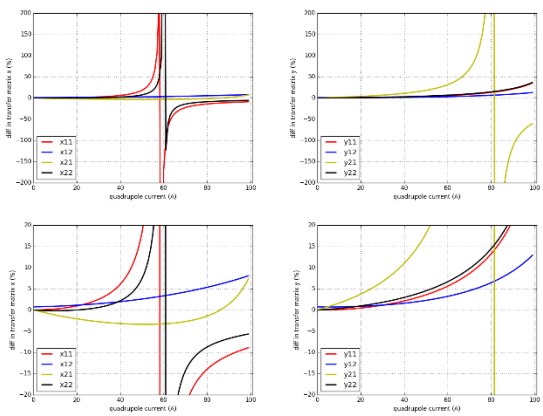

Figure 9: Transfer matrix elements difference of the first three quadrupoles with Q1 focusing in x plane (left up) and y plane (right up), with Q1 defocusing in x plane (left down) and y plane (right down).

By using the fringe field overlap model in beam tracking simulation, we have got good agreement with emittance measurement [3]. If we use the hard edge model, the emittance will have large discrepancies.

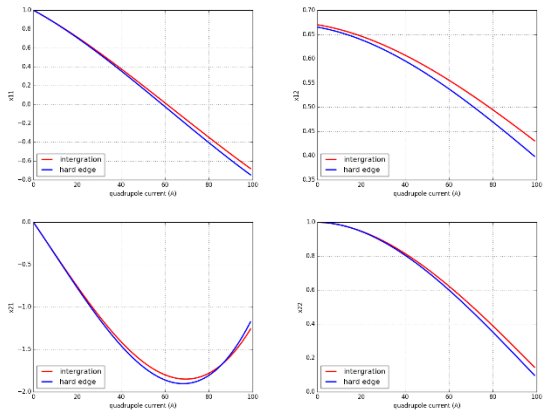

Figure 10: Transfer matrix elements of the three quadrupoles' fringe field overlap model (red) and hard edge model (blue) in x plane.

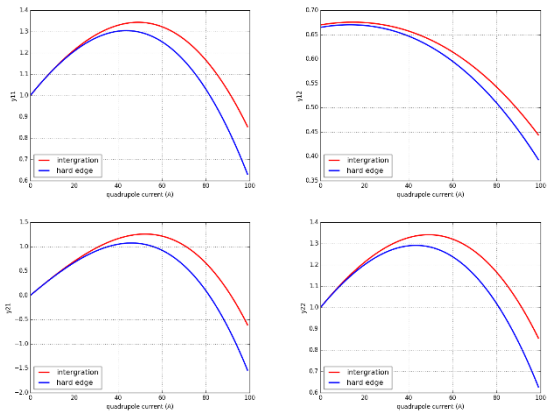

Figure 11: Transfer matrix elements of the three quadrupoles' fringe field overlap model (red) and hard edge model (blue) in y plane.

## CONCLUSION

The hard edge model is not "right" considering the fieldmap distribution in "thin" quadrupoles.

Tracking in Field map shows that when the quadrupole current increase, there will be larger difference between the hard edge model and the fieldmap model

Overlap of the fieldmap enlarges the difference between the hard edge model and fieldmap model by changing the overall field distribution of nearby quadrupoles.

In the future design and tuning of beam lines with "thin" and adjacent quadrupoles, the real fieldmap distribution and their overlap should be considered directly in beam dynamics.

## ACKNOWLEDGEMENT

The author would like to acknowledge Andrei Shishlo at SNS, ORNL for useful discussions about the fringe field overlap model.

ISBN: 978-3-95450-199-1 doi:10.18429/JACoW-SAP2017-MOPH31



## REFERENCES

[1] Jia Huan, He Yuan, Yuan Youjin *et al.*, "Design and construction of the MEBT1 for CADS injector scheme II", *Chinese Physics C*, 39, 10 (2015) 107003.

[2] G.R.Moloney *et al.*, "Analysis of the fringe field region of magnetic quadrupole lenses: field measurements and ion optical calculations", *NIM. B*, vol. 130, pp. 97-103, 1997.

[3] Huan Jia, "Lessons of high-power CW beam commissioning of injector II of Chinese ADS", talk at HB2016, Malmo, Sweden.

[4] Klaus G.Steffen, "High Energy Beam Optics", Interscience Publishers, 1965, pp. 56-76.

[5] Helmut Wiedemann, "Particle Accelerator Physics", Springer, Fourth Edition, 2015, pp. 187-190.

ISBN: 978-3-95450-199-1 doi:10.18429/JACoW-SAP2017-MOPH32

# BEAM PARAMETER RECONSTRUCTION AT THE INPUT OF LEBT OF C-ADS INJECTOR II*

W. L. Chen,W. S. Wang , Y. S. Qin, S. H. Liu, W. P. Dou, C. Wang, Z. J. Wang, Y. He
Institute of Modern Physics (IMP), Chinese Academy of Sciences, Lanzhou, China

*Abstract*

The Injector II for the C-ADS is designed to accelerate a proton beam to 10 MeV in continuous wave (CW) mode with beam current up to 10 mA, which is the demonstration of the key technologies for CiADS. The LEBT section physical length and dynamic lattice is calibrated recently, and the more receivable beam parameters has been reconstructed at the input of LEBT. AS the transport of high current beams at low energies is critical, for at kinetic energies of a few MeV, the beams are space charge dominated. This paper will introduce beam parameters reconstruction based on emittance measurement experiment and PIC code TraceWin to reconstruct with space charge considered.

## INTRODUCTION

A project named China Accelerator Driven Sub-Critical System (C-ADS) has been proposed to treat the spent nuclear fuel and began construction since 2011 [1]. Under six years commissioning, the demo facility had accelerated 12.6 mA Pulse proton beam to 26.06 MeV, 170 uA CW proton beam had accelerated up to 25 MeV, and recently the project of C-ADS demo facility just has completed the acceptance. The layout of the demo facility is shown in Figure 1.

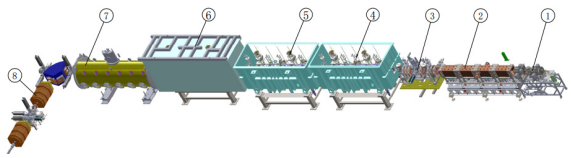


Figure 1: The layout of the demo facility of C-ADS.
① LEBT section ② RFQ ③ MEBT section ④ CM1(HWR010) ⑤ CM2(HWR010) ⑥ CM3(Taper HWR015) ⑦ CM4 (Spoke021) ⑧ HEBT section

The LEBT is designed by Y.Yao [2], the Layout of the LEBT is shown in Figure 2. As the project tasks arranged so compact, the beam parameters had not measured so clear at the beginning of the LEBT commissioning. The LEBT beam parameters of injector II are copied by injector I at IHEP, for the two LEBT designed all by IMP is very similar.

The LEBT physical length has been alignment recently by machinery group, but the collimation error is far away from the dynamic length. Using the initial beam parameters and the actual solenoid magnetic field values for beam transport simulation and tracking, the beam parameters at the end of the LEBT cannot match well with the download section (RFQ). Figure 3 is the beam phase space out of RFQ tracking by matched beam. But for the mismatched beam the transmission of the RFQ is about 98%, and the beam emittance growth is almost 47%. Table1 shows the comparison of these.

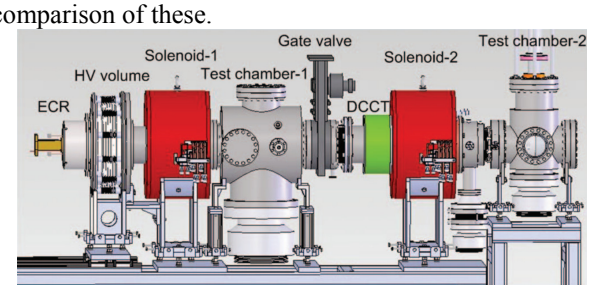


Figure 2: The layout of the LEBT of C-ADS.

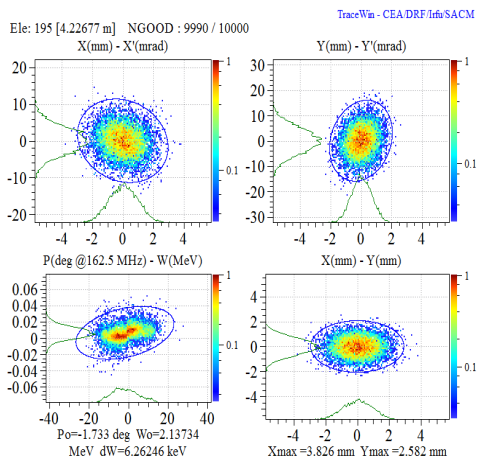


Figure 3: Phase space out of the RFQ.

For getting the real beam initial parameter at the LEBT input, a beam dynamic code named TraceWin combined with python is used for beam parameter reconstruction.

Table 1:Comprision of the Match or Mismatch Beam Parameters out of RFQ

| | α x | β x | Ex (RMS) | α y | β y | Ey (RMS) |
|---|---|---|---|---|---|---|
| LEBT Input | 0 | 0.16 | 0.189 | 0 | 0.16 | 0.189 |
| Matched beam | 0.1551 | 0.2646 | 0.2257 | -0.1945 | 0.1316 | 0.2229 |
| Mismatched beam | 0.1554 | 0.2574 | 0.2916 | -0.2294 | 0.1312 | 0.2767 |

*Work supported by National Science Foundation of China (Grant No. 91426303 and No.11525523)

ISBN: 978-3-95450-199-1 doi:10.18429/JACoW-SAP2017-MOPH32



## ARITHMETIC FOR RECONSTRUCTION

To get the initial beam parameter at the input of the LEBT, the code named TraceWin is used for reconstruction. This code is based on PIC arithmetic for low energy section beam space charge simulation. By using python calls TraceWin, it can be used for scanning the entrance beam Twiss parameters map and comparing the tracked results at the end of the LEBT with the RFQ matched input parameters to get the target LEBT input parameters.

Oscillation of the beam projections will be added when the injected beam ellipse is not match with the focusing elements. The conception of beam mismatch factor is proposed [3] to describe the quality of the beam matching results. At different location, the Courant-Snyder ellipse parameters $\alpha$, $\beta$, $\gamma$ defined for represent the beam space phase.

Suppose the matched beam ellipse is defined by

$$\gamma_m x + 2\alpha_m x x' + \beta_m x'^2 = \varepsilon$$

And the mismatched beam ellipse is defined by

$$\gamma x + 2\alpha x x' + \beta x'^2 = \varepsilon$$

Then the mismatch factor is defined by

$$M = \left[1 + \frac{H + \sqrt{H(H+4)}}{2}\right]^{1/2} - 1$$

Where

$$H = (\Delta\alpha)^2 - \Delta\beta\,\Delta\gamma$$

And $\Delta\alpha = \alpha - \alpha_m$, $\Delta\beta = \beta - \beta_m$, $\Delta\gamma = \gamma - \gamma_m$.

Different like actual beam matrix $\sigma_m$

$$\sigma_m = \begin{bmatrix} \beta_m & -\alpha_m \\ -\alpha_m & \gamma_m \end{bmatrix}$$

Where the $\Delta\sigma$ is useful to express as

$$H = \Delta\sigma = \begin{bmatrix} \Delta\beta & -\Delta\alpha \\ -\Delta\alpha & \Delta\gamma \end{bmatrix}$$

Mismatch factor M is used for comparing the track beam by TraceWin and the matched initial beam parameter input of the RFQ system. By searching the beam Twiss parameter map input of the LEBT, the more reasonable value can be found.

This beam track by PIC code TraceWin considered with the space charge compensation effect, the SCC. factor is defined as 0.87[4].

The RFQ input matched beam parameters are shown in Table 2.

Table 2: Required Parameters before the RFQ

| Parameters | Numbers | Units |
|---|---|---|
| Energy | 35 | KeV |
| Current | 15 | mA |
| Pulse width | CW | - |
| Twiss parameter $\alpha$ | 1.21 | - |
| Twiss parameter $\beta$ | 0.0479 | mm/π.mrad |
| $\epsilon(nRMS)$ | <0.2 | π.mm.mrad |
| Proton fraction | >95 | % |

## EXPERIMENT AND SIMULATION

As it is described in the introduction, the physical length of the LEBT had been calibrated recently, the layout of the LEBT mechanical drawings is shown in Figure4.

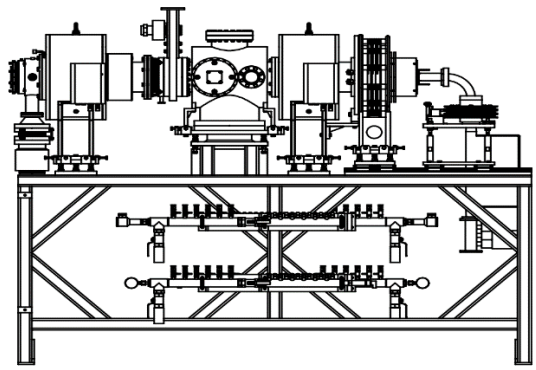

Figure 4: The layout of the LEBT mechanical drawings.

Some experiment has been done for studying the match between LEBT and RFQ. During the experiment, it has shown that the mismatch will lead the beam emittance growth during transport though the RFQ accelerator [5]. The results are shown in Figure 5. (Five group of different solenoids of G2 had be set for studying, but some mistake happened during the Last group G2=280A.)

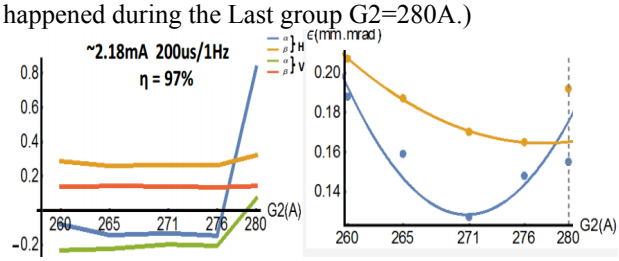


Figure 5: LEBT and RFQ match research.

During the study, the G1 is set as 215A, the beam is about 5mA. From the figure 4, it is still seen that the G1 = 215A, G2 =275A (G1=1980Gs, G2=2533Gs) is the match point of the LEBT and RFQ.

After calibration of the dynamic lattice length, the results of beam track though the LEBT is shown in table 3. For dynamic simulation, the solenoid field map is used, so the length of it is more than the real length. As the results, the input location of the LEBT is almost nearby the extraction electron, the initial beam parameter used previously at the input of LEBT may not too reasonable.

Table 3: Beam Parameters out of LEBT and RFQ

| | α x | β x | Ex (RMS) | α y | β y | Ey (RMS) |
|---|---|---|---|---|---|---|
| LEBT Input | 0 | 0.16 | 0.189 | 0 | 0.16 | 0.189 |
| Out of LEBT | 0.261 | 0.038 | 0.207 | 0.259 | 0.038 | 0.209 |
| Out of RFQ | 0.191 | 0.259 | 0.288 | -0.198 | 0.133 | 0.283 |

ISBN: 978-3-95450-199-1 doi:10.18429/JACoW-SAP2017-MOPH32

During the scanning of the input beam parameters of the LEBT, G1=1980Gs G2=2533Gs is chosen as the fixed value for reconstraction. The step length of the Twiss parameters input of the LEBT is about 0.01for both horizontal and vertical of the beam. Figure 6 shows the beam parameters out of the LEBT.

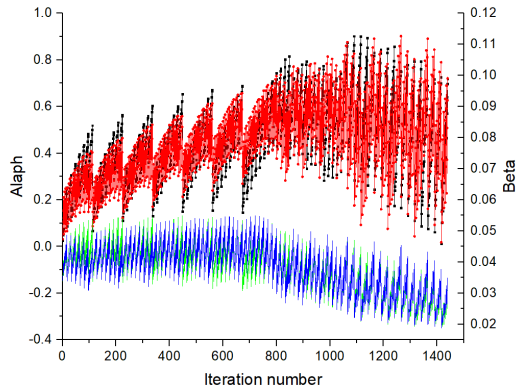


Figure 6: Beam parameters out of the LEBT. (the red for $\beta_x$, black for $\beta_y$, blue for $\alpha_x$, green for $\alpha_y$)

The minimum value of the sum of mismatch factor both in the horizontal and vertical indicates the best match point of the LEBT and RFQ. Figure 7 shows the scaning results.

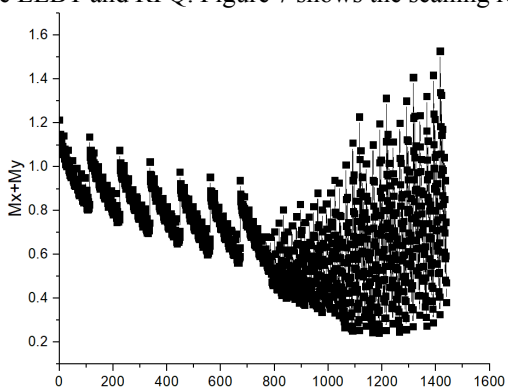


Figure 7: The sum of mismatch factor both of horizontal and vertical direction.

Finally, sorting the simulation results of the mismatch factor at the cross section of the LEBT and RFQ, the minimum data of the sequence corresponding to the input beam parameters of the LEBT is the scanning solution.

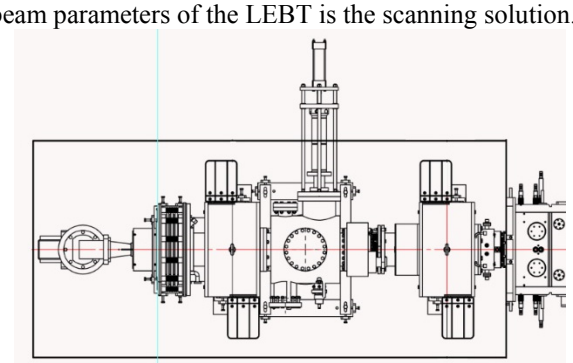

Figure 8: The flat view of the LEBT.

The scanning results of the initial beam parameters at the LEBT input section is shown in Table 4 and the sum mismatch factor is 0.199, beam tracking results at the RFQ input section is shown in Table 5.

Table 4: Initial Beam Parameters at Input of LEBT

| | α x | β x | α y | β y |
|---|---|---|---|---|
| Twiss parameters | 1.0 | 0.24 | 1.0 | 0.24 |

Table 5: Beam Tracking Results out of LEBT

| | α x | β x | α y | β y |
|---|---|---|---|---|
| Twiss parameters | 0.916 | 0.0476 | 0.979 | 0.0490 |

## SUMMARY AND CONCLUSIONS

In Figure 8 the blue line shows the real input location of the LEBT. This section nearby the extraction electron of the ion source. Comparing with the simulation results of the beam parameters map scanning, it is more reasonable to accept the initial input parameters at the LEBT entrance.

## REFERENCES

[1] W. Zhijun, *et al.*, "End-to-end simulation of the C-ADS Injector II with a 3-D field map," *Chinese Phys. C*, vol. 37, no. 4, p. 047003, 2013.

[2] Y. Yang, *et al.*, "A low energy beam transport system for proton beam", *Review of scientific instruments*, 84, 033306, 2013.

[3] Crandall, K.R., *Trace 3-D Documentation*, 2nd ed., Los Alamos Report LA-UR-90-4146, 1990.

[4] Tan Biao, "Research of space charge neutralization level for low energy intense beam", dissertation for master's degree, University of Science and Technology of China. Lanzhou, 2015.

[5] Z.J. Wang, "Beam commissioning activities at domo facility of C-ADS Injector II", presented in the 6th open collaboration meeting on superconducting linacs for high power proton beams, Daresbury, UK., May 2016.

ISBN: 978-3-95450-199-1 doi:10.18429/JACoW-SAP2017-MOPH33

# BEAM OPTICS VERIFICATION FOR A QWR*

Y. S. Qin†, Z. J. Wang, H. Jia, Y. He, S. H. Liu, W. L. Chen, C. Wang, Y. Z. Jia, P. H. Gao
Institute of Modern Physics (IMP), Chinese Academy of Sciences, Lanzhou, China

*Abstract*

Quarter-wave resonators (QWRs) are being widely used in linear accelerators (linac) for acceleration of ions with low-β velocity. Two effects of this kind of cavities are the beam steering effect and RF defocusing effect caused by geometric asymmetry and the offset of input beam. Measurement for these two effects has been conducted by beam position monitors (BPM) and wire in a QWR type buncher whose frequency is 162.5 MHz at Institute of Modern Physics (IMP), Chinese Academy of Sciences (CAS). Since the experimental result and simulation result matches well, beam optics has been verificated, such that beam central position and beam envelope could be predicted in simulation and an online orbit correction program will be developed in the future.

## INTRODUCTION

QWRs, being widely studied and built in many laboratories for accelerating of ions in the velocity range from 0.01c to 0.3c[1], are cylindrical and coaxial cavities who have an up-down asymmetry with respect to the beam axis. Because of lacking of symmetry, QWR will lead to beam steering and RF de-focusing. Both horizontal magnetic field and vertical electric field will produce steering in the direction of the resonator axis. The beam deflection, moreover, depends on the particle position, which will create emittance growth and beam spill, especially in high intensity proton linac[2]. Beam envelope will also increase because of RF defocusing effect.

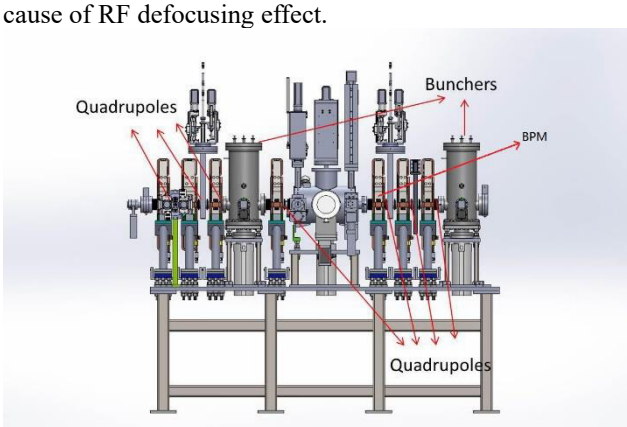


Figure 1: Layout of MEBT of C-ADS Injector II.

Based on the initial simulation and beam experiment, QWR will lead to considerable beam deflection and beam envelope increase. Beam optics verification for the QWR has been carried out based on beam experiment which is conducted on the MEBT of C-ADS injector II. In the experiment, the first buncher and the BPM are used as shown in Figure 1[3]. By comparing the experimental result with the simulation result, beam steering effect and RF defocusing effect could be calculated.

The simulation code we used is TraceWin.

## BEAM STEERING EFFECT IN QWR

Figure 2 shows the QWR buncher cavity and the electromagnetic field distribution. The blue line presents the longitudinal electric field Ez along the cavity axis, the red line presents the vertical electric field Ey×10, and the black line presents the horizontal magnetic field cBx. Compared with the accelerating component Ez, the transverse electric field Ey and the horizontal magnetic field Bx will cause dipole component field. Thus, both horizontal magnetic field and vertical electric field will produce beam steering in the vertical direction and RF defocusing in transverse direction[4].

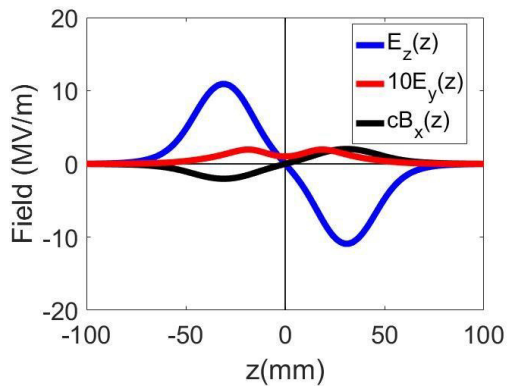


Figure 2: QWR field distribution.

In a RF cavity, beam energy gain is associated with the cavity voltage V0 and the RF phase φ as shown in the following equation:

$$\Delta U = qV_0TL\cos\varphi$$

Considering the asymmetrical electric and magnetic field, beam steering effect will vary with the voltage and RF phase:

$$\Delta y' = -\frac{\Delta U}{\gamma mc^2\beta}\tan\varphi\left[\frac{\cos(\frac{\pi d_y}{\beta\lambda})}{\beta\sin(\frac{\pi d_y}{\beta\lambda})}K_{EY}(y)+K_{BX}(y)\right]$$

where $\Delta y' \approx \Delta p_y / p$ is the deflection angle produced by the QWR, and $\Delta U, m, \varphi, \lambda$ are the particle energy gain, rest mass, RF phase and RF wavelength respectively. While d is the gap-to-gap distance, $d_y$ is an effective gap-to-gap distance for the transverse electric field $E_y$. The

* Supported by the National Natural Science Foundation of China (Grant No. 91426303 and No. 11525523)
† E-mail: marshal@impcas.ac.cn

ISBN: 978-3-95450-199-1 doi:10.18429/JACoW-SAP2017-MOPH33

electric deflection and the magnetic deflection is shown in the up equation where $K_{EY} = \overline{E_Y}(y) / \overline{E_Z}$ and $K_{BX} = \overline{B_Y}(y) / \overline{E_Z}$.

## RF DEFOCUSING IN QWR

For longitudinal stability, it is longitudinal focusing, which requires the synchronous phase to be negative. Thus, the RF fields are increasing in time and it is generally incompatible with local radial focusing from those fields.

The nonzero field components of the synchronous space harmonic experienced by a particle of phase $\varphi_s$ were obtained as

$$E_z = E_0 TI_0(Kr)\cos\varphi_s$$

$$E_r = -\gamma_s E_0 TI_1(Kr)\sin\varphi_s$$

$$B_\theta = -\frac{\gamma_s \beta_s}{c} E_0 TI_1(Kr)\sin\varphi_s$$

The radial momentum impulse delivered to a particle over a length L is

$$\Delta(\gamma\beta\gamma') = -\frac{\pi q E_0 TL\sin\varphi_s}{mc^2\gamma_s^2\beta_s^2\lambda} r$$

For longitudinal stability, the sign of $\varphi_s$ is negative, therefore the radial impulse is positive, which means an outward or defocusing impulse[5].

## BEAM EXPERIMENT

The beam experiment was conducted on the MEBT of C-ADS injector II at IMP and the beam status is shown below:

Table 1: Beam Status

| Parameter | Value | Unit |
|---|---|---|
| Particle | proton | — |
| Energy | 2.12 | MeV |
| Current | 2.3 | mA |
| Pulse width | 80 | us |
| Pulse frequency | 1 | Hz |

### *Beam Steering*

In the experiment, beam steering effect is affected by the voltage, the RF phase and beam input position at the entrance of the buncher. Beam center position at the BPM is recorded by scanning the three parameters.

In a phase sweeping period, beam center position detected by BPM varied because of beam steering effect as shown in figure 3. The variation was different according to different voltage and RF phase of the buncher.

Since beam steering effect could be expressed by the peak-to-peak value of beam center position at BPM during phase seeping, beam steering effect contributed by x is 0.600 mm, while it is 0.609 mm when considering both x and x'. The ratio of the two contribution is 1.5%. It suggests that beam steering effect contributed by the input angle x' is 1.5% of that contributed by the input position x.

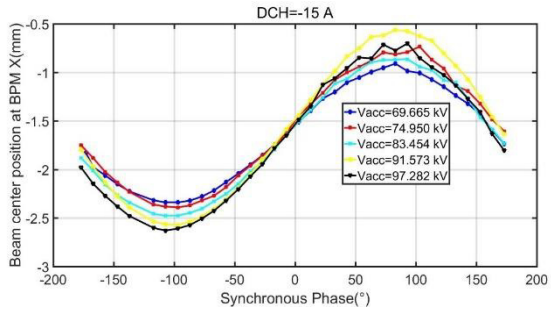


Figure 3: Beam center position at BPM.

Considering electrical and magnetic field distribution, the buncher is symmetrical in horizontal direction but asymmetrical in vertical direction, so beam center position at BPM doesn't vary during phase sweeping when horizontal input position x=0, but it still varies in vertical direction even if vertical input position y=0.

In simulation, beam input position x and y at the entrance of the buncher is scanned from -3 mm to 3 mm. Each result in different voltage and different DCH/DCV is compared with the experimental result, until the error between experimental result and simulation result is the least. At x=-0.98 mm and y=0.63 mm, the result nearest to the experiment is found as shown in Figure 4.

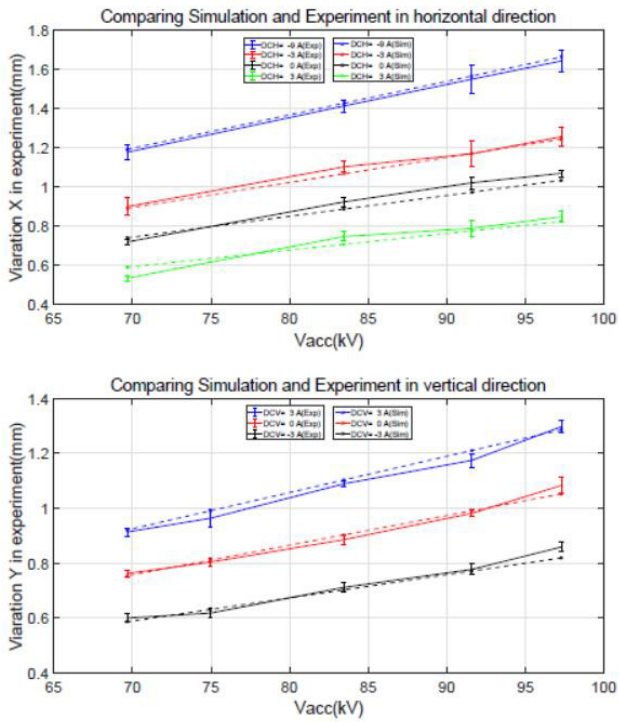


Figure 4: Simulation and experiment comparison.

The root-mean-square (RMS) error is $3.36\times10^{-2}$ mm and $4.13\times10^{-2}$ mm in horizontal and vertical direction respectively, about 4% of the experimental result.

### *RF Defocusing*

RF defocusing effect is affected by the voltage of the RF phase of the QWR. In the experiment, the synchronous phase was set at -90° to guarantee that the longitudinal

ISBN: 978-3-95450-199-1 doi:10.18429/JACoW-SAP2017-MOPH33



focus is the most, thus, the RF defocusing effect is transverse direction is the biggest. By scanning the amplitude of the QWR, beam profile is measured by moving the wire.

In the measurement, the wire scans from -25 mm to 25 mm with the step length of 0.5 mm in horizontal and vertical directions. The simulation and experiment is shown in figure 5.

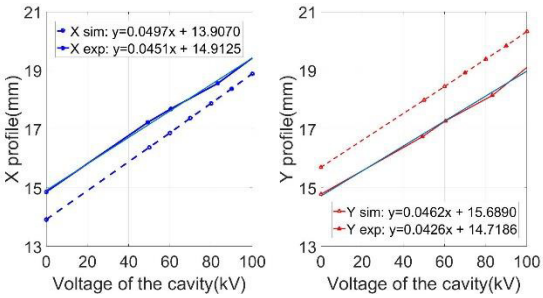


Figure 5: Beam profile.

Since the linear coefficient $R^2$ is 0.9987 in the two directions correspondingly, the measurement result is very close to linearity.

The slope represents RF defocusing effect, and the slope deviation between experiment and simulation in the two directions is less than 10%:

$$Ds_x = \left|\frac{0.0497 - 0.0451}{0.0497}\right| = 9.3\%$$

$$Ds_y = \left|\frac{0.0462 - 0.0426}{0.0462}\right| = 7.8\%$$

## CONCLUSION

Beam steering effect and RF defocusing effect are measured in the QWR type buncher. The simulation result and experimental result matches well and the beam optics of the cavity has been verified. By comparing the measurement result and the simulation result, the input position at the entrance of the buncher is calculated and the result is x=-0.98 mm and y=0.63 mm. Thus, beam center position and beam profile can be predicted in simulation as long as the machine parameters are given, based on which a program for online orbit correction will be developed.

## REFERENCES

[1] C. Zhang *et al.,* Analytical study on beam steering in low-β superconducting quarter wave resonators, *Nuclear Physics Review* 27 (4), 2010, pp. 436-439.

[2] A. Facco *et al.,* "Study on beam steering in intermediate β superconducting quarter wave resonators", in *Proc. PAC2001,* pp. 1095-1097.

[3] S. C. Huang *et al.,* Design and RF test of MEBT buncher cavities for C-ADS Injector II at IMP, *Nuclear Instruments and Methods in Physics Research A,* 799 (2015) pp. 44-49.

[4] H. Jia *et al.,* Analytical study on beam steering in low-β superconducting quarter wave resonators, *Nuclear Physics Review* 27 (4), 2010, pp. 436-439.

[5] T. P. Wangler *et al., RF Linear Accelerator,* 2008, pp. 436-439.

ISBN: 978-3-95450-199-1 doi:10.18429/JACoW-SAP2017-MOPH34

# BEAM DYNAMICS DESIGN OF CIADS SUPERCONDUCTING SECTION *

Shuhui Liu, Zhijun Wang,Yuan He, Insititution of Modern Physics, China

*Abstract*

China Initiative Accelerator Driven system (CiADS) is a strategic plan to solve the nuclear waste problem and the resource problem for nuclear power plants in China, and it aims to design and build an ADS demonstration facility with 500 MeV in energy and 5mA in beam current. CiADS contains driver linac, target and reactor. In this paper, the beam dynamics philosophy applied to the design of the superconducting part of the linac as well as the beam dynamics performance of this structure are focused on.

## INTRUDUCTION

The CiADS linac, to be built in Huizhou, Guangdong, is a CW proton accelerator. The driven linac will deliver a 500 MeV, 5 mA proton beams in CW operation mode. The general layout is shown in Figure 1. The driver linac is composed of two major sections. One is the normal conducting section and the other is the superconducting (SC) section. The normal conducting section is composed of an electron cyclotron resonance (ECR) ion source with frequency of 2.45 GHz, a low energy beam transport (LEBT) line, a four-vane type copper structure radio frequency quadrupole (RFQ) with frequency of 162.5 MHz and a medium energy beam transport (MEBT) line. The normal conducting section will accelerate proton beam to 2.1 MeV. The SC section as the main accelerating section will accelerate the proton beam from 2.1 MeV up to 500 MeV. Then, the beam is transported to the beam dump going through the high energy beam transport (HEBT) line.

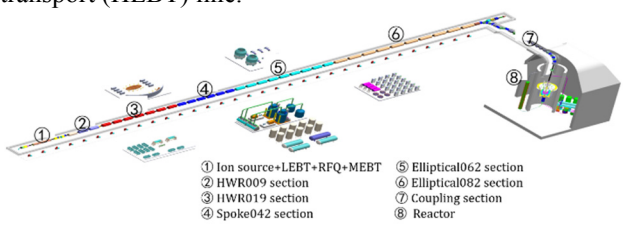


Figure 1: General layout of the CiADS linac.

In this paper, the design considerations of the superconducting section with different types cavity is discussed and the multi-particle simulation results are also presented.

## GENERAL CONSIDERATION AND PHILOSOPHY ON SC SECTION DESIGN

Hands on maintenance and machine protection set strict limits,1 W/m and 0.1 W/m respectively, on beam losses and have been a concern in high power linacs [1]. Therefore, it is crucial to design a linac, which does not excite beam halo and keeps the emittance growth at a minimum level to avoid beam loss. Given the demands of stability and reliability, some guidelines are required to be considered in the design process. Although a lot of the design philosophy for the linac has been addressed in previous literature, we still consider some of them so important to be stated here, and the most important factors in designing our machine are the following [2]:

(1) Transverse period phase advances for zero current beams should be below 90° to avoid the structure resonance.

(2) Wave numbers of oscillations need change adiabatically along the linac, especially at the lattice transitions with different types of focusing structure and inter-cryostat spaces.

(3) Avoid strong space charge resonances through the judgment of Hofmann's Chart.

(4) Minimize the emittance growth and beam halo formation caused by mismatching in the lattice transition section.

(5) Enough redundancy to avoid the beam loss along the linac.

## LATTICE DESIGN

Five types cavities are adopted in SC section based on the analytical results of optimization code. The general parameters of these cavities are determined through optimization as shown in table1. For beam dynamics design and simulation, Epeak is 75% of designed performance, and another 25% is used for element failure compensation, and this redundancy also benefits the cavity reliability.

Table 1: Parameters of the Cavities in the SC Section

| Cavity type | βg | Frequency MHz | Emax MV/m | Bmax mT |
|---|---|---|---|---|
| HWR | 0.10 | 162.5 | 28 | 56.75 |
| | 0.19 | 162.5 | 32 | 58.24 |
| Spoke | 0.42 | 325 | 35 | 65.91 |
| Elliptical | 0.62 | 650 | 35 | 67.34 |
| | 0.82 | 650 | 35 | 68.30 |

The optimized lattice structures for each section of the SC segment are shown in Figure 2. In the first segment with HWR010 cavity, in order to overcome the emittance growth and beam loss caused by strong space charge effect and nonlinear effect, short and compact structure is used, which is also beneficial to raise the accelerating efficiency and increase the longitudinal acceptance for the RFQ output beam. The output energy is about 8MeV. In

*Work supported by National Science Foundation of China (Grant No.91426303 and No.11525523)

ISBN: 978-3-95450-199-1 doi:10.18429/JACoW-SAP2017-MOPH34



the second segment with HWR019 cavity, quasi-period structure, which is beneficial for matching between cryomodules, is adopted. The output energy is 44MeV. In the last three segments, full period structure is used considering the matching between different structures.

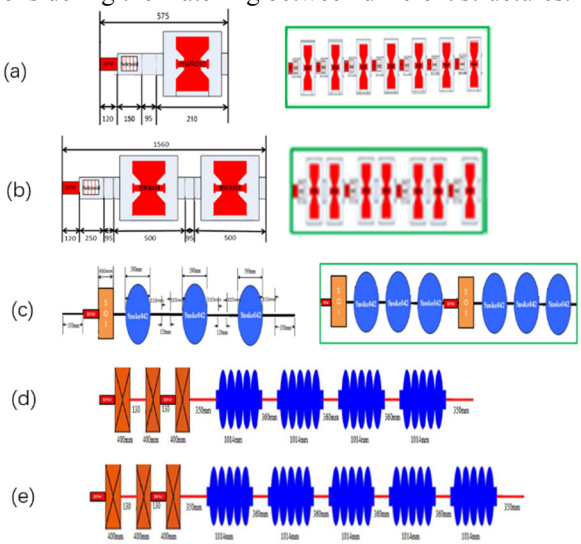


Figure 2: Lattice structures of each section. (a) HWR010 segment, (b) HWR019 segment, (c) spoke042 segment, (d) elliptical062 segment, (e)elliptical082

The phase advance in the three planes are kept below 90° to avoid the parametric resonance. The focusing fields in both the transverse and longitudinal directions are kept almost constant in each section to have almost constant envelope amplitude when the rms emittance is shrinking along the acceleration [3]. This also means constant phase advance in each section, but the absolute value of the synchronous phase decreases from the lower-energy section to the higher-energy section to obtain higher acceleration rate. Because of the limitation in the longitudinal phase advance per cell, a big synchronous phase (absolute value) should be kept ensuring longitudinal acceptance, therefore, the cavity voltages at the beginning parts of the SC section may not be fully exploited. The period phase advance and synchronous phase evolution of the SC section are shown in Figure 3 and Figure 4.

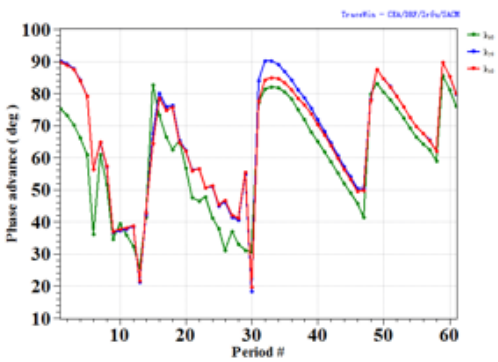


Figure 3: Period phase advance of SC section.

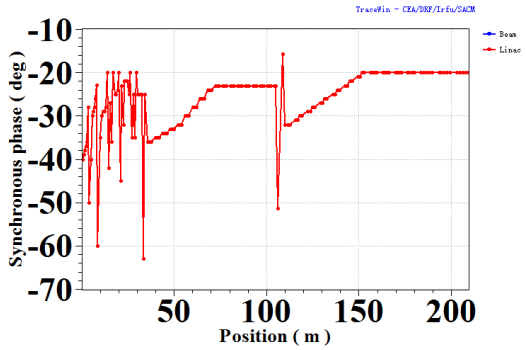


Figure 4: Synchronous phase of SC section.

## MULTI-PARTICLE SIMULATION

The multi-particle simulation is performed with 100000 micro particles with TraceWin [4] code. The beam current is 5mA. The initial beam emittances at the entrance to the SC section are 0. 216mm.mrad in the transverse planes and 0. 25mm.mrad in the longitudinal plane which are the beam parameters out of normal conducting section. The input beam distribution is initially at 3sigma Gaussian distribution in the transverse plane and 5sigma Gaussian distribution in the longitudinal plane respectively. The simulations carried out here assumes error free lattice. The 2D PICNIC space charge routine with a 30*50mesh is employed for space charge calculations. The 2.1MeV proton beam will be accelerated up to 500MeV. The figure 5 shows the beam density distribution of the SC section, and the Figure 6 shows the RMS beam emittance evolution. The maximum beam size is at least half of the aperture, and the particles are all in bucket. The normalized RMS emittance growths are 5%, 7.6% and 3% (x, y and z planes) respectively. During the design, the normalized RMS emittance growths are considered as one major criterion for determining the matching results between the two CMs.

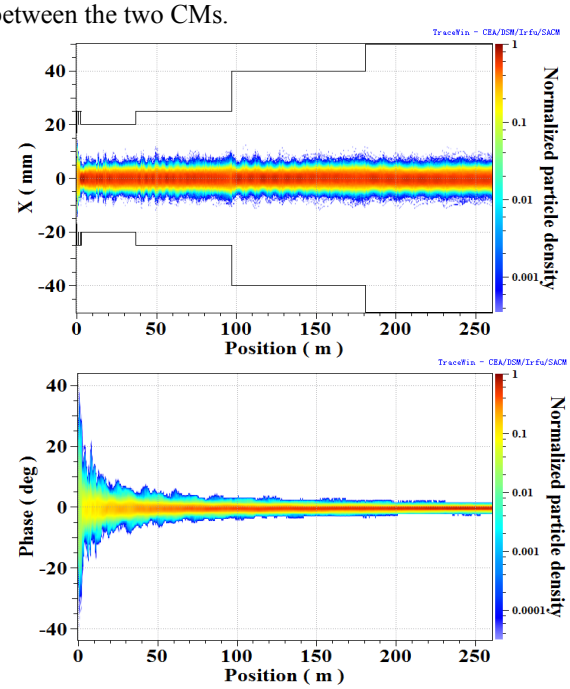


Figure 5: Beam density distribution of SC section.

ISBN: 978-3-95450-199-1 doi:10.18429/JACoW-SAP2017-MOPH34

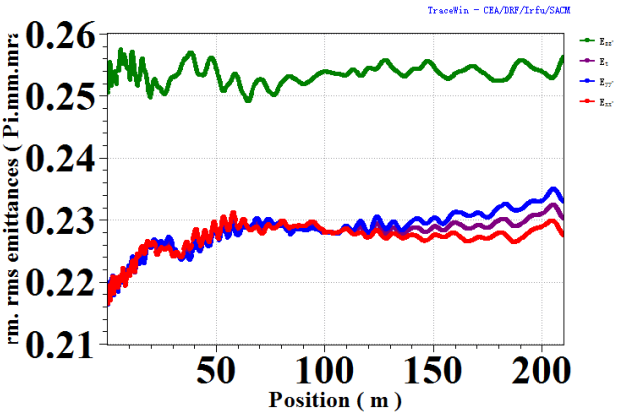


Figure 6: Normalized RMS emittance evolution.

The halo development due to errors, mismatches and resonances is the key causing beam loss, it becomes the central focus of the beam dynamics studies. The emittance evolutions for RMS, 95%, 99%, 99.99% beam fractions have been studied, using TraceWin [4] code. The number of macro-particles is 100000 for the simulations. The Figure 7, Figure 8 and Figure 9 are listed the emittance evolutions in three directions. The emittances with different fractions of particles indicate that the basic design is robust.

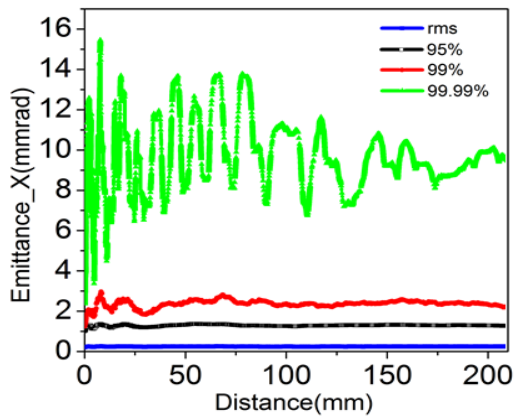


Figure 7: Emittance evolution in X direction.

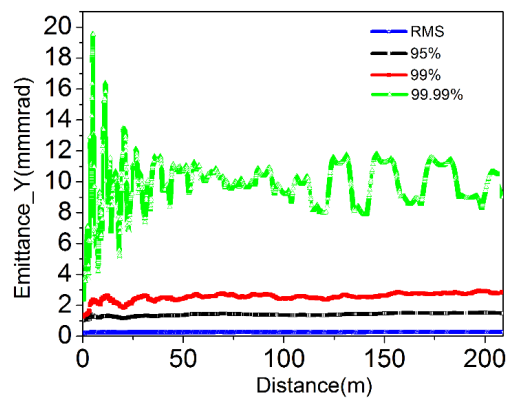


Figure 8: Emittance evolution in X direction.

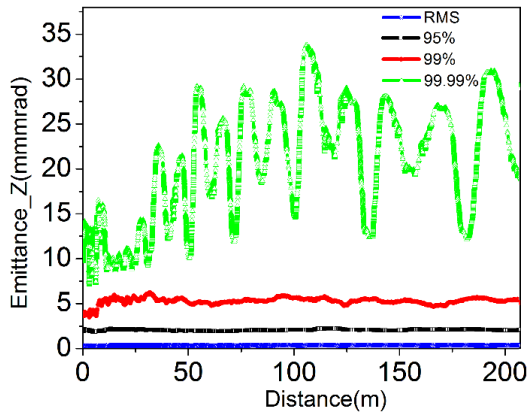


Figure 9: Emittance evolution in X direction.

## SUMMARY

The physics design of the CIADS SC section is presented which considered the rules of the thumb in high intensity ion linacs. Period phase advance at zero current less than 90° are considered to avoid resonance and to reduce the possible beam losses. Multi-particle simulation results with Gussian distribution are shown. The RMS emittance growths are 5%, 7.6% and 3% in the x, y and z planes, respectively. Emittance evolution with different fractions of particles are studied in three plane phases, and the results indicate that the basic design is robust. Further optimizations and other discussions will be carried out in the future.

## ACKNOWLEGEMENT

The authors express the sincere thanks to the colleagues in the CiADS accelerator team for their valuable inputs and discussions.

## REFERENCES

[1]M. Eshraqi, H. Danared, R. Miyamoto, in *Proc. HB2012*, Beijing China, TUO3B02, pp. 278-282
[2]Shu-Hui Liu, Zhi-Jun Wang, Huan Jia et al., Physics design of the CIADS 25MeV demo facility , *Nuclear Instruments and Methods in Physics Research A*. 843(2017):11-17.
[3]M.Rerser, N.Brown, *Phys.Rev. Lett*. 74(1995) 11 11.
[4]D.Uriot. http://irfu.cea.fr/Sacm/logiciels/index3.php,2011.

ISBN: 978-3-95450-199-1 doi:10.18429/JACoW-SAP2017-MOPH35

# ORBIT CORRECTION STUDY BASED ON SIMULATION FOR INJECTOR II

W.S.Wang, Z.J.Wang, C.Jin, Y.He, S.H.Liu, P.Y.Jiang, W.P.Dou, W.L.Chen, Y.S.Qin
Institute of Modern Physics (IMP), Chinese Academy of Sciences, Lanzhou, China

## *Abstract*

Orbit correction is one of the most fundamental processes used for beam control in accelerators. The CADS is a CW machine and a few particle loss will cause serious damage to the machine. Therefore, the quality of the orbit control is an essential component towards the efficiency in operation, flexibility in machine studies. This paper describes an orbit correction implementation using singular value decomposition (SVD) of the response matrix and the simulation of its application to the CIADS injector II. This effort was achieved by exploiting the capabilities of Python, which provided the hands-on modules to develop the GUI code easily. Also involved in this effort was the code TraceWin, which was used to construct the virtual machine by providing the parameters of the Linac optics. Several iterations of the orbit correction may be required in order to obtain a satisfactory control of the orbit, because the the response matrix changes with iteration in an attenuating mode. After appropriate removal the redundancy steerers, a promising result of the orbit control was achieved.

## *Introduction*

The CIADS project aims to deliver high power proton beams for nuclear transmutation. The neutrons created in the target from a spallation reaction between protons and heavy elements drive the subcritical reactor for sustained chain reaction. CIADS will be a continuous wave (CW), proton RF superconducting linear accelerator with current (10mA) and final energy 1.5GeV. The pre-feasibility study facility, injector II established mainly by IMP, was successfully commissioned in June 2017 with the jointed efforts of IMP and IHEP. The overall architecture of injector II is shown in Fig. 1. The chosen sequence of accelerating sections is quite standard for modern pulsed linac designs. The ion source is followed by a Radio Frequency Quadrupole (RFQ), a MEBT and the superconducting accelerating structures. Four cryomodules of the accelerating structures bring the energy from 2.1MeV at the exit of RFQ up to 25MeV: the first three cryomodules and the last one are fabricated by IMP and IHEP respectively.

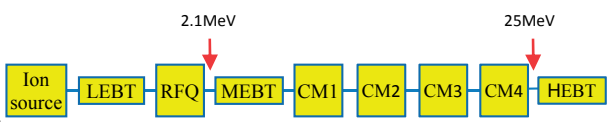


Figure 1: Scheme of Injector II.

* Work supported by National Science Foundation of China (Grant No.91426303 and No.11525523)
† email address: wwshunan@impcas.ac.cn

CIADS is designed to enable hands-on maintenance and minimize the performance deterioration of superconducting cavities caused by particle loss, which means that its beam loss will be below 1 W/m for the entire accelerator. These specifications will place CIADS in line with the next generation of accelerators worldwide. In real life errors will be present: misalignments, incorrect field settings, magnetic field inhomogeneities, etc. These errors can cause unacceptably large deviation of the orbit. Usually the distorted orbit can be corrected using the dipole correctors and BPMs. In this paper, we select a partial section of injector II, consisting of MEBT and the first three cryomodules, to conduct the correction study. The distribution of correctors and BPMs is shown in Fig. 2. MEBT includes 7 quadrupoles, each of which contains a pair of horizontal and vertical steerers, and there are 4 BPMs separately installed at the center of 1th, 4th, 5$^{th}$ and 7th quadrupoles. Each cryomodule consists of a series of periods and there are a magnet assembly of focusing solenoid and corrector coils, a cavity and a BPM cell in each period.

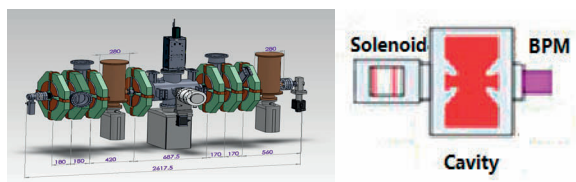


Figure 2: The layout of MEBT and a cryomodule period

In the orbit correction study, we use TraceWin to simulate the behaviour of proton beams in the accelerator and displace the central orbit at the accelerator entrance in the transversal direction to introduce an artificial orbit deviation. As a preliminary attempt, a well-known orbit correction approach using SVD of the response matrix was implemented on the accelerator to estimate the correction effect on bringing back the beam orbit.

## *Orbit Correction Method*

According to accelerator theory the transfer matrix R between positions 1 and 2 is given by [1]:

$$\mathrm{R} = \begin{bmatrix} R_{11} & R_{12} \\ R_{21} & R_{22} \end{bmatrix} \quad (1)$$

The elements of the matrix are as follows:

$$R_{11} = \sqrt{\beta_2/\beta_1}\,(cos\Delta\psi + \alpha_1 sin\Delta\psi)$$
$$R_{12} = \sqrt{\beta_1\beta_2}\,sin\Delta\psi$$
$$R_{21} = -[(1+\alpha_1\alpha_2)sin\Delta\psi + (\alpha_2-\alpha_1)cos\Delta\psi]/\sqrt{\beta_1\beta_2}$$
$$R_{22} = \sqrt{\beta_2/\beta_1}\,(cos\Delta\psi - \alpha_1 sin\Delta\psi)$$

where $\beta_i$ and $\alpha_i$ ( i=l, 2) are the machine functions; $\Delta\psi$ is the phase difference between positions 1 and 2.

ISBN: 978-3-95450-199-1 doi:10.18429/JACoW-SAP2017-MOPH35

Assume an orbit corrector is located at position 1 and a position monitor is located at position 2. A kick $\Delta x_1'$ created by an orbit corrector at position 1 will cause a distortion $\Delta x_2$ of the orbit, which can be observed at position 2 by a position monitor. This signal can be described as:

$$\Delta x_2 = R_{12}\Delta x_1' = \Delta x_1'\sqrt{\beta_1\beta_2}sin\Delta\psi \quad (2)$$

If there are some other orbit correctors installed along the accelerator, then at the $j_{th}$ monitor (j = 1, ..., N) the signal $\Delta x^j$ will be the sum of all of those signals $\Delta x_i^j$ (i = 1, ..., M), caused by the $i_{th}$ orbit corrector, which gives the kick $\Delta x_i'$:

$$\Delta x^j = \sum_{i=1}^{M}\Delta x_i^j = \sum_{i=1}^{M}(R_{12})_{ji}\,\Delta x_i' \quad (3)$$

Two vectors X and X' are introduced. X contains the signals $\Delta x^j$ from position monitors and X' contains the kicks $\Delta x_i'$ from orbit correctors:

$$X = \begin{pmatrix}\Delta x^1\\ \vdots \\ \Delta x^N\end{pmatrix} \qquad X' = \begin{pmatrix}\Delta x_1'\\ \vdots \\ \Delta x_M'\end{pmatrix} \quad (4)$$

The equation for describing the relation between signal X (displacement of orbit) received from position monitors and the kicks X' created by orbit correctors can be written as:

$$X = AX' \quad (5)$$

where the N x M matrix A is the so-called response matrix. Its elements $A_{ji}$ relates the orbit displacement $\Delta x^j$ at $j_{th}$ BPM to the dipole kick change $\Delta x_i'$ at $i_{th}$ corrector. In reality X will be measured by BPM and A will be obtained from calculation or measurements.

Linear orbit correction reduces to inverting the (usually non-square) A matrix, or solving this system of linear equations with a linear least-squares method. One then has a set of equations that give the set of corrector changes necessary to produce a given orbit change on all BPMs. Putting in the negative of the measured BPM positions for this given orbit change will give a set of corrector strengths that make all BPM positions zero and thus correct the orbit.

Traditional linear algebra courses teach methods to create square matrix inverses, but don't teach the more general approach to finding an optimal solution for a non-square linear problem.

Singular value decomposition (SVD) is the most common approach to producing a "pseudo-inverse" for A. Background information is in the corresponding Wikipedia article [2] but the approach is fairly straightforward and well-supported by standard linear algebra environments like Python numpy. We write A as a product of three matrices U, Σ, and V as

$$A = U\Sigma V^T \quad (6)$$

where U is a N x N orthogonal matrix and V is a M x M orthogonal matrix, while Σ is a N x M diagonal matrix with positive or zero values on the diagonal with descending magnitude which represents the sensitive of the orbit displacements at BPMs to the kick changes at correctors. For small singular values that are "near zero", we can set them to zero. This gives the opportunity to filter out noise in the measurement. We calculate the pseudo-inverse of Σ by replacing all non-zero diagonal terms $s_i$ of Σ with their inverses $1/s_i$. Then the pseudo-inverse of A is constructed as

$$A^{-1} = V\Sigma^{-1}U^T \quad (7)$$

where $U^T$ is the transpose of U.

This provides the solution of the corrector changes necessary to remove the measured orbit displacements:

$$X' = A^{-1}X \quad (8)$$

### *Correction Results*

We used two basic software tools for orbit correction study: TraceWin for tracking the beam orbit in the accelerator and python for data processing. TraceWin is a global tool box oriented to accelerator design and realistic simulations with many useful features. One of the main specificity of TraceWin, probably unique in the plethora of existing codes, is to make possible to run different models with various levels of sophistication. Thus, model complexity can be gradually increased from envelope optic with hard edge linearized elements and space-charge to massive tracking 3D simulations using PIC space-charge, field maps, and use of automatic tuning procedures in realistic (imperfect) accelerators. Python is free and open source which includes natively an impressive number of general-purpose or more specialized libraries, and yet more external libraries are being developed by Python enthusiasts.

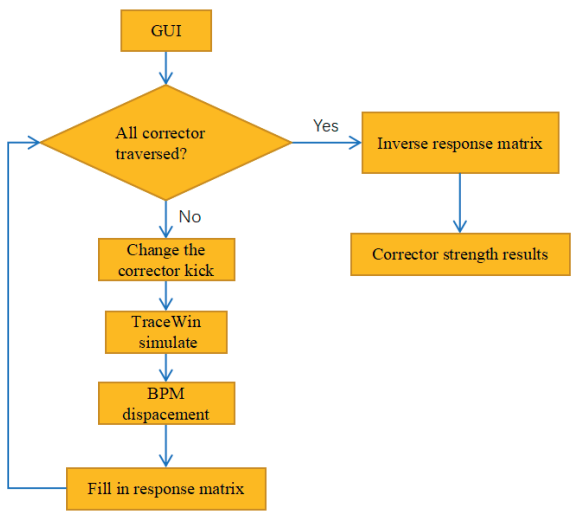


Figure 3: Orbit correction workflow diagram.

For ease of use we have developed a python GUI code for users to select the correctors and BPMs involved in the orbit correction and launch the automatic correction process. In the underlying orbit correction process python calculates the response matrix iteratively from the first column to the last column, where a certain column is obtained by giving a unit kick change to a given corrector, running the TraceWin simulation on the specified accelerator, recording the corresponding displacements of the downstream BPMs and restoring the corrector to the original status. When the response matrix is obtained, the off-the-shelf tool SVD in Python numpy will be used to calculate the pseudo-inverse of the response matrix

ISBN: 978-3-95450-199-1 doi:10.18429/JACoW-SAP2017-MOPH35



and finally the set of corrector changes required can be easily calculated. Figure 3 shows the entire workflow for the orbit correction.

To produce an articifial orbit deviation, we simulate the behavior of the beam in a perfect accelerator except a transrverse orbit displacement at the accelerator entrance. Since the beam do not pass through the magnetic center of the magents, a focusing or defocusing force acting on the beam will deflect the orbit more and more deviated from the reference orbit. Of course orbit corrections were carried out in the immediate following. Sometimes several iterations of orbit corrections are necessary in order to get a better correction effect at the expense of time, because the response matrices vary from iteration to iteration until the orbit does not change any more. When there are more correctors than BPMs a multiplicity of solutions is possible. In this case some correctors do not contribute to observable orbit distortion and can be discarded[3]. This is the reason for setting the singularity rejection parameter to reject the correctors having little correction ability. The correction results for the case of the beam with a 2.5mm horizontal displacement are shown in Fig. 4.

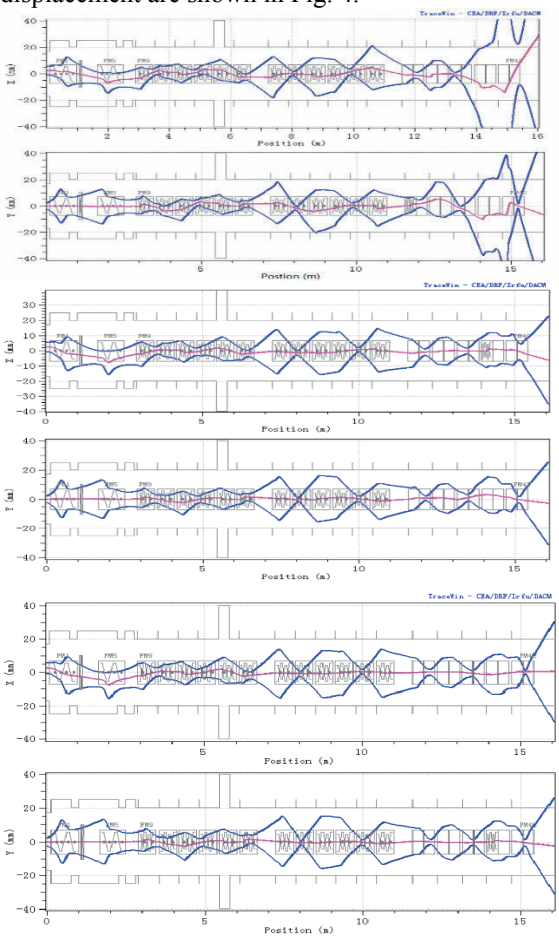


Figure 4: Figures from top to bottom respectively represent orbits before correction, after first correction and after second correction while a 2.5mm horizontal displacement was applied to the input beam.

In the above orbit corrections we only considered the simplest alignment error, an transversal orbit displacement of the input beam, and more comprehensive errors are needed to be assined to imitate the real accelerator with various misalignment errors like displacement and rotation of the magnets.

## *Conclusions*

The orbit correction performed on the virtual machine of injector II, in which the beam behavior is simulated by TraceWin, has a satisfactory result. It was just a trial of the algorithm of the response matrix, and more studies will be done to optimize the correction scheme. We also consider applying it to the actual machine in the future.

## REFERENCES

[1] K.L. Brown, R.V. Servranckx., "Optics Modules for Circular Accelerator Design", *Nucl. Instr. Meth.,* vol. 258, pp. 480-502, 1987.

[2] Wiki, https://en.wikipedia.org/wiki/Singular_value_de composition

[3] Y. Chung, G. Decker, K. Evans, "Closed orbit correction using singular value decomposition of the response matrix", in *Proc. PAC'09*, pp. 2263-2265.

ISBN: 978-3-95450-199-1 doi:10.18429/JACoW-SAP2017-MOPH36

# THE PRGRESS OF THE CHINA MATERIAL IRRADIATION FACILITY RFQ*

Weiping Dou†, Zhijun Wang, Chenxing Li, Yuan He, Fengfeng Wang, Xianbo Xu, Shuhui Liu, Zhouli Zhang, Institute of Modern Physics, Lanzhou, China

*Abstract*

The design and low power RF measurement of the radio frequency quadruple (RFQ) for the front end of China Material Irradiation Facility (CMIF), which is an accelerator based neutron irradiation facility for fusion reactor material qualification, has been completed. The RFQ, which operated under CW mode, is specified to accelerate 10 mA deuteron beam from the energy of 20 keV/u to 1.5 MeV/u. To reduce the possibility of beam loss in supper conducting section, the output longitudinal emittance need be optimized. The idea of "Kick-drift" is adopted in beam dynamic design. The challenge for CW RFQ is not only the beam dynamic design but also in the design of cavity structure and cooling of structure. With the experience obtained in the design of the RFQ for CIADS injector II, the structure design and cooling design have been finished. The results of low power RF measurement show the flatness and asymmetry are below 4% for each module.

## INTRODUCTION

The China Material Irradiation Facility (CMIF) will be established by the Institute of Modern Physics (IMP), Chinese Academy of Science. CMIF is a new compact neutron source with less cost and low level risk than the project IFMIF. The schematic diagram of CMIF is illustrated in Fig. 1. It consists of ion source, LEBT, RFQ, MEBT, superconducting section, HEBT, and granular beryllium alloy particle target [1]. The RFQ operated under CW mode, as a key equipment of the CMIF linac, is specified to accelerate deuteron beam with intensity high to 10mA from the energy of 20 keV/u to 1.5 MeV/u.

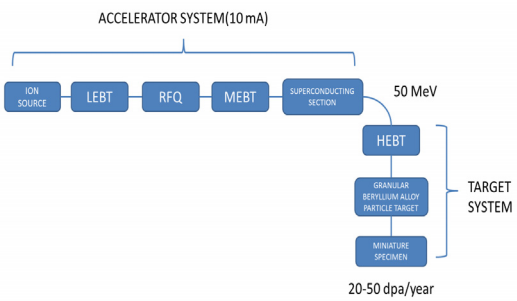


Figure 1: The schematic diagram of CMIF.

## BEAM DYNAMIC DESIGN

The main RFQ parameters are shown in Table 1.

Table 1: CMIF RFQ Design Parameters

| Particle | Value | Unit |
|---|---|---|
| Beam current | 10 | mA |
| I/O energy | 0.02-1.5 | MeV/u |
| Vane voltage | 65 | kV |
| Vane length | 526.43 | cm |
| Max.surface filed | 19.01 | MV/m |
| Transmission rate | 98.2 | % |
| Tr.n.r.emittace | 0.203 | pi.mm.mrad |
| 99.99% long.emittace | 3.5 | pi.mm.mrad |

These goals of RFQ beam dynamic studies usually are minimize the vane length, beam loss and emittance growth. For CMIF RFQ, two special goal are optimized Kilpatrick factor and output longitudinal emittance. PARMTEQM code [2], which was developed at Los Alamos National Laboratory, is used to generate RFQ parameters. The Kilpatrick factor was optimized to 1.4 computed by PARMTEQM code, which is small enough for avoiding any possible breakdown and reducing time of conditioning of the resonator. The output longitudinal emittance need be optimized to 3.5 pi.mm.mrad to reduce the possibility of beam loss in supper conducting section. The idea of "kick-drift" and Four-Section Procedure are adopted in beam dynamic optimized design. The "kick-drift" act as internal bunch system to bunch beam in short distance. The longitudinal emittance growth and bunch efficient with different electrode modulation factor and drift length have been studied in Fig. 2. The results show when max electrode modulation is 1.02 and the distance is appropriate, the longitudinal emittance growth is smaller and the phase spread is about ± 30 deg.

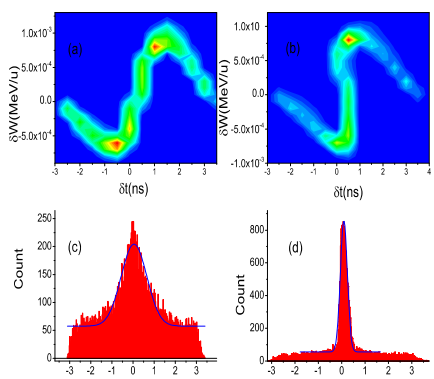


Figure 2: The evolution of longitudinal phase space with different electrode modulation factor and drift length.

* Work supported by National Science Foundation of China (Grant No.9142603) and National Magnetic confinement Fusion Science Program of China (Grant No.2014GB104001)
† email address: douweiping@impcas.ac.cn

ISBN: 978-3-95450-199-1 doi:10.18429/JACoW-SAP2017-MOPH36

The beam simulation by PARMTEQM code is in Fig. 3. The initial beam is water bag. The beam transmission efficient is 98.2%. In Fig. 4, the longitudinal 99.9% emittance at the RFQ exit is optimized to 3.5 pi.mm.mrad. The longitudinal acceptance of downstream supper conducting accelerator is 27 pi.mm.mrad. The ration is 1 to 7.7.

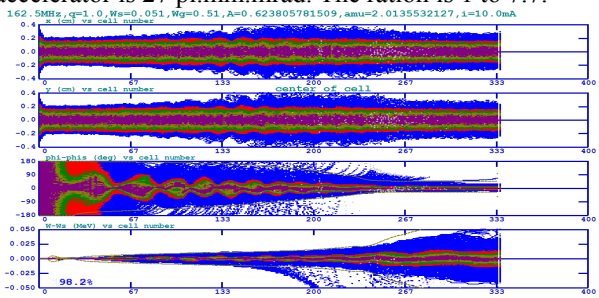


Figure 3: The beam simulation used PARMTEQM.

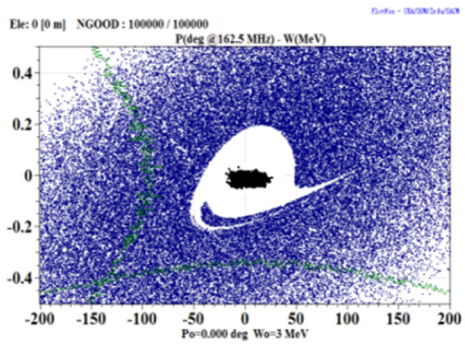


Figure 4: The 99.9% longitudinal emittance and longitudinal acceptance of supper conducting section.

## RF DESIGN

The RF design and study have included the RF design of 2D cross section, 3D RF simulation of period structure and RF simulation of the whole length. Though the study of the 2D cross section, the mesh study is completed and the optimized cross section parameter to get low power consumption is got. The approximate 2D simulation can be performed by the 3D code CST MWS [3]. The geometry parameters of the cross section is shown in Fig. 5 and table 2. Finally the frequency is 162.491MHz. The dipole mode frequency is 157MHz. The power loss per length is 16.5 W/mm.

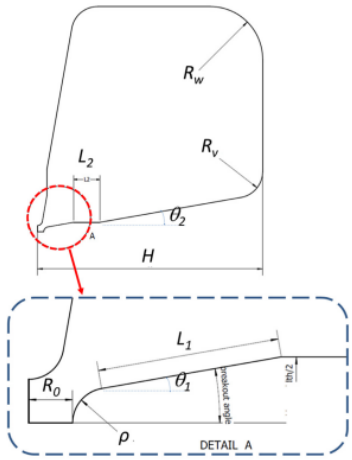


Figure 5: The cross section of CMIF RFQ.

Table 2: The Parameters of the Cross Setion

| Variables | Value | Unit |
|---|---|---|
| $R_0$ | 4.807 | mm |
| $R_0/\rho$ | 0.8 | |
| $L_1$ | 27.82 | mm |
| $L_2$ | 11.89 | mm |
| $\theta_1$ | 7.1 | deg |
| $\theta_2$ | 10 | deg |
| $R_v$ | 20 | mm |
| $R_w$ | 40 | mm |
| H | 169.3 | mm |
| $\rho$ | 3.85 | mm |

The 3D RF simulation of period structure have included $\pi$-mode stabilizing loops (PISLs) [4] and tuner period structure. The parameters of PISLs are optimized to separate the frequency of the quadruple and dipole. The period structure of PISLs is shown in Fig. 6. The frequency shift of quadruple mode due to PISLs is 5.5 MHz and that of the dipole mode frequency is 17.5 MHz. The tuner will be used to compensate the construction errors after the cavity was brazed. The structure of the tuner period is shown in Fig. 7. For the tuner period, the tuning sensitivity for one tuner inserting one millimeter is 22KHz. The tuning range can be reached to about 1.5MHz for the whole length cavity.

ISBN: 978-3-95450-199-1 doi:10.18429/JACoW-SAP2017-MOPH36

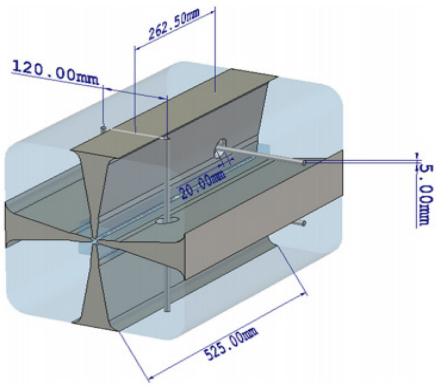


Figure 6: The period structure of PISLS.

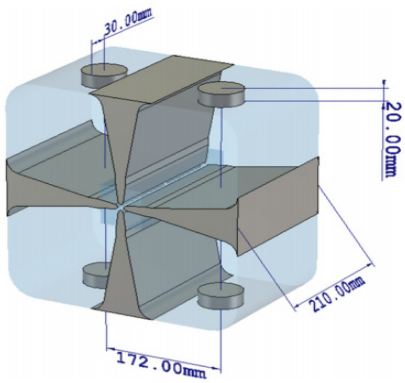


Figure 7: The period structure of tuner.

After the period simulation, the precise RF simulation of whole length model with modulation is performed. Some dimensions are adjusted to reach the design targets including frequency and field flatness. The dimensions of the inputs cutback and output cutbacks are shown in Fig. 8. The distance between vane tips and the surface of end-plate is adjusted to get optimized filed flatness. Finally the filed flatness is in range of 2%.

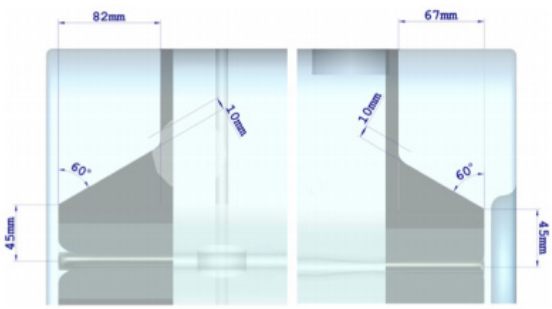


Figure 8: The dimensions of input (left) and output cutbacks (right).

## COOLING DESIGN

The thermal analysis and cooling design have been carried out by the the software ANSYS [5]. The water cooling channels and their positions are shown in Fig. 9. Inlet temperature of cooling water is 20 ℃, the velocity of the cooling water is 2.29 m/s. The temperature distribution is shown in Fig. 10.

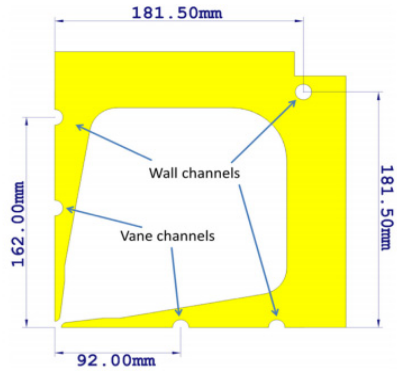


Figure 9: The water cooling channels.

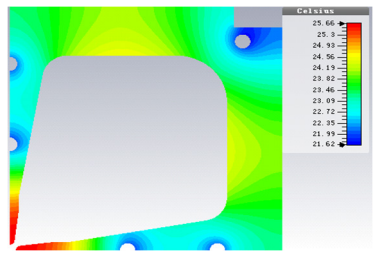

Figure 10: The temperature distribution.

## LOW POWER RF MEASUREMENT

Before braze and after braze, the cold model tests were performed for each module. The results of low power RF measurement show in Figure 11, it show the flatness and asymmetry are below 4% which is within the tuning range. The discrepancy between simulated frequency and measured frequency is below 500 kHz which is also within the range of tuning.

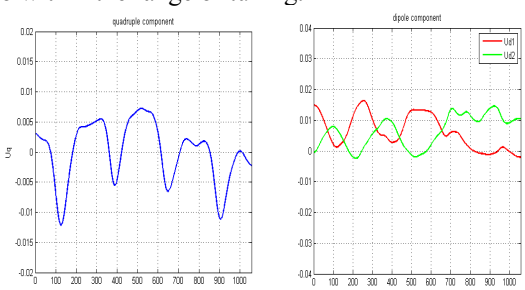


Figure 11: The flatness and asymmetry.

## SUMMARY AND PLAN

The beam dynamic design, RF design and cooling design of RFQ for CMIF project are presented. The results of low RF measurement show the flatness and asymmetry are below 4% for each module. The whole length cold model test and tuning is under progress and will be finished this month. The high power conditioning will be on October.

ISBN: 978-3-95450-199-1 doi:10.18429/JACoW-SAP2017-MOPH36



## REFERENCES

[1] L.Yang, W.L. Zhan *et al.*, "New concept for ADS spallation target: gravity-driven dense granular flow target", *Sci. China Technol*. Sci.58(10) (2015) 1705-1711

[2] Crandall K R *et al.*, 1998 RFQ Design code: LA-UR-961836

[3] CTS STUDIO SUITE, *http://www.cst.com*

[4] A. Uenoi, Y.Yamazaki, "New filed stabilization method of a four-vane type RFQ", *Nucl. Instrum, Methods Phys.Res.A* 300 (1).(1991) pp. 15-24.

[5] ANSYS, *http://www.ansys.com*

ISBN: 978-3-95450-199-1 doi:10.18429/JACoW-SAP2017-MOPH37

# CALIBRATION OF THE BPM OFFSETS IN CRYOMODULE AT CiADS INJECTOR II

C. Feng*, Z. J. Wang, W. S. Wang, Y. He
Institute of Modern Physics (IMP), Chinese Academy of Sciences, Lanzhou, China

*Abstract*

China Initiative Accelerator Driven System (CiADS) project is a strategic plan to solve the nuclear waste problem and the resource problem for nuclear power plants in China. For CiADS driven linac, which has a long superconducting accelerator section, traditional ways to calibrate the Beam Position Monitor (BPM) are not always available. In order to calibrate the BPM offsets in cryomodule so as to adjust the beam orbit effectively and accurately, we have tried to scan the superconducting solenoid's current, read the BPM values, and fit the data to get BPM offsets.

## INTRODUCTION

The Injector Scheme II which is being built at IMP is composed of an ion source, a low energy beam transport line (LEBT), a 162.5 MHz radio frequency quadrupole accelerator (RFQ), a medium energy beam transport line (MEBT) and a superconducting Half Wave Resonator (HWR) accelerator section. In superconducting accelerator section, beam loss is particularly deleterious. Large beam orbit excursion is one of the major reasons causing beam loss. In order to align the beam orbit accurately to the centroid of the accelerator components, calibration of the BPM offsets is essential.

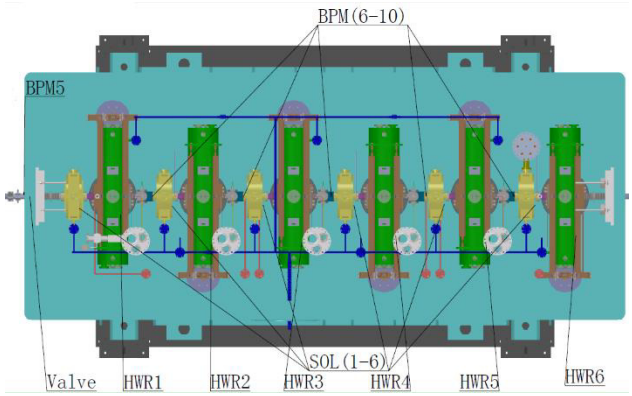


Figure 1: Layout of CM1 of C-ADS Injector II.

Traditional methods of calibrating BPM offsets always need quadrupoles [1]. But in cryomodule, such as CM1 shown in Fig. 1, there is no quadrupole. On this occasion, solenoid may be a substitute. In this report, the formulations of calibration of the BPM offsets with solenoid will be briefly described in the second section. The experiment designs and results are demonstrated in the third section. Finally, the summary of the studies will be given and some ideas for further studies will also be discussed in the last section.

## MATHEMATICAL THEORY

Let x, x', y, and y' be coordinates of the particle and the subscript 0 and 1 denote the beginning and ending point of the lattice, we get

$$\begin{pmatrix} x_1 \\ x_1' \\ y_1 \\ y_1' \end{pmatrix} = M \cdot \begin{pmatrix} x_0 \\ x_0' \\ y_0 \\ y_0' \end{pmatrix}, M = \begin{bmatrix} m_{11} & m_{12} & m_{13} & m_{14} \\ m_{21} & m_{22} & m_{23} & m_{24} \\ m_{31} & m_{32} & m_{33} & m_{34} \\ m_{41} & m_{42} & m_{43} & m_{44} \end{bmatrix}$$

where M is the total transfer matrix which can be calculated by [2]

$$R_{drift} = \begin{bmatrix} 1 & L & 0 & 0 \\ 0 & 1 & 0 & 0 \\ 0 & 0 & 1 & L \\ 0 & 0 & 0 & 1 \end{bmatrix}$$

$$R_{solenoid} = \begin{bmatrix} cos^2(kL) & \frac{1}{2k}sin(2kL) & \frac{1}{2}sin(2kL) & \frac{1}{k}sin^2(kL) \\ \frac{-k}{2}sin(2kL) & cos^2(kL) & -ksin^2(kL) & \frac{1}{2}sin(2kL) \\ -\frac{1}{2}sin(2kL) & -\frac{1}{k}sin^2(kL) & cos^2(kL) & \frac{1}{2k}sin(2kL) \\ ksin^2(kL) & -\frac{1}{2}sin(2kL) & -\frac{k}{2}sin(2kL) & cos^2(kL) \end{bmatrix}$$

Define $x_{off}$ and $y_{off}$ as offsets of the BPM next the solenoid, there are

$$\langle x_1 \rangle = m_{11}\langle x_0 \rangle + m_{12}\langle x_0' \rangle + m_{13}\langle y_0 \rangle + m_{14}\langle y_0' \rangle - x_{off}$$
$$\langle y_1 \rangle = m_{31}\langle x_0 \rangle + m_{32}\langle x_0' \rangle + m_{33}\langle y_0 \rangle + m_{34}\langle y_0' \rangle - y_{off}$$

Respectively, the following equations can be obtained:

$$\begin{pmatrix} \langle x_1 \rangle \\ \cdots \\ \langle x_N \rangle \\ \langle y_1 \rangle \\ \cdots \\ \langle y_N \rangle \end{pmatrix} = A \cdot \begin{pmatrix} x_0 \\ x_0' \\ y_0 \\ y_0' \\ x_{off} \\ y_{off} \end{pmatrix},$$

$$\mathrm{A} = \begin{bmatrix} m_{11}^{(1)} & m_{12}^{(1)} & m_{13}^{(1)} & m_{14}^{(1)} & -1 & 0 \\ \cdots & \cdots & \cdots & \cdots & \cdots & \cdots \\ m_{11}^{(N)} & m_{12}^{(N)} & m_{13}^{(N)} & m_{14}^{(N)} & -1 & 0 \\ m_{31}^{(1)} & m_{32}^{(1)} & m_{33}^{(1)} & m_{34}^{(1)} & 0 & -1 \\ \cdots & \cdots & \cdots & \cdots & \cdots & \cdots \\ m_{31}^{(N)} & m_{32}^{(N)} & m_{33}^{(N)} & m_{34}^{(N)} & 0 & -1 \end{bmatrix}$$

With enough measured $\langle x_i \rangle$ and $\langle y_i \rangle$ values, the quantity of $x_{off}$ and $y_{off}$ can be fitted by using the least square method, which can be simplified as [3]

* E-mail: fengchi@impcas.ac.cn

ISBN: 978-3-95450-199-1 doi:10.18429/JACoW-SAP2017-MOPH37



$$\begin{pmatrix} x_0 \\ x_0' \\ y_0 \\ y_0' \\ x_{off} \\ y_{off} \end{pmatrix} = (A^T A)^{-1} A^T \begin{pmatrix} \langle x_1 \rangle \\ \cdots \\ \langle x_N \rangle \\ \langle y_1 \rangle \\ \cdots \\ \langle y_N \rangle \end{pmatrix}$$

## EXPERIMENT AND RESULTS

The calibration was carried out on the Injector Scheme II Cryomodule 1. During the experiment, the beam was operated at a pulse width of 50 microseconds with the frequency of 1Hz and intensity of 2mA. By scanning the current of SOL1 from -100A to 100A, we acquired a series of values of beam positions.

Table 1: The First Experimental Data of SOL1

| Current(A) | -100 | -90 | … | 90 | 100 |
|---|---|---|---|---|---|
| X(mm) | 0.58 | 1.01 | … | -0.17 | -0.22 |
| Y(mm) | 3.20 | 2.84 | … | -0.17 | 0.14 |

The raw data from BPM6 and the fitted curve are shown in Fig. 2.

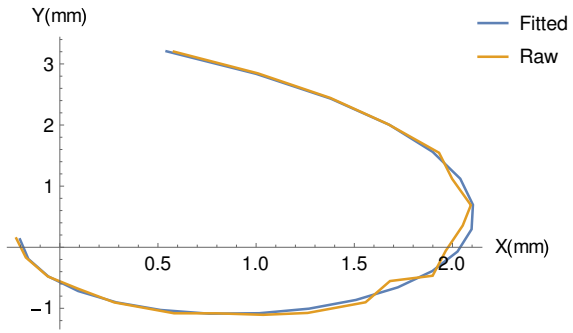


Figure 2: The first fitting result of SOL1.

After fitting, we acquired $x_{off} = 1.61mm$ and $y_{off} = -2.10\text{mm}$. Then change the beam position and direction before SOL1 and repeat the experiment to benchmark the result. The raw data and the fitted curve are shown in Fig. 3.

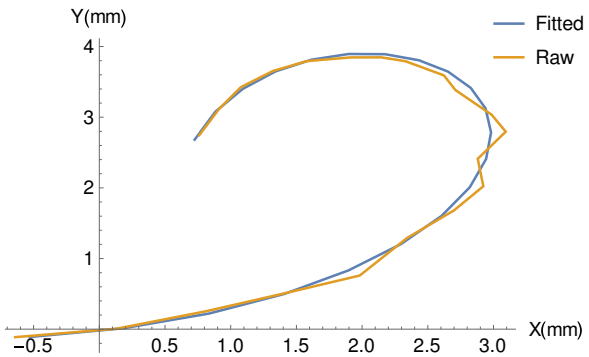


Figure 3: The second fitting result of SOL1.

We got $x_{off} = 1.52mm$ and $y_{off} = -2.01\text{mm}$, which was close to the first result.

Table 2: Fitting Results of BPM7 and BPM9

| | BPM7 | BPM9 |
|---|---|---|
| $x_{off}$(mm) | -1.39 | -2.20 |
| $y_{off}$(mm) | -4.45 | -3.70 |

At last we calibrated BPM7 and BPM9 respectively by using SOL2 and SOL4. The results are shown in Table 2. And the data with fitted curves are plotted in Fig. 4 and Fig. 5.

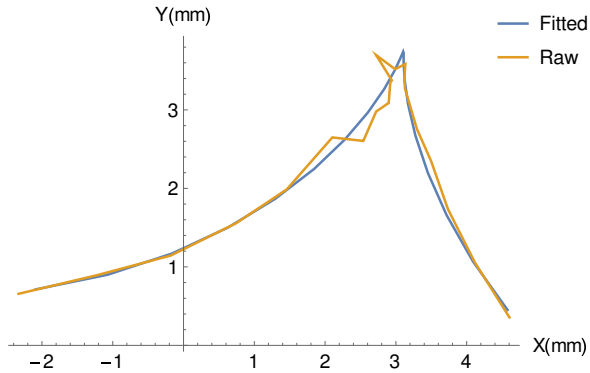


Figure 4: Fitting result of SOL2.

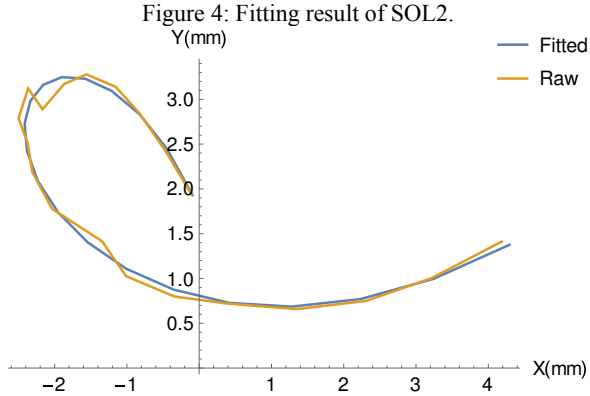


Figure 5: Fitting result of SOL4.

## SUMMARY

In cryomodule, solenoid is likely an alternative to quadrupole to calibrate the BPM offset, which means the displacement between the magnetic axis of the solenoid and the electric center of the BPM. But the experiment is only at an early stage of feasibility study. As the step further, error analysis will be made. In addition, the availability of this method need to be verified in practice.

## REFERENCES

[1] Zhang CaiXia, Liu Weibin, Ye Qiang, Atomic Energy, 44(2). Feb. (2010)

[2] D.N.Edwards, B. Rose, An extension of the transfer matrix method to a beam transport system containing a solenoid[J], Nuclear Instruments & Methods, 1960, 7(2):135-144.

[3] G. Strang, Linear algebra and its applications[M], Academic Press, 1976.

ISBN: 978-3-95450-199-1 doi:10.18429/JACoW-SAP2017-TUAH4

# USING A BESSEL LIGHT BEAM AS AN ULTRA-SHORT PERIOD HELICAL UNDULATOR

B. C. Jiang, Q. L. Zhang, J. H. Chen and Z. T. Zhao, Shanghai Institute of Applied Physics, Chinese Academy of Sciences, Shanghai, China

*Abstract*

An undulator is a critical component to produce synchrotron radiation and free electron laser. When a Bessel light beam carrying the orbit angular momentum co-propagates with an electron beam, a net transverse deflection force will be subjected to the latter one. As a result of dephasing effect, the deflection force will oscillate and act as an undulator. For such a laser based undulator, the period length can reach sub-millimeter level, which will greatly reduce the electron energy for the required X-ray production.

## INTRODUCTION

A magnetostatic undulator is in periodic structures of dipole magnets [1, 2]. The static magnetic field of the undulator is perpendicular to the electron beam trajectory, and periodically changes its directions, which causes an electron beam bunch to follow an undulating trajectory, hence the energy radiations. The radiation brightness from an undulator at the resonance wavelength is $N^2$ times higher than that from a single bending magnet, where N is total period number of the undulator.

The radiation wavelength can be calculated by Eqs. (1) and (2) [2, 3]:

$$\lambda_{\mathrm{rad}} = \frac{\lambda_{\mathrm{u}}}{2\gamma^2}\left(1 + \frac{K^2}{2} + \gamma^2\theta^2\right), \qquad (1)$$

$$K = \frac{eB\lambda_{\mathrm{u}}}{2\pi m_e c} = 0.934B(T)\,\lambda_{\mathrm{u}}(\mathrm{cm}), \qquad (2)$$

where, $\lambda_u$ is period length of the undulator; $B$ is peak magnetic field of the undulator; $\lambda_{rad}$ is the radiation wavelength; $\theta$ is the radiation angle; $\gamma$, $e$ and $m_e$ are the Lorentz factor, charge and rest mass of electron, respectively; and $c$ is the speed of light.

An important direction of the undualtor improvement is to decrease the period length. The shorter is the period length of undulator, the lower is the electron energy required for a desired X-ray, hence a great reduction of the facility scale and cost.

For a practical configuration, $K$ value of an undulator should be in order of 1. To this end, the shorter the period length, the higher the peak magnetic field should be. This prevents the undulator period from being ultra-short. In-vacuum undulator was developed for short period approach [4, 5]. In this type of undulator, the permanent magnets are installed in a vacuum tank, thus the undulator pole gap can be much smaller, the peak field can be increased, and the period length can be reduced.

The discovery of increasing remanent field and coercivity of the permanent magnet at low temperatures provides the possibility of building cryogenic permanent magnet undulator (CPMU) [6, 7] with a shorter period, a little bit, though, at the cost of an additional liquid nitrogen cryogenic system. The superconducting technology helps to build undulators of even shorter periods [8, 9]. However, even for the state-of-the-arts technology, the period length of a magnetostatic undulator is beyond 1 mm [10]. It is possible for an RF undulator [11, 12] to achieve period length of shorter than 1 mm. However, for lacking of high power THz source, it is still hard to realize a millimeter-period undulator.

Optical undulator has been proposed for compact FEL purpose for years. When an intense and long enough laser pulse counter-propagates with the electron beam, the laser may act as an undulator [13–16]. The period length of optical undulator is in micron range. This requires that the electron beam is orders of magnitude brighter than the existing electron source for FEL generation. Laser plasma undulator [16, 17] was just proposed to build sub-millimeter period undulator, but the fact that the electrons do not pass through free space may prevent its use in storage rings.

In the following sections we will show that a Bessel light beam can be used for undulating relativistic electrons when it is co-propagating as shown in Figure 1. With the advent of high power laser, it is possible to achieve $K$ value of around 1 for Bessel light beam undulator (BLU) with period length approaching sub-millimeter.

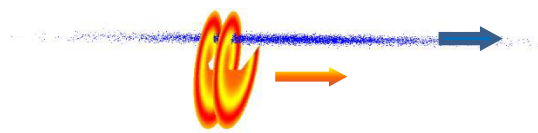

Figure 1: Sketch of Bessel light beam (red-orange vortex) interaction with electron beam (blue dot).

## TRANSVERSE FORCE OF BESSEL LIGHT BEAM TO THE RELATIVISTIC ELECTRON

For a monochromatic Bessel light beam, in the dimensionless system *(c=1)*, the electric and magnetic fields of the wave in the Cartesian coordinate for paraxial approximation can be expressed as [18]:

$$\begin{pmatrix}\mathcal{E}_x\\ \mathcal{E}_y\\ \mathcal{E}_z\end{pmatrix} = \begin{pmatrix}\kappa_- C_{M+1} + \kappa_+ C_{M-1}\\ \kappa_- S_{M+1} - \kappa_+ S_{M-1}\\ 2S_M\end{pmatrix}, \qquad (3\text{-a})$$

$$\begin{pmatrix}\mathcal{B}_x\\ \mathcal{B}_y\\ \mathcal{B}_z\end{pmatrix} = \begin{pmatrix}\kappa_- S_{M+1} + \kappa_+ S_{M-1}\\ -\kappa_- C_{M+1} + \kappa_+ C_{M-1}\\ 2C_M\end{pmatrix}, \qquad (3\text{-b})$$

$$C_M = cos(k_\parallel z - \chi\omega t + M\phi)\, J_M(k_\perp \rho), \qquad (4\text{-a})$$

$$S_M = sin(k_\parallel z - \chi\omega t + M\phi)\, J_M(k_\perp \rho), \qquad (4\text{-b})$$

where, $z$ is the light propagation direction, $\rho = \sqrt{x^2+y^2}$ is the transverse distance to the $z$ axis, $\phi$ is the azimuthal phase to the z axis, $M$ is the order of Bessel beam, and

ISBN: 978-3-95450-199-1 doi:10.18429/JACoW-SAP2017-TUAH4



$$\boldsymbol{\kappa}_{\pm} = \frac{\boldsymbol{k} \pm \boldsymbol{k}_{\parallel}}{\boldsymbol{k}_{\perp}}. \quad (5)$$

In this paper, we only consider the forward propagated wave with $\boldsymbol{\chi} = \mathbf{1}$. The wavenumbers have the following relationships,

$$\boldsymbol{k} = \sqrt{\boldsymbol{k}_{\parallel}{}^2 + \boldsymbol{k}_{\perp}{}^2}, \quad (6)$$

$$\boldsymbol{\omega} = \boldsymbol{c}\,\boldsymbol{k}, \quad (7)$$

The Lorentz force in the horizontal (x) and vertical (y) planes for a co-propagated relativistic electron ($v \cong$ c) can be derived by:

$$F_x(z,t,\rho,\phi) = -e\left(\boldsymbol{\mathcal{E}}_x - c\,\boldsymbol{\mathcal{B}}_y\right) = -2e\boldsymbol{\kappa}_{-}\boldsymbol{C}_{M+1}(z,t,\rho,\phi), \quad (8\text{-a})$$

$$F_y(z,t,\rho,\phi) = -e\left(\boldsymbol{\mathcal{E}}_y + c\,\boldsymbol{\mathcal{B}}_x\right) = -2e\boldsymbol{\kappa}_{-}\boldsymbol{S}_{M+1}(z,t,\rho,\phi). \quad (8\text{-b})$$

Forces in x and y planes expressed in Eq. (8) oscillate in a sin waveform with phase difference of π/2, forming a force like a helical undulator.

From Eqs. (4), (6) and (7), it can be found that the phase velocity of the Bessel beam is faster than the light speed. As the relativistic electron is in velocity of $v \cong c$, the phase slip of a relativistic electron to the light produces upconversion undulate period of the laser wavelength:

$$\lambda_{\mathrm{u}} = \frac{1}{1-\boldsymbol{k}_{\parallel}/\boldsymbol{k}}\lambda_{\mathrm{laser}}. \quad (9)$$

The key factor for a Bessel light to undulate the relativistic electron is that its phase velocity is faster than the light speed. The magnetic field can't be cancelled completely by the electric field when it is seen by a co-propagated relativistic electron, leaving a net periodic oscillated deflecting force. As EM field of Bessel light rotates in the transverse plane, by neglecting energy absorption from the laser to the electrons, BLU only produces circular polarized radiations.

## LASER POWER REQUIREMENT

An ideal Bessel light beam has an infinitely extended transverse profile and carries infinite power, but Bessel light beams in practice cannot be ideal, with finite radius and power. A non-ideal Bessel beam in radius $R$ has diffraction distance [19]:

$$L = R\frac{k}{\boldsymbol{k}_{\perp}}, \quad (10)$$

The Bessel light beam holds N rings within radius $R$ will be diffracted layer by layer until the innermost ring diffracts away at the end of diffraction distance.

For $k_{\perp}/k \ll 1$, the laser power is mainly determined by the EM term in right hand of Eq.(3) with $\boldsymbol{\kappa}_{+}$ coefficient. The power can be integrated approximate as:

$$P \approx 2\boldsymbol{\kappa}_{+}{}^2 \int_0^{2\pi} \mathrm{d}\phi \int_0^{R} \rho J_{M-1}(\boldsymbol{k}_{\perp}\rho)^2\, d\rho \quad (11)$$

Eq. (11) is in normalized form as it is directly derived from Eq. (3). For power calculation, a factor $cB_0^2/2\mu_0$ should be multiplied, where $B_0$ is the normalized magnetic field for Eq. (3), $\mu_0$ is the permeability of vacuum.

Take a $CO_2$ laser in wavelength of 10.6 μm for example, to produce an undulator of 47 periods, $\lambda_u$=0.53 mm, and $K_x$=0.5, a laser power of 9.3 TW is needed. The laser beam parameters are listed in Table 1.

Table 1: BLU Parameters

| | |
|---|---|
| Laser wavelength /μm | 10.6 |
| $\boldsymbol{k}_{\perp}/\boldsymbol{k}$ | 0.199 |
| $\boldsymbol{k}_{\parallel}/\boldsymbol{k}$ | 0.98 |
| M | 2 |
| $\lambda_{\mathrm{u}}$ / mm | 0.53 |
| R / mm | 5 |
| L / mm | 25 |
| Periods | 47 |
| Laser power / TW | 9.3 |
| Kx(K) | 0.5 (0.707) |

In Ref. [20] a laser carries OAM at TW level demonstrated the feasibility of building a BLU for X-ray production.

## BEAM TRACKING AND PHOTON FLUX

Here we take Shanghai soft X-ray linac beam [21] as an example for tracking, whose electron energy is 840 MeV. With BLU parameters listed in Table 1, 1.2 Å hard X-ray will be produced.

To maximize the deflection force, it is nature to align the electron beam at the place where $\boldsymbol{J}_{M+1}(\boldsymbol{k}_{\perp}\boldsymbol{\rho})$ gets its peak value, and where the deflecting force has a small range of flat top in amplitude in the radial direction, which allows a relatively large part of an electron beam to radiate monochromatically.

In the tracking, both transverse and longitudinal parts of the EM fields are counted while radiation effect is neglected. The tracking is mainly focused on finding out the electron trajectory which can be used for undulator phase error evaluation.

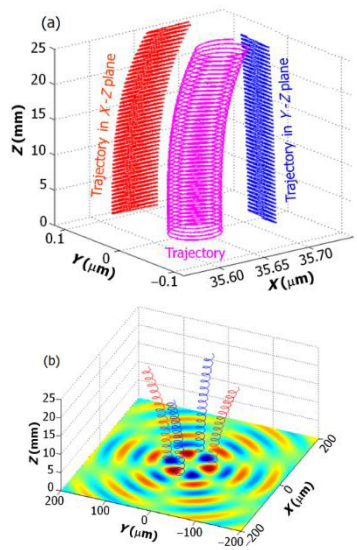


Figure 2: Tracking result of electron trajectory (a); and the defocus effect (b), with the zoomed beam trajectory for a clear view, and with the electrical field rotating anticlockwise in the bottom.

ISBN: 978-3-95450-199-1 doi:10.18429/JACoW-SAP2017-TUAH4

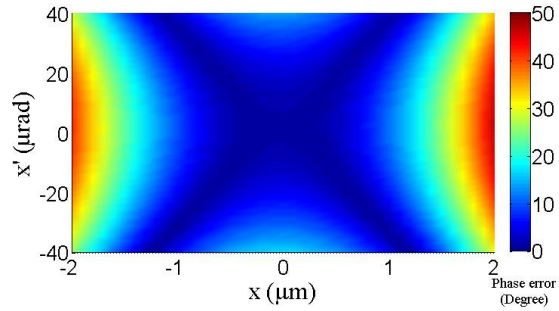


Figure 3: Radiation phase errors for electrons with different initial x-x' conditions.

In the tracking, it is found that the longitudinal electrical field causes an energy modulation of the electron beam, resulting in a deflecting effect in the radial direction. The defecting force is in axial symmetry, so the focus (for left handed helix) or defocus (for right handed helix) effects are in transverse directions as shown in Fig.2.

To evaluate how many radiations from the electrons in transverse phase space are monochromatic, the radiation phase error is calculated from electron trajectory. As shown in Figure 3, the BLU is sensitive to the transverse place where electron passes through, however it is tolerant to slope angle of the electron. It also shows that a monochromatic radiation is produced with the transverse acceptance of just around 2 microns, which requires a novel focus lattice design for the electron beam at the end of the linac [22].

## DISCUSSIONS

The BLU has unique properties that other types of undulators do not have. It only undulates a part of the electrons when the laser pulse is shorter than the electron beam. Because the Bessel light beam is at the speed of light, the interaction is limited at the place where electrons and the laser overlap in the longitudinal coordinate. This property can be used for short pulse (femtosecond) X-ray production with picosecond electron beam bunch.

The undulated electrons may shift backward in longitudinal coordinate, as the interaction is located in a part of longitudinal area of the electron beam, which may cause an electron beam density modulation.

From the preliminary tracking results, it can be found that BLU may radially focus (or defocus) electrons, which is different to quadrupoles and solenoids. More research efforts are needed for applications of the effects.

## ACKNOWLEDGMENTS

The authors thank Prof. Alex Chao greatly for useful discussions. Thanks also go to Prof. Qiaogen Zhou for discussion on undulator performances and Prof. Sheng Kanglong for language polishing.

## REFERENCES

[1] Julian Schwinger, *Phys. Review.* 75, 1912-1925, 1949.

[2] Kwang-Je Kim, *AIP Conference Proceedings* 184, 565(1989).

[3] Laser handbook, edited by W.B. Colson, C. Pellegrini and A. Reniery ( Elsevier Science Publisher B. V. , Amsterdam, 1990) Vol.6.

[4] W. Gudat *et al., Nucl. Instru. Meth.* A 246, 50, (1986).

[5] S. Yamamoto *et al., Rev. Sci. Instru.* 63, 400 (1992).

[6] T. Hara *et al., Phys. Rev. Spec. Top. Accel. Beams* 7, 050702 (2004).

[7] J. Chavanne *et al., Proc. of EPAC2008,* Genoa, Italy, 2243-2245.

[8] Casalbuoni S *et al., Synchrotron radiation news* 24-3, 14-19 (2011).

[9] Ivanyushenkov Y *et al.,*in *Proc. of PAC11,* New York, 1286.

[10]J. Clarke, The Science and Technology of Undulators and Wigglers (Oxford University Press, New York, 2004).

[11] Tsumoru Shintake *et al., Japanese Journal of Applied Physics,* 22-5, 844-851, (1983).

[12] Sami Tantawi *et al., Phys. Rev. Lett.* 112, 164802 (2014).

[13] M. Zolotorev, *Nucl. Instrum. Methods Phys. Res., Sect. A,* 483, 445 (2002).

[14]A. Bacci, M. Ferrario, C. Maroli, V. Petrillo, and L. Serafini, *Phys. Rev. ST Accel. Beams.* 9, 060704 (2006)

[15]P. Sprangle, B. Hafizi, and J. R. Penano, *Phys. Rev. ST Accel. Beams.* 12, 050702 (2009)

[16] S. G. Rykovanov, C. B. Schroeder, E. Esarey, C. G. R. Geddes, and W. P. Leemans, *Phys. Rev. Lett.* 114, 145003 (2015).

[17] S. G. Rykovanov, J.W. Wang, V. Yu. Kharin, B. Lei, C. B. Schroeder, C. G. R. Geddes, E. Esarey, and W. P. Leemans, *Phys. Rev. ST Accel. Beams.* 19, 090703 (2016)

[18] David L. Andrews, Mohamed Babiker, *The angular momentum of light,* Cambridge University Press, 2013.

[19] B. Hafizi, E. Esarey and P. Sprangle，*Physical Review E* 55, 3539.

[20] Yin Shi, Baifei Shen, Lingang Zhang, Xiaomei Zhang, Wenpeng Wang and Zhizhan Xu, *Phys. Rev. Lett.* 112, 235001 (2014)

[21] Z.T. Zhao and D. Wang,in *Proc. of FEL2010,* Malmo, Sweden, 15.

[22] Raimondi P, Seryi A. , Novel final focus design for future linear colliders. *Phys. Rev. Lett.,* 2001, 86(17): 3779.

ISBN: 978-3-95450-199-1 doi:10.18429/JACoW-SAP2017-TUBH2

# PIC SIMULATION OF THE HIGH CURRENT BEAM FOR THE LIA

Liao Shuqing, He Xiaozhong, IFP, CAEP, Mianyang, China
Liu Shuang, DEP, TSINGHUA. Beijing, China

*Abstract*

High current beams emitting and transport of the linear induction accelerator (LIA) injector are simulated by a PIC code. And then beam transport and accelerated with space charge from injector exit to the LIA exit is simulated by another PIC simulation code and the slice beam parameters variability are also presented by this paper.

## INTRODUCTION

The new type linear induction accelerator DRAGON-II is performed a multi-pulse x-ray flash radiography. The accelerator is delivered several about 20MeV (about 2% over the flattop), 2.0kA, 90ns(FWHM), 2000mm.mrad beams. To achieve the radiographic performance specifications, the time integrated beam spot size on the target should be less than 2mm. However, the interactions between the high energy intensity beams with the target may disrupt the beam spot size. These beam parameters make the new accelerator transport system the complicated system ever designed to transport a high current, high energy and long pulse beam. And designing the new accelerator transport system is challenging.

The DRAGON-II consists of pulse power system (triggering synchronizer, Marx generators and Blumlein lines), accelerator platform (injector, accelerator modules, beam transport system, beam downstream system), auxiliary system (vacuum system, isolated gas supply and water-cooling device). The pulse system that powers the injector for the new accelerator is capable of producing a 2.5-3 MV output pulse that is 90ns (FWHM). With the 2.5-3 MV diode voltage the cathode emits an about 2.0-2.5 kA pulse electron beam with more than 90ns (FWHM) current/energy "flat-top". After leaving the diode, the beam is accelerated by induction cells to 2.5-3MeV. Following the injector, these are a series of accelerator cells which consist of four accelerator cells and a vacuum cell. At the accelerator exit the beams are accelerated by all cells to about 20MeV. The beam downstream system focuses the high energy beams to target less than 2mm for the x-ray flash radiography.

The accelerator transport system consists of three sections. The first, a solenoid transport system consists of several large size solenoids which diameter are about 450mm. Namely the first transport system is the injector beam transport system. The second section consists of a series of solenoids which named accelerator cell solenoid. The second system transports the beam between the injector and the accelerator exit. The third transport system is the beam downstream system, the target beam line. In this paper we discuss the model of the transport sections; from the cathode to the accelerator exit.

## THE INJECTOR

A particle simulation code named CHIPIC [1] is utilized to model the transport of a 90ns pulse beam from the cathode emitting, through the anode hole, and to the injector exit. Particle simulations can provide additional information on the performance of the beam line, for example the beam slice emittance. Figure 1 shows the geometry for the PIC simulation and the transport solenoids.

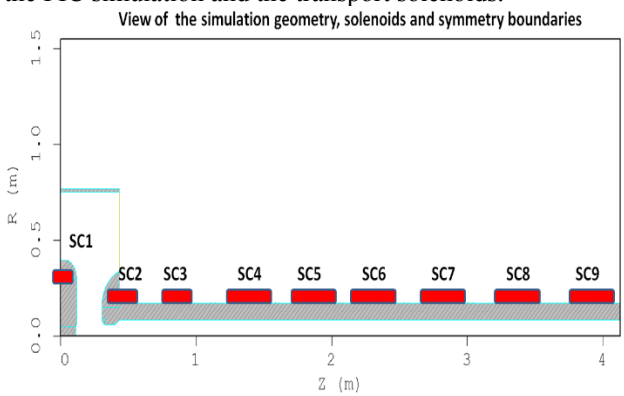


Figure 1: The geometry for the Injector simulation.

By the POSSION/SUPERFISH code, we obtain the injector axial magnetic field that Figure 2 shows. All the solenoids are designed at a lower tilt/offset that about 1mrad/0.5mm for the corkscrew control.

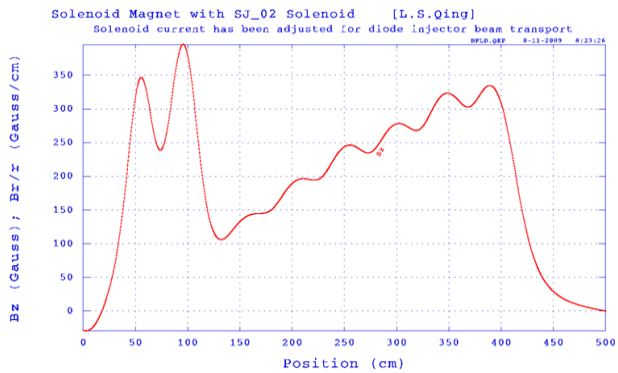


Figure 2: The axial magnetic field of the Injector.

A voltage pulse V(t) is applied to the injector. The different voltages lead to the different emit beam currents and the different cathode-anode gaps also lead to the different beam currents that Table.1 shows.

Table 1: Emit Beam Currents with the Voltages

| Voltage Mv | Emit current A |
|---|---|
| 1.2 | 738 |
| 2.4 | 1893 |
| 3 | 2543 |
| 3.6 | 3231 |
| 4.8 | 4679 |

ISBN: 978-3-95450-199-1 doi:10.18429/JACoW-SAP2017-TUBH2

The transport of the high current electronic diode beams is simulated in different excitation currents for solenoids. The slice beam emittance is less than 220mm.mrad and the envelope radius is lower 10mm at the injector exit that meet with the goal of controlling the emittance/radius at the injector exit for the accelerator. These beam parameters are decided by the all solenoids and the beam transport can be optimized by the PIC simulation. Figure 3 shows the beam transport which has been optimized. The optimized beam radius is about 9mm and the beam current is about 2.54kA. The slice beam rms emittance is about 100mm.mrad.

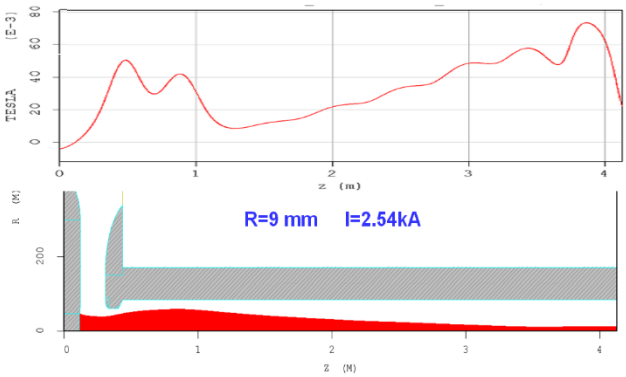


Figure 3: The beam transport which has been optimized.

## THE ACCELETATOR

This section reports the results of PIC simulations for beam transport from the injector exit to the LIA accelerator exit. We use particle simulation code named OPAL [2] to model the slice beam about 5ns pulse width transport.

The initial beam parameters are about 2.6MeV, 1000 mm-mrad. The slice beam is transported through the LIA accelerator using solenoidal magnetic focusing fields which is an efficient and convenient means that has been used in all LIAs. The magnetic field produced by these magnets is called the tune of the accelerator. Figure 4 shows a plot of the axial magnetic flux density on axis as calculated by the POSSION/SUPERFISH code.

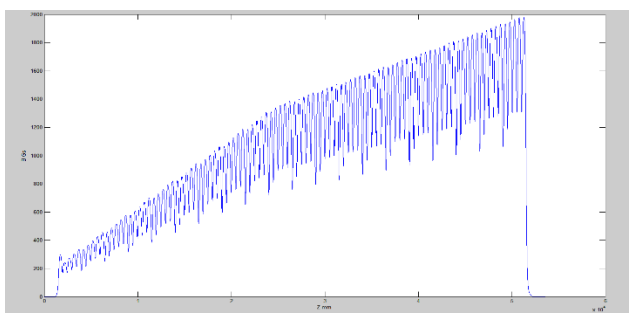

Figure 4: The axial magnetic field of the Accelerator.

We also use the POSSION/SUPERFISH code for the accelerator gap electric field calculation. Figure 5 shows the electrostatic potentials for this simulation with 200 kV across the gap. Only the features of the gap region that might affect the field on axis were included. Figure 6 shows the resulting field on axis, which was used with the gap locations to create an input file for PIC simulations.

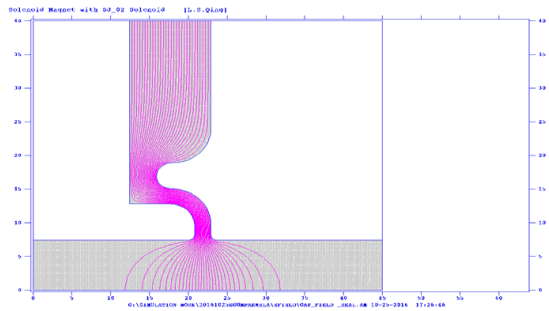

Figure 5: Equipotentials of the accelerating electric field in the region of the DRAGON-II gap for 200-kV gap voltage. Simulation was performed using the POSSION/SUPERFISH code.

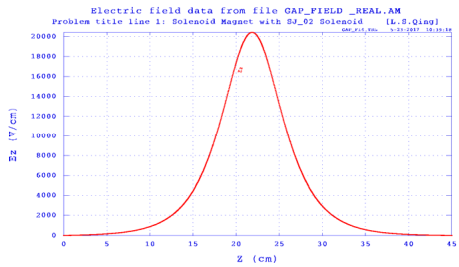


Figure 6: Accelerating electric field on axis calculated by POSSION/SUPERFISH for the DRAGON-II cell.

We use the PIC code OPAL to simulate beam transport from the injector exit to the accelerator exit for the DRAGON-II within the beam pulse. Space charge in particle slices are included in the simulations.

Figure 7 shows the particle load of 1000000 particles for a 5ns pulse of a nominal 2.6MeV, 2kA Gaussian distribution beam with a normalized emittance of 1000 mm-mrad at the injector exit of DRAGON-II.

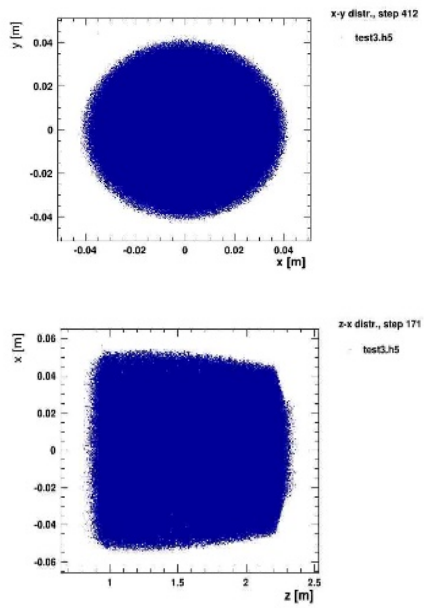


Figure 6: Initial particles space at injector exit for a 2.6 MeV, 2 kA and 1000 mm-mrad beam.

Figure 7 shows the particle longitudinal load for the 5ns pulse at the accelerator axis position about 1.5m, 10m, 20m and 30m of DRAGON-II. And figure 8 shows the reference particle energy gains via the accelerator gap voltage.

ISBN: 978-3-95450-199-1 doi:10.18429/JACoW-SAP2017-TUBH2



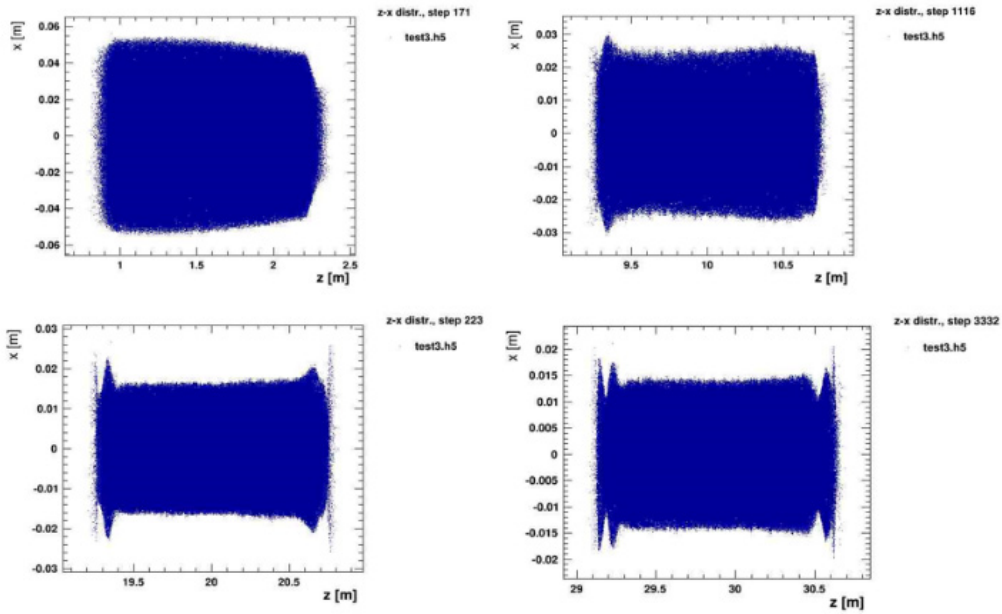


Figure 7: Particles longitudinal space at the different axis position about 1.5m, 10m, 20m and 30m of DRAGON-II.

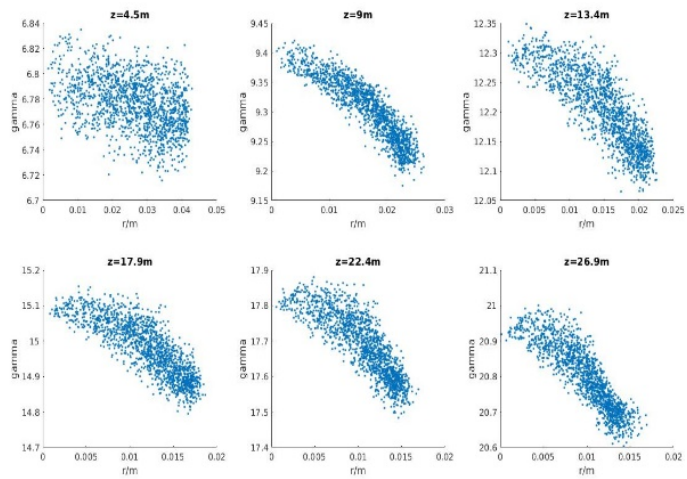


Figure 9: The slice beam(~0.25ns) energy spectrum.

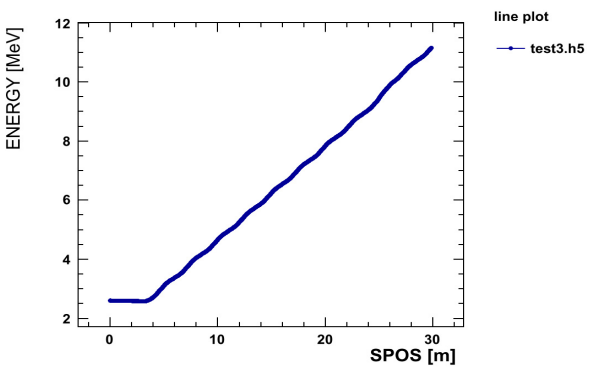


Figure 8: The reference particle energy.

An important figure of merit in the performance of DRAGON-II is the slice beam energy spectrum variability.Figure 9 shows the slice beam (~0.25ns) energy spectrum at the accelerator different axis position.

## CONCLUSIONS

PIC simulations provide significant information about the performance of the LIA beamline by including a variety of physics models for transport components. Simulations for the DRAGON-II beamline have been performed including space charge and other effects. Estimates of the energy variation of the slice beam and particles longitudinal space at the different axis position can be determined with different transport magnetic fields.

## REFERENCES

[1] DI Jun,Zhu Da-jun,LIU Shenggang, "Electromagnetic Field Algorithms of CHIPIC Code," *journal of UEST of China*,Vol.34, No.4, Aug. 2005.

[2] The OPAL Framework User's Reference Manual, PSI-PR-08-02.

ISBN: 978-3-95450-199-1 doi:10.18429/JACoW-SAP2017-TUBH4

# CENTRAL REGION DESIGN OF THE HUST SCC250 SUPERCONDUCTING CYCLOTRON *

Z. J. Zeng†, K. J. Fan, Huazhong University of Science and Technology, Wuhan, China

*Abstract*

A superconducting cyclotron based proton therapy system is being developed at Huazhong University of Science and Technology (HUST). The compactness of superconducting cyclotron imposes a challenge to the central region design. This paper describes beam dynamic studies in the central region. Beam performance at the initial 4 or so turns is crucial that determines the beam emittance, energy divergence and extraction efficiency. Therefore, considerable efforts have been made to the central region design and optimization. The electric and magnetic field distribution are numerically calculated by the program OPERA. Particle trajectories are simulated by means of the computer code Z3CYCLONE and the track command in OPERA. Finally, an optimum central region configuration is obtained which meets the stringent requirements and further studies is carried out about the beam radial and axial motion based on the designed central region.

## INTRODUCTION

Proton therapy has shown advantages in treating several kinds of cancer and has become a favorable treatment option for patients, which shows considerable advantages over conventional photon therapy. In recent years, there has been a massive growth in the development of proton therapy centers in the world particularly in China. The cancer incidence in China is the greatest in the world, and cancer is the leading cause of death, which has become a major public health problem in China. In order to meet the fast growing demand for proton therapy, Chinese government decided to support the development of a superconducting cyclotron based proton therapy facility in the National Key Research and Development Program at 2016. This project is being taken by several institutes and Huazhong University of Science and Technology (HUST) plays a crucial role in this program.

The superconducting cyclotron HUST-SCC250 has the advantage of minimizing the size, however, it has as a drawback of difficult to design a very compact central region. The central region uses an internal cold cathode PIG source to simplify the structure. The configuration of the central region is optimized by using the OPREA code, which can numerically simulate the electric and magnetic field distribution exactly. The beam dynamics studies in the central region are carried out using the beam tracking codes Z3CYCLONE and the track command in OPERA.

* Work Work supported by national key R & D program, 2016YFC0105303
† zengzhijie@hust.edu.cn

## CENTRAL REGION DESIGN

One of the challenging design tasks of a superconducting cyclotrons is the central region, where the initial proton orbits are crucial in determining the properties of the final beam.

To study the beam dynamics in the central region, considerable efforts have been made to optimize the central region geometry. The optimum central region design could be achieved using iterative process. Two main problems concerning the central region are the axial motion and radial motion [1].The main parameters of the central region are listed in Table 1.

Table 1: Basic Parameters

| Parameters | Value |
|---|---|
| DEE width | 50° |
| DEE voltage | 60 kV |
| Harmonic mode | 2 |
| RF frequency | 75.52 MHz |
| Injection radius | 1.18 cm |
| Injection angle | 122° |
| Central magnetic field | 2.476 T |

The design process of central region is illustrated as follows,

1) Assuming a uniform magnetic field in the central region, the initial condition of the beam after circulating one turn is obtained based on the ideal energy gain. Then, the initial condition is revised in order to make beam be centered.

2) Using backward algorithm to determine the position of the ion source.

3) Beam forward tracking algorithm is again used to optimize the electrode structure.

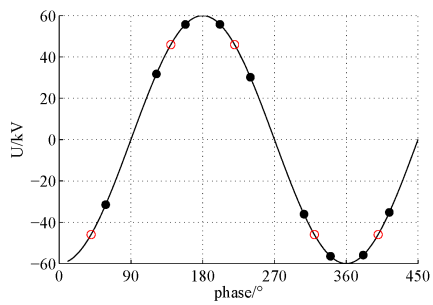


Figure 1: RF phase of the proton crossing the DEE boundary.

Ignoring the transition effect of the accelerating gap, the maximum energy gain on certain RF phases can be obtained, which is shown in Fig. 1 marked as the hollow circles.

ISBN: 978-3-95450-199-1 doi:10.18429/JACoW-SAP2017-TUBH4



In comparison, the RF phases when the proton crosses the DEE boundaries are shown as the solid circles in Fig. 1. The electrode structure is revised precisely to adjust the RF phase in order that the energy gain for beam of a certain initial RF phase can be reasonable. Simultaneously, beam for a certain range of initial phases can have better energy gain when crossing the gaps. The radial acceptance of beam can be adjusted in that way [2–5].

## ELECTRIC AND MAGNETIC ANALYSIS

The parameterized model of central region is made using SOLIDWORKS at first, then it is imported into the Finite Element Analysis (FEA) software OPERA to calculate the electric field [6, 7]. Then beam dynamics analysis is carried out by using the track command in OPERA. The parameterized model is in turn revised to meet the requirements for the stable beam radial motion. Finally, the optimized electrode structure in the central region is designed as shown in Fig. 2, and correspondingly the potential map of the central region is shown in Fig. 3.

The axial focusing force of the magnetic field is small for the radial logarithmic gradient of the magnetic field is higher than zero. To optimize the axial focusing of the beam, the magnet pole shape is initially designed. The average magnetic field distribution is shown in Fig. 4 and the radial distribution of the vertical focusing tunes is shown in Fig. 5.

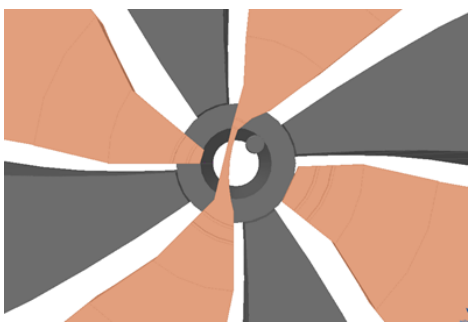

Figure 2: Structure diagram of the central region electrode.

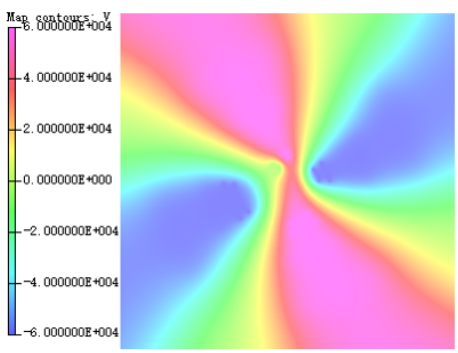


Figure 3: Potential distribution diagram calculated by TOSCA.

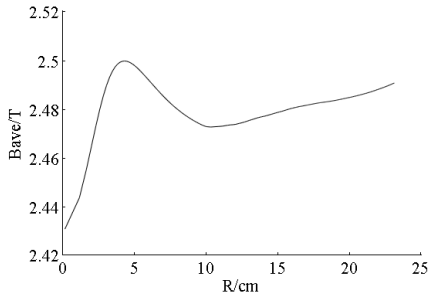


Figure 4: Radial distribution of the central region average magnetic field.

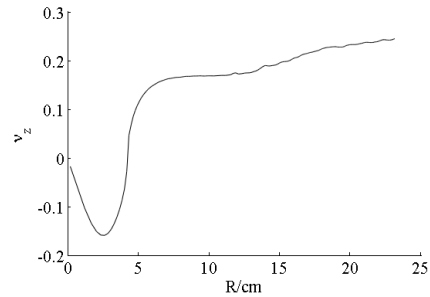


Figure 5: Radial distribution of the vertical focusing tunes.

## BEAM DYNAMICS IN THE CENTRAL REGION

### *Radial Movement Analysis*

Z3CYCLONE is adopted to calculate the beam orbit parameters at different initial conditions [8, 9]. The injection radius is 1.18 cm, the injection angle is 122° and several initial RF phases are selected for comparison. As shown in Fig. 6, the radial RF phase acceptance is about 20°, from 242° to 262°.

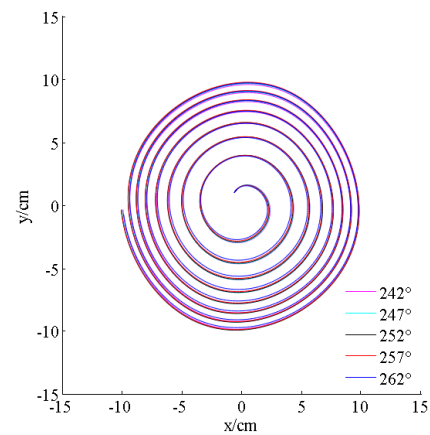


Figure 6: Particle orbit diagram for the initial phase ranging from 242° to 262°.

Ignoring the transition effect in the accelerating gaps, the theoretical energy gain per turn is given,

ISBN: 978-3-95450-199-1 doi:10.18429/JACoW-SAP2017-TUBH4

$$E_{gain} = n \cdot U_m \cdot \sin(\frac{\theta_{DEE} \cdot h}{2}) = 8 \times 0.06 \times \sin(\frac{50 \times 2}{2}) = 0.3677 MeV \quad (1)$$

In numerical tracking, the maximum energy gain of one turn is 0.35 MeV, which is 17.7 keV smaller than the theoretical value (as shown in Fig. 7).

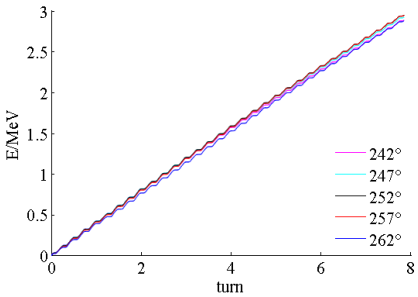


Figure 7: Energy gain diagram.

Figure 8 shows the maximum deviation between the instantaneous beam curvature center and the center of the cyclotron. The deviation is less than 1.8 cm in both x and y direction which is acceptable.

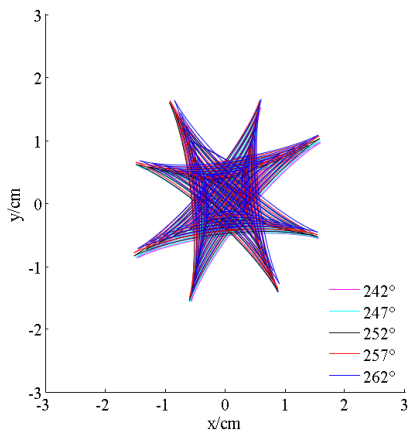


Figure 8: Particle orbit curvature center diagram.

Similarly, the calculated result of energy gain with Z3CYCLONE is cross checked by using the track command in OPERA, which is shown in Fig. 9. The relative error of energy gain for the first 4 turns is less than 1%, which shows the reliability of the orbit dynamics results.

### *Axial Movement Analysis*

The axial movement of the beam is subjected to the electromagnetic force. Considering the half height of the ion source slit is 0.275 cm, axial movements of the beam starting form different initial conditions are analyzed here and shown in Fig. 10 and Fig. 11. The half height of the channel within r=5 cm is about 0.45 cm, thus the beam will not be

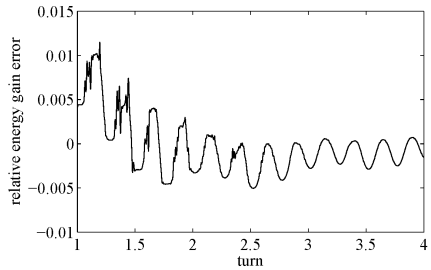


Figure 9: Relative energy gain error for OPERA vs Z3CYCLONE.

lost as shown in the figures. At the same time, the electric focusing force is greater for beam of positive phases which is in good agreement with the theoretical result.

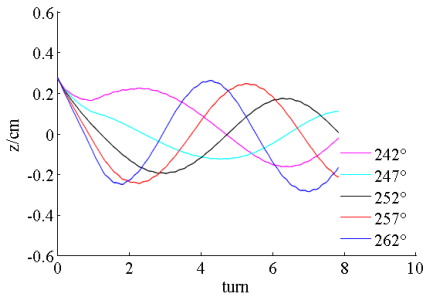


Figure 10: The vertical motion of various RF phase beams starting at z=0.275 cm, $p_z$=0.

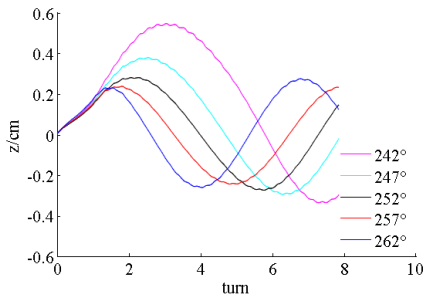


Figure 11: The vertical motion of various RF phase beams starting at z=0, $p_z$=0.0203 cm.

## CONCLUSION

This paper introduces the design process of the central region of the superconducting cyclotron HUST-SCC250 for proton therapy. The compactness of the cyclotron makes the design difficult. The central region is optimized iteratively by using several codes, SOLIDWORKS, OPERA and Z3CYCLONE, which finally meets the requirements for proton therapy. The optimal parameters are as follows, the phase acceptance is about 20°, the maximum deviation between the instantaneous beam curvature center and the center of the cyclotron is controlled within 1.8 cm.

ISBN: 978-3-95450-199-1 doi:10.18429/JACoW-SAP2017-TUBH4



## REFERENCES

[1] J. W. Kim, "Magnetic fields and beam optics studies of a 250MeV superconducting proton radiotherapy cyclotron," *Nucl. Instr. Meth*, vol. 582, pp. 366-373, (2007)

[2] V. Smirnov *et al.*, "Design study of an ultra-compact superconducting cyclotron for isotope production," *Nucl. Instr. Meth*, vol. 763, pp. 6-12, (2014)

[3] S. Y. Jung *et al.*, "Central region of SKKUCY-9 compact cyclotron," *Journal of Instrumentation*, 9(04): T04005, (2014)

[4] D. Toprek and L. Milinkovic, in *Proc. EPAC'94*, pp. 2361-2363

[5] D. Campo *et al.*, "Central region and static orbit study for the 300 A MeV superconducting cyclotron," *Cyclotrons and Their Applications*, pp. 391-393, (2007)

[6] Vector Fields Limited, OPERA-3D User Guide & Reference Manual, Oxford, (2006)

[7] H. Houtman, F. W. Jones and C. J. Kost, *Computers in Physics*, 8(4): 469, (1994)

[8] MSU NSCL Accelerator Group, *Z3CYCLONE. Instruction Manual*, Version 4.0., MSU, USA, (1993)

[9] C. Baumgarten *et al.*, "A beam profile measurement in the ACCEL 250MeV medical proton cyclotron," *Nucl. Instr. Meth*, vol. 569, pp. 706-712, (2006)

ISBN: 978-3-95450-199-1 doi:10.18429/JACoW-SAP2017-TUCH3

# INCOHERENT TRANSVERSE TUNE SHIFT CAUSED BY SPACE-CHARGE EFFECTS IN HEPS STORAGE RING AND BOOSTER

Chongchong Du†, Jiuqing Wang, IHEP, Beijing, China

*Abstract*

In cases of low beam energy and high particle densities, space-charge effects become necessary discussions on transverse beam dynamics. It may cause a big enough tune shift in a circular accelerator moving the beam onto a resonance. In this paper, the transverse tune shift in High Energy Photon Source (HEPS) storage ring and booster ring caused by space-charge effects is firstly estimated based on the existing theory. Since the tune shift is at the level of 0.2, it may move the beam onto a resonance in the operation mode with high bunch charges. Then some simulations are made by tracking particles with elegant in the HEPS storage ring and booster including the space-charge effects. During the tracking, some particles are lost in HEPS booster ring with bunch charge of 14.4nC for the so called "swap-out" mode. Further simulation shows that no particles would be lost if the charge of single bunch was less than 8.6nC in HEPS booster.

## INTROUDUCTION

The High Energy Photon Source (HEPS), with a beam energy of 6 GeV, a natural emittance of 59.4 pm·rad and a storage ring circumference of 1295.6m, is a diffraction-limited storage ring to be built in Beijing [1]. The beam current is 200mA, and currently two filling patterns are under consideration. One is the high brightness mode with 648 bunches and the other one is the timing mode with 60 bunches.

The space-charge effect forces the beam to defocus transversely to produce tune shift, which may cause the particles to cross the resonance lines during the accumulation and acceleration process, resulting in loss of the beam or deterioration of the beam quality. Although space-charge effects is often overlooked in the discussion of high-energy accelerators, it must be taken into account in the case of low energy and high particle density. Considering the ultra-low-emittance and the mode of 60 bunches with single bunch charge 14.4 nC in HEPS storage ring, space-charge effects may result in deterioration of the beam quality. Also, the booster is ramping from low energy 300 MeV, and the single bunch charge is large with "swap-out" mode, space-charge effects may result in loss of the beam. So we study the transverse tune shift in HEPS storage ring and booster ring caused by space-charge effects.

In this paper, based on current parameters [2], the transverse tune shift in HEPS storage ring and booster ring caused by space-charge effects is firstly estimated based on the existing theory. Some simulations are made by tracking particles with elegant [3] in HEPS storage ring and booster ring including the space-charge effects.

† ducc@ihep.ac.cn

## TUNE SHIFT THEORY

Due to the nonuniform charge distribution within a beam, tune shifts are not the same for all particles. Only particles close to the beam center suffer the maximum tune shift, but less affect betatron oscillation amplitudes. The space-charge effects therefore introduces a tune spread rather than a coherent tune shift and we refer to this effect as the incoherent space-charge tune shift.

The incoherent space-charge tune shift is [4]

$$\Delta\nu_{x,y} = -\frac{\lambda r_c}{(2\pi)\beta^2\gamma^3}\left[\oint \frac{\beta_{x,y}}{\sigma_{x,y}(\sigma_x+\sigma_y)}dz + 2(1+\beta^2\gamma^2 B)\int_0^{L_{vac}}\frac{\varepsilon_1\beta_{x,y}}{b^2}dz 2\beta^2\gamma^2 B\int_0^{L_{mag}}\frac{\varepsilon_2\beta_{x,y}}{g^2}dz\right] \quad (1)$$

where $\lambda = \frac{N_{tot}}{n_b l_b} = \frac{N_{tot}}{n_b\sqrt{2\pi}\sigma_l}$ is the linear particle density, $N_{tot}$ is the total number of particle in the circulating beam, $n_b$ is the number of bunches, $\sigma_l$ is the standard bunch length for a Gaussian distribution, $r_c = \frac{q^2}{4\pi\epsilon_0 mc^2}$ is the classical particle radius, $\sigma_{x,y}$ is the beam size, $B = \frac{n_b l_b}{2\pi R}$ is the bunch occupation along the ring circumference, b is the vertical half axis of an elliptical vacuum chamber, a is the horizontal half axis, as shown in Fig. 1, $\varepsilon_1$ and $\varepsilon_2$ are the Laslett form factors, $\varepsilon_2 = \frac{\pi^2}{24}$, $\varepsilon_1$ is compiled in Table 1.

Table 1: Laslett Incoherent Tune Shift form Factors for Elliptical Vacuum Chamber[4,5]

| a/b | 1 | 6/5 | 5/4 | 4/3 | 3/2 | 2/1 | ∞ |
|---|---|---|---|---|---|---|---|
| $\varepsilon_1$ | 0 | 0.065 | 0.09 | 0.107 | 0.134 | 0.172 | $\frac{\pi^2}{48}$ |

In equation (1), the loop integral is equal to the total length of the ring, the integration length $L_{vac}$ is equal to the total length of the vacuum chamber, $L_{mag}$ is the total length of magnets along the ring circumference.

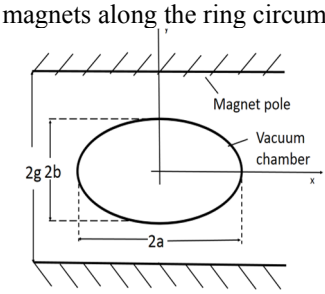


Figure 1: Metallic vacuum chamber and ferromagnetic boundaries.

## TUNE SHIFT IN STORAGE RING

The main parameters of the HEPS storage ring used for

ISBN: 978-3-95450-199-1 doi:10.18429/JACoW-SAP2017-TUCH3



space chare effect calculation are listed in Table 2. The natural emittance and the circumference are 59.4 pm·rad and 1295.6 m, respectively. The radius of circular vacuum chamber is 11mm in HEPS storage ring with $\varepsilon_1 = 0$, $\varepsilon_2 = \frac{\pi^2}{24}$.

Table 2: Main Parameters of the HEPS Storage Ring [2]

| Parameter | Symbol,unit | HEPS |
|---|---|---|
| Beam energy | E, GeV | 6 |
| Beam current | $I_0$, mA | 200 |
| Bunch number | $n_b$ | 648/60 * |
| Bunch population | N | 8.33e9/9e10 |
| Bunch current | $I_b$, mA | 0.3/3.3 |
| Bunch length | $\sigma_z$, mm | 3 |
| Emittance | $\varepsilon_x/\varepsilon_y$, pm·rad | 59.4/5.94 |
| Betatron tune | $\nu_x/\nu_y$ | 116.16/41.12 |

*For the mode of 648 bunches, single bunch population is 8.33e9 and single bunch charge is 1.33 nC; for the mode of 60 bunches, single bunch population is 9e10 and single bunch charge is 14.4 nC.

The calculation of incoherent space-charge tune shift is listed in Table 3. The range of incoherent tune shift with 648 bunches and 60 bunches in resonance lines diagram are shown in Fig. 2. Note that the incoherent tune shift with 648 bunches is far from the resonance lines, however, the incoherent tune shift with 60 bunches cross the resonance lines. So we studied the case of 14.4nC bunch charge for the mode of 60 bunches with elegant [3].

Table 3: The Calculation of Incoherent

| | Tune shift | Bunch number | |
|---|---|---|---|
| HEPS | | 648 | 60 |
| 6GeV | $\Delta\nu_x$ | -3.2e-3 | -0.035 |
| | $\Delta\nu_y$ | -1.82e-2 | -0.196 |

Particles are tracked through a zero length multipole to simulate space charge effects in elegant [3]. 10000 particles are tracked with only the space-charge effects for 10000 turns, and no particles are lost. We recorded each of particle coordinates, then processed frequency of each particle by using Fourier Transforms. The particle statistics of tune shift caused by space-charge effects in the horizontal and vertical direction are shown in Fig 3. The average value of $\Delta\nu_x$ is –0.0343, and the average value of $\Delta\nu_y$ is –0.164. It can be seen that the simulation results are consistent with the calculated results (Table 3).

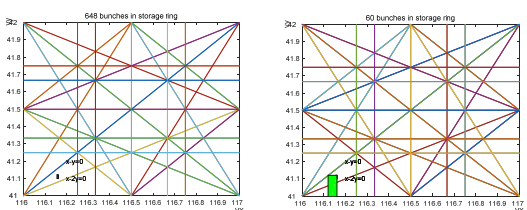


Figure 2: The range of incoherent tune shift with 648 bunches and 60 bunches in resonance lines diagram.

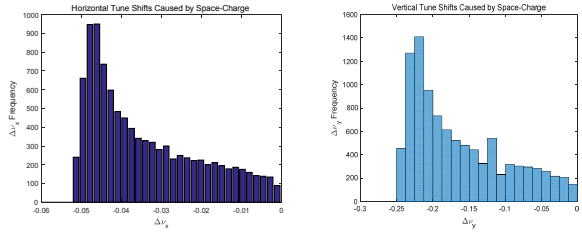


Figure 3: The particle statistics of tune shift caused by space-charge effects in the horizontal (x) and vertical direction (y), respectively.

## TUNE SHIFT IN BOOSTER

The main parameters of the HEPS booster used for space chare effect calculation are listed in Table 4. The circumference is 431.77 m. The vertical and horizontal half axis of elliptical vacuum chamber are 12.5mm and 15mm in HEPS booster, with $\varepsilon_1 = 0.065$, $\varepsilon_2 = \frac{\pi^2}{24}$.

Table 4: Main Parameters of the Booster [2]

| Parameter | Symbol, unit | Low energy | High energy |
|---|---|---|---|
| Beam energy | E, GeV | 0.3 | 6 |
| Beam current | $I_0$, mA | 15 | 15 |
| Bunch number | $n_b$ | 30 | 30 |
| Bunch current | $I_b$, mA | 0.5 | 0.5 |
| Bunch population | N | 4.5e9 | 4.5e9 |
| Bunch length | $\sigma_z$, mm | 30 | 10 |
| Emittance | $\varepsilon_x/\varepsilon_y$,nm·rad | 70/70 | 4.1/0.4 |
| Betatron tune | $\nu_x/\nu_y$ | 26.3/8.13 | |

The calculation of incoherent tune shift with 300MeV and 6GeV are listed in Table 5. The range of incoherent tune shift with 300MeV is shown in Fig.4. Fig 5 shows the change of tune shift with ramping in booster. Note that the incoherent tune shift with 300MeV is far from the resonance lines, then we studied incoherent tune shift for the "swap out" mode.

Table 5: The Calculation of Incoherent Tune Shift with 300MeV and 6GeV in Booster

| | Tune shift | N=4.5e9 |
|---|---|---|
| 300MeV | $\Delta\nu_x$ | -5.1e-4 |
| | $\Delta\nu_y$ | -7.1e-4 |
| 6GeV | $\Delta\nu_x$ | -1.49e-5 |
| | $\Delta\nu_y$ | -2.91e-5 |

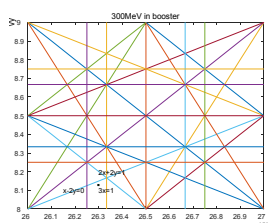


Figure 4: The range of incoherent tune shift with 300MeV in resonance lines diagram.

ISBN: 978-3-95450-199-1 doi:10.18429/JACoW-SAP2017-TUCH3

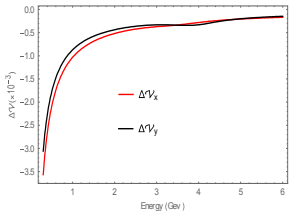


Figure 5: the change of tune shift with ramping in booster.

In the "swap-out" mode [1], the bunch charge of Booster is the same as that of the storage ring. Other parameters and simulations are the same as Table 4. The calculation of incoherent tune shift with 300MeV and 6GeV are listed in Table 6. The range of incoherent tune shift with 300MeV for "swap-out" mode with 14.4 nC single bunch charge is shown in Fig. 6. The change of tune shift with ramping in booster with 14.4 nC bunch charge are shown in Fig. 7. The particle statistics of tune shift caused by space-charge effects in the horizontal and vertical direction with 14.4nC bunch charge are shown in Fig 8. The average value of $\Delta\nu_x$ is –0.015, and the average value of $\Delta\nu_y$ is –0.0145. It can be seen that the simulation results are consistent with the calculated results (Table 6). However, some particles are lost in the case of 14.4nC bunch charge. This may be the result of some particles reaching the vertical aperture in the case of large charge and low energy. No particles would be lost if the charge of single bunch was less than 8.6nC in HEPS booster.

Table 6: The Calculation of Incoherent Tune Shift for "swap-out" Mode in Booster

| | Tune shift | N=8.33e9 (1.33nC) | N=9e10 (14.4nC) |
|---|---|---|---|
| 300MeV | $\Delta\nu_x$ | -9.44e-4 | -1.02e-2 |
| | $\Delta\nu_y$ | -1.3e-3 | -1.42e-2 |
| 6GeV | $\Delta\nu_x$ | -2.76e-5 | -2.98e-4 |
| | $\Delta\nu_y$ | -5.39e-5 | -5.82e-4 |

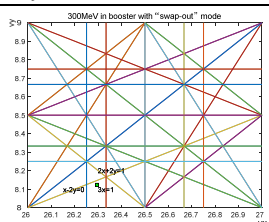


Figure 6: The range of incoherent tune shift with 300MeV for "swap-out" mode with 14.4 nC single bunch charge.

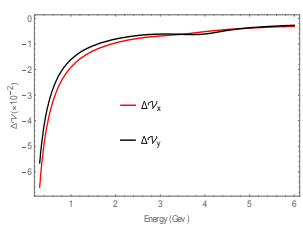


Figure 7: The change of incoherent tune shift with ramping in booster with 14.4 nC single bunch charge.

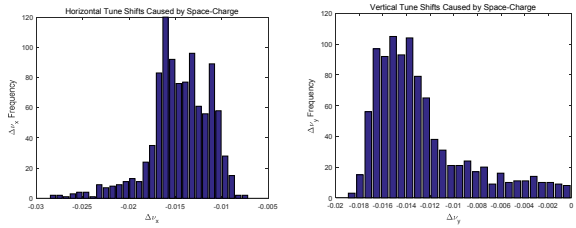


Figure 8: The particle statistics of tune shift caused by space-charge effects in the horizontal and vertical direction with14.4nC bunch charge, respectively.

## CONCLUSION

Since the vertical tune shift is at the level of 0.2 in the operation mode with 14.4nC bunch charge, it move the beam onto a resonance. However, it does not affect the beam from the results of particle tracking, the tune shift of simulation results are also consistent with that of calculated results. I suggest that stretch beam length and adjust the tune shift. Moreover, we calculate the change of tune shift with ramping in booster. In the "swap-out" mode, the tune shift of simulation results are also consistent with that of calculated results with 14.4nC bunch charge at 300MeV. However, some particles are lost. This is the result of some particles reaching the vertical aperture in the case of large charge and low energy, the reason of reaching the vertical aperture is under discussion. I suggest that bunch charge should be less in the case of low beam energy. After simulating different bunch charge, no particles would be lost if the charge of single bunch was less than 8.6nC in HEPS booster.

## ACKNOWLEDGENMENT

The author would like to thank Saike Tian for help with the elegant code.

## REFERENCES

[1] G. Xu, Y. Jiao and Y. Peng, *Chin. Phys. C*, 40 (2): 027001.

[2] HEPS Accelerator Physical Group, Progress Report of the Physical Design and Study on the HEPS *Accelerator Physics*, 12-04, 2016.

[3] M. Borland, "elegant: A Flexible SDDS-Compliant Code for Accelerator Simulation," Advanced Photon Source LS-287, September 2000.

[4] Helmut Wiedemann, *Particle Accelerator Physics*, third edition.

[5] L.J. Laslett, *BNL Report* 7534(1963), p.324.

ISBN: 978-3-95450-199-1 doi:10.18429/JACoW-SAP2017-TUDH2



# MEGA-ELECTRON-VOLT ULTRAFAST ELECTRON DIFFRACTION AND MICROSCOPE AT TSINGHUA UNIVERSITY*

Z. Zhou, Y.C. Du, L.X. Yan, W.H. Huang† and C.X. Tang
Department of Engineering Physics, Tsinghua University, Beijing, China

*Abstract*

Photocathode gun enabled high brightness, relativistic electron beams with femtoseconds to picosecond tuneable time structure are powerful tools for structural dynamics study. A prototype MeV UED system has been built and operated at Accelerator laboratory of Tsinghua University since a decade ago. Experiments of high quality single-shot static diffraction as well as pump-probe based dynamical process have been successfully conducted, especially the pump-probe experiment in continuously-time resolved mode to achieve better temporal resolution. These studies demonstrated the sub-picosecond timescale and atomic length resolving capabilities of our UED facility. To meet the growing interest of ultrafast sciences based on MeV UED facility, we are upgrading it to a user facility. Meanwhile the concept design of ultrafast electron microscope is proceeding. The current status of UED/UEM facility will be reported in this paper.

## INTRODUCTIONS

High brightness electron beams with ultrashort pulse duration are suitable probes for observing structural changes with ultrahigh spatiotemporal resolution. Compared to X-ray probes, electrons serve several unique advantages: $10^4$-$10^6$ times larger scattering cross sections, $10^3$ times less radiation damage and much easier manipulability [1]. Moreover, electrons are sensitive to both electrons and nuclei in material, thus making it an ideal complementary tools for understanding ultrafast structural dynamics.

In 1980s, the concept of ultrafast electron diffraction (UED) was proposed and demonstrated by G. Mourou et al [2], based on pump-probe method, where the electrons are generated by high voltage photocathode DC gun, and then probe the laser pumped sample structures on the atomic level and ps time domain. Following this novel and powerful technique, numbers of UED facilities have been constructed and many remarkable experimental results have been generated [3]. However, the temporal resolution of DC-based keV UED facility is limited to picosecond scale because of the strong space charge effect, which causes severe pulse elongating with increasing charge density and drift length. To overcome these barriers, photocathode rf gun was proposed to serve as the high brightness beam source for UED facility [4], in which the electrons are quickly accelerated to a few MeV and space charge force is dramatically suppressed since it scales as $\gamma^{-3}$, where $\gamma$ is the Lorentz factor. Meanwhile, utilization of MeV electron probes also solves the problems of velocity mismatch, where electron travels slower then light in sample, especially in gas sample or surface. Since then, intensive efforts have been devoted to development of MeV UED facilities [5-9], including machine performance, methodology and science application.

On the other hand, diffraction patterns are the Fourier transformation of the nuclei and electrons density distribution of the sample, thus no spatial resolution is achievable is UED. Therefore, to observe directly the image of the sample with sub-angstrom space resolution and sub-ps time resolution is indispensable, which is the main purpose of ultrafast electron microscope (UEM). Currently, most widely used UEM facility are based on photocathode DC gun, where the electron energy is limited to hundreds of keV due to the limited accelerating gradient. Problems of strong space charge effected are also encountered in keV UEM, resulting in pulse duration and energy spread increasing during propagations.

To overcome these problems, a S-band photocathode rf gun based UED prototype has been constructed in Tsinghua university since 2008, both high quality static diffraction and pump-probe experiments were successfully conducted. Now we are upgrading it to a user facility using a more flexible and versatile beamline design and a state-of-out new power source. Meanwhile, the design of UEM is ongoing, where a set of permanent magnet quadruplets (PMQs) are employed as a single imaging unit, different to the commonly used superconducting solenoids. The summary of previous work and the current status of the UED/UEM facility in Tsinghua will be present in this paper.

## UED RESEARCH AT THU

The schematic of the prototype UED instrument is shown in Fig.1 [10], where the electrons are generated by a S-band photocathode rf gun and focused by a magnetic solenoid. The collimator located just before the sample is used to select a small portion of electrons to improve diffraction pattern quality. A plug-in Faraday cup is to measure the bunch charge. A pair of steering coils are used to correct possible misalignments and fine tune the beam trajectory. Bunch duration is measured by the deflecting cavity, which also enables the UED system working on the so-called "continuously time resolved (CTR)" mode. The diffraction patterns are captured by the detector system, comprised of a phosphor screen, a 45-deg mirror and an EMCCD perpendicular to the beamline.

A set of machine parameters are optimized by thorough, start-to-end simulations, under the guidance of which a high quality single-shot diffraction pattern of a ~200nm polycrystalline aluminium foil is gained, as shown in Fig.2. It is easy to see that the (111) ring and (200) ring are clearly

* Work supported by NSFC Grants No. 11375097and No. 11435015.
† huangwh@mail.tsinghua.edu.cn

ISBN: 978-3-95450-199-1 doi:10.18429/JACoW-SAP2017-TUDH2

distinguished, indicating a good reciprocal space resolution.

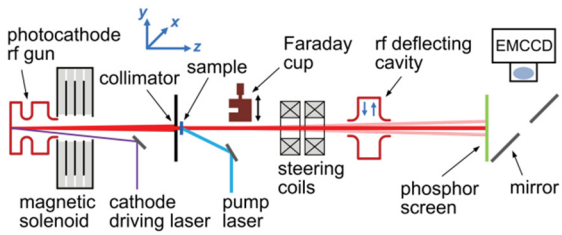


Figure 1: Schematic of the MeV UED system.

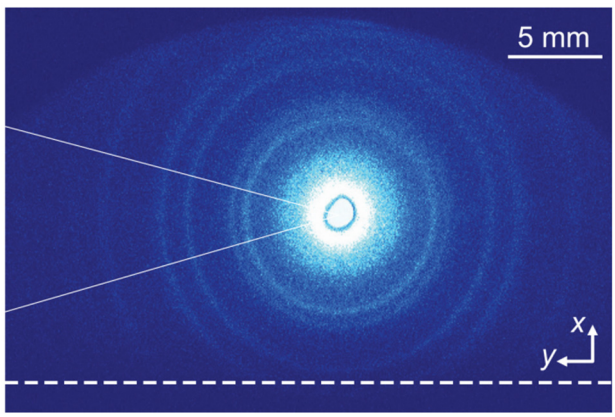


Figure 2: A single-shot MeV UED diffraction pattern.

Apart from static diffraction, pump-probe experiment of single crystal gold sample has been conducted [11]. Typically, the intensity changes of diffraction spot before and after pump ware gained by scanning the time delay between the pump laser and the electron probe. In our experiment, a 10ps long electron pulse is generated and used to probe the sample, then streaked by the deflecting cavity.

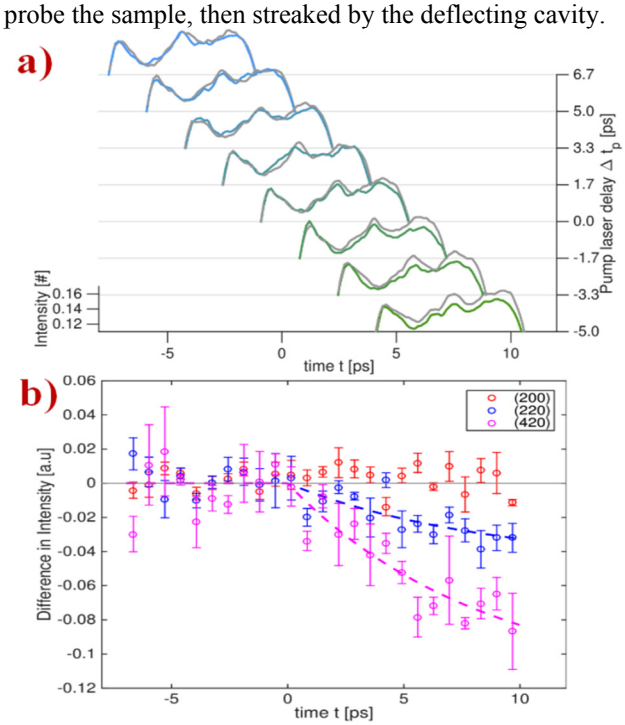


Figure 3: a) intensity of streaked diffraction spot (420) varies with respect to time zero, with pump (colored) and without pump (grey); b) The statistical result of slices of the diffraction patterns at different time delay.

The measured intensity of the streaked (420) diffraction spot at different time delay to pump laser is shown in Fig 3 a), and these in a clear drop in intensity when pump laser is ahead of the electron probe, known as the Debye-Waller effect. The statistical result of slices of the diffraction patterns of (200), (220) and (420) before and after time zero is shown in Fig 3 b). The intensity decay after time zero is fitted with an exponential function of constant of 8.4 ps, which is the Debye-Waller factor.

## FUTURE PLAN OF UED/UEM PROJECT

To meet the urgent need of high quality and high stability machine performance for user experiments, we have a newly designed UED/UEM beamline with the following improvement over the prototype:

- A new, state-of-the-art modulator is employed to reduce the amplitude and phase error of the rf system.
- An auxiliary solenoid identical to a C-band photocathode gun solenoid is used to adjust the beamsize on the sample, from a few micrometers to hundreds of micrometers.
- A versatile sample chamber is installed to meet different environment requirement of different user experiments, such as solid sample, gas sample or even liquid sample.

The most significant goal of UED facility is the 100fs time resolution, which is square root of quadratic sum of four items: electron probe length, pump laser length, arrival time error between electrons and lasers at sample and velocity mismatch in sample. Among these factors, electron bunch duration and time-of-arrival jitter are the most concerned ones, since the pump laser is a few to tens of femtoseconds decided by the laser system and velocity mismatch is negligible in thin samples.

In order to get 100fs time resolution, it is necessary to keep the electron bunch length shorter than 100fs. Considering that our current laser shortest duration at 266 nm wavelength is ~127fs, the required bunch length has to be got by lowering the bunch charge, in together with gun compression at low launching phase. We have simulated the bunch length at sample located at 1.5m downstream, as shown in Fig.4.

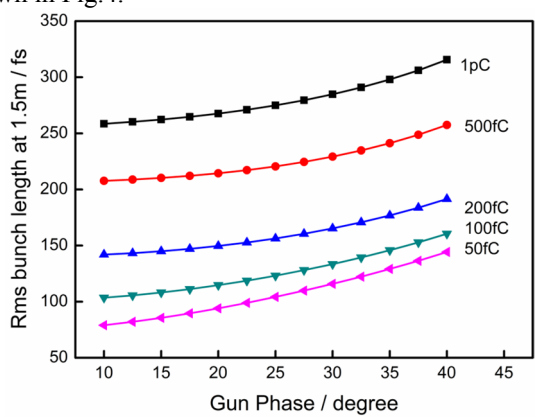


Figure 4: Bunch length vs launching phase.

ISBN: 978-3-95450-199-1 doi:10.18429/JACoW-SAP2017-TUDH2



It is obvious to see that the bunch charge should be kept below 100 fC, and lower launching phase helps to compress the beam.

The time jitter between the electron probe and pump laser is caused by the amplitude fluctuation of the rf system and laser launching phase error, which includes phase error of the rf system and laser to low level rf (LLRF) phase error. The effect of time of arrival (TOA) jitter with respect to launching phase and rf amplitude jitter is simulated and fitted respectively. Simulation results showed that a degree launching error can cause 670fs TOA jitter, while 0.1% fluctuation of rf amplitude introduces 110fs. Since the laser to LLRF phase error can be controlled between rms 70fs with our current LLRF system, an upgraded modulator with tiny high voltage fluctuation is demanded. With the stability of peak to peak 0.1%, the rf amplitude jitter is about 0.04% and phase error is about rms 40fs. The laser to RF error is then about 80fs and induces a TOA jitter of rms 55fs, while the rf amplitude jitter contributes a TOA jitter of rms 10fs, thus the whole TOA jitter is kept below rms 60 fs. The final time resolution is estimated to be rms 127 fs, which will enable the real-time observation of many ultrafast processes.

As to the design of UEM, permanent magnet quadrupoles (PMQ) are considered as the focusing elements. Typically, solenoids are used as the imaging lens. Reliable and convenient as it is, solenoid coil is often bulky and heavy in MeV UEM. Another alternative option is using PMQ, which is more efficient in focusing high energy electrons than solenoids. A PMQ can offer a high gradient of a few hundreds of T/m with a typical romance of 1.2T~1.4T in material and inner bore of a few millimeters. Recently, a prove-of-principle experiment of using a PMQ based triplet for transmission electron microscope is demonstrated [12]. Since a single PMQ focuses beam in one direction while defocuses in the other, at least two of them need work together to form a focusing element in both x/y directions. Among different configurations, a Russian quadruplet is a promising choice, where the polarities and the strengths of the four quadrupoles are sorted as +A-B+B-A, while the length of the quads(l) and distance (s) between them are l1–s1–l2–s2–l2–s1–l1, thus making this configuration antisymmetric. A single imaging unit based on a Russian quadruplet is designed, the whole transfer matrix of which is:

$$R_{x,y} = \begin{pmatrix} -29.63 & 0 \\ -49.94 & -0.03 \end{pmatrix}. \quad (1)$$

Where $R_{11}$=-29.83 is the magnification factor, $R_{12}$=0 is requirement of point-to-point imaging, the $R_{21}$ element equals -1/f, and the focusing length is then about 2cm.

Parameters of the Russian quadruplet is listed in Table 1. A start-to-end imaging simulation using such a single imaging unit of a virtual sample is present in Fig 5. The beam energy here is 4MeV with rms 0.1% energy spread, while the beam emittance is 100nm and beamsize at sample is 50um.

Table 1: Russian Quadruplet Parameters

| Number | Thick | Gradient | Position |
|---|---|---|---|
| Q1 | 5mm | 178.76 T/m | 9.9mm |
| Q2 | 5mm | -423 T/m | 15.9mm |
| Q3 | 5mm | 423 T/m | 22.55mm |
| Q4 | 5mm | -178.76 T/m | 28.55mm |

This clear image proves the reliability of PMQ based imaging system. Cascading of 2~3 imaging units will gain a magnification factor over 1000 times, and then the whole resolution of the UEM is expected to reach tens of nm.

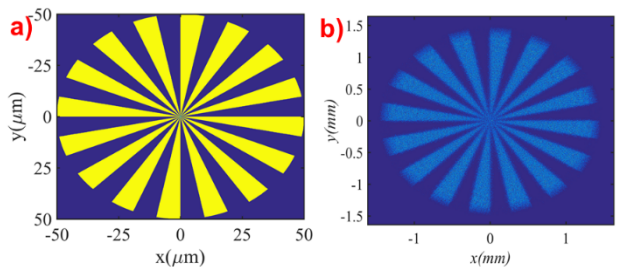


Figure 5: a) distribution of the virtual sample; b) image of a virtual sample with ~30 times magnified.

## SUMMARY

Previous work of UED research has laid a solid foundation for the future UED/UEM facility in Tsinghua. The new facility will be installed soon and is expected to serve as a reliable tool for ultrafast sciences.

## ACKNOWLEDGEMENT

The authors want to thank Dr. Li Renkai and Dr. Lu Xianhai for their fruitful work in Tsinghua and helpful suggestions.

## REFERENCES

[1] R.K. Li, “Theoretical and experimental investigation of mega-electron volt ultrafast electron diffraction”, Ph.D. thesis, Tsinghua university, 2010.

[2] Mourou, Gerard, and Steve Williamson, "Picosecond electron diffraction", *Applied Physics Letters* 41.1 (1982): 44-45.

[3] X.H. Lu, “Optimization Study and Application Exploration of Mega-Electron-Volt Ultrafast Electron Diffraction”, Ph.D. thesis, Tsinghua university, 2014.

[4] X.J. Wang *et al.*, "Potential of femtosecond electron diffraction using near-relativistic electrons from a photocathode RF electron gun", JOURNAL-KOREAN PHYSICAL SOCIETY 48.3 (2006): 390.

[5] P. Musumeci, J. T. Moody, and C. M. Scoby, "Relativistic electron diffraction at the UCLA Pegasus photoinjector laboratory", Ultramicroscopy 108.11 (2008): 1450-1453.

[6] Pengfei Zhu, *et al.,* "Dynamic separation of electron excitation and lattice heating during the photoinduced melting of the periodic lattice distortion in 2H-TaSe2", *Applied Physics Letters* 103.7 (2013): 071914.

[7] S. P.Weathersby *et al.*,"Mega-electron-volt ultrafast electron diffraction at SLAC National Accelerator Laboratory", Review of Scientific Instruments 86.7 (2015): 073702.

ISBN: 978-3-95450-199-1 doi:10.18429/JACoW-SAP2017-TUDH2

[8] Jinfeng Yang *et al.,* "100-femtosecond MeV electron source for ultrafast electron diffraction", *Radiation Physics and Chemistry* 78.12 (2009): 1106-1111.

[9] Renkai Li *et al*., "Experimental demonstration of high quality MeV ultrafast electron diffraction", *Review of Scientific Instruments* 80.8 (2009): 083303.

[10] R. K. Li *et al*., "Recent progress of MeV ultrafast electron diffraction at Tsinghua University", in *Proceedings of IPAC' 10* , pp. 229-231.

[11] X.H. Lu *et al.*, "Continuously time-resolved process of laser pumped single crystal gold by MeV ultrafast electron diffraction", unpublished.

[12] D. Cesar *et al.,* "Demonstration of single-shot picosecond time-resolved MeV electron imaging using a compact permanent magnet quadrupole based lens", *Physical review letters* 117.2 (2016): 024801.

ISBN: 978-3-95450-199-1 doi:10.18429/JACoW-SAP2017-TUDH3

# ELECTRON OSCILLATIONS IN THE INTENSE LASER PRODUCED THREE-DIMENSIONAL POST-SOLITON ELECTROMAGNETIC FIELD

Dongning Yue, Xiaohui Yuan, Min Chen†
Key Laboratory for Laser Plasmas (Ministry of Education), School of Physics and Astronomy, Shanghai Jiao Tong University, Shanghai, China
Collaborative Innovation Center of IFSA, Shanghai Jiao Tong University, Shanghai, China

*Abstract*

Electron oscillations in the three-dimensional post-soliton electromagnetic field generated by ultrashort intense laser in near-critical density plasma were studied using 3D particle-in-cell (PIC) simulations. Two types of post-solitons were observed. We found that unlike the ions, which are expelled from the centre of post-soliton, electrons oscillate around the centre of a post-soliton and the resultant poloidal electric vector field behaves like an oscillating electric dipole. The toroidal magnetic field also oscillates along with electrons. On the timescale of $\omega_{pi}^{-1}$, where $\omega_{pi}$ is the ion plasma frequency, protons have evolved into multi-shell structures due to Coulomb explosion in the post-soliton. The polarization of the post-soliton is found to be different from that of the driver laser beam.

## INTRODUCTION

Nonlinear localized coherent electromagnetic (EM) modes have been found in the interaction of ultra-intense ($I \geq 10^{18}$ Wcm$^{-2}$) laser pulse with underdense plasma ($\omega_{pe} < \omega_L$, where $\omega_L$ is the laser frequency, $\omega_{pe} = \sqrt{4\pi n_e e^2/m_e}$ is the electron plasma frequency, $n_e$ is the electron density). A laser pulse depletes its energy into plasma on a spatial scale of the order of $l_{depl} \approx l_{pulse}(\omega_L/\omega_{pe})^2$ during propagation, where $l_{pulse}$ represents the laser pulse length [1]. With the laser energy loss, the laser frequency undergoes a redshift. The laser experiences locally overcritical density plasma and is trapped in the plasma cavity. This coherent structure shows excellent stability in one-dimensional PIC simulation and propagates with a velocity that is well below the speed of light or almost equal to zero in homogeneous plasma [2]. Since the low frequency EM wave confined inside the slowly expanding plasma cavity is normally generated in the wake of the driver laser pulse, it is therefore denoted as "post-soliton".

A model called "snowplow" has been proposed to explain the generation and evolution of the two-dimensional *s*-polarized post-soliton [3, 4]. Experimental and PIC simulation results show that the structure of the three-dimensional post-soliton is anisotropic like a prolate spheroid [4, 5] and depends on the plasma parameters [6].

In this paper, the EM field structure of the three-dimensional post-soliton, electron oscillations in this field and multi-shell like structure of protons will be presented. The polarization of post-soliton is different from that of laser, which has not been reported before as far as we know.

## SIMULATION RESULTS

Three-Dimensional Particle-In-Cell (3D-PIC) code OSIRIS was used in this study [8]. In the simulation, the laser pulse propagates along $x_1$ direction and is linearly polarized along $x_2$ axis. The normalized electric vector is $a = eE/(m_e\omega c) = 1$ with pulse duration of 40 fs corresponding to 15 $T_0$ which $T_0 = \lambda_0/c$ and laser wavelength $\lambda_0$ is 0.8 $\mu$m. The laser pulse has a transversely Gaussian envelope and its focal plane is at a distance of 20 $\mu$m from the back of plasma slab. The laser pulse starts at $x_1$ = 15 $\mu$m (the front of the plasma slab). The plasma slab is 30 $\mu$m thickness and the homogenous density is $n_e$ = 0.28 $n_{cr}$. The simulation box is $x_1 \times x_2 \times x_3$ = 45 $\mu$m × 14 $\mu$m × 14 $\mu$m and is divided into 900 × 280 × 280 cells. Protons are set to be mobile in the simulations.

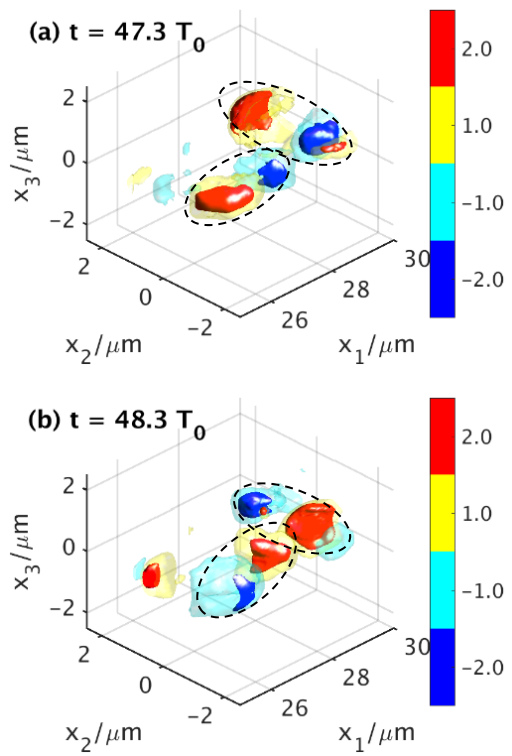


Figure 1: Distributions of transverse electric field $E_2$ at t = 47.3 $T_0$ (a) and t = 48.3 $T_0$ (b), respectively. Dotted line areas highlight the electric fields that are trapped inside the post-soliton structure.

† minchen@sjtu.edu.cn

ISBN: 978-3-95450-199-1 doi:10.18429/JACoW-SAP2017-TUDH3

Figure 1 shows the distributions of transverse electric field $E_2$ at two time snaps after the laser pulse arrival. Part of the electric field is trapped inside the post-soliton structure and oscillates like a standing wave. Two different modes are observed. One oscillates along $x_1$ direction (i.e. the laser propagation axis), and the other along $x_2$ direction (i.e. along laser polarization direction). Both post-soliton modes oscillate in a frequency lower than that of the driver laser.

We denote the post-soliton that oscillates along $x_2$ direction as transverse post-soliton and the other as longitudinal post-soliton. Figure 2 shows the transverse electron density distributions of the transverse post-soliton in the middle plane for two time snaps. It is clear that the structure elongates along the laser polarization direction. When electrons concentrate on one side, the other side will be a proton cavity. The cavity size is 2 $\mu$m in $x_3$ direction and 4 $\mu$m in $x_2$ direction, respectively. The concentrated electron density could be as high as 1.5 $n_c$, while the electron density on the wall is 0.84 $n_c$.

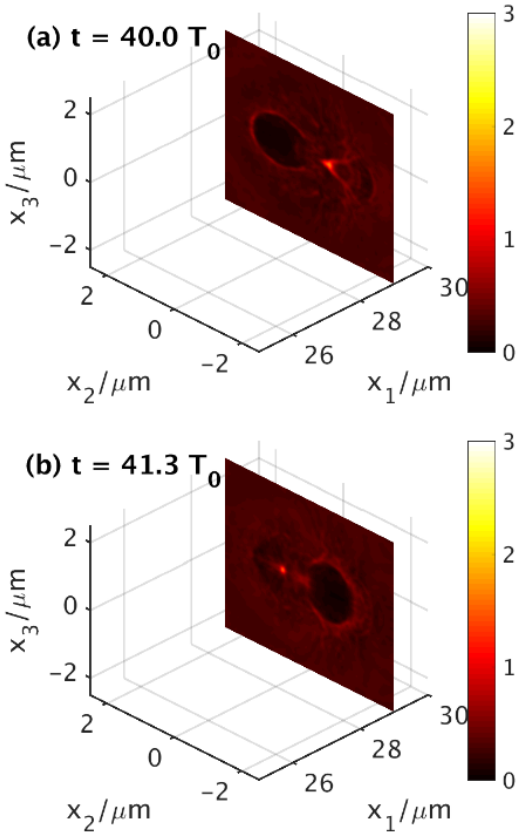


Figure 2: Electron density distributions of transverse post-soliton at t =40.0 $T_0$ (a) and t = 41.3 $T_0$ (b). The cross section is at $x_1$=29.0 $\mu$m and the density is normalized with critical density $n_c$.

The electric vector field distributions are shown in Fig. 3 at the same time as in Fig. 2. This electric vector field oscillates like an electric dipole, i.e. its poles follow the electrons' movement shown in Fig. 2. This field also shows the anisotropic structure.

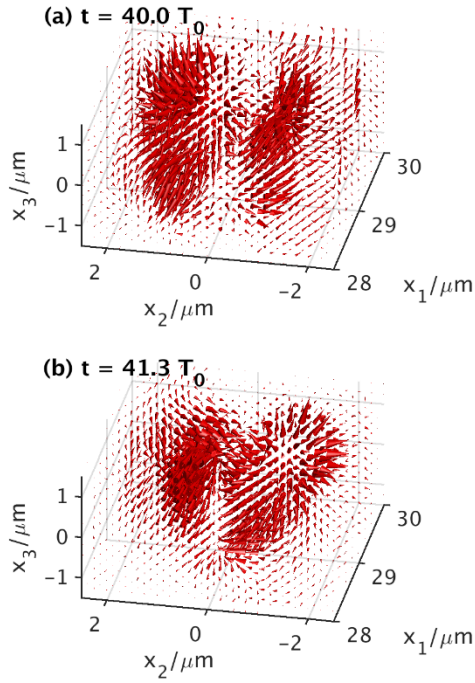


Figure 3: The electric vector field distributions inside transverse post-soliton at t = 40.0 $T_0$ (a) and t = 41.3 $T_0$ (b). The strength of electric field has been normalized.

The vortex-like magnetic field structure was shown in Fig. 4, which has a similar oscillation mode to Fig. 2 and Fig. 3. The toroidal direction of magnetic field is counter-clockwise with respective to the +$x_1$ direction.

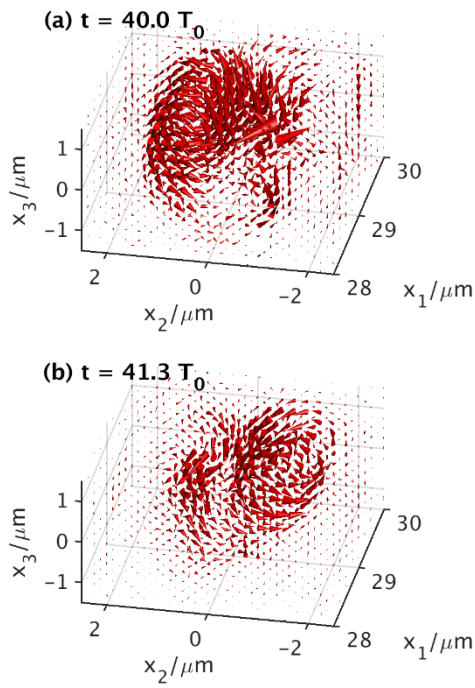


Figure 4: The magnetic vector field distributions inside the transverse post-soliton at t = 40.0 $T_0$ (a) and t = 41.3 $T_0$ (b). The strength of magnetic field has been normalized.

ISBN: 978-3-95450-199-1 doi:10.18429/JACoW-SAP2017-TUDH3



In Fig. 5 we show the phase space distribution of protons in the transverse post-soliton. Protons are accelerated by the field inside the post-soliton. This process resemble to Coulomb explosion, which drives the cavity expanding slowly. We could see clearly there are two (three at most) antisymmetric regions both in $p_2x_2$ and $p_3x_3$ phase spaces. This suggests that at least two proton shells exist in the post-soliton structure. Protons pile up on the wall of the cavity and are pushed away from the cavity centre. More protons are involved in this process and start to move along the expanding direction. Protons could be accelerated to tens of keV energy on the cavity wall at time t = 68.8 $T_0$. The inner shell distribution of protons in $p_2x_2$ space is not as antisymmetric as in $p_3x_3$ space. This could be attributed to the influence of the other nearby post-soliton. Unlike the multi-shell structure found in electron vortex, which leads to a number of multi-stream instabilities, no instability is found in the process of post-soliton evolution in our simulation time window [7].

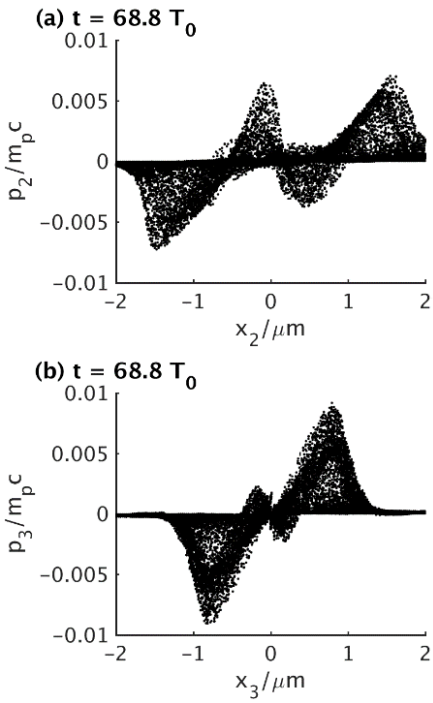


Figure 5: Proton distribution of transverse post-soliton in phase space of $p_2x_2$ (a) and $p_3x_3$ (b) at t = 68.8 $T_0$.

## CONCLUSION

Electron and fields oscillations in a three-dimensional post-soliton electromagnetic field have been studied numerically by 3D-PIC simulations. We found that electron oscillation plays an important role in sustaining the stability of a post-soliton. Poloidal electric field and toroidal magnetic field also oscillate with electrons. Ions acceleration during cavity expansion is observed in such post-soliton structure.

## ACKNOWLEDGEMENT

The authors would like to acknowledge the OSIRIS-Consortium, consisting of UCLA and IST (Lisbon, Portugal) for the use of OSIRIS and the visXD framework. The work was supported by National Basic Research Program of China (Grant No. 2013CBA01502), National Natural Science Foundation of China (Grant Nos. 11121504 and 11205100), and National Key Scientific Instrument Development Project (Grant No.2012YQ030142).

## REFERENCES

[1] Bulanov S V, Inovenkov I N, Kirsanov V I *et al.,* "Nonlinear depletion of ultrashort and relativistically strong laser pulses in an underdense plasma", *Physics of Fluids B Plasma Physics*, 1992, 4(7):1935-1942.

[2] Esirkepov T Z, Kamenets F F, Bulanov S V *et al.,* "Low-frequency relativistic electromagnetic solitons in collisionless plasmas", *Journal of Experimental & Theoretical Physics Letters*, 1998, 68(1):36-41.

[3] Naumova N M, Bulanov S V, Esirkepov T Z *et al.,* "Formation of Electromagnetic Postsolitons in Plasmas", *Physical Review Letters*, 2001, 87(18):231-295.

[4] Sarri G, Singh D K, Davies J R *et al.,* "Observation of postsoliton expansion following laser propagation through an underdense plasma", *Physical Review Letters,* 2010, 105(17):175007.

[5] Esirkepov T, Nishihara K, Bulanov S V *et al.,* "Three-dimensional relativistic electromagnetic subcycle solitons", *Physical Review Letters,* 2002, 89(27):275002.

[6] Sarri G, Kar S, Romagnani L *et al.,* "Observation of plasma density dependence of electromagnetic soliton excitation by an intense laser pulse", *Physics of Plasmas*, 2011, 18(8):696.

[7] Lezhnin K V, Kamenets F F, Esirkepov T Z *et al.,* "Explosion of relativistic electron vortices in laser plasmas", *Physics of Plasmas*, 2016, 23(9):175002-335.

[8] Fonseca R A, Silva L O, Tsung F S *et al.,* "OSIRIS: A Three-Dimensional, Fully Relativistic Particle in Cell Code for Modeling Plasma Based Accelerators", International Conference on Computational Science. Springer-Verlag, 2002:342-351.

ISBN: 978-3-95450-199-1 doi:10.18429/JACoW-SAP2017-TUPH01

# 2σ SIGNALS FOR THE ELECTRO-GRAVITATIONAL INDUCTION BASED ON BEAM INSTABILITY IN CHARGED PARTICLE STORAGE RINGS *

Dong Dong †
Institute of High Energy Physics, Chinese Academy of Sciences, Beijing, China

*Abstract*

Changes in beam position within charged particle accelerator storage rings have been observed due to changes in gravity caused by the moon and sun. The terrestrial tidal model has been used to explain this type of beam instability. Further analysis reveals that these instabilities arise from changes in the electron beam energy, that may not only come from movements of the accelerator components due to terrestrial tidal forces, and may caused by the unsighted process. We try to induce an electromotive force along the ring, referred to as electro-gravitational induction (EGI). The circular motion of the charged particles causes the accumulation of the EGI in the storage ring, turn by turn. We used existing data from storage ring beam signals to estimate the maximum value of the gravity coefficient of the induced electromotive force.

## INTRODUCTION

LEP and Spring8 have observed COD changes, the period of 12 hours, comes from the gravity changes, the change of acceleration of gravity g, delta g caused by the moon and sun moving relative to the earth[1-2]. See the Figure 1 and 2.

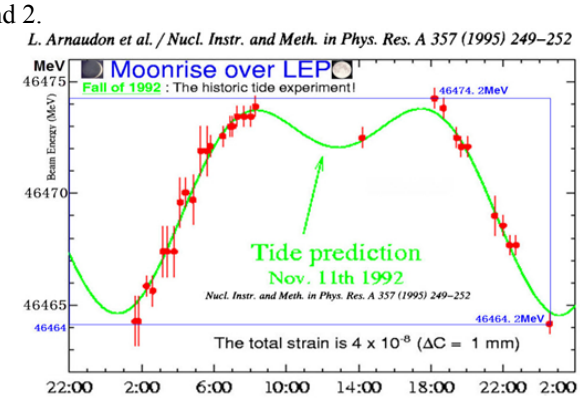


Figure 1: LEP Observation, see reference [1].

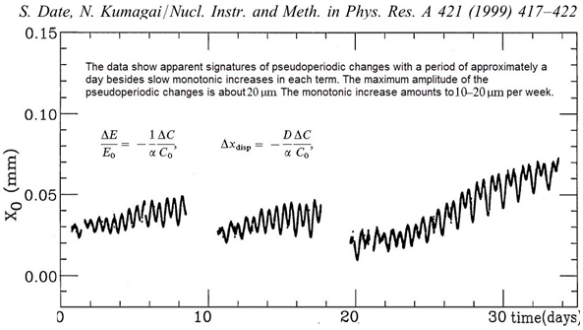


Figure 2: SPrng8 observation, see reference [2].

* Work supported by the National Natural Science Foundation of China under Grant No. 11575215, partly.
† email address dongd@ihep.ac.cn

Phenomenology, we would assume that the gravity changes caused by the moon and sun moving at the storage ring have caused the beam energy changes in the storage ring [3].

$$\Delta E = \xi \cdot \Delta g \quad (1)$$

Which $\Delta E$ is the beam energy changes, caused by gravity changes $\Delta g$. If it is true, then it may be the electro-gravitational induction (EGI). We have discussed the possibility of EGI, and estimate the maximum value of the gravity coefficient of the induced electromotive force by using the existing beam data from the storage rings.

The EGI coefficient $\xi$ is found to be less than $3.78\ \mathrm{statcoul}^{-1} \cdot \mathrm{m}^{-1} \cdot \mathrm{kg} \cdot \mathrm{sec}$. There is still a question of whether the value $\xi$ actually exists or zero; we may be able to obtain a more accurate measurement from a setup with no feedback systems in place, that is, no beam energy compensation systems, beam orbit correction systems, and so on.

Furthermore, the EGI coefficient $\xi \leq 3.78\ \mathrm{stat}coul^{-1} \cdot m^{-1} \cdot \mathrm{kg} \cdot \mathrm{sec}$ can also be formulated using the existing constants, G and $\kappa_e$:

$$\xi \leq 9.7 \times 10^{-4} \left( \frac{1}{c} \sqrt{\frac{\kappa_e}{G}} \right) \quad (2)$$

where G is the gravitational constant, $\kappa_e$ is the dielectric constant, and c is the speed of light in a vacuum. From equation (6), we see that the resulting value of $\xi$ would be less than that obtained above, if the EGI does in fact exist.

## DISCUSSION

The changes of COD predicts by the EGI is in a same-phase transformation with the changes caused by the Newton tidal force. However, EGI, if exist, will affects the positive charged particle and negative charged particle in opposite way, one is accelerated and another is decelerated at same time, in same place. For example, if we have two same size rings, located in the same site of ground, one is electron ring another is positron ring, moving in same direction; we can measure the COD of these two similar storage rings respectively at same time, and noted as $\mathrm{COD}_+(t)$ for the closed obit distortion of the positive particles beam, $\mathrm{COD}_-(t)$ for the negative particles beam, respectively. So we can obtain the $\Delta\mathrm{COD}(t)$, $\Delta\mathrm{COD}(t) = \mathrm{COD}_+(t) - \mathrm{COD}_-(t)$, see the Figure3. Therefore, $\Delta\mathrm{COD}(t)$ signals will be independent on the terrestrial tidal force. So the effect of the EGI model will be $\Delta\mathrm{COD}(t)/2$. Here, we must consider all the influence

ISBN: 978-3-95450-199-1 doi:10.18429/JACoW-SAP2017-TUPH01



Table 1: Parameters for Different Storage Rings

| | NL Northern latitude | $L_0$(m) Ring circumference | $E_0$(GeV) Beam energy | $\Delta L_{max}$ measured COD changes | $\xi$ (maximum) $\left(10^{-2}\ \mathrm{stat}coul^{-1} \cdot m^{-1} \cdot \mathrm{kg} \cdot \mathrm{s}\right)$ EGI coefficient |
|---|---|---|---|---|---|
| LEP[1] | 46 | 26658.9 | 91 | 0.1mm | 3.76 |
| SPring8[2] | 34.9 | 1435.9 | 8 | 56$\mu$m | 2.09 |
| APS[3] | 41.7 | 1105 | 7 | 40$\mu$m | 3.78 |

NL: Northern latitude; $L_0$: Expected path perimeter; $E_0$: Beam energy in GeV; $\Delta L$: measured COD changes; $\Delta L_{max}$: maximum COD change per day; $\xi$: calculation of the EGI coefficient in $\mathrm{stat}coul^{-1} \cdot m^{-1} \cdot \mathrm{kg} \cdot \mathrm{s}$.

of other factors, such as the synchronization, RF system and feedback systems and others when we check EGI, in practice.

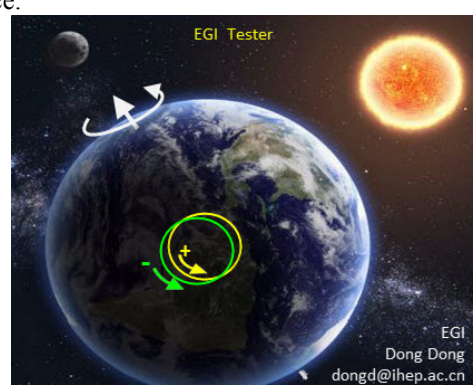


Figure 3: Two ring for checking EGI effect.

For example, based the Beijing Electron and Positron Collider (BEPC), which has two rings, one is electron ring and the other is positron, if we modify the machine so that the electron and positron beam moves at the same direction in the two ring at same time, then we can check the EGI model true or false by measuring $\Delta\mathrm{COD}(t)$, in future.

## REFERENCES

[1] L. Arnaudon et al., "Effects of terrestrial tides on the LEP beam energy". *Nucl. Instr. Meth*. **A357**,249-252 (1995).
[2] S. Date, N. Kumagai, "A long term observation of the DC component of the horizontal COD in the storage ring of Spring-8". *Nucl. Instr. Meth.***A421**, 417-422 (1999).
[3] Junyi Dong, etc, "On the Electro-Gravitational Induction Predicted by Beam Instability in Charged Particle Storage Rings". *e-Print Archive chinaXiv:201609.00255.*

ISBN: 978-3-95450-199-1 doi:10.18429/JACoW-SAP2017-TUPH08

# A PROPOSAL OF USING IMPROVED RHODOTRON AS A HIGH DOSE RATE MICRO-FOCUSED X-RAY SOURCE*

Xiaozhong He†, Liu Yang, Shuqing Liao, Wei Wang, Jidong Long, Jinshui Shi, Institure of Fluid Physics, Chinese Academy of Engineering Physics, Mianyang, China

*Abstract*

High energy X-ray computer tomography has wide application in industry, especially in quality control of complicated high-tech equipment. In many applications, higher spatial resolution is needed to discover smaller defects. Rhodotron have been used to produce high power CW electron beam in hundreds of kilowatts level. In this paper, we propose to use an improved Rhodotron to generate high brightness electron beam with high average power. Beam dynamics study shows that when producing tens of kilowatts electron beam, the normalized RMS emittance can be lower than 10 μm, and the relative RMS energy spread can be lower than 0.2%. The beam can be focused to a spot size of about 100μm, and converted to X-Ray by using a rotating target within several kilowatts beam power. Improved Rhodotron proposed in this paper is a good candidate of X-ray source for high resolution high energy industrial CT systems.

## INTRODUCTION

High energy industrial CT has shown to be of great value in the research and development of the high-end equipments (large locomotives, engines, nuclear weapons, etc.). But it is still urgent need for higher resolution to detect smaller defects in high-end equipments. To meet the needs, a micro-focused accelerator with high dose rate will be needed.

Traditional used accelerator used for this purpose is RF traveling or standing wave linear accelerator. There are many commercial companies such as VARIAN in American, GUHONG in China, providing linear accelerators for high energy CT inspection. The typical beam energy for high energy CT inspection is 9-15MeV, the dose rate for 9MeV is about 3000 Rad/min, and the X-ray spot size is about 1-2mm. There are also many micro-focused X-ray source products using a DC acceleration tube and a rotating target, the X-ray spot-size can be small as 0.2mm at the electron beam power of 750W and the beam energy of 750kV. For the CT inspection of large equipment with large aerial density, especially in the case of high resolution is needed, one need a X-ray source with high energy (not less than 9MeV), and with high dose rate (not less than 3000 Rad/min), and a very small spot size (not more than 0.2mm).

To generate micro-focused high dose rate X-ray, high brightness electron beam is needed. More specific, electron beam with high average power, low emittance and low energy spread is needed, so one can use a not so complicated focus system to get a small spot size such as 0.2mm. On other side, one should deal with the target temperature rise when producing high dose rate X-ray at a very small spot size. Even use the rotating target system, high duty factor accelerator is needed to avoid the target melting problem.

Some type of accelerators such as Rhodotron [1-8], Rdigetron [9], Fabitron [10], can accelerate electron beam many times using the same RF structure, and can work at very high duty factor, and sometimes work at continuous wave mode. In this paper, it is proposed that using Rhodotron and a rotating target to generate a high dose rate micro-focused X-ray. A layout is shown in Figure 1. The Rhodotron is designed to produce high power electron beam with high brightness.

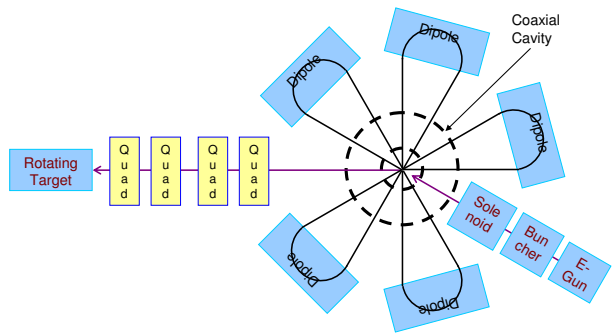


Figure 1: Layout of the proposed micro-focused X-ray source.

Main specification of the proposed micro-focus X-ray source is listed in Table 1.

Table 1: Main specifications of the proposed X-ray source.

| Parameters | Value |
|---|---|
| electron beam energy | 9 MeV |
| dose rate of X-ray at 1m from target | ≥ 3000 Rad/min |
| X-ray spot size (FWHM) | ≤ 0.2mm |
| time structure | 10% duty factor, and at 100 Hz |

## PRELIMINARY BEAM DYNAMICS DESIGN

To generate the proposed dose rate, the needed average power of the electron beam is about 1kW. This value is far less than that has been achieved at high power Rhodotron, in which several hundreds of kW electron beam was produced. So the beam current in our design is relatively low, and the electron beam can be bunched to shorter phase width to acquire high brightness, and a smaller cathode can be used to archive smaller emittance. Additional to the buncher used in low energy section, the acceleration phases in the RF cavity are also chosen to

* Work supported by R&D PROJECT OF IFP/CAEP
† hexiaozhong@caep.cn

ISBN: 978-3-95450-199-1 doi:10.18429/JACoW-SAP2017-TUPH08

bunch the electron beam. In other words, the acceleration phase choice and the non-zero R56 of the dipoles make every dipole can work as a magnetic compressor.

The code PARMELA was used to simulate the beam dynamics in the accelerator. At the end of the accelerator, the normalize RMS emittance of x and y direction are both lower than 8 mm·mrad, the peak current is about 1 Ampere, and the RMS energy spread is about 0.2% (Figure 2).

Using the focus system consisting 4 quadroples, the electron beam can be focused to be smaller than 0.15mm (FWHM, see Figure 3). The dispersion effect and the chromatism effect are included in the simulation by the code PARMELA. At the rotating target, the electron beam is scattered by the target material, and the spot size of X-ray beam may be larger than the beam size simulated by the beam tracking code. The diffusion process of the electron in the target is simulated by the code GEANT4. The simulation shows that there is not obvious difference between the X-ray spot size and the electron beam spot size even with a focus spot of 0.1mm.

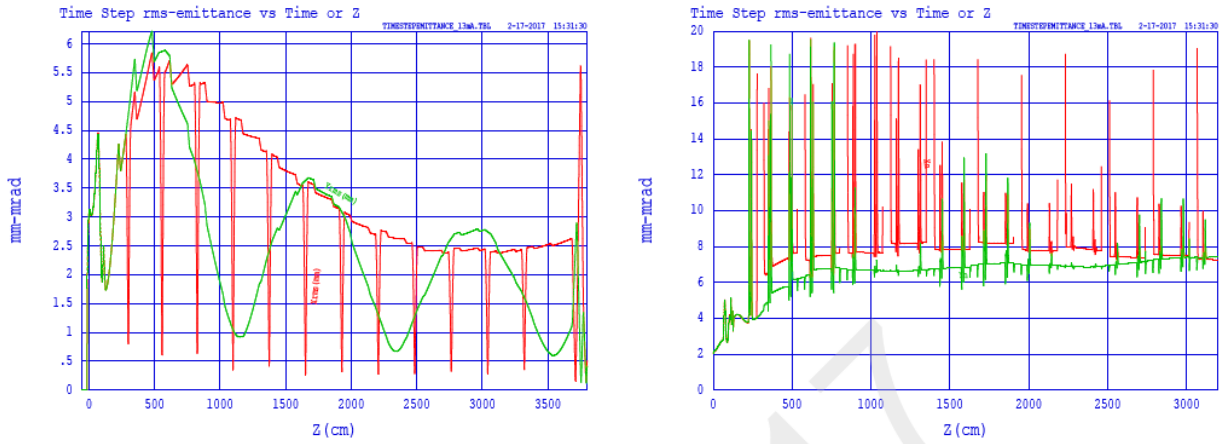


Figure 2: The beam envelope and emittance of the electron beam in the accelerator.

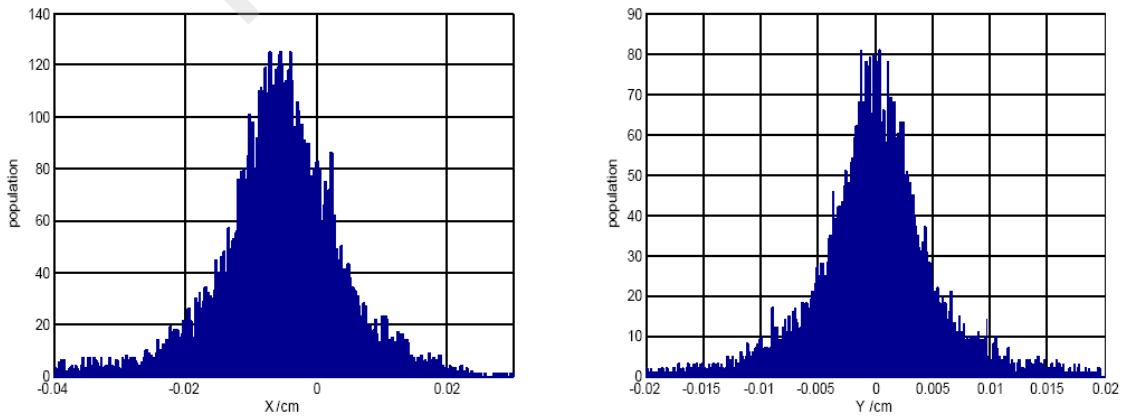


Figure 3: Distribution of the electron focus spot in x and y direction.

ISBN: 978-3-95450-199-1 doi:10.18429/JACoW-SAP2017-TUPH08

## KEY TECHNOLOGY NEEDED TO REALIZE THE PROPOSED DESIGN

Main technologies needed are coaxial cavity with large dimension, dipole magnet with high accuracy to provide proper transverse focusing, rotating bremsstrahlung targets in vacuum. Besides these key technologies, high voltage pulsed power supply with very high repetition rate may be needed to avoid the overlapping of the beam track in the center of the accelerator. To avoid the overlapping, we proposed to generate one electron bunch every 10 RF cycles. That is to say, for a RF frequency of 108MHz, the power supply of the grid should work at repetition rate of 10.8MHz, and produce a pulse of FWHM less than about 3 nanosecond which is about 1/3 one RF period. There is a R&D project in progress to develop key technologies including the generation of electric pulse with needed repetition rate, RF cavities, the high accuracy dipole magnet, rotating target, and also the beam dynamics optimization.

## CONCLUSION AND FUTURE WORK

Methode of using improved Rhodotron as micro-focused X-ray source is proposed. Beam dynamics design of the improved Rhodotron are carried out to generate X-ray with high dose rate and very small focus spot. Beam dynamics study shows that when producing tens of kilowatts electron beam, the normalized RMS emittance can be lower than 10 μm, and the relative RMS energy spread can be lower than 0.2%. The beam can be focused to a spot size of about 100μm.

There is a R&D project in progress in CAEP to develop key technologies including the generation of electric pulse with needed repetition rate, RF cavities, the high accuracy dipole magnet, rotating target, and also the beam dynamics optimization.

## ACKNOWLEDGEMENT

Thanks to the useful discussion with Weiping Xie, Jinshui Shi, Yufei Peng.

## REFERENCES

[1] J. Pottier *et al.*, "A new type of RF electron accelerator: the Rhodotron", *Nucl. Instrum. Methods-Phys.Res.B*, 40/41(1989)943.

[2] A. Nguyen *et al.*, in *Proc. 2nd European. Particle Accelerator Conf.,* Nice, France, 1990, p . 1840.

[3] J. M. Bassaler *et al.*, "Rhodotron: an accelerator for industrial irradiation", *Nucl. Instrum. Methods-Phys.Res.B*, 1989, B68 (1992) 92-95.

[4] D. Defrise *et al.*, "Technical Status Of The First Industrial Unit of The 10 MeV, 100kW Rhodotron", Radiat. Phys. Chem, 46(4-6), page 473-476.

[5] Y.Jongen *et al.*, "The Rhodotron: a 10 MeV, 100 kW beam power metric waves, CW electron accelerator", *Nucl. Instrum. Methods-Phys.Res.B*, 79(1993)865.

[6] Y. Jongen *et al.*, "RHODOTRON ACCELERATORS FOR INDUSTRIAL ELECTRON-BEAM PROCESSING : A PROGRESS REPORT", in *Proc. EPAC96.*

[7] Abs M *et al.*, "The IBA Rhodotron T T1000: a very high power E beam accelerator", *Radiation Physics and Chemistry*, 2004, 71: 285-288.

[8] J.M. Bassaler *et al.*, "Project of a free electron laser in the far infrared using a Rhodotron accelerator", *Nucl. Instrum. Methods-Phys.Res. A* 304 (1991) 177-180.

[9] Hayashizaki N *et al., Nucl. Instrum. Methods-Phys.Res. A*, 1999, A427: 28.

[10] Kwon H J *et al.*, in *Proc. of PAC 99,* 1999, 4: 2558- 2560.

ISBN: 978-3-95450-199-1 doi:10.18429/JACoW-SAP2017-TUPH09

# SPONTANEOUS RADIATION OF HIGH-ORDER MAGNETIC FIELD UNDULATOR

Tao Wei †, Peng Li, China Academy of Engineering Physics, Mianyang, China
Joachim Pflueger, Yuhui Li, European XFEL Gmbh, Schenefeld, Germany

*Abstract*

Based on the purpose of concision, nearly all the undulator radiation formulas have maken an assumption that the guiding magnetic field is a sinusoid wave. The assumption is consistent with the truth if the ratio of undulator gap to period length is large enough. However, high-order magnetic field exists widely in most undulators, especially those with long period length and short gap. This paper will derive the radiation output equations of high-order magnetic field undulator, what's more, the formulas are validated through numerical simulation with code SPECTRA.

## INTRODUCTION

The undulators have been widely used as insertion devices in synchrotron sources and free electron laser (FEL) to generate magnetic field which is periodic along the electron beam direction. The simplest case is the planar undulator which presents a sinusoid field perpendicular to the electron beam path. It is the most popular undulator model, the characteristic of its radiation have been discussed in many references [1, 2].

Taking into account a practical undulator, high-order magnetic field exists more or less. This paper will derive the far-field radiation of high-order planar undulator and discuss the influence of high-order magnetic field.

## SPONTANEOUS RADIATION EQUATION

The magnetic field of planar undulator should be periodic along the beam direction, in addition, the integral of the magnetic field over a single period length vanished [3]. Without loss of generality, the planar undulator which contains high-order magnetic field can be described as

$$\vec{B} = \sum_{m=1}^{+\infty} B_m \sin(mk_u z - \delta\phi_m)\,\vec{e_y}\,. \tag{1}$$

In which $k_u = 2\pi/\lambda_u$, $\lambda_u$ is the period length of undulator. To simplify the expression, the phase of fundamental magnetic field was chosen zero ($\delta\phi_1 = 0$).

The electron motion equation in the undulator can be described as

$$\gamma m_e \dot{\vec{v}} = -e\vec{v} \times \vec{B}\,. \tag{2}$$

This results in two coupled equations for the undulator with field distribution (1),

$$\ddot{x} = \frac{e}{\gamma m_e} B_y\,\dot{z}\,, \quad \ddot{z} = -\frac{e}{\gamma m_e} B_y\,\dot{x}\,. \tag{3}$$

In which $m_e$ and $e$ are the mass and charge of electron, $\gamma$ is the Lorentz factor, $z$-axis is the direction of electron beam moving forward. The formula (3) can be solved iteratively. To obtain the first-order motion solution we assume $v_z$ keep constant ($v_z = \dot{z} \approx \bar{\beta}_s c$), in which $\bar{\beta}_s$ is the average velocity in the forward direction. For the case of high energy electron, $\bar{\beta}_s$ is infinitely close to 1, i.e. $\bar{\beta}_s \to 1$. Then $z \approx \bar{\beta}_s ct$ and the transverse component of electron trajectory is

$$x(t) \approx -\frac{ec}{\gamma m_e \omega_u^2} \sum_{m=1}^{+\infty} \frac{B_m \sin(m\omega_u t - \delta\phi_m)}{m^2}, \tag{4}$$

in which $\omega_u = \frac{k_u z}{t} \approx k_u c$. The relative transverse velocity is

$$\beta_x = \frac{v_x}{c} = \frac{\dot{x}(t)}{c} \approx -\frac{e}{\gamma m_e \omega_u} \sum_{m=1}^{+\infty} \frac{B_m \cos(m\omega_u t - \delta\phi_m)}{m}. \tag{5}$$

As the energy of the electron is fixed, the electron velocity $\beta$ is also fixed. Therefore any variation in $\beta_x$ must result in a corresponding change in $\beta_s$ because of $\beta^2 = \beta_x^2 + \beta_s^2$. From this we have

$$\bar{\beta}_s \approx 1 - \frac{1}{2\gamma^2} - \frac{e^2}{4\gamma^2 m_e^2 c^2 k_u^2} \sum_{m=1}^{+\infty} \left(\frac{B_m}{m}\right)^2. \tag{6}$$

The fundamental radiation wavelength in the laboratory system [4] is thus

$$\begin{aligned} \lambda_r &= \lambda_u\left(1 - \bar{\beta}_s \cos\vartheta\right) \\ &\approx \frac{\lambda_u}{2\gamma^2}\left\{1 + \frac{e^2}{2m_e^2 c^2 k_u^2} \sum_{m=1}^{+\infty} \left(\frac{B_m}{m}\right)^2 + \gamma^2\vartheta^2\right\}. \end{aligned} \tag{7}$$

In which $\vartheta$ is the emission angle respect to the beam direction. Here we define the undulator parameter K as

$$\mathrm{K} = \frac{e}{m_e c k_u} \sqrt{\sum_{m=1}^{+\infty} \left(\frac{B_m}{m}\right)^2}. \tag{8}$$

Then formula (7) returns to the familiar expression as

$$\lambda_r = \frac{\lambda_u}{2\gamma^2}\{1 + \mathrm{K}^2/2 + \gamma^2\vartheta^2\}. \tag{9}$$

Let's consider of the second-order motion solution,

$$\begin{aligned} \ddot{z} &= \frac{e^2 c}{\gamma^2 m_e^2 \omega_u} \sum_{j,k=1}^{+\infty} \frac{B_j B_k \sin(j\omega_u t - \delta\phi_j)\cos(k\omega_u t - \delta\phi_k)}{k} \\ &= \frac{e^2 c}{2\gamma^2 m_e^2 \omega_u} \left[ \begin{aligned} &\sum_{j,k} \frac{B_j B_k \sin(j\omega_u t + k\omega_u t - \delta\phi_j - \delta\phi_k)}{k} \\ &+ \sum_{j,k} \frac{B_j B_k \sin(j\omega_u t - k\omega_u t - \delta\phi_j + \delta\phi_k)}{k} \end{aligned} \right]. \end{aligned} \tag{10}$$

† email address: weitaocaep@qq.com

ISBN: 978-3-95450-199-1 doi:10.18429/JACoW-SAP2017-TUPH09

So the $z$ component of electron trajectory is written as

$$z = \bar{\beta}_s ct - \frac{e^2 c}{2\gamma^2 m_e^2 \omega_u^3}\left[\sum_{j,k}\frac{B_j B_k \sin(j\omega_u t + k\omega_u t - \delta\phi_j - \delta\phi_k)}{k\,(j+k)^2} + \sum_{j\neq k}\frac{B_j B_k \sin(j\omega_u t - k\omega_u t - \delta\phi_j + \delta\phi_k)}{k\,(j-k)^2}\right]. \quad (11)$$

Combine (4) and (11), the electron motion causes a figure '8' [1] in the co-moving frame.

The spectral angular energy density radiated by an electron [2] in far-field is

$$\frac{d^2W}{d\Omega d\omega}\Big|_{\substack{\omega=h\omega_r\\ on-axis}} = \frac{e^2 h^2 \omega_r^2 N^2}{16\pi^3 c\varepsilon_0} L\left(\frac{N\Delta\omega}{\omega_r}\right)\left|\int_{-\frac{\lambda_u}{2c\bar{\beta}_s}}^{\frac{\lambda_u}{2c\bar{\beta}_s}} -\beta_x\, e^{ih\omega_r\left(t-\frac{z}{c}\right)} dt\right|^2$$

$$= \frac{e^4 h^2 N^2 \gamma^2}{4\pi^3\varepsilon_0 c m_e^2 (1+\mathrm{K}^2/2)^2} L\left(\frac{N\Delta\omega}{\omega_r}\right)\left|\int_{-\frac{\lambda_u}{2c\bar{\beta}_s}}^{\frac{\lambda_u}{2c\bar{\beta}_s}} \sum_m \frac{B_m \cos(m\omega_u t - \delta\phi_m)}{m} e^{i(1-\bar{\beta}_s)h\omega_r t + \frac{ihe^2\omega_r}{2\gamma^2 m_e^2\omega_u^3}\left[\sum_{j,k}\frac{B_j B_k \sin(j\omega_u t + k\omega_u t - \delta\phi_j - \delta\phi_k)}{k\,(j+k)^2} + \sum_{j\neq k}\frac{B_j B_k \sin(j\omega_u t - k\omega_u t - \delta\phi_j + \delta\phi_k)}{k\,(j-k)^2}\right]} dt\right|^2$$

$$= h^2 D\left|\int_{-\frac{\lambda_u}{2c\bar{\beta}_s}}^{\frac{\lambda_u}{2c\bar{\beta}_s}} \sum_m \frac{B_m \cos(m\omega_u t - \delta\phi_m)}{m} e^{ih\omega_u t + ihA\left[\sum_{j,k}\frac{B_j B_k \sin(j\omega_u t + k\omega_u t - \delta\phi_j - \delta\phi_k)}{k\,(j+k)^2} + \sum_{j\neq k}\frac{B_j B_k \sin(j\omega_u t - k\omega_u t - \delta\phi_j + \delta\phi_k)}{k\,(j-k)^2}\right]} dt\right|^2 \quad (13)$$

In which

$$D = \frac{e^4 N^2 \gamma^2}{4\pi^3\varepsilon_0 c m_e^2 (1+\mathrm{K}^2/2)^2} L\left(\frac{N\Delta\omega}{\omega_r}\right) \text{ and}$$

$$A = \frac{e^2\omega_1}{2\gamma^2 m_e^2 \omega_u^3} = \frac{e^2}{m_e^2 \omega_u^2 (1+\mathrm{K}^2/2)} \quad (14)$$

$$\frac{d^2W}{d\Omega d\omega} = \frac{e^2\omega^2 N^2}{16\pi^3 c\varepsilon_0} L\left(\frac{N\Delta\omega}{\omega_r}\right)\left|\int_{-\frac{\lambda_u}{2c\bar{\beta}_s}}^{\frac{\lambda_u}{2c\bar{\beta}_s}} (\vec{n}\times(\vec{n}\times\vec{\beta}))\, e^{i\omega(t-\frac{\vec{n}\cdot\vec{r}}{c})} dt\right|^2 \quad (12)$$

In order to deal with a periodic undulator with $N$ periods, we introduce the distribution function $\left(\frac{N\Delta\omega}{\omega_r}\right) = \frac{\sin^2\left(\frac{N\pi\Delta\omega}{\omega_r}\right)}{N^2\sin^2\left(\frac{\pi\Delta\omega}{\omega_r}\right)}$, in which $\omega_r = \frac{2\pi c}{\lambda_r} \approx \frac{\omega_u}{(1-\bar{\beta}_s\cos\vartheta)}$. For simplification, the energy density on-axis ($\vartheta = 0$) can be expressed as

The Bessel function relationship

$$e^{ix\sin\theta} = \sum_{p=-\infty}^{+\infty} J_p(x) e^{ip\theta}, \quad (15)$$

can be used to rewrite (13) as

$$\frac{d^2W}{d\Omega d\omega}\Big|_{\substack{\omega=h\omega_r\\ on-axis}} = h^2 D\left|\int_{-\frac{\lambda_u}{2c\bar{\beta}_s}}^{\frac{\lambda_u}{2c\bar{\beta}_s}} \sum_m \frac{B_m \cos(m\omega_u t - \delta\phi_m)}{m} e^{ih\omega_u t} \prod_{j,k} e^{\frac{ihAB_j B_k \sin(j\omega_u t + k\omega_u t - \delta\phi_j - \delta\phi_k)}{k\,(j+k)^2}} \prod_{j\neq k} e^{\frac{ihAB_j B_k \sin(j\omega_u t - k\omega_u t - \delta\phi_j + \delta\phi_k)}{k\,(j-k)^2}} dt\right|^2$$

$$= h^2 D\left|\int_{-\frac{\lambda_u}{2c\bar{\beta}_s}}^{\frac{\lambda_u}{2c\bar{\beta}_s}} \sum_m \frac{B_m \cos(m\omega_u t - \delta\phi_m)}{m} e^{ih\omega_u t} \prod_{j,k}\left\{\sum_{p_{jka}} J_{p_{jka}}\left[\frac{hAB_k}{k\,(j+k)^2}\right] e^{ip_{jka}(j\omega_u t + k\omega_u t - \delta\phi_j - \delta\phi_k)}\right\} \prod_{j\neq k}\left\{\sum_{p_{jkb}} J_{p_{jkb}}\left[\frac{hAB_j B_k}{k\,(j-k)^2}\right] e^{ip_{jkb}(j\omega_u t - k\omega_u t - \delta\phi_j + \delta\phi_k)}\right\} dt\right|^2 \quad (16)$$

If we set

$$M = \sum_{j,k} p_{jka}(j+k) + \sum_{j\neq k} p_{jkb}(j-k),\ \Theta = \sum_{j,k} p_{jka}(\delta\phi_j + \delta\phi_k) + \sum_{j\neq k} p_{jkb}(\delta\phi_j - \delta\phi_k) \quad (17)$$

Then the spectral angular energy density on-axis can be written as

$$\frac{d^2W}{d\Omega d\omega}\Big|_{\substack{\omega=h\omega_r\\ on-axis}} = h^2 D\left|\sum_m \sum_{h+M=\pm m}\left\{\frac{B_m}{m}\prod_{j,k} J_{p_{jka}}\left(\frac{hAB_j B_k}{k\,(j+k)^2}\right)\prod_{j\neq k} J_{p_{jkb}}\left(\frac{hAB_j B_k}{k\,(j-k)^2}\right)\int_{-\frac{\lambda_u}{2c\bar{\beta}_s}}^{\frac{\lambda_u}{2c\bar{\beta}_s}} \cos(m\omega_u t - \delta\phi_m)\, e^{i(h\omega_u t + M\omega_u t - \Theta)} dt\right\}\right|^2$$

$$= \frac{h^2 D\lambda_u^2}{4c^2}\left|\sum_m \sum_{h+M=\pm m}\left\{\frac{B_m}{m}\prod_{j,k} J_{p_{jka}}\left(\frac{hAB_j B_k}{k\,(j+k)^2}\right)\prod_{j\neq k} J_{p_{jkb}}\left(\frac{hAB_j B_k}{k\,(j-k)^2}\right)\cos(-\delta\phi_m \pm \Theta)\right\}\right|^2 \quad (18)$$

## COMPARISION WITH SPECTRA SIMULATIONS

For a pure sinusoid magnetic field undulator, $\vec{B} = B_1\sin(k_u z)\,\vec{e_y}$, the spectral angular energy density on-axis is

$$\frac{d^2W}{d\Omega d\omega}\Big|_{\substack{\omega=h\omega_r\\ on-axis}} = \frac{h^2 D\lambda_u^2 B_1^2}{4c^2\bar{\beta}_s^2}\left|J_{\frac{1-h}{2}}(hAB_1^2/4) + J_{\frac{-1-h}{2}}(hAB_1^2/4)\right|^2. \quad (19)$$

If only the 3rd order magnetic field introduced, $\vec{B} = [B_1\sin(k_u z) + B_3\sin(3k_u z - \delta\phi_3)]\,\vec{e_y}$, the energy density become more complicated. Considering that high order field strength is much lower than the fundamental one ($B_3 \ll B_1$), the fundamental energy density on-axis can be written as

ISBN: 978-3-95450-199-1 doi:10.18429/JACoW-SAP2017-TUPH09

$$\left.\frac{d^2W}{d\Omega d\omega}\right|_{\substack{\omega=\omega_r\\on-axis}} \approx \frac{h^2 D\lambda_u^2}{4c^2\overline{\beta}_s^2}\cdot \left|\begin{array}{l} B_1 J_0\left(\frac{AB_1B_1}{4}\right) J_0\left(\frac{AB_1B_3}{48}\right) J_0\left(\frac{AB_3B_1}{16}\right) J_0\left(\frac{AB_3B_3}{108}\right) J_0\left(\frac{AB_1B_3}{12}\right) J_0\left(\frac{AB_3B_1}{4}\right) + \\ B_1 J_1\left(\frac{AB_1B_1}{4}\right) J_0\left(\frac{AB_1B_3}{48}\right) J_0\left(\frac{AB_3B_1}{16}\right) J_0\left(\frac{AB_3B_3}{108}\right) J_1\left(\frac{AB_1B_3}{12}\right) J_0\left(\frac{AB_3B_1}{4}\right)\cos(\delta\phi_3) + \\ B_1 J_{-1}\left(\frac{AB_1B_1}{4}\right) J_0\left(\frac{AB_1B_3}{48}\right) J_0\left(\frac{AB_3B_1}{16}\right) J_0\left(\frac{AB_3B_3}{108}\right) J_{-1}\left(\frac{AB_1B_3}{12}\right) J_0\left(\frac{AB_3B_1}{4}\right)\cos(\delta\phi_3) + \\ B_1 J_1\left(\frac{AB_1B_1}{4}\right) J_0\left(\frac{AB_1B_3}{48}\right) J_0\left(\frac{AB_3B_1}{16}\right) J_0\left(\frac{AB_3B_3}{108}\right) J_0\left(\frac{AB_1B_3}{12}\right) J_{-1}\left(\frac{AB_3B_1}{4}\right)\cos(\delta\phi_3) + \\ B_1 J_{-1}\left(\frac{AB_1B_1}{4}\right) J_0\left(\frac{AB_1B_3}{48}\right) J_0\left(\frac{AB_3B_1}{16}\right) J_0\left(\frac{AB_3B_3}{108}\right) J_0\left(\frac{AB_1B_3}{12}\right) J_1\left(\frac{AB_3B_1}{4}\right)\cos(\delta\phi_3) + \\ B_1 J_{-1}\left(\frac{AB_1B_1}{4}\right) J_0\left(\frac{AB_1B_3}{48}\right) J_0\left(\frac{AB_3B_1}{16}\right) J_0\left(\frac{AB_3B_3}{108}\right) J_0\left(\frac{AB_1B_3}{12}\right) J_0\left(\frac{AB_3B_1}{4}\right) + \\ B_1 J_0\left(\frac{AB_1B_1}{4}\right) J_0\left(\frac{AB_1B_3}{48}\right) J_0\left(\frac{AB_3B_1}{16}\right) J_0\left(\frac{AB_3B_3}{108}\right) J_1\left(\frac{AB_1B_3}{12}\right) J_0\left(\frac{AB_3B_1}{4}\right)\cos(\delta\phi_3) + \\ B_1 J_0\left(\frac{AB_1B_1}{4}\right) J_0\left(\frac{AB_1B_3}{48}\right) J_0\left(\frac{AB_3B_1}{16}\right) J_0\left(\frac{AB_3B_3}{108}\right) J_{-1}\left(\frac{AB_1B_3}{12}\right) J_0\left(\frac{AB_3B_1}{4}\right)\cos(\delta\phi_3) + \\ \frac{B_3}{3} J_1\left(\frac{AB_1B_1}{4}\right) J_0\left(\frac{AB_1B_3}{48}\right) J_0\left(\frac{AB_3B_1}{16}\right) J_0\left(\frac{AB_3B_3}{108}\right) J_0\left(\frac{AB_1B_3}{12}\right) J_0\left(\frac{AB_3B_1}{4}\right)\cos(\delta\phi_3) + \\ \frac{B_3}{3} J_0\left(\frac{AB_1B_1}{4}\right) J_0\left(\frac{AB_1B_3}{48}\right) J_0\left(\frac{AB_3B_1}{16}\right) J_0\left(\frac{AB_3B_3}{108}\right) J_{-1}\left(\frac{AB_1B_3}{12}\right) J_0\left(\frac{AB_3B_1}{4}\right) + \\ \frac{B_3}{3} J_0\left(\frac{AB_1B_1}{4}\right) J_0\left(\frac{AB_1B_3}{48}\right) J_0\left(\frac{AB_3B_1}{16}\right) J_0\left(\frac{AB_3B_3}{108}\right) J_0\left(\frac{AB_1B_3}{12}\right) J_1\left(\frac{AB_3B_1}{4}\right) + \\ \frac{B_3}{3} J_0\left(\frac{AB_1B_1}{4}\right) J_{-1}\left(\frac{AB_1B_3}{48}\right) J_0\left(\frac{AB_3B_1}{16}\right) J_0\left(\frac{AB_3B_3}{108}\right) J_0\left(\frac{AB_1B_3}{12}\right) J_0\left(\frac{AB_3B_1}{4}\right)\cos(2\delta\phi_3) + \\ \frac{B_3}{3} J_0\left(\frac{AB_1B_1}{4}\right) J_0\left(\frac{AB_1B_3}{48}\right) J_{-1}\left(\frac{AB_3B_1}{16}\right) J_0\left(\frac{AB_3B_3}{108}\right) J_0\left(\frac{AB_1B_3}{12}\right) J_0\left(\frac{AB_3B_1}{4}\right)\cos(2\delta\phi_3) \end{array}\right|^2 \quad (20)$$

As shown in Fig.1 is the relative variation of undulator parameter ($\frac{K-K_1}{K}$) due to high-order magnetic field, where $K_1$ represents the undulator parameter caused by fundamental magnetic field $K_1 = \frac{eB_1}{m_e c k_u}$, and K represents the one described in equation (8). In consideration of the tolerable K error less than $5\times10^{-5}$, the influence of radiation wavelength caused by high-order magnetic field cannot be ignored.

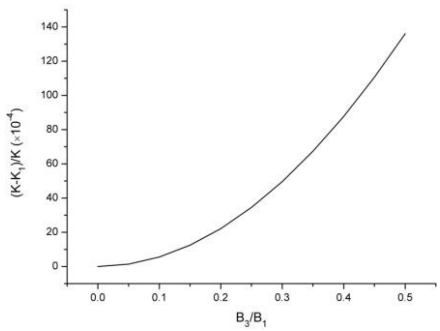


Figure 1: The relative variation of the undulator parameter due to high-order magnetic field. The horizontal coordinate is the ratio of $B_3$ to $B_1$.

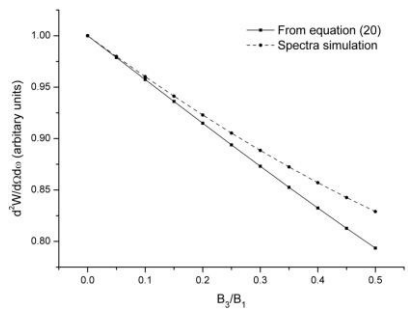


Figure 2: The variation of the fundamental spectral angular energy density with $B_3/B_1$ (phase $\delta\phi_3 = 0$). The solid line is the one from equation (20), the dashed line comes from Spectra simulation.

In studying the radiation influence of high-order magnetic field, we keep the radiation wavelength unchanged, i.e. the undulator parameter shown in equation (8) remains constant. As shown in Fig.2, if we choose phase shift zero ($\delta\phi_3 = 0$), the fundamental spectral angular energy density on-axis varies with the ratio of $B_3$ to $B_1$, and the result is very similar with Spectra [5] simulation.

In fact, the phase cannot be ignored completely. Figure 3 shows the variation of the fundamental spectral angular energy density on-axis with phase. It can be seen the radiation intensity fluctuates according to the magnetic phase.

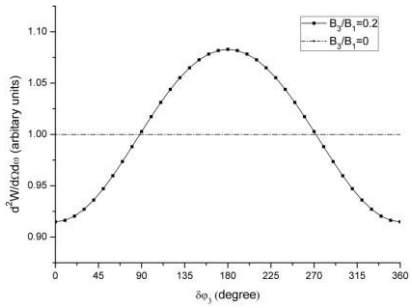


Figure 3: The variation of the fundamental spectral angular energy density with magnetic phase $\delta\phi_3$ ($\frac{B_3}{B1} = 0.2$).

As shown in Fig.3, the magnetic phase will influence the radiation output, the minimum value of radiation intensity appears at $\delta\phi_3 = 0$ and the maximum value at $\delta\phi_3 = \pi$. Both magnetic field distributions are shown in Fig.4, it looks the bigger peak field results in stronger radiation.

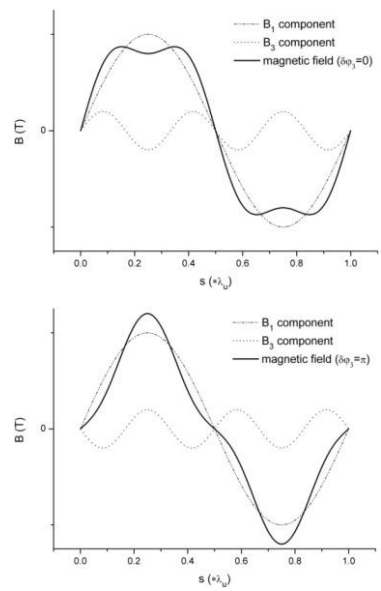


Figure 4: The variation of the fundamental spectral angular energy density with magnetic phase $\delta\phi_3$ ($\frac{B_3}{B1} = 0.2$).

## CONCLUSION

The high-order magnetic field is small mount compared with the fundamental one. Normally the ratio is less than 0.2. The influence of high-order magnetic field to the radiation output is lower than 10%.

It is worth noting that the influence of high-order magnetic field to the wavelength cannot be ignored, and the undulator parameter as described in equation (8) is the right one for high-order undualtor.

ISBN: 978-3-95450-199-1 doi:10.18429/JACoW-SAP2017-TUPH09

## REFERENCES

[1] Thomas C. Marshall, "Free-electron lasers", *Macmillan publishing company*, 1985, ISBN-13: 9780070406094.

[2] James A. Clarke, "The science and technology of Undulators and Wigglers", *Oxford university press*, 2004, ISBN-13: 9780198508557.

[3] H. Onuki and P. Elleaume, "Undulators, Wigglers and their applications", *Taylor & Francis*, First published 2003, ISBN: 0-415-28040-0.

[4] Peter Schmuser, Martin Dohlus and Jorg Rossbach, "Undulators, Ultraviolet and soft X-Ray Free-electron lasers", *Springe-Verlag Berlin Heidelberg*, 2008, ISBN: 978-3-540-79571-1.

[5] T. Tanaka and H. Kitamura, "SPECTRA - a synchrotron radiation calculation code", *J. Synchrotron Radiation*, 8 (2001) 1221.

ISBN: 978-3-95450-199-1 doi:10.18429/JACoW-SAP2017-TUPH10

# ELECTRON COOLING OF BUNCHED ION BEAM IN STORAGE RING *

Lijun Mao†, He Zhao, Meitang Tang, Jie Li, Xiaoming Ma, Xiaodong Yang, Jiancheng Yang
Insitute of Modern Physics, Lanzhou, China

*Abstract*

A combination of electron cooling and RF system is an effective method to compress the beam bunch length in storage rings. Bunched ion beam cooling experiments have been carried out in the main cooling storage ring (CSRm) of the Heavy Ion Research Facility in Lanzhou (HIRFL), to investigate the minimum bunch length obtained by the cooling method, and study the dependence of the minimum bunch length on beam and machine parameters. It is observed that the IBS effect is dominant for low intensity beams, and the space charge effect is much more important for high intensity beams. The experimental results in CSRm shown a good agreement with the analytical model in the IBS dominated regime. Meanwhile, the simulation work offers us comparable results to those from the analytical model both in IBS dominated and space charge dominated regimes.

## INTRODUCTION

The HIRFL accelerator complex is a multipurpose research facility for nuclear physics, atomic physics and applied research in medicine, biology and materials science. It consists of two cyclotrons, two storage rings and several experimental terminals[1]. Two electron coolers installed in the storage rings CSRm and CSRe (experimental Cooling Storage Ring) are applied to the stored ion beams for the phase space compression. The electron coolers were designed and manufactured in the cooperation between IMP China and BINP Russian[2]. The layout of HIRFL accelerator complex is shown in Fig. 1.

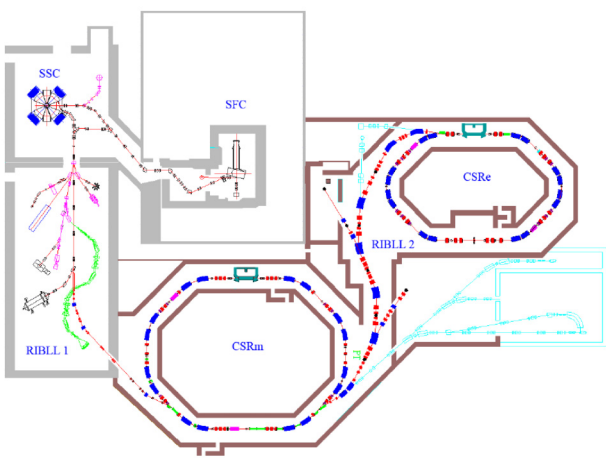


Figure 1: Layout of HIRFL accelerator complex.

Electron cooling is a powerful method for shrinking the size, the divergence and the momentum spread of stored charged-particle beams in storage rings for precision experiments. It also supports beam manipulations involving RF system to provide beam with short bunch length. Short-bunched ion beam has a wide range of application in rare isotope production, high energy density physics experiment, collider and cancer therapy. In order to study the cooling process of bunched ion beam, a series of experiments have been done in several cooling storage rings, such as HIMAC, ESR, IUCF and CSRe[3-5]. The results shown that the minimum bunch length of cooled-beam is affected by the equilibrium between electron cooling, IBS effect, ion beam space charge field and RF voltage, but the dependence of the minimum bunch length on the beam parameters has a slight difference in those experiments.

In this paper, we present the recent experimental results which was done at CSRm, and compare with the simulation results based on the multi-particle tracking method. Bothe experimental and simulated results shown a good agreement with the analytical model.

## BUNCH LENGTH MEASUREMENT

The experiments were performed with $^{112}Sn^{36+}$ beam at the energy of 3.7 MeV/u and $^{12}C^{6+}$ beam at the energy of 6.9 MeV/u, respectively. The range of stored particle number was from $10^6$ to $10^9$. A flat distribution electron beam with diameter around 50 mm was used for beam cooling. The electron beam current was set as 135 mA for $^{112}Sn^{36+}$ beam and 44 mA for $^{12}C^{6+}$ beam, respectively. A sinusoidal RF voltage from 0.2 to 2.3 kV was applied with the harmonic number of 2.

A typical experimental cycle is as follow: heavy ions are injected, accumulated and cooled with the help of continuous electron beam, and then a sinusoidal RF voltage is switched on with 2nd harmonic number of revolution frequency. The bunch length after 2 seconds of turning on the RF system is measured by a position pick up with the length of 150 mm and the capacitor of 120 pF. The voltage drop at a 50 Ohms resistor between the pick up and ground is amplified by a pre-amplifier with the gain factor of 54 dB. An oscilloscope with bandwidth of 1 GHz is used to read the signal from the pre-amplifier. A RMS bunch length value is evaluated from a Fokker-Plank fitting result of this voltage signal. As an example, a measurement of the voltage signal from pick up for $^{112}Sn^{36+}$ beam is shown in Fig. 2. In this case, the beam longitudinal linear charge density is obtained by the integration of the pick up voltage signal. The RMS bunch length $\sigma_t$ is evaluated by the Fokker Plank fitting result of the bunch shape data.

* Work supported by National Natural Science Foundation of China No. 11575264, No. 11375245, No. 11475235 and the Hundred Talents Project of the Chinese Academy of Sciences
† email address: maolijun@impcas.ac.cn

ISBN: 978-3-95450-199-1 doi:10.18429/JACoW-SAP2017-TUPH10

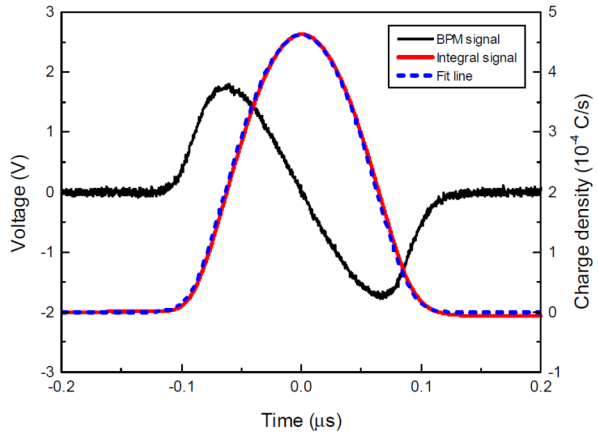


Figure 2: Voltage signal of bunched beam acquired from BPM and the linear charge density calculated by BPM signal with its Fokker Plank fitting result.

The stored beam current was measured by the DC current Transformer (DCCT) in CSRm the particle number per bunch is calculated by Eq. (1):

$$N = \frac{I}{eZhf}. \quad (1)$$

Where $I$ is the beam current measured by DCCT, $Z$ is the charge state of particle, $h$ is the harmonic number and $f$ is the revolution frequency.

## EXPERIMENTAL RESULTS

The experimental results of $^{112}Sn^{36+}$ and $^{12}C^{6+}$ beam are shown in Fig. 3, in which the dependency of the minimum bunch length n particle number at different RF voltage is presented. It is observed that the bunch length increases proportionally to $N^k$, and the range of $k$ is from 0.22 to 0.28 for such low ion intensities and energies. For space charge dominated beam, $k$ is close to 1/3 which have been measured and analysed in references. According to these results, the beam charge density in longitudinal is determined by the geometrical factor $g$ and $\sigma$, where the value of $g$ influences the width of the central part and $\sigma$ defines the tails. In our case, we think the bunched beam after cooling belongs to IBS domain and the beam bunch length is mainly determined by IBS effect, even the central part of the beam is strongly affected by space charge effect. As the results shown in reference, the evolution of RMS momentum spread show a different rule with the total beam current and the peak current respectively.

In the experiments, the stored particle number per bunch is from $10^6$ to $10^8$. Accordingly, the IBS effect is the main heating source to affect the bunch length for such low ion intensity and low energy, in which the space charge effect only exit at the central part of beam that with quite small momentum spread. Therefore, the distribution of bunched beam is mainly determined by the particles outside the canter that with large momentum spread relatively. The space charge potential can be ignored for the particle outside the centre, and the synchrotron motion of these particles can be described by small amplitude oscillation in RF bucket:

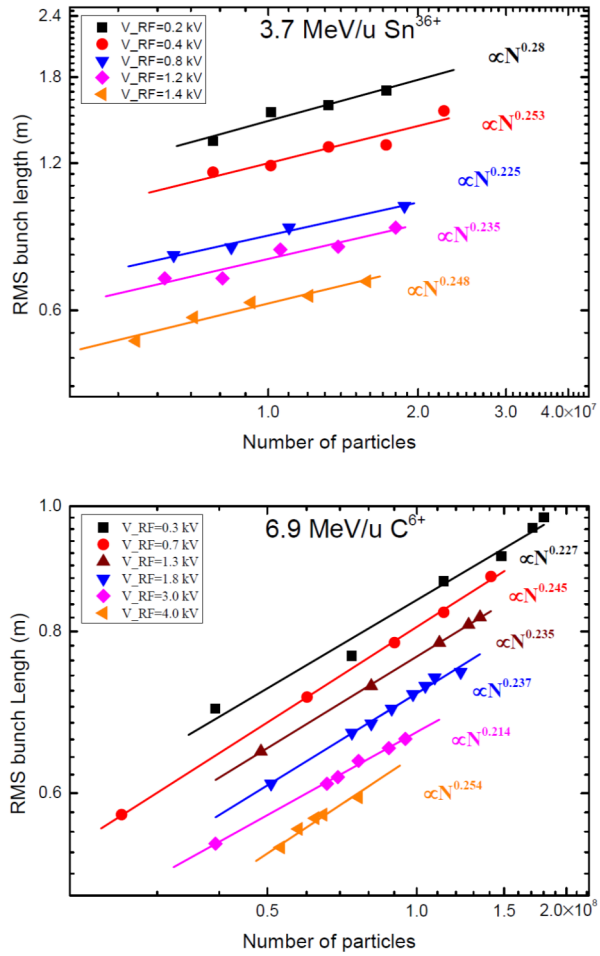


Figure 3: Dependency of the RMS bunch length on the stored particle number for different RF voltages for $^{112}Sn^{36+}$ and $^{12}C^{6+}$ ion beams, respectively. The solid lines are fitted to the experimental data.

$$\frac{\delta}{\theta} = \left(\frac{ehV_{RF}|\cos\emptyset_s|}{2\pi\beta^2 E|\eta|}\right)^{1/2} = \frac{Q_{s0}}{|\eta|} \quad (2)$$

where $\delta$ and $\theta$ are the maximum amplitudes of the phase space ellipse, $E$ is the total energy of ions, $\eta$ is the slip factor and $Q_{s0}$ is the synchrotron tune. It is clear that the bunch length for small amplitude oscillation increases linearly with the momentum spread for a certain RF amplitude. In the cooling process, the evolution of momentum spread satisfies the differential equation:

$$\frac{1}{\delta_p}\frac{d\delta_p}{dt} = \frac{1}{\tau_{cooling}} + \lambda_{heating} \quad (3)$$

here the $\tau_{cooling}$ is the cooling time and $\lambda_{heating}$ is the heating rate. For low ion intensities and energies, the heating rate is determined by the IBS heating rate, and when the equilibrium is achieved, we can get:

$$\frac{1}{\tau_{cooling}} = \lambda_{IBS} \quad (4)$$

ISBN: 978-3-95450-199-1 doi:10.18429/JACoW-SAP2017-TUPH10



According to the electron cooling theory, the cooling force value on particle with small momentum deviations $\Delta p$ is a linear function $F=k\Delta p$, where $k$ is the slop of the longitudinal cooling force which is a constant for a certain electron beam setting. Therefore, the cooling time for the cold beam at equilibrium status with small momentum spread $\delta_p$ is:

$$\frac{1}{\tau_{cooling}} = \frac{F}{p_0} = k\delta_p \tag{5}$$

The gas relaxation model can be used for the calculation of IBS heating rate, the longitudinal heating rate for bunched beam is given by:

$$\lambda_{IBS} = \frac{1}{2\delta_p^2}\frac{d\delta_p^2}{dt} = \frac{r_i^2 c N_i \Lambda}{16\beta^2\gamma^3\varepsilon_\perp^{3/2}\langle\beta_\perp^{3/2}\rangle\sqrt{\pi/2}\sigma_b\delta_p^2} \tag{6}$$

Where $\Lambda$ is the coulomb logarithm, $\varepsilon_\perp$ is the transverse emittance, $\beta_\perp$ is the beta function, $N_i$ is the particle number per bunch corresponds to 92% of ion beam in longitudinal direction. In the equilibrium state, we get

$$k\delta_p = \frac{r_i^2 c N_i \Lambda}{16\beta^2\gamma^3\varepsilon_\perp^{3/2}\langle\beta_\perp^{3/2}\rangle\sqrt{\pi/2}\sigma_b\delta_p^2} \tag{7}$$

According to the Eqs. (2-7), the minimum bunch length after cooling is increase proportionally to:

$$\sigma_b \propto N^{1/4} \tag{8}$$

which has a good agreement with the experiment results shown in Fig. 3.

## SIMULATION

A simulation code based on multi particle tracking method was developed, in which the ion beam is represented by a number of model particles and the beam dynamics is calculated by statistical method. The cooling, IBS, space charge field and synchrotron motion are considered in simulation.

In order to investigate the limitation of bunch length under different beam intensities, a calculation of $^{12}C^{6+}$ beam with RF voltage 1.0 kV were done, the other parameters are the same as experiments. Figure 4 shows a comparison of the simulation results to the experimental results. According to the results considered the IBS effect only, the experimental results are clearly belong to the IBS dominant regime. The bunch length is proportional to $N^{1/4}$. The space charge dominated beam will attained when the particle number per bunch exceeds $6\times10^8$. When only space charge effect is considered, it is observed that the dependency of the particle number is divided into two regions. The expected dependence of the bunch length shown in Figure 4 is close to $N^{1/3}$ for the particle number less than $10^9$. Such results can be explained rather well by the equilibrium between the space charge effect and RF voltage. Beyond this particle number, an additional increase of the bunch length occurs, proportional to $N^{3/4}$, it is also observed that the particles almost out the RF bucket for much high beam density.

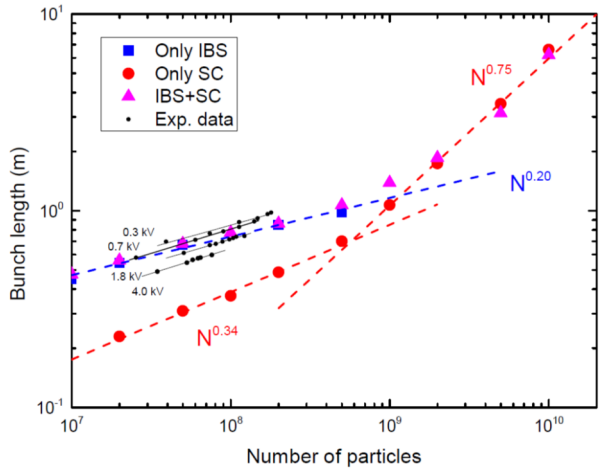


Figure 4: The bunch length versus particle number in simulation and experiment. The dash lines are fitted to the simulation results.

## CONCLUSION

In this paper, we reported the experimental and simulated results of the minimum ion beam bunch length obtained by a combination of electron cooling and RF system. It is obvious that such combination is an effective method for beam bunch compression. Both results show that the minimum bunch length increase proportionally to the particle number in bunches with $N^{\alpha}$. The dependence can be divided into two conditions. For small particle number, the IBS effect is dominant and the exponent is 1/4. For higher intensity the ion beam space charge effect is dominant and the exponent is 1/3. Additionally, when more particles applied, some blow up effect will happen and the beam almost cannot be bunched in the RF bucket. The experimental results in CSRm shown a good agreement with the simulation results in the IBS dominated regime.

## REFERENCES

[1] J.W.Xia, W.L.Zhan, B.W.Wei *et al.*, *Nucl. Instrum. Methods Pys. Res., Sect. A* 488, 11 (2002).

[2] X.D.Yang, H.W.Zhao, J.W.Xia *et al.*, in *Proc. APAC'01*, Beijing, China, p.777.

[3] G.Kalisch, K.Beckert, B.Franzke *et al.,* in *Proc. European Particle Accelerator Conference*, Berlin, Germany, 1992, p.780.

[4] T.J.P.Ellison, S.S.Nagaitsev, M.S.Ball *et al.*, *Phys. Rev. Lett.* 70, p.790.

[5] L.J.Mao, H.Zhao, X.D.Yang *et al.*, *Nucl. Instrum. Methods Pys. Res., Sect. A* 808, 29 (2016)

ISBN: 978-3-95450-199-1 doi:10.18429/JACoW-SAP2017-TUPH11

# RESONANCE STOP-BANDS COMPENSATION FOR THE BOOSTER RING AT HIAF*

J. Li†, J. C. Yang, HIAF design group, Institute of Modern Physics, CAS, Lanzhou, China

*Abstract*

The Booster Ring (BRing) of the new approved High Intensity heavy-ion Accelerator Facility (HIAF) in China is designed to stack $1.0{\cdot}10^{11}$ number of $^{238}U^{35+}$ ions at the injection energy of 17MeV/u and deliver over such intensity beam to SRing (Spectrometer Ring) at 800MeV/u. However such intensity beam causes low-order resonances crossing during RF bunching. To keep a low beam loss, resonance stop-band compensation scheme is proposed covering the process from RF capture to the first stage of acceleration below 200 MeV/u.

## INTRODUCTION

### *Layout of the HIAF*

The High Intensity heavy-ion Accelerator Facility (HIAF) is a new heavy ion accelerator complex under detailed design by Institute of Modern Physics [1]. Two typical particles of $^{238}U^{35+}$ and proton is considered in the design. The beam is generated by a Superconducting Electron Cyclotron Resonance (SECR) ion source or an intense proton source, and accelerated mainly by an ion linear accelerator (iLinac) and an booster ring (BRing). The iLinac is designed to deliver $H_2^+$ at 48 MeV and $^{238}U^{35+}$ at 17 MeV/u. Before entrancing the BRing, $H_2^+$ is stripped to proton, and then accumulated by two-plane painting and accelerated to 9.3 GeV. The $^{238}U^{35+}$ is injected by multi-turn two-plane painting scheme, after accumulation or cooling by a electron cooler at the BRing, then accelerated to 0.2-0.8 GeV/u for extraction. After being stripped at the HIAF FRagment Separator (HFRS), the secondary beam like $^{238}U^{92+}$ is injected to the Spectrometer Ring (SRing) for the high precision physics experiments. Besides, five external target stations of T1 - T5 is planned for nuclear and atomic experimental researches with the energy range from 5.8-800 MeV/u for uranium beam.

### *Overview of the BRing*

The BRing is designed to accumulate beam intensity up to space charge limit at the injection energy and deliver over $1.0\cdot10^{11}$ $^{238}U^{35+}$ ions or $1.0\cdot10^{12}$ proton to SRing in extraction. Two operation modes of fast and slow are considered. Fast mode feathers multi-turn two-plane painting injection within around 120 revolution turns whereas the slow one by over 10 s injection time for electron cooling helped accumulation. Main parameters of the BRing are listed in Table 1. The BRing has a three-folding symmetry lattice around its circumference of 549.45 m. Each super-period consists of an eight-FODO-like arc and an over 70 m long dispersion-free straight section featured with a length of 15.7 m drift reserved for electron cooler, two-plane painting injection, or RF cavities. Lattice layout of the BRing for one super-period is shown in Fig. 1.

Table 1: Main Parameters of $^{238}U^{35+}$ at the BRing

| | |
|---|---|
| Circumference | 549.45 m |
| Max. magnetic rigidity | 34 Tm |
| Periodicity | 3 |
| Injection energy | 17 MeV/u |
| Betatron tune | (8.45,8.43) |
| Acceptance ( $H/V, \delta p/p$ ) | $200/100\pi mmmrad$, ±5.0‰ |

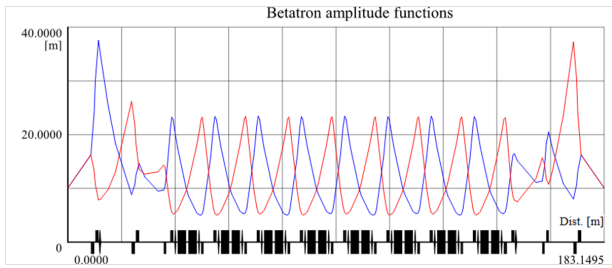


Figure 1: BRing lattice for one super-period.

## RESONANCE AND STOP-BANDS

### *Betatron Resonances*

The charged particle beam produces repulsive force and results in depressed tune distribution in tune diagram. During the injection and accumulation process of $^{238}U^{35+}$ beam at the BRing, the nominal working point is set as (8.45, 8.43) with safety distance from dangerous low order structure resonances e.g., $2Q_y - Q_x = 9$ and $2Q_x - Q_y = 9$. The only structure resonances appear in Fig. 2 are four $4th$-order ones shown as pink lines. They will be ignored due to weak effect considering the operation experiences. Thus, no structure resonances will be considered at our case.

The tune spread of $^{238}U^{35+}$ at the design intensity of $1.0{\cdot}10^{11}$ is shown in Fig. 2 as the blue dots when the transverse emittance equals to acceptance. The red dots give the spread information of cooled beam when the emittance is decreased to $50/50\pi mmmrad$ [2]. For the two cases above, the uranium beam has a momentum spread of ±2.0‰ and bunching factor of 0.4 after RF capture. The design intensity produces a vertical tune spread about 0.16 for $200/100\pi mmmrad$ and 0.33 for the cooled beam. The figure also indicates an overlapping of tune spread with four $3^{rd}$-order betatron resonances and a linear coupling difference resonance at the both situation. The overlapping of tune

* Work supported by NSFC (Grant No. 11475235, 11375245, 11575264)
† lijie@impcas.ac.cn

ISBN: 978-3-95450-199-1 doi:10.18429/JACoW-SAP2017-TUPH11



spread with these resonances will induce emittance variation and even beam loss.

To enlarge valid tune space for beam accumulation, new correction fields are introduced to counteract with stop-bands derived from the magnets imperfection and unwanted multi-pole fields. Correction or compensation of the following low-order betatron resonance stop-bands is considered for intensive $^{238}U^{35+}$ beam operation at the BRing.

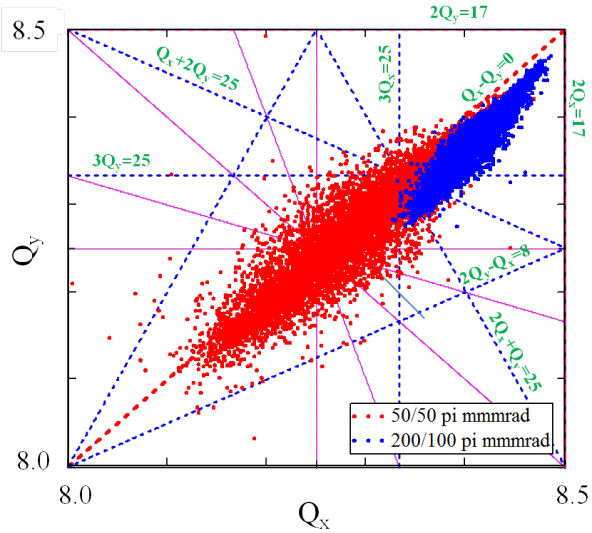


Figure 2: Resonances in tune diagram at the BRing i.e., linear difference coupling (red dotted line), $3^{rd}$-order betatron (blue dotted line), $4^{th}$-order structure (pink solid line), and two half-integer resonances; The nominal working point for $^{238}U^{35+}$ injection is set as (8.45, 8.43).

### *Stop-bands Compensation*

Resonance causes emittance growth or beam loss when the tune of ion sits on the stop-bands. The main sources of related resonance stop-bands at the BRing are listed as below:

(a) Half-integer ones of $2Q_x = 17$ and $2Q_y = 17$

derives from quadruple fields imperfection and high order field component of magnets; to be compensated with normal quadrupole field

(b) Linear coupling difference of $Q_x - Q_y = 0$

derives from longitudinal fields by solenoid, rotation of quadruples, vertical offset of sextuple, and high order field component; to be compensated with skew quadrupole fields

(c) $3^{rd}$-order of $3Q_x = 25$, $Q_x + 2Q_y = 25$, and $2Q_y - Q_x = 8$

derives from sextuple alignment and high-order components of magnets; to be compensated with normal sextuple field

(d) $3^{rd}$-order of $3Q_y = 25$, $2Q_x + Q_y = 25$

derives from sextuple alignment and high-order components of magnets; to be compensate with skew sextuple field

where $Q_x$ and $Q_y$ is the betatron tune values.

### *Tune Spread Dependence on Energy*

The time length for one fast cycle is about 3 s that consists of 20 ms for ramping up to the injection plateau, 2 ms for painting injection, 60 ms for RF capture, 73 ms at the $1^{st}$ stage of acceleration, 90 ms for RF debunching, 120 ms for the $2^{nd}$ stage of RF capture, 973 ms for the $2^{nd}$ stage of acceleration, 40 ms at top plateau, and ramping down in 1580 ms. If we take 0.4 as the maximum valid vertical tune space for the spread of stored beam, then it will shrink to 0.093 when the synchrotron ramps up to the middle plateau of 200 MeV/u according calculation of tune spread [3]. That means the effect of low order resonance will be eliminated due to not overlapping any more low-order resonances. Therefore, the compensation becomes necessary only below 200 MeV/u for the current nominal working point at the BRing. The dependence of maximum allowed tune spread upon energy is shown in Fig. 3.

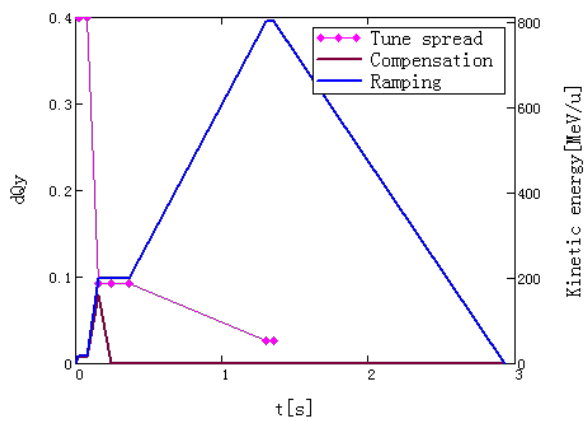


Figure 3: Dependence of allowed tune spread upon kinetic energy at the BRing at the fast cycle mode.

## COMPENSATION SCHEME

We assume that the misalignment errors of dipole, quadruple, and sextuple magnets have a random distribution with transverse offset $\delta x = 0.2$ mm, $\delta x = 0.2$ mm, rotation $\delta\phi_t = 0.2$ mrad, and longitudinal offset $\delta s = 0.2$ mm and rotation $\delta\phi_s = 0.2$ mrad, and multi-pole field error $\delta B/B = 3 \cdot 10^{-4}$. For the case of applying the electron cooling, at the straight section for electron cooler, a longitudinal magnetic field is introduced by cooling section solenoid and two toroids with an equivalent length of 9.6 m and a strength of 0.08 T.

For stop-band compensation, the phase advance $\Delta\phi$ between compensating elements demands the following rela-

ISBN: 978-3-95450-199-1 doi:10.18429/JACoW-SAP2017-TUPH11

tionship:

$$\frac{\Delta\phi}{Q_{x,y}} \cdot M \rightarrow (n + \frac{1}{2})\pi \quad (1)$$

where $Q_{x,y}$ the horizontal or vertical working point and $M$ is the resonance number of $jQ_x + kQ_y = M$. And $j, k, n$, are any integers. Meanwhile, A large ratio between the two transverse betatron functions of the compensation elements is demanded because it can release the strength requirement for compensation magnet.

### *Half-integer Resonance*

The compensation of half-integer resonance is reserved for setting new working points out range of the tune area shown in Fig. 1. The misalignment and multi-pole field errors list above bring a resonance stop-band width of 0.003 for $2Q_x = 17$, and 0.004 for $2Q_y = 17$ at the injection energy. According to the phase advance and betatron function, we use two group of trim coils added upon existed quadruples of QFS2K and QFSK, QDSK and QD1 within the same straight section to make the horizontal and vertical compensation separately. The designed strength is 0.0015 $m^{-2}$ or about 0.6% of that for the standard quadrupole at injection energy.

### *Linear Difference Coupling*

According to the calculation of stop-band width of linear difference coupling resonance of $Q_x - Q_y = 0$, the contribution to resonance excitation from the longitudinal fields introduced by switching on electron cooler is six times larger than that by misalignment and field errors that corresponds a stop-band width of 0.025 and 0.004 respectively

Four group of skew quadruple field families are considered for horizontal compensation with SQH01 and SQH02, and for the vertical one with SQV01 and SQV02. In each family, the two skew quadruple elements locates at the straight section but separated by the arc section. The skew field is generated by winding additional coils upon the close orbit dipole corrector. This type of corrector is designed with four magnet cores with two opposite ones providing dipole field and all the four ones produce skew quadruple field through additional windings. To release the strength of skew field in the case of compensation longitudinal field by cooler., eight skew quadruple element is considered with a strength of 0.025 $m^{-2}$. They have the same length of 0.3 m as dipole correctors.

### *$3^{rd}$-order Resonance*

The misalignment and field errors around the synchrotron create a stop-band width of 0.0002 for $Q_x + 2Q_y = 25$ and 0.001 for $3Q_x = 25$ at injection energy. According to formula (1), four trim sextuples used for chromaticity correction at the arc section are considered to generate normal sextuple field for the compensation with a strength of 0.02 $m^{-3}$. That's a strength of 0.1% of the standard sextuple magnet. The misalignment and error also induced a stop-band of 0.0006 for $2Q_y - Q_x = 8$, that will been corrected by four trim sextuple for chromaticity correction at the arc section with a strength of $0.01m^{-3}$ and length of 0.4 m .

The stop-band width produced by the errors listed above is 0.0002 for $2Q_x + Q_y = 25$ and 0.0006 for $3Q_y = 25$ at injection energy. Four new skew sextuples with strength of 0.02 $m^{-3}$ are planned to compensate the two resonances. They locates the straight section but separated by the arc section.

## CONCLUSION

Accumulation of uranium beam to its design intensity at the BRing induces an overlapping between tune spread and several low-order resonances. Compensation of these resonances below 200 MeV/u are considered. The preliminary compensation scheme is introduced for the resonances concerned.

## REFERENCES

[1] J.C. Yang *et al.*, "High Intensity heavy ion Accelerator Facility (HIAF) in China", *Nucl. Instr. and Meth. B*, vol. 317, p. 263-265, 2013.

[2] L.J. Mao, private communication, Mar. 2016.

[3] J. Li, *et al.*, "simulation of beam intensity limitations under space charge effects at BRing of HIAF", *This proceeding*, Aug. 2017.

ISBN: 978-3-95450-199-1 doi:10.18429/JACoW-SAP2017-TUPH21



# MAGNETIC MEASUREMENT OF THE UNDULATOR U38 FOR THZ-FEL

L. G. Yan, D. R. Deng, P. Li, J. X. Wang, H. Zhang, M. Li, X. F. Yang
Institute of Applied Electronics, China Academy of Engineering and Physics, Mianyang, China

*Abstract*

The high average power terahertz free electronic laser facility (THz-FEL) has one undulator named U38. As one of the most important components, U38 has a significant effect on entire facility. So, we measure the magnetic field of U38 to confirm its field qualities using magnetic field measurement bench before installation. The measurement gaps include 19 mm, 21 mm, 24 mm, 25.6 mm and 28 mm, and the longitudinal distribution of magnetic field on five lines at transverse positions of -6 mm, -3 mm, 0 mm, 3 mm and 6 mm are scanned. Electronic trajectory, peak field vs gap curve and peak-to-peak error are calculated based on the longitudinal distribution of magnetic field. We also measure the transverse distribution of magnetic field to test the good field region. In this proceeding, the measurement method is described and the results are presented and discussed.

## INTRODUCTION

The high average power terahertz source at CAEP (China Academy of Engineering Physics) is based on the routine of free electronic laser (FEL), which will output with the average power 10 W between the range of 100-300 μm. Undulator is one of the most important components in FEL and has a significant effect on spontaneous radiation, gain and saturation [1,2]. THz-FEL has one undulator named U38, which is manufactured by SINAP (Shanghai Institute of Applied Physics) at Shanghai. The magnetic structure of U38 consists of two standard Halbach-type permanent magnet arrays with period length 38 mm and gap range of 18-32 mm, which can generate max peak field of 0.55 T. Some errors must be decreased, such as peak-to-peak error (<1%), center trajectory deviation (<0.1 mm) and deviation error in 12 mm good field region (<0.5%) [3]. Before installation, it is indispensable to measure and characterize the magnetic field of U38 precisely in order to achieve high magnetic performances. In 2017, U38 is measured at Chengdu using magnetic filed measurement bench. In this proceeding, the measurement method is described and the results are presented and discussed.

## INSTRUMENT AND METHOD

A magnetic field measurement bench (MFMB) has been constructed to confirm the field qualities of U38, which transports Hall probe through the undulator straightly and precisely. The figure 1 shows the measurement site. The total length of MFMB is 3 m, which is enough to measure 1.64-m-long U38. Positioning errors of MFMB are better than 10 μm in all three moving axis, which limits errors in the probe motion through the undulator and in turn decreases measurement errors. Before measurement, the rough alignment is done by laser tracker to parallel the three center planes of MMFB and U38, and then the fine alignment is done by measuring and analyzing the magnetic field in horizontal and vertical plane to fix the position of Hall probe in U38. MMFB works on go-stop mode with step length of 0.5 mm and pause time of 0.5 s. Local magnetic field is acquired by Bell 8030 that is a three dimensions Gaussmeter with accuracy of ±0.05%. The room temperature is controlled within 23±0.5 °C to minimize the field variation of U38 and ensure an acceptable stability of the MFMB.

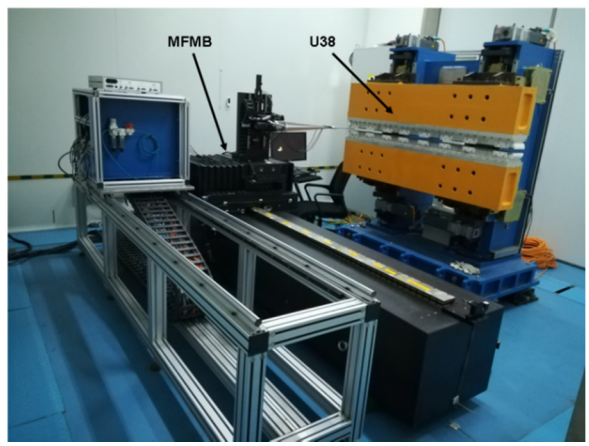


Figure 1: Measurement site.

## RESULTS AND DISCUSSION

The vertical component of earth field in our lab is about 0.3 Gs. It is known a small field can influence undulating field obviously and then damage the straightness of trajectory. So, there is a long coil on both of upper and lower beam to cancel the residual dipole field and earth field in gap. In the following data, if not specified, the optimal current has been applied on the long coil.

The measurement gaps include 19 mm, 21 mm, 24 mm, 25.6 mm and 28 mm. We scan five lines in the transverse position from 6 mm to -6 mm with step length of 3 mm along the U38 at every gap. The total measurement points are 4600, which correspond to a measurement distance of 2.3 m. The margin length on both sides is 0.33 m.

ISBN: 978-3-95450-199-1 doi:10.18429/JACoW-SAP2017-TUPH21

### *The Longitudinal Distribution of Magnetic Field*

All the longitudinal distribution of magnetic field curves are sine-like and antisymmetric type. Due to limited paper space, we won't show raw measurement results except for gap 24 mm. Commonly, we can only get discrete magnetic field values because of the limited measurement points on the five lines in horizontal plane. Here, we concluded magnetic field at any point in the horizontal plane by two dimensions interpolation based on the discrete data that we have. The result at the gap of 24 mm is shown in figure 2(a), and the longitudinal distribution of magnetic field at the transverse position of 2 mm is concluded and shown in figure 2(b). There is similar case in other gaps, so we won't show more figures.

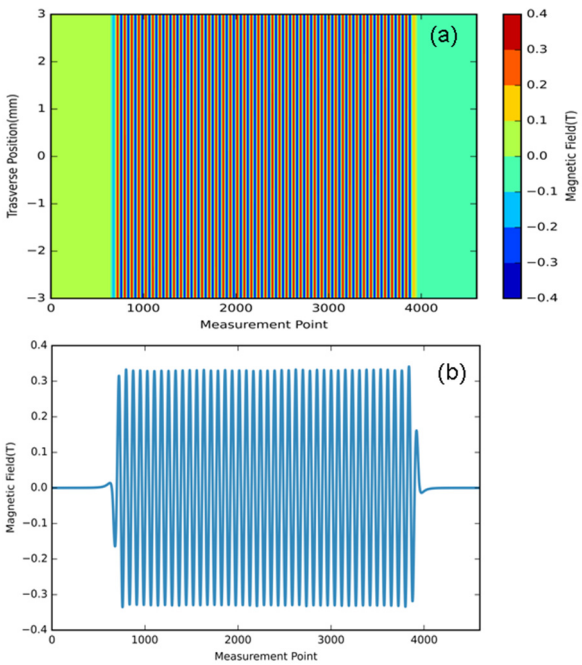


Figure 2: The magnetic field distribution in the horizontal plane (a) and at the transverse position of 2 mm (b) at the gap of 24 mm.

### *Electronic Trajectory*

Electronic trajectory is calculated by integrating the longitudinal field distribution twice, in where the kinetic energy 8 MeV of electronic is applied. The trajectories at the transverse position from 6 to -6 is shown in figure 3. The center trajectory (transverse position 0 mm) must be less than 0.1 mm to ensure the overlap of electronic beam and light beam in FEL scheme. In the other transverse positions, we have added a offset in figure 3. It is obvious that there is a weak focus in the horizontal plane. So the transport matrix in horizontal plane is not a drift type but a focus type, which is different from the ideal case.

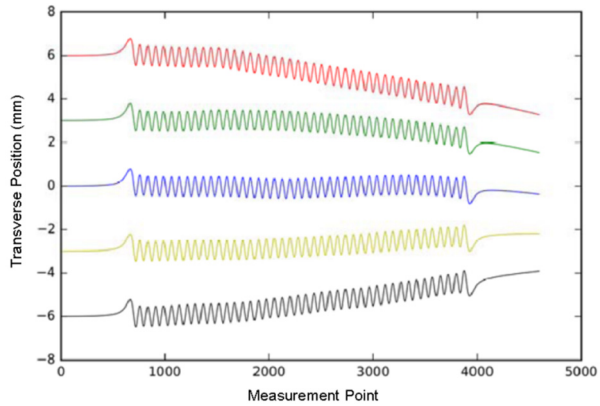


Figure 3: Electronic trajectories in the horizontal plane at the transverse position of -6 mm, -3 mm, 0 mm, 3 mm and 6 mm.

### *Peak Field vs Gap*

The wavelength of radiation light is determined by peak field of undulator and energy of electronic, so a continuous curve of peak field and gap is needful in application. Commonly, the peak field of undulator decreases exponentially with increasing of the gap. In previous studies, equation (1) has been attained experimentally, in which $B_0$ is peak field, $\lambda_u$ is period length, and $g$ is gap. The three coefficients a, b and c must be determined with given undulator [4]. At every gap, the root mean square value of peak field of U38 is calculated from all of 84 ordinary peak field values, and then a, b and c is determined by fitting equation (1) using least square method ($R^2$=1). They are a=2.991, b=-3.736 and c=0.379. Figure 4 shows the raw data (red point) and the fitting curve (blue line). Now, peak field at any gap can be concluded by equation (1).

$$B_0 = a * e^{b*\frac{g}{\lambda_u} + c*(\frac{g}{\lambda_u})^2} \quad (1)$$

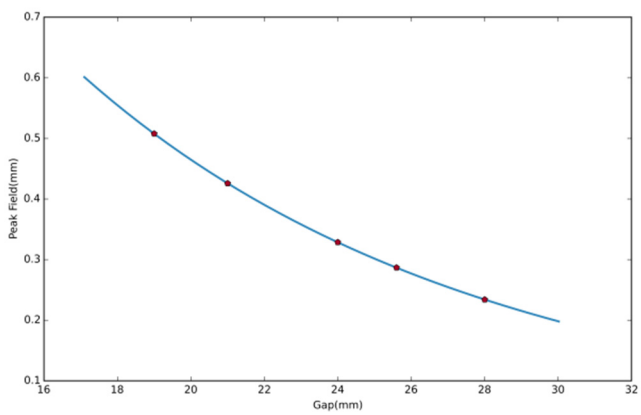


Figure 4: Peak field vs gap from 19 mm to 28 mm.

ISBN: 978-3-95450-199-1 doi:10.18429/JACoW-SAP2017-TUPH21



### *Peak-to-peak Error*

The peak-to-peak error is calculated by the root mean square value of peak field dividing mean value of peak field. The peak-to-peak error vs gap is shown in figure 5. All the errors are less than the required value of 0.5%. We also see the peak-to-peak error decreases with increasing the gap dramatically. It is because the influence of local error due to machining error and slight inhomogeneity of material on axis magnetic field becomes weak duo to the increase of distance of magnetic structure and horizontal plane.

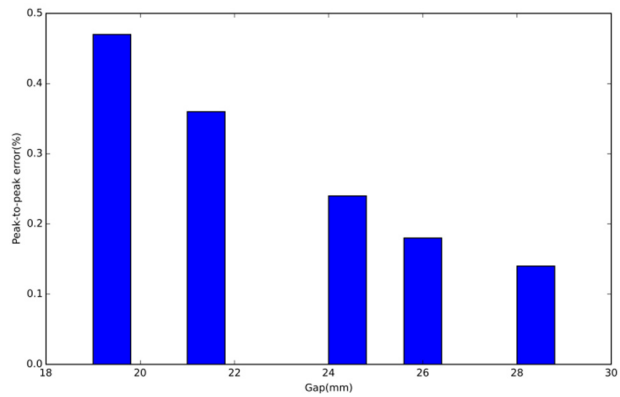


Figure 5: Peak-to-peak error at the gap of 19 mm, 21 mm, 24 mm, 25.6 mm and 28 mm.

### *Good Field Region*

The width of magnetic structure must be wide enough to cover the width the transverse motion of electronic beam. In U38, 12 mm good field region with error of 0.5% is required. The transverse distribution of magnetic field between the transverse position of -18 mm and 18 mm is measured, which is show in figure 6. There is a flat-top at all of the measurement gap, and the error in good field region is below 0.5%.

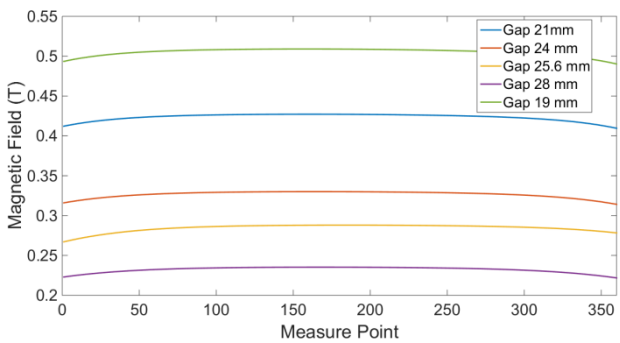


Figure 6: The transverse distribution of magnetic field.

## SUMMARY

We measured the longitudinal and transverse distribution of magnetic field of U38 using magnetic field measurement bench to check its field qualities. Electronic trajectory, peak field vs gap curve and peak-to-peak error were calculated based on longitudinal distribution and good field region was concluded from transverse distribution. The results show that all the requirements of U38 are met.

## ACKNOWLEDGMENT

The work is supported by Ministry of Science and Technology under the project of the national large-scale instrument development (No. 2011YQ130018) and China NSAF Fund under grant of 11505174.

## REFERENCES

[1] N. Vinokurov, “Free Electron Lasers as a High-power Terahertz Sources”, *Journal of Infrared, Millimeter, and Terahertz Wave*, vol. 32, pp. 1123-1143, 2011.

[2] J. Feldhaus *et al.,* “X-ray free-electron lasers*”, J. Phys. B: At. Mol. Opt. Phys.*, vol.38, pp.799 – 819, 2005.

[3] Y. H. Li *et al.,* “Undulator system tolerance analysis for the European x-ray free-electron laser”, *Physical Review Special Topics - Accelerators and Beams*, vol.11. p. 100701, 2008.

[4] H. Onuki *et al.,* “Undulators, Wigglers and Their Applications”, Taylor & Francis Inc., USA, 2002.

ISBN: 978-3-95450-199-1 doi:10.18429/JACoW-SAP2017-TUPH23

# BEAM LOSS SIMULATION AND GAS DESORPTION MEASUREMENT FOR HIAF*

P. Li , J†C. Yang , Z.Q. Dong, W.H. Zheng, W.J. Xie, J.J. Chang, X.J. Liu, M. Li, Y.J. Yuan, J. Meng , CH. Luo, R.S. Mao, W.L. Li
Institute of Modern Physics, Chinese Academy of Sciences, Lanzhou, China

*Abstract*

Large dynamic vacuum pressure rises of orders of magnitude which caused by the lost heavy ions can seriously limit the ion intensity and beam lifetime of the intermediate charge state heavy ion accelerator. The High Intensity heavy ion Accelerator Facility (HIAF) which will be built by the IMP will accumulate the intermediate charge state ion $^{238}U^{35+}$ to intensity $3\times10^{10}$ ppp to different terminals for nuclear physics, nuclear astrophysics and so on. In order to control the dynamic vacuum effects induced by the lose beams and design the collimation system for the BRing of the HIAF, a newly developed dynamic vacuum simulation program is conducted to optimize the collimation efficiency. Furthermore, two dedicated desorption measurement setups have been established at the terminal of the CSRm and 320 kV HV platform to study the molecular desorption process and do the benchmarking of the simulation code. This presentation will describe the collimation efficiency optimization, measurement results with Sn beam at the CSRm and withthe Xe beam in the HV platform.

## INTRODUCTION

The HIAF project consists of ion sources, Linac accelerator, synchrotrons and several experimental terminals. The Superconducting Electron-Cyclotron-Resonance ion source (SECR) is used to provide highly charged ion beams, and the Lanzhou Intense Proton Source (LIPS) is used to provide $H_2^+$ beam. The superconducting ion Linac accelerator (iLinac) is designed to accelerate ions with the charge-mass ratio Z/A=1/7 (e.g. $^{238}U^{35+}$) to the energy of 17 MeV/u. Ions provided by iLinac will be cooled, accumulated and accelerated to the required intensity and energy (up to $3\times10^{10}$ and 800 MeV/u of $^{238}U^{35+}$) in the Booster Ring (BRing), then fast extracted and transferred either to the external targets or the Spectrometer Ring (SRing) [1].

The intermediate charge state $^{238}U^{35+}$ has been chosen as the reference ion for the facility HIAF. Intermediate charge state particles are much easier lost when they collide with the rest gas atoms and change to other charge states. The resulting change in the mass over charge ratio m/q leads to modified trajectories in dispersive beam transport elements, and finally to the loss of the particle at the vacuum chamber. Secondary particles are produced at the impact position by ion-induced desorption and as a result the pressure in the vacuum chamber is increased locally. This local rise in pressure enhances the charge changing processes, and at extremely bad conditions, it can cause an avalanche process resulting in a complete loss of the beam during a few turns in the synchrotron. The layout of the HIAF project is shown in Fig. 1.

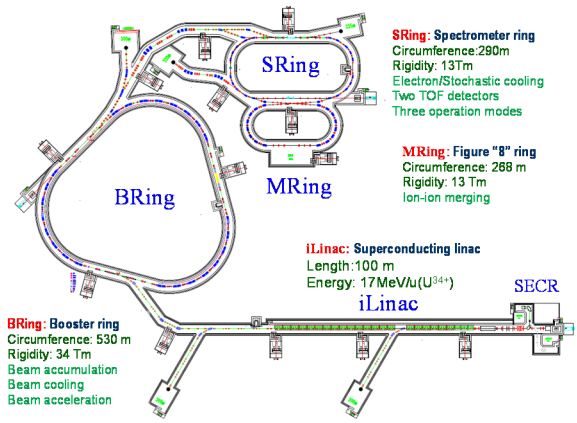


Figure 1: Layout of HIAF project.

## BRING COLLIMATION EFFICIENCY

The Booster Ring (BRing) of the HIAF project has a threefold- and mirror-symmetric lattice over its circumference of 530.8 m. Each super period consists of 8 DF structure arc and FODO straight sections. Beam loss distribution is calculated by the new developed simulation program.

In order to simulate the charge exchange driven beam loss and dynamic vacuum effects in heavy ion synchrotrons, a new program package (ColBeam) designed for optimizing the collimation efficiency is developed by taking different types of errors into account in the accelerator [2].

The particles can be tracked in a ring during multiple turns or in a beamline just one-pass. Firstly the software package must load a lattice file which contains essential element parameters of the ring or beamline, such as element type, length, strength, vacuum chamber aperture and so on. The lattice file with extension “LAT” for the simulation software Winagile [3] is used as the default input file.

More than thirty lattices for the Bring have been simulated and the collimation efficiency was optimized. Collimation efficiency is defined as the ration of the particles hitting the collimators $N_c$ and the wall $N_w$.

$$\theta = \frac{N_c}{N_w + N_c} \quad (1)$$

The final accepted lattice is the DF structure and its collimation efficiency is 100% according to the simulation result. With a constant vacuum pressure around the ring, the

* Work supported by National Natural Science Foundation of China (11675235) and Youth Innovation Promotion Association of Chinese Academy of Sciences 2016364.
† Email address LIPENG@IMPCAS.AC.CN

ISBN: 978-3-95450-199-1 doi:10.18429/JACoW-SAP2017-TUPH23



beam trajectory for one electron-loss $^{238}U^{36+}$ is illustrated in Fig 2. The loss position and intensity of the charge exchanged particle at each point is also counted and shown in the Fig 2.

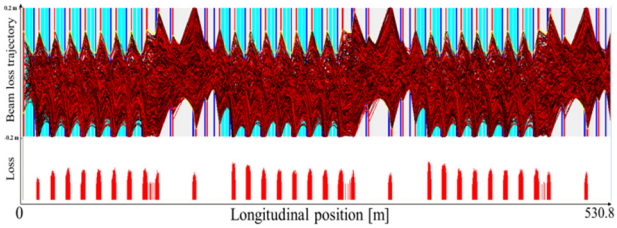


Figure 2: Beam loss trajectory and the beam loss distribution of the simulation results for one electron-loss $^{238}U^{36+}$.

The beam trajectory of the lost beam with the collimator is shown in Fig 3. No beam is lost on the vacuum chamber wall and the collimation efficiency is 100%.

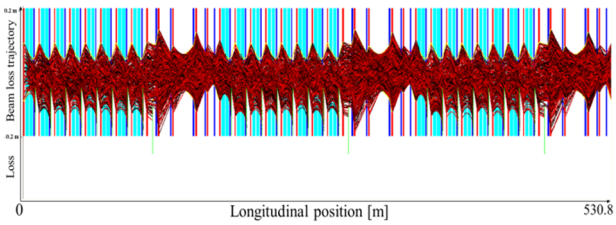


Figure 3: Beam loss trajectory and the beam loss distribution of the simulation results for one electron-loss $^{238}U^{36+}$ with collimators.

## GAS DESORPTION MEASUREMENT

### *Low Energy Measurement Platform*

The gas desorption yield experiment has been conducted at the 320 kV high voltage platform in IMP. The 320 kV HV platform, based on the ECR ion source and built in 2007, is the one that can supply 320 kV high voltage and electrostatic acceleration of various high charge state ion beams[4]. This platform can provide stable and continuous low energy heavy ion beams. Figure 4 shows an overview of the experimental setup, including three quadrupoles (Q1~Q3), vacuum chamber (l = 545 mm), a short vacuum chamber (l = 340 mm) as experiment chamber, a slit, a fluorescent screen (VS) with a TV camera, a Faraday cup (FC) and a target. The three quadrupoles at the starting position are used to optimize the beam size. To make sure that the data collected by the vacuum gauge is all from the target, which means all particles should impact on the target surface instead of the vacuum chamber wall, a slit (square: 90 × 90 mm$^2$) with a small hole (12 mm) is installed in the long vacuum chamber. Behind the slit, a fluorescent screen with a TV camera is used to cooperate with the hole on the slit to ensure that the beam would bombard the target perpendicularly by adjusting the beam to the center of the fluorescent screen. The beam current is measured by the Faraday cup. The target, which is made of oxygen-free copper (cube: 50×50×50 mm$^3$) and has been cleaned by alcohol first, is installed in a short test vacuum chamber which is located at the end of the beam line.

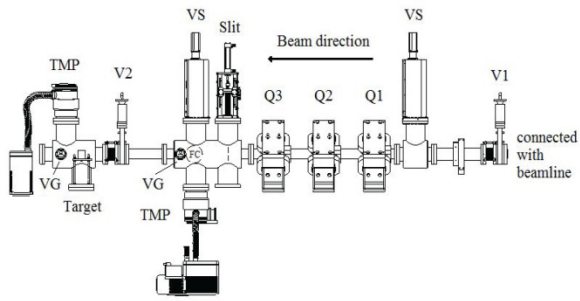


Figure 4: Experimental setup used for ion-induced gas dsorption yield measurement on the 320 kV HV platform at the IMP.

Table 1 lists the beam parameters for the desorption measurement. The spot size of the beam is about 10 × 20 m$^2$, monitored by fluorescent screen after the slit.

Table 1: Beam Parameters used in the Gas Desorption Yield Measurement

| Beam | Charge state | Energy (keV) | Current (μA) |
|---|---|---|---|
| Xe | 10+ | 1000 | 3.91 ± 0.21 |
| | | 1500 | 4.01 ± 0.07 |
| | | 2000 | 3.98 ± 0.18 |
| | | 2500 | 3.89 ± 0.14 |
| O | 1+ | 100 | 4.95 ± 0.06 |
| | | 150 | 5.20 ± 0.10 |
| | | 200 | 5.00 ± 0.06 |
| | | 250 | 4.97 ± 0.21 |

Figure 5 shows a typical pressure evolution in the experimental chamber with the copper target bombarded continuously with 2500 keV $Xe^{10+}$ ions [5].

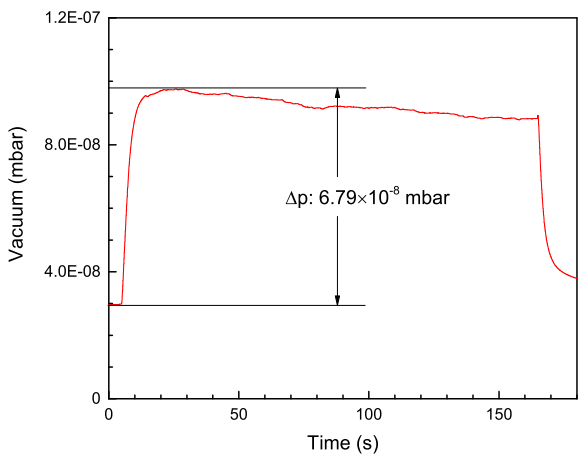


Figure 5: Pressure evolution in experimental chamber during a period of continuous bombardment. The copper target is bombarded by 2500 keV $Xe^{10+}$ beam with a loss about 2.43×10$^{12}$ particles per second.

The results of continuous bombardment measurements of Xe10+ and O+ are shown in Fig. 6. The two figures show the Xe10+ data and O+ data divided by 10 respectively. The chosen energy regimes of Xe10+ beam and O+ beam are both well below the Bragg-Peak, and one can find

ISBN: 978-3-95450-199-1 doi:10.18429/JACoW-SAP2017-TUPH23

that the measured gas desorption yields are increasing with increase of ion energy. From the Fig.6, it can be seen that in the applied energy regime the nuclear energy loss is dominating for the Xe beam, and the electronic energy loss is dominating for the O beam [6].

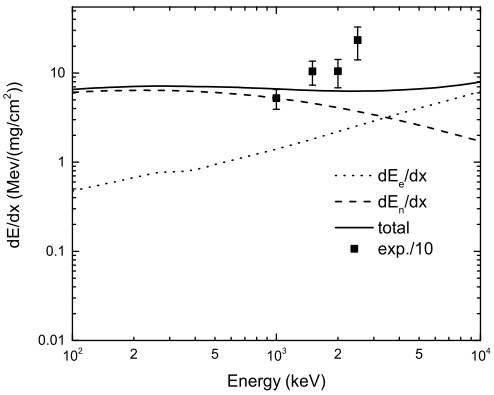


Figure 6(a): Nuclear energy loss $dE_n/dx$ and electronic energy loss $dE_e/dx$ for projectile lost perpendicularly on the surface of copper target for Xe beam.

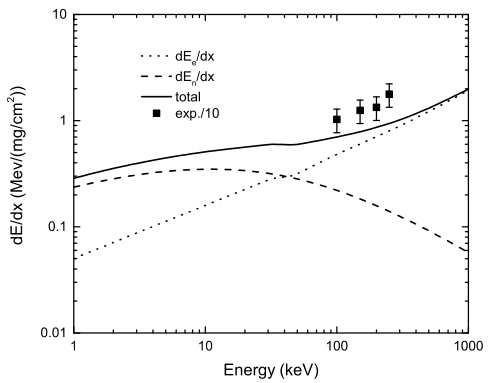


Figure 6(b): Nuclear energy loss $dE_n/dx$ and electronic energy loss $dE_e/dx$ for projectile lost perpendicularly on the surface of copper target for O beam.

### *High Energy Measurement Platform*

High energy experimental setup to measure the ion induced desorption rate is designed and installed at the CSRm. Figure 7 shows the layout of this setup [6].

This setup consists of three chambers: first chamber which installed an Integrating Current Transformer (ICT), $Al_2O_3$ fluorescence screen is used to measure the beam current and align the incoming beam; the second chamber which installed a TSP, SIP and NEXTorr is used to pump out the desorption gases; the experimental chamber is equipped with a pressure (extractor) gauge and a residual gas analyzer (RGA) to measure the total pressure increase and the partial pressure distribution during ion bombardment.

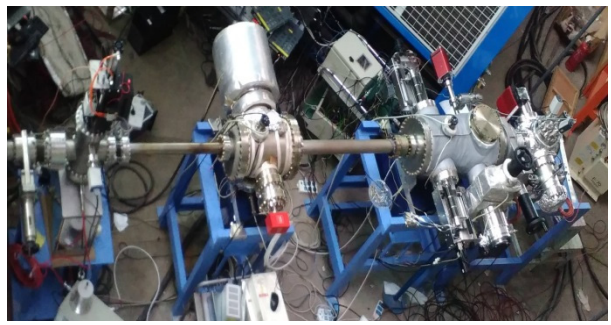

Figure 7: The layout of experimental setup.

The first beam measurement in this setup was conducted in 2015 with the $Sn^{26+}$ beam. The beam intensity was low to decrease the measurement noise. Therefore, more beam with high energy are needed in this setup to measure the gas desorption.

## CONCULSION

The heavy-ion induced gas desorption yield measurement shows the relationship between the desorption yield and the beam energy. With the increase of projectile energy, the change of desorption is up to 4 times for Xe beam and 2 times for O beam. The results indicate that the desorption yield scales with the $(dE_e/dx)^2$ roughly.

These results will support future dynamic pressure simulation and optimization of the position and efficiency of the collimators to be installed on the BRing at HIAF, which the gas desorption part of outgassing rate would increase and influence the localized pressure profile when charge-exchanged particles hit chamber wall or collimators in tracking simulation.

## ACKNOWLEDGEMENT

We thank 320 kV platform staff J.Y. Li, T.M. Zhang, H.P. Liu and L. Kang for their valuable support and providing an excellent beam.

## REFERENCES

[1] HIAF Conceptual Design Report, unpublished.

[2] Peng Li *et al.*, "Beam loss distribution calculation and collimation efficiency simulation of a cooler storage ring in a heavy ion research facility", *Phys. Rev. ST Accel. Beams*, vol. 17, p. 084201, 2014.

[3] P.J. Bryant, in *Proc. EPAC'00*, Vienna, Austria, p 1357.

[4] Ma X, Liu H P, Sun L T *et al.*, *Journal of Physics: Conference Series*. IOP Publishing, 2009, 163(1): 012104.

[5] Z.Q Dong, Peng Li, J.C Yang *et al.*, Measurement on the gas desorption yield of the oxygen-free copper irradiated with low energy Xe10+ and O1+, *Nuclear Instruments and Method in the in Physics Research A* 2017.(Accepted).

[6] P. Li *et al.*, "PRESSURE PROFILES CALCULATION FOR THE CSRM AND BRING", in *Proc. 57rd ICFA Advanced Beam Dynamics Workshop on High Intensity and High Brightness Hadron Beams*, Malmo, Sweden, 2016.

ISBN: 978-3-95450-199-1 doi:10.18429/JACoW-SAP2017-TUPH26



# NUMERICAL ASSESSMENT OF BEAM DIAGNOSTIC CALORIMETER FOR EAST NEUTRAL BEAM INJECTOR*

Yongjian Xu, Chundong Hu, Yahong Xie, Yuanlai Xie, Ling Yu, Lizhen Liang†
Institute of Plasma Physics, Chinese Academy of Sciences, Hefei, China

*Abstract*

Neutral beam injection is one of the most effective means of plasma heating and has been also verified to be applicable for current driving. In order to support the physical research of EAST, two neutral beam injectors (NBI, 80keV, 4 MW) have been developed and constructed in Institute of Plasma Physics, CAS. In order to evaluate beam intensity distribution and divergence, a moveable sophisticated copper short-pulse beam diagnostic calorimeter is designed and installed on the NBI test stand. In this article, the structure of calorimeter, the operating parameters are introduced. The new diagnostic calorimeter plate bombarded by the beam adopts blocking design and there is no heat transfer between adjacent block. Thermocouples are installed into the block, so the temperature can be measured precisely. Based on the data obtained by thermocouples, the beam pattern can be plotted. In order to ensure the diagnostic calorimeter work safely, the operating parameters are explored using FEM. As a new beam diagnostic calorimeter, it solves the problem of mutual interference due to the heat transfer of each block, it can give more precise beam property comparing with the present calorimeter.

## INTRODUCTION

Neutral beam injection is one of the most effective means of plasma heating and has been also verified to be applicable for current driving[1-5]. In order to support the physical research of the Experiment Advanced Superconductive Tokomak (EAST), two identical neutral beam injectors (NBI, 80 keV, 4 MW) have been developed and constructed in Institute of Plasma Physics, Chinese Academy of Sciences [6-11]. In order to evaluate more precisely the beam intensity distribution, divergence and uniformity [12-16], a moveable sophisticated copper short-pulse beam diagnostic calorimeter is designed and installed on the NBI test stand. The new diagnostic calorimeter plate bombarded by the beam adopts blocking design and there is no heat transfer between adjacent block. Thermocouples are installed into the block, so the temperature can be measured precisely. Based on the data obtained by thermocouples, the beam pattern, divergence can be obtained. Considering the limitation of the heat exchange capacity, the diagnostics calorimeter only works in short-pulse mode, in order to determine the operation parameter, the diagnostics calorimeter is analyzed by FEM. In this article, the structure of calorimeter, the primary simulation results are introduced. Simulation results give the maximum operation pulse length at different beam energy.

As a new beam diagnostic calorimeter, it solves the problem of mutual interference due to the heat transfer of each block. Comparing with the present calorimeter, it can give more precise beam property.

## SIMULATION AND ANALYSIS

### *Layout and Design of Diagnostics Calorimeter*

Short-Pulse beam diagnostic calorimeter is installed between the gas baffle and bending magnet. Diagnostic calorimeter can be moved left and right under the traction of steel cable (see Fig.1). The diagnostic calorimeter will be moved out of beam channel during long pulse beam extraction.

The diagnostic calorimeter is designed to be operated inertially. It is made of a cooling back plate with a cooling circuit and 5×19 copper blocks which are brazed on the "beam side". Each block is inertially cooled via small cooling channels in the back plate and through a small ø10 mm×2 mm copper cylinder that acts as a thermal resistance between cooling plate and block. Each block has a surface of 30 mm×30 mm and a thickness of 25 mm. Each block is separated from adjacent blocks by a 2 mm gap (see Fig.2). With this solution the transversal heat transmission between blocks during the beam phase is practically negligible. 34 sheath thermocouples (K-Type) are used for temperature measure of the calorimeter (see Fig.3). The embedded thermocouples are positioned at half depth (12.5 mm) of a block (which is 25 mm thick) in order to provide a good assessment of the average block temperature. According to the temperature rise of the blocks, the beam profile in vertical and horizontal direction can be obtained.

### *FEM Analysis of Diagnostics Calorimeter*

The incidence angle of the beam on the calorimeter is supposed to be 90°. The simulations have been performed with pulse length 1s, heat flux 10MW/m$^2$ (uniform distribution). The flow rate of cooling water is 2m/s and the origin temperature is 293K. The thermal radiation between the adjacent blocks is ignored. The model is shown in Fig.4.

**Relationship between Inclination Angle and Surface Temperature of Block** In order to decrease thermal radiation between the adjacent blocks, the black is designed as regular hexahedron (see Fig.5a). For the difference of heat transfer path, there is a big gap between edge and center (see Figs.5b, 5c) with the change of inclination angle α. As the softening temperature of the material of

* Work supported by the National Natural Science Foundation of China (NNSFC) (Contract No. 11575240) and the Foundation of ASIPP (Contract No. DSJJ-15-GC03)
† Email: address: lzliang@ipp.ac.cn

ISBN: 978-3-95450-199-1 doi:10.18429/JACoW-SAP2017-TUPH26

diagnostics calorimeter (oxygen-free copper, OFC) is about 573K, the edge of block inevitably become priority concerned point. Figure 5d gives the relationship between the inclination angle and the temperature difference between edge and center. It can provide certain reference for designing head-loading components.

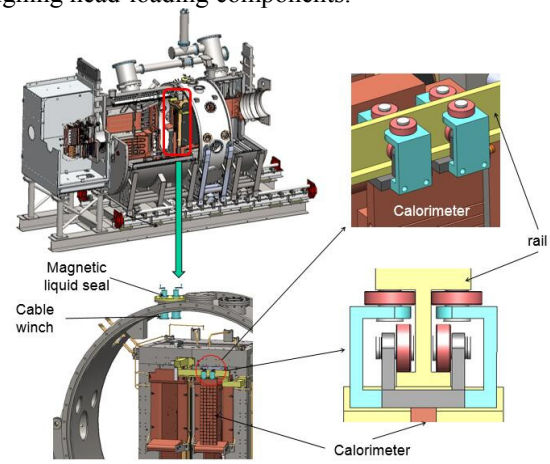


Figure 1: The layout of short-pulse diagnostics calorimeter.

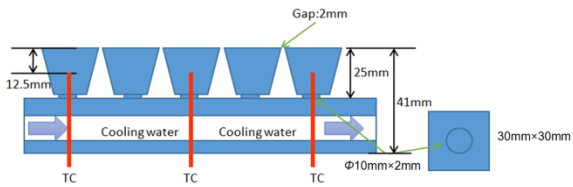


Figure 2: The design of short-pulse diagnostics calorimeter.

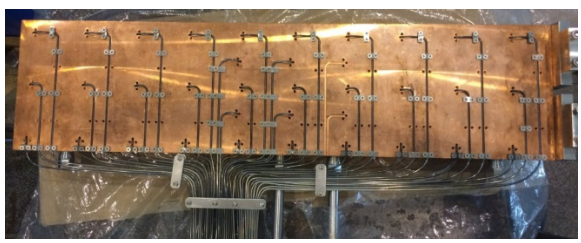

Figure.3: The installation of thermocouple in short-pulse diagnostics calorimeter.

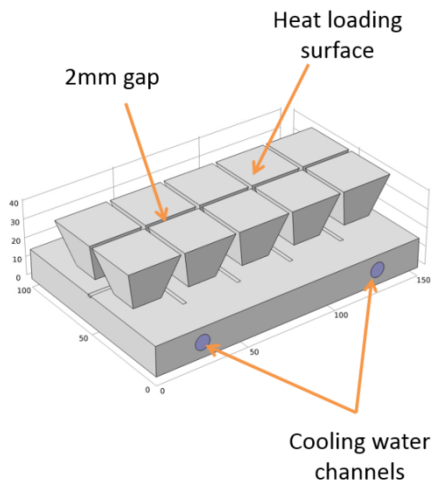


Figure 4: The model of FEM simulation for short-pulse diagnostics calorimeter.

**Three-dimention Temperature Distribution Varying with Time** The temperature of block is measured by the thermocouples embedded in it. The beam parameters, such as beam profile, divergence angle and uniformity and so on, can be calculated. Figure 6 gives the 3D simulation temperature distribution of diagnostic calorimeter at the end of beam extraction. It shows that there is a difference of more than 120 degree centigrade. In order to analyze the temperature change of the calorimeter during the beam extraction, the curves of temperature rise are plotted for the edge, center and the installation site of thermocouple (see Fig.7).

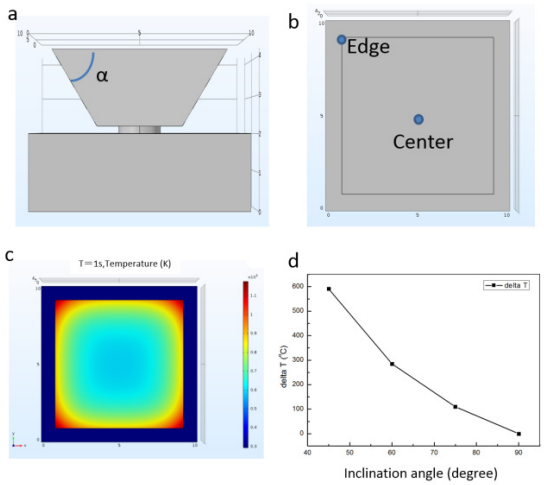


Figure 5: Inclination angle and surface temperature of a block: a. the section of block; b. the top view of block; c. the surface temperature distribution of black; d. relationship between inclination angle and surface temperature difference between edge and center.

**Three-dimention Temperature Distribution Varying with Time** The temperature of block is meausred by the thermocouples embedded in it. The beam parameters, such as beam profile, divergence angle and uniformity and so on, can be calculated. Figure 6 gives the 3D simulation temperature distribution of diagnostic calorimeter at the end of beam extraction. It shows that there is a difference of more than 120 degree centigrade. In order to analyze the temperature change of the calorimeter during the beam extraction, the curves of temperature rise are plotted for the edge, center and the installation site of thermocouple (see Fig.7).

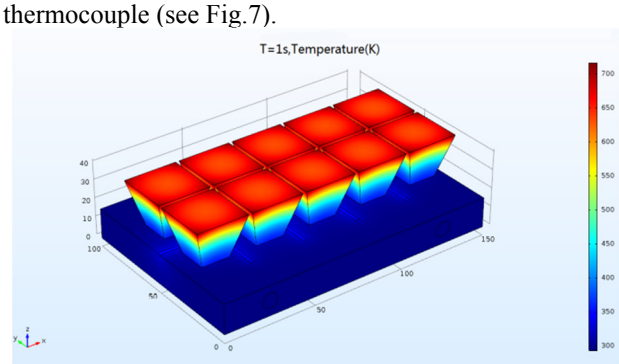


Figure 6: The 3D simulation temperature distribution of diagnostic calorimeter at the end of beam extraction.

ISBN: 978-3-95450-199-1 doi:10.18429/JACoW-SAP2017-TUPH26



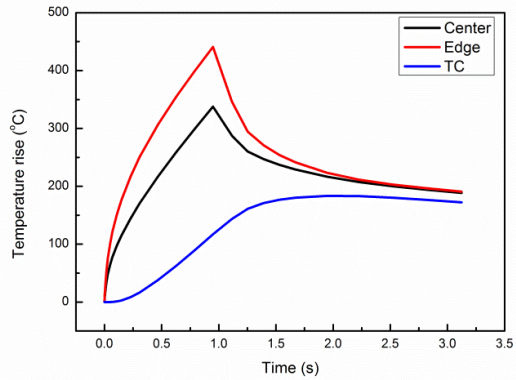


Figure 7: The curve of temperature rise varying with time.

**Operation Pulse Length of Calorimeter at Different Beam Energy.** The temperature rise of calorimeter is determined by the beam power density and pulse length. Fig.8 gives the beam average power density varying with beam energy at optimum perveance. Set the softening temperature of OFC 593K as safety threshold, the maximum operational pulse length is shown in Fig.9.

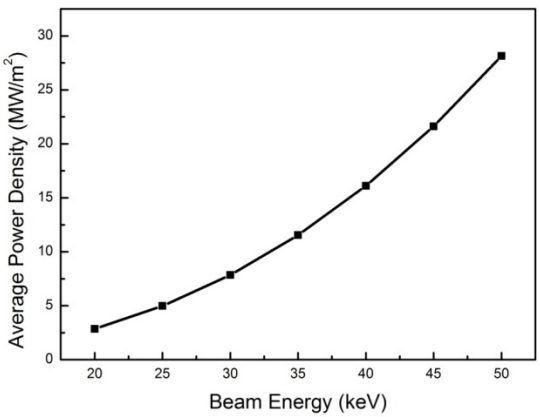


Figure 8: The beam average power density varying with beam energy.

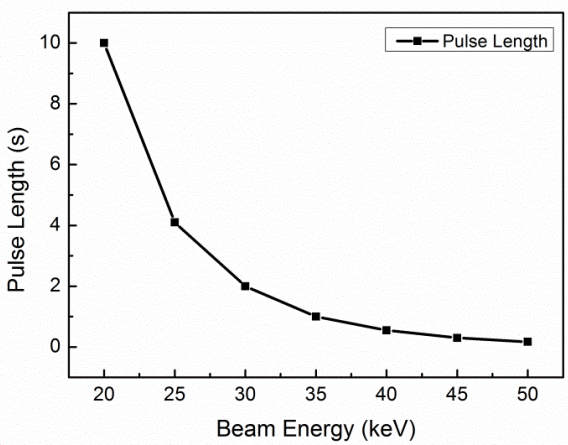


Figure 9: The maximum operational pulse length at different beam energy.

## CONCLUSION

Comparing with the current calorimeter, the new diagnostics calorimeter can provide up to 30mm high spatial resolution. Simulation results show that (1) the spatial resolution of calorimeter is determined by the scale of block; (2) the operational pulse length obvious decrease with the increase of beam energy. The application of new diagnostics calorimeter can provide more precise results of beam parameters and lay a foundation for optimization and development of ion source.

## REFERENCES

[1] C. Hu *et al.*, "Preliminary Results of Ion Beam Extraction Tests on EAST Neutral Beam Injector", *Plasma Sci. Technol.*, vol.14, no.10, p.871, Oct, 2012.

[2] A. Kojima *et al.*, "Progress in long-pulse production of powerful negative ion beams for JT-60SA and ITER", *Nucl. Fusion*, vol.55, no.6, p.063006, Jun, 2015.

[3] R. Maurizio *et al.*, "Characterisation of the properties of a negative hydrogen ion beam by several beam diagnostic techniques", *Nucl. Fusion*, vol.56, no.6, p.066012, Jun, 2016.

[4] C. Hu *et al.*, "Design of Neutral Beam-Line of EAST", *Plasma Sci. Technol.*, vol.13, no.5, p.541, Oct, 2011.

[5] B Wu *et al.*, "Neutral beam injection simulation of EAST", *Fusion Eng. Des.*, vol.86, no.6-8, p.947, Oct, 2011.

[6] C. Hu *et al.*, "Achievement of 100 s Long Pulse Neutral Beam Extraction in EAST Neutral Beam Injector", *Plasma Sci. Technol.*, vol.15, no.3, p.201, Mar, 2013.

[7] C. Hu *et al.*, "Overview of Development Status for EAST-NBI System", *Plasma Sci. Technol.*, vol.17, no.10, p.817, Oct, 2015.

[8] C. Hu *et al.*, "First Achievement of Plasma Heating for EAST Neutral Beam Injector", *Plasma Sci. Technol.*, vol.17, no.1, p.1, Jan, 2015.

[9] C. Hu *et al.*, "The Recent Development of the EAST Neutral Beam Injector", *Chinese Phys. Lett.*, vol.32, no.5, p.052901, May, 2015.

[10] C. Hu *et al.*, "Performance of positive ion based high power ion source of EAST neutral beam injector", *Rev. Sci. Instrum.*, vol.87, no.2, p.02B301, Feb, 2016.

[11] Y. Xie *et al.*, "Upgrade of accelerator of high current ion source for EAST neutral beam injector", *Fusion Eng. Des.*, vol.100, no.7, p.265, Jul, 2015.

[12] L. Yu *et al.*, "Temperature Measurement System of EAST Neutral Beam Injector", *J. Fusion Enger .*, vol. 34,no.2, p.245,Feb,2014.

[13] Y.Xu *et al.*, "A new method of rapid power measurement for MW-scale high-current particle beams", *Nucl. Instrum. Meth.* A, vol.795, p.196, Sep, 2015.

[14] Y. Xu *et al.*, "Progress of beam diagnosis system for EAST neutral beam injector", *Rev. Sci. Instrum .*, vol.87, no.2, p.02B934, Feb, 2016.

[15] R. Nocentini *et al.*, "Beam diagnostic tools for the negative hydrogen ion source test facility ELISE", *Fusion Eng. Des .*, vol.88, no.6-8,p.913,Jul,2013.

[16] C. Hu *et al.*, "Analysis of the Pipe Heat Loss of the Water Flow Calorimetry System in EAST Neutral Beam Injector", *Plasma Sci. Technol.*, vol.18, no.11, p.1139, Nov, 2016.

ISBN: 978-3-95450-199-1 doi:10.18429/JACoW-SAP2017-TUPH27

# ELECTROMAGNETIC, THERMAL, STRUCTURAL ANALYSIS FOR THE RF-CAVITY OF A RHODOTRON ACCELERATOR *

L. Yang†, X. Z. He, H. Li, Institute of Fluid Physics, CAEP, Mianyang, Sichuan, China

*Abstract*

A Rhodotron-based electron accelerator served as micro-focused X-ray source at a high repetition rate of 10.75 MHz is proposed at IFP, CAEP. The RF-cavity, running in long pulse/ CW mode, will deliver 9 MeV energy gain to the charged beam at the exit by taking its advantage of multiple accelerations with the same field at a frequency of 107.5MHz. A substantial amount of power loss will be dissipated on the RF surface of the cavity within beam time. Further electromagnetic (EM) optimization was performed on a standard coaxial model with slight modifications aiming to achieve a higher shunt impedance, thus less power loss on surfaces. A proper water cooling design is still required to prevent large scale temperature rise on the cavity wall. The corresponding effects on cavity mechanical stability and resonant frequency shifting are concerned. This paper will present the details in the EM, thermal, structural analysis of the RF-cavity.

## INTRODUCTION

Rhodotron, as a kind of compact electron accelerator with high efficiency of energy transfer to charged beams, has been widely employed to generate X-ray for industrial irradiation since the concept of multiple accelerations in the same field supplied by a half wave resonator (HWR) was raised by J. Pottier [1]. With several bend magnets azimuthally surrounding to an HWR, Electron beams could re-entry into the cavity and be re-accelerated at each time passing through a bend. A schematic view is shown in Figure 1. A high energy in the order of 10MeV which well meets the energy level of industrial irradiation sources, could be achieved with a relatively low field intensity. Hence long-pulse mode with large duty factor and fully continuous wave mode (CW) at an acceptable power loss level ~100kW are applicable and not often seen in normal conducting electron accelerators. Variable designs but in the same principle could be referred in these literatures [2-5]. We propose a micro-focused X-ray source at a high repetition rate of 10.75 MHz by adopting a 107.5MHz Rhodotron being able to accelerate electron beams with initial energy 40keV up to 9 MeV after 10 times across. Great efforts have been put on the beam dynamics design to form a 0.2 mm beam spot at the target location other than a typical size of 2 mm for normal industrial CT machines, which in details is documented in the paper ([6] A proposal of using improved Rhodotron as a high dose rate micro-focused X-ray source) of this conference. This paper is focusing on some specific cavity design issues.

One important thing should be carefully concerned is water cooling for CW running mode or high duty cycle mode. Large surface loss density in an order of $10^6$ w/cm$^2$ is concentrated on the areas at the strong magnetic field zone considering OFC material being penetrated by RF field. Since the cavity body will be made out of stainless steel with OFC coated on the inner surface, the high surface loss density areas should be fully covered by forced water where efficient heat convection would occur. With the known heat convection status, one can perform the thermal analysis in those commonly used FEA codes to predict the steady temperature pattern over the cavity wall, which is of an important body load for the subsequent structural analysis and coupled thermal induced frequency drift estimation. The heat convection coefficient regarding to normal water cooling problems with regular meanders and uniform heat flux has been well developed in theory and usually adopted by the thermal simulations for normal conducting RF guns, cavities [7-8]. In our case, however, the heat convection highly depends on the local heat flux and varied fluid field due to the non-regular cavity geometry, therefore theoretical approximation is too roughly to calculate the distribution of heat convection coefficient. Thanks to the heat transfer enabled fluent package in ANSYS [9], the heat convection is internally computed and coupled with fluid calculation. The data mapping technology in Workbench allows load import between different physics fields that even don't share the same mesh and node pattern. By taking such advantages, we have done a complete coupled EM, thermal, fluid and structural simulation during the cavity design stage, which along with EM optimization will be presented in following sections.

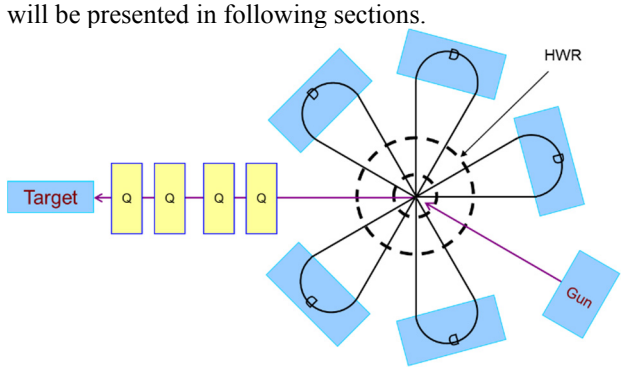


Figure 1: Layout of a Rhodotron.

## EM OPTIMIZATION

EM optimization started with a standard initial coaxial line model resonating at the targeting frequency 107.5MHz. The outer conductor diameter **D** was set to 1.6m in order to keep an appropriate room for installing beam diagnostic elements on the beam line section between the cavity and the bend magnets. The inner conductor diameter **d** was defined to 0.25**D** where reaches the maximum shunt impedance by taking the transit time effect into account. A further optimization step with a

* Work supported by R&D project of IFP/CAEP
† yyperf57@163.com

ISBN: 978-3-95450-199-1 doi:10.18429/JACoW-SAP2017-TUPH27



cone feature and radial bend adding in the short ends was taken to get another 10% improvement on the shunt impedance. A longer cavity was resulted to fix the resonating frequency. This modification rather than a totally flat short plate, on the other hand, would increase the mechanical stability of the cavity. The whole set of RF parameters were calculated in HFSS. A wedge model (1/40 of the full model) was used for less mesh generation benefitting from symmetrical boundary conditions. Figure 2 shows the field patterns in the RF. Table 1 lists the comparison of key RF parameters and geometric parameters between the initial and final model.

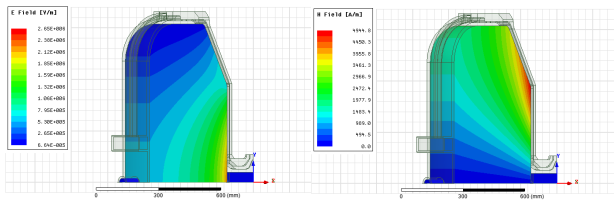

Figure 2: Electric field and magnetic field intensity. The cavity wall dressed with water cooling jacket appears as the transparent portion.

Table 1: RF Parameters and Key Geometric Parameters of the Initial, Final Models

| Parameters | Initial model | Final model |
|---|---|---|
| $Q_0$(Copper) | 42554 | 49086 |
| Shunt impedance | 10.6MΩ | 11.8MΩ |
| Power loss | 76kW | 68kW |
| Cavity Height | 1.39m | 1.55m |
| Outer Diameter | 1.6m | 1.6m |
| Inner Diameter | 0.4m | 0.4m |

## COUPLED ANALYSIS

The complete coupled analysis engages 3 physics packages, EM, heat transfer enabled fluid and static structural with data links between each other to forecast the steady temperature rise in cavity body at a certain RF power level and flow rate of water, accordingly, the frequency shift due to thermal expansion, and the maximum thermal stress. All these packages are assembled in ANSYS, and should share the same model to carry out data access each other. A work flow is plotted in Figure 3 which also illustrates the data transfer network.

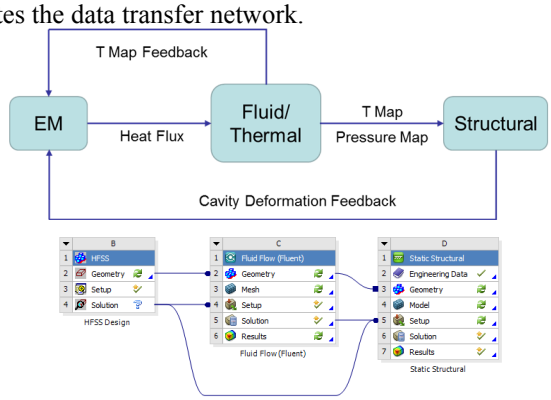


Figure 3: The work flow of the coupled analysis and a snapshot in ANSYS user interface.

The surface loss density calculated by HFSS is imported into Fluent as an energy source which will be conducted through the cavity wall in the solid zone and taken away by water flow in the fluid zone. The temperature distribution over the solid zone will be feedback to HFSS from Fluent. Since the resistance of the coated copper on the cavity inner surface is temperature dependent, an updated heat flux resulted from another run in HFSS will be reloaded into Fluent, and accordingly, the temperature distribution could be renewed. One can perform this iterative process couple times to meet the convergence threshold. In our case, single iteration has already shown a reasonable convergence. The final temperature distribution and the pressure load applied by the water flow will go forward into the static structural package. The deformation induced by thermal expansion and pressurized water and also the vacuum load in RF volume could be independently calculated or linearly superposed. The overall maximum stress is predicted by the latter one. The deformation will be captured by HFSS and mapped onto the mesh pattern for the new eigen mode calculation. The frequency shift is taking the difference to the initial eigen mode result.

### *Cooling Layout and Model Setup*

The final RF model was translated into a shell model as the cavity wall with thickness of 15 mm, see Figure 4. The cooling layout over cavity wall was designed in a way that cooling efficiency and mechanical stability were both considered. The inner conductor and the short ends are fully covered by a jacket with a 5 mm gap, while the outer conductor is cooled by numbers of regular meanders evenly distributed along the cavity circumference. Pressurized water will be injected towards the blind plates in the medium region of the inner conductor. All the water flows drained out of these meanders are collected by a belt like buffer and circulated back to a chiller. These meanders play another import role of stiffening rings to keep the large cavity body rigid against water pressure, vacuum in RF volume, and thermal expansion. Similar to the EM calculation, symmetrical boundary conditions allow using a reduced model with water volume filled in all the gaps and meanders for the coupled simulation.

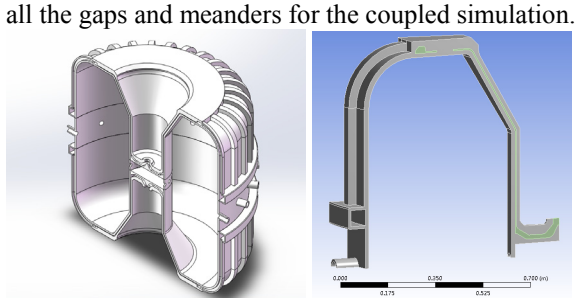

Figure 4: Left: Full cavity mechanical model; right: reduced model for coupled simulation, the water volume is coloured in green.

### *Simulation Setup and Single Pass Result*

The field intensity in HFSS was adjusted to an overshot operational level (CW) with 15% margin to 68kW given

ISBN: 978-3-95450-199-1 doi:10.18429/JACoW-SAP2017-TUPH27

by the EM optimization as possible $Q_0$ degradation might take place during cavity fabrication. Temperature dependence of copper electric conductivity was enabled for the afterwards calculation with temperature feedback. The water flow rate was set to 55.7L/min which is equivalent to an average temperature rise of 10K at the outlet with respect to 77.5kW energy absorption by water. The water flow was injected at a typical temperature 300K. A rough estimation of Reynolds number in the areas with high flow velocities gives a range of 470~967. Hence, the fluid problem mostly falls in Laminar flow category (Re<2000). The configuration in Fluent doesn't require much attention to these complex models particularly solving turbulence problems. Large number of mesh in an order of million is required for a reasonable result even though a significantly reduced model was used. The RAM memory consuming is able to be handled by a modern desktop yet, and the time cost up to convergence is about 5 min, which is fairly acceptable.

After 40 iterations, the maximum temperature monitored in the entire processing reaches steady. The ramped up trace could be seen in Figure 5. The water temperature distribution in transverse plane on the outlet yields a mass-weighted average rise 9.94 K, and well consistent with the one predicted by a given flow rate. Figure 6 shows the temperature distribution with the initial heat flux load and the convection coefficient calculated from postprocessing. The coefficient varies in a broad range of -126.3 ~912.9 W/K·m$^2$, which is far beyond the estimations by theoretical models. The negative value means heat transfer back to some areas at low temperature. There are two regions with appreciable temperature rise, the one undergoing high loss density and the other one located in the medium of two adjacent meanders where water cooling doesn't reach and the heat has to be conducted away by stainless steel wall with poor thermal conductivity.

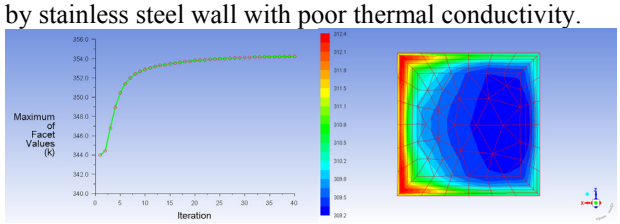


Figure 5: Left: maximum temperature trace over 40 iterations; right: water temperature distribution in transverse plane on the outlet.

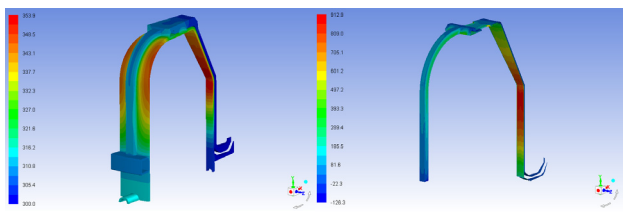

Figure 6: Temperature rise under initial heat flux load and the calculated convection coefficient

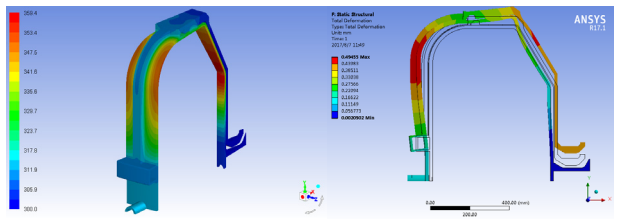

Figure 7: Updated temperature rise and induced deformation, note the frame in solid line is undeformed.

A 5% of Q0 drop after temperature feedback was seen, and in turn caused additional 5.6K (see Figure 7) rise to the initial maximum temperature, 353.9K. The heated cavity due to thermal expansion induces deformation with a maximum displacement of 0.495mm, and shifts the resonating frequency by a mount of -30.3 kHz to the one of a cold cavity.

### *Sweeping Flow Rate*

More simulations have been done by sweeping the flow rate. The flow rate was adjusted from 27.9 to 139.3 L/min, coordinating to the mean temperature rise in fluid at the outlet, 4~20K. The maximum temperature and the induced frequency shift are plotted in Figure 8. When the flow rate is being increased over 60 L/min, the temperature drop starts to be slow down, where the high temperature spots on the outer conductor mainly cooled by thermal conducting become dominant. The optimized flow rate to this particular cooling layout, therefore could be defined at somewhere close to 60L/min.

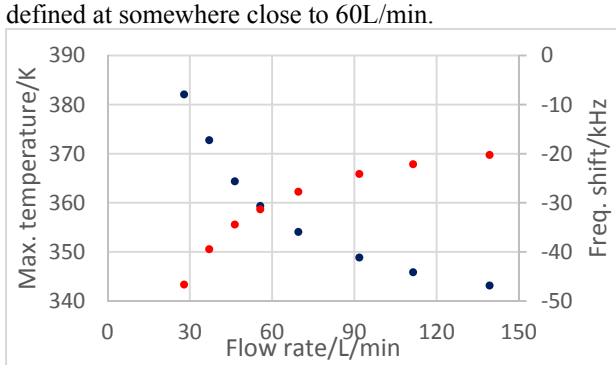


Figure 8: The maximum temperature (blue) varies with the flow rate and the corresponding frequency shift (red).

## CONCLUSION

Calculation techniques for comprehensive EM, thermal, fluid and structural coupled simulation of RF cavities have been described extensively. Reasonable prediction on RF induced temperature rise is applicable owing to the heat transfer enabled fluid simulation with internally computation on the convection coefficient, which must have to be accurately given in advance in a sole thermal analysis. Cooling layout was severely designed for this specific RF cavity of a Rhodotron and verified in simulation with a controllable temperature rise at a full power level. The optimized flow rate to the cooling design has been forecasted by parameter sweeping.

ISBN: 978-3-95450-199-1 doi:10.18429/JACoW-SAP2017-TUPH27



## REFERENCES

[1] J. Pottier *et al.*, "A new type of RF electron accelerator: the Rhodotron", *Nucl. Instrum. Methods-Phys.Res.B*, 40/41,p. 943, 1989.

[2] Y.Jongen *et al.*, "The Rhodotron: a 10 MeV, 100 kW beam power metric waves, CW electron accelerator", *Nucl. Instrum. Methods-Phys.Res.B*, 79, p.865, 1993.

[3] Abs M *et al.*, "The IBA Rhodotron T T1000: a very high power E beam accelerator", *Radiation Physics and Chemistry*, 2004, 71: 285-288.

[4] I. Jabbari *et al.*, "Design study of double-layer beam trajectory accelerator based on the Rhodotron structure", *Nucl. Instrum. Methods-Phys.Res.A*, 828, pp.72–80, 2016.

[5] R. Y. Song *et al.*, "Design of resonant cavity of petal shaped accelerator", *High power laser and particle beams*, Vol. 21, No. 12, Dec. , 2009.

[6] X. Z. He *et al.*, "A proposal of using improved Rhodotron as a high dose rate micro-focused X-ray source", presented at *Proc. SAP2017*, Jishou, China, 2017, this proceedings, paper TUPH08.

[7] F. Marhauser, "Finite Element Analyses for RF Photoinjector Gun Cavities", BESSY GmbH, Germany, TESLA FEL Report 2006 - 02.

[8] N. Hartman *et al.*, "Electromagnetic, Thermal, and Structural Analysis of RF Cavities Using ANSYS", in *Proc. PAC2001*, Chicago, USA, 2001, paper MPPH060, pp.912-914.

[9] ANSYS, http://www.ansys.com

ISBN: 978-3-95450-199-1 doi:10.18429/JACoW-SAP2017-TUPH30

# REDUNDANCY ANALYSIS OF SOLID-STATE AMPLIIFERS FOR CIADS ACCELERATOR *

Penghui Gao†, Zhijun Wang, Institute of Modern Physics, CAS, Lanzhou, China
Yi Xiong, Beijing BBEF Science and Technology Co., Ltd, Beijing, China
Yuan He, Yuanshuai Qin, Weiping Dou, Shuhui Liu, Wangsheng Wang, Weilong Chen, Huan Jia, Peiyong Jiang, Chi Feng, Yongzhi Jia, Chao Wang, Haoye Wang, Institute of Modern Physics, CAS, Lanzhou, China

*Abstract*

The solid-state amplifier(SSA) will be applied in China Initial Accelerator Driven System (CiADS) accelarator. 20KW SSA is the basis of RF power systems. With considering power loss redundancy of the main amplifier(MA) is analyzed by builting k/N reliability model for various redundancy. 26/30 redundancy is optimal for 20KW SSA in term of reliability.

## INTRODUCTION

The solid-state amplifier has proved to be quite reliable as well as easy maintenance compared to tetrode and klystron, so it will satisfy high availability of CiADS accelarator. CiADS amplifiers have four types: 20KW, 40KW, 60KW and 80KW [1] and they are combined by 20KW SSA.

Redundancy of SSA is analyzed by the fault tree(FT) model in IFMIF [2]. However, power loss is not considered and causes a large effect for availability analysis.

With considering power loss, k/n RBD model of MA is built and MTBF of various redundancy is calculated in this paper.

## THE PRICIPLE OF 20KW SSA

20KW SSA is composed by RF chain, central control, the cooling system and power assembly. There are many componets, such as limiter, attenuator, RF switch, 1:6 splitter, pre-amplifier which has six 50W-SSA, 6:1 combiner, 1:22 splitter, the mian amplifier that has twenty-two 1KW-SSA, 22:1 combiner and coupler in RF chain. As is shown in Figure 1. The cooling system includes cooling pipe, pump and flowmeter. Central control is combined by an industrial computer and monitoring circuits.

Low level radio frequency(LLRF) transimit a signal to limiter which discriminates range of amplitude. Attenuator can amplifying signal and RF switch controls signal output. Small power amplifys to 20KW through the pre-amplifier and MA. The data that coupler moniters the power is transimited to central control which gives commands to every component. The cooling system cools large-power components and power assembly complishes 220V or 380V conversion.

* Work supported by Strategic Priority Research Program-Future Advanced Nuclear Fission Energy (Grant No. Y102070ADS)
† gaoph2016@impcas.ac.cn

## K/N RBD MODEL OF MA

### *Component Definition*

Componet definition is different between physical modle and RBD model. 20KW SSA is composed by components such as input control, splitter, the pre-amplifier, combiner, equivalent splitter, 1KW SSA, equivalent combiner, the cooling system and central control in RBD model. Here concepts of equivalent splitter and combiner are put forword to solve redundancy analysis of MA. If one 1KW-SSA is wrong, 20KW SSA which has twenty-two 1KW-SSA can not output rated power. If MA has twenty-four 1KW-SSA, 20KW SSA can tolerate one 1KW-SSA is wrong. Styles of splitting and combineing which are different for various redundancy are unified with concepts of equivalent splitter and combiner and it will not affect reliability analysis.

### *Redundancy Analysis of MA*

Insertion loss of equivalent combiner and equivalent splitter is 0.4dB. If guaranteeing Po of SSA output is 20 KW, Pm of the main amplifier must equal 21.93KW according to the equation(1).

$$10 * lg(P_m/P_o) = 0.4 \quad (1)$$

(Pm-Po) is insertin loss of equivalent combiner. If the power source outputs 20KW, MA at least needs twenty-two 1KW-SSA. This situation is no redundancy. Any amplifier which is fault can cause the fault of the power source. If applying more than 22 amplifiers, the power source could tolerate one or a few amplifiers which are fault. However, in this case inconsistency of amplitude and phase will bring about additional power loss. N represents the number of total amplifiers and n represents the most number of amplifiers that are wrong. And k=N-n. We can caculate Pm acoording to equation(2) and equation(3). Pi represents the power output of k amplifiers. Different redundancy is as followed table1.

$$P_i = P_o * (N/(N-n))^2 \quad (2)$$

$$10 * lg(P_m/P_i) = 0.4 \quad (3)$$

In conlusion, 24 amplifiers can tolerate at most one which is fault. 26 amplifiers can tolerate at most two which are fault. 32 amplifiers can tolerate at most five which are fault. k/N RBD model of MA is as followed Figure 2.

ISBN: 978-3-95450-199-1 doi:10.18429/JACoW-SAP2017-TUPH30



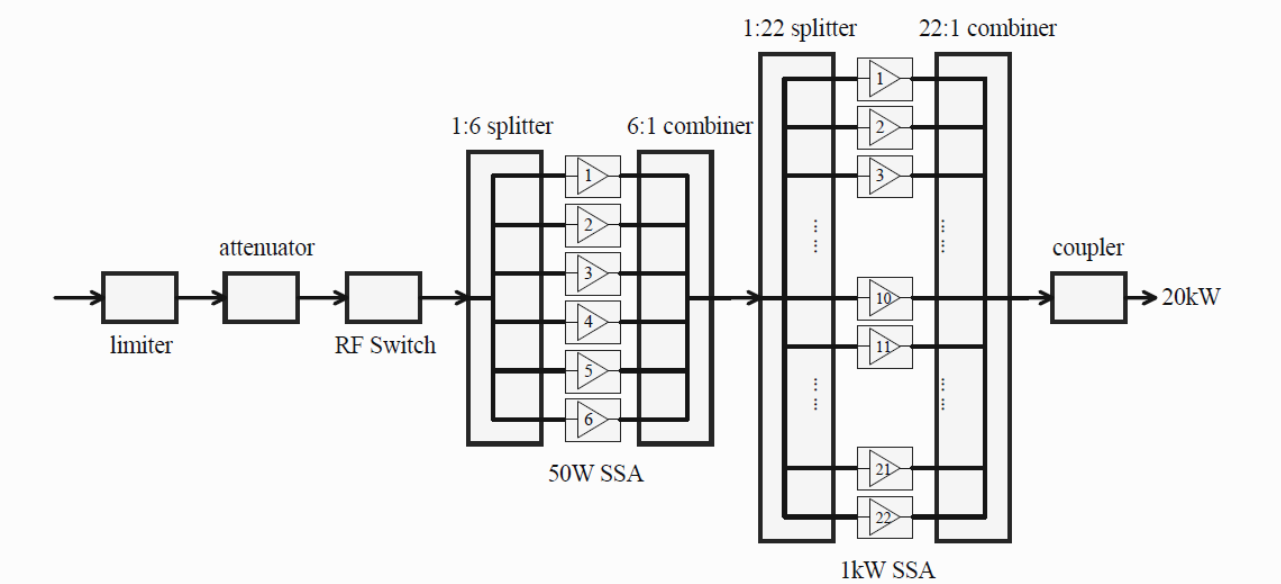


Figure 1: The schematic diagram of 20KW SSA.

Table 1: Various Redundancy of 20KW SSA

| N | n | redundancy |
|---|---|---|
| 22 | 0 | 22/22 |
| 24 | 1 | 23/24 |
| 26 | 2 | 24/26 |
| 28 | 3 | 25/28 |
| 30 | 4 | 26/30 |
| 32 | 5 | 27/32 |
| 33 | 6 | 27/33 |

### *The Weakness of 20KW SSA*

MTBF of the system must be smaller than every component, so improving MTBF of the module which is high fault rate, reliability of the system increases more fast compared to the module that is low fault rate. According to running experience, 1KW SSA has the highest fault rate compared to other components. MA which is the weakness of 20KW SSA will apply degraded redundancy to improvre MTBF of it. In general, MTBF of other components is longer than MTBF of MA.

### *Hypotheses and Assumptions*

Using assumptions are as follows:

(1)All components have only two states: fault and running.

(2)The fault density of components obeys exponential distribution and Fault rate is reciprocal of MTBF. Every fault disables the component and it must be maintained.

(3)There is no contact between components. The fault of one component can not cause non-function of other components.

(4)MTBF of 1KW amplifiers is constant below rated power.

(5)Definition of fault: components or systems do not complish desired function.

## MTBF CACULATION OF MA

The k/n reliability model of MA is built by Reliasoft. MTBF of 1KW SSA is 100000 hours in RBD model. MTBF of MA is calculate as Table 2.It is not difficult that MTBF of other components realises 200000 hours. Because other components can not reach 700000 hours, MA of 26/30 redundancy is not weakness of 20KW SSA. Considering cost and reliability, 27/32 or more reduandancy is not taken account of.

Table 2: MTBF of MA in Various Redundancy

| redundancy | MTBF(h) |
|---|---|
| 22/22 | 4550 |
| 23/24 | 14924 |
| 24/26 | 49268 |
| 25/28 | 171702 |
| 26/30 | 700985 |
| 27/32 | 3052783 |
| 27/33 | 21052180 |

## SUMMARY

26/30 redundancy is optimal for 20KW solid-state amplifiers. Because other components can not reach 700000 hours, MA of 26/30 redundancy is not weakness of 20KW SSA.

## REFERENCES

[1] Design Report of China Initial Accelerator Driven System, IMPCAS etc, 2017.

[2] ENRIC BARGALLÓ, IFMIF accelerator facility RAMI analyses engineering design phase, 2014.

ISBN: 978-3-95450-199-1 doi:10.18429/JACoW-SAP2017-TUPH30

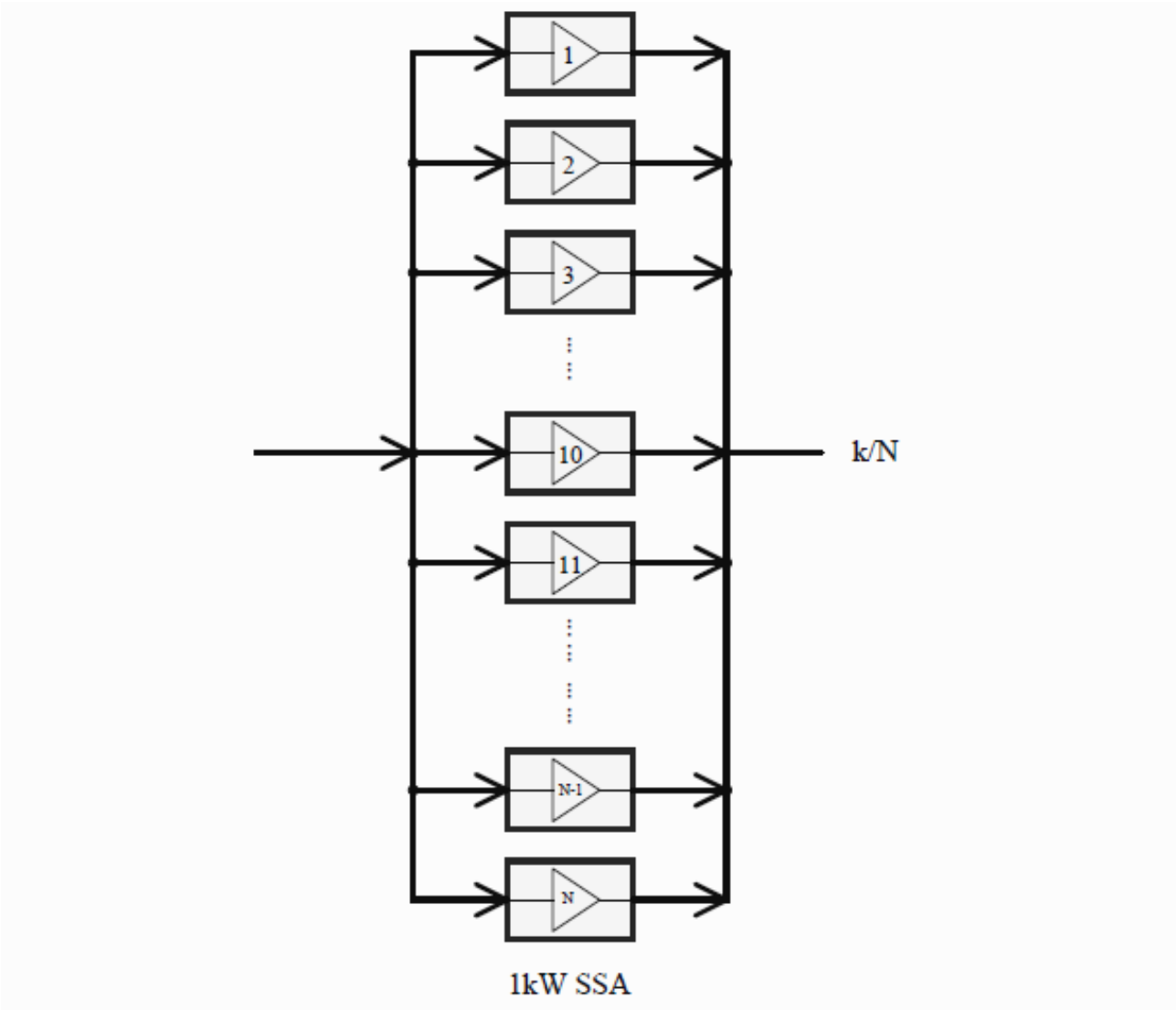


Figure 2: k/N RBD model of MA.

ISBN: 978-3-95450-199-1 doi:10.18429/JACoW-SAP2017-WEAH4

# BUNCH LENGTH MEASUREMENT SYSTEM FOR 500 kV PHOTOCATHODE DC GUN AT IHEP

O. Z. Xiao[1], J. R. Zhang, X. P. Li, X.J.Wang, D.R.Sun
Institute of High Energy Physics, Chinese Academy of Sciences, Beijing, China
[1]also at Key Laboratory of Particle Acceleration Physics and Technology,
Institute of High Energy Physics, Chinese Academy of Sciences, Beijing, China

*Abstract*

In September of 2011, a 500 kV photocathode DC gun was proposed for FEL-ERL two purpose facility at Institute of High Energy Physics (IHEP). So far, the whole system has been installed and the preliminary high voltage conditioning has been carried out. Since the photocathode response time influence the beam quality, the bunch length measurement system is required, which consist of a solenoid, a 1.3 GHz standing wave deflecting cavity, a slit and a YAG screen. In this paper, the design of a deflecting cavity with $TM_{210}$ mode is presented. In addition, the beam dynamics study of the bunch measurement system is performed using ASTRA and the layout of the bunch measurement system is determined. The bunch length in simulation is in good agreement with theoretical calculation.

## INTRODUCTION

High voltage DC electron guns based on GaAs photocathode are proposed for energy recovery linac and free electron laser in many laboratories around the world. Compared with RF guns, DC guns can produce high average current beam with low emittance and operate at CW mode. As a key technology for future advanced light source, the R&D of photocathode dc electron gun was supported at IHEP in 2012. So far, the construction of the DC gun had been completed and a preliminary high voltage conditioning was carried out up to 440 kV [1]. The performance of photocathode depends on many factors such as cathode material, the preparation and activation condition, which will influence the beam parameter. For example, the photocathode with slow response time will generate a long tail compared with laser pulse width, which will cause the emittance growth. For this reason, a bunch length and longitudinal profile measurement system based on deflecting cavity is essential to investigate cathode property.

## BUNCH LENGTH MEASUREMENT SYSTEM DESIGN

To reduce the space charge effect in the gun region, the laser pulse illuminating the photocathode is necessary to shape and extend to tens of picoseconds. In our case, the laser pulse is like plateau distribution with flat top of 20 ps and rise and fall time each of 2 ps. The beam longitudinal distribution is almost the same as the laser pulse when the photocathode response time is rapid. In order to study the properties of photocathode, a bunch length measurement system is proposed, which includes a solenoid, a 1.3 GHz standing wave deflecting cavity, a slit and a YAG screen. The deflecting cavity is 1.15 m away from the cathode of the electron gun. A YAG screen to measure the transverse beam profile is put at downstream of 1.4 m from deflecting cavity. To improve the resolution length of measurement, a solenoid after the gun and a slit before the deflecting cavity are used to reduce the horizontal beam size. The resolution length determine the measurement accuracy, which is defined as

$$L_{res\_t} = \frac{\sigma_{x0}(E/e)}{wV_{def}L} \quad (1)$$

Where $\sigma_{x0}$ is the horizontal beam size at screen with deflecting cavity turn-off, E is the beam energy, $V_{def}$ is the deflecting voltage, $w$ is the circular frequency of cavity. The layout of the bunch measurement system is shown in Fig. 1.

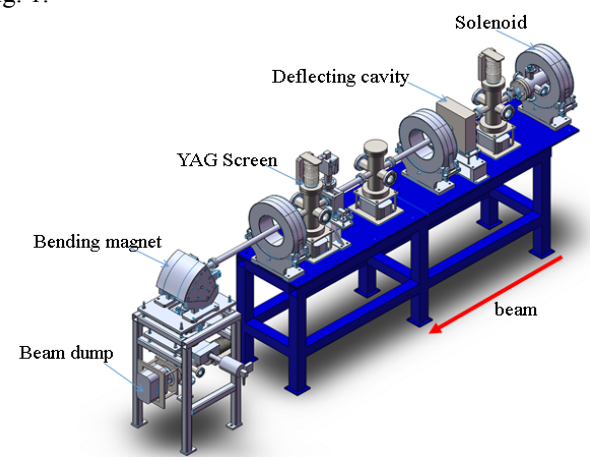


Figure 1: The layout of the bunch measurement system.

The parameters of the bunch measurement system are presented in Table 1. Using these parameters, the relation between the resolution length and the input power is shown in Fig. 2.

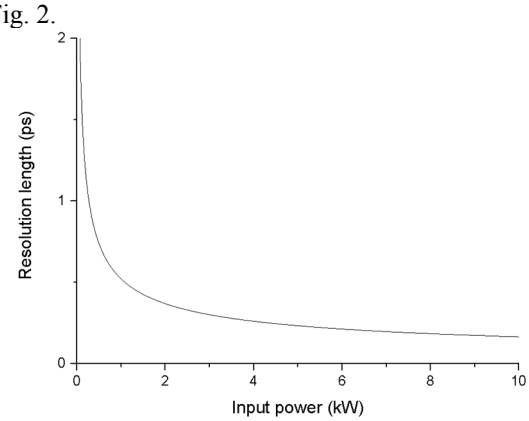


Figure 2: The relation between the resolution length and the input power.

ISBN: 978-3-95450-199-1 doi:10.18429/JACoW-SAP2017-WEAH4

Table 1: The Parameters for Bunch Measurement System

| Parameters | Value |
|---|---|
| Beam Energy(MeV) | 0.5 |
| Beam Normalized Emittance(mm.mrad) | 0.3 |
| Bunch Total Length(ps) | 30 |
| Bunch RMS Length(ps) | 6 |
| Beam Size without Deflecting Cavity(mm) | 0.5 |
| Resolution length(ps) | 1 |
| Drift Length（m） | 1.4 |
| Deflecting Cavity Frequency（GHz） | 1.3 |
| Deflecting Voltage(kV) | 23 |
| Input Power(W) | 250 |
| Solenoid Magnetic Field（Gs） | 310 |

## DEFLECTING CAVITY DESIGN AND MEASUREMENT RESULTS

The multi-cell deflecting cavity can be used for high energy or low energy beam. However the beam energy of 0.5 MeV is relative low, a single-cell cavity will be applied to reduce the complexity of cavity design. The cavity operating at $TM_{210}$ is similar to the RF deflector at KEK [2]. The amplitude of transverse deflecting voltage acting on a beam on axis is

$$V_\perp = \left| c\int_{-\infty}^{\infty} B_\perp(z).e^{jkz/\beta}dz - j\frac{1}{\beta}\int_{-\infty}^{\infty} E_\perp(z).e^{jkz/\beta}dz \right| \quad (2)$$

where $B_\perp(z)$ and $E_\perp(z)$ are the transverse components of the magnetic and electric fields on axis, k is the wave number, z is the longitudinal coordinate, c is the speed of light, β is the particle relative velocity. According to the Panofsky-Wenzel theorem, the deflecting voltage can be defined as

$$V_\perp = \left| \frac{1}{\beta ka}\int_{-\infty}^{\infty} E_z(z).e^{jkz/\beta}dz \right| \quad (3)$$

The transverse shunt impedance is defined as

$$Z_\perp = \left| \frac{V_\perp^2}{2P} \right| \quad (4)$$

P is the power dissipated in the cavity walls. The higher the transverse impedance value, the less power is required to get a certain deflecting voltage. The cavity shape and dimension is optimized to maximize $Z_\perp$ and unloaded Q factor using CST [3]. To separate the orthogonal dipole modes, the cavity horizontal width is slight larger than vertical width. The parasitic modes are also simulated, which should not be exited. The oxygen free high conductivity copper material is used for fabrication of the cavity because of the low ohmic losses and the high thermal conductivity. After the cavity was fabricated and assembled, some characteristic parameters are measured with a network analyser. Table 2 and Table 3 summarize cavity parameters and the frequency of parasitic modes respectively. The vacuum leak detection of the cavity is shown in Fig. 3. The electromagnetic field pattern of $TM_{210}$ is shown in Fig. 4.

Table 2: Comparison of Cavity Parameters

| Parameters | Simulation | Test |
|---|---|---|
| f (GHz) | 1.3 | 1.3 |
| $Q_0$ | 23323 | 20964 |
| $Z_\perp$(Mohm) | 0.88 | - |
| β | 1.02 | 1.01 |

Table 3: Parasitic Modes Frequency

| Mode | Frequency (MHz) |
|---|---|
| $TM_{110}$ | 849.6 |
| $TM_{120}$ | 1363 |
| $TM_{220}$ | 1692 |
| $TM_{310}$ | 1838 |

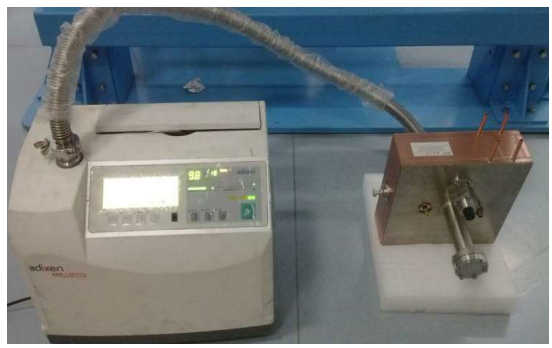

Figure 3: The vacuum leak detection of the cavity.

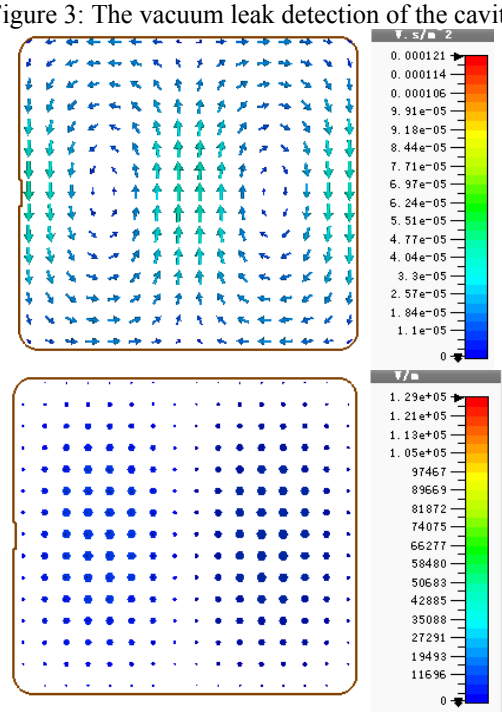


Figure 4: Electromagnetic field pattern of $TM_{210}$ with 1 W input power.

## BEAM DYNAMIC SIMULATION

The beam dynamics of the whole bunch measurement system is simulated in two different cases using ASTRA [4]. One case is low input power of 250 Watts with slit to collimate the beam in horizontal direction, and the other case is high input power of 1000 Watts without slit.

ISBN: 978-3-95450-199-1 doi:10.18429/JACoW-SAP2017-WEAH4



The resolution length of both cases is almost the same. After the deflector, the beam longitudinal position relative to the bunch centre is transformed into transverse displacement on the screen. Then the bunch length can be calculated according to bunch spot size, which is defined as

$$\sigma_t = \frac{(E/e)}{2\pi f V_{def} L}\sqrt{\sigma_x^2 - \sigma_{x0}^2} \quad (5)$$

Where $\sigma_x$ is the beam spot size on screen in horizontal direction when the deflector is turn-on. The bunch length calculation results of both cases are summarized in Table 4, which are agreement with the bunch length of 6.15 ps before deflecting cavity.

Table 3: The Bunch Length Calculation Results

| Parameters | Case1 | Case2 |
|---|---|---|
| $V_{def}$(kV) | 42 | 21 |
| $\sigma_{x0}$(mm) | 1.08 | 0.58 |
| $\sigma_x$(mm) | 5.96 | 3.02 |
| $\sigma_t$(ps) | 6.1 | 6.18 |

The electromagnetic field along the longitudinal direction of the latter case is shown in Fig. 5.

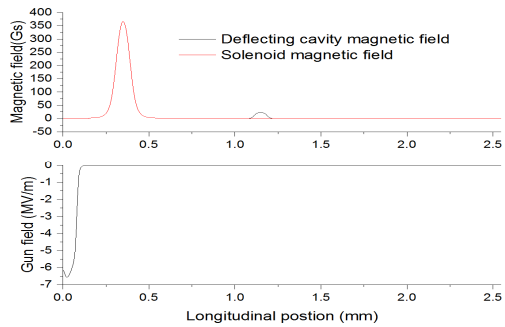


Figure 5: Electromagnetic field along the longitudinal direction.

The evolution of the bunch transverse distribution and phase space of both cases are shown in Figs. 6 and 7.

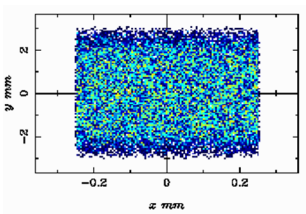

a)Transverse distribution before deflector

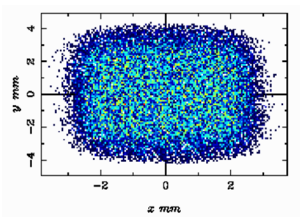

b)Transverse distribution after deflector

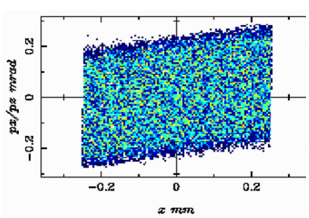

c)Horizontal space phase before deflector

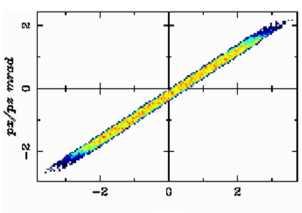

d) Horizontal space phase after deflector

Figure 6: The transverse beam distribution with slit.

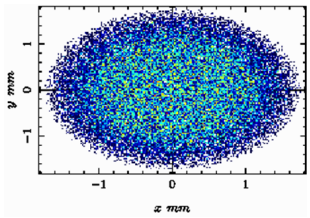

a)Transverse distribution before deflector

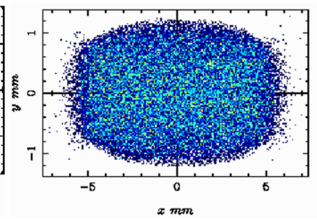

b)Transverse distribution after deflector

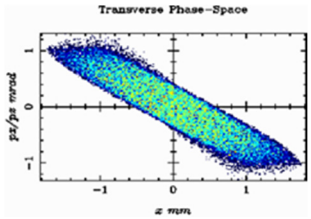


c)Horizontal space phase before deflector

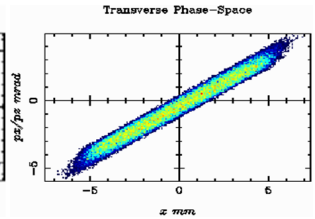


d) Horizontal space phase after deflector

Figure 7: The transverse beam distribution without slit.

The Figs. 6 and 7 indicate that the beam horizontal energy spread and spot size increase due to the horizontal kick of deflector. Also the horizontal distribution on the screen can be converted to longitudinal profile after some mathematical treatment, as shown in Fig. 8. The profile from the screen is in agreement with that before deflector.

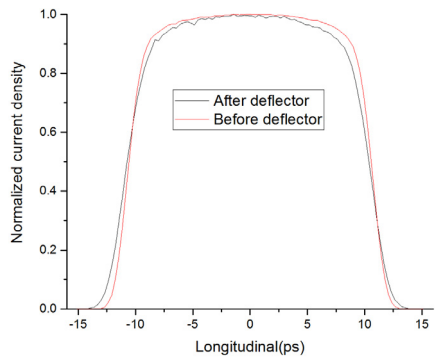


Figure 8: Comparison of the beam longitudinal profile.

## CONCLUSION

The transverse deflecting cavity is an accurate and effective means to measure bunch length and distribution. This paper presented the bunch measurement system based on deflector for 500 kV photocathode dc gun at IHEP. A 1.3 GHz rectangular deflecting cavity operating at $TM_{210}$ mode has been designed and fabricated. The cold test has been completed and the characteristic parameters are in good agreement with simulation in CST. So far all components used in the beam length measurement system have been installed. The beam dynamics of the bunch length measurement system has been simulated. The slit before the deflecting cavity can be used to reduce the input power requirement. The error analysis and simulation are in progress.

ISBN: 978-3-95450-199-1 doi:10.18429/JACoW-SAP2017-WEAH4

## REFERENCES

[1] Xiao-Ping Li, Jiu-Qing Wang ,Jin-Qiang Xu *et al*., "Constructions and Preliminary HV Conditioning of a Photocathode Direct-Current Electron Gun at IHEP", *Chin. Phys. Lett* ,Vol. 34, No. 7 ,2017.

[2] S. Matsuba *et al*., "Deflecting cavity for bunch length diagnostics at compact ERL Injector", in *Proc. IPAC'10*, Kyoto, Japan, 2010.

[3] *CST 2017 Manual*, 2017.

[4] Klaus Floettmann, *ASTRA Manual V3*, 2011.

ISBN: 978-3-95450-199-1 doi:10.18429/JACoW-SAP2017-WEBH3

# EXPERIMENTAL POLARIZATION CONTROL OF THOMSON SCATTERING X-RAY SOURCE

Zhang Hongze†
Tsinghua University, Beijing, China

*Abstract*

Thomson scattering of intense laser pulses from relativistic electrons allows us to generate high-brightness and tunable-polarization X/γ-ray pulses. In this paper, we demonstrate the polarization control of the Thomson scattering source experimentally. We control the incident laser polarization by rotating a quarter-wave plate, thus controlling X/γ-ray polarization. In order to measure the polarization, we use Compton scattering method. Meanwhile, stokes parameters of X/γ-ray whose energy varies between tens of keV and MeV are simulated. The simulation results show that with the increasing of X-ray Energy, X-ray polarization is a constant value in a small cone of motivation. According to modulation curves analysed from experiment results, we can get the conclusion that the polarization of Thomson scattering source is tunable and controllable.

## INTRODUCTION

Polarized X/γ-ray has been studied and widely used in various scientific field. Polarization of X/γ-ray can provide unique information addition to X-ray imaging and analysis of spectroscopy for researchers. In astrophysics, polarimetric observations of neutron stars provide the information of the intensity and geometry of the magnetic field [1-4]. In material science and biology, polarized X-rays can enhance the sensitivity of X-ray fluorescence analysis [5]. In nuclear physics, polarized γ-rays plays an important role in studying nuclear property. We can study the structure of nuclear by nuclear resonance fluorescence with polarized X/γ-ray (NFR) [6-9]. And the polarized state of γ-rays is also important for the measurements of the parity of the nuclear states [10], the investigation of giant resonances of nuclei and the scattering reactions between photons and nuclei [11,12].

Compton scattering is the elastic scattering of a photon from a free electron, for the low energy electron(~MeV), it is also called as Thomson scattering [13-15]. Compton(Thomson) scattering X-ray source has been studied and developed for decades [16-20]. Comparing to the mechanism of other radiation sources, it can produce ultrashort, energy continuously tunable, high brightness, well-collimate and high polarized X-ray beams by laser photons scattering from free relativistic electrons [21-24]. Because of the advantages in X-ray application, Thomson scattering X-ray source is utility in material, medical and biological areas [24-28]. In our experiment, we change the polarization of X-ray by adjusting the polarization of laser beams since the polarization of laser is directly transferred to the scattered photons.

† zhz16@mails.tsinghua.edu.cn

## EXPERIMENT

We carry out the X-ray polarization control and measurement experiment on Tsinghua Thomson scattering X-ray source (TTX) platform. TTX is set up with a linac system and a femtosecond laser system. The linac system consists of a S-band photocathode RF gun, a magnet compressor and two x-band harmonic structures to generate high brightness electron pulse. The laser system can generate 266-nm ultraviolet pulse for the photocathode and 800-nm infrared pulse for the scattering interaction. The energy of X-ray photons is 50-keV and the flux is about $10^7 s^{-1}$[29]. In our experiment, laser photons track through the quarter-wave plate and have a head-on interaction with the high-quality electron beams in the vacuum interaction room. The polarization of scatted photons is determined by the incident laser beams, which are controlled by the quarter-wave plate precisely.

In our experiment, we use the Compton scattering method, a kind of polarization-sensitive process which is more accurate than before, to measure the polarization of X-ray beams. According to the Klein-Nishina formula [30], for linear incident X/γ-ray photon, the azimuthal distribution of the scattered photons is strongly depended on the X-ray polarization. A target, made from polyethylene, is placed after the titanium window of the beam pipe. The size of the cylinder target is 5-cm in height and 0.75-cm in radius. X-ray pulses irradiate on the end of the cylinder and generate scattered photons. We use an image plate wrapping around the cylinder to record scattered photons (Figur 1). Meanwhile, we use two thin aluminium rings locked to both ends of the polyethylene cylinder to support the image plate. The curved image plate is 2.5-cm in radius.

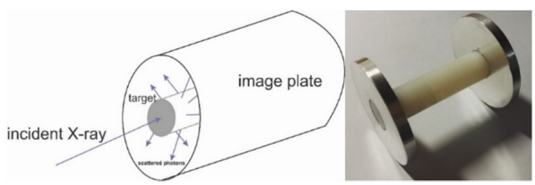


Figure 1: Schematic and real picture of target.

## RESULTS

Figures 2-4 show the experiment results recorded by image plate and the simulation results done with Geant4.

ISBN: 978-3-95450-199-1 doi:10.18429/JACoW-SAP2017-WEBH3

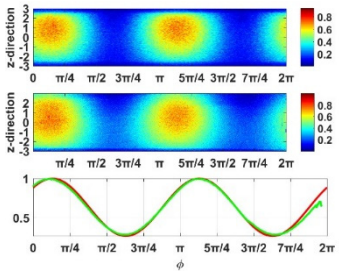


Figure 2: Linear polarized incident laser beams. First subpicture: Simulation result of the scattered photons recorded by the image plate. Second subpicture: experiment result of the scattered photons recorded by the image plate. Third subpicture: Calculated results from the simulation (red) and experiment (green) results.

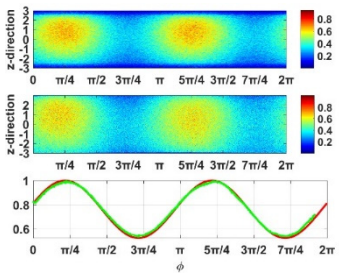


Figure 3: Ellipse polarize incident laser beams.

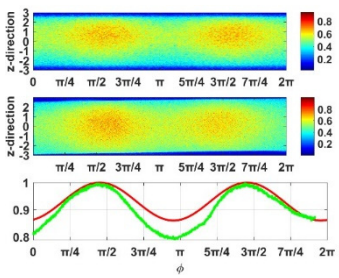


Figure 4: Circle polarized incident laser beams.

In Figs 2-4, for each polarization result, we sum the photons recorded by the image plate in the z-direction and get modulation curves. According to the modulation curves, we calculate the modulation amplitude and polarization of different polarized X-ray pulses. The modulation curves' amplitudes vary from the maximum value for linear polarization to the minimum value for circle polarization. The reasons, affecting the accuracy of the results, include the jitter of the electron pulse and laser pulse. Also, we assume that the X-ray bunches are parallel after tracking through the filter. But there is still a small divergence for each X-ray bunch in the forward direction.

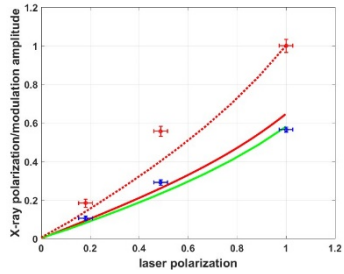


Figure 5: Red line: the theory result of modulation amplitude. Green line: the simulation result of modulation amplitude. Red dot line: the simulation result of polarization. Red spots: experiment results of polarization. Blue spots: experiment results of modulation amplitude.

Simulated result (green line) is smaller than the theory result (red line). Because when we calculate the theory result, we only consider primary scattering process and ignore the background. The variation trend of the experiment result fits the simulation results. However, there is still one point doesn't fit the simulation results well. Because the simulation process is done under an ideal condition. The polarization of X-ray irradiated on the target is supposed to be the same. However, X-rays generated by Thomson scattering sources have a small divergence in forward direction. It results in the polarization of X-ray irradiated on the target varies between a small region. We can reduce the target's cross section radius to improve the accuracy of the experiment.

The X-ray energy is about 50-keV in our experiment and the X-ray polarization is nearly a constant value. In order to verify the polarizaiton relationship between incident laser pulses, electron beams in high energy section, we calculate stokes parameters of X-rays under different electron beams energy. Limited by the experiment condition, we simulate the interaction process with Cain program. Stokes parameter $S_2$ represents the circle polarization and $S_3$ represents the linear polarization. $S_2 = 1$ or $S_2 = -1$ represents clockwise and counterclockwise. And $S_1(S_3) = 1$ or $S_1(S_3) = -1$ represents two polarized directions which are orthogonal to each other. Complete polarized states have $S^2 = 1 (S^2 = S_1^2 + S_2^2 + S_3^2)$, but mixed states have $S^2 < 1$. Changing energies of electron beams in Cain, the average value of $S_2$ and $S_3$ in a small cone (θ=1⁄5γ) under different X-ray energys are shown in Fig. 6.

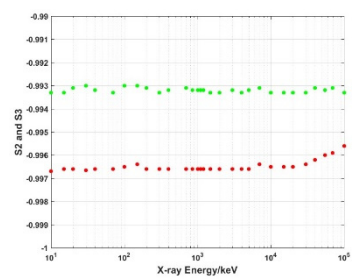


Figure 6: Stokes parameters. Green line: average value of S_2 under different X-ray energy. Red line: average value of S_3 under different X-ray energy.

ISBN: 978-3-95450-199-1 doi:10.18429/JACoW-SAP2017-WEBH3



In Fig. 5, Stokes parameters are almost invariant with X-ray energy increasing in a constant small cone($\theta=1/5\gamma$). This means energies of electron beams doesn't affect the polarization of X-ray with a wide range of energy in a small cone. In order to measure the high-energy X-ray polarization, a smaller cross section target is useful. But with high energy X-ray, about 10-Mev or more, the effect of pair production will affect the accuracy of the measurement.

## CONCLUSION

Thomson Scattering Source is an important way to generate polarized X/γ -ray pulses which are tunable and controllable. Polarized X/γ-ray pulses are important and useful in various scientific area. Our experiment is the first time that try to precisely measure the polarization of Thomson Scattering Sources and verify the relationship of polarization between the incident laser beams and scattered X-ray beams. We use Compton scattering method, applicable in the energy range keV ~ MeV, to measure the polarization of X-ray beams. The experiment results show that we can produce accuracy polarization γ-ray/X-ray pulses by changing the polarized state of incident laser beams. And X-ray polarization are nearly constant value in a small cone under different X-ray energy.

## REFERENCES

[1] P. A. Connors and R. F. Stark, *Nature 269*, 8 (1977).

[2] E. Costa, P. Soffitta, R. Bellazzini, A. Brez, N. Lumb and G. Spandre, *Nature 411*, 662 (2001).

[3] J. R. P. Angel, R. Novick, P. V. Bout and R. Wolff, *Phys. Rev. Lett. 22*, 861(1969).

[4] G. Bao, P. J. Witta and P. Hadrava, *Phys. Rev. Lett*. 77, 12(1996).

[5] J. O. Christoffersson and S. Mattsson, *Phys. Med. Biol.* 28, 1135(1983).

[6] L. I. Schiff, *Phys Rev.,* 70, 761(1946).

[7] U. Kneissl, H. H. Pitz, A. Zilges and Prog. Part. *Nucl. Phys*., 37, 349(1996).

[8] M. E. Rose and R. L. Carovillano, *Phys. Rev*., 122, 1185 (1961).

[9] C. T. Angell, R. Hajima, T. Hayakawa, T. Hayakawa, H. J. Karwowski, and J. Silano, *Phys. Rev. C* , vol. 90, 054315(2014).

[10] N. Pietralla, Z. Berant *et al., Phys. Rev. Lett*., vol. 88, 012502 (2001).

[11] H. Arenhövel, and E. Hayward, *Phys. Rev*., vol. 165, 1170(1968).

[12] E. Hayward, W. C. Barber and J. Sazama, *Phys. Rev. C*, vol. 8, 1065 (1973).

[13] A. H. Compton, *Phys. Rev*., vol. 21, 483(1923).

[14] R. H. Milburn, *Phys. Rev. Lett*., vol. 10, 75(1963).

[15] G. Fiocco, and E. Thompson, *Phys. Rev. Lett*., vol. 10, 89(1963).

[16] F. R. Arutyunian, and V. A. Tumanian, *Phys. Lett*., vol. 4, 176 (1963).

[17] A. M. Sandorfi *et al*., *IEEE Tran. Nucl. Sci*. vol. 30, 3083 (1983).

[18] R. W. Schenlein *et al*., *Science,* vol. 274, 236(1996).

[19] C. Bula *et al*, *Phys. Rev. Lett.*, vol. 76, 3116(1996).

[20] A. Ting *et al*., *J. Appl. Phys*, vol. 78(1), 575(1995).

[21] V. N. Litvinenko *et al*., *Phys. Rev. Lett*., vol. 78, 4569 (1997).

[22] I. V. Pogorelsky *et al*., *Phys. Rev. ST Accel. Beams*, vol. 3, 090702 (2000).

[23] D. J. Gibson *et al*., *Phys. Rev. ST Accel. Beams*, vol. 13, 070703 (2010).

[24] P. Oliva *et al*., *Appl. Phys. Lett*., vol. 97, 134104(2010).

[25] K. Yamada *et al*., *Nucl. Instr. Meth. A*, vol. 608, S7 (2009).

[26] R. Kuroda *et al*., *Nucl. Instr. Meth. A*, vol. 608, S28 (2009).

[27] J. Abendroth *et al*., *Journal of structural and functional genomics*, vol. 11, 91 (2010).

[28] M. Bech *et al*., Journal of synchrotron radiation 16, 43 (2009).

[29] Y. Du *et al., Nucl. Instr. Meth. A*, vol. 637, S168 (2011).

[30] L. W. Fagg, S. S. Hanna, *Rev.Mod.Phys*. vol. 31, 711(1959)

ISBN: 978-3-95450-199-1 doi:10.18429/JACoW-SAP2017-WEBH4

# BEAM OPTIMIZATION AND MEASUREMENT OF CAEP FEL-THz INJECTOR*

D. Wu, D. X. Xiao, P Li, J. X. Wang†, X. K. Li, X. Luo, K. Zhou, C. L. Lao,
Q. Pan, S. F. Lin, L. J. Shan, H. B. Wang, X. F. Yang, M. Li
Institute of Applied Electronics, China Academy of Engineering Physics (CAEP/IAE),
Mianyang, P. R. China

*Abstract*

The FEL-THz facility in Chinese Academy of Engineering Physics (CAEP) requires high brightness high repetition electron beam, which needs optimization of multi-parameter and multi-objective, such as emittance, energy spread, bunch length, etc. In this paper, some studies of beam optimization based on differential evolution (DE) algorithm and Astra code are shown. Dozens of the DC-SRF-injector parameters have been considered in the optimization. Some measurements of the electron beam are also introduced, including emittance measurement with the three-profile method, energy spread measurement with analyzing magnet and beam length diagnostics with zero-phasing method. These studies indicate that the injector beam quality satisfies the requirement of the FEL-THz facility.

## INTRODUCTION

High average power high-brightness electron source plays a significant role in the path to the realization of the future high repetition short-wave free electron lasers (FELs) and energy recovery linacs (ERLs)[1, 2]. With the construction of European XFEL[3], and with some new projects put forward, such as LCLS-II[4] and MaRIE[5], the X-ray free electron lasers are moving in the direction of high repetition or even continuous-wave mode. These new developments have proposed some new requirements of the high brightness electron sources. The biggest challenge is to maintain the high brightness (electron charge ~200 pC, emittance <0.5 mm·mrad, longitudinal length <1 ps and energy spread ~ $10^{-5}$) of the electron beams at high average current (~MHz repetition and ~100 mA average current).

High-voltage (HV) DC photocathode injector with superconducting RF accelerator could provide high brightness electron beams in CW mode, which makes it a hotspot in short-wave FEL research. One of the best results[6] is achieved by CLASS team in Cornell university, who has get a 0.3 mm·mrad emittance (95% core ) at 100 pC CW mode with 1.3 GHz repetition. The dynamics design of the Cornell beamline is optimized by a multivariate genetic algorithm[7].

In China, the CAEP FEL-THz facility is the first high average Tera-Hertz source based on FEL, which is driven by a DC gun with GaAs photocathode and two 4-cell 1.3 GHz super-conducting radio frequency (SRF) accelerator[8–12]. This is also the first DC-SRF-injector designed for high-Brightness electron beams In China.The repetition of FEL-THz is 54.167 MHz, one in twenty-fourth of 1.3 GHz. The effective accelerator field gradient is about 10 MV/m. The injector could provide high-brightness CW electron beam for the oscillator Tera-Hertz free electron laser. And the beam quality could be optimized better than the FEL-THz requirements. In this paper, an optimization with differential evolution genetic algorithm is discussed. And the beam measurement is shown, including emittance, energy spread and bunch length.

## BEAM OPTIMIZATION

### *DE Algorithm*

Differential evolution (DE) algorithm is a heuristic global optimization based on population, works on Darwin's concept of survival of the fittest[13, 14]. DE and other evolutionary algorithms are often used to solve the beam dynamic optimization[7, 15–17]

DE starts with a population of $NP$ candidate solutions, which may be represented as $X_{i,G}$, $i = 1, 2, ...NP$, where $i$ index denotes the population and $G$ denotes the generation to which the population belongs. DE uses mutation, crossover and selection to solve problems, which are shown in Fig. 1.

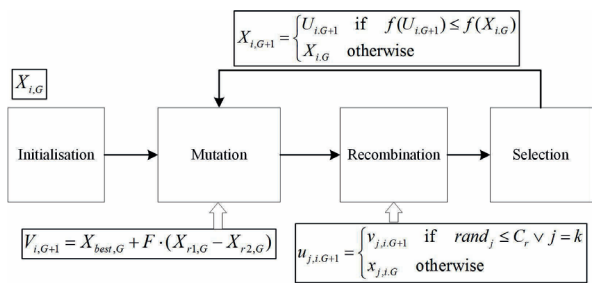


Figure 1: DE flow chart.

The mutation operator is the prime operator of DE. In this paper, a so-called 'best-strategy-type-1' is used[18], where $F \in [0, 1]$ is the control parameter. $r_i \in \{1, ...NP\}$ is a random selection and $r_1 \neq r_2$. The operator recombination and selection are also shown in Fig. 1 The crossover rate $C_r \in [0, 1]$ is the other control parameter of DE.

The most important part in the selection operator is the objective function $f$. In the one-objective situation, $f$ is often as simple as normalized emittance or energy spread

* Work supported by China National Key Scientific Instrument and Equipment Development Project (2011YQ130018), National Natural Science Foundation of China with grant (11475159, 11505173, 11576254 and 11605190)
† jianxinwang1026@163.com

ISBN: 978-3-95450-199-1 doi:10.18429/JACoW-SAP2017-WEBH4



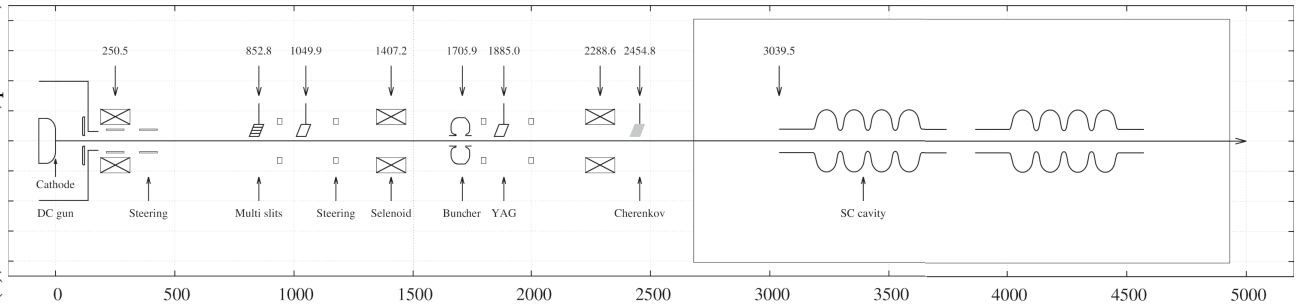


Figure 2: The layout of FEL-THz photo-injector(unit:mm).

in a specific location. But the beam optimization is a multi-objective problem, which means many parameters should be considered together, such as emittance, energy spread, bunch length and transverse beam size. In this paper, two linear objective functions are considered as:

$$f(x) = \sum_i \omega_i f_i(x) \quad \text{or} \quad f(x) = \sum_i \omega_i \left| \frac{f_i(x) - f_{i,0}}{f_{i,0}} \right| \quad (1)$$

where $\omega_i > 0$ is artificially given parameters to highlight main goal. In the left function the magnitude of each objective should be estimated in advance. Its advantage is to be able to search for a better solution than expected. The right one have an ideal solution when $f_i = f_{i,0}$, where $f_{i,0}$ is the preset target for each goal.

### *Optimiaztion Results*

The location of injector elements are shown in Fig. 2. There are three solenoids and one RF buncher upstream of the 2×4-cell superconducting RF accelerator. The first solenoid is used for the emittance compensation[19]. The second and the third ones are used to adjust the transverse beam size before the buncher and accelerator, respectively.

The range of design parameters are shown in Table 1.$B_{si}$ is the center magnetic field along beamline. $E_{b,avg}$ is the average electric field gradient of the buncher. $\phi_b$ and $\phi_{sc}$ are the phase of buncher and accelerators, respectively. The gradient of SC accelerator is preset as 8 MV/m. The beam dynamics is simulated by ASTRA code[20], in which the relative phase is used, making $\phi = 0$ the maximum accelerating phase. $\sigma_r$ is the RMS beam size on the cathode with a two-dimension Gaussian distribution, the lower limit of which is given by the space charge limit (SCL)[21]:

$$\sigma_{r,\min,gaussian} = \sqrt{\frac{Q}{2\pi\varepsilon_0 E_0}} \quad (2)$$

where $Q$ is the beam charge and $E_0$ the electric field gradient on the cathode.

The objective function is to minimize the emittance, bunch length, energy spread at the exit of the accelerator, in which the emittance has the largest weighting factor $\omega$. One of the results is shown in Fig. 3, where (a) is the convergence process of every individual's normalized emittance (unit:mm·mrad) in generations. (b)-(f) are the normalized emittance, the transverse RMS beam size, the longitudinal FWHM length, the energy spread and the kinetic energy along the beam direction $z$, respectively.

Table 1: Range of Design Parameters

| Parameter/Unit | Lower limit | Upper limit |
|---|---|---|
| $\sigma_r$/mm | 0.66 | 2 |
| $B_{s1}$/Gs | 240 | 320 |
| $B_{s2}$/Gs | 90 | 200 |
| $B_{s2}$/Gs | 90 | 200 |
| $E_{b,avg}$/MV·m$^{-1}$ | 0.6 | 2 |
| $\phi_b$/deg | -110 | -70 |
| $\phi_{sc1}$/deg | -20 | 10 |
| $\phi_{sc2}$/deg | -20 | 20 |

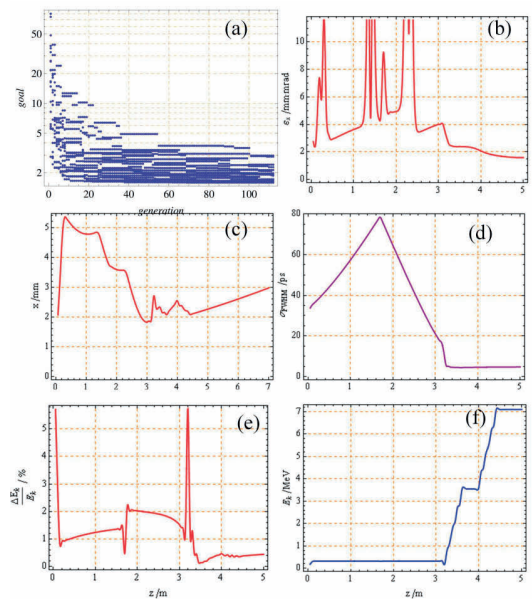


Figure 3: One optimization result with DE algorithm.

ISBN: 978-3-95450-199-1 doi:10.18429/JACoW-SAP2017-WEBH4

The optimization in 100 generations shows that the emittance can be 1.86 mm·mrad and other parameters can also meet the requirements of FEL-THz facility when $Q$=92 pC, $\sigma_r$=0.7 mm, $B_{s1}$ =278 Gs, $B_{s2}$ =121 Gs, $B_{s3}$ =149 Gs, $E_{b,avg}$ =1.2 MV/m, $\phi_b = -85°$, $\phi_{sc1} = -10°$ and $\phi_{sc2} = -5°$.

## BEAM MEASUREMENT

### *Emittance*

The three-profile method[22] is used to measure the emittance downstream of the accelerator. The transverse beam distribution and the normalized emittance are shown in Fig. 4 and Table. 2. The result is larger than the simulation because of space charge force and low beam energy.

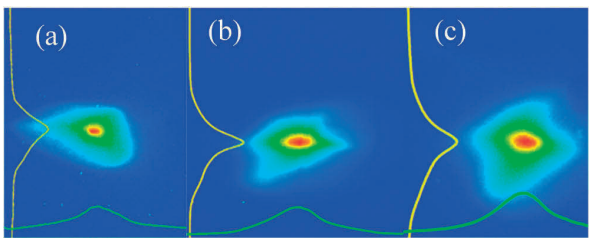


Figure 4: The three profiles for emittance measurement.

Table 2: Emittance measurement result

| $\sigma_{xa}$ | $\sigma_{xb}$ | $\sigma_{xc}$ | $l_{ab}$ | $l_{bc}$ | $E_k$ | $\varepsilon_{n,x}$ |
|---|---|---|---|---|---|---|
| 1.53 mm | 1.07 mm | 1.01 mm | 1662 mm | 2503 mm | 8.1 MeV | 8.2 mm·mrad |

### *Energy Spread*

Fig. 5 shows the energy spread versus buncher field scanning. There is a 90° analysis magnetic system with a slit and a YAG screen. The distance between the slit and the magnet is 300mm, the same as the one between the magnet and the creen. The buncher field is measured by the pickup power. The $E_b$ in this picture presents the peak field and is much larger than the simulation. The minimized FWHM energy spread is 0.3% when the peak field $E_b$ =1.7 MV/m.

### *Bunch Length*

The beam bunch length is measured with zero-phasing method[23, 24]. Because the length change is small after the first 4-cell SC cavity according to the simulation, the second 4-cell one is used to measure the bunch length, making the kinetic energy much smaller than the full power operation. Fig. 6 (a)-(c) are the energy spread when the second 4-cell accelerator is turn-off, in the rising zero phase and in the descending zero phase, respectively. (d)-(f) are the projection of the images (a)-(c) in $x$ direction. The second peak in Fig. 6 (d) is due to the ghost pulses which should be ignored.

Solve the following equation and the bunch length can be achieved in Table. 3. The result is larger than the simulation

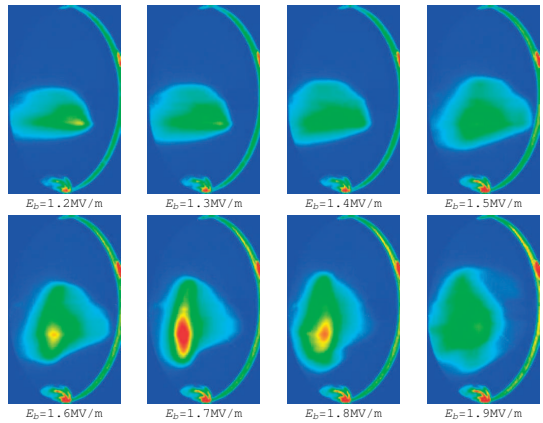


Figure 5: Energy spread scanning.

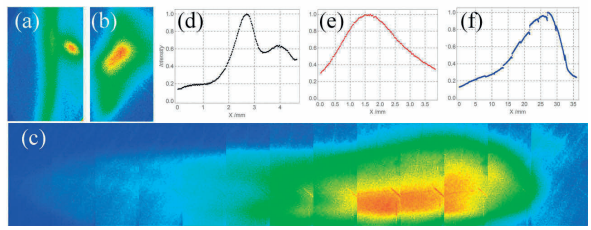


Figure 6: Energy distribution for zero-phasing method

also because of space charge force and low beam energy.

$$\sigma_x = \sqrt{\sigma_{x0}^2 + \sigma_z^2 \eta^2 \left[ \frac{1}{E_0} \left( \frac{\mathrm{d}E}{\mathrm{d}z} \right)_0 + \frac{2\pi e V_{\mathrm{rf}}}{\lambda_{\mathrm{rf}} E_0} \right]^2} \quad (3)$$

Table 3: Bunch Length Measurement Result

| $\sigma_{x0}$ | $\sigma_{x,0}$ | $\sigma_{x,\pi}$ | $E_0$ | $\lambda_{rf}$ | $\eta$ | $\sigma_z$ |
|---|---|---|---|---|---|---|
| 0.5 mm | 0.94 mm | 8.05 mm | 3.1 MeV | 0.23 m | 0.3 m | 0.94 mm |

## SUMMARY

In this paper, the simulation optimization with differential evolution algorithm and ASTRA code are introduced. The emittance of the FEL-THz photo-injector can be reduced to less than 2 mm·mrad, with all the other beam parameters meet the facility requirements. The normalized emittance is measured as 8.2 mm·mrad with 3-profile method. The energy spread is proved to be as small as 0.3%. And a 0.94 mm RMS bunch length is measured by the means of zero-phasing method. This research indicates that DE algorithm is effective on the beamline optimization, and all the beam micro-pulse parameters fulfil the requirements of FEL-THz facility.

ISBN: 978-3-95450-199-1 doi:10.18429/JACoW-SAP2017-WEBH4



## REFERENCES


[1] D. Dowell *et al.*, "Cathode r&d for future light sources," *Nuclear Instruments and Methods in Physics Research Section A: Accelerators, Spectrometers, Detectors and Associated Equipment*, vol. 622, no. 3, pp. 685–697, 2010.

[2] T. Rao and D. H. Dowell, *An engineering guide to photoinjectors*. 2014.

[3] M. Altarelli *et al.*, "The European X-ray free-electron laser," DESY, Tech. Rep., 2006, pp. 1–26.

[4] J. N. Galayda, "The LCLS-II project," Tech. Rep., 2014.

[5] J. Lewellen *et al.*, "Status of the MaRIE X-FEL accelerator design," in *Proceedings of IPAC'15*, Richmond, VA, USA, 2015, pp. 1894–1896.

[6] A. Bartnik, C. Gulliford, I. Bazarov, L. Cultera, and B. Dunham, "Operational experience with nanocoulomb bunch charges in the cornell photoinjector," *Physical Review Special Topics-Accelerators and Beams*, vol. 18, no. 8, p. 083 401, 2015.

[7] I. Bazarov and C. Sinclair, "Multivariate optimization of a high brightness DC gun photoinjector," *Physical Review Special Topics - Accelerators and Beams*, vol. 8, no. 3, p. 034 202, 2005.

[8] P. Li, Y. Jiao, W. Bai, H. B. Wang, X. H. Cui, and X. K. Li, "Start-to-end simulation of CAEP FEL-THz beamline," *High Power Laser and Particle Beams*, vol. 26, no. 8, p. 083 102, 2014.

[9] M. Zheng-Hui *et al.*, "Design and test of frequency tuner for a CAEP high power THz free-electron laser," *Chinese Physics C*, vol. 39, no. 2, p. 028 102, 2015.

[10] X. Luo *et al.*, "Design and fabrication of the 2×4-cell superconducting linac module for the free-electron laser," *Nuclear Instruments and Methods in Physics Research Section A: Accelerators, Spectrometers, Detectors and Associated Equipment*, vol. 871, pp. 30–34, 2017.

[11] K. Zhou *et al.*, "Progress of the 2×4-cell superconducting accelerator for the CAEP THz-FEL facility," in *Proceedings of the 18th International Conference on RF Superconductivity*, Lanzhou China, Jul. 2017, unpublished.

[12] X. Luo *et al.*, "Design of the 2×4-cell superconductng cryomodule for the free-electron laser," in *Proceedings of the 18th International Conference on RF Superconductivity*, Lanzhou, China, Jul. 2017, unpublished.

[13] R. Storn and K. Price, "Differential evolution–a simple and efficient heuristic for global optimization over continuous spaces," *Journal of global optimization*, vol. 11, no. 4, pp. 341–359, 1997.

[14] M. Ali, M. Pant, and A. Abraham, "A simplex differential evolution algorithm: Development and applications," *Transactions of the Institute of Measurement and Control*, vol. 34, no. 6, pp. 691–704, 2012.

[15] J. Qiang, Y. Chao, C. Mitchell, S. Paret, and R. Ryne, "A parallel multi-objective differential evolution algorithm for photoinjector beam dynamics optimization," in *Proceedings of IPAC'13*, 2013, pp. 1031–1033.

[16] Y. Zhang and D. Zhou, "Application of differential evolution algorithm in future collider optimization," in *7th International Particle Accelerator Conference (IPAC'16), Busan, Korea, May 8-13, 2016*, JACOW, Geneva, Switzerland, 2016, pp. 1025–1027.

[17] L. Y. Zhou *et al.*, "Design of an X-band photocathode rf gun for tsinghua thomson scattering X-ray source," in *IPAC'17*, 2017, pp. 1025–1027.

[18] W. Gong, A. Fialho, and Z. Cai, "Adaptive strategy selection in differential evolution," in *Proceedings of the 12th annual conference on Genetic and evolutionary computation*, ACM, 2010, pp. 409–416.

[19] B. Carlsten, "Space-charge-induced emittance compensation in high-brightness photoinjectors," in *PAC'95*, vol. 49, 1995, pp. 27–65.

[20] K. Flöttmann, "Astra: A space charge tracking algorithm," *Manual, Version*, vol. 3, 2011.

[21] J. Rosenzweig *et al.*, "Initial measurements of the ucla RF photoinjector," *Nuclear Instruments and Methods in Physics Research Section A: Accelerators, Spectrometers, Detectors and Associated Equipment*, vol. 341, no. 1-3, pp. 379–385, 1994.

[22] R. Cutler, J. Owen, and J. Whittaker, "Performance of wire scanner beam profile monitors to determine the emittance and position of high power cw electron beams of the nbs-los alamos racetrack microtron," in *Proceedings of the 1987 IEEE particle accelerator conference: Accelerator engineering and technology*, 1987.

[23] D. X. Wang, G. A. Krafft, and C. K. Sinclair, "Measurement of femtosecond electron bunches using a rf zero-phasing method," *Phys. Rev. E*, vol. 57, pp. 2283–2286, 2 Feb. 1998.

[24] W. Graves *et al.*, "Ultrashort electron bunch length measurements at DUVFEL," in *PAC'01*, vol. 3, 2001, pp. 2224–2226.

ISBN: 978-3-95450-199-1 doi:10.18429/JACoW-SAP2017-WECH2

# OVERALL DESIGN AND PROGRESS OF XiPAF PROJECT

S.X. Zheng, Q.Z. Xing, X.L. Guan, H.J. Yao, C. Cheng, T.B. Du, K.D. Man, H.Y. Zhang, G.R. Li, P.F. Ma, R.Tang, M.W. Wang, Y. Yang, H.J. Zeng, Q. Zhang, C.B. Bi, C.T. Du, Q.K. Guo, W.H. Huang, C.X. Tang, H.B. Chen, D. Wang, X.W. Wang†, Key Laboratory of Particle & Radiation Imaging (Tsinghua University), Ministry of Education, Beijing, China
also at Laboratory for Advanced Radiation Sources and Application, Tsinghua University, Beijing, China
also at Department of Engineering Physics, Tsinghua University, Beijing, China
Z.M. Wang, C. Zhao, B.C. Wang, C.Y. Wei, Y.P. Wang, Y.H. Yan, H. Zhang,W.L. Liu, D. Wang, M.C. Wang,Y.M. Fu, E.Y. Qu, M.T. Qiu, W. Chen,
State Key Laboratory of Intense Pulsed Radiation Simulation and Effect (Northwest Institute of Nuclear Technology), Xi'an, China
W.Q. Guan, Y. He, J. Li, NUCTECH Co. Ltd., Beijing, China

*Abstract*

Xi'an Proton Application Facility (XiPAF) which consists of one 230 MeV proton accelerator and irradiation stations, will be constructed in Xi'an city, Shaanxi, China. The facility is composed of a 230 MeV synchrotron, a 7 MeV H- linac injector and two experimental stations. It can provide a flux of $10^5$~$10^8$ p/cm$^2$/s with the uniformity of better than 90% on the 10 cm×10 cm sample. The overall design of XiPAF accelerator is presented in this paper. And the progress of project is reported also.

## INTRODUCTION

To fulfil the need of the experimental simulation of the space radiation environment, especially the investigation of the single event effect, the project of Xi'an Proton Application Facility (XiPAF) is under construction in Xi'an City, Shaanxi China. The facility is mainly composed of a 230 MeV synchrotron with a 7 MeV $H^-$ linac injector and two experimental stations. A proton flux of $10^5$~$10^8$ p/cm$^2$/s with the uniformity of better than 90% on the 10 cm×10 cm sample is designed [1]. Table 1 shows the main parameters of the synchrotron and linac injector.

Table 1: Main Parameters of the XiPAF

| Parameter | Injector | Synchrotron |
|---|---|---|
| Ion type | $H^-$ | Proton |
| Output energy (MeV) | 7 | 60~230 |
| Peak current (mA) | 5 | |
| Repetition rate (Hz) | 0.1~0.5 | 0.1~0.5 |
| Beam pulse width | 10~40 μs | 1~10 s |
| Max. average current (nA) | 100 | 30 |
| Flux (p/cm$^2$/s) (10×10cm$^2$) | | $10^5$~$10^8$ |

The schematic layout of the XiPAF Accelerator system is presented in Fig. 1. The $H^-$ beam is produced at the ion source (IS), accelerated to 7 MeV in linac injector, and then transferred to synchrotron through Medium Energy Beam Transport line (MEBT). This $H^-$ beam is stripped into protons by carbon foil in synchrotron and it is accelerated up to 230 MeV. Then the beam is extracted to experimental station through High Energy Beam Transport line (HEBT). The HEBT have two beamlines, where T2 is used for 60 to 230 MeV proton application extracted from synchrotron directly, and the T1 can degrade the proton energy from 60 MeV to 10 MeV for low energy application. The lowest extraction energy from the synchrotron is 60 MeV.

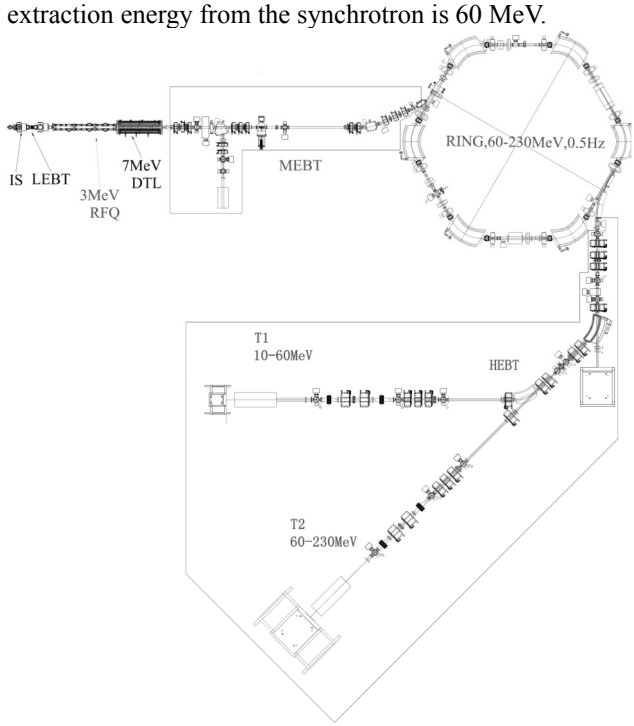


Figure 1: Layout of XiPAF accelerator system.

The main features of this accelerator are listed as follow:

- $H^-$ injection enables transverse space painting flexibility in order to alleviate space charge effects at low energy [2].
- The 6-fold "Missing-dipole" FODO structure simplifies the lattice design and work point tuning. And it supply large space for injecting and extraction.
- The magnet-alloy loaded cavity simplifies the accelerating system and provides wide beam frequency swing.

† wangxuewu@tsinghua.edu.cn

ISBN: 978-3-95450-199-1 doi:10.18429/JACoW-SAP2017-WECH2



- Slow extraction with the 3rd integer resonance can provide stable, uniform and low current for proton irradiation requirement [3].

### *Synchrotron*

Fig. 2 shows layout of synchrotron. The $H^-$ beam is striped into proton beam by carbon foil in injection system of synchrotron, then proton beam is adiabatically captured by RF bucket. The captured 7 MeV proton beam can be accelerated up-to 230 MeV in 0.5 second. The proton beam will be slow-extracted in 1 to 10 s. table 2. List the main parameters of the synchrotron lattice.

Table 2: Main Parameters of the Synchrotron Lattice

| Parameter | Value | Unit |
|---|---|---|
| Circumference | 30.9 | m |
| Dipole effective length | 1.6 | m |
| Dipole bending angle | 60 | degree |
| Dipole edge angle | 30 | degree |
| Maximum beta function(x/y) | 5.7/6.0 | m |
| Maximum dispersion | 2.6 | m |
| Tune at extraction(x/y) | 1.68/1.79 | |
| Chromaticity(x/y) | -0.2/-2.3 | |
| Transition energy | 1.64 | |

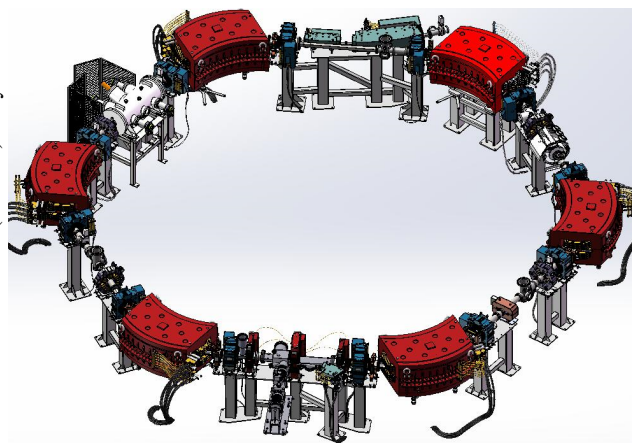

Figure 2: 3-dimension layout of synchrotron.

### *Injector*

The 7 MeV linac injector [4] is composed of the 50 keV $H^-$ ion source, Low Energy Beam Transport line (LEBT), 3 MeV four-vane type Radio Frequency Quadrupole (RFQ) accelerator, 4MeV (from 3 to 7MeV) Alvarez-type Drift Tube Linac (DTL), and the corresponding RF power source system. The designed number of the accumulated protons in each pulse in the synchrotron is $2\times10^{11}$. We choose the injection energy of 7 MeV for both achievable particle intensity and the cost of the linac injector [4]. Layout of 7 MeV H- injector is shown in Fig. 3.

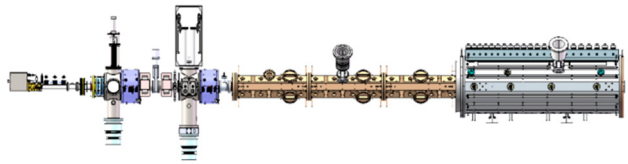

Figure 3: Layout of 7 MeV H- injector.

### *HEBT and Experimental Stations*

The main function of the HEBT is to uniformly irradiate the accelerated proton beam from the synchrotron to the target in experimental station. 2 Step-like field magnets (SFMs) are used for the beam spot homogenization.

## PROGRESS

Manufacture of the accelerator equipment were started after Primary Design Review which was held on November 2015. The R&D on key components and technology has been started before the PDR. All components are expected to be finished at the first half year of 2018. Following sections are some examples of project progress.

### *Permanent Magnetic Quadrupole (PMQ)*

PMQs are used in DTL beam focusing. Procedure for high quality and precision PMQ manufacture was established. Special tools are developed for PMQ measurement. HOMs can be controlled under 1%. Fig. 4 is the photo of PMQs.

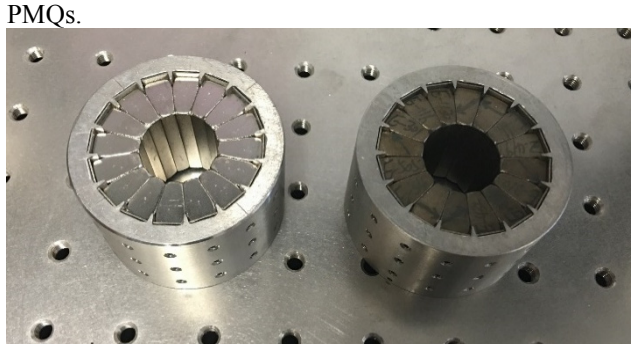

Figure 4: Photo of PMQs.

### *Magnet-alloy Loaded Cavity*

The magnet-alloy (MA) loaded broadband coaxial cavity system is adopted due to its good frequency characteristics and high saturation flux density characteristics.

The main parameters of MA cavity are listed in table 3.. The required accelerating voltage is 800 V.

Table 3: The Main Parameters of MA Cavity

| Parameter | Value | Unit |
|---|---|---|
| Operation frequency range | 1~6 | MHz |
| Acceleration voltage | 800 | V |
| Core number | 6 | |
| **Cavity size** | | |
| Length (flange to flange) | 630 | mm |
| Outer diameter | 550 | mm |
| Inner conductor diameter | 120 | mm |

ISBN: 978-3-95450-199-1 doi:10.18429/JACoW-SAP2017-WECH2

| | | |
|---|---|---|
| Acceleration gap length | 30 | mm |
| **Core size** | | |
| Outer diameter | 450 | mm |
| Inner diameter | 300 | mm |
| Thickness | 25 | mm |
| **Electrical parameter (3 MHz)** | | |
| Serial inductance (per core) | ~1.6 | H |
| Serial impedance (per core) | ~57 | Ω |
| Parallel inductance (per core) | ~7.3 | H |
| Cavity capacitance | ~30 | pF |
| Cavity shunt impedance | ~440 | Ω |
| Cavity power consumption | ~730 | W |

The key component of the cavity, large size MA cores, are made in domestic manufacture. Test results show it has good characteristics similar with foreign mature products. The parameters are stable during 3 hour running at 1kV level. And the maximum temperature is stable under 60 degree as shown in Fig5. Fig. 6 is the photo of cavity.

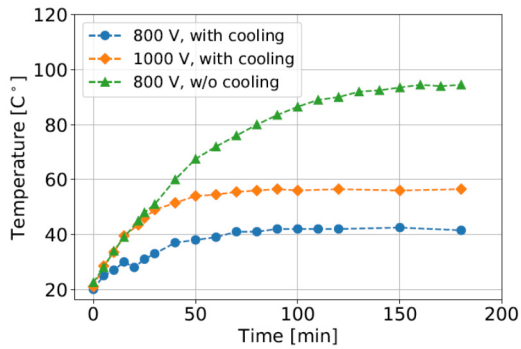


Figure 5: Maximum temperature rising as a function of time with constant gap voltage.

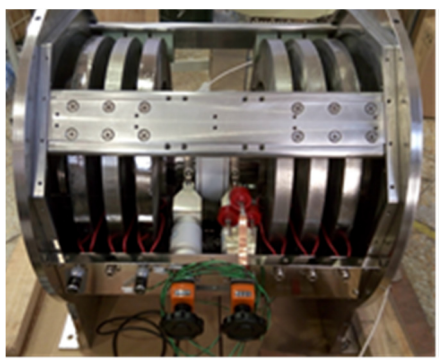

Figure 6: Photo of MA cavity.

## *Beam Position Monitor (BPM)*

Both button type and shoe-box type BPM will be adopted in XiPAF. Fig. 7 are the photos of button and shoe-box BPM.

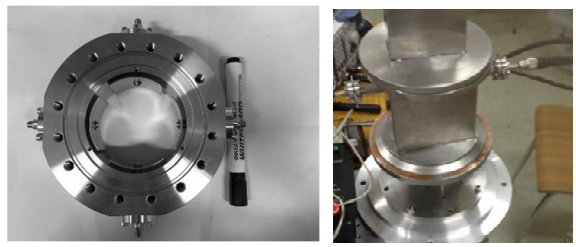

Figure 7: Photos of button (L) and shoe-box (R) BPM.

Button type BPM will be used at MEBT, to measure beam position, energy and current. And prototype has been tested at Compact Pulsed Hadron Source (CPHS) in Tsinghua University. The experimental results show that resolutions of position and phase measurement of XiPAF BPM are better than 60 μm and 0.74°, respectively, and accuracy of absolute position measurement is ±0.34 mm. The prototype satisfies the requirements of XiPAF well.

Shoe-box type BPM will be used in synchrotron. Offline tests show BPM system fulfils all XiPAF requirements.

## *Slow Extraction at Low Energy*

The third resonant slow extraction and RF-Knockout technology was adopted in XiPAF. To fulfil the requirement of irradiation requirement, research on slow extraction at low energy is conducted. Li-tracker, a C++ code for slow extraction was developed. The influence of the quadrupoles/dipoles on extracted spill was investigated in theory and by this code. Some methods other than RF-KO is investigated.

## CONCLUSION

The construction of XiPAF is underway after PDR. It is a proton application facility based on 230 MeV synchrotron. The R&D on key components and technology are progressing smoothly. We expect the manufacture of all components can be finished at the first half of next year. And beam commissioning can start at 2018 also.

## ACKNOWLEDGEMENT

Many institutes, universities and experts give us a lot of help for XiPAF project. We cannot list all names here. Special acknowledgements should be given to Institute of Modern Physics, Institute of High Energy Physics, Institute of Applied Physics, and University of Science and Technology of China.

## REFERENCES

[1] G. R. Li et al., "Design of the key parameters in an advanced radiation proton synchrotron", *Modern Applied Physics*, 6, 2015.

[2] H. J. Yao et al., "H- charge exchange injection for XiPAF synchrotron", in *Proc. HB'16*, Malmö, Sweden, July 2016 pp. 49-51.

[3] H. J. Yao et al., "RF-Knockout Slow Extraction Design for XiPAF Synchrotron", in *Proc. HB'16*, Malmö, Sweden, July 2016 pp. 52-54.

[4] Q. Z. Xing et al., "Design of the 7MeV linac injector for the 200MeV Synchrotron of the Xi'an Proton Application Facility", in *Proc. IPAC2016*, Korea, 2016, pp. 426-428.

ISBN: 978-3-95450-199-1 doi:10.18429/JACoW-SAP2017-WECH2

ISBN: 978-3-95450-199-1

# *List of Authors*

**Bold** papercodes indicate primary authors; ~~crossed out~~ papercodes indicate 'no submission'

ISBN: 978-3-95450-199-1

ISBN: 978-3-95450-199-1

ISBN: 978-3-95450-199-1

ISBN: 978-3-95450-199-1

# *Institutes List*

**ASIPP**
Hefei, People's Republic of China
- Hu, C.D.
- Liang, L.Z.
- Xie, Y.H.
- Xie, Y.L.
- Xu, Y.
- Yu, Yu, L.

**BNL**
Upton, Long Island, New York, USA
- Weng, W.-T.

**CAEP/IAE**
Mianyang, Sichuan, People's Republic of China
- Deng, D.R.
- He, T.H.
- Lao, C.L.
- Li, M.
- Li, P.
- Lin, S.F.
- Luo, X.
- Pan, Q.
- Shan, L.J.
- Shen, X.M.
- Shen, X.
- Wang, H.
- Wang, J.
- Wu, D.
- Xiao, D.X.
- Yan, L.G.
- Yang, X.
- Zhang, H.
- Zhou, K.

**CAEP/IFP**
Mainyang, Sichuan, People's Republic of China
- Chen, S.
- Fan, P.L.
- He, X.
- Li, H.
- Li, Y.D.
- Liao, S.Q.
- Long, J.
- Lu, Y.
- Pang, J.
- Shi, J.
- Wang, W.
- Wei, T.
- Yang, L.

**CIAE**
Beijing, People's Republic of China
- An, S.
- Cao, L.C.
- Cui, T.
- Ge, T.
- Guan, F.P.
- Hou, S.G.
- Ji, B.
- Ji, L.Y.
- Jia, X.L.
- Li, M.
- Li, P.Z.
- Lu, X.T.
- Lv, Y.L.
- Qin, J.C.
- Song, G.F.
- Wang, C.
- Wang, F.
- Wang, L.
- Wang, Y.
- Wei, S.M.
- Wen, L.P.
- Yin, Z.G.
- Zhang, D.S.
- Zhang, T.J.

**HUST**
Wuhan, People's Republic of China
- Fan, K.
- Hu, S.
- Li, L.X.F.
- Mei, Z.Y.
- Zeng, Z.J.
- Zhang, L.G.

**HZCY Technologies Co., Ltd.**
Beijing, People's Republic of China
- Sun, Z. Sun.
- Zhang, D.

**IHEP**
Beijing, People's Republic of China
- Bian, T.J.
- Chi, Y.L.
- Cui, X.
- Dong, D.
- Du, C.C.
- Duan, Z.
- Gao, B.
- Gao, J.
- Geng, H.
- Gong, D.J.
- Guo, Y.Y.
- Ji, D.
- Jiao, Y.
- Li, J.L.
- Li, X.P.
- Li, X.Y.
- Li, Y.
- Meng, C.
- Pei, G.

ISBN: 978-3-95450-199-1



- Pei, S.
- Peng, Y.M.
- Qin, Q.
- Sha, B.
- Shi, H.
- Sun, D.R.
- Sun, Y.S.
- Tian, S.K.
- Wang, D.
- Wang, J.Q.
- Wang, N.
- Wang, S.
- Wang, X.
- Wang, Y.
- Wei, Y.
- Wu, J.
- Xu, G.
- Xu, H.S.
- Xu, S.Y.
- Yan, F.
- Yu, C.H.
- Zhai, J.Y.
- Zhang, J.R.
- Zhang, Y.
- Zhao, Y.L.

**IMP/CAS**
Lanzhou, People's Republic of China
- Chang, J.J.
- Chen, W.L.
- Dou, W.P.
- Feng, C.
- Gao, P.H.
- Ge, W.W.
- Gu, K.
- He, Y.
- Jia, H.
- Jia, Y.Z.
- Jiang, P.
- Jing, L.
- Li, C.X.
- Li, G.H.
- Li, J.
- Li, M.
- Li, P.
- Li, W.L.
- Li, X.N.
- Liu, S.H.
- Liu, X.J.
- Luo, C.L.
- Ma, X.M.
- Mao, L.J.
- Mao, R.S.
- Meng, J.
- Qin, Y.S.
- Shen, G.D.
- Tang, M.T.
- Wang, C.
- Wang, F.F.
- Wang, P.P.
- Wang, W.S.
- Wang, Z.J.
- Wei, W.
- Wu, J.X.
- Xie, W.J.
- Xu, X.B.
- Yan, T.L.
- Yang, J.C.
- Yang, X.D.
- Yin, D.Y.
- Yuan, Y.J.
- Zhang, Z.L.
- Zhao, H.
- Zheng, W.H.

**Institute of High Energy Physics (IHEP), Chinese Academy of Sciences**
Beijing, People's Republic of China
- Shu, S.

**Institute of High Energy Physics (IHEP)**
People's Republic of China
- Xiao, O.

**Institute of Physics, Chinese Academy of Sciences**
Beijing, People's Republic of China
- Li, Y.

**LLP**
Shanghai, People's Republic of China
- Chen, M.
- Yuan, X.H.
- Yue, D.N.

**National University of Defense Technology**
Changsha, Hunan, People's Republic of China
- Yin, Y.

**NINT**
Xi'an, People's Republic of China
- Chen, W.

**NUCTECH**
Beijing, People's Republic of China
- Guan, W.Q.
- He, Y.
- Li, J.
- Liu, D.H.
- Luo, L.

**ORNL**
Oak Ridge, Tennessee, USA
- Plum, M.A.

**PKU**
Beijing, People's Republic of China
- Chen, J.E.

ISBN: 978-3-95450-199-1

- Feng, L.W.
- Hao, J.K.
- Huang, S.
- Li, L.R.F.
- Liao, Q.
- Lin, C.
- Lin, L.
- Liu, K.X.
- Lu, H.Y.
- Lu, X.Y.
- Lu, Y.R.
- Ma, W.J.
- Quan, S.W.
- Wang, F.
- Wu, Wu,M.J.
- Xie, H.M.
- Xu, X.
- Yan, X.Q.
- Yang, L.
- Zhang, A.L.
- Zhao, Y.Y.
- Zhu, F.
- Zhu, J.G.
- Zhu, K.

**SINAP**
Shanghai, People's Republic of China
- Chen, J.H.
- Deng, H.X.
- Jiang, B.C.
- Liu, B.
- Wang, Z.
- Zhang, Q.L.
- Zhao, Z.T.

**SLAC**
Menlo Park, California, USA
- Chao, A.

**State Key Laboratory of Intense Pulsed Radiation Simulation and Effect, Northwest Institute of Nuclear Technology**
Shannxi, People's Republic of China
- Fu, Y.M.
- Liu, W.L.
- Qiu, M.T.
- Qu, E.Y.
- Wang, B.C.
- Wang, D.
- Wang, M.C.
- Wang, Y.P.
- Wang, Z.M.
- Wei, C.Y.
- Yan, Y.H.
- Zhang, H.Z.
- Zhao, C.

**Tsinghua University**
Beijing, People's Republic of China
- Su, Q.
- Zhang, H.

**TUB**
Beijing, People's Republic of China
- Bi, C.B.
- Cao, D.Z.
- Chen, H.B.
- Cheng, C.
- Cheng, Z.
- Du, C.T.
- Du, T.B.
- Du, Y. C.
- Du, Y.-C.
- Gai, W.
- Guan, X.
- Guo, Q.K.
- Hua, J.F.
- Huang, S.
- Huang, W.-H.
- Jin, Q.X.
- Li, F.
- Li, G.R.
- Li, X.
- Liao, S.Q.
- Lu, W.
- Ma, P.F.
- Man, K.D.
- Pai, C.H.
- Peng, M.M.
- Shi, J.
- Tan, C.J.
- Tang, C.-X.
- Tang, R.
- Wan, Y.
- Wang, D.
- Wang, P.
- Wang, W.
- Wang, X.W.
- Wu, Y.P.
- Xing, Q.Z.
- Yan, L.X.
- Yang, Y.
- Yao, H.J.
- Zeng, H.J.
- Zha, H.
- Zhang, H.Y.
- Zhang, J.
- Zhang, Q.
- Zhang, Z.
- Zheng, S.X.
- Zhou, S.Y.
- Zhou, Z.

**UCLA**
Los Angeles, California, USA
- An, W.
- Joshi, C.
- Mori, W.B.
- Xu, X.L.

ISBN: 978-3-95450-199-1

**USTC/NSRL**
Hefei, Anhui, People's Republic of China
- Bai, Z.H.
- Liu, G.
- Pei, Y.J.
- Tang, Zh. X.
- Wang, L.
- Xu, D.R.
- Xu, H.
- Yang, P.H.

**XFEL. EU**
Hamburg, Germany
- Li, Y.
- Pflüger, J.